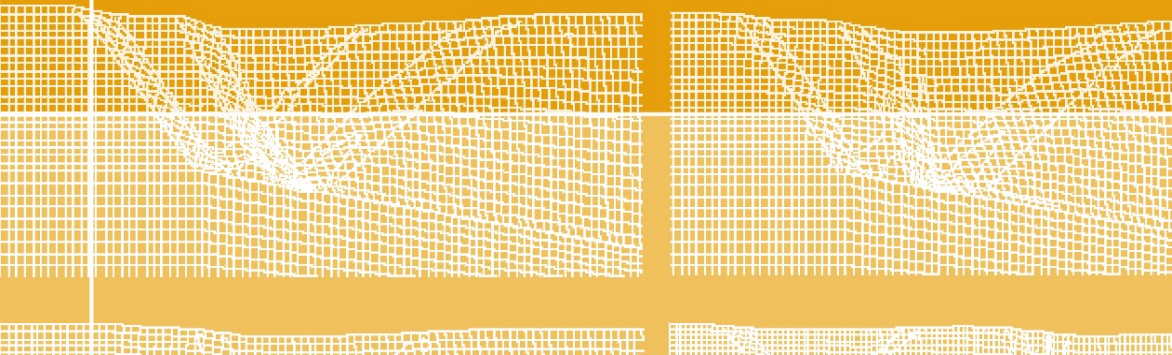


George E. Exadaktylos
Ioannis G. Vardoulakis
(Eds.)



Bifurcations, Instabilities, Degradation in Geomechanics



Springer

George E. Exadaktylos

Ioannis G. Vardoulakis

Editors

**Bifurcations, Instabilities, Degradation
in Geomechanics**

George E. Exadaktylos
Ioannis G. Vardoulakis
Editors

Bifurcations, Instabilities, Degradation in Geomechanics

with 230 Figures and 17 Tables

 Springer

Mr. George E. Exadaktylos
Technical University Crete
Dept. Mineral Resources Engineering
University Campus, Akrotiri, Chania
731 00 Crete
Greece

Email: exadaky@mred.tuc.gr

Dr. Ioannis G. Vardoulakis
National Technical University
Dept. Mechanical Engineering
Zografou
157 80 Athens
Greece

Library of Congress Control Number: 2006936091

ISBN-13 978-3-540-49341-9 Springer Berlin Heidelberg New York

This work is subject to copyright. All rights are reserved, whether the whole or part of the material is concerned, specifically the rights of translation, reprinting, reuse of illustrations, recitation, broadcasting, reproduction on microfilm or in any other way, and storage in data banks. Duplication of this publication or parts thereof is permitted only under the provisions of the German Copyright Law of September 9, 1965, in its current version, and permission for use must always be obtained from Springer-Verlag. Violations are liable to prosecution under the German Copyright Law.

Springer is a part of Springer Science+Business Media
springer.com
© Springer-Verlag Berlin Heidelberg 2007

The use of general descriptive names, registered names, trademarks, etc. in this publication does not imply, even in the absence of a specific statement, that such names are exempt from the relevant protective laws and regulations and therefore free for general use.

Cover design: de'blik, Berlin
Production: Almas Schimmel
Typesetting: camera-ready by the editors

Printed on acid-free paper 30/3141/as 5 4 3 2 1 0

Preface

The 1st International Workshop on "Localisation of Soils" was held in Karlsruhe, Germany on February 22-25, 1988. It was followed by the 2nd International Workshop in Gdansk, Poland on September 25-30, 1989. The first two events emphasised fundamental aspects of bifurcation theory applied to Soil Mechanics, and they were sponsored by the German and Polish Research Councils. The 3rd International Workshop on "Localisation and Bifurcation" was held in Aussois, France on September 6-9, 1993, and the topics were extended to accommodate Rock Mechanics; generous support was provided by the French Research Council. The 4th and 5th Workshops held in Gifu, Japan and Perth, Australia. The University of Minnesota was selected as the place for the 6th International Workshop on "Bifurcations and Instabilities in Geomechanics". The event was hosted at the St. John's University in Collegeville, Minnesota U.S.A. on June 2 - 5, 2002 and was supported by a grant from the NSF and has generously received Corporate support (BP Amoco-Houston, Schlumberger-Houston-Cambridge, Shell-Houston), MTS-Minneapolis, Itasca-Minneapolis).

The objective of all these workshops has been to bring together international researchers and practitioners dealing with bifurcations and instabilities in Geomechanics. The focus was to collect and debate the developments and applications that have taken place since the first workshop in 1988. The topics covered included modelling of bifurcation, structural failure of geomaterials and geostructures, advanced analytical, numerical and experimental techniques, application and development of generalised continuum models etc. The scope of these workshops included analytical solutions, numerical methods, experimental techniques, and case histories. Besides the presentation of fundamental research findings, applications in geotechnical, petroleum, mining, and bulk materials engineering were emphasised.

These workshops have provided a forum for researchers and practitioners to present their findings, interact formally and informally on a person-to-person basis, and exchange ideas on problems and solutions with colleagues from other countries. Exchange of ideas is an important ingredient in the professional growth and development of engineers. Our workshop has offered excellent opportunities for such growth.

The papers presented in this special issue and those published in a special Volume entitled *Bifurcations, Instabilities and Degradation in Geomechanics* (George Exadaktylos and Ioannis Vardoulakis, editors) Springer Verlag (2006) give the picture of the state of the art in the area of

contemporary Geomechanics. At this point, the Guest Editors of this special Issue of the IJNAMG and Organizers of the 7th IW BIDG would like to acknowledge the support of the following contributors and sponsors: Technical University of Crete (TUC), National Technical University of Athens (NTUA), EDRASIS S.A., Hellenic Society for Soil Mechanics and Geotechnical Engineering, DIGA Research Training Network, A.L.E.R.T. Geomaterials, TC34 of ISSMGE, and the Technical Chamber of Greece.

The assistance of Mr. Pantelis Liolios, Mr. Sotiris Alevizos, Mrs. Stavroula Tsouvala, Mr. George Xiroudakis, and Mr. Manolis Veveakis during the successful organization and execution phases of this workshop is deeply acknowledged here. Last, but not least, we deeply acknowledge the contribution of Mr. George Barakos who significantly assisted the Guest Editors for the edition of this volume.

G.E. Exadaktylos, TUC
I.G. Vardoulakis, NTUA

Organization of the 7th International Workshop

At the board meeting in St. John's University it was decided that the next event will be hosted jointly by the National Technical University of Athens and the Technical University of Crete, at the City of Chania in the Northwest part of the island of Crete, in Greece. The event is entitled as the "7th International Workshop on "Bifurcations, Instabilities and Degradation in Geomechanics".

For the organization of the 7th IWBIDG in Chania the following committees have been formed:

- Local Organizing Committee
- International Advisory Board
- International Scientific Committee

A number of topics were attacked in this Workshop such as:

1. Advanced Experimental Techniques
2. Micromechanical approaches
3. Constitutive modeling
4. Mathematical analyses
5. Numerical analyses
6. Failure mechanics, damage mechanics and fracture mechanics
7. Multiphase flow and granular flow aspects

Particular attention is also given to be plenty of time for presentations and fruitful discussions among the participants.

Contents

Introduction	1
1 The Concept of Bifurcation in Geomechanics.....	3
Part I - Experimental Aspects	1
Third Invariant Dependent Single Yield Surface Model and Localization Conditions for High Porosity Sandstone	17
1 Introduction.....	18
2 Constitutive Relation	21
3 Localization Conditions	26
3.1 Hardening Modulus (h) Expression.....	26
3.2 Determination of Critical Hardening Modulus (h_{cr})	27
4 Results.....	30
4.1 Specialized Deviatoric and Stress State Parameters.....	31
4.2 Band Orientation Predictions: Limiting Conditions	32
4.3 Axisymmetric Compression	33
4.4 J_3 Independent SYSM: P_1 Stress State.....	35
4.5 J_3 Dependent SYSM: P_1 Stress State, $\xi = \psi$	36
4.6 J_3 Dependent SYSM: P_1 Stress State, $\xi \neq \psi$	40
5 Summary and Conclusions	43
Appendix A.....	46
Interpretation of the Scale Effect in Perforation Failure	53
1 Introduction.....	53
2 Mathematical Model	56
3 Model Calibration	61
4 Results and Discussion	63
5 Conclusions.....	69
Experimental Investigation of Instabilities of Granular Materials in Relation to Dilatancy and Fabric Issues	71
1 Introduction.....	72

2 Proportional Strain Paths	73
3 Biaxial Testing Apparatus	74
4 Proportional Strain Path Testing	76
4.1 7 mm Pentagonal Disks	76
4.2 7 mm Circular Disks.....	83
4.3 5 mm Circular Disks.....	83
5 Stress (Strain) Response Envelopes and Anisotropy	85
5.1 Stress Response Envelope and Effect of Stress History	85
5.2 Strain Response Envelopes and Uniqueness of Incremental Plastic Strain Direction	89
6 Conclusions.....	91

**Compactive Cataclastic Flow in Tuffeau de Maastricht Calcarenite:
Mechanical Deformation & Permeability Reduction 95**

1 Introduction.....	96
2 Experimental Procedure and Mechanical Data.....	98
3 Infinitesimal Deformation Theory of Bifurcation of Elastoplastic Solids – Calibration of the Lade and Kim’s Model.....	103
3.1 General Analysis of the Deformation Bands.....	103
3.2 Constitutive Model Developed by Lade and Kim	106
3.2.1 Plastic Potential Function.....	107
3.2.2 Determination of the Parameters c_3, c_0, μ	108
3.2.3 Failure Criterion.....	110
3.2.4 Yield Criterion and Hardening/Softening Law	110
3.2.5 Parameter Determination for Yield Criterion	111
3.2.6 Hardening Law.....	112
3.2.7 Variation of q	114
3.2.8 Softening Law	115
3.2.9 Determination of the Parameters A and B	115
3.3 Theoretical Parameters	29
4 Back Test Analysis	116
5 Permeability Reduction.....	119
6 Concluding Remarks.....	123

**Local Second Gradient Models and Damage Mechanics: 1D Post-
Localization Studies in Concrete Specimens 127**

1 Introduction.....	127
2 Scalar Damage Model.....	128
3 Local Second Gradient Model	130
4 1D Numerical Simulations.....	133

5 Expansion of the Plastic Region	137
6 Conclusions.....	139
Part II - Micromechanical Aspects.....	143
Entropy and Material Instability in the Quasi-Static Mechanics of Granular Media	145
1 Statistics of Kinematics and Stress	145
1.1 Delaunay Triangulation, Deformation and Stress	145
2 Maximum Entropy & Virtual Thermodynamics.....	148
3 Material Instability.....	151
4 Conclusions.....	153
A DEM Study of Compaction Band Formation.....	155
1 Introduction.....	156
2 The Discrete Element Method	157
2.1 Simulations on Sandstone.....	158
2.2 Simulations on Sand	159
3 Results.....	161
3.1 Sand Simulations	161
3.2 Sandstone Simulations.....	164
4 Proposed Statistical Approach	166
5 Conclusions.....	170
Shear Zone Formation in 2D Random Granular Specimens within Enhanced Hypoplasticity	173
1 Introduction.....	173
2 Hypoplasticity	175
3 Micro-Polar Hypoplastic Law	178
4 Non-Local Hypoplastic Law.....	181
5 Second-Gradient Hypoplastic Law	181
6 FE-Input Data	183
7 FE-Results.....	188
8 Conclusions.....	194
A Rational Approach to Stress-Dilatancy Modelling Using an Explicit Micromechanical Formulation	201

1 Introduction.....	202
2 Rowe’s Stress-Dilatancy Formulation Revisited	204
3 Effect of Fabric on Stress-Dilatancy Relations.....	206
3.1 Simple Cases: Regular Packing.....	206
3.2 Random Packing.....	211
4 Stress-Dilatancy Formulation with Micromechanical Considerations .	213
4.1 Stress-Dilatancy Formulation: Generalities.....	213
4.2 Nominal Friction Angle φ_f on Sliding Plane and Critical State Friction Angle φ_{cv}	217
5 Verification	218
6 Simplified Procedure and Modified Rowe’s Stress-Dilatancy Relation	219
6.1 Mean Sliding Direction and Nominal Friction Angle φ_f	220
6.2 Comments on and	224
7 Closing Remarks.....	227
Micro-Fracture Instabilities in Granular Solids.....	231
1 Introduction.....	231
2 RVE Problem.....	232
3 Macroscopic Loss of Ellipticity	236
4 Numerical Examples and Discussion.....	237
Part III - Constitutive Aspects	243
Entropy and Material Instability in the Quasi-Static Mechanics of Granular Media	245
1 Statistics of Kinematics and Stress	246
2 Single Crack Mechanics	248
2.1 Short Review of Griffith’s Crack Propagation Criterion.....	248
2.2 Energy Released by Penny-Shaped Cracks Propagating in Mode I under Uniaxial and Triaxial Stress States	249
3 Representative Volume Elements Damaged by many Interacting Microcracks	255
3.1 Representative Volume Element (RVE) and Material Phases [17, 40, 31]	255
3.2 Stress / Strain Averaging and Concentration [17, 39, 40, 41]	257
3.3 Stiffness Estimation on the Basis of Eshelby’s Matrix - Inclusion Problem [39, 40, 41]	258
3.4 Open and Empty Penny-Shaped Cracks.....	260

3.5 Linking Macroscopic Stresses to Single-Crack Related Crack Propagation Criteria262

4 Effective Stress-Strain Behavior of Microcracked Brittle Materials – Assessment of Griffith’s Energy Release Rate Criterion263

4.1 Uniaxial Macroscopic Tension – Tensile Mode I Micro-cracking. 263

4.2 Uniaxial Macroscopic Compression – Axial Splitting265

4.3 Determination of the Initial Microcrack Radius and of the Initial Microcrack Half-Opening from the Uniaxial Tensile Strength and the Uniaxial Compressive Strength.....268

4.4 Confined Macroscopic Compression – Axial Splitting270

5 Conclusions.....272

Modeling the Influence of Pressure and Moisture Content on the Disintegration of Weathered Rockfill Materials277

1 Introduction.....278

2 Granular Hardness and Pressure Dependent Limit Void Ratios279

3 Hypoplastic Model.....284

3.1 Inelastic Material Properties284

3.2 Density, Pressure and Moisture Dependent Properties.....285

3.3 Comparison of Numerical Simulations with Experiments289

4 Shear Band Analysis or Plane Strain Compression292

5 Conclusions.....296

Shear Zone Formation in 2D Random Granular Specimens within Enhanced Hypoplasticity301

1 Introduction.....302

2 Mechanism of Crack Propagation in Non-Uniform Stress Fields305

3 Statistical Properties of Non-Uniform Stress Field Created by Many Wing Cracks309

4 A Mechanism of Splitting and Oblique Failure in Compression.....313

5 Conclusions.....315

A Rational Approach to Stress-Dilatancy Modelling Using an Explicit Micromechanical Formulation319

1 Introduction.....319

2 Constitutive Models for Concrete.....320

2.1 Elasto-Plastic Model.....320

2.2 Damage Model321

3 Non-Local Approach323

4 FE - Simulations	324
4.1 Uniaxial Tension	324
4.1.1 Elasto-Plastic Model	324
4.1.2 Damage Model	327
4.2 Three-Point Bending	330
4.2.1 Elasto-Plastic Model	331
4.2.2 Damage model	334
5 Conclusions.....	336

Kinematics of Shear Zone Deformation in Soft Sensitive Clays..... 341

1 Introduction.....	342
2 Governing Equation for Coupled Flow.....	343
3 Pore Water Pressure Generation Dissipation Equation.....	345
4 Finite Element Simulation of Coupled Pore Water and Strain Localization	348
5 Results and Discussion	349
5.1 Evaluation of Strain Localization	349
5.2 Effect of Excess Pore Water Pressure	352
5.3 Material Behavior.....	353
6 Conclusions.....	356

Part IV - Numerical Aspects..... 359

**Numerical Analysis of Deformation of Methane Hydrated Contained
Soil due to the Dissociation of Gas Hydrate 361**

1 Introduction.....	361
2 Simulation Method	363
2.1 Multiphase Mixture Theory	363
2.2 General Setting	363
2.3 Conservations of Mass.....	364
2.4 Skeleton Stress.....	365
2.5 Conservation of Momentum.....	365
2.6 Conservation of Energy	367
2.7 Suction-Saturation Relation.....	368
3 Dissociation of Hydrates.....	368
4 Constitutive Model for Soil	369
4.1 Elasto-Viscoplastic Model for Unsaturated Soil	369
4.2 Overconsolidation Boundary Surface.....	370
4.3 Static Yield Surface.....	371

4.4 Viscoplastic Potential Surface	371
4.5 Viscoplastic Flow Rule.....	372
5 Simulation Examples	373
6 Conclusions.....	379
Numerical Prediction of Impact Force of Geomaterial Flow against Retaining Structure using CIP Method	381
1 Introduction.....	381
2 Numerical Framework	383
2.1 Constitutive Model	383
2.2 Governing Equations	387
2.3 Numerical Scheme.....	388
3 Laboratory Experiment.....	392
4 Conclusions.....	400
Numerical Simulation of the Cracked Brazilian Disc under Diametral Compression	403
1 Introduction.....	403
2 The Problem.....	406
2.1 The Scope	406
2.2 The Intact Brazilian Disc	406
2.3 The Cracked Brazilian Disc	408
2.4 Geometry	409
2.5 Material Models and Boundary Conditions.....	410
3 Numerical Analysis and Results	411
3.1 Stress Distributions.....	411
3.2 Distributions of Stress Intensity Factors.....	417
4 Discussion.....	420
4.1 Stress - Griffith Strength Criterion	420
4.2 Stress Intensity Factors.....	421
5 Conclusions.....	427
Stress Analysis of Multiply Fractured Porous Rocks	431
1 Introduction.....	431
2 Formulation of the (a) Short-Term and (b) Long-Term Problems.....	432
3 The First Fundamental Boundary Value Problem of the Cracked Body (Prescribed Normal and Tangential Stresses on Cracks).....	435
3.1 Formulation for a Single Crack	437
3.2 Formulation for a System of Non-Intersecting Cracks	442

3.3 Numerical Solution for a Single Crack.....	443
3.4 Numerical Solution for a System of Non-Intersecting Cracks	445
4 Solution of the Pore Pressure.....	448
5 Numerical Examples.....	449
5.1 Example 1: Single Linear Crack on Ox Axis	449
5.2 Example 2: System of Three Parallel Cracks	454
5.3 Example 3: Multiple (40) Cracks Ahead of a Horizontal Crack under Uniform Pore Pressure (Steady State).....	458
Index.....	463

Introduction

1 The Concept of Bifurcation in Geomechanics

Contemporary localization theory [24] is a natural extension of Mohr's [12] original strength theory published in the year 1900 in a milestone paper with the title, "*Welche Umstände bedingen die Elastizitätsgrenze und den Bruch eines Materials?*". Mohr's question cannot be answered without resorting to experiments carefully and systematically run. Experiments, however do not give definite answers, since they are always subject to theoretical interpretation: In order to arrive to some conclusion one needs a theoretical framework within which the experiment is run and interpreted. In that sense Mohr's fundamental geometrical theory of stress analysis provided a useful tool for engineering design. Fig. 1.1 is taken from Mohr's paper and is usually referred to as the graphical representation of the 'Mohr-Coulomb' failure criterion; although in Mohr's original paper no explicit reference to Coulomb's work [4] is made. Unfortunately as a result of traditionalism it is customary to give more than necessary emphasis to the Mohr-Coulomb linear regression parameters, C and φ , namely the renowned "cohesion" and "friction angle" of the material.

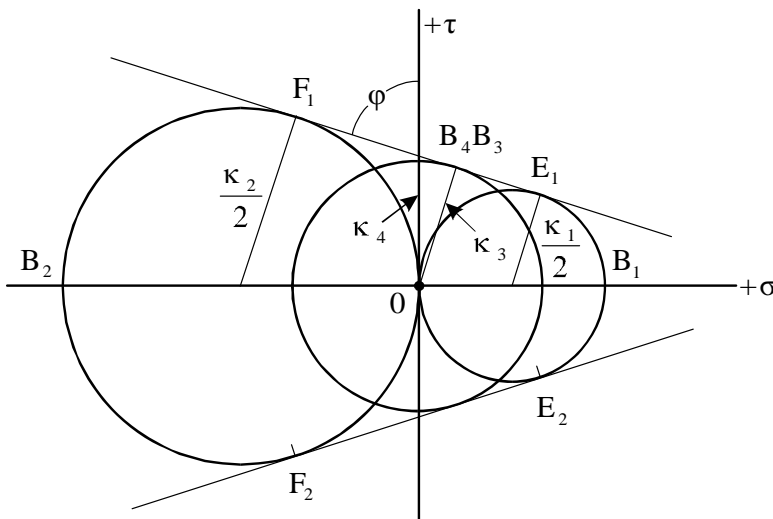


Fig. 1.1. Mohr's original failure criterion for a cohesive-frictional or 'Coulomb' material

In the aforementioned paper Mohr summarizes his observations by pointing to the following general property of *localized* deformation: “...*The deformations observed in a homogeneous body after the elasticity limit [is reached] are not confined in the smallest domains of the body. They consist more or less in that, parts of the body of finite dimension displace with respect to each other on two sets of slip bands...*”. Indeed one basic property of localization phenomena is some degree discontinuity of the deformation. Today we know that prior to *localization* the governing partial differential equations of the underlying quasi-static rate-boundary-value problem are elliptic and exclude discontinuous solutions. At the onset of localization these equations are changing type and from elliptic they turn hyperbolic. *Slip-lines* and *shear-bands* are thus identified with the characteristic lines of the governing hyperbolic partial differential equations. Presently we are not only interested in states of *incipient failure*. One is increasingly interested in ways to trace the deformation in the so-called *post-failure* regime. Since at *failure* the underlying mathematical problem is changing type (an elliptic-to-hyperbolic transition), post-failure we deal in general with mathematically ill-posed problems which need some degree of regularization.

Granular materials are ideal examples of *plastic*¹ solids, showing predominantly irreversible deformations. Besides *internal friction* granular media show predominant *plastic dilatancy* [17,10].

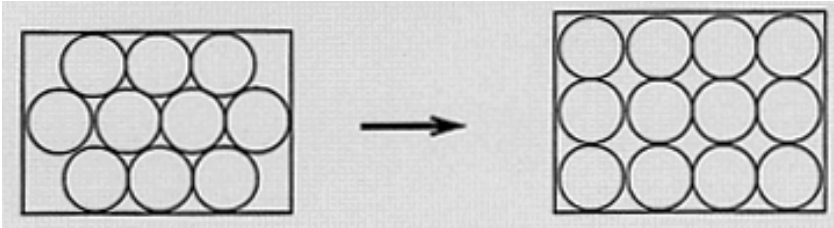


Fig. 1.2. Dilatancy of a regular dense packing into a loose packing due to shear

¹

Πλάσσω: to form, mould, shape

(Liddle and Scott's, *Greek-English Lexicon*, Calendron Press 1889)

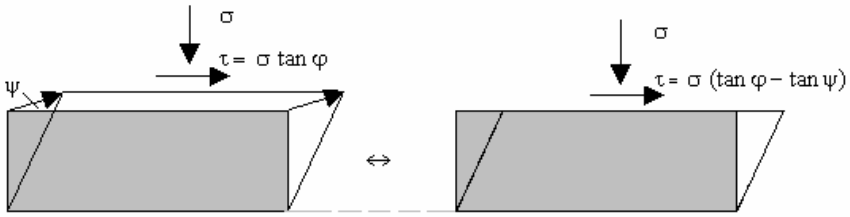


Fig. 1.3. Stresses and velocities in direct shear of: a) a 'real' frictional-dilatant medium like dry sand and b) an equivalent, from the point of view of energy dissipation, model frictional material

Accordingly Taylor's stress-dilatancy condition [21, 25] constitutes the simplest generalization of the *normality condition* of classical flow theory of plasticity, which is included in it for the degenerate case of zero effective friction coefficient. It is customary, however, to call the corresponding flow-rule *non-associated* [13], although Taylor's rule provides a simple way to relate the normals to the plastic potential- and yield-surface. It should be noticed also that Rowe [19] and de Joselin de Jong [5] have used the same concept as Taylor. In these attempts of deriving macroscopic equations from simple micro-mechanical models they have introduced a 'true' angle of friction and identified it with the inter-particle friction coefficient.

Recently non-associative elasto-plastic behavior has been related to flutter-type instabilities [2], instabilities in the form of failure of Hill's condition [5] and to loss of controllability at the element level [15]. Some of these instabilities may be physical and some are perhaps purely mathematical. This state of affairs raises naturally the question if classical non-associative plasticity theory and equivalent variants of it constitute after all useful soil models or not.

In granular materials shear-band localization induces intense inter-granular slip, which in turn leads to strong dilatancy and large deformations of the material inside the localized zone [7], as is shown for example in Fig. 1.4 in three sequential X-ray plates of shear-banding in sand specimen emerging out of soft-sand lens. Strong localized material dilatancy, due to grain rearrangement and grain rotation are the dominant micro-kinematical features of shear banding. Increasing porosity reduces naturally the coordination number of the granular assembly, yielding progressively to a weaker granular structure. On top of that and from the microstatistical point

of view an important structure that appears to dominate this type of localized deformation is the formation and collapse (buckling) of grain columns [16], which in turn lead to a basic asymmetry of shear stress and probably to micro-polar effects [14].

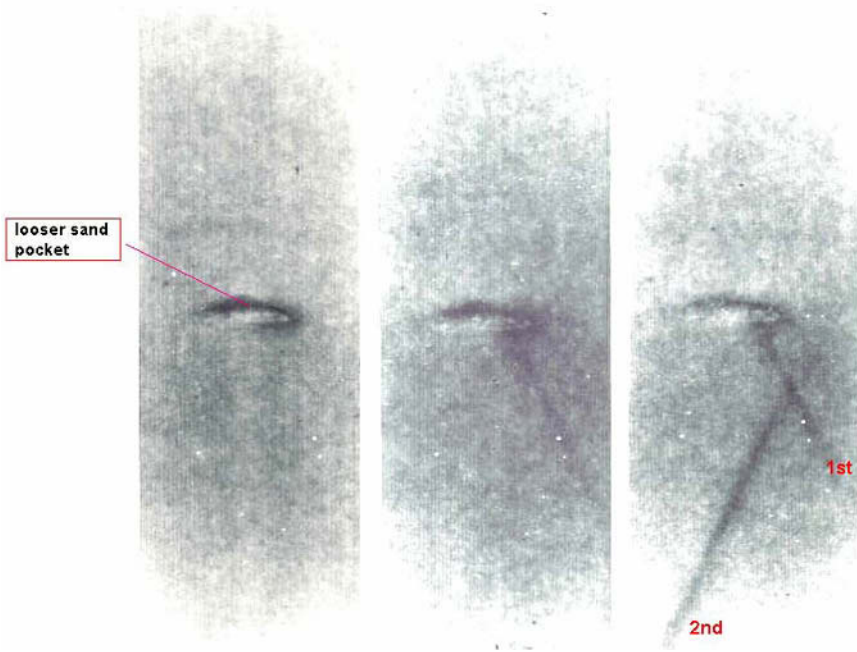


Fig. 1.4. Evolution of dilatancy localization in a sand specimen under biaxial compression [20]

Reduction of coordination number and grain-column buckling lead both to macroscopic (*structural*) *softening* of the material inside the localized zone. For equilibrium reasons the material outside the localized zone is unloading. Thus we perceive the shear-band as being separated from the rest material by a set of parallel discontinuity surfaces at some distance $2d_B$, the so-called shear-band boundaries. The shear-band boundaries may be modeled as elasto-plastic boundaries; i.e. material surfaces, which separate the elasto-plastically softening shear band from its elastically unloading neighborhood.

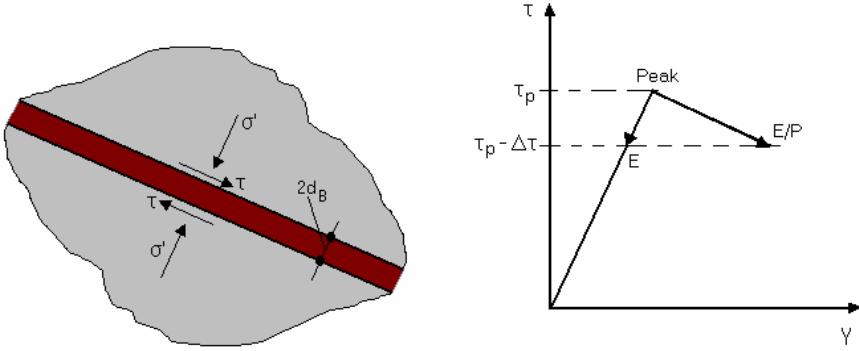


Fig. 1.5. The elasto-plastic shear-band model

The problem of modeling localized deformation in geomaterials is quite a challenging task and has been addressed in all previous Workshops of the present series. This is due to the mathematical difficulties, which are encountered while dealing with non-associate and softening material behavior and boundary-value problems with moving internal elasto-plastic boundaries. Thus, as first addressed by Mandel [11], questions of uniqueness and stability of solutions arise naturally within the context of shear-band analysis. It turns out that the result of such analyses depends primarily on the assumed physical non-linearities, which are inherent to the underlying constitutive description [3] and, in a much lesser degree, it is influenced by geometrical non-linearities.

The various drawbacks and shortcomings of the classical continuum and constitutive theories in connection with strain localization or, more generally, for problems where loss of ellipticity of the governing partial differential equations is taking place, have been discussed extensively in many recent papers [1]. The origin of this undesirable situation can be traced back to the fact that conventional constitutive models do not contain material parameters with the dimension of length, so that the shear-band thickness or the dominant surface buckling mode are vanishingly small, which in turn leads to mathematical ill-posedness of the related linearized problem [20].

Already in the early 70's the Karlsruhe group under the leadership of Professor Gerd Gudehus [22] has conjectured that spontaneous loss of homogeneity in the form of shear-band formation is a clear indication for the existence of material length scale. Indeed, there is ample experimental evidence that shear-bands in granular materials engage a significant number of grains. Based on direct experimental observations, Roscoe [18]

proposed that the width of shear-bands is about 10 times the average grain diameter.

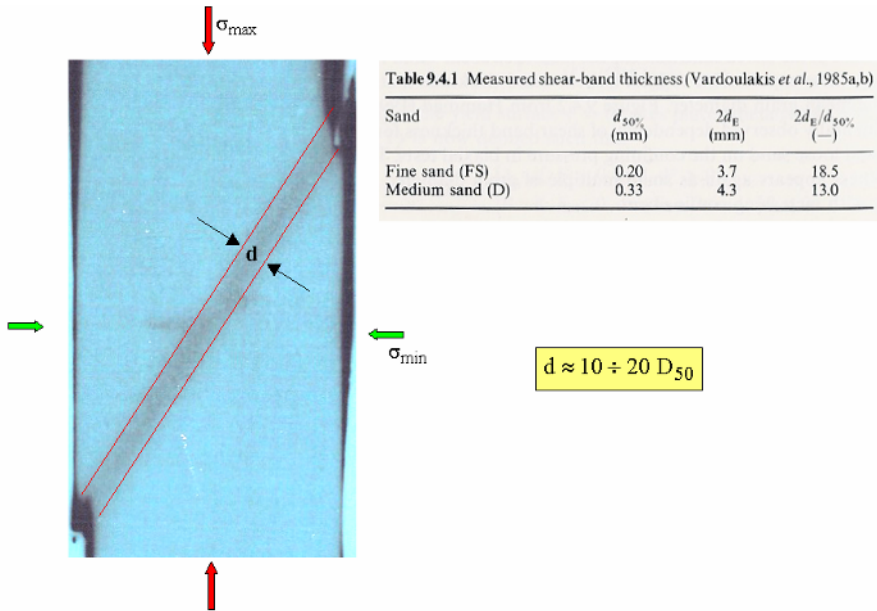


Fig. 1.6. Shear-band thickness correlation to grain size [24]

Localization of deformation leads to a change of scale of the problem, so that phenomena occurring at the scale of the grain cannot be ignored anymore in the mechanical modeling process of the macroscopic behavior of the material. Thus in order to describe correctly localization phenomena it appears necessary to resort to continuum models with micro-structure. These generalized continua usually contain additional kinematical degrees of freedom and/or higher deformation gradients. These observations have prompted the extension of classical continuum mechanical descriptions for geomaterials past the softening regime by resorting to the so-called *Cosserat* or *Gradient models*. Cosserat continua and higher gradient continua belong to a general class of constitutive models, which account for the material's micro-structure. The description of statics and kinematics of continuous media with microstructure has been studied systematically by many authors in the past [8, 9] and several important contributions appeared in the present series of Workshops. The consideration of higher order continuum models is however not free of new problems and challenges. Issues of extra boundary conditions, physical parameter identification,

computational issues and thermodynamical considerations are presently at the drawing board of researchers and engineers.

There is also interest in Structural Geology where shear bands appear as faults (Fig. 1.7a,b & c) which among other things give clues to the history, the magnitude and the orientation of tectonic stresses. Advanced studies in coupled phenomena related with localized deformations are now applied to understand the effects of fluid flow and temperature changes on the behavior of active fault zones. Further, other tectonic processes as folds may be studied in the context of bifurcation theory as presented in the pioneering work of Maurice Biot.

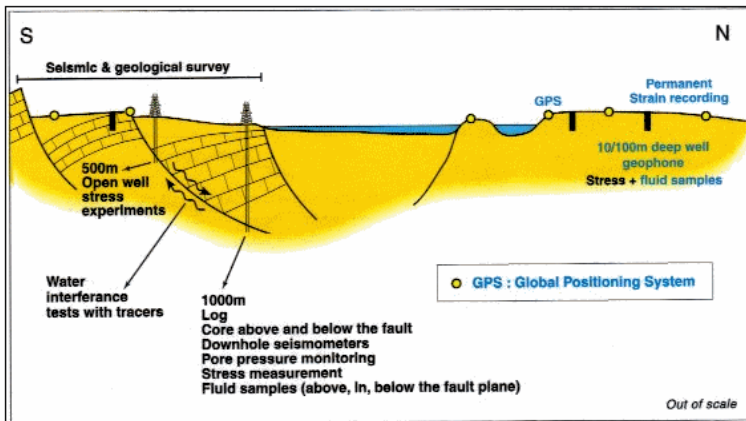


Fig. 1.7a: (a) Pyrgaki normal fault at Aigion region and
 (b) Rough sketch of the normal faults forming the Gulf of Corinth
 (<http://www.corinth-rift-lab.org>)

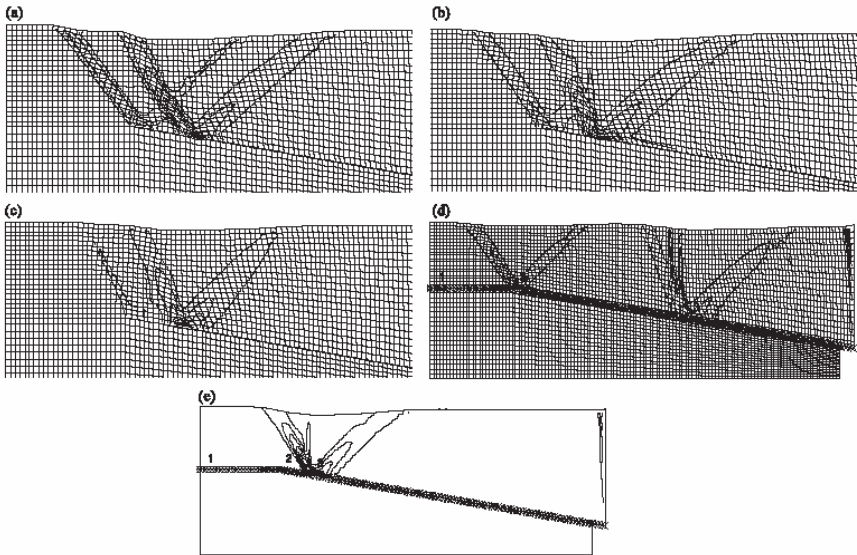


Fig. 1.7b : Normal and antithetic faults delineated from inversion of seismological measurements at the Gulf of Corinth [26]

Dissemination of bifurcation theory: Bifurcation and stability analyses focusing mainly on the constitutive behavior of geomaterials (soils, rocks and concretes) can be viewed as an extension of classical strength of materials. In its early development, bifurcation theory applied to geomechanics was used by very few researchers and was not appreciated by the engineering community, because it requires a more advanced mathematics and continuum mechanics background. The “7th International Workshop on Bifurcations, Instabilities and Degradation in Geomechanics (**IWBIDG 2005**)” organized jointly by the National Technical University of Athens and the Technical University of Crete aims at a significant dissemination of bifurcation theory. A new breed of young engineers from Europe and abroad have presented developments in advanced mathematical, constitutive and numerical modeling, as well as in experimental techniques.

Education of decision-making civil and mining engineers: It appears that some of the important modeling work in civil and mining engineering as well as in geology is increasingly performed by applied mathematicians and physicists. This is because some of the more conventional civil engineering, mining engineering, geological engineering and geology schools do not prepare their students for advanced needs, which call for top skills

in applied mathematics, mechanics, computer aided analysis and experimentation. The trouble in choosing scientists to play the role of civil and mining engineers lies in the fact that the former, coming from a university environment with different views on applied and fundamental research, may, in many occasions, lead to 're-inventing the wheel'. On the other hand geologists know rocks very well, but often they shy away from mathematical presentations concerning the physical and mechanical properties of rocks. The reverse can also be true: engineers do not always know the history of the rocks on which they have accumulated substantial data. This is another manifestation of the loss of engineering know-how, which is the delayed effect of not supporting engineering faculty to be active in advanced fundamental research.

The forthcoming **8th International Workshop on "Bifurcation, Instabilities and Degradation in Geomechanics"** will cover the "classical" subjects of contemporary constitutive theory, bifurcation, localization and stability theories, methods of numerical simulations, and advanced experimental techniques, and hopes also to extend the scope into the subjects of *degradation* and *phase changes* of Geomaterials and monumental stones, being these of purely mechanical or physicochemical origin. Another aim is to bring closer geologists with engineers in order to jointly attack the problems related with the mechanics of jointing, faulting and folding in geological materials.

References

1. Benallal, A., Bilardon, R. and Geymonat G. (1989). Conditions de bifurcation à l'intérieur et aux frontières pour une classe de matériaux non standards. Acad. Sci., Paris, 308, série II, 893-898.
2. Bigoni, D and Petryk, H (2002). A note on divergence and .utter instabilities inelastic –plastic materials. International Journal of Solids and Structures, 39, 911 –926.
3. Chambon, R. and Caillerie, D. (1999). Existence and uniqueness theorems for boundary value problems involving incrementally non-linear models. Int. J. Solids, and Structures, 36, 5089-5099.
4. Coulomb Charles-Augustin. *Essai Sur une application des règles de Maximis & Minimis à quelques Problèmes de Statique, relatifs à l'Architecture*, 1773. In: J. Heyman, Coulomb's Memoir on Statics, Cambridge University Press, 1972.
5. Darve F., Laouafa F. (2000). Instabilities in granular materials and application to landslides, Int. J. Mech. of Cohes. Frict. Materials, 5(8), 627-652.
6. De Josselin de Jong (1976). Rowe's stress-dilatancy relation based on friction. Géotechnique, 26, 527-534.

7. Desrues, J., Chambon, R., Mokni, M. and Mazerolle, F. (1996). Void ratio evolution insideshear bands in triaxial sand specimens studied by computed tomography. *Géotechnique*, 46, 529-546.
8. Germain P. (1973). La méthode des puissances vituelles en mécanique des milieux continus. Part I, *J. de Mécanique*, 12, 235-274.
9. Germain P. (1973). The Method of virtual power in continuum mechanics. Part 2: Microstructure. *SIAM J. Appl. Math.*, 25, 556-575.
10. Goddard, J.D. and Bashir Y.M. (1990). On Reynolds dilatancy, recent developments in structured contunua. (eds. Dekee, D. and Kaloni, P.W.), Vol. 2, 23-35.
11. Mandel, J.. *Propagation des surfaces de discontinuite dans un milieu elasto-plastique*. In: *Stress Waves in Anelastic Solids*. Springer, Berlin, 331-341, 1964.
12. Mohr, O. (1900). Welche Umstände bedingen die Elastizitätsgrenze und den Bruch eines Materials? *Zeitschrift des Vereines deutscher Ingenieure*, 44, 1-12.
13. Mroz, Z. (1963). Non-associate flow laws in plasticity. *J. de Mécanique*, 2, 21-42.
14. Mühlhaus, H.-B. and Vardoulakis, I.(1987). The thickness of shear bands in granular materials. *Géotechnique*, 37, 271-283.
15. Nova, R. (1994). Controllability of the incremental response of soil specimens subjected to arbitrary loading programes, *J. of Mech. of Beh. Materials*, 5(2), 193-201.
16. Oda, M., Kazama, H. and Konishi, J.. (1997). Effects of induced anisotropy on the development of shear bands in granular materials. *Mechanics of Materials*, 25.
17. Reynolds, O. (1885). On the dilatancy of media composed of rigid particles in contact. With experimental illustrations. *Phil. Mag.* (2) 20, 469-481. Also: Truesdell, C. and Noll, W.: *The Non-Linear Field Theories of Mechanics*, *Handbuch der Physik Band III/3*, section 119, Springer 1965.
18. Roscoe, K.H. (1970). The influence of strains in Soil Mechanics. *Géotechnique*, 20,129-170.
19. Rowe, P.W. (1962). The stress-dilatancy relation for static equilibrium of an assembly of particles in contact. *Proc. Roy. Soc.*, 269, 500-527.
20. Schaeffer, D. (1990). Instability and ill-posedeness in the deformation of granular materials. *Int. J. Num. Anal. Methods in Geomechanics*, 14, 253-278.
21. Taylor, D.W. *Fundamentals of Soil Mechanics*. John Wiley, 1948.
22. Vardoulakis I. *Berechnungsverfahren für Erdkörper mit plastischer Ver- und Entfestigung: Entstehung und Ausbreitung von Scherfugen*. DFG Report GU 103/16, 1974.
23. Vardoulakis, I. and Graf B. (1982). Imperfection sensitivity of the biaxial test on dry sand. *IUTAM Conf. on Deformation and Failure of Granular Materials*, Delft, 485-491, A.A. Balkema.
24. Vardoulakis I. and Sulem J. *Bifurcation Analysis in Geomechanics*, Blackie Academic and Professional (Chapman & Hall) 1995.

25. Wan, R.G. and Guo, P.J. (1999). A pressure and density dependent dilatancy model for sand for granular materials. *Soils and Foundations*, **39**, 1-11.
26. G.E. Exadaktylos, Vardoulakis, I., M.C. Stavropoulou and Tsombos, P. (2003), Analogue and numerical modeling of normal fault patterns produced due to slip along a detachment plane, *Tectonophysics*, 376, Nos. 1-2, pp. 117-134.

Part I

Experimental Aspects

Third Invariant Dependent Single Yield Surface Model and Localization Conditions for High Porosity Sandstone

Dr. Vennela Challa¹, Dr. Kathleen A Issen²

¹1342 S Finley Rd., 3E,
Lombard, IL – 60148
E-mail: vennelac@gmail.com
Phone: 216-375-5064
Fax: 315-268-6695

²Associate Professor
Mechanical & Aeronautical Engineering
207 CAMP, Box 5725
8, Clarkson Avenue
Clarkson University
Potsdam, NY 13699-5725
E-mail: issenka@clarkson.edu
Phone: 315-268-3880
Fax: 315-268-6695

Summary

High porosity sandstones are observed to fail by the formation of localized bands in field and laboratory settings. Compaction bands form perpendicular to the direction of maximum compression, with pure compactant strain, while shear bands form at an angle to the direction of maximum compression, with shear strain accompanied by either compactant or dilatant strain normal to the band. Recent experimental evidence indicates that mechanical behavior of some high porosity sandstones depends on the third invariant of deviatoric stress (J_3). In this work, a J_3 dependent single yield surface constitutive model was developed, and band orientation predictions determined using the Rudnicki and Rice bifurcation theory. While in the laboratory, high porosity sandstones are typically tested under axisymmetric compression (ASC; intermediate principal stress equal to the least compressive principal stress), stress states in the field are often non-axisymmetric. Therefore, localization conditions were determined under

P_1 , a stress state perturbed from ASC. For ASC, the localization conditions resulting from the J_3 dependent model are identical to those from the J_3 independent model. The most favorable conditions for compaction band formation occur under ASC, while under P_1 , localization conditions favor shear band formation. Mild to moderate J_3 dependence favors formation of shear bands over compaction bands, and a strong J_3 dependence prohibits localized deformation band formation. These results provide one possible explanation for relatively few field observations of compaction bands versus more commonly observed shear bands.

1 Introduction

The phenomenon of strain localization has been identified as a common deformation mode in high porosity sandstones, both in the field and in laboratory test specimens. Localized deformation is observed to occur at scales ranging from intragranular to global (Aydin 1978; Mollema and Antonellini 1996; Olsson 1999; Olsson and Holcomb 2000; Wu et al. 2000; Cashman and Cashman 2000; Klein et al. 2001; Wong et al. 2001; Du Bernard et al. 2002; Baud et al. 2004a; Baud et al. 2004b; Sternlof and Chapin, 2004). Deformation structures are typically classified depending on the dominant strain component as: compaction bands, which form perpendicular to the direction of maximum compression, and are identified as planar structures with pure compressional deformation; dilation bands, which form perpendicular to the direction of minimum compression/maximum extension with pure dilational deformation; and, shear bands, which form at an angle to the direction of maximum compression, and are characterized by shear deformation, often coupled with either dilatant or compactant deformation normal to the band. In the laboratory, high porosity sandstones are commonly tested under axisymmetric compression (ASC). The ASC stress state is traditionally obtained by holding the confining pressure constant (intermediate principal stress equal to the minimum compressive stress) while increasing the axial compressive stress. Therefore in the traditional ASC test the lateral stresses are maintained at a constant value, unlike in an oedometric test where zero lateral strain is maintained. Under ASC, laboratory specimens are generally observed to fail by the formation of either shear bands and/or compaction bands, depending on the confining pressure under which the material is tested (Dunn et al. 1973; Scott and Neilsen 1991; Wong et al. 1992; Zhang et al. 1993; Wong et al. 1997; Olsson 1999; Mair et al. 2000;

Olsson and Holcomb 2000; Wu et al. 2000; Klein et al. 2001; Wong et al. 2001; Du Bernard et al. 2002; Baud et al. 2004a; Baud et al. 2004b).

Typically, localized deformation band formation in high porosity sandstones is accompanied by a change in porosity within the band, compared to the base material. As a result of a local change in porosity within the band, permeability variations are also reported (Zhu et al. 1997; Olsson and Holcomb 2000; Baud et al. 2004b). It has been suggested that the formation of localized bands in high porosity sandstones could alter fluid flow pathways within reservoirs, due to changes in permeability (Zhu et al. 1997; DiGiovanni et al. 2000; Olsson 2001; Olsson et al. 2002; Baud et al. 2004b). Sand production during bore hole drilling could be due to the formation of compaction bands perpendicular to the drilling direction; the crushed material within compaction bands is washed out by drilling fluid (Haimson and Song 1998; Haimson 2001). Additionally, the efficiency of porous sandstones for use in sequestration applications could be influenced by the formation of localized bands (Wawersik et al. 2001). Zones of localized compaction have also been observed in porous cellular materials such as metal foams, honeycombs and cancellous bone (Odgaard et al. 1989; Papka and Kyriakides 1999; Ashby et al. 2000; Bastawros and Evans 2000). In both granular and cellular solids compaction localization is characterized by a band of reduced porosity. Whereas, in granular materials, the porosity reduction mechanism inside the band is grain crushing and/or grain rotation, in cellular solids, compaction bands form via cell collapse.

Rudnicki and Rice (1975) determined the conditions governing formation of shear bands in low porosity rocks by incorporating a single yield surface constitutive model (SYSM) within the framework of a bifurcation theory. Subsequently, compaction bands were identified as a new mode of localized deformation within high porosity sandstones in the field, and in laboratory specimens (Mollema and Antonellini 1996; Olsson 1999; Olsson and Holcomb 2000; Klein et al. 2001; Wong et al. 2001; Sternlof et al. 2004). Following experimental studies of Castlegate sandstone tested under ASC, Olsson (1999) proposed that compaction band formation could be explained using the Rudnicki and Rice (1975) localization theory. Issen and Rudnicki (2000, 2001) determined conditions for compaction band formation by re-examining the results obtained by Rudnicki and Rice (1975), and considering work done by Ottosen and Runesson (1991) and Perrin and Leblond (1993). According to the constitutive model considered by these authors (Rudnicki and Rice 1975; Ottosen and Runesson 1991; Perrin and Leblond 1993; Issen and Rudnicki 2000; Issen and Rudnicki 2001), the mechanical behavior of high porosity sandstones was assumed to be independent of the third invariant

of deviatoric stress (J_3). However, recent experimental evidence indicates that some high porosity sandstones display J_3 dependence (Drs. T. -f. Wong and P. Baud, personal communication). For such materials, the yield stress under compression is greater than that under extension i.e., the portion of the yield surface accessed by the stress path for extension is closer to the mean stress axis than that accessed under compression. While the mechanical behavior of some geomaterials has been described using J_3 dependent constitutive models (Lade 1977; Desai 1980; Desai and Faruque 1983; Desai et al. 1986; Desai and Salami 1987; Brown and Yu 1988; Lade and Kim 1988; Sture et al. 1989; Bardet 1990; Ottosen and Runesson 1991; Lade and Kim 1994; Schwer and Murray 1994; Fossum and Fredrich 2000; Krenk 2000), none of these models were extended to discuss the conditions governing localized deformation.

Motivated by recent experimental observations, a J_3 dependent SYSM is developed in this work. Localization conditions and theoretical band orientation predictions are determined by incorporating this J_3 dependent SYSM within the framework of the Rudnicki and Rice bifurcation theory. While the behavior of high porosity sandstone is typically investigated under ASC in the laboratory, stress states in the field are certainly not limited to ASC, and there is some question as to whether this stress state is common. Additionally, field observations of compaction bands are rare compared to shear bands. One possible reason for this is that compaction bands are either under-identified or misdiagnosed. Another possible explanation is that the ASC stress state, while identified as the theoretically most favorable for compaction band formation (Issen and Rudnicki 2000), is not common in the field. Therefore, in order to understand whether non-axisymmetric stress states produce conditions favoring compaction band formation, the present work investigates band orientation predictions for a stress state perturbed from ASC. Note that this analysis can be conducted for any number of stress states between ASC and axisymmetric extension (ASE, intermediate principal stress equal to the maximum compressive principal stress). However, since the focus of this investigation is on compaction bands, which are reported to form under ASC or near-ASC conditions, this work examines results for a stress state slightly perturbed from ASC. In the succeeding analyses, the engineering convention for principal stresses is used to derive the theoretical results: $\sigma_I \geq \sigma_{II} \geq \sigma_{III}$, positive in tension, where *III* corresponds to the direction of maximum compressive stress. In geomechanics notation, the principal stresses are traditionally defined as: $\sigma_1 = -\sigma_{III}$, $\sigma_2 = -\sigma_{II}$, and $\sigma_3 = -\sigma_I$.

2 Constitutive Relation

The expressions defining the yield and plastic potential surfaces for the J_3 dependent SYSM are similar to those proposed by Holcomb and Rudnicki (2001) for a J_3 independent SYSM. The J_3 dependence is incorporated within the constitutive relations through a similarity angle, θ . The yield surface, F , and the plastic potential surface, Γ , are defined as

$$F_{J_3} = \tau - f(\sigma, \theta, \gamma^p) \quad (2.1)$$

$$\Gamma_{J_3} = \tau - g(\sigma, \theta, \gamma^p) \quad (2.2)$$

where the subscript ' J_3 ' indicates a J_3 dependence. In (2.1) and (2.2), the dependence on the first and second invariants of stress is through the mean stress, σ ($= -I_1/3$), and the Mises equivalent shear stress, τ ($= \sqrt{J_2}$), respectively. The first invariant of principal stress is $I_1 = \sigma_{kk}$ (positive in tension); and the second invariant of deviatoric stress is $J_2 = (1/2)s_{ij}s_{ij}$, where the deviatoric stress is $s_{ij} = \sigma_{ij} - \sigma_{kk}\delta_{ij}/3$. The similarity angle is $\theta = (1/3)\cos^{-1}(3\sqrt{3}J_3/2\tau^3)$, where $J_3 = (1/3)s_{ij}s_{jk}s_{ki}$. The similarity angle, θ , is used to incorporate the J_3 dependence instead of the Lode angle because of the convenience afforded during constitutive model development. It is related to the Lode angle, α , as: $\cos 3\theta = -\sin 3\alpha$, such that the similarity angle varies smoothly from 0 to $\pi/3$ between ASE and ASC, while the Lode angle varies from $-\pi/6$ to $\pi/6$. The accumulated inelastic shear strain, γ^p , tracks inelastic deformation. The inelastic strain increment, obtained by incorporating the plastic potential expression (2.2) within the non-associated flow rule, $d\epsilon_{ij}^p = d\lambda(\partial\Gamma/\partial\sigma_{ij})$, is

$$\left(d\epsilon_{ij}^p\right)_{J_3} = d\lambda \left(\frac{\partial\tau}{\partial\sigma_{ij}} - \frac{\partial g}{\partial\sigma} \frac{\partial\sigma}{\partial\sigma_{ij}} - \frac{\partial g}{\partial\theta} \frac{\partial\theta}{\partial\sigma_{ij}} \right) \quad (2.3)$$

where $d\lambda$ is a non-negative scalar. The requirement that the material continues to experience inelastic deformation with continued loading past the elastic limit, is satisfied by the consistency condition, $dF = 0$. This condition, using the expression for the yield surface 2.1, becomes

$$(dF)_{J_3} = d\tau - \frac{\partial f}{\partial \sigma} d\sigma - \frac{\partial f}{\partial \theta} d\theta - \frac{\partial f}{\partial \gamma^p} d\gamma^p = 0 \quad (2.4)$$

In (2.3) and (2.4), $\partial f / \partial \sigma$ and $\partial g / \partial \sigma$ are the components of the gradient, with respect to σ , of the yield and plastic potential surfaces, respectively. These gradient components are defined as: $\partial f / \partial \sigma = -\mu$ and $\partial g / \partial \sigma = -\beta$, where μ (the friction coefficient) and β (the dilation coefficient) are the local slopes, in the $\tau - \sigma$ plane, of the yield and plastic potential surfaces, respectively (Fig. 2.1).

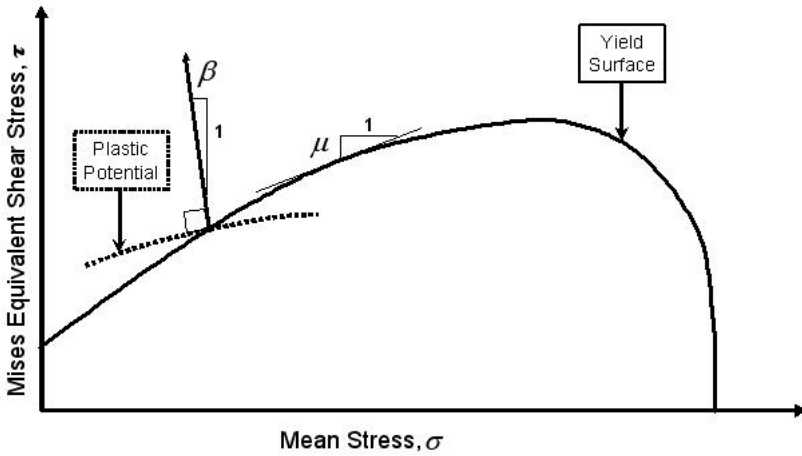


Fig. 2.1. Single yield surface for high porosity sandstone. The friction factor, μ , defines the slope of the yield surface. The dilation coefficient, β , defines the slope of the plastic potential surface, which is perpendicular to the inelastic strain increment

In 2D space, the slope of a curve at a specific point (point O in inset, Fig. 2.2) is defined as:

$$m_o = \frac{r + \tan \vartheta \frac{\partial r}{\partial \vartheta}}{-r \tan \vartheta + \frac{\partial r}{\partial \vartheta}} \quad (2.5)$$

where, r is the radius of the curve at 'O', and ϑ is the angle made by 'O' with the x -axis (inset, Fig. 2.2). Relating these terms to the parameters in the deviatoric plane, r corresponds to the shear stress τ , and ϑ corresponds

to the similarity angle, θ . The partial derivative $\partial r / \partial \mathcal{G}$ corresponds to $\partial \tau / \partial \theta \Leftrightarrow -(\partial F / \partial \theta) / (\partial F / \partial \tau)$ for the yield surface, and to $\partial \tau / \partial \theta \Leftrightarrow -(\partial \Gamma / \partial \theta) / (\partial \Gamma / \partial \tau)$ for the plastic potential surface. Substituting these terms in 2.5 and rearranging, the definitions for the gradients $(\partial \Gamma / \partial \theta) / (\partial \Gamma / \partial \tau)$ and $(\partial F / \partial \theta) / (\partial F / \partial \tau)$ are given by:

$$\frac{\partial \Gamma / \partial \theta}{\partial \Gamma / \partial \tau} = \frac{\tau(1 + m_p \tan \theta)}{(\tan \theta - m_p)} = \tau \zeta \tag{2.6}$$

$$\frac{\partial F / \partial \theta}{\partial F / \partial \tau} = \frac{\tau(1 + m_y \tan \theta)}{(\tan \theta - m_y)} = \tau \psi \tag{2.7}$$

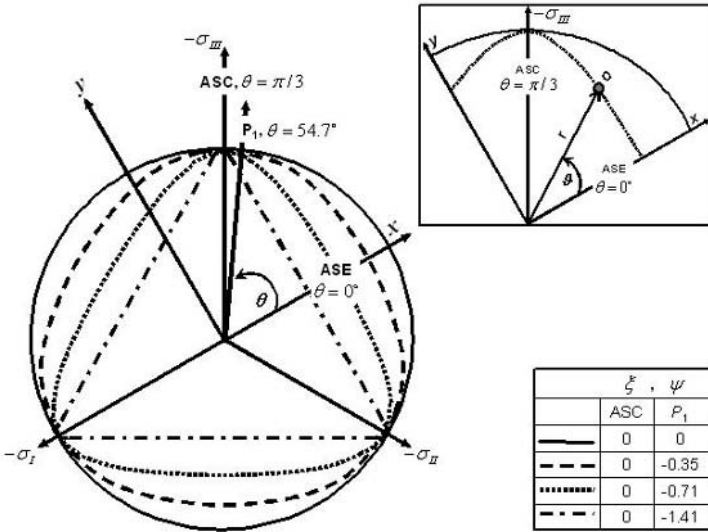


Fig. 2.2. Yield/plastic potential surfaces and stress paths in the deviatoric plane. The circle represents a yield/plastic potential surface with no J_3 dependence, and the triangle represents a strong J_3 dependence. The similarity angle, θ , is measured from the ASE axis. The slope of a curve at point O (in inset) is defined as a function of r , the radius of the curve at O , and ϑ , the angle made by point O with the x -axis. These can be related to the constitutive parameters as: $r \Leftrightarrow \tau$ and $\vartheta \Leftrightarrow \theta$, and used to define the deviatoric parameters ζ and ψ . Inset table gives values of ζ and ψ for the ASC and P_1 stress states

In (2.3) and (2.4), $\partial g / \partial \theta$ and $\partial f / \partial \theta$ are the components of the gradient, with respect to θ , of the plastic potential and yield surfaces, respectively. These components are related to the gradients defined in (2.6) and (2.7) as $\partial g / \partial \theta = -(\partial \Gamma / \partial \theta) / (\partial \Gamma / \partial \tau) = -\tau \xi$ and $\partial f / \partial \theta = -(\partial F / \partial \theta) / (\partial F / \partial \tau) = -\tau \psi$. The deviatoric parameters ξ and ψ are related to the local slopes, in the deviatoric plane, of the plastic potential (m_p) and yield surface (m_y), and the similarity angle (θ) as

$$\xi = \frac{m_p \tan \theta + 1}{\tan \theta - m_p} \quad (2.8)$$

$$\psi = \frac{m_y \tan \theta + 1}{\tan \theta - m_y} \quad (2.9)$$

Using the tensor definitions of $d\tau$, $d\sigma$ and $d\theta$, and substituting the gradient components defined above into (2.3) and (2.4), the inelastic strain increment, $d\varepsilon_{ij}^p$, and the inelastic shear strain increment, $d\gamma^p$, are found to be

$$\left(d\varepsilon_{ij}^p \right)_{J_3} = d\lambda \left(\frac{s_{ij}}{2\tau} + \frac{\beta}{3} \delta_{ij} + \xi S_{ij} \right) \quad (2.10)$$

$$\left(d\gamma^p \right)_{J_3} = \frac{1}{(\partial f / \partial \gamma^p)} \left(\frac{s_{ij}}{2\tau} + \frac{\mu}{3} \delta_{ij} + \psi S_{ij} \right) d\sigma_{ij} \quad (2.11)$$

where

$$S_{ij} = \frac{1}{\sin 3\theta} \left(\frac{\delta_{ij}}{\sqrt{3}} + \frac{\cos 3\theta}{2} \frac{s_{ij}}{\tau} - \frac{\sqrt{3}}{2} \frac{s_{ik}s_{kj}}{\tau^2} \right) \quad (2.12)$$

In (2.11), $\partial f / \partial \gamma^p = h$, which is a hardening modulus defined as the slope of the shear stress – inelastic shear strain curve at constant mean stress. The inelastic strain increment, $d\varepsilon_{ij}^p$, is related to the inelastic shear strain increment, $d\gamma^p$, as $d\gamma^p = 2d\varepsilon_{ij}^p d\varepsilon_{ij}^p - (2/3)d\varepsilon_{kk}^p d\varepsilon_{mm}^p$ (derived from the relation $d\gamma^p = \sqrt{2de_{ij}^p de_{ij}^p}$ and the definition of the deviatoric

strain $de_{ij}^p = d\varepsilon_{ij}^p - d\varepsilon_{kk}\delta_{ij}/3$). Using this relation and (2.10), the inelastic shear strain increment is found to be $d\gamma^p = d\lambda\sqrt{1+\xi^2}$. Comparing this definition for the inelastic shear strain increment, with that given in (2.11), $d\lambda$ is found to be

$$d\lambda = \frac{1}{h\sqrt{1+\xi^2}} \left(\frac{s_{ij}}{2\tau} + \frac{\mu}{3}\delta_{ij} + \psi S_{ij} \right) d\sigma_{ij} \quad (2.13)$$

Finally, substituting (2.13) into (2.10), the total inelastic strain increment is

$$\begin{aligned} & \left(d\varepsilon_{ij}^p \right)_{J_3} \\ &= \frac{1}{h\sqrt{1+\xi^2}} \left(\frac{s_{ij}}{2\tau} + \frac{\beta}{3}\delta_{ij} + \xi S_{ij} \right) \left(\frac{s_{kl}}{2\tau} + \frac{\mu}{3}\delta_{kl} + \psi S_{kl} \right) d\sigma_{kl} \end{aligned} \quad (2.14)$$

As will be discussed later, when the J_3 dependence is removed, ξ and ψ equal zero; in which case the J_3 independent expression for $d\varepsilon_{ij}^p$, determined by Rudnicki and Rice (1975), is recovered from (2.14).

The elastic strain increment, assuming isotropic elasticity, is defined as $d\varepsilon_{ij}^e = [1/2G] [\delta_{ik}\delta_{jl} - \delta_{ij}\delta_{kl}\nu/(1+\nu)] d\sigma_{kl}$. Therefore, the total strain increment is given by $d\varepsilon_{ij} = d\varepsilon_{ij}^e + d\varepsilon_{ij}^p = R_{ijkl} d\sigma_{kl}$. Inverting this strain – stress relation results in $d\sigma_{ij} = L_{ijkl} d\varepsilon_{kl}$, where L_{ijkl} is a modulus tensor. The expression for the modulus tensor, L_{ijkl} , for the J_3 dependent SYSM, is given by

$$L_{ijkl} = M_{ijkl} - \frac{1}{H} A_{ij} B_{kl} \quad (2.15)$$

where

$$M_{ijkl} = G \left[\left(\delta_{ik}\delta_{jl} + \delta_{il}\delta_{jk} \right) + \frac{2\nu}{1-2\nu} \delta_{ij}\delta_{kl} \right] \quad (2.16)$$

$$A_{ij} = GN_{ij} + K\beta\delta_{ij} + 2G\xi S_{ij} \quad (2.17)$$

$$B_{kl} = GN_{kl} + K\mu\delta_{kl} + 2G\psi S_{kl} \quad (2.18)$$

$$H = h\sqrt{1 + \xi^2} + K\beta\mu + G\xi\psi + G \quad (2.19)$$

In (2.16) – (2.19) G is the elastic shear modulus, K is the elastic bulk modulus, N_{ij} are the stress state parameters defined as $N_{ij} = s_{ij} / \tau$, and ν is the elastic Poisson's ratio.

3 Localization Conditions

3.1 Hardening Modulus (h) Expression

Rudnicki and Rice (1975) modeled localized deformation as a bifurcation from homogeneous deformation due to instability in the constitutive framework used to describe the behavior of an inelastically deforming material. Localized deformation, in the form of a planar band whose orientation is defined by the band normal \underline{n} , is possible when $\det[n_i L_{ijkl} n_l] = 0$ is satisfied. When the combination of material parameters is such that this condition is satisfied, band formation is predicted. Substituting (2.15) into the localization condition and solving for h , results in

$$\frac{h_{J_3}}{G} = \frac{1}{\sqrt{1 + \xi^2}} \left[\frac{h_{RR}}{G} + (\beta\xi + \mu\psi)H_1 + (\xi + \psi)H_2 + \xi\psi H_3 \right] \quad (3.1)$$

where the H_1 , H_2 and H_3 terms, defined in Appendix A, are functions of θ , n_K and N_K . In (3.1), h_{RR} is equivalent to the hardening modulus expression from the J_3 independent Rudnicki and Rice (1975) SYSM, and is given by

$$\frac{h_{RR}}{G} = \frac{G(N_{22} + K\beta/G)(N_{22} + K\mu/G)}{\left(K + \frac{4}{3}G\right)} + (N_{12}^2 + N_{23}^2) - (K\beta\mu/G + 1) \quad (3.2)$$

In (3.2), the stress state parameters (expressed in a local coordinate system where the 2-direction is defined as perpendicular to the band; see Rudnicki and Rice 1975), represented by combinations of N_{ij} and Y_{ij} terms, are defined as

$$N_{22} = n_I^2 N_I + n_{II}^2 N_{II} + n_{III}^2 N_{III} \quad (3.3)$$

$$Y_{22} = n_I^2 N_I^2 + n_{II}^2 N_{II}^2 + n_{III}^2 N_{III}^2 \quad (3.4)$$

$$N_{12}^2 + N_{23}^2 = Y_{22} - N_{22}^2 \quad (3.5)$$

$$Y_{12}^2 + Y_{23}^2 = n_I^2 N_I^4 + n_{II}^2 N_{II}^4 + n_{III}^2 N_{III}^4 - Y_{22}^2 \quad (3.6)$$

$$N_{12} Y_{12} + N_{23} Y_{23} = n_I^2 N_I^3 + n_{II}^2 N_{II}^3 + n_{III}^2 N_{III}^3 - N_{22} Y_{22} \quad (3.7)$$

where n_K are band normal components ($K = I, II, III$ are the principal stress directions), and N_K are stress state parameters in the principal stress directions, defined as: $N_K = s_K / \tau$, and their values are specific to the stress state under consideration. In (3.3) – (3.7), Y_{ij} are stress state parameters (expressed in the local coordinate system) defined as: $Y_{ij} = s_{ik} s_{kj} / \tau^2$. Typically, the value of the hardening modulus, h , is observed to decrease with continued inelastic loading. Therefore, the band orientation that produces the maximum value for h_{J_3} is predicted to form. Note that, when the J_3 dependence is removed, ζ and ψ equal zero, and (3.1) reduces to (3.2).

3.2 Determination of Critical Hardening Modulus (h_{cr})

Equations (3.3) – (3.7) can be simplified using the assumption that $n_{II} = 0$, corresponding to localized deformation in the plane of maximum shear (Rudnicki and Rice 1975). Recall that the band orientation with the maximum value of the hardening modulus is the orientation theoretically predicted to form. Therefore, using the method of Lagrange Multipliers, the expression defining the maximum h , and the corresponding predicted band orientation, are determined. This expression for h is referred to as the critical hardening modulus, h_{cr} . Analytical expressions are determined for two cases: (1) one of the n_K in (3.1) is zero, corresponding to maximizing h_{cr} for shear bands, and (2) two of the n_K are zero ($n_I = n_{II} = 0$ corresponds to compaction bands, and $n_{II} = n_{III} = 0$ to dilation bands). The h_{cr} expression for shear bands is given by

$$\frac{(h_{\text{cr}}^{\text{II}})_{J_3}}{G} = \frac{1}{\sqrt{1+\xi^2}} \left\{ \frac{(1-2\nu)^2 (T_1 S_2 + T_2 S_1)^2}{8(1-\nu) S_1 S_2} - \frac{2(1+\nu)}{3(1-2\nu)} \beta \mu \right. \\ \left. - \frac{1}{2} \left[(1+\nu) N_{\text{II}}^2 + 2(N_I N_{\text{II}} - N_{\text{III}}^2) \right] S_1 S_2 \right. \\ \left. - \frac{(1-2\nu)}{2} N_{\text{II}} (T_1 S_2 + T_2 S_1) - \xi \psi - 1 + \frac{(1-2\nu)}{2(1-\nu)} T_1 T_2 \right\} \quad (3.8)$$

where the terms T_1 , T_2 , S_1 and S_2 , defined in Appendix A, are functions of the variables β , μ , ψ , ξ and θ . The angle between the band normal corresponding to the plane of localization, and the direction of maximum compression, is: $\phi = \sqrt{(\kappa - N_{\text{III}}) / (N_I - \kappa)}$, where κ is given by

$$\kappa = \frac{(1-2\nu)}{2} \left(\frac{T_1}{S_1} + \frac{T_2}{S_2} \right) - (1-\nu) N_{\text{II}} \quad (3.9)$$

Under general loading conditions, the solution given by (3.8) is valid when the following inequality is satisfied

$$N_{\text{III}} \leq \frac{(1-2\nu)}{2} \left(\frac{T_1}{S_1} + \frac{T_2}{S_2} \right) - (1-\nu) N_{\text{II}} \leq N_I \quad (3.10)$$

which is determined from the requirement that the squares of the components of the band normal must be positive: $n_K^2 \geq 0$. If the left side of the inequality is violated, compaction bands are predicted, and if the right side is violated, dilation bands are predicted.

When two of the n_K are equal to zero, the third equals unity following the restriction $n_I^2 + n_{\text{II}}^2 + n_{\text{III}}^2 = 1$. When $n_{\text{II}}^2 = n_{\text{III}}^2 = 0$ and $n_I^2 = 1$, the band is perpendicular to the direction of minimum compression/maximum extension, and is defined as a dilation band. Similarly, when $n_I^2 = n_{\text{II}}^2 = 0$ and $n_{\text{III}}^2 = 1$, this corresponds to a compaction band, which is perpendicular to the direction of maximum compression. The h_{cr} for these orientations is

$$\frac{(h_{cr}^J)_{J_3}}{G} = \frac{1}{\sqrt{1+\xi^2}} \left\{ \frac{(1-2\nu)}{2(1-\nu)} \left[N_J (q_1^J + q_2^J) + q_1^J q_2^J \right] \right. \\ \left. + \frac{(1+\nu)}{3(1-\nu)} \left[\beta q_1^J + \mu q_2^J \right] - \xi \psi + \frac{(h_{cr}^J)_{RR}}{G} \right\} \quad (3.11)$$

where $J = III$ for compaction bands, and $J = I$ for dilation bands. The terms q_1^J and q_2^J , defined in Appendix A, are functions of the variables ψ , ξ , θ and N_J . In (3.11), $(h_{cr}^J)_{RR}$ is the expression for the critical hardening modulus obtained from the J_3 independent SYSM used by Rudnicki and Rice (1975), and defined as (Issen and Rudnicki 2000).

$$\frac{h_{cr}^J}{G} = \frac{(1+\nu)}{9(1-\nu)} (\beta - \mu)^2 - \left(1 - \frac{3}{4} N_J^2 \right) \\ - \frac{(1+\nu)}{(1-\nu)} \left[\frac{1}{2} N_J - \frac{1}{3} (\beta + \mu) \right]^2 \quad (3.12)$$

3.3 Theoretical Parameters

In (3.1) – (3.12), the stress state parameters, N_K , and the similarity angle, θ , are functions of the stress state. For example, the similarity angle (see Fig. 2.2) is equal to $\pi/3$ for ASC, $\pi/6$ for pure shear (PS), and 0 for ASE. The stress state parameters for ASC are defined as: $N_I = N_{II} = 1/\sqrt{3}$, $N_{III} = -2/\sqrt{3}$; and for ASE are given by: $N_I = 2/\sqrt{3}$, $N_{II} = N_{III} = -1/\sqrt{3}$. The values of the deviatoric parameters, ψ and ξ , depend on the similarity angle, and the shapes of the yield and plastic potential surfaces in the deviatoric plane. Two important assumptions are considered to limit the shapes of these surfaces: (1) The material is assumed to be isotropic prior to inception of localized deformation, therefore, the shape of the yield surface is constrained to be symmetric about the principal stress axes in the deviatoric plane, (2) It is required that the yield and plastic potential surfaces remain convex, therefore, the limiting shapes for these surfaces are assumed to be a circle, corresponding

to no J_3 dependence, and a triangle, corresponding to extreme J_3 dependence (see Fig. 2.2).

For circular surfaces, the slopes (in Cartesian coordinates) of the yield and plastic potential surfaces are given by: $m_y = m_p = -1/\tan\theta$. Substituting this into (2.8) and (2.9) reveals that, for circular surfaces, $\psi = \xi = 0$ is always true, irrespective of the stress state under which the material is loaded (i.e., any stress state between and including ASC and ASE). When $\xi = \psi = 0$ is substituted into (3.1), the expression for h_{J_3} reduces to h_{RR} , which is equivalent to the h from the J_3 independent SYSM used by Rudnicki and Rice (1975). Similarly, when $\xi = \psi = 0$ is substituted into (3.11), the expression for $(h'_{cr})_{J_3}$ reduces to $(h'_{cr})_{RR}$, the result from the J_3 independent SYSM defined in (3.12). Since the J_3 independent model can be recovered from the J_3 dependent model by setting $\psi = \xi = 0$, circular surfaces correspond to no J_3 dependence under any stress state. Conducting a similar analysis for triangular surfaces, it is determined that $\psi = \xi = 0$ under ASE ($\theta = 0^\circ$), while, for PS ($\theta = \pi/6$), $\psi = \xi = -1/\sqrt{3}$. Under ASC there is a sharp vertex, and the strain direction is undefined. To avoid this singularity, the vertices of the triangle are typically rounded, such that $\xi = \psi = 0$ is again true for ASC. Therefore under ASC or ASE, $\xi = \psi = 0$ is always true irrespective of the shape of the yield and plastic potential surfaces, and the localization conditions reduce to those from the J_3 independent SYSM. For non-circular yield and plastic potential surfaces, the influence of the J_3 dependence can be significant for stress states perturbed from ASC and ASE.

4 Results

In prior sections, constitutive relations and localization conditions for a J_3 dependent material were derived for a general stress state. Next, we examine the influence of J_3 dependence on band orientation predictions for the ASC stress state and a stress state P_1 perturbed from ASC. To determine the h_{cr} for any stress state, first the values of N_K , θ , ξ and ψ , specific to the stress state, must be determined. The stress state parameters were previously defined for ASC and ASE. Issen and Challa (submitted) used sample principal stress values to determine the N_K parameters for

stress states perturbed from axisymmetric. Note that the deviatoric stress states are characterized by the value of the intermediate principal stress (σ_{II}), with respect to the values of the other two principal stresses (σ_I, σ_{III}). For ASC and ASE, σ_{II} is equal to either σ_I or σ_{III} , respectively, which is no longer true for stress states perturbed from axisymmetric. Fixed numerical values were assumed for the minimum and maximum principal stresses, and values of σ_{II} were assumed to range between $\sigma_{II} = \sigma_I$ (corresponding to ASC) and $\sigma_{II} = \sigma_{III}$ (corresponding to ASE). While Issen and Challa (submitted) investigated a range of stress states between ASC and ASE, in this work only the P_1 stress state will be discussed, in addition to reviewing the results under ASC.

4.1 Specialized Deviatoric and Stress State Parameters

In the current analysis, the assumed minimum and maximum principal stress values are: $\sigma_{III} = -200$ MPa and $\sigma_I = -100$ MPa, respectively. Additionally, the elastic Poisson's ratio, ν , is assumed to be 0.2. While, for ASC, $\sigma_{II} = -100$ MPa, for the P_1 stress state, $\sigma_{II} = -110$ MPa. The similarity angle, θ , for the P_1 stress state is found to be equal to 54.7° , and the values of the stress state parameters are determined to be: $N_I = 0.667$, $N_{II} = 0.483$ and $N_{III} = -1.15$. While specific stress values were used to facilitate the analysis, the results discussed below are not limited to these specific values; results are applicable to all stress states that produce the same values of N_I , N_{II} and N_{III} (for example, $\sigma_{III} = -100$ MPa, $\sigma_{II} = -55$ MPa, and $\sigma_I = -50$ MPa).

For circular yield and plastic potential surfaces, $\xi = \psi = 0$ is true for all stress states. For triangular surfaces (for non-axisymmetric stress states), $\xi, \psi = -\tan\theta$, so for the P_1 stress state ($\theta = 54.7^\circ$), $\xi, \psi = -1.41$. Therefore, for the P_1 stress state, the values associated with the deviatoric parameters vary from 0 to -1.41 , for surfaces varying between a circle and a triangle (see table inset, Fig. 2.2). In (3.1), for any specific stress state (ASC, P_1 , ASE, etc.), the values of N_K and θ are fixed. Additionally, for a specified stress state, after the shapes of the yield and plastic potential surfaces in the deviatoric plane are defined, the values of the deviatoric parameters ξ and ψ are also fixed. Therefore, for a specific stress state with defined shapes for the yield and plastic potential surfaces,

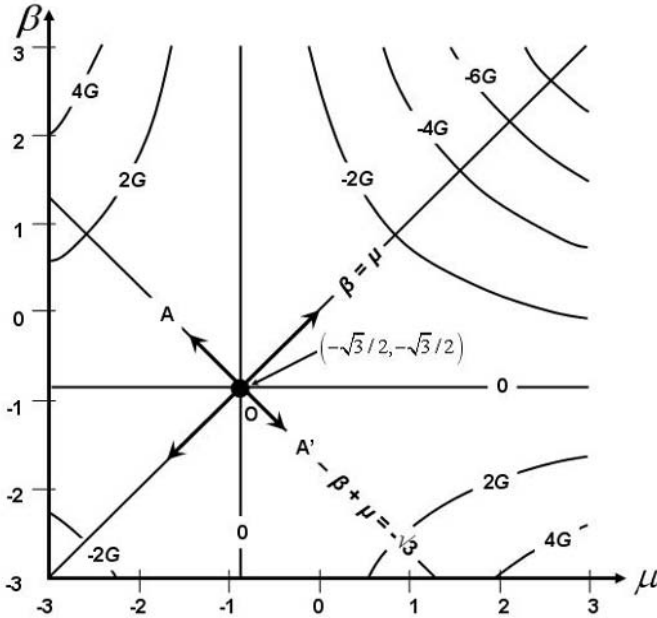


Fig. 4.1. Contours of constant h_{cr}^{III} in the $\beta - \mu$ plane, using equation (3.12). Moving outward from O , along normality ($\beta = \mu$), h_{cr} is always negative and compaction band formation is inhibited. Moving outward along AA' ($\beta + \mu = \sqrt{3}$), $h_{cr} > 0$ and compaction band formation is predicted prior to the peak stress

the h in (3.1) is a function of only the band normal component n_t , and the parameters β and μ . Consequently, the band orientation predictions for the ASC and P_1 stress states are investigated by plotting the results on the $\beta - \mu$ plane.

4.2 Band Orientation Predictions: Limiting Conditions

In this work, conditions are defined as being theoretically “favorable” for band formation when $h_{cr} > 0$ is true, since this corresponds to the inception of localized deformation earlier in the loading program. Conditions for localized deformation are theoretically “unfavorable” when h_{cr} is negative, since this corresponds to band formation after the peak in the stress-strain curve. This distinction is based on current experimental observations, which indicate that compaction band formation initiates pre-peak or at peak, rather than post-peak. Note that, although band formation is still

possible for small negative values of h_{cr} , when h_{cr} is a large negative number (e.g., $h_{cr} < -G/2$), localized deformation is likely to be completely prohibited (Challa and Issen 2004; Issen and Challa 2005). The value of h_{cr} varies significantly, depending on the values of β and μ . This is shown in Fig. 4.1, which plots contours of constant h_{cr} for ASC, using the h_{cr}''' expression for compaction bands from (3.12).

Band orientation predictions for the ASC and P_1 stress states are illustrated in Figs. 4.2 – 4.8. In these plots, compaction bands are predicted below line AA', dilation bands above line BB' and shear bands between these two bounding lines. The equations defining lines AA' and BB' are determined using inequality (3.10). The value of h_{cr} , determined from (3.8) and (3.11), is positive in the shaded regions and negative in the unshaded regions. Experimental data from Olsson (1999) and Wong et al. (2001), where compaction bands and/or shear bands were observed to form under ASC, are represented by ovals. The dots represent β and μ values determined using data from Bentheim sandstone tested under ASC (Baud et al. 2004a) where compaction bands and/or shear bands were observed. We know of no reported experimental data from high porosity sandstones tested under the P_1 stress state, which could be used to evaluate theoretical predictions for this stress state. However, while the β and μ values for this stress state will not likely be exactly the same as those for ASC, it does not seem unreasonable to assume that the deviation would not be too large. Therefore, the ASC data values are also shown on Figs. 4.3 – 4.8, for the P_1 stress state, to provide a rough estimate of how theoretical predictions might be expected to compare with experimental data. Existing experimental data from laboratory tests on high porosity sandstones indicate that while non-normality is typically true for these materials, large deviations from $\beta = \mu$ do not occur (Olsson 1999; Wong et al. 2001; Baud et al. 2004a). Therefore, band orientation predictions in Figs. 4.2 – 4.8 are investigated only for values of β and μ satisfying normality, or corresponding to a small deviation from normality.

4.3 Axisymmetric Compression

Expression (3.12) represents a hyperbolic paraboloid (saddle shape) in the $h - \beta - \mu$ space, and Fig. 4.1 shows the $\beta - \mu$ plane obtained by taking a section through $h = 0$. The saddle point falls at $\beta = \mu = -\sqrt{3}/2$, and $h_{cr} = 0$ along the lines $\beta = -\sqrt{3}/2$ and $\mu = -\sqrt{3}/2$. As the values of β

and μ move outward from O , along the $\beta = \mu$ line, h_{cr}^{III} becomes increasingly negative. Therefore, under ASC, when normality is true, h_{cr}^{III}

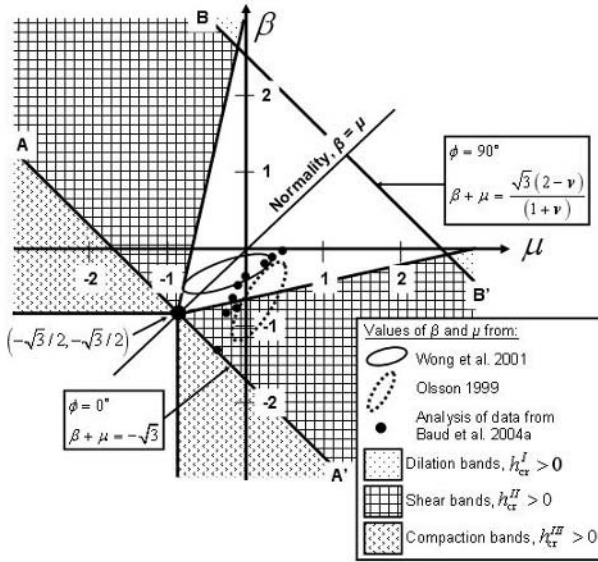


Fig. 4.2. Band orientation predictions as a function of β and μ for ASC ($\psi = \xi = 0$). The $h_{cr} > 0$ in the shaded regions. Compaction bands ($\phi = 0^\circ$) are predicted below $\beta + \mu = -\sqrt{3}$, and dilation bands ($\phi = 90^\circ$) are predicted above $\beta + \mu = \sqrt{3}(2-\nu)/(1+\nu)$. Shear bands, with $0^\circ \leq \phi \leq 90^\circ$, are predicted between AA' and BB' . The compaction band orientation, represented by the AA' line passes through the saddle point $(-\sqrt{3}/2, -\sqrt{3}/2)$. The band orientation, ϕ , is the angle between the band normal and the axial direction. Only shear bands are predicted for reported values of β and μ , while compaction bands and/or shear bands were observed

is always negative, so band formation is predicted later in the loading program, and localization conditions are defined as being “unfavorable”. However, as the values of β and μ move outward from the saddle point, along the $\beta + \mu = -\sqrt{3}$ line, h_{cr}^{III} is always positive and becomes increasingly positive for increasing deviations from normality. Thus, theory predicts increasingly favorable localization conditions for increasing deviations from normality; however, experiment results typically demonstrate only modest deviations from normality. Therefore, the optimal conditions for localization occur for the band angle that

produces the largest positive h_{cr} for the smallest deviation from normality. We refer to this band orientation as the “optimal band angle.” As shown in Fig. 4.2, for ASC, the compaction band is the orientation corresponding to the optimal localization conditions, since the compaction band boundary (line AA’ in Fig. 4.2) goes through the saddle point and always lies in the region where $h_{cr} \geq 0$. Therefore, conditions for the formation of compaction bands are defined as being “favorable” for combinations of β and μ values that fall on (or slightly below) line AA’.

Under ASC, regardless of J_3 dependence (Fig. 4.2), shear bands are predicted between the bounds defined by $-\sqrt{3} \leq \beta + \mu \leq \sqrt{3}(2 - \nu)/(1 + \nu)$. There is a smooth transition in the predicted band angles, from low angle compacting shear bands just above line AA’, to high angle dilating shear bands just below line BB’. However, as reported by other authors (Olsson 1999; Issen and Rudnicki 2000; Issen and Rudnicki 2001; Wong et al. 2001; Baud et al. 2004a) the data falls entirely in the region where shear bands are predicted, so the observed shear bands are predicted, but not the observed compaction bands. Improved agreement can be obtained through use of a J_3 independent two yield surface model (Issen 2002; Challa and Issen 2004; Issen and Challa 2005). Incorporation of J_3 dependence into a two yield surface model is significantly more complex than for the SYSM discussed in this work, and therefore, will be examined in a forthcoming paper.

4.4 J_3 Independent SYSM: P_1 Stress State

Figure 4.3 shows band orientation predictions for the P_1 stress state, using the J_3 independent model. The predictions are largely similar to those for ASC, and $h_{cr} < 0$ is again true along normality. The saddle point is at $(-0.73, -0.73)$, which has moved up slightly along the $\beta = \mu$ line, compared to the location for ASC. Unlike ASC, where AA’ (corresponding to compaction bands) passes through the saddle point, under P_1 , the CC’ contour, corresponding to an 18° compacting shear band (characterized as a shear band with a compaction strain component normal to the band), passes through the saddle point. Therefore, line CC’ corresponds to the largest range of β and μ values along which $h_{cr} > 0$ is always true. Thus, for a slight perturbation from ASC, the most favorable localization conditions exist for the 18° band orientation, in contrast to ASC, where conditions for compaction bands were the most favorable. Shear bands are

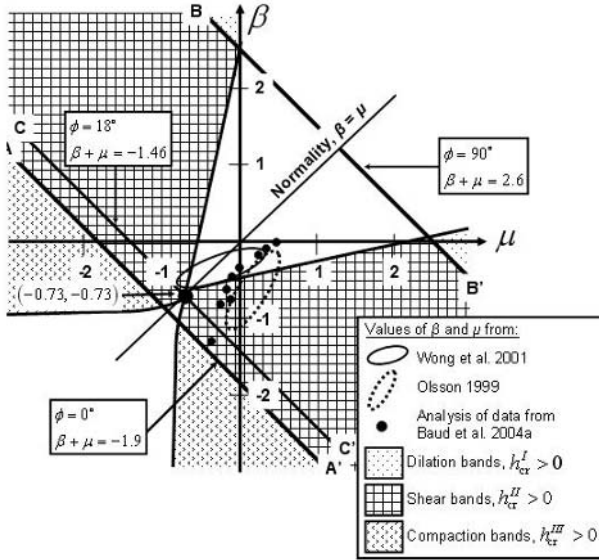


Fig. 4.3. Band orientation predictions as a function of β and μ for P_1 (J_3 independent SYSM, $\psi = \zeta = 0$). The $h_{cr} > 0$ in the shaded regions. Compaction bands ($\varphi = 0^\circ$) are predicted below $\beta + \mu = -1.9$, and dilation bands ($\varphi = 90^\circ$) are predicted above $\beta + \mu = 2.6$. Shear bands, with $0^\circ \leq \varphi \leq 90^\circ$, are predicted between AA' and BB'. The 18° shear band orientation is predicted along the CC' line ($\beta + \mu = -1.5$). The CC' line passes through the saddle point $(-0.73, -0.73)$, which has moved up along the $\beta = \mu$ line compared to ASC in Fig. 4.2

predicted between the bounds defined by: $-1.9 \leq \beta + \mu \leq 2.6$ (for $\nu = 0.2$). Compared to the results from the ASC stress state, the bounding lines (AA' and BB') for the P_1 stress state shift outward slightly. Therefore, shear bands are predicted in a slightly larger area of the $\beta - \mu$ plot. For both the ASC and P_1 stress states, using the J_3 independent model, only shear bands are predicted whereas shear and/or compaction bands were observed experimentally.

4.5 J_3 Dependent SYSM: P_1 Stress State, $\zeta = \psi$

Using the J_3 dependent model, two cases were investigated for the P_1 stress state: (1) assuming deviatoric normality ($\xi = \psi$), and (2) assuming deviatoric non-normality ($\xi \neq \psi$). For the first case, when the plastic

potential and yield surfaces are close to a circle ($\xi = \psi = -0.35$), band orientation predictions are shown in Fig. 4.4. Compared to the J_3 independent case (Fig. 4.3), the bounding lines AA' and BB' have moved out, so shear bands are predicted in a much larger region: $-2.5 \leq \beta + \mu \leq 2.7$ (for $\nu = 0.2$). Along $\beta = \mu$, and for small deviations from normality, the critical hardening modulus is always negative, and band formation is inhibited.

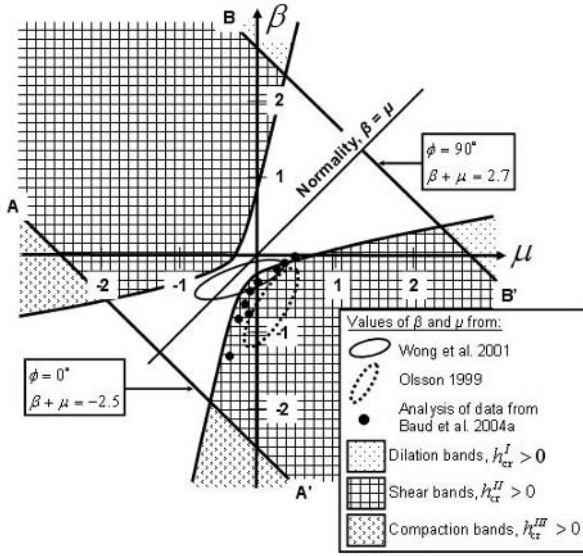


Fig. 4.4. Band orientation predictions as a function of β and μ for P_1 (J_3 dependent SYSM, $\xi = \psi = -0.35$, corresponding to a mild J_3 dependence). In the unshaded regions $h_{cr} < 0$ (always true along $\beta = \mu$). Compaction bands ($\phi = 0^\circ$) are predicted below $\beta + \mu = -2.5$, and dilation bands ($\phi = 90^\circ$) are predicted above $\beta + \mu = 2.7$. Shear bands, with $0^\circ \leq \phi \leq 90^\circ$, are predicted between AA' and BB'. Shear band conditions are more favorable than compaction band conditions

Although some of the experimental data lies within the region where $h_{cr} > 0$ (corresponding to localized deformation pre-peak), only shear bands are predicted. Compaction bands are predicted with $h_{cr}^{III} > 0$ only for large deviations from normality, with improbably large negative values of either β or μ . Therefore, the compaction band conditions are significantly less favorable for a stress state perturbed from ASC, if the material has a small J_3 dependence.

Figure 4.5 shows predictions when the yield and plastic potential surfaces are triangles, with $\xi = \psi = -1.41$ (corresponding to a large J_3 dependence). Compared with a small J_3 dependence (Fig. 4.4), the compaction band boundary, AA', has moved down significantly, such that compaction band formation is only possible for strongly negative values of

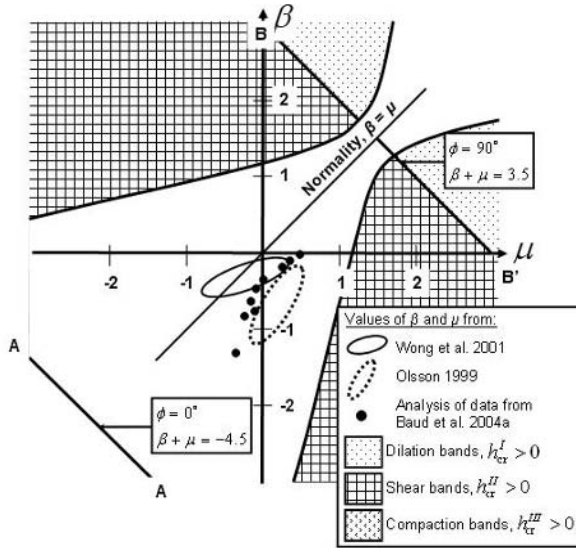


Fig. 4.5. Band orientation predictions as a function of β and μ for P_1 (J_3 dependent SYSM, $\psi = \xi = -1.41$, corresponding to a strong J_3 dependence). The $h_{cr} > 0$ in the shaded regions. Compaction bands ($\phi = 0^\circ$) are predicted below $\beta + \mu = -4.5$, and dilation bands ($\phi = 90^\circ$) are predicted above $\beta + \mu = 3.5$. Shear bands, with $0^\circ \leq \phi \leq 90^\circ$, are predicted between AA' and BB'. The $h_{cr} < 0$ in the unshaded regions and is always true along $\beta = \mu$. Localized deformation band formation is theoretically inhibited for possible values of β and μ

β and μ . Additionally, the boundary line for dilation bands, BB', moves up slightly. For this case, shear bands are predicted within a large region of the $\beta - \mu$ plot defined by the bounds: $-4.5 \leq \beta + \mu \leq 3.5$. However, $h_{cr} > 0$ is possible only with large deviations from normality. While the strongly negative values of β and μ required for compaction band formation might be possible for loading paths intersecting the cap portion of the yield surface (very close to the mean stress axis, at high confining pressures), the strong deviations from normality required are unlikely to occur for these loading paths. Additionally, all of the ASC experimental

data falls in a region where h_{cr} is a large negative number, indicating that localized deformation is inhibited. Therefore, for this case, for possible values of β and μ , the inception of localization should be prohibited. This is in accordance with results from high confining pressure ASC experiments, where uniform cataclastic flow, not strain localization, was observed (Wu et al. 2000).

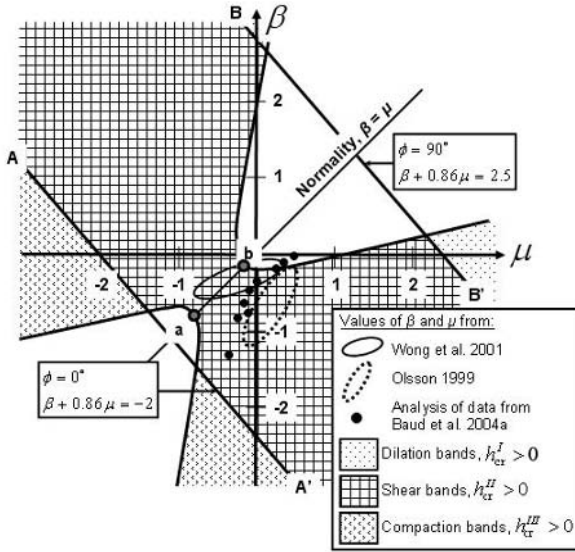


Fig. 4.6. Band orientation predictions as a function of β and μ for P_1 (J_3 dependent SYSM, $\psi = -0.35$, $\zeta = 0$, the plastic potential surface is independent of J_3 while the yield surface is mildly J_3 dependent). The $h_{cr} > 0$ in the shaded regions. Compaction bands ($\phi = 0^\circ$) are predicted below $\beta + 0.86\mu = -2$, and dilation bands ($\phi = 90^\circ$) are predicted above $\beta + 0.86\mu = -2.5$. Shear bands, with $0^\circ \leq \phi \leq 90^\circ$, are predicted between AA' and BB'. At points a and b, the 19° and 38° band orientations are predicted, respectively, with $h_{cr} > 0$. Conditions for low angle compacting shear bands are more favorable than those for compaction bands

Next, the influence of deviatoric non-normality ($\xi \neq \psi$) is investigated for the P_1 stress state. Unfortunately, we know of no experimental results for high porosity sandstones that could be used to guide selection of appropriate values for ξ and ψ , and there are many theoretically possible permutations. Therefore, the current work will explore only a few of the possible values for ξ and ψ , which satisfy deviatoric non-normality. Should

experimental results become available in the future, certainly a similar process could be used to conduct a more comprehensive evaluation.

4.6 J_3 Dependent SYSM: P_1 Stress State, $\xi \neq \psi$

Figure 4.6 shows band orientation predictions when the plastic potential surface is independent of J_3 , and the yield surface has a mild J_3 dependence so it is nearly circular ($\xi = 0$, $\psi = -0.35$). Shear bands are predicted between the bounding surfaces defined by: $-2 \leq \beta + 0.86\mu \leq 2.5$. The first band orientation predicted with $h_{cr} > 0$ along the $\beta = \mu$ line is the 19° shear band, which is indicated by point **a** in Fig. 4.6. At point **b** the 38° shear band is predicted with a positive h_{cr} . Therefore, shear bands with $22^\circ \leq \phi \leq 38^\circ$ are predicted to form with $h_{cr} > 0$ along normality, and for deviations from normality. Note that, when $\xi = \psi$, the AA' and BB' lines are symmetric about and perpendicular to $\beta = \mu$; this is no longer true when deviatoric non-normality is assumed. Conditions for the formation of compaction bands are again less favorable than for no J_3 dependence, since these bands are predicted with $h_{cr}^{III} > 0$ only for large deviations from normality and with large negative values of either β or μ .

When the yield surface is in between a circle and a triangle ($\psi = -0.71$), corresponding to a moderate J_3 dependence, and the plastic potential has mild J_3 dependence (closer to a circle, $\xi = -0.35$), the band orientation predictions are shown in Fig. 4.7. Along normality, shear bands within the range $\phi = 33^\circ$ (point **a**) and $\phi = 62^\circ$ (point **b**) are predicted with $h_{cr} > 0$, for small positive to small negative values of β and μ . Shear bands are predicted within the bounds defined by: $-2.8 \leq \beta + 0.86\mu \leq 2.6$. Compared to the case where deviatoric normality was assumed with a moderate J_3 dependence (Fig. 4.4), with increasing deviatoric non-normality, the AA' and BB' lines move outward, increasing the region on the $\beta - \mu$ plot where shear bands are predicted (Fig. 4.7).

When the yield surface is strongly J_3 dependent (a triangle, $\psi = -1.41$), and the plastic potential is mildly J_3 dependent (close to a circle, $\xi = -0.35$), band orientation predictions are illustrated in Fig. 4.8.

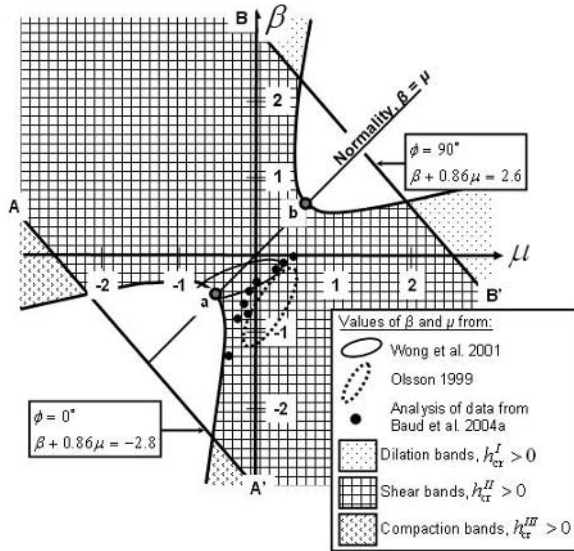


Fig. 4.7. Band orientation predictions as a function of β and μ for P_1 (J_3 dependent SYSM, $\psi = -0.71$, $\zeta = -0.35$). The $h_{cr} > 0$ in the shaded regions. Compaction bands ($\phi = 0^\circ$) are predicted below $\beta + 0.86\mu = -2.8$, and dilation bands ($\phi = 90^\circ$) are predicted above $\beta + 0.86\mu = 2.6$. Shear bands, with $0^\circ \leq \phi \leq 90^\circ$, are predicted between AA' and BB'. At points a and b, 33° and 62° band orientations are predicted, respectively, with $h_{cr} > 0$

Along normality, bands orientations varying from shear bands with $\phi = 47^\circ$ (point a), to dilation bands ($\phi = 90^\circ$, at point b), are predicted with a positive h_{cr} . Similar to the results discussed in the previous case (Fig. 4.7), compaction bands are predicted with $h_{cr} > 0$ only for large deviations from normality, and for large negative values of β ; both conditions are not commonly reported when compaction bands are observed experimentally. However, analogous to the prior discussion regarding Fig. 4.5, values of β and μ sufficiently positive to fall in the large region in Fig. 4.8 where $h_{cr} > 0$ (where dilating shear bands are predicted,

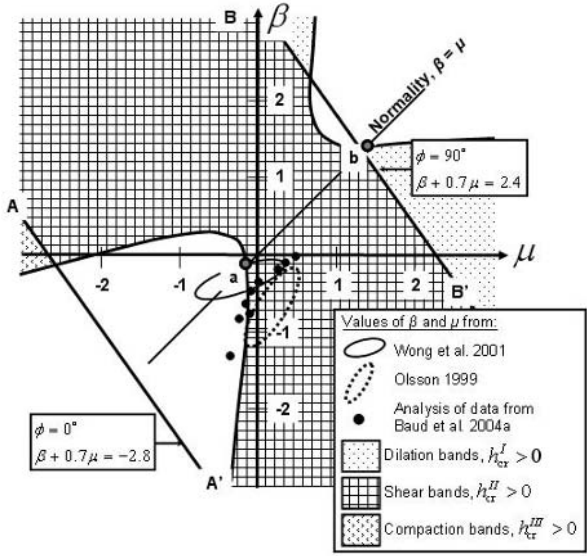


Fig. 4.8. Band orientation predictions as a function of β and μ for P_1 (J_3 dependent SYSM, $\psi = -1.41$, $\zeta = -0.35$). The $h_{cr} > 0$ in the shaded regions. Compaction bands ($\phi = 0^\circ$) are predicted below $\beta + 0.7\mu = -2.8$, and dilation bands ($\phi = 90^\circ$) above $\beta + 0.7\mu = 2.4$. Shear bands, with $0^\circ \leq \phi \leq 90^\circ$, are predicted between AA' and BB'. At point a, a 47° shear band is predicted, and at point b, dilation bands are predicted, both with $h_{cr} > 0$. Compaction bands are predicted only with large deviations from normality, and for improbably large negative values of β and μ

e.g., between points a) and b), could be produced by conducting experiments using a proper low mean stress loading path.

For non-normality in the deviatoric plane, the band orientation predictions are no longer arranged symmetrically on the $\beta - \mu$ plane (lines AA' and BB' in Figs. 4.6 – 4.8 are not perpendicular to the $\beta = \mu$ line). This asymmetry can be explained analytically by substituting the appropriate deviatoric and stress state parameters into 3.10 and expanding. For the P_1 stress state, when deviatoric normality is true, 3.10 simplifies to

$$-0.76 \leq \frac{0.4(\beta + \mu) - 0.37\xi}{1 - 0.45\xi} \leq 1.05 \tag{4.1}$$

For fixed values of $\xi (= \psi)$, the coefficients of β and μ in (4.1) are equal. Therefore, the bounding surfaces (AA' and BB' in Figs. 4.2 – 4.5) are symmetric about $\beta = \mu$. For deviatoric non-normality, (3.10) simplifies to:

$$-0.76 \leq \frac{0.4\beta - 0.187\xi}{1 - 0.45\xi} + \frac{0.4\mu - 0.187\psi}{1 - 0.45\psi} \leq 1.05 \quad (4.2)$$

where, due to the denominators in (4.2), the coefficients of β and μ are no longer equal. Therefore, bounding surfaces AA' and BB' (Figs. 4.6 – 4.8) are not symmetric about $\beta = \mu$.

To summarize, assuming deviatoric non-normality ($\xi \neq \psi$) for the P_1 stress state, with increasing J_3 dependence and increasing deviatoric non-normality, the $h_{cr} = 0$ lines, and the bounding lines within which shear bands are predicted, move further apart (Figs. 4.6 – 4.8). Additionally, for increasing deviatoric non-normality, along the $\beta = \mu$ line, shear bands with larger band angles are predicted with a positive h_{cr} . With increasing deviatoric non-normality and increasing J_3 dependence, the region on the $\beta - \mu$ plot where h_{cr} is positive becomes larger, and conditions become more favorable for shear band formation; conditions become less favorable for the formation of compaction bands. Although most of the experimental data falls in a region where $h_{cr} > 0$, conditions are observed to be more favorable for the formation of shear bands than for compaction bands. While the shear bands observed in ASC tests are predicted theoretically, the observed compaction bands are not predicted in any of these three cases investigated.

5 Summary and Conclusions

Recent experimental evidence suggests that the mechanical behavior of high porosity sandstones depends upon the third invariant of deviatoric stress (J_3). While J_3 dependent constitutive models have been developed by researchers (Lade 1977; Desai 1980; Desai and Faruque 1983; Desai et al. 1986; Desai and Salami 1987; Brown and Yu 1988; Lade and Kim 1988; Sture et al. 1989; Bardet 1990; Ottosen and Runesson 1991; Lade and Kim 1994; Schwer and Murray 1994; Fossum and Fredrich 2000; Krenk 2000) to describe the behavior of geomaterials, the analyses were not extended to determine conditions under which localized deformation could be possible. Additionally, while laboratory specimens are frequently tested under

axisymmetric stress states, there is some question whether stress states in the field are limited to these stress states. Therefore, there is a gap in the understanding of the behavior of this material, in particular the localization behavior, under non-axisymmetric stress states.

In this work, a J_3 dependent single yield surface constitutive model (SYSM) was developed for high porosity sandstones, and the conditions for the formation of localized bands were determined. Additionally, band orientation predictions were determined using this J_3 dependent SYSM for two stress states: ASC, and a stress state, P_1 , slightly perturbed from ASC. Analyses focused on examining conditions required for compaction band formation, since these bands have recently been identified in field settings and in laboratory specimens and their formation could influence fluid flow, and impact fluid extraction and storage applications.

The analyses conducted in this work reveal that the ASC stress state is a specialized case, where theoretical band orientation predictions remain insensitive to a dependence on J_3 . Therefore, under ASC (or ASE) the localization conditions, and the band orientation predictions, remain the same as those from the J_3 independent SYSM. For non-axisymmetric stress states, incorporating a J_3 dependence results in a large variation in the band orientation predictions for stress states even slightly perturbed from ASC. A similar analysis conducted for stress states slightly perturbed from ASE (results not presented here) reveals that the variation in band orientation predictions is small to moderate.

This work defined conditions for formation of a particular band orientation as “favorable,” when $h_{cr} \geq 0$ (where h is the hardening modulus, and $h_{cr} \geq 0$ corresponds to localization at or prior to the peak stress) is possible for normality ($\beta = \mu$, where β is the dilation coefficient, and μ is the friction factor) and/or for small deviations from normality. Conversely, conditions were defined as “unfavorable” when large deviations from normality are required to obtain $h_{cr} \geq 0$. The “optimal” band angle, for a given stress state, is that which provides the largest h_{cr} value for the smallest deviation from normality. For ASC (with or without J_3 dependence), the optimal band angle is a compaction band. For P_1 , when the material is independent of J_3 , the optimal band angle is an 18° shear band (a compacting shear band). For this case while compaction bands are possible when $\beta + \mu \leq -1.9$, for ASC, the less restrictive condition, $\beta + \mu \leq -\sqrt{3}$, is required for compaction band formation. For P_1 , shear bands are predicted on a larger area of the $\beta - \mu$ plot and compaction bands are predicted with $h_{cr} > 0$ only for large deviations from normality. Thus, conditions for compaction band formation are most favorable under ASC.

Several possible forms of J_3 dependence were examined for the P_1 stress state. For normality in the deviatoric plan, when a mild J_3 dependence is incorporated, compaction bands are only possible for $\beta + \mu \leq -2.5$, while for a strong J_3 dependence, $\beta + \mu \leq -4.5$ is required. As J_3 dependence increases, increasing deviations from normality are required to predict compaction bands with $h_{cr} \geq 0$. Additionally, for strong J_3 dependence, it seems unlikely that any form of localized deformation band formation is possible. Assuming deviatoric non-normality, there exists a region along normality where $h_{cr} > 0$ for a range of shear band angles. For mild to moderate J_3 dependence (and mild to moderate deviatoric non-normality), band angles between 19° and 62° correspond to $h_{cr} > 0$. For strong J_3 dependence (and larger deviatoric non-normality), the range of band angles is 47° to 90° . Therefore, the P_1 stress state with a J_3 dependent material, results in conditions favorable for shear band formation, but unfavorable (possibly prohibitive) for compaction band formation. Thus, if stress states in the field are even slightly perturbed from ASC, the preceding discussion provides a possible explanation for why shear bands are more frequently reported in the field than compaction bands.

The band orientation predictions from the ASC and P_1 stress states, with and without J_3 dependence, were compared with the available experimental data from ASC tests (data not available for P_1). For reported values of β and μ , the observed shear bands are predicted, but not the observed compaction bands. Some authors (Zhang et al. 1990; Wong et al. 1992; Menéndez et al. 1996; Wong et al. 1997; Wong et al. 2001) have reported that compaction bands typically form when high porosity sandstone is tested under stress states where multiple deformation mechanisms appear to be active. A J_3 independent two yield surface constitutive model (TYSM) (Issen 2002; Challa and Issen 2004; Issen and Challa 2005) predicts both experimentally observed compaction bands and shear bands for reported values of key material parameters. Additionally, predicted shear band angles generally agree with the range of reported band angles. The TYSM incorporates multiple active deformation mechanisms by considering a shear yield surface which corresponds to a dilatant, frictional mechanism and a cap which corresponds to a compactant mechanism. These results suggest that use of a TYSM may be more appropriate for describing the behavior of high porosity sandstone for stress states corresponding to the brittle – ductile transition, where compaction bands are commonly observed in experiments. Therefore, in an ensuing paper, a J_3 dependent TYSM will be developed, and the consequent localization conditions and band angle predictions investigated.

In the current work, experimental data from existing ASC tests on high porosity sandstones were used to conduct preliminary evaluations of the predictions from the J_3 dependent SYSM. However, the existing data cannot be used to determine accurate values of the deviatoric parameters specific to the J_3 dependent constitutive models, since ASC tests are not sufficient to characterize the shapes of the yield and plastic potential surfaces in the deviatoric plane. Additionally, we know of no existing experimental results for the P_1 stress state, which can be directly compared to the predictions for this stress state. Therefore, there is a definite need for additional experimental work, to examine the behavior of high porosity sandstones under non-axisymmetric stress states. These experimental results could be used to determine the degree of J_3 dependence of these materials and rigorously evaluate the theoretical predictions for loading under non-axisymmetric stress states. Additionally, findings from these experiments would enable determination of bounds on stress states that produce compaction bands, which could ultimately be useful in understanding compaction band formation in field settings.

Appendix A

The parameters that appear in (3.1) are defined as follows

$$H_1 = \frac{K}{3\cos 3\theta} \frac{\left(3\tan 3\theta \cos 3\theta N_{22} + 3\sqrt{3}Y_{22} - 2\sqrt{3}\right)}{\left(K + \frac{4}{3}G\right)} \quad (\text{A.1})$$

$$H_2 = \frac{1}{3\cos 3\theta \left(K + \frac{4}{3}G\right)} \left\{ \sqrt{3}GN_{22} (3Y_{22} - 2) \right. \\ \left. + 3\tan 3\theta \cos 3\theta \left[GN_{22}^2 + \left(K + \frac{4}{3}G\right)(N_{12}^2 + N_{23}^2) \right] \right. \\ \left. + 3\sqrt{3} \left(K + \frac{4}{3}G\right) (N_{12}Y_{12} + N_{23}Y_{23}) \right\} \quad (\text{A.2})$$

$$\begin{aligned}
 H_3 = & \frac{1}{\cos^2 3\theta \left(K + \frac{4}{3}G \right)} \left\{ \left(K + \frac{4}{3}G \right) (3Y_{12}^2 + 3Y_{23}^2 - \cos^2 3\theta) \right. \\
 & + 2\sqrt{3} \tan 3\theta \cos 3\theta \left[GN_{22}Y_{22} + 2 \left(K + \frac{4}{3}G \right) (N_{12}Y_{12} + N_{23}Y_{23}) \right] \\
 & + \tan^2 3\theta \cos^2 3\theta \left[\left(K + \frac{4}{3}G \right) (N_{12}^2 + N_{23}^2) + GN_{22}^2 \right] \\
 & \left. - \frac{4}{\sqrt{3}} \tan 3\theta \cos 3\theta GN_{22} + G_{22} (3Y_{22} - 4) + 4G/3 \right\}
 \end{aligned} \tag{A.3}$$

where N_{ij} and Y_{ij} are defined in (3.3) – (3.8). Terms H_1 , H_2 and H_3 in (A.1) – (A.3) are always negative for the P_1 stress state, and zero for the axisymmetric stress states. The parameters T_1 , T_2 , S_1 and S_2 , appearing in (3.9) – (3.12), are defined as:

$$T_1 = \left(\frac{K\beta}{G} + \frac{2\xi}{\sqrt{3} \sin 3\theta} \right) + \frac{\sqrt{3}\xi N_I N_{III}}{\sin 3\theta} \tag{A.4}$$

$$T_2 = \left(\frac{K\mu}{G} + \frac{2\psi}{\sqrt{3} \sin 3\theta} \right) + \frac{\sqrt{3}\psi N_I N_{III}}{\sin 3\theta} \tag{A.5}$$

$$S_1 = 1 + \xi \cot 3\theta + \frac{\sqrt{3}\xi N_{II}}{\sin 3\theta} \tag{A.6}$$

$$S_2 = 1 + \psi \cot 3\theta + \frac{\sqrt{3}\psi N_{II}}{\sin 3\theta} \tag{A.7}$$

In (3.12) the terms q_1^J and q_2^J are defined as

$$q_1^J = \psi \left[-\frac{\sqrt{3}N_J^2}{\sin 3\theta} + N_J \cot 3\theta + \frac{2}{\sqrt{3}\sin 3\theta} \right] \tag{A.8}$$

$$q_2^J = \xi \left[-\frac{\sqrt{3}N_J^2}{\sin 3\theta} + N_J \cot 3\theta + \frac{2}{\sqrt{3}\sin 3\theta} \right] \tag{A.9}$$

It is important to note that, when $\xi = \psi = 0$ (corresponding to (1) circular yield and plastic potential surfaces, and (2) ASC and ASE stress states), the variables in (A.4) – (A.9) simplify to $T_1 = K\beta/G$, $T_2 = K\mu/G$, $S_1, S_2 \rightarrow 1$ and $q_1^J, q_2^J \rightarrow 0$.

Acknowledgements

The authors gratefully acknowledge Dr. T.-f. Wong and Dr. P. Baud for allowing us access to their triaxial test data. We also acknowledge financial support from the National Science Foundation, Directorate for Geosciences, Division of Earth Sciences, grants EAR-0106932 and EAR-0310085 to Clarkson University, in collaboration with Dr. T.-f. Wong of SUNY Stony Brook. Any opinions, findings and conclusions or recommendations expressed in this paper are those of the authors and do not necessarily reflect the views of the National Science Foundation.

References

1. Ashby MF, Evans AG, Fleck NA, Gibson LJ, Hutchinson JW, Wadley HNG (2000) *Metal Foams: A Design Guide*. Massachusetts: Butterworth-Heinemann
2. Aydin A (1978) Small faults formed as deformation bands in sandstone. *Pure and Applied Geophysics*: 116: 913–930
3. Bardet JP (1990) Lode dependences for isotropic pressure-sensitive elastoplastic materials. *Journal of Applied Mechanics*: 57: 498–506
4. Bastawros A, Evans AG (2000) Deformation heterogeneity in cellular Al alloys. *Advances in Engineering Materials*: 2: 210–214
5. Baud P, Klein E, Wong T-f (2004a) Compaction localization in porous sandstones: spatial evolution of damage and acoustic emission activity. *Journal of Structural Geology*: 26: 603–624
6. Baud P, Vajdova V, Wong T-f (2004b) Shear-enhanced compaction and strain localization: Mechanical deformation and constitutive parameters for porous sandstones. Submitted to *Journal of Geophysical Research*
7. Brown ET, Yu HS (1988) A model for the ductile yield of porous rock. *International Journal for Numerical and Analytical Methods in Geomechanics*: 12: 679–688
8. Cashman S, Cashman K (2000) Cataclasis and deformation-band formation in unconsolidated marine terrace sand, Humboldt County, California. *Geology*: 28(2): 111–114

9. Challa V, Issen KA (2004) Conditions for compaction band formation in porous rock using a two yield surface model. *Journal of Engineering Mechanics*: 130(9): 1089–1097
10. Desai CA (1980) A general basis for yield, failure, and potential functions in plasticity. *International Journal for Numerical and Analytical Methods in Geomechanics*: 4: 361–375
11. Desai CS, Faruque MdO (1983) Constitutive model for (geological) materials. *Journal of Engineering Mechanics*: 110(9): 1391–1408
12. Desai CS, Salami MR (1987) A constitutive model and associated testing for soft rock. *International Journal of Rock Mechanics and Mining Sciences and Geomechanical Abstracts*: 24(5): 299–307
13. Desai CS, Somasundaram S, Frantziskonis G (1986) A hierarchical approach for constitutive modelling of geologic materials. *International Journal for Numerical and Analytical Methods in Geomechanics*: 10: 225–257
14. DiGiovanni AA, Fredrich JT, Holcomb DJ, Olsson WA (2000) Micromechanics of compaction in an analogue reservoir sandstone. *Proceedings of the North American Rock Mechanics Symposium*: 1153–1158, Ed. J Girard, M Liebman, C Breeds, T Doe, AA, Pub. AA Balkema
15. Du Bernard X, Eichhubl P, Aydin A (2002) Dilation bands: A new form of localized failure in granular media. *Geophysical Research Letters*: 29(24): 2176. DOI:10.1029/2002GL015966
16. Dunn DE, LaFountain LJ, Jackson RE (1973) Porosity dependence and mechanisms of brittle fracture in sandstones. *Journal of Geophysical Research*: 78(14): 2403–2471
17. Fossum FA, Fredrich JT (2000) Cap plasticity models and compactive and dilatant pre-failure deformation. *Pacific Rocks 2000, Proceedings of the 4th North American Rock Mechanics Symposium*: 1169–1176
18. Haimson BC (2001) Fracture-like borehole breakouts in high porosity sandstone: Are they caused by compaction bands? *Physics and Chemistry of the Earth (A)*: 26(1-2): 15–20
19. Haimson BC, Song I (1998) Borehole breakouts in Berea sandstone: two porosity-dependent distinct shapes and mechanisms of formation. *Rock Mechanics in Petroleum Engineering: Society of Petroleum Engineers*, 1: 229–238
20. Holcomb DJ, Rudnicki JW (2001) Inelastic constitutive properties and shear localization in Tennessee marble. *International Journal for Numerical and Analytical Methods in Geomechanics*: 25: 109–129
21. Issen, KA (2002) The influence of constitutive models on localization conditions for porous rock. *Engineering Fracture Mechanics*: 69: 1891–1906
22. Issen KA, Challa V (2005) Strain Localization Conditions in Porous Rock Using a Two Yield Surface Constitutive Model. *SP245 High-Strain Zones: Structure and Physical Properties*: edited by D. Bruhn and L. Burlini, Geological Society of London Special Publications

23. Issen KA, Challa V (submitted) Influence of the Intermediate Principal Stress on the Strain Localization Mode in Porous Rock. *Journal of Geophysical Research*.
24. Issen KA, Rudnicki JW (2000) Conditions for compaction bands in porous rock. *Journal of Geophysical Research*: 105(B9): 21529–21536
25. Issen KA, Rudnicki JW (2001) Theory of compaction bands in porous rock. *Physics and Chemistry of the Earth*: 26(1-2): 95–100
26. Krenk S (2000) Characteristic state plasticity for granular materials Part I: Basic theory. *International journal of Solids and Structures*: 37: 6343–6360
27. Lade PV (1977) Elasto-plastic stress-strain theory for cohesionless soil with curved yield surfaces. *International Journal of Solids and Structures*: 13: 1019–1035
28. Lade PV, Kim MK (1988) Single hardening constitutive model for frictional materials II. Yield criterion and plastic work contours. *Computers and Geotechnics*: 6: 13–29
29. Lade PV, Kim MK (1994) Single hardening constitutive model for soil, rock and concrete. *International Journal of Solids and Structures*: 32(14): 1963–1978
30. Klein E, Baud P, Reuschlé T, Wong T-f (2001) Mechanical behavior and failure mode of Bentheim sandstone under triaxial compression. *Physics and Chemistry of the Earth*: 26(1-2): 21–25
31. Mair K, Main I, Elphick S (2000) Sequential growth of deformation bands in the laboratory. *Journal of Structural Geology*: 22: 25–42
32. Menéndez B, Zhu BW, Wong T-f (1996) Micro mechanics of brittle faulting and cataclastic flow in Berea sandstone. *Journal of Structural Geology*: 18(1): 1–16
33. Mollema PN, Antonellini MA (1996) Compaction bands: a structural analog for anti-mode I cracks in Aeolian sandstone. *Tectonophysics*: 267: 209–228
34. Odgaard A, Hvid I, Linde F (1989) Compressive axial strain distributions in cancellous bone specimens. *Journal of Biomechanics*: 22(8/9): 829–835
35. Olsson WA (1999) Theoretical and experimental investigation of compaction bands in porous rocks. *Journal of Geophysical Research*: 104(B4): 7219–7228
36. Olsson WA (2001) Quasistatic propagation of compaction fronts in porous rocks. *Mechanics of Materials*: 33: 659–668
37. Olsson WA, Holcomb DJ (2000) Compaction localization in porous rock. *Geophysical Research Letters*: 27(21): 3537–3540
38. Olsson WA, Holcomb DJ, Rudnicki JW (2002) Compaction localization in porous sandstone: Implications for reservoir mechanics. *Oil & Gas Science and Technology*: 57: 591–599
39. Ottosen NS, Runesson K (1991) Properties of discontinuous bifurcation solutions in elasto-plasticity. *International Journal of Solids and Structures*: 27(4): 401–421
40. Papka SD, Kyriakides S (1999) Biaxial crushing of honeycombs – Part I: Experiments. *International Journal of Solids and Structures*: 36: 4367–4396

41. Perrin G, Leblond JB (1993) Rudnicki and Rice's analysis of strain localization revisited. *Journal of Applied Mechanics*: 60: 842–846
42. Rudnicki JW, Rice JR (1975) Conditions for the localization of deformation in pressure-sensitive dilatant materials. *Journal of Mechanics and Physics of Solids*: 23: 371–394
43. Schwer LE, Murray YD (1994) A three-invariant smooth cap model with mixed hardening. *International Journal for Numerical and Analytical Methods in Geomechanics*: 18: 657–688
44. Scott TE, Nielsen KC (1991) The effects of porosity on the brittle-ductile transition in sandstones. *Journal of Geophysical Research*: 96(B1): 405–414
45. Sternlof KR, Chapin JR, Pollard DD, Durlafsky LJ (2004) Permeability effects of deformation band arrays in sandstone. *AAPG Bulletin*: 88(9): 1315–1329
46. Sture S, Runesson K, Macari-Pasqualino EJ (1989) Analysis and calibration of a three-invariant plasticity model for granular materials. *Ingenieur-Archiv*: 59: 253–366
47. Wawersik WR, Orr Jr FM, Rudnicki JW, Ortoleva PJ, Dove P, Richter F, Harris J, Warpinski NR, Logan JM, Wilson JL, Pyrak-Nolte L, Wong T-f (2001) Terrestrial sequestration of CO₂: An assessment of research needs. *Advances in Geophysics*: 43: 97–177
48. Wong T-f, Baud P, Klein E (2001) Localized failure modes in a compactant porous rock. *Geophysical Research Letters*: 28(13): 2521–2524
49. Wong T-f, David D, Zhu W (1997) The transition from brittle faulting to cataclastic flow in porous sandstones: Mechanical deformation. *Journal of Geophysical Research*: 102(B2), 3009–3025
50. Wong T-f, Szeto H, Zhang J (1992) Effect of loading path and porosity on the failure mode of porous rocks. *Applied Mechanics Review*: 45(8): 261–293
51. Wu XY, Baud P, Wong T-f (2000) Micromechanics of compressive failure and spatial evolution of anisotropic damage in Darley Dale sandstone. *International Journal of Rock Mechanics and Mining Sciences*: 37: 143–160
52. Zhang J, Davis DM, Wong T-f (1993) The brittle-ductile transition in porous sedimentary rocks: geological implications for accretionary wedge aseismicity. *Journal of Structural Geology*: 15(7): 819–830
53. Zhang J, Wong T-f, Davis DM (1990) Micromechanics of pressure-induced grain crushing in porous rock. *Journal of Geophysical Research*: 95(B1): 341–352
54. Zhu W, Montesi LG.J, Wong T-f (1997) Shear-enhanced compaction and permeability reduction: Triaxial extension tests on porous sandstone. *Mechanics of Materials*: 25: 199–214

Interpretation of the Scale Effect in Perforation Failure

Panos Papanastasiou

Department of Civil and Environmental Engineering
University of Cyprus
P.O. Box 20537, 1678 Nicosia, Cyprus
E-mail: panospap@ucy.ac.cy

Summary

In this paper we examine a borehole failure model which is based on fracture mechanics and layer buckling theories in the light of experimental data. The model assumes that the main mechanism of borehole collapse takes place in the form of (pre-existing or formed) layers buckling [1]. The model introduces a combination of fracture mechanics parameters with length dimension that scale the size of the holes allowing for size effect predictions. We present and compare the model predictions with available experimental data. For the model predictions as well the experimental data we found a strong correlation between hole strength normalized by the uniaxial compressive strength and hole size normalized by the square of the division of rock fracture toughness over its tensile strength. These findings can be used for constructing mechanical models to predict failure in small size holes such as perforations.

1 Introduction

Hollow cylinder tests on different size holes showed that the most dominant factor in the range of perforation size (less than 25 mm) is the scale effect. Results on the dependence of the hole strength on its size were presented in references [2], [6], [10] and in other studies over the last three decades. From all these results it was made clear that small holes are much stronger than large holes.

For practical applications modelling of the dependence of the hole strength on its size (scale effect) becomes important in the case where the stability of wellbore in the field is assessed using hollow cylinder test data. The existence of the scale effect was ignored for many years and the

Elastic models were blamed for failing to predict correctly the hollow cylinder experimental data. Later it was made clear that plasticity models are also inadequate to predict the scale effect since they are short of an internal length (microstructure) for scaling the size of a hole. Nevertheless, a properly calibrated plasticity model is in a position to predict correctly the stability of a large size wellbore as long no attempt is made to calibrate it with hollow cylinder tests.

The importance of the scale effect is much more important for predicting failure around a perforation since the size of the perforations fall in the range where the scale effect is dominant. We mention here that sanding experiments run in hollow cylinders indicated that in weakly consolidated rocks, stress induced failure occurs before sand production. The role of fluid-flow is mainly restricted in transferring the loose sand grains which fall into the cavity after failure. During field production, failure takes place mainly due to increase of the effective stresses after depletion and secondary due to increase of draw-down pressure. Therefore, in the sand prediction modelling emphasis was put on predicting and avoiding rock failure.

Models which can account for the scale effect in borehole failure were based on bifurcation analyses with higher order continuum models. These models introduce the microstructure of the rock into the constitutive equations in the form of extra degrees of freedom such as grain rotation [8], [9] or higher order terms of the deformation gradient [13]. As an example we show in Figure 1.1 the predictions of a Cosserat model for the load at which bifurcation takes place (dashed line) and the peak load (solid line) as a function of the hole radius normalized by an internal length related to the average grain size [9]. The computations were performed for material parameters of Castlegate sandstone and models with different internal radii but with fixed ratio 5:1 of the external radius to the internal. It is clear that both bifurcation and peak loads increase as the hole radius decreases. For very small holes bifurcation does not take place and limit point is reached. Smaller holes bifurcate with lower warping modes. The scale effect fades out rapidly with increasing hole size. As the hole gets bigger, the scale effect becomes less pronounced, a tendency also observed in the experiments of references [2], [6], [10]. The scale effect fades out also for very small hole size because bifurcation disappears and the load reaches a limit value. This finding is also supported by experimental results discussed in detail in reference [11]. Such models are usually employed in non-linear finite element analyses that are computationally intensive and not easy to use for practical applications. In addition, the use of such models is limited also by the issue of material parameters determination, such as the rate of softening and the value of the internal

length. The rate of softening can not be measured directly in a mechanical test and an inverse matching procedure of the test results with a localization model shall be employed. For the identification of the internal length it was suggested that is related to the average diameter of the sandstone grain or to the assembly of grains. An account of these models for borehole failure prediction was presented in reference [9] in a hierarchical approach covering a wide range of models from linear elasticity to post-bifurcation analysis. It is also true that the scale effect observed in hollow cylinder tests is more dramatic than the predictions of Figure 1. However, the predicted scale effect of Figure 1 may become more pronounced by varying the model parameters such as the rate of softening or the dilation angle.

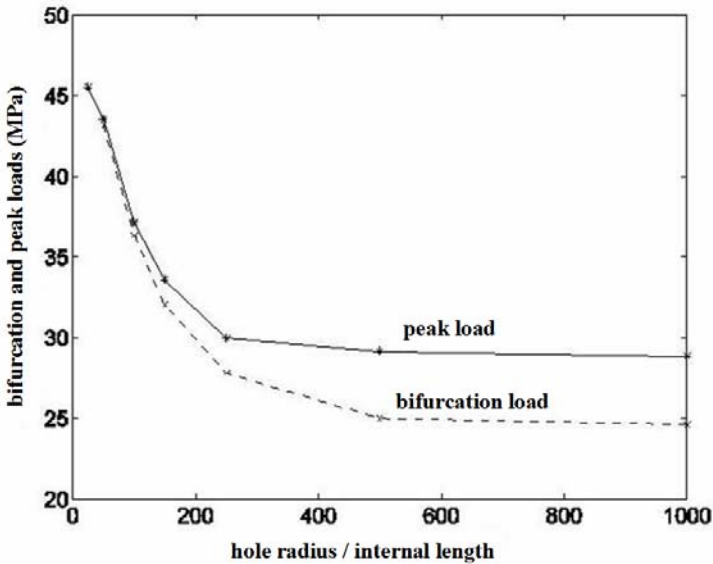


Figure 1.1. Bifurcation and peak loads versus normalized hole radius as predicted by Cosserat model

Due to the importance of the size effect on hole strength and in general of the collapse mechanism around a borehole, we investigate in this study an alternative approach based on fracture mechanics and buckling theories. The objective is always to derive an analytical solution for predicting hole collapse taking into account the size effect. We follow the model proposed in [1] and we examine its predictions in the light of the available experimental data. The model considers buckling of layers as the main

mechanism of borehole instability. The layers pre-exist or formed due to crack growth. This type of failure mechanism was clearly seen in laboratory experiments performed on shale samples [5].

In the next section, we present the basic equations upon which the model is based. In section 3 we present the calibration of the model and in section 4 we present and discuss the results of parametric studies in comparison with experimental data. The main conclusions are summarized in section 5.

2 Mathematical Model

A number of papers assumed that the main mechanism of borehole collapse takes place in the form of buckling layers (pre-existing or formed). These theories introduce micro-mechanical parameters related to the layer thickness and fracture mechanics parameters. Such approach was examined first in composite materials in [3] considering the failure stress required to buckle a thin surface of layer material under compression. In rock mechanics, the layer buckling approach, among others, was adopted in [12], [1] and recently in [4] for modelling rockburst and breakouts near an underground opening. In this study we will investigate the model presented in [1]. In the following, we summarize the basic equations of the model.

A borehole of radius R is embedded in an infinite elastic medium and is subjected to a uniform remote stress field. The deformation perpendicular to the hole axis is in plane strain state. The failure in general, tends to enlarge the hole axis to an elliptical shape in the direction of breakouts which is usually along the minimum *in situ* stress. It is assumed that the shape of the wellbore does not change in the other perpendicular direction along which the wellbore remains circular of radius R (Figure 2.1).

As it is mentioned the breakout area is formed by buckling of layers which pre-exist, like in the case of laminated shales [5], or formed due to growth of axial splitting cracks in mode-I. The length of these layers are bounded by the formation of shear bands or mode-II cracks. These shear bands or mode-II cracks are bending to meet each other in some distance in the interior of the rock. Therefore, the length of the buckling layers decreases with the distance from the hole center suggesting that the failure process will stabilize at some depth beyond the hole boundary for constant applied stress field. Furthermore, research work to consider anisotropic rocks is currently under progress.

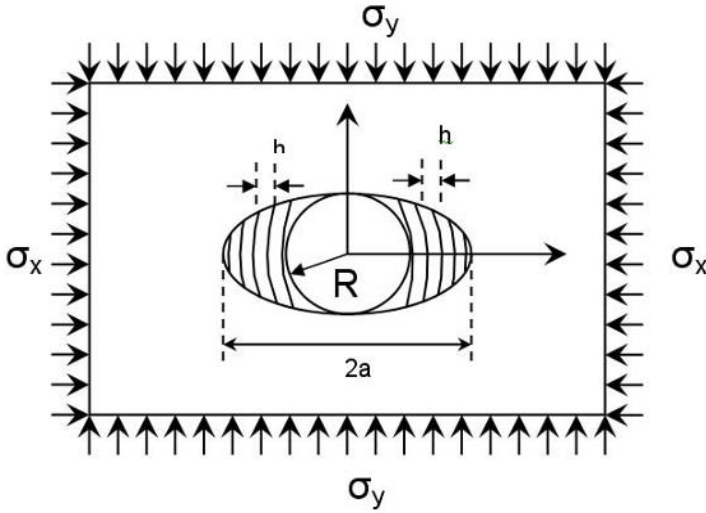


Figure 2.1. Failure around a hole in the form of buckling and growth of the cavity in elliptical shape

Based on Eshelby's solution, the energy release due to growth (or cutout) of an elliptical cavity of long axis $a > R$ in an initially uniformly stressed infinite elastic space is

$$\Delta\Pi_1 = -\frac{\pi}{2E'} \left[(a + 2R)R\sigma_x^2 + (2a + R)a\sigma_y^2 - 2aR\sigma_x\sigma_y \right] \quad (2.1)$$

where $E' = E/(1 - \nu^2)$ is the plane strain modulus. $\Delta\Pi_1$ represents the sum of the work of the stresses on the strain changes outside the ellipse which is non-uniformly distributed and decay with distance from the ellipse, and the work of the stresses on the strain changes inside the elliptical cut-out which, according to Eshelby's theorem, are uniformly distributed. Equation (2.1) gives the potential energy when the stresses within the ellipse are reduced to zero. The potential energy change when the initial stress σ_y is reduced to a critical stress value σ_{cr} , rather than zero is [1]

$$\Delta\Pi_1' = -\frac{\pi}{2E'} \left[(a + 2R)R\sigma_x^2 + (2a + R)a\sigma_y^2 - 2aR\sigma_x\sigma_y - 2a^2\sigma_{cr}^2 \right] \quad (2.2)$$

In the limit case of $R \rightarrow 0$, the elliptical hole becomes a crack and equation (2.1) yields the expression for the energy loss for creating a crack of length $2a$ in an infinite space,

$$\Delta\Pi_1 = -\frac{\pi}{E'}\sigma_y^2 a^2 \quad (2.3)$$

The potential energy change for the case of no cavity to the case of a circular cavity of radius R is obtained from (2.1) by setting $a=R$

$$\Delta\Pi_0 = -\frac{\pi R^2}{2E'}[3\sigma_x^2 + 3\sigma_y^2 - 2\sigma_x\sigma_y] \quad (2.4)$$

The potential energy change when the stress in the area between the original circle and the circumscribed ellipse is reduced from σ_y to σ_{cr} is obtained by subtracting (2.4) from (2.2)

$$\Delta\Pi_1' = \Delta\Pi_1' - \Delta\Pi_0 = -\frac{\pi}{2E'} \left[(aR - R^2)\sigma_x^2 + (2a^2 + Ra - 3R^2)\sigma_y^2 + 2R(R - a)\sigma_x\sigma_y - 2a^2\sigma_{cr}^2 \right] \quad (2.5)$$

Fracturing under compression creates a system of parallel, equidistant, splitting cracks parallel to the direction of the maximum principal stress σ_y (Figure 2.1). The stress carried by the slabs of thickness h between the cracks is limited by elastic buckling, analogous of a fixed-end column of length $2L$ equal to the crack length. Therefore, the vertical compressive stress will not be zero but will have the Euler bifurcation load given by

$$\sigma_{cr} = -\frac{\pi^2}{L^2} \frac{E'h^2}{12} \quad (2.6)$$

Assuming that the mode of failure in small and large holes is geometrically similar, the half-length of the cracks can be expressed as

$$L = \kappa R \quad (2.7)$$

where κ is empirical constant usually less than 1.

In addition, in compressive buckling the crack opening displacement is zero and due to the roughness of the crack faces in the rock, a shear stress is transmitted resulting in increase of the critical stress according to [1]

$$\sigma_{cr} = -\frac{\pi^2}{L^2} \frac{E'h^2}{12} - \frac{h}{\lambda} G \quad (2.8)$$

where λ is an empirical length (material property) and G is the elastic shear modulus. The work of shear stress is neglected at the initiation of buckling.

The residual strain energy contained in the zone between ellipse and the initial circle is given by the bending energy of all the slabs, approximately expressed as

$$\Pi_{cr} = (\pi\alpha R - \pi R^2) \frac{\sigma_{cr}^2}{2E'} = \frac{\pi R(\alpha - R)}{2E'} \left(\frac{\pi^2}{\kappa^2 R^2} \frac{E'h^2}{12} + \frac{h}{\lambda} G \right)^2 \quad (2.9)$$

The energy loss due to changing from a circular hole in elastic rock to a damaged elliptical zone of splitting cracks is

$$\Delta\Pi = \Delta\Pi_1' - \Delta\Pi_0 + \Pi_{cr} \quad (2.10)$$

On the other hand, the dissipated energy in rock fracturing is the sum of the energy dissipated in all the splitting cracks [1]

$$\Delta W_f = (\pi\alpha R - \pi R^2) \frac{G_f}{h} \quad (2.11)$$

The energy balance requires that

$$-\Delta\Pi = \Delta W_f \quad (2.12)$$

Assuming that the parallel cracks are formed progressively, equation (2.12) can be differentiated with respect to α to derive the incremental energy balance relation

$$-\frac{\partial(\Delta\Pi)}{\partial\alpha} = \frac{\partial(W_f)}{\partial\alpha} \quad (2.13)$$

which results in

$$\begin{aligned} \frac{\pi}{2E'} \left[R\sigma_x^2 + (4a + R)\sigma_y^2 - 2R\sigma_x\sigma_y - 4a\sigma_{cr}^2 \right] = \\ \frac{\pi R}{2E'} \left(\frac{\pi^2 E'h^2}{12\kappa^2 R^2} + \frac{h}{\lambda} G \right)^2 + \frac{\pi R G_f}{h} \end{aligned} \quad (2.14)$$

The initiation of breakouts occurs for $\alpha=R$, and for this value of α in equation (2.14) we obtain

$$\left[\sigma_x^2 + 5\sigma_y^2 - 2\sigma_x\sigma_y - 4\sigma_{cr}^2\right] = \left(\frac{\pi^2 E' h^2}{12\kappa^2 R^2} + \frac{h}{\lambda} G\right)^2 + \frac{2E'G_f}{h} \quad (2.15)$$

Noticing that the remote effective applied stress can be expressed by

$$\sigma_{ef}^2 = (\sigma_x^2 + 5\sigma_y^2 - 2\sigma_x\sigma_y) / 5 \quad (2.16)$$

equation (2.15) is written in the form

$$\sigma_{ef}^2 = \left(\frac{\pi^2 E' h^2}{12\kappa^2 R^2} + G \frac{h}{\lambda}\right)^2 + \frac{2E'G_f}{5h} \quad (2.17)$$

The minimum applied stress σ_{ef} will occur for the width of splitting crack spacing h that minimizes the *RHS* of equation (2.17) [1]. This value can be obtained from differentiation of the *RHS* of equation (2.17) with respect to h resulting in

$$\frac{5\pi^4 E'^2}{72\kappa^4 R^4} h^5 + \frac{15\pi^2 E'G}{12\kappa^2 R^2 \lambda} h^4 + \frac{5G^2}{\lambda^2} h^3 - E'G_f = 0 \quad (2.18)$$

The algebraic equation (2.18) can be solved numerically to obtain the value of h and then the applied effective stress σ_{ef} from equation (2.17). Bounds for the solution of h are derived for holes of small radius R by neglecting the 2nd and 3rd terms, in comparison with the 1st term,

$$h = \left(\frac{72\kappa^4 G_f}{\pi^4 E'}\right)^{1/5} R^{4/5} \quad (2.19)$$

and for holes of very large R

$$h = \left(\frac{E'G_f \lambda^2}{5G^2}\right)^{1/3} \quad (2.20)$$

Equation (2.19) suggests that the splitting crack spacing h will increase with radius R but will reach a constant value for sufficient large holes.

Bazant et al. [1] obtained the solution for small holes by replacing the value of h from equation (2.19) in equation (2.17),

$$\sigma_{ef} = C_1 R^{-2/5}, C_1 = \left(\frac{\pi^2 5^{1/2}}{48\kappa^2} E'^3 G_f^2\right)^{1/5} \quad (2.21)$$

and the solution for large holes by replacing the value of h from equation (2.20) in equation (2.17),

$$\sigma_{ef} = C_0, \quad C_0 = 3 \left(\frac{GE'G_f}{5\lambda} \right)^{1/3} \quad (2.22)$$

For the intermediate values of R they suggested an approximate solution by combining equations (2.21) and (2.22)

$$\sigma_{ef} \approx C_1 R^{-2/5} + C_0 \quad (2.23)$$

As we can see in the next section of the results, the proposed approximate solution (2.23) is not that close to the full solution (2.17) for practical applications.

3 Model Calibration

In this section we will explain how we obtained the different parameters required by the model in equations (2.17) to (2.22). Table 3.1 shows the material parameters of three sandstones which were used in hollow cylinder experiments [6], [11], the results of which will be compared with the model predictions in the next section. These parameters are the Young's modulus E and the Poisson's ratio ν , the Uniaxial Compressive Strength, UCS, and an approximate value for the fracture toughness, K_{IC} . The values for the shear modulus, G , and the plane strain elastic modulus, E' are given by

$$G = \frac{E}{2(1+\nu)}, \quad E' = \frac{E}{(1-\nu^2)} \quad (3.1)$$

The energy release rate G_f per crack tip can be calculated from

$$G_f = K_{IC}^2 / E' \quad (3.2)$$

The numbers of the fracture toughness shown in Table 3.1 are approximate values since there are no known data for fracture toughness for these particular rocks. These values are in the expected range for weak rocks, $0 - 2.5 \text{ MPa m}^{1/2}$, nearly proportional to the rock strength and in particular to the tensile strength. A good approximate value for the tensile strength of a rock is about,

$$\sigma_T \approx UCS/10 \quad (3.3)$$

Nevertheless, in the next section we will show sensitivity of the results to the fracture toughness value. In order to determine the unknown parameter λ , we used first the asymptotic solution for large holes shown by the experimental results

$$C_0 = \left(\frac{4}{5}\right)^{1/2} 1.43 UCS \quad (3.4)$$

and then we solved for λ equation (2.22). The factor coefficient 1.43 is obtained from the asymptotic solution for large holes suggested by experimental data [6], [10]. The factor $\left(\frac{4}{5}\right)^{1/2}$ in equation (3.4) is due to the relation (2.16) for isotropic loading

$$s_{ef} = \left(\frac{4}{5}\right)^{1/2} HCS \quad (3.5)$$

Table 3.1. Calibration parameters for fracture mechanics model

Sandstone	Elastic modulus (MPa)	Poisson's ratio	Uniaxial Compressive Strength (MPa)	Tensile Strength = UCS/10 (MPa)	Fracture toughness (MPa m ^{1/2})
Berea	17300	0.27	27	2.7	2.5
Castlegate	6830	0.178	10	1.0	1.0
Red Wildmoor	3400	0.20	6	0.6	0.5

Another relatively unknown parameter in the model is κ which gives the half length of the splitting cracks as a proportion of the hole radius in equation (2.7). Bazant et al. [1] suggested a value near 0.25 which is found

in this study to produce good results. Experimental results [5] and finite element modeling [8] suggest that the value of κ may vary in the range of 0 to 1. In anyway, sensitivity of the results to the parameter κ will also be investigated in the next section.

4 Results and Discussion

Figure 4.1 shows the predicted hole strength by the model for different values of the parameter κ and comparison with experimental data on Berea sandstone. It is clear that the model gives almost accurate predictions for κ close to 0.25 which means that the length of the splitting cracks and formed slabs are close to $0.5R$. Figure 4.2 shows the calculated width of the slabs normalized by the grain size of Berea sandstone. The results show that for very small holes the calculated theoretical width can be less than the grain size. This suggestion is not appear to be realistic. Greater range of small hole size where the results can be permissible is obtain again for κ close to 1.

Figure 4.3 shows the sensitivity of the model to the value of the rock fracture toughness. The results are quite sensitive to the fracture toughness value in the range of the very small holes. For small size holes the width of the slab is almost independent of the fracture toughness but it varies for medium and large holes (Figure 4.4). For a constant fracture toughness the slab width reaches an asymptotic value above a certain hole radius.

Figure 4.5 shows the predictions of the hollow cylinder strength for different values of fracture toughness and comparison with experimental results on Castlegate sandstone. Similar results are shown in Figure 4.6 for Red Wildmoor sandstone. The relative variation of fracture toughness is greater in Figure 4.6 since the larger spread of the predicted results. Figure 4.7 shows the best predictions obtained by the model in comparison with the experimental results on the three sandstones. The same results are also compared in Figure 4.8 with the approximate solution suggested in reference [1], equation (2.23). We observe that the approximate solution deviates significantly from the full solution.

In Figure 4.9 we attempted normalization of all the theoretical and experimental results shown in Figure 4.7. The results in the vertical axis were normalized by the UCS of each rock. The results in the horizontal axis were normalized by the parameter $(K_{IC} / \sigma_T)^2$ which has a length unit in order to obtain a final dimensionless form. After normalization the dimensionless results collapse in a narrow band supporting a strong correlation. This correlation suggests that it is possible to derive an appa-

rent strength model which can be further employed in a stress analysis for predicting perforation failure. The model is based on parameters which are measurable and easy to obtain or interpret. The only parameter that appears to be difficult to obtain from the field data is the rock fracture toughness. Nevertheless, it may be possible to interpret it from correlation functions with UCS.

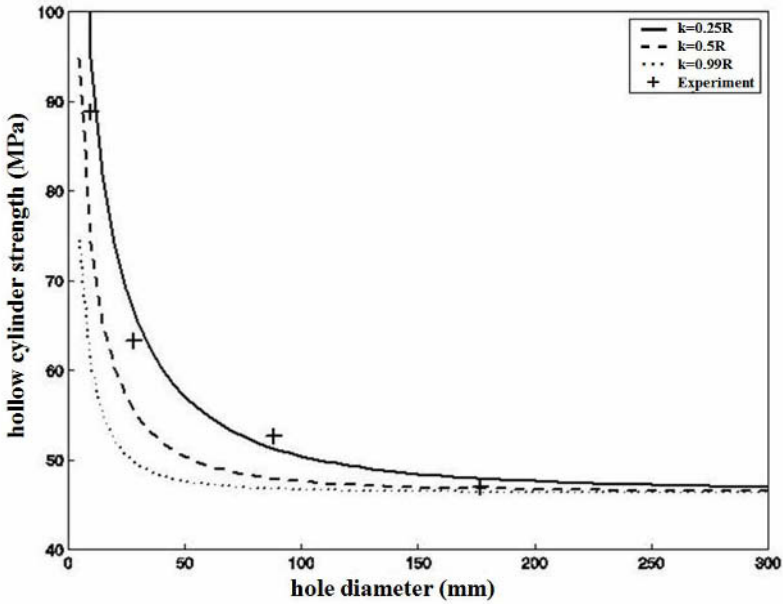


Figure 4.1. Prediction of the hole strength for different values of the parameter κ and comparison with experimental results on Berea sandstone

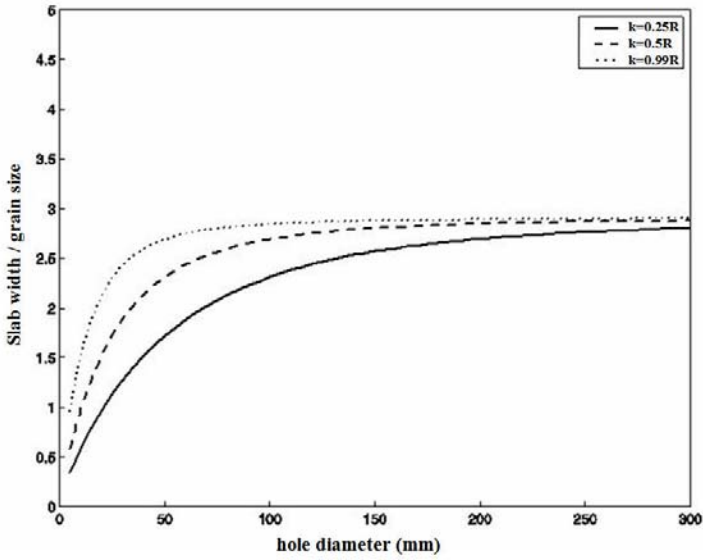


Fig. 4.2. Normalized slab width h for different values of the parameter κ

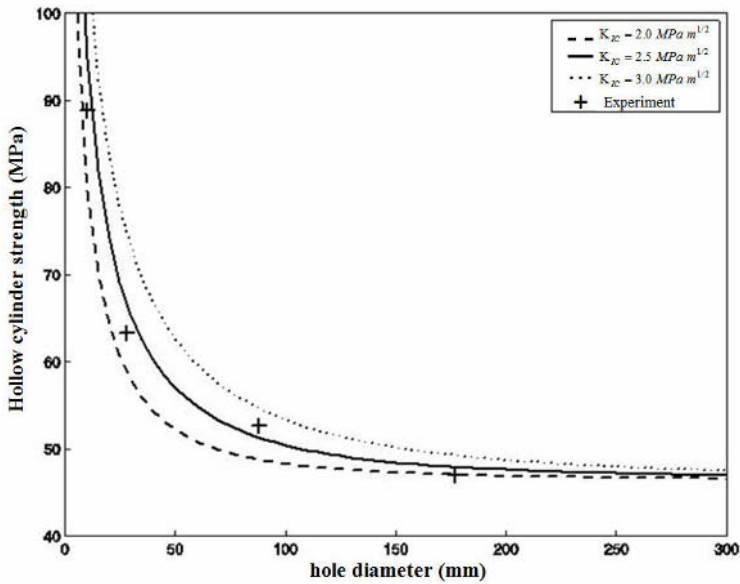


Fig. 4.3. Prediction of the hole strength for different values of fracture toughness and comparison with experimental results on Berea sandstone

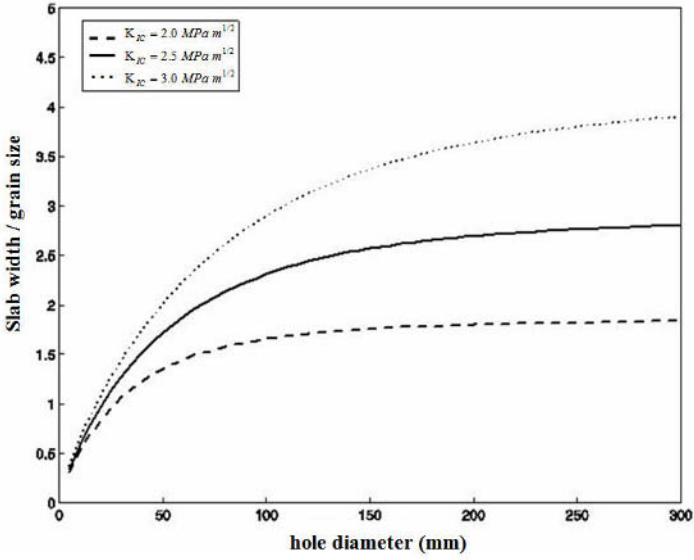


Fig. 4.4. Normalized slab width h for different values of fracture toughness

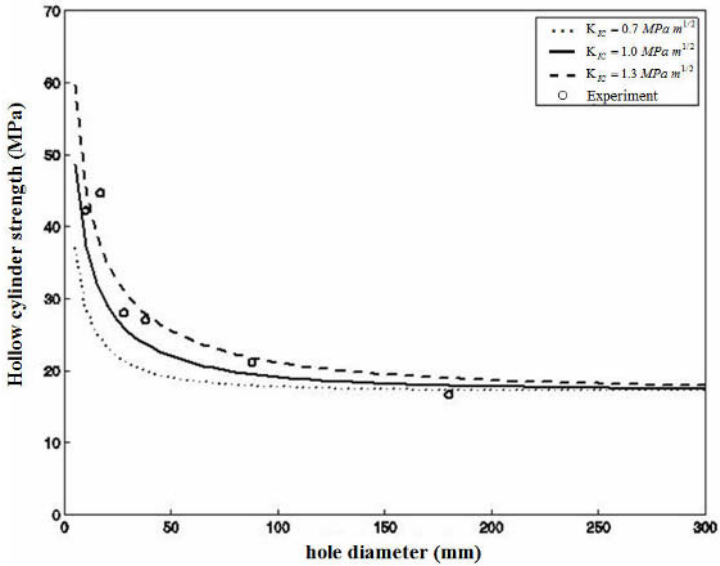


Fig. 4.5. Prediction of the hole strength for different values of fracture toughness and comparison with experimental results on Castlegate sandstone

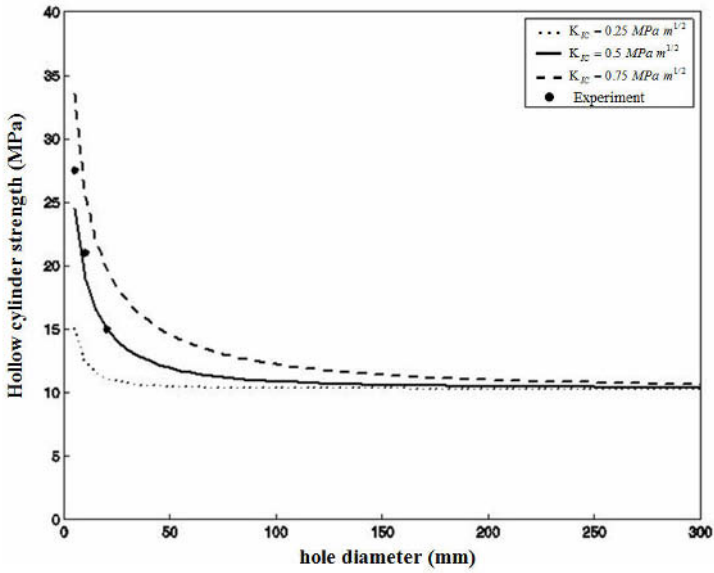


Fig. 4.6. Predictions of the hole strength for different values of fracture toughness and comparison with experimental results on Red Wildmoor

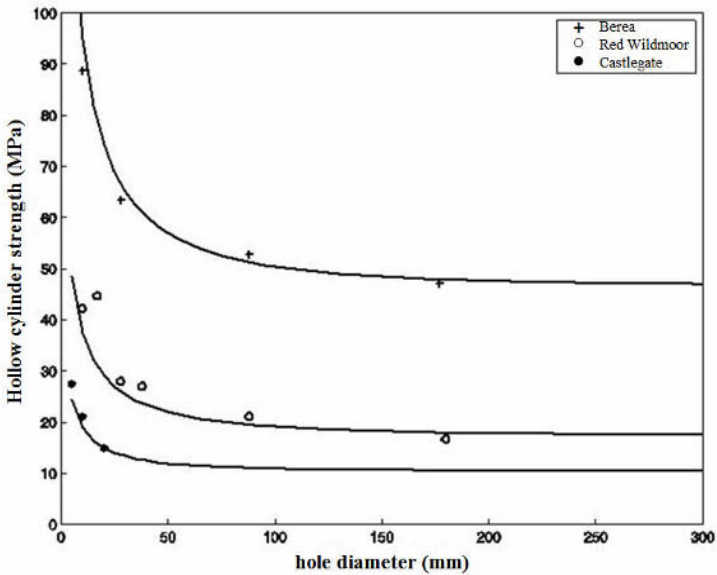


Fig. 4.7. Model predictions and comparison with experimental data

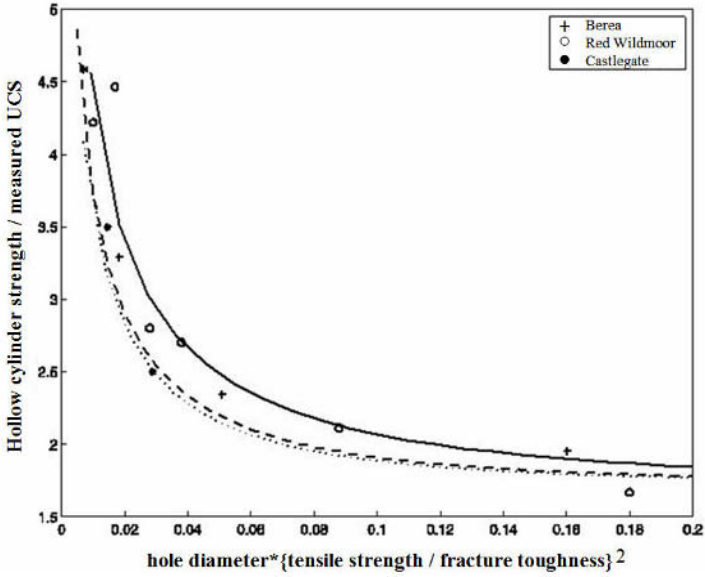


Fig. 4.8. Comparison of the predictions of (a) full model (solid lines) and (b) approximate model equation (2.23) (dashed lines) with experimental data

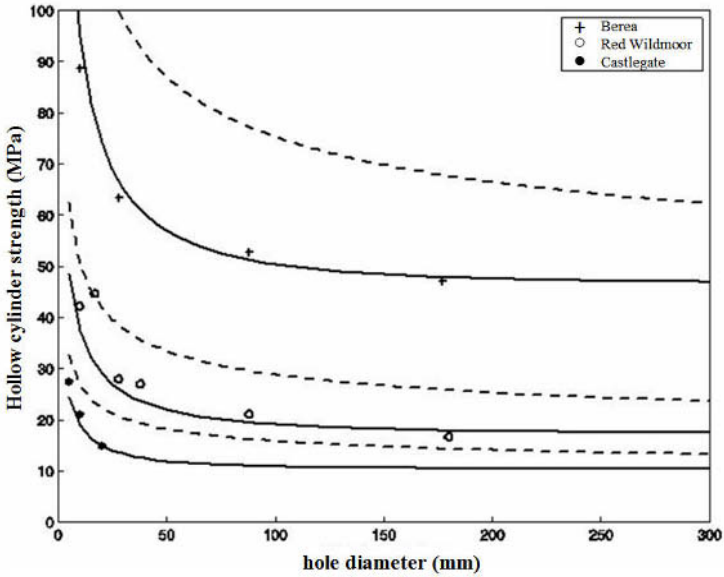


Fig. 4.9. Model predictions and experimental results in a normalized form

5 Conclusions

In this paper we examined a model originally proposed in reference [1] for predicting borehole collapse based on fracture mechanics and layer buckling theories. The model considers that the main mechanism of borehole collapse takes place in the form of (pre-existing or formed) layers buckling. A combination of the fracture mechanics parameters introduced by the model allows scaling of the hole size and prediction of the dependence of load collapse on its radius. We presented sensitivity of the model to the most uncertain parameters and compared the results with available experimental data. We showed that the model is capable of producing results close to experimental data following a strong scale dependence of the hole strength on its radius. In addition, for model predictions as well experimental data we found a strong correlation between hole strength normalized by the Uniaxial Compressive Strength of the rock and hole size normalized by the square of division of rock fracture toughness divided by tensile strength. These results can be used for deriving an apparent strength model which can be further employed in mechanical models for predicting the strength of small holes like perforations.

Acknowledgements

This research was supported by Schlumberger Cambridge Research.

References

1. Bazant Z, Lin F-B, Lippmann H (1993) Fracture energy release and size effect in borehole breakout. *Int. J. Num. Anal. Meth. Geomech.*, 17: 1-14.
2. Haimson B, Herrick C (1989) Borehole breakouts and in situ stress. In: *Proc., Drilling Symp. At ATCE-ASME Conference, Houston*, pp 17-22.
3. Kachanov LM (1988) *Delamination Buckling of Composite Materials*. Kluwer Academic Publishers, Dordrecht, Boston, London.
4. Germanovich LN, Dyskin AV (2000) Fracture mechanisms and instability of openings in compression. *Int. J. Rock Mech. Min. Sci.* 37: 263-284.
5. Oakland, D. and Cook, J. M. (1998) Bedding-related instability in high-angle wells. In *SPE/ISRM Eurock 98, vol.1*, pp 413-422.
6. Papamichos E, van den Hoek P (1995) Size dependency of Castlegate and Berea sandstone hollow-cylinder strength on the basis of bifurcation theory. In: *Proc. 35th US Symp. Rock Mechanics*, pp 301-306.

7. Papanastasiou P, Vardoulakis I (1989) Bifurcation analysis of deep boreholes: II. Scale effect. *Int. J. Num. Anal. Meth. Geomech.*, 13:183-198.
8. Papanastasiou P, Vardoulakis I (1992) Numerical treatment of progressive localization in relation to borehole stability. *Int. J. Num. Anal. Meth. Geomech.*, 16: 389-424, (1992)
9. Papanastasiou P, Zervos A (2004) Wellbore stability analysis: from linear elasticity to post-bifurcation modeling. *Int. J. Geomechanics, ASCE*, 4: 2-12.
10. Tronvoll J, Papamichos E, Kessler N (1993) Perforation cavity stability: Investigation of failure mechanisms. In: *Proc. Symp. Hard Soils, Soft Rocks, Athens*
11. Van den Hoek P (2001) Prediction of different type of cavity failure using bifurcation theory. In: *Proc. U.S. Rock Mechanics Symposium, Washington DC*.
12. Vardoulakis I, Papamichos E (1991) Surface instabilities in elastic anisotropic media with surface-parallel Griffith cracks. *Int. J. Rock Mech. Min. Sci.*, 28: 163-173.
13. Zervos A, Papanastasiou P, Vardoulakis I (2001) Modelling of localization and scale effect in thick-walled cylinders with gradient elastoplasticity. *Int. J. Solids Struct.*, 38: 5081-5095.

Experimental Investigation of Instabilities of Granular Materials in Relation to Dilatancy and Fabric Issues

Richard Wan¹, Mohammed Al-Mamun², and Peijun Guo³

¹Professor
Civil Engineering Department,
University of Calgary,
2500 University Dr. NW,
Calgary, Alberta, T2N 1N4, Canada
E-mail: wan@ucalgary.ca
Phone: +1 (403) 220-5504
Fax: +1 (403) 282-7026

²Geotechnical Engineer
Klohn Crippen Berger Ltd
Calgary, Alberta, T2E 7H7, Canada

³Assistant Professor
Department of Civil Engineering
Mc Master University
Hamilton, ONT L8S 4L7, Canada

Summary

The paper examines an experimental evaluation of the intertwined effects of microstructure (fabric) and dilatancy on the stability and strength of granular materials. The basic premise is that a granular material such as sand has at the outset a certain potential to dilate by an amount commensurate with the nature of the applied external loads (stress or strain imposed) and how conducive they are to fabric changes. As such, the deformation of dense packings of two-dimensional photoelastic disks of various cross-sections is investigated along so-called proportional strain paths that correspond to various dilation rates. Several stress (strain) paths together with stress (strain) probes are performed in the context of biaxial element tests, and the resulting strain (stress) response envelopes are determined. This is a more objective way of evaluating the stress-strain behaviour of granular soils with reference to anisotropy and dilatancy. One

of the findings of this investigation is the elucidation of the microstructural changes accompanying the instability behaviour of granular materials when all effective stresses nullify such as in static liquefaction. It is found that strong force chains develop in a dilating specimen, and that a flow type of failure is due to the buckling of these force chains. Instability is also more formally analyzed within the framework of Hill's second order work. It is interesting to note that experimental results obtained in such a 'coarse' two-dimensional material (200-400 particles with mean diameter of 5-7 mm) are very consistent with simulation results from a micromechanically based plasticity model reported in a previous publication. This confirms the pivotal importance of microstructure in any constitutive modelling endeavour.

1 Introduction

Granular materials are endowed with a microstructure (fabric) that evolves during the course of deformation history. On the other hand, it is well-known that dilatancy can be interpreted as volume changes that arise from kinematical constraints imposed by the grain connectivity against applied external loads. Hence, dilatancy and fabric are invariably intimately linked and involve important micro-kinematics such as relative sliding and rolling of particles, including microstructural features such as force chains that control both material strength and stability. It is believed that such micromechanical information must be incorporated into any constitutive model, if salient behavioural features of granular materials such as shear banding, strain localization, dilatancy and material instability are to be appropriately captured. Yet, one of the obstacles to overcome in any micromechanically formulated constitutive law is the mathematical description of fabric and its evolution with deformation history. There have been many attempts to visualize the evolution of the microstructure, and hence the development of anisotropy, in a deforming sand by using CT X-ray scans; see a comprehensive review expounded in Oda and Iwashita (1999). On the other hand, simpler ways of observing the micro-kinematics of granular material deformation involve the use of an analogue 2-D Schneebeli material which consists of a stack of several rods of different diameters as used by Calvetti et al. (1997). In order to examine the statics of the granular assembly, force contact chain (network) development can be optically rendered by using photoelastic disks of various shapes and sizes. The first attempt to put such a contact force network into evidence

was due to Drescher and de Jong (1972). Oda et al. (1982), and others have followed with the characterization of fabric tensors.

In this paper, we use techniques of photoelasticity to investigate the failure behaviour of a 2-D analogue granular material when subjected to proportional strain paths with imposed dilation or contraction rate under biaxial loading. The motivation behind such a study stems from the fact that in many geotechnical applications, e.g. submarine slopes, soils could still display unstable behaviour (liquefy) while undergoing some degree of dilation in conditions other than undrained such as partial drainage. Hence, the experiments reported in this paper will focus on the failure and material instability issues in a 2-D analogue photoelastic granular material using microstructural and fabric arguments. The experimental results will be useful in developing microstructurally based constitutive models.

2 Proportional Strain Paths

We refer to loading along proportional strain paths with a constant imposed deformation rate \mathcal{G} defined as the rate of volumetric strain ($d\varepsilon_v$) over that of shear strain ($d\gamma$). As such, the special case of isochoric deformations corresponds to the condition of $\mathcal{G} = 0$, while imposed dilation and compaction refer to $\mathcal{G} < 0$ and $\mathcal{G} > 0$ respectively. Such strain path controlled experimental studies are scarce in the literature, with the exception of the work reported by Chu et al. (1992) that probes sand behaviour along proportional strain paths with reference to strain softening, localization, as well as material stability. On the other hand, there have also been various numerical explorations of material behaviour in proportional strain paths; see Darve & Laouafa (2002), and Wan & Guo (2004). From a practical viewpoint, Vaid and Sivathayalan (2000) have also investigated strain path tests by controlling the drainage conditions in the test specimen so that the rate at which water flows into or out of it would produce either dilation or contraction. The rationale of such tests is that under ‘real’ field conditions, soils deform in a partially drained condition. Another instance of this occurs during gas ex-solution in gassy soils where the rate of production of gas makes the soil skeleton deform along strain paths with sensibly constant dilation rates.

3 Biaxial Testing Apparatus

We study the issue of fabric and microstructural changes in two-dimensions by loading biaxially an assembly of flat photoelastic particles, and thereafter optically observing the particle force chains developed through a network of fringes.

Fig. 3.1 shows the schematics of a biaxial tester that was designed, and consisting of four sliding loading beams that enclose the test specimen (100 x 100 mm). The test specimen is composed of an assembly of particles made of flat pentagons (circumscribing circle of 7 mm in diameter) that are cut out from a sheet of photoelastic polyurethane material, 10 mm in thickness. A typical specimen contains about 220 pentagons depending on the packing. Custom made disks of circular cross-sections can also be used to constitute the specimen. These were prepared by casting the material into moulds of various sizes to produce the desired disk diameter (5 and 7 mm).

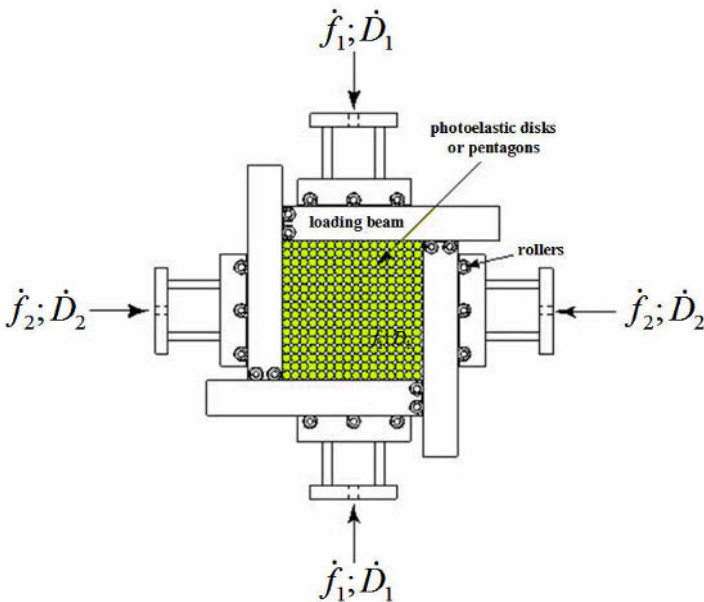


Fig. 3.1. Schematics of biaxial testing apparatus

Fig. 3.2 shows the various photoelastic disks used in this study. The physical and optical properties of the photoelastic material are as follows:

material fringe value $F=0.15$ kPa/fringe/m, elastic modulus $E=4$ MPa, and Poisson's ratio $\nu=0.5$. The material fringe value is a parameter that links optical information to applied stresses as a function of the light wavelength used.

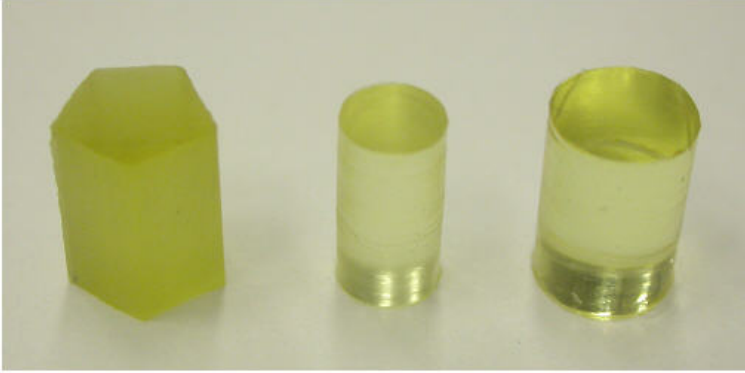


Fig. 3.2. Photoelastic disks: from left to right: 7 mm equivalent diameter pentagonal disk, 5 mm diameter circular disk, and 7 mm diameter circular disk

By using a circular polariscope arrangement, consisting of crossed polarizers, it is possible to visualize fringes (hence force chain networks) as well as estimate forces at the particle level (Fig. 3.3). Basically, as the pentagons are stressed, a ray of polarized light gets resolved along two principal stress directions with each of these components experiencing different refractive indices due to the phenomenon of birefringence. These two light wave components suffer a phase retardation that is a function of applied stress, and hence produces an interference (fringe) pattern visible in a system of crossed polarizers. The reader is referred to Coker and Filon (1931) for a classic treatise on photoelasticity.

Finally, the loading system is set up such that either displacements (D_1 and D_2) or loads (f_1 and f_2) can be independently controlled in both axial and lateral directions.

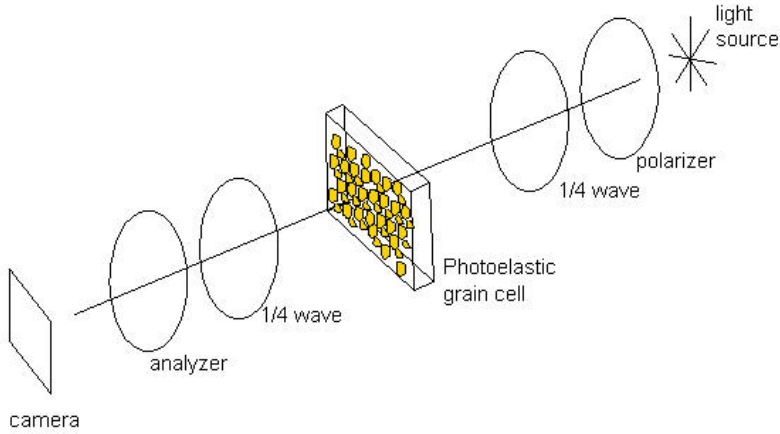


Fig. 3.3. Schematics of photoelastic setup and polarizer

4 Proportional Strain Path Testing

In view of testing the material along proportional strain paths, both axial and lateral displacement rates (\dot{D}_1 & \dot{D}_2 respectively) are applied in a ratio defined as $\mathcal{G}^* = (\dot{D}_1 + \dot{D}_2)/(\dot{D}_1 - \dot{D}_2)$. Hence, forced dilatant and contractant strain paths refer to negative and positive \mathcal{G}^* values respectively, whereas the isochoric deformation condition is given by $\mathcal{G}^* = 0$. The axial and lateral forces arising from the applied displacements are also measured as \dot{f}_1 and \dot{f}_2 respectively.

4.1 7 mm Pentagonal Disks

A relatively dense packing of pentagons is achieved by carefully placing the particles one by one in a consistent manner following a given pattern so that the initial packing of the specimen is repeatable. Then, the specimen is stressed at a targeted confining pressure, and thereafter forced to deform along various strain paths of \mathcal{G}^* values corresponding to a particular prescribed dilation or contraction rate.

Fig. 4.1 shows the force response paths resulting from shearing the specimen along some selected strain paths that range from imposed compaction to dilation. One immediate observation is the material response is not bounded by the ones given in the constant lateral

confinement (akin to a drained test) and the isochoric (akin to an undrained test) conditions. In other words, the densely packed granular material may well display unstable behaviour if it were taken along a dilatant path (e.g. $\mathcal{G}^* = -0.67$ and -1.5), while it would display a stable hardening behaviour when forced to compact (e.g. $\mathcal{G}^* = 0.6$ and 1.2).

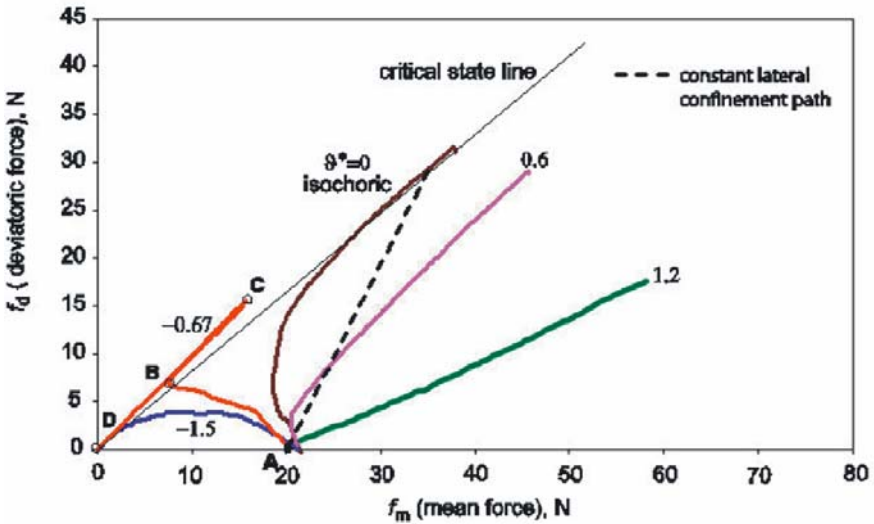


Fig. 4.1. Force path response for various constant rates of dilation and compaction

Amongst all force response paths, it is of interest to examine the one path pertaining to an imposed dilation rate of $\mathcal{G}^* = -0.67$ which displays an initial hardening phase (BC) followed by a snap back phase (CD), whereby the material suffers an abrupt collapse. To further examine this phenomenon, the evolutions of axial (f_1), lateral (f_2) and mean (f_m) forces are shown in Fig. 4.2. There is a general increase in axial forces during the hardening phase while the lateral forces are small and continually drop.

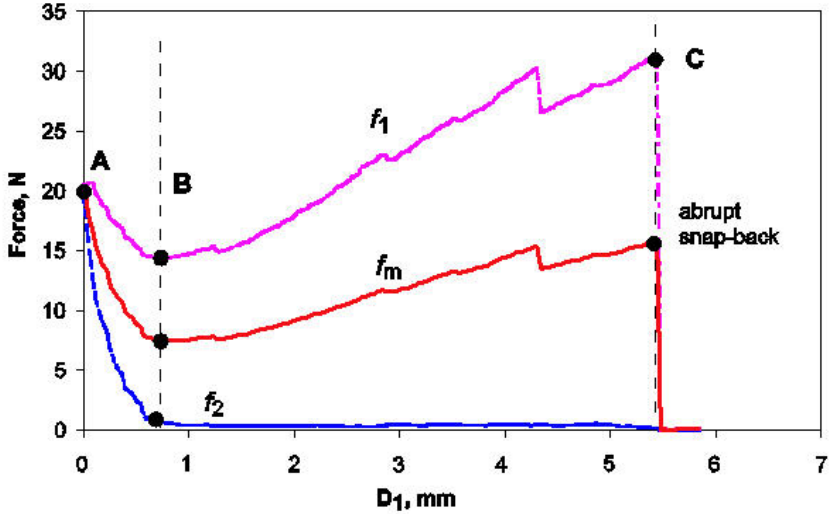


Fig. 4.2. Force component evolutions: dilatant path $\mathcal{G}^* = .67$

In order to pursue an investigation of fundamentals at the microscopic level, Fig. 4.3 gives the contact force chain and associated structure at key points A, B and C on the force response curve plotted in Fig. 4.2. The fringe patterns indeed reveal the formation of contact force chains along path A-B, while both axial and lateral loads are being reduced. Between B and C, additional force chains develop in the axial direction as the axial load picks up. At the same time, in order to sustain the imposed deformations as prescribed by \mathcal{G}^* value, the lateral load has to decrease so as to allow the required dilation. The force chains ultimately buckle at point C, giving an abrupt snap back in load response. At this point, the material response is very unstable with failure associated to a complete loss of load bearing capacity due to the disaggregation of particles. This is germane to a percolation threshold at which all the contact forces (effective stresses) vanish. It is also interesting to note that a two-phase structure emerges with the force chains seen embedded into a matrix of apparently less loaded particles. This observation was reported by Radjai et al. (1996) in numerical simulations of granular packings using the discrete element method.

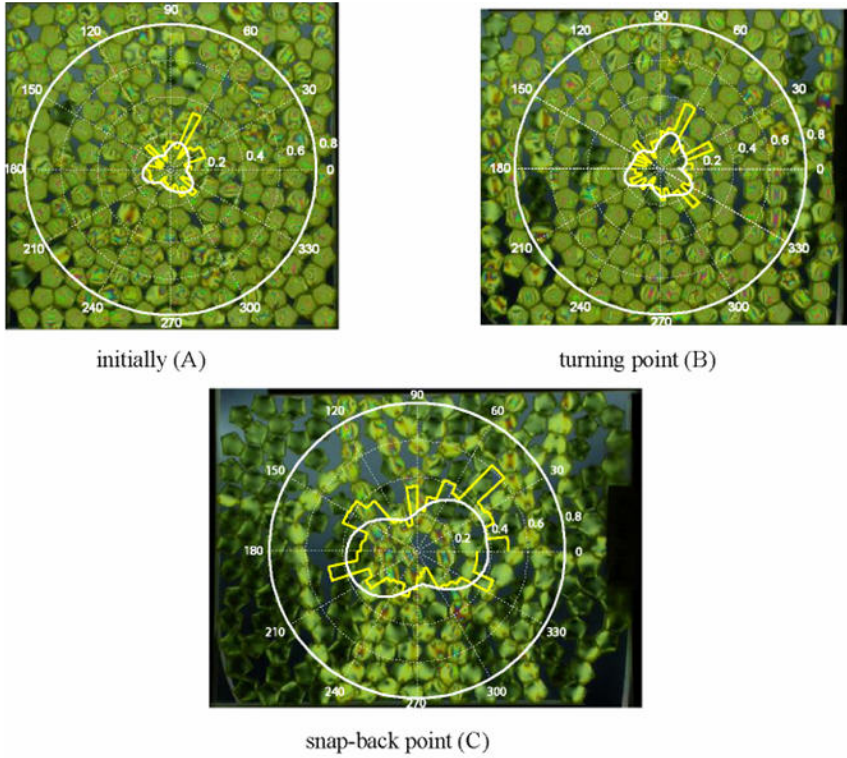


Fig. 4.3. Fabric evolution along dilatant strain path ABC: compaction of grains, formation of strong force columns, and spontaneous buckling of force chains due to loss of lateral confinement. Also, the evolution of the directional void ratio plot confirms the mechanism of deformation

They defined two ‘populations’ of contact networks, a weak and a strong one depending on whether the transmitting forces are below and above a mean force value respectively. The strong contact network can be identified with strong force chains. The experimental results reported herein suggests that in the development of a microstructurally oriented constitutive law, the average stress, σ , in a granular material could potentially be decomposed into partial stresses, σ^w and σ^s , corresponding to the weak and strong contact networks respectively, i.e.

$$\sigma = \alpha_s \sigma^s + (1 - \alpha_s) \sigma^w \quad (4.1)$$

where α_s is the relative proportion of strong contacts in the system.

Superimposed on the images in Fig. 4.3, are the polar plots of void ratio distributions conveying their directional nature as a function of loading history along path ABC. The directional void ratio plots were created by drawing a series of scan lines radiating from the centre of the specimen. Each radial line intersects a number of grains as well as voids along its run. The lineal void ratio along a scan line is simply defined as the ratio of the length of intersected voids to that of solid. The raw data has also been smoothed out using a high order Fourier series as shown by the continuous void ratio distribution. Initially, at point A, the packing is almost isotropic with an average lineal void ratio of approximately 0.2. At the turning point (pt. B), the formation of force chains in the axial direction is reflected by a generalized reduction in void ratio in that same direction, while void ratio tends to increase in other directions. At the point of collapse (C), the buckling of the columns produces a loosening of the packing in the lateral direction as confirmed by the rotation of the void ratio distribution.

In order to formally examine material stability issues, the second order work as stipulated by Hill (1958) is advocated. Basically, a sufficient condition for material stability is that the second order work, $d^2W = d\boldsymbol{\sigma} \cdot d\boldsymbol{\varepsilon}$, must be positive in any increment during deformation history. By material stability, we mean that the material response is small in the neighborhood of a stress and strain state for any small perturbation in loading, see Darve and Laouafa (2002). Here, in 2-D deformation conditions, the second order work expressed in terms of force and displacement increments gives:

$$d^2W = df_1 dD_1 + df_2 dD_2 = \left(df_1 - \frac{df_2}{\mathfrak{R}} \right) dD_1 \quad (4.2)$$

where $\mathfrak{R} = (1 + \mathcal{G}^*) / (1 - \mathcal{G}^*) = -dD_1 / dD_2$. Hence, a peak in the plot of $(f_1 - f_2 / \mathfrak{R})$ against D_1 signals a zero second order work, or material instability. Fig. 4.4 depicts such plots for the selected \mathcal{G}^* paths in Fig. 4.1. The analysis shows that for $\mathcal{G}^* \leq -0.67$, material instability prevails as revealed by noticeable peaks (zero slope) on the second order work curves. On the other hand, material stability is ensured for path with $\mathcal{G}^* > 0$.

The essentials of the results are next summarized in the deviatoric (f_d) versus mean (f_m) force space shown in Fig. 4.5. The force (stress) space is divided into dilation and compaction regions as distinguished by negative and positive \mathcal{G}^* values respectively. Interestingly, it is found that there are certain forced dilatant \mathcal{G}^* paths for which the material response can still be stable with the value $\mathcal{G}^* \sim 0.67$ as threshold for this case. Those

force response paths, found within the “forced dilation and stable” region, refer to a dilatant hardening behaviour. In these cases, strong contacts prevail over weak ones in the force network throughout deformation history.

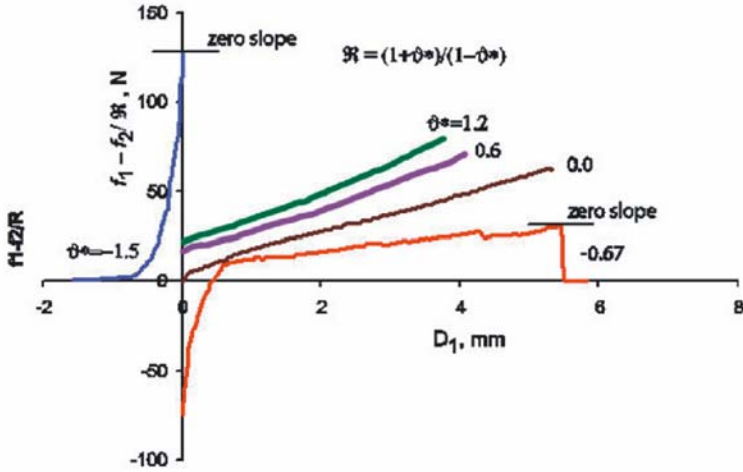


Fig. 4.4. Investigation of material instability through second order work plot

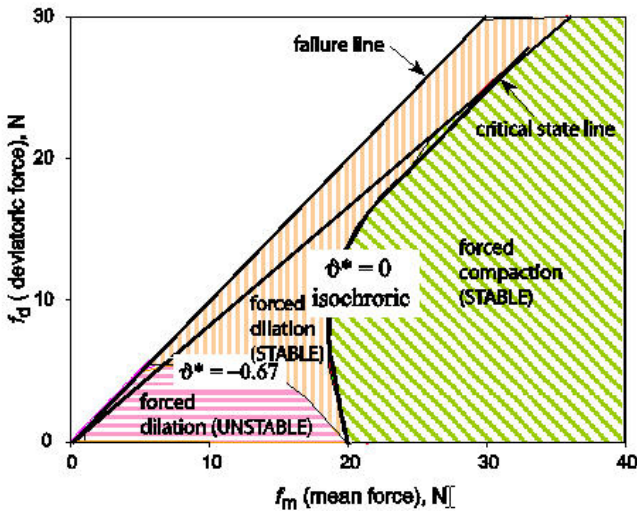


Fig. 4.5. Zones of stability and instability under forced compaction and dilation

Next, it is worthwhile to establish the contribution of dilatancy to shear strength as deduced from some apparent friction angle φ^p calculated from the asymptotic part of force response paths given in Fig. 4.1. If α is the angle of inclination of the asymptotic part of the force response path in the f_m versus f_d axes, and invoking a Mohr-Coulomb failure criterion, it turns out that $\sin \varphi^p = \tan \alpha$. In addition, recalling the imposed dilation rate as $\mathcal{G}^* = (\dot{D}_1 + \dot{D}_2)/(\dot{D}_1 - \dot{D}_2)$, we can obtain a dilatancy angle ψ based on kinematical conditions, and considering the Mohr's circle of strains (Hansen 1958), it follows that

$$\sin \psi = \frac{\dot{D}_1 + \dot{D}_2}{\dot{D}_1 - \dot{D}_2} = \mathcal{G}^* \quad (4.3)$$

Since for each test, the enforced dilation rate \mathcal{G}^* (hence dilation angle ψ) is known, a relationship between the apparent friction angle, φ^p , as derived from α and dilation angle ψ can be established. Table 4.1 shows the measured as well as transformed data from a more complete set of tests than the ones given in Fig. 4.1. From the data, we arrive at the following simple relationship, i.e.

$$\varphi^p = \varphi_{cv} + 0.4\psi \quad (4.4)$$

where φ_{cv} refers to the friction angle of constant volume (critical state). We note that the above established relationship is similar to the one developed by Bolton (1986), i.e.

$$\varphi^p = \varphi_{cv} + 0.8\psi \quad (4.5)$$

which was derived from experimental data on sand.

Table 4.1. Dilation angles as observed from static and kinematic analyses

\mathcal{G}^*	α (deg)	φ^p (deg)	$\varphi^p - \varphi_{cv}$ (deg)	$\sin^{-1}(\mathcal{G}^*)$
0	39.8	56.4 (= φ_{cv})	0	0
-0.2	41.5	62.1	5.7	11.5
-0.33	42.1	64.5	8.1	19.3
-0.60	43.18	69.8	13.4	36.8
-0.67	44	74.9	18.5	42.0
-0.75	45	90	33.6	48.6

4.2 7 mm Circular Disks

We next investigate the effect of particle shape by replacing the pentagonal disks with circular ones of the same diameter, i.e. 7mm. Fig. 4.6b shows the force response path for the strain path $\mathcal{G}^* = \tilde{0.67}$. There is no snap-back phenomenon as seen in the case of the pentagonal disk assembly. In fact, both axial and lateral forces (f_1 and f_2) steadily decrease throughout deformation history (Fig. 4.6a). In order to get more insight in the development of characteristic failure mechanisms during loading history, the disk packing corresponding to the different stages of the force response path are subsequently shown in Figs. 4.6c, d, e and f. At point B, some disks in the central part of the specimen are highly stressed in comparison to other ones at the two lateral sides. As the peak point (point C) on the force response path is reached, a general weakening of the central core occurs, until finally at point D and beyond, the fringes correlating to intensity of contact forces disappear for most of the disks in a diffuse manner. The latter corresponds to a progressive softening of the sample that exacerbates in time to eventually lead to its collapse. It is clear from the images that the sample never hardens, which is in contrast with the pentagonal disk case where the sample showed remarkable hardening due to interlocking until it could no longer hold loads anymore so as to succumb and collapse as force chains buckled. In general, the degree of interlocking in a circular disk assembly is much less than in the case of pentagonal disks.

4.3 5 mm Circular Disks

Circular disks of smaller diameter (5 mm) were tested along the same strain path $\mathcal{G}^* = \tilde{0.67}$ as in the previous subsection. Images of the microstructure at different points on the force path are shown in Fig. 4.7. It is interesting to note that a change in disk diameter leads to a different response in spite of the same packing and void ratio. In this case (5mm disk) hardening behaviour is observed compared to the 7 mm disk case (Fig. 4.6). Fig. 4.7a shows that the mean force (f_m) after reaching a peak drops to a constant value for large shearing (from pt B to D). For the 7 mm disk sample, no such response was observed (see Fig. 4.6a), where the mean force dropped all the way down. The characteristic response of the 5 mm disk assembly can be explained from the images. In the image corresponding to point B (Fig. 4.7d), a visible core of highly stressed region develops in the middle to support increasing stresses along the axial direction. With further shearing at point C, the sample begins to soften, whereby disks along diagonal directions start to slip with each other with the strong core vanishing.

Once this mechanism is initiated, the disks slip forming a wedge (as shown at point D, Fig. 4.7f) to lead to sample instability.

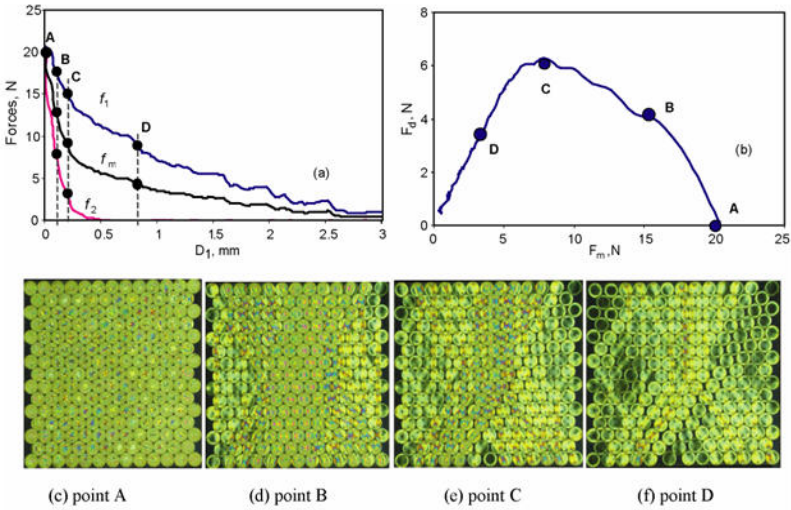


Fig. 4.6. Force components, force response path, and microstructure at key points for 7 mm circular disks

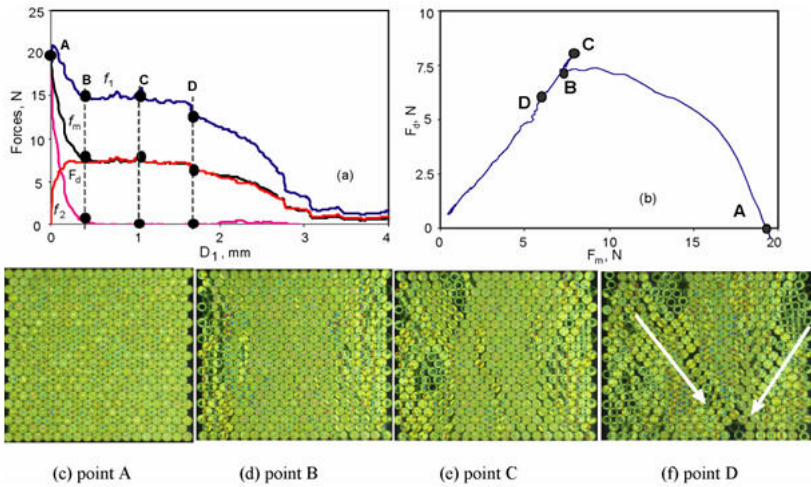


Fig. 4.7. Force components, force response path, and microstructure at key points for 5 mm circular disks

5 Stress (Strain) Response Envelopes and Anisotropy

We next turn to the characterization of the constitutive behaviour at the macroscopic scale with underlying microstructural changes. The concept of response envelopes, as first introduced by Gudehus (1979), is herein adopted in order to examine the nature of the constitutive behaviour of the tested 2-D analogue granular material with respect to anisotropy and loading history. Basically, for a given stress (strain) state, a series of strain (stress) probes of a predetermined magnitude is applied to the granular material. By plotting the corresponding responses in the stress or strain space, and depending on the nature of the probing, a stress or strain envelope can be drawn. From the elasticity equations, we can easily determine that an elastic response is characterized by an ellipse centered about the initial stress (or strain) point with the major (or minor) principal axis oriented at 45° with the horizontal in either the stress or strain space. Any rotation of the ellipse would indicate anisotropic elastic behaviour, whereas a translation about the initial stress (strain) point refers to inelastic behaviour, see Wu and Kolymbas (2002).

From a constitutive viewpoint, a response envelope generally conveys the notion of the directional loading dependence of material behaviour, while its shape depicts the variation of directional compliance or stiffness. Also, any discontinuity in the response envelope reveals a non-continuity of incremental response between tensorial zones as defined by Darve and Laouafa (2000), which may signal material instability.

5.1 Stress Response Envelope and Effect of Stress History

In the following, the effect of stress history is investigated by examining the response of a system of pentagonal disks (circumscribing circle diameter of 7 mm) against strain probes of different magnitudes for two cases. In the first case, the probes are applied to the specimen which was anisotropically stressed up to a state, $f_1 = 40$ N and $f_2 = 20$ N. The second case involves applying the strain probing after the specimen has undergone an initial isotropic compaction followed by a preshear so as to reach the same state as previously.

Fig. 5.1 shows the response envelopes measured for selected strain probes of magnitudes 0.5 and 1.0 mm after initial anisotropic compaction. In order to facilitate the discussion, the elastic response envelopes are also plotted in dotted lines and compared with the ones obtained by fitting the experimental data into a surface. The measured response envelopes deviate

from the baseline elliptical (elastic) ones in that the former are rotated, and also are unsymmetrical with respect to the initial force (stress) state point A. This signifies that the material response is predominantly anisotropic with some plastic deformation, the degree of which increases with probing strain level.

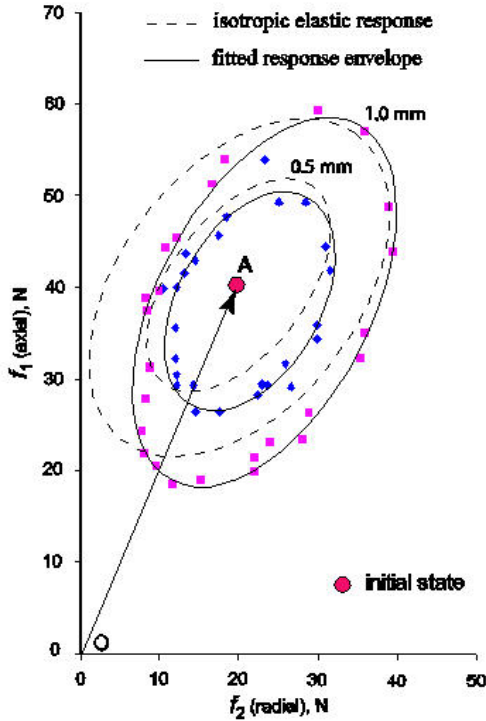


Fig. 5.1. Force response envelopes for strain probes applied after isotropic compaction (OA)

Fig. 5.2 shows the response envelopes for strain probes applied to the same pentagonal disk assembly subjected to a different stress history that involves a preshear in addition to an initial isotropic compaction. In contrast with the previous case (Fig. 5.1), the deviation of material response from the elastic one is larger for both strain probe levels of 0.5 and 1.0 mm. This is probably because the fabric change induced prior to strain probing is less than in the previous case. Along the isotropic compaction path OC, virtually no stress induced fabric change is to be expected so that the only fabric change is due to path CA. Hence, when the

strain probing is applied, there is much potential for the development of plastic deformations and anisotropy.

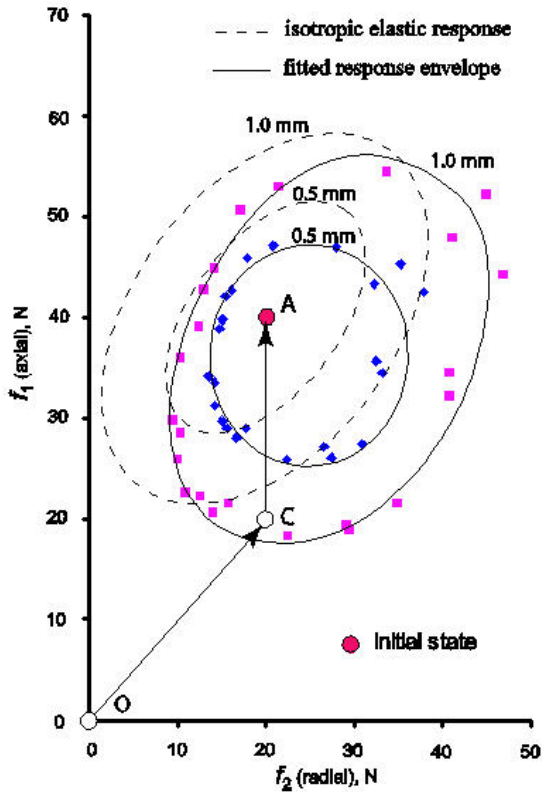


Fig. 5.2. Force response envelopes for strain probes applied after a combination of isotropic compaction (OC) and preshear (CA)

Finally, Figs. 5.3 and 5.4 show the evolution of stress envelopes for both stress histories as the level of probing strain is increased. It is observed that at higher probing strain levels ($D = 2$ and 3 mm), the response envelopes are no longer elliptical in shape and are unsymmetrical about the initial stress state, thus showing substantial deviation from an elastic behaviour. Also, comparing Figs. 5.3 and 5.4, the response envelopes at higher probing strain levels are found to be similar in each case. This suggests that the effect of preshear is virtually erased at higher probing strain levels as the plasticity induced fabric changes are so large that the preshear memory is swept away.

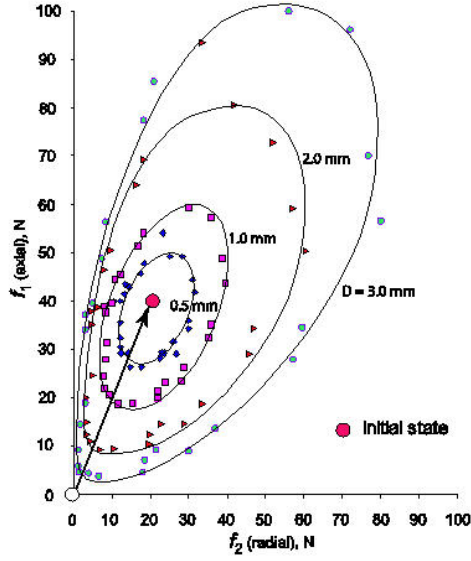


Fig. 5.3. Complete force envelopes for anisotropically compacted specimen

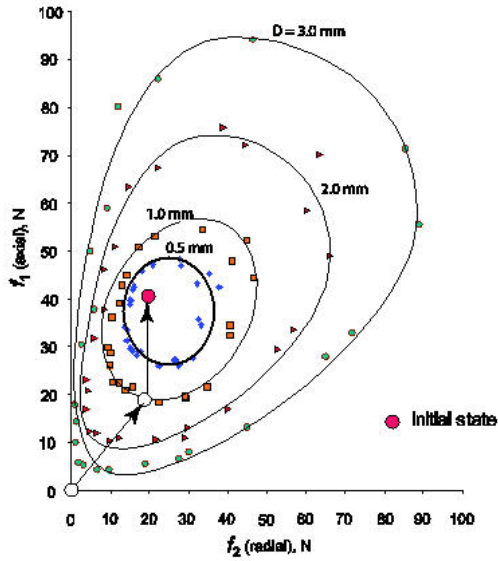


Fig. 5.4. Complete force envelopes for specimen compacted isotropically followed by a preshear

5.2 Strain Response Envelopes and Uniqueness of Incremental Plastic Strain Direction

The two cases pertaining to two different stress histories that lead to the same initial state are now subjected to force (stress) probes of magnitudes 10 and 15 N along 8 different directions in the force space. Figs. 5.5 and 5.6 show the strain response envelopes for a force probe level of 10 and 15 N respectively, when the specimen was isotropically compacted followed by a preshear. By unloading at the end of each force probing direction, the amount of elastic deformation was measured. Hence, any plastic strain increment developed during probing could be deduced. In Figs. 5.5 and 5.6, it is found that all force probings give a strain envelope that collapses into a line, resulting into a single plastic strain increment direction defined by $\dot{D}_1 / \dot{D}_2 = \tan \theta \approx 2$, no matter the force probing level and direction. The same conclusion was reached for the other stress history involving an anisotropically compacted specimen to the same initial state prior to probing. This means that a single plastic strain increment vector is obtained irrespective of the incremental stress direction and history, which means that the granular assembly deforms according to a regular plasticity flow rule.

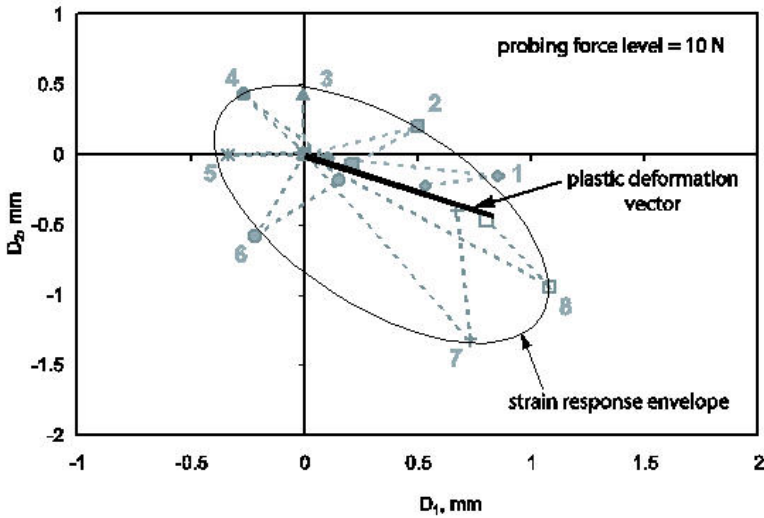


Fig. 5.5. Strain response envelope for isotropically compacted and presheared specimen at force probe of 10 N

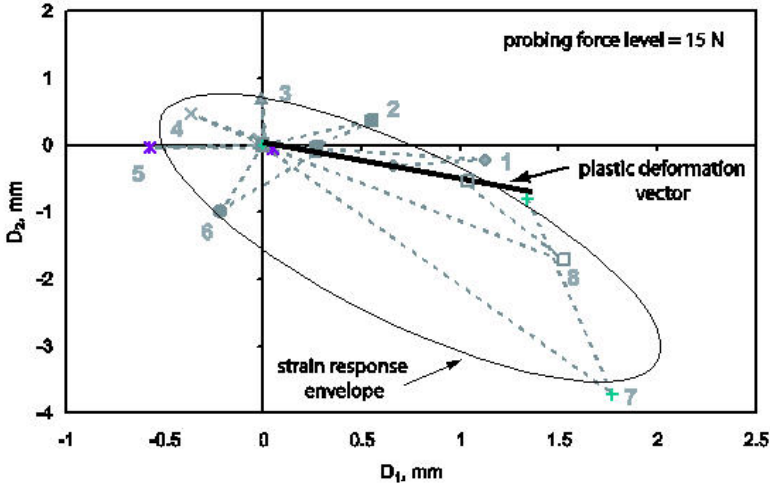


Fig. 5.6. Strain response envelope for isotropically consolidated and presheared specimen at force probe level of 15 N

Finally, Fig. 5.7 summarizes all experimental results showing the deduced plastic strain increment vector, and the probable yield and plastic potential surfaces by invoking the theory of plasticity. The experimental results of Figs. 5.5 and 5.6 showing the existence of a regular plasticity flow rule imply that the granular assembly can be described using any classic elastoplastic constitutive model. However, subtle material responses such as described in the beginning of the paper involving instability and force chain collapse can only be modelled by enriching an elastoplastic constitutive law with microstructural information, see for example, Wan et al. (2005). The validity of a regular plasticity flow rule in describing the behaviour of a granular material is subject of debate in the literature; see Darve and Nicot (2005). For instance, a regular plasticity flow rule may only hold under two dimensional stress/strain conditions, but may not apply to three dimensions where the response is manifestly a function of the direction of loading increment as advocated in incremental constitutive laws of the type first proposed by Darve and Labanieh (1982).

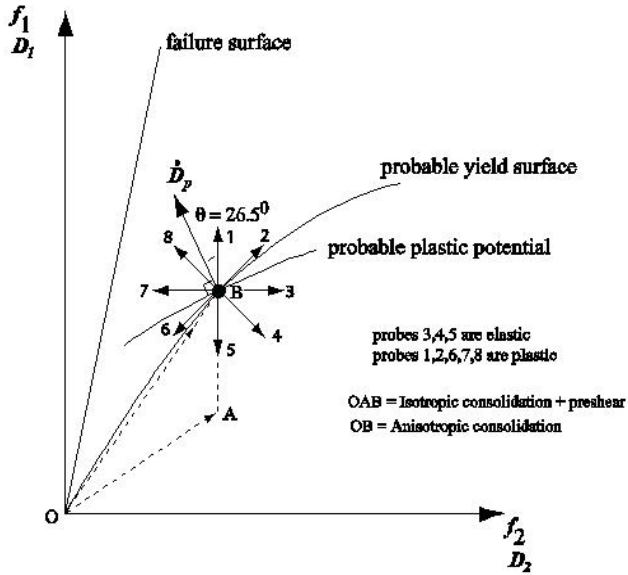


Fig. 5.7. Uniqueness of plastic strain increment direction and probable yield and plastic potential surfaces

6 Conclusions

The experimental results presented in this paper demonstrate the possibility of evaluating microstructural changes through the visualization of force networks that control the macroscopic response of granular materials by using an analogue photoelastic material. The importance of testing the material response along proportional strain paths with an imposed constant rate of dilation is identified. These strain paths generalize the conventional undrained and drained triaxial testing in soil mechanics in that they refer to various degrees of drainage under in-situ conditions. The experimental results obtained in this study demonstrate the failure mechanisms leading to collapse under forced dilation strain paths. Material stability as described by hardening behaviour corresponds to the formation of strong force columns in the central core of the specimen. It is the lateral confinement that dictates the strength of the central core which can locally collapse, and hence lead to failure at the macroscopic level. It was also observed that a two-phase structure emerges with the force chains seen embedded into a matrix of apparently less loaded particles as found in discrete element modelling, see Radjai et. al. (1996) and Goddard (2002).

Stress and strain response envelopes have also been determined experimentally for various stress and strain probes. One of the main findings is that stress history memory is swept away at high probing strain levels. More importantly, when imposing stress probes on a material with two different stress histories, it is found that the resultant plastic strain envelope collapses into a single line defining the direction of plastic strain increment vector. This observation remains true at least for the two dimensional case, and hence a regular plasticity flow rule within the theory of non-associated plasticity can be used to model granular materials at the continuum level. In three dimensional conditions, the dependence of the plastic strain increment vector on the direction of loading (stresses) may be destroyed as advocated by Darve and Nicot (2005) using micromechanical arguments. Basically, in two dimensions, the sliding direction between a pair of grains is kinematically constrained along a line, and is independent of the loading direction. In three dimensions, the problem is less constrained as the sliding direction, while depending on the loading direction, may be anywhere within the contact plane.

All the results reported in this paper are consistent with simulation results obtained from a constitutive model developed at a continuum level, based on the theory of plasticity and enriched with microstructural information; see Wan et al. (2005) for instance. By incorporating microstructural information through an embedded fabric tensor, it is possible to describe micro/meso phenomena through the model in the above cited work. This further underscores the importance of microstructure information in any constitutive modelling endeavour.

Acknowledgements

Funding provided by the Natural Science and Engineering Council of Canada, and the Alberta Energy Research Institute, is gratefully acknowledged.

References

1. Bolton MD (1986) The strength and dilatancy of sands. *Géotechnique* 35(2):99-112
2. Calvetti F, Combe G, Lainer J (1997) Experimental micromechanical analysis of a 2D granular material: relation between structure evolution and loading path. *Mechanics of Cohesive-Frictional Materials* 2:121-163

3. Chu J, Lo SCR, Lee IK (1992) Strain-softening behaviour of granular soil in strain-path testing. *J. Geotech. Eng. ASCE* 118(2):191-208
4. Coker EG, Filon LNG (1931) *A treatise on photo-elasticity*. Cambridge University Press, England, 720p
5. Darve F, Labanieh S (1982) Incremental constitutive laws for sands and clays: Simulations of monotonic and cyclic tests. *Int. J. for Num. and Anal. Meth. in Geomech.*, 6:243-275
6. Darve F, Laouafa F (2002) Constitutive equations and instabilities of granular materials. In: C. Gianfranco, N. Vito, and G. Pasquale (eds.), *Modeling and Simulation in Science, Engineering and Technology*, Birkhauser, pp 3-43
7. Darve F, Laouafa, F (2000) Instabilities in granular materials and application to landslides. *Mech. of Cohes. Frict. Mater* 5:627-652
8. Darve F, Nicot F (2005) On flow rule in granular media: phenomenological and multi-scale views (part II). *Int. J. Numer. Anal. Meth. Geomech* 29:1411-1432
9. Drescher A, Josselin de Jong G (1972) Photoelastic verification of mechanical model for the flow of a granular material. *J. Mech. Phys. Solids* 20(5):337-351
10. Goddard JD (2002) Material instability with stress localization. *Proceedings of the International Workshop on Bifurcations and Instabilities in Geomechanics*, Minnesota, June 2-5, pp 57-64
11. Gudehus G (1979) A comparison of some constitutive laws for soils under radially symmetric loading and unloading. In: Wittke (ed.), *Proc. 3rd Int. Conf. on Numerical Methods in Geomechanics* 1309-1323
12. Hansen B (1958) Lines ruptures regarded as narrow rupture zone, basic equation based on kinematic conditions. *Proceedings of Conference of earth pressure Problems*, Brussels, Belgium 39-51
13. Hill R (1958) A general theory of uniqueness and stability in elastic-plastic solids. *J. Mech. Phys. Solids* 6:239-249
14. Oda M, Iwashita K (1999) *Mechanics of Granular Materials: An Introduction*. A.A. Balkema, Rotterdam Netherlands 382 p
15. Oda M, Konishi J, Nemat-Nasser S (1982) Experimental micromechanical evaluation of strength of granular materials: effects of particle rolling. *Mechanics of Materials* 1(4):269-283
16. Radjai F, Moreau JM, Roux S (1996) Force distributions in dense two dimensional granular systems. *Phy. Rev. Lett.*, vol 77, p. 274
17. Vaid YP, Saivathayalan S (2000) Fundamental factors affecting liquefaction susceptibility of sands. *Can Geotech. J.* 37:592-606
18. Wan R, Guo PJ, Al-Mamun, M (2005) Behaviour of granular materials in relation to their fabric dependencies. *Soils and Foundations* 45(2):77-86
19. Wan R, Guo PJ (2004) Stress dilatancy and fabric dependencies on sand behavior. *Journal of Engineering Mechanics, ASCE* 130(6):635-64
20. Wu W, Kolymbas D (2002) Hypo-plasticity then and now. In: D. Kolymbas (ed.), *Constitutive Modelling of Granular Materials*, Springer-Verlag 57-105

Compactive Cataclastic Flow in Tuffeau de Maastricht Calcarenite: Mechanical Deformation & Permeability Reduction

Theocharis Baxevanis¹ and Euripides Papamichos²

¹ Department of Applied Mathematics,
University of Crete,
714 09 Heraklion, Greece,
Tel: +30-2810-393727,
E-mail: theocharis@tem.uoc.gr

² Civil Engineering Department,
Aristotle University,
Thessaloniki, Greece

Summary

The mechanical behavior and permeability of the Tuffeau de Maastricht calcarenite under compactive cataclastic flow have been studied. The model used to back-test analyze the experimental results was the one developed by Lade and Kim, which employs all three invariants. The model parameters were calibrated based on conventional triaxial and hydrostatic experiments. In order to predict the formation of localization zones, bifurcation analysis was applied. The localization point was identified to be the onset of shear-enhanced compaction (a threshold in differential stress after which significant reduction of porosity is induced). The numerical results proved to be in good agreement with the experimental ones. As for the permeability measurements, K-constant as well as conventional triaxial experiments were conducted. The effective mean stresses were in the "transitional" regime between brittle faulting and cataclastic flow. Before the onset of shear-enhanced compaction, permeability was primarily controlled by the effective mean stress, independent of the deviatoric stresses. With the onset of shear-enhanced compaction, however, coupling of the deviatoric and hydrostatic stresses induced considerable permeability and porosity reduction.

1 Introduction

Compaction bands are localized, planar zones of compressed material that form normal to the most compressive stress. Compaction bands were found by Mollema and Antonellini 1996 in a porous sandstone from the Navajo Formation. More recently, Sternlof and Pollard 2001 documented field observations of compaction bands in the Jurassic Aztec sandstone of southeastern Nevada. Such bands have been observed also in the laboratory (Olsson 1999; Olsson and Holcomb 2000; Wong et al 2001), in high porosity rocks that failed by cataclastic flow, as well as in polycarbonate honeycombs (Papka and Kyriakides 1998), steel foams (Park and Nutt 2001) and plaster (Lajtai 1974). Within these bands in high porosity sandstones, microstructural observations in laboratory samples revealed intragranular cracks - recent field observations of Sternlof et al 2005 show almost no cracking - that extend across the grains and result in comminution and pore collapse (Baud et al 2004). These field and laboratory results suggest that compaction bands are probably a common feature in high porosity rocks.

The evolution of compaction bands has been observed to take several forms: once initiated a compaction band may widen to accommodate the cumulative strain (diffuse bands) (Olsson and Holcomb 2000; Baud et al 2004), or alternatively further compaction is accommodated by the initiation of additional bands that remain relatively narrow (discrete bands); alternating bands of compacted and uncompacted material (Wong et al 2001; Klein 2001; Baud et al 2004). There is little understanding so far for the origins of these different morphologies although Baud et al 2004 have pointed out some of the key microstructural attributes that are favorable for the development of compaction localization in the form of discrete bands. The relationship of the laboratory compaction bands to those observed in the field has not, also, been fully established. Microscopic differences regarding the amount of the grain-scale fracturing indicates that further study is needed to determine the exact relationship.

Because the material within the compaction bands is more dense, it has lower permeability than the surrounding material (Holcomb and Olsson 2003, Vajdova et al 2004). Hence, compaction bands constitute barriers to fluid flow, adversely affecting the injection and extraction of fluids for storage or energy production. The presence of compaction bands affects the overall mechanical strength of the formation as well. The grain breakage and microstructural weakening within the compaction bands could lead to breakout phenomena causing increased sand production (Haimson 2003; Haimson and Song 1998; Haimson and Lee 2004).

Permeability reduction and increased sand production are of economic significance in the oil industry.

Systematic studies (Wong et al 2001; Baud et al 2004) have demonstrated that compaction localization is associated with stress states in the transitional regime from brittle faulting to cataclastic flow where two different damage mechanisms are active (axial microcracks that grow and coalesce, and pores that collapse while grains are crushed). In the cataclastic flow, it is known that application of nonhydrostatic stresses causes the pore space in a high porosity rock to compact (shear-enhanced compaction) and permeability to decrease. In the brittle regime, contradictory observations in sandstones were reported. Nevertheless, Zhu et al 1997 observed that permeability in four different sandstones with porosity above 15% consistently decreased with increasing stress. The current understanding of the effect of stress on permeability in porous rock is not quite comprehensive. Experimental studies (Holt 1989; Rhett and Teufel 1992; Zhu and Whong 1997) revealed that permeability in sandstones is very sensitive to loading path through the interplay of hydrostatic and deviatoric loadings. On the other hand, Somerton et al 1975 concluded that in coal, permeability is affected primarily by the mean effective stress and that the nonhydrostatic stress has negligible influence.

Since the pioneering work of Rudnicki and Rice 1975, the onset of localized deformation has been interpreted as instability in the constitutive description of the deforming homogeneous material. To date, most of the modeling efforts for the prediction of compaction bands have focused on two invariant constitutive descriptions of the homogeneous deformation. Rudnicki and Rice 1975, Olsson 1999 and Issen and Rudnicki (2000, 2001) adopted a simple constitutive framework whereby the yield envelope and inelastic volumetric change can be characterized by the pressure sensitivity parameter and the dilatancy factor, respectively. Their results are roughly consistent with the conditions under which compaction bands form. Recently, Issen 2002 proposed a two-yield surface model to capture the combined effect of the two different damage mechanisms active in the transitional regime from brittle faulting to cataclastic flow, where compaction bands form, in which the shear yield surface and cap meet at a vertex. The bifurcation analysis for this model is elaborate, but analytical results are available for some special cases. The results obtained, have extended the range of parameters over which compaction bands form. However, laboratory and numerical work suggest that the third stress invariant may play a significant effect on the description of the mechanical response of geomaterials (Kim and Lade 1988; Lade and Kim 1988^{1,2}; Borja 2002; Borja 2004; Borja and Aydin 2004). Nevertheless, bifurcation

analysis applies only to the onset of localization and further analyses are required to elucidate the development of the localized failure.

The present study identifies the development of compaction bands in a sedimentary limestone, namely the Tuffeau de Maastricht calcarenite. The experimental results are presented in Section 2. Section 3 revisits the general localization theory of deformation bands. Section 3 also presents the formulation and calibration of an elastoplastic constitutive model developed by Kim and Lade (Kim and Lade 1988^{1,2}; Lade and Kim 1988) on the basis of the experimental observations of the mechanical behavior of the tested rock. The developed model is used in Section 4 for back analysis of the experimental results. Conclusions concerning the permeability evolution and its dependence on the stress states and formation of compaction bands are drawn in Section 5. In the last Section (Section 6) follows an overall discussion of the study. In matters of terminology, compactive stresses and strains are taken positive.

2 Experimental Procedure and Mechanical Data

The tested rock, the Tuffeau de Maastricht calcarenite, is a high-porosity outcrop yellowish-white porous sedimentary limestone. The Tuffeau is a siliceous limestone formed from the erosion of other rocks by marine sedimentation 90 million years ago. The word "Tuffeau" comes from the Latin *tofus* meaning spongy stone (Beck et al 2003).

All tests were conducted on right circular cylinders (approximately 38 mm in diameter and 76 mm in height, that is a height:diameter ratio of 2:1), under triaxial and K-constant compression. Cores were drilled in the same direction to eliminate the possibility of lithological variations and anisotropy influencing the results. The tolerance of the samples was within the ISRM requirements. Thin nitrile sleeves were used to separate the dry samples from the confining fluid while for the saturated samples FEP teflon sleeves were used. Axial deformations were measured using LVDTs (Linear Variable Differential Transformer), while radial ones were measured in two orthogonal directions using cantilevers jigs. The samples were tested at room temperature inside a pressure vessel. Both the axial force and the confining pressure were applied by servo-controlled hydraulic systems.

In tests performed for permeability measurements, the samples were saturated with purified kerosene. Each steel piston used, had two fluid ports delivering the fluid to a centered hole in the piston front face. Sintered steel disks were placed at the end faces of the saturated samples to

distribute the fluid over the cross section. Volumetric flow rates were recorded by the fluid delivery pumps (Quizix SP-5200), while a differential pressure transducer recorded the pressure drop across the sample.

A set of mechanical data for Tuffeau de Maastricht calcarenite is shown in Fig. 2.1. The axial stress is plotted against the axial strain for specimens that tested in conventional triaxial experiments with confining pressures as indicated in the figure. The samples deformed uniaxially and at confining pressure 0.5 MPa are representative of the brittle faulting regime. The axial stress attained a peak, beyond which the stress progressively dropped (strain softening). The peak stress shows a positive correlation with mean stress (Fig. 2.2). At 0.5 MPa confining pressure the volumetric strain initially increased, but near the peak stress it reversed to a decrease (Fig. 2.3). Visual inspection of the tested samples confirmed the development of shear localization.

In the "transitional" regime between brittle faulting and cataclastic flow (deformation at confining stresses 2, 2.5, 4, 4.5 and 5 MPa) the volumetric strain increased in all experiments monotonically with ongoing deformation (Fig. 2.3). A peak in the differential stress and strain softening (negative slope in the axial stress vs. axial strain curve) are evident at the deformation behavior of the samples tested at 2, 2.5, 4 and 5 MPa confining pressure. CT scans and microscopic observations confirmed the formation of compaction bands and development of several conjugate shear bands of "high" angle in the samples tested at 4.5 and 5 MPa confining pressure. The CT scan of the sample tested at 4.5 MPa confining pressure revealed the formation inside the sample of fractures (dark areas) that were not visible in the outer surface (Fig. 2.4). The fractures were generated in high angles (almost normal some of them) to the plug axis that is the direction of the most compressive stress. The whole specimen was first impregnated by blue-stained epoxy and then petrographic thin sections (30 mm thick) were taken and examined by transmitted light microscopy. The thin section presented in Fig. 2.5 was located to a part of the plug where an open fracture had been observed in the CT image and demonstrates the presence of released grains in the fractures. In another thin section (Fig. 2.6) crushed grains close to a fracture and some micro cracks oriented orthogonal to the fracture can be seen. The CT scan of the sample tested at 5 MPa confining pressure (Fig. 2.7) reveals also fractures oriented in high angles to the most compressive stress. In both samples grain packing is evident across the fractures (Fig. 2.8). Grain breakage and packing along the fractures but not in the large fragments in between them suggest that localization occurred in the loading phase. In the unloading phase (elastic phase), due to stress release, fractures emerged inside the localization zones since the grain bonds were broken and fragments were not

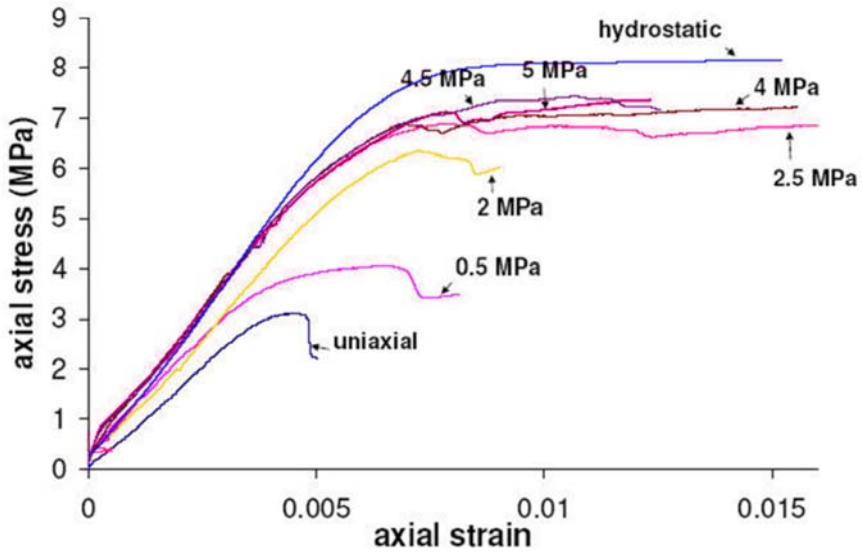


Fig. 2.1. Axial stress vs axial strain curves obtained from conventional triaxial experiments performed at confining pressures as indicated in the figure.

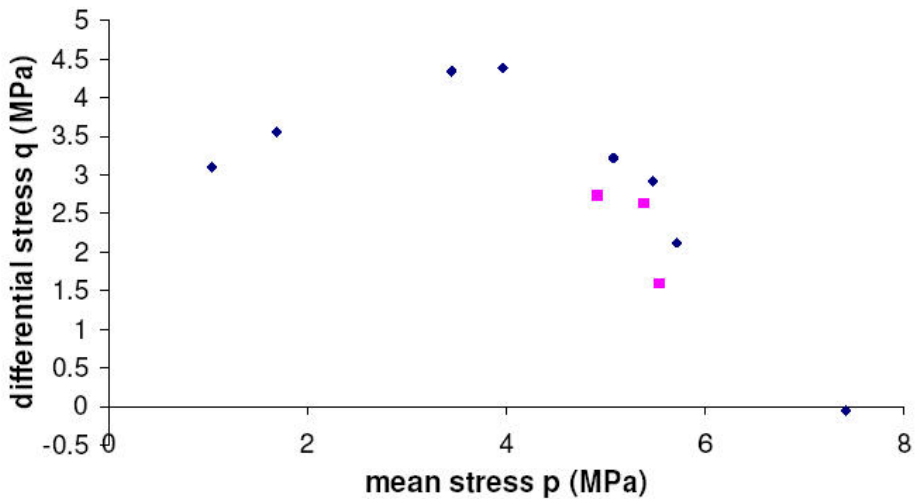


Fig. 2.2. Failure envelope of the tested rock. In "■", data from tests not presented in Fig. 2.1

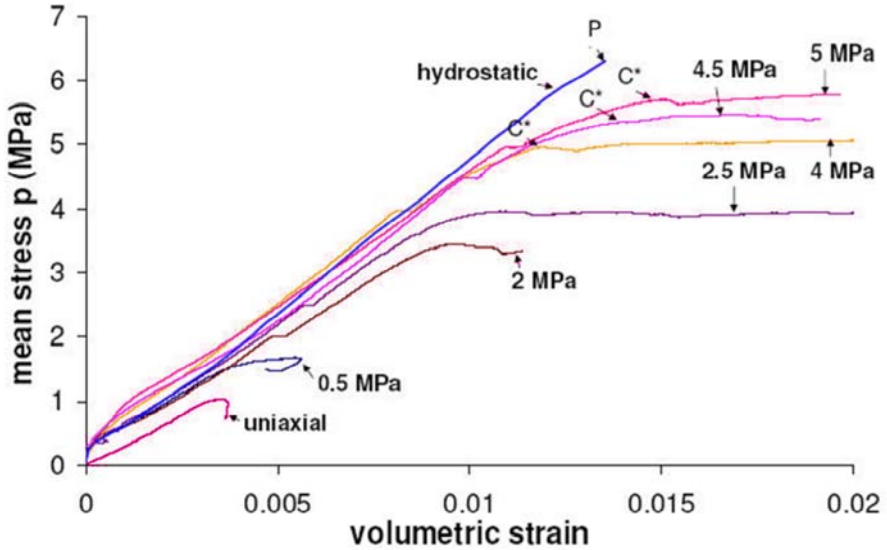


Fig. 2.3. Mean stress vs volumetric strain curves for a set of conventional triaxial tests performed at confining pressures as indicated in the figure.

attached to each other by cement (released gains). The orientation of some of the fractures (normal to the most compressive stress) suggests the formation of compaction bands.

Additional insight is gained by examining the effects of the hydrostatic and deviatoric stresses on volumetric strain (Fig. 2.3). There is a point in the hydrostat denoted P_* which corresponds to the onset of grain crushing and pore collapse. Deviations from the hydrostat imply that additional volumetric strain change is induced by the deviatoric stresses. In the transitional regime between brittle faulting and cataclastic flow, beyond the stress levels, denoted by C^* in Fig. 2.3, that correspond approximately to the first local peak stresses, deviatoric stresses provides a significant contribution to the compactive volumetric strain (shear-enhanced compaction). In contrast, in the brittle faulting regime deviatoric stresses induced the volumetric strain to decrease (shear-enhanced dilation). The mean stress-volumetric strain curves describing the experiments at 2 and 2.5 MPa have the qualitative descriptions of the others in the transitional type of failure. That is, before the peak stress was attained, the volumetric strain increased somewhat relative to the hydrostat, but then a pronounced increase occurred post-peak.

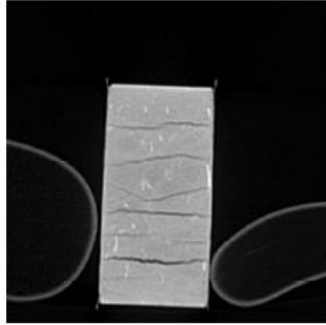


Fig. 2.4. CT-scan of a sample tested triaxially at 4.5 MPa confining pressure

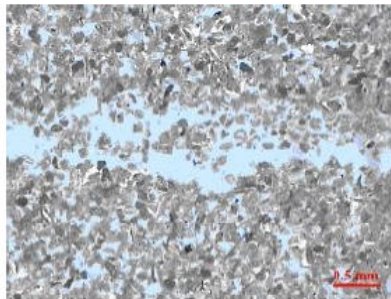


Fig. 2.5. Thin section photo of the sample tested at 4.5 MPa confining pressure showing released grains in fracture. A 0.5 mm scale bar is shown

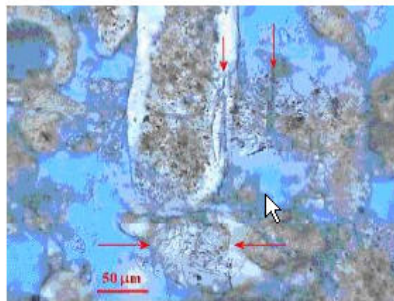


Fig. 2.6. Thin section photo of the sample tested at 4.5 MPa confining pressure showing crushed grains close to a fracture. Some micro cracks (upper arrows) are oriented orthogonal to the fracture (horizontal, just above the photo). A 0.5 mm scale bar is shown

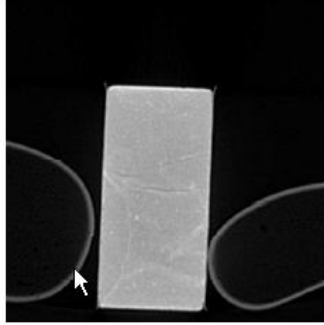


Fig. 2.7. CT-scan of a sample tested triaxially at 5 MPa confining pressure

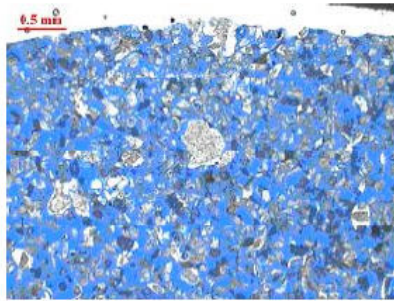


Fig. 2.8. Thin section photo of the sample tested at 5 MPa confining pressure showing possible denser grain packing close to large fragments that are not compressed. A 0.5 mm scale bar is shown

3 Infinitesimal Deformation Theory of Bifurcation of Elastoplastic Solids – Calibration of the Lade and Kim’s Model

In this section we revisit the general localization theory of deformation bands and calibrate the elastoplastic model developed by Lade and Kim to the experimental data.

3.1 General Analysis of the Deformation Bands

We assume an elastoplastic material with a yield function F and a plastic potential function Q . If plastic volumetric strain v_p is used as the only

parameter to keep track of the history of inelastic deformation, then the yield condition can be written as

$$F(\sigma_{ij,k}) = 0 \quad (3.1)$$

where $k := k(v_p)$ is a function of the plastic volumetric strain v_p induced by the stresses σ_{ij} ($i, j = 1, 2, 3$).

When the stress state is on the yield surface, the inelastic strain increments $d\varepsilon_{ij}^p$ ($i, j = 1, 2, 3$) are assumed to be normal to the plastic potential Q , thus are assumed to be expressed by the following relation:

$$d\varepsilon_{ij}^p = d\lambda_p \frac{\partial Q}{\partial \sigma_{ij}} \quad (3.2)$$

where $d\lambda_p$ is a non-negative factor of proportionality and ∂ denotes partial differentiation with respect to the indicated variable. Then, the rate constitutive equation takes the form:

$$d\sigma_{ij} = C_{ijkl}^\varepsilon \left(d\varepsilon_{kl} - d\lambda_p \frac{\partial Q}{\partial \sigma_{ij}} \right) \quad (3.3)$$

where with isotropy in the elastic response, the elasticity tensor reads:

$$C_{ijkl}^\varepsilon = \frac{E}{2(1+\nu)} \left(-\frac{2\nu}{1+\nu} \delta_{ij} \delta_{kl} + \delta_{ik} \delta_{jl} + \delta_{il} \delta_{jk} \right) \quad (3.4)$$

E and ν denote Young's modulus and Poisson's ratio, respectively, and δ_{ij} is the Kronecker's delta.

Because v_p changes with inelastic deformation, so that the stress state remains on the yield surface, the following consistency condition must be satisfied:

$$dF = \frac{\partial F}{\partial \sigma_{ij}} d\sigma_{ij} + \frac{\partial F}{\partial k} \frac{dk}{dv_p} dv_p \quad (3.5)$$

Substituting

$$dv_p = d\varepsilon_1^p + d\varepsilon_2^p + d\varepsilon_3^p = d\lambda_p \sum_{i=1}^3 \frac{\partial Q}{\partial \sigma_i} \quad (3.6)$$

where $\sigma_i (i=1,2,3)$ denote the principal stresses and $d\varepsilon_i^p (i=1,\dots,3)$ denote the principal plastic strain increments, into (3.5), solving for $d\lambda_p$ and substituting the result into (3.5) yields the following expression for the stress increments:

$$d\sigma_{ij} = C_{ijkl}^{ep} d\varepsilon_{kl} \quad (3.7)$$

where the elastoplastic constitutive operator C_{ijkl}^{ep} is given by

$$C_{ijkl}^{ep} = C_{ijkl}^{\varepsilon} - \frac{C_{ijmn}^{\varepsilon} \frac{\partial F}{\partial \sigma_{mn}} \frac{\partial F}{\partial \sigma_{pq}} C_{pqkl}^{\varepsilon}}{\frac{\partial F}{\partial \sigma_{rs}} C_{rstu}^{\varepsilon} \frac{\partial F}{\partial \sigma_{tu}} + H} \quad (3.8)$$

and

$$H = -\frac{\partial F}{\partial k} \frac{dk}{dv_p} \sum_{i=1}^3 \frac{\partial Q}{\partial \sigma_i} \quad (3.9)$$

is the plastic hardening modulus.

The loading criterion for a given strain increment reads:

$$\left\{ \begin{array}{l} \frac{\partial F}{\partial \sigma_{ij}} C_{ijkl}^{\varepsilon} d\varepsilon_{kl} > 0, \quad \text{loading;} \\ \frac{\partial F}{\partial \sigma_{ij}} C_{ijkl}^{\varepsilon} d\varepsilon_{kl} = 0, \quad \text{neutral loading;} \\ \frac{\partial F}{\partial \sigma_{ij}} C_{ijkl}^{\varepsilon} d\varepsilon_{kl} < 0, \quad \text{unloading.} \end{array} \right. \quad (3.10)$$

Rudnicki and Rice 1975 showed that localized deformation in a planar zone with unit normal \mathbf{n} is a bifurcation from homogeneous deformation if a non trivial solution exists to the following eigenvalue problem:

$$\{n_i C_{ijkl}^{ep} n_l\} m_k = 0 \quad (3.11)$$

A non-trivial solution for the m_k is possible only when

$$\det \{n_i C_{ijkl}^{ep} n_l\} = 0 \quad (3.12)$$

$n_i C_{ijkl}^{ep} n_l$ is the acoustic tensor and \mathbf{m} its eigenvector. The localization condition is the result of the requirements that the traction rates be continuous across the band boundary and that the velocity field be continuous at the instant of band localization. The nature of the deformation band at localization depends on the inner product (\mathbf{n}, \mathbf{m}) of the vectors \mathbf{n} and \mathbf{m} :

$$\left\{ \begin{array}{ll} (n, m) = -1, & \text{pure dilation band;} \\ -1 < (n, m) < 0, & \text{dilatant shear band;} \\ (n, m) = 0, & \text{pure shear band;} \\ 0 < (n, m) < 1, & \text{compactive shear band;} \\ (n, m) = 1, & \text{pure compaction band.} \end{array} \right. \quad (3.12)$$

3.2 Constitutive Model Developed by Lade and Kim

Kim and Lade (Kim and Lade 1988^{1,2}; Lade and Kim 1988) developed a single hardening constitutive model for frictional materials. The model incorporates all three stress invariants and it was validated by the authors for sand and plain concrete. It consists of twelve parameters that are to be calibrated from at least a hydrostatic, a uniaxial and a conventional triaxial experiment in the brittle faulting regime. The restricted number of tests necessary for the calibration of the model is of importance, since the number of in situ cores available for testing is often restricted as well. It should be noted however that the presence of the third invariant is not necessary for the simulation of the experiments performed.

In table 3.1 values of Young's modulus E and Poisson ratio ν obtained from unloading-reloading cycles performed at different conventional triaxial experiments are given. The averaged values, together with the parameters of model that are calibrated below, are used in order to calculate the elastoplastic tensor C_{ijkl}^{ep} of Section 3.1.

Table 3.1. Determination of Young's modulus E and Poisson ratio ν for Tuffeau de Maastricht rock from unloading-reloading cycles in conventional triaxial experiments at confining pressures as indicated in the table

Triaxial compression tests performed at	E (MPa)	ν
0 MPa	2807.65	0.23
0.5 MPa	2648.24	0.223
2 MPa	3161.27	0.202
2.5 MPa	3158.48	0.206
averaged $E \approx 2943.91$		averaged $\nu \approx 0.215$

3.2.1 Plastic Potential Function

The plastic potential function is expressed as a function of the three stress invariants I_1 , I_2 and I_3 in the following form:

$$Q = \left(c_0 - \frac{I_1^2}{I_2} + c_3 \frac{I_1^3}{I_3} \right) I_1^\mu \quad (3.13)$$

where the subscript "1" denotes the direction of the most compressive stress.

The parameter c_0 controls the intersection with the hydrostatic axis, the parameter c_3 acts as a weighting factor between the triangular shape (from the I_3 term) and the circular shape (from the I_2 term), and the exponent μ determines the curvature of the meridians. A constant stress α (tensile strength) must be added to stresses before substituting them to the invariants. α is a cohesion like parameter. If a uniaxial extension test is not available then α can be approximated reasonably well from the compressive strength σ_c , using the relation

$$\alpha = -0.22\sigma_c^{0.75} \quad (3.14)$$

which holds for sedimentary rocks (Kim and Lade 1984). The above relation yields $\alpha = 0.5142 \text{ MPa}$ for the tested Tuffeau. In what follows we will keep the notation used for the stresses and for the stress invariants to denote the translated stresses and translated stress invariants respectively.

3.2.2 Determination of the Parameters c_3, c_0, μ

In Kim and Lade 1988¹, it was shown for various frictional materials that c_3 decreases as the rigidity of the materials increase, and the cross-section of the plastic potential surface changes from a triangular to a rounded shape. The effect of material rigidity was also observed in the characteristics of the failure surfaces. Thus the curvature of failure surface meridians increases with increasing rigidity. This curvature is modeled by the parameter m in the failure criterion below. The relation between c_3 and m for frictional materials can be expressed as a power function

$$c_3 = 0.00155m^{-1.27} \quad (3.15)$$

giving $c_3 = 0.0007$, since $m = 1.853$ (see Failure Criterion below).

By defining now

$$v_p = -\frac{d\varepsilon_3^p}{d\varepsilon_1^p} \quad (3.16)$$

and substituting the plastic strain increments using the plastic flow rule, under triaxial compression conditions, we obtain

$$c_3 \frac{I_1^3}{I_3} - \frac{I_1^2}{I_2} = \frac{1}{\mu} \left(\frac{1}{1+v_p} \left(\frac{I_1^3}{I_2^2} (\sigma_1 + \sigma_3 + 2\sigma_1 v_p) + c_3 \frac{I_1^4}{I_3^2} (\sigma_1 \sigma_3 + \sigma_3^2 v_p) \right) \right) - c_0 \quad (3.17)$$

$$\left(-3c_3 \frac{I_1^3}{I_3} + 2 \frac{I_1^2}{I_2} \right)$$

or

$$f_1 = \frac{1}{\mu} f_2 - c_0 \quad (3.18)$$

Then the parameters μ , and c_0 can be determined by linear regression from several data points (Fig. 3.1). For the tested rock $\mu = 4.32$ and $c_0 = -2.96$. Notice that the condition of irreversibility that is plastic work should be positive whenever a change in plastic strain occurs (Kim and Lade 1988²), is satisfied since

$$\mu > 0 \tag{3.19}$$

$$c_0 > -(27c_3 + 3) \tag{3.20}$$

The plastic potential surface for Tuffeau de Maastricht has the shape of an asymmetric cigar in the principal stress space (Fig. 3.2). The surface is continuous throughout the stress space except at the intersection with the hydrostatic axis behind the origin of the space.

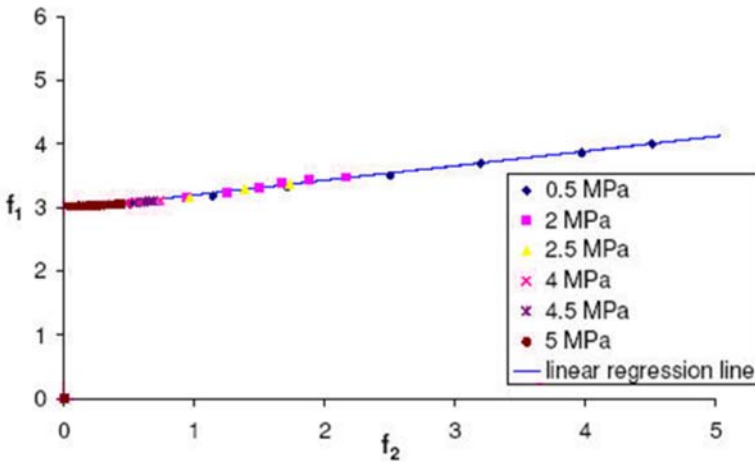


Fig. 3.1. Determination of the parameters μ and c_0 by linear regression from several data points

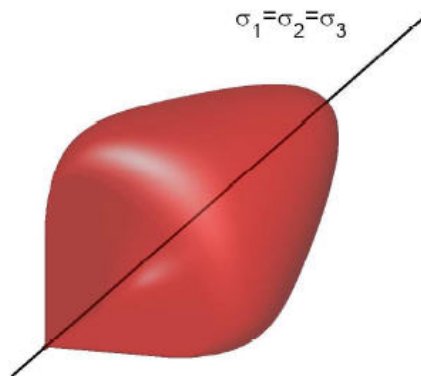


Fig. 3.2. Plastic potential surface for Tuffeau de Maastricht calcarenite in principal stress space

3.2.3 Failure Criterion $F_f = \left(I_1^3 / I_3 - 27\right) I_1^m = \eta$

The above criterion was proposed by Kim and Lade 1984 based on data for different types of rock. The constant parameters m and η can be determined by plotting $\left(\frac{I_1^3}{I_3} - 27\right)$ vs $\left(\frac{1}{I_1}\right)$ at failure in a log-log diagram and locating the best fitting straight line. The intercept of this line with $\left(\frac{1}{I_1}\right) = 1$ is the value of $\eta = 1127.716$ and $m = 1.863$ is the slope of the line (Fig. 3.3).

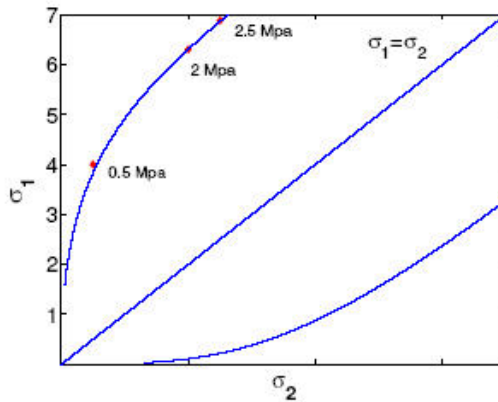


Fig. 3.3. Failure envelope for Tuffeau de Maastricht rock in a diagram of the first and second principal stresses

3.2.4 Yield Criterion and Hardening/Softening Law

The proposed isotropic yield function is expressed as follows:

$$F = f(\sigma_i) - k(v_p) \quad (3.21)$$

in which

$$f(\sigma_i) = \left(c_3 \frac{I_1^3}{I_3} - \frac{I_1^2}{I_3} \right) I_1^h e^q \quad (3.22)$$

and $k(v_p)$ keeps track of the history of inelastic deformation based solely in the plastic volumetric strain (v_p). The parameter c_3 was determined in the plastic potential function. Parameters h (constant) and q (variable) control the meridional curvature of the yield surface.

The yield surface together with the compactive yield cap have the shape of an asymmetric tear drop with a smoothly rounded triangular cross section as shown in Fig. 3.4.

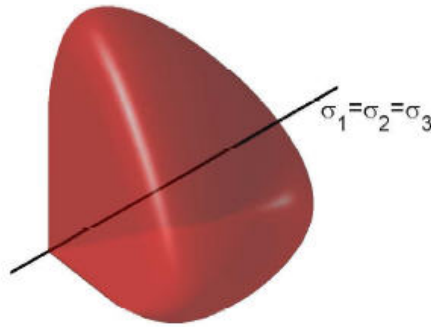


Fig. 3.4. Yield envelope for Tuffeau de Maastricht calcarenite in principal stress space

3.2.5 Parameter Determination for Yield Criterion

Consider two stress points A and B on the same plastic volumetric strain contour (plastic volumetric strain contours coincide with yield surfaces). We suppose that q , which is variable, is 1 at the failure point B and 0 at the point A which lies on the hydrostatic axis. Then $F(\sigma_i)_{atA} = F(\sigma_i)_{atB}$ or

$$h = \frac{\ln \left(\frac{c_3 \frac{I_{1B}^3}{I_{3B}} - \frac{I_{1B}^2}{I_{2B}}}{27c_3 + 3} \right) e}{\ln \frac{I_{1A}}{I_{1B}}} \tag{3.23}$$

In table 3.2 the values of h , in the conventional triaxial experiments at confining pressures that correspond in the brittle faulting regime and in the transition regime between brittle faulting and cataclastic flow, are given.

Table 3.2. Determination of the parameter h for Tuffeau de Maastricht rock

Triaxial compression tests performed at	h
0.5 MPa	3.25
2 MPa	3.64
2.5 MPa	3.08
averaged $h \approx 3.324$	

The parameter q is a function of stress level such that

$$\begin{cases} q = 0, & \text{during hydrostatic compression;} \\ 0 < q < 1, & \text{during hardening;} \\ q = 1, & \text{at failure stresses.} \end{cases} \quad (3.24)$$

The dependence of q on the stress level in the hardening regime will be investigated in the sequel. We have to keep in mind though, that $q = 0$ during hydrostatic compression in order to calibrate the parameters of the hardening law that follows.

3.2.6 Hardening Law $k := f'(v_p)$

The translated hydrostatic pressure may be modeled by a quadratic function of the plastic volumetric strain, up to a value v_p^{in} chosen for the best fitting possible, but otherwise arbitrary:

$$I_1 = K v_p^2 + L v_p + W \quad (3.25)$$

where the parameters K , L and W are all constants. Then, the parameters of the quadratic function (K , L and W) update so that

$$K(v_p^{in})^2 + Lv_p^{in} + W = \left(K(v_p^{in})^2 + Lv_p^{in} + W \right)_{updated} \quad (3.26)$$

$$2Kv_p^{in} + LW = \left(2Kv_p^{in} + L \right)_{updated} \quad (3.27)$$

$$\left(-\frac{L}{2K} \right)_{updated} = v_p^* \quad (3.28)$$

(3.26) and (3.27) yield that the curve which simulates the translated hydrostatic pressure is C^1 differentiable (Fig. 3.5), while due to (3.28) the transition from hardening to softening occurs when the plastic volumetric strain takes the value v_p^* (see also Softening law).

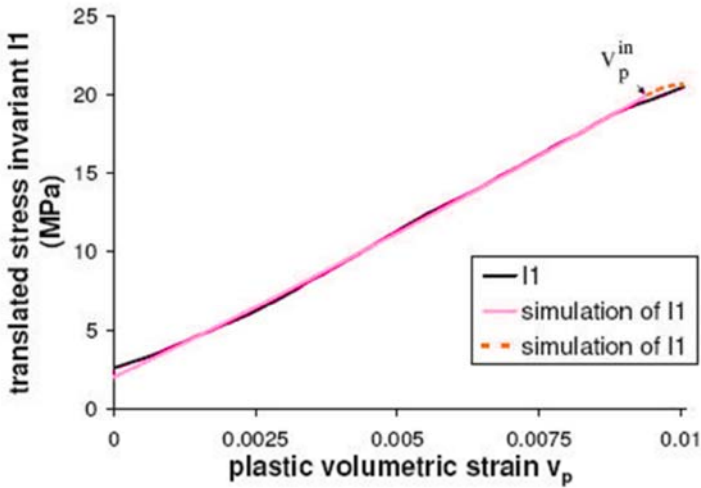


Fig. 3.5. Simulation of the translated hydrostatic principal stress I_1 as a function of plastic volumetric strain

The plastic volumetric strain contour at v_p^* approximates the compactive failure cap, that is the curve defined by the stress states C^* (Table 3.3). So for a hydrostatic compression test ($q = 0$, q defined in the yield criterion)

$$f(\sigma_i) = f'(v_p) \Rightarrow f'(v_p) = (27c_3 + 3)(Kv_p^2 + Lv_p + W)^h \quad (3.29)$$

3.2.7 Variation of q

The stress level $S = \frac{F_f}{n}$ varies from 0 on the hydrostatic axis to 1 at the failure surface. S is a hyperbolic function of

Table 3.3. Values of v_p on the compactive failure cap for different triaxial compression

Triaxial compression tests performed at	v_p
2.5 MPa	0.00913
4 MPa	0.00915 and 0.0123
4.5 MPa	0.0138 and 0.0128
5 MPa	0.0118
averaged $v_p^* \approx 0.0115$	
Hydrostatic experiment	0.0149

$$q = \ln \left(\frac{f'(v_p)}{\left(c_3 \frac{I_1^3}{I_3} - \frac{I_1^2}{I_3} \right) I_1^h} \right) \tag{3.30}$$

that is $S = \frac{q}{\beta + \gamma q}$ where β and γ are constant parameters. Since the curve passes through (1, 1) we obtain

$$q = \left(\frac{\beta S}{1 - (1 - \beta)S} \right) \tag{3.31}$$

Fig. 3.6 presents the variation of q with respect to the stress level for the tested Tuffeau. β was found to be approximately 0.7.

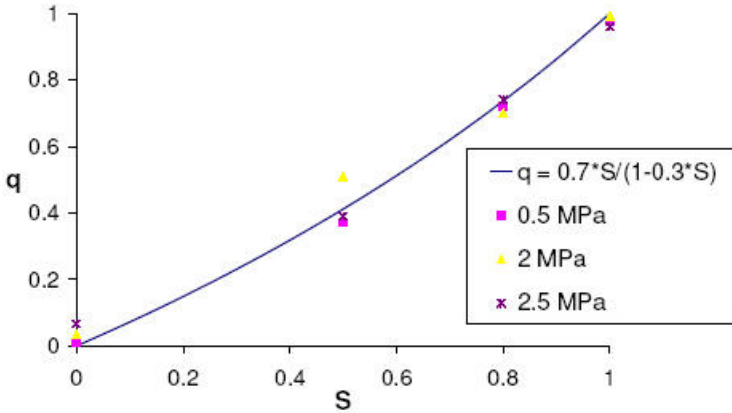


Fig. 3.6. Variation of q as a function of the stress state S

3.2.8 Softening Law $k := f''(v_p)Ae^{-Bv_p}$

Softening may begin anywhere along the monotonically increasing hardening curve and is initiated when $q=1$, which in turn occurs when $S=1$. Softening may also occur when the plastic volumetric strain takes the value v_p^* of the plastic volumetric strain contour that approximates the failure cap that is in the case of Tuffeau de Maastricht rock the value 0.0115 strain (table 3.3). This value must be equal to $v_p^* = -\frac{L}{2K}$ for which the hardening modulus $H = (27c_3 + 3)h(Kv_p^2 + Lv_p + W)^{h-1}(2Kv_p + L)$ becomes zero and softening begins.

3.2.9 Determination of the Parameters A and B

The slope of the softening curve is set equal to one tenth the negative slope of the hardening curve at the peak point. This assumption enables us to calculate both parameters

$$A = (f')_{peak} e^{B(v_p)_{peak}} \quad (3.32)$$

$$B = \frac{1}{10} \left(\frac{df''}{dv_p} \right)_{hard, peak} \frac{1}{(f')_{peak}} \quad (3.33)$$

The values of all the parameters that are needed for the calculation of the elasto-plastic tensor C_{ijkl}^{ep} of the tested rock are listed in table 3.4.

Table 3.4. Parameters needed for the calculation of the elasto-plastic tensor C_{ijkl}^{ep} of Tuffeau de Maastricht rock

E (MPa)	ν	α	m	η
2943,91	0.215	0.5142	1.853	1127.716
c_0	c_3	μ	h	β
-2.96	0.0007	4.32	3.324	0.7

4 Back Test Analysis

The back analysis of the triaxial tests used for the calibration of the elasto-plasticity model follows. Because of the non-linear constitutive model, the simulation of the tests is performed incrementally using numerically Euler forward integration.

Fig. 4.1 shows the numerical simulation in comparison with the experimental data of a hydrostatic test up to point P^* that corresponds to the onset of grain crushing and pore collapse. In the uniaxial compressive test the numerical data is roughly consistent with the experimental data,

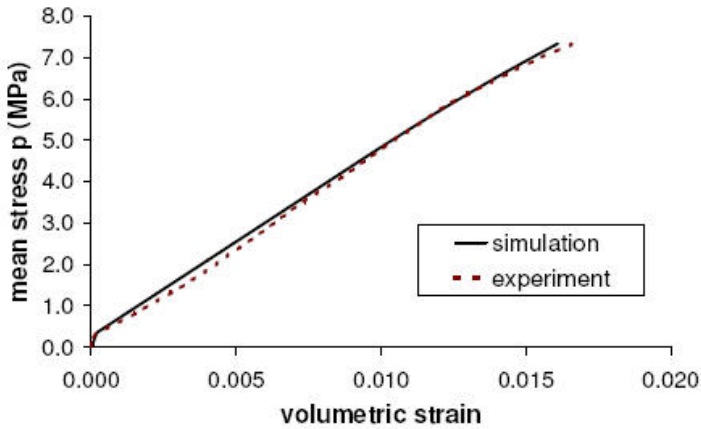


Fig. 4.1 Experimental data and numerical simulation of a hydrostatic test

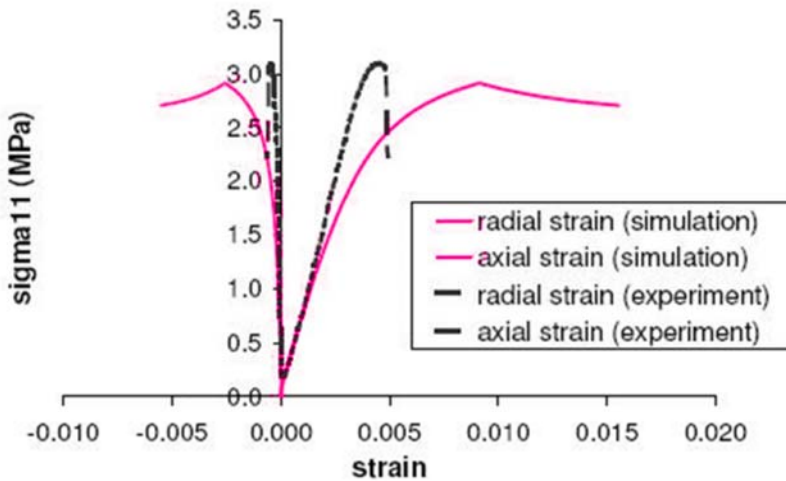


Fig. 4.2. Experimental data and numerical simulation of a uniaxial test. The two left curves represent the radial strains (experimental and simulated)

and the reason is that in the calibration as customary the uniaxial test was not taken into account (Fig. 4.2).

The comparison of the numerical simulation of the conventional triaxial experiment at 0.5 MPa confining pressure with the experimental data (Fig.

4.3), together with the back analysis of the other tests below, shows that the model of Lade and Kim does capture the behavior of Tuffeau rock.

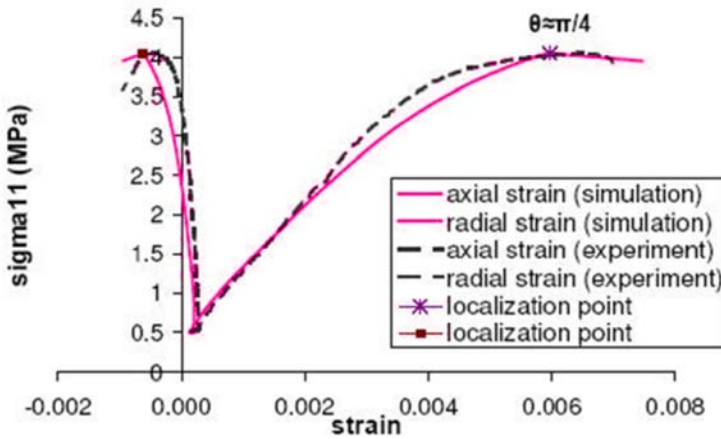


Fig. 4.3. Experimental data and numerical simulation of a conventional triaxial test at 0.5 MPa confining pressure. The two left curves represent the radial strains (experimental and simulated).

The bifurcation analysis for this test predicts a localization of the homogeneous deformation in a dilatant (almost isochoric) shear band ($0 < (n, m) = \mathbf{O}(10^{-2})$) in the softening regime. The angle between the plane of localization and the most compressive stress is approximately 0.241π . In the next figure (Fig. 4.4) the back analysis of a conventional triaxial test with 2 MPa confining pressure is presented. The predicted localization band that forms in the softening regime, is in this case a compactive shear band ($(n, m) < 0$) with the aforementioned angle being approximately 0.345π . The same angle between the plane of the predicted localization band and the most compressive stress in the conventional triaxial experiment at 2.5 MPa confining pressure is 0.342π approximately (Fig. 5.1). The onset of the predicted compactive shear band occurs again post-peak. The above tests were representatives of the brittle faulting regime and the transitional regime between brittle faulting and cataclastic flow. In the conventional triaxial experiments that follow with confinements in the cataclastic flow regime, namely at 4, 4.5 and 5 MPa confining pressures, the model predicts pure compaction bands ($(n, m) \approx -1$) pre-peak. The comparison of the experimental data with the numerical simulation as well as the predicted onsets of the pure compaction bands are given in Figs. 5.2,

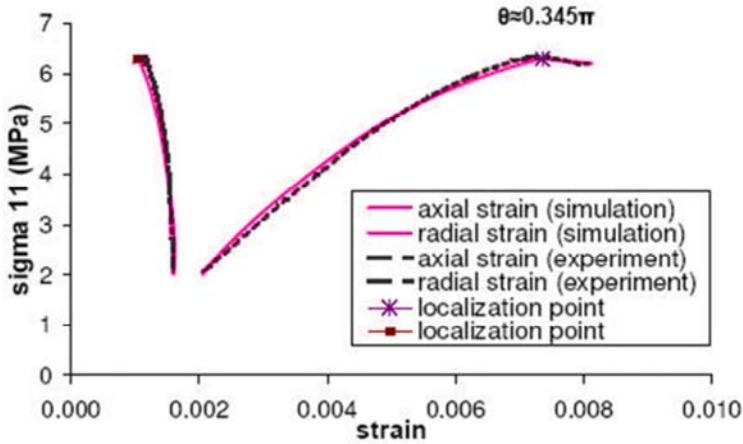


Fig.4.4. Experimental data and numerical simulation of a conventional triaxial test at 2 MPa confining pressure. The two left curves represent the radial strains (experimental and simulated).

5.3 and 5.4 for the tests at confining pressures 4, 4.5 and 5 MPa, respectively. Again only the deviatoric part of the tests is considered.

5 Permeability Reduction

There was an appreciable scatter in permeability between different samples. Instead of presenting the normalized data from all the experiments performed, we prefer to show the primary data of those samples with comparable permeabilities.

In Fig. 5.5 the axial stress as a function of the axial strain at conventional triaxial experiments performed at 4, 4.5 and 5 MPa effective pressures and a K -constant experiment for $K=0.7$ (the ratio σ_2 / σ_1 is equal to 0.7, where $\sigma_2 = \sigma_3$ and $\sigma_i (i=1, \dots, 3)$ are the principal stresses), are shown. The tests were drained with the pore pressure kept constant at 2 MPa. The stress-strain curves of the conventional triaxial experiments in Fig. 4.4 are similar to those of the samples that were subjected to loading at corresponding confining pressures. However, there is a difference in the strength, due to the presence of kerosene used to saturate the samples and to creep since at 0.5 MPa effective mean stress some preliminary

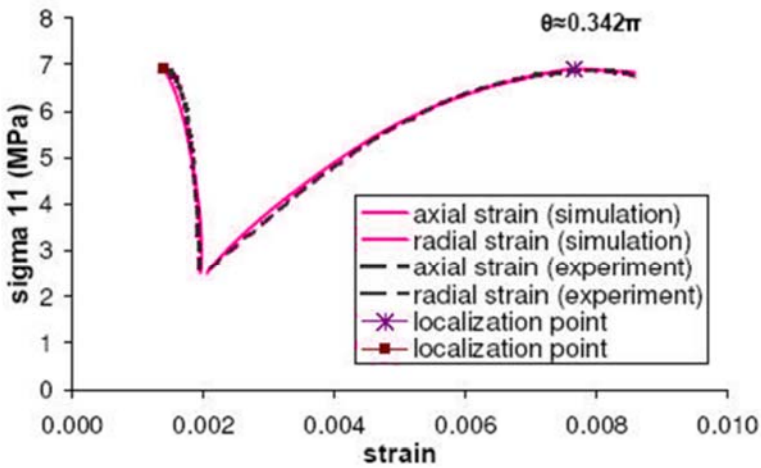


Fig. 5.1. Experimental data and numerical simulation of a conventional triaxial test at 2.5 MPa confining pressure. The two left curves represent the radial strains (experimental and simulated)

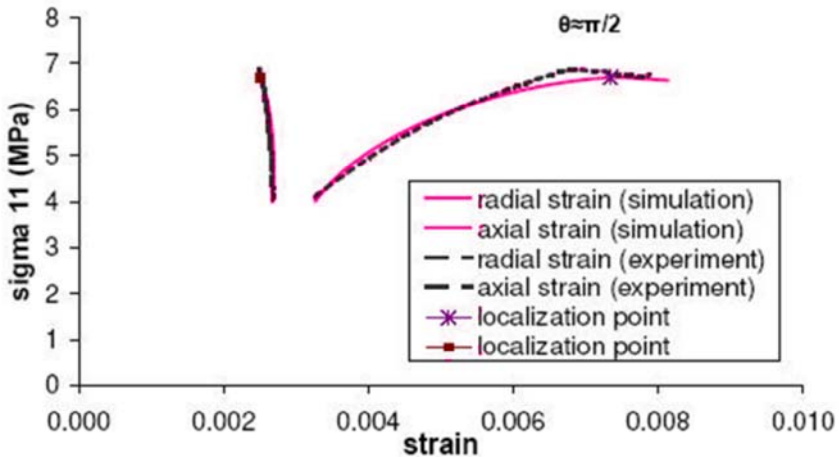


Fig. 5.2. Experimental data and numerical simulation of a conventional triaxial test at 4 MPa confining pressure. The two left curves represent the radial strains (experimental and simulated)

permeability measurements had to be recorded. This difference is approximately 13.6% of the strength of the dry samples. All the above experiments are performed at effective pressures that correspond to the cataclastic flow regime. Permeability consistently decreases with increasing strain, independently of whether the sample showed hardening or softening. The mechanical data presented in Section 2 indicate that with the onset of shear-enhanced compaction C^* (a threshold in differential stress) coupling of the deviatoric and hydrostatic stresses induce considerable volumetric strain increase. The critical stress levels C^* mark the onset of significant reduction in permeability as well. Before the onset of shear-enhanced compaction permeability is primarily controlled by the effective mean stress, independent of the deviatoric stresses. With the onset of shear-enhanced compaction, however, the nonhydrostatic loading exerts dominant control over permeability (Fig. 5.6).

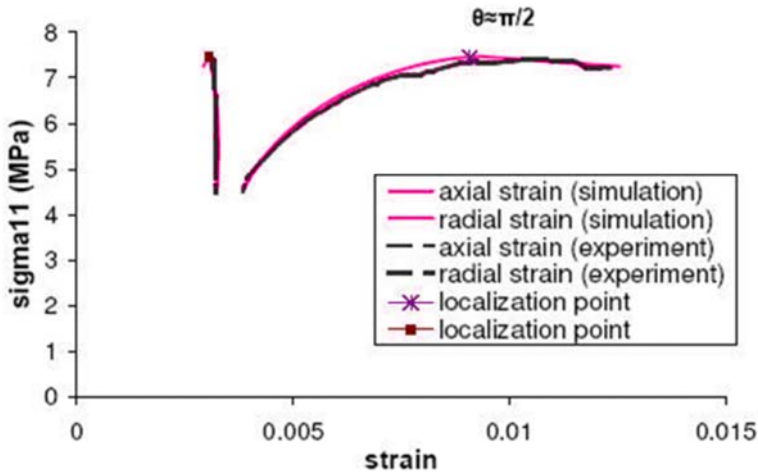


Fig. 5.3. Experimental data and numerical simulation of a conventional triaxial test at 4.5 MPa confining pressure. The two left curves represent the radial strains (experimental and simulated)

Minor differences can be seen between the hydrostatic and triaxial experiments when permeability is plotted as a function of volumetric strain (overall positive correlation).

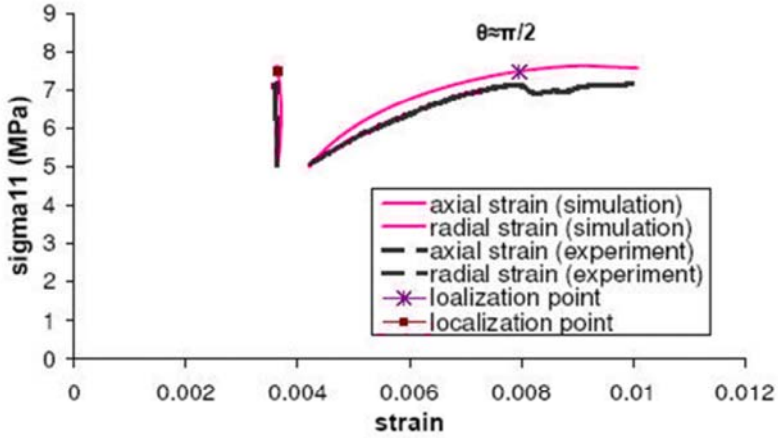


Fig. 5.4. Experimental data and numerical simulation of a conventional triaxial test at 5 MPa confining pressure. The two left curves represent the radial strains (experimental and simulated)

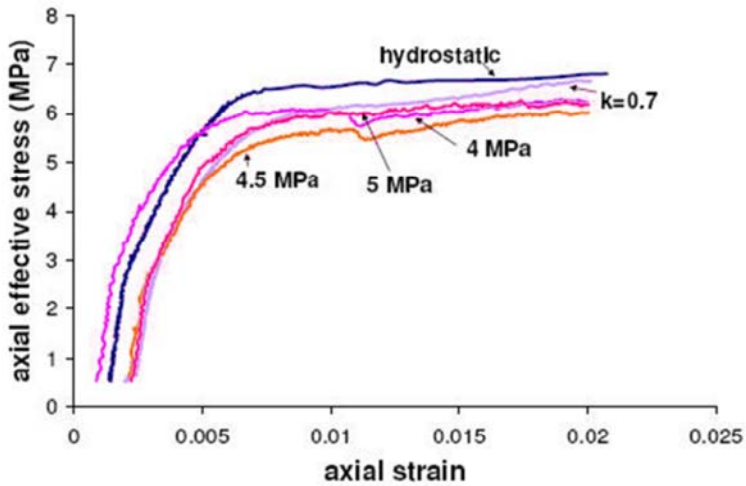


Fig. 5.5. Axial effective stress vs axial strain curves obtained from conventional triaxial and a K -constant experiments performed for testing permeability evolution

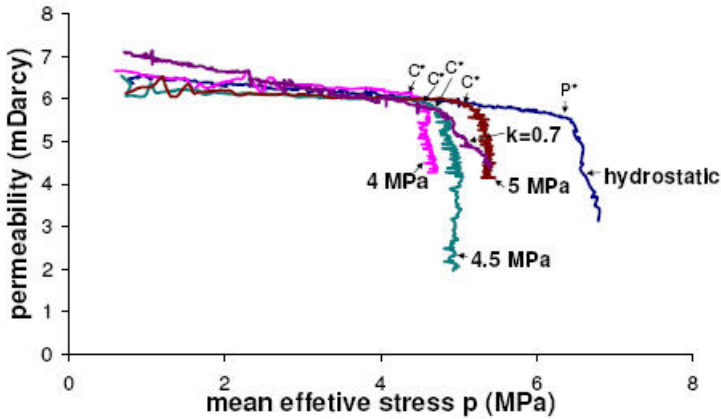


Fig. 5.6. Permeability plotted against mean effective stress for conventional triaxial experiments in the cataclastic flow regime.

6 Concluding Remarks

The mechanical behavior of Tuffeau de Maastricht calcarenite was studied. Dry conventional triaxial and hydrostatic experiments were performed. The data obtained was used to calibrate the parameters of the single hardening elasto-plastic model developed by Kim and Lade. The numerical results were in good agreement with the experimental ones. The tested samples were CT scanned and petrographic thin sections were taken based on these CT scans, in an effort to identify the presence of deformation bands.

The model predicts dilatant shear bands in the brittle faulting regime in accordance with the experimental observation, while in the transitional regime between brittle faulting and cataclastic flow predicts compactive shear bands and almost pure compaction bands. The localization points in the cases of dilatant shear bands and compactive shear bands occur post-peak (after the peak in the stress-strain curve is attained). Almost pure compaction bands are predicted before the onset of shear-enhanced compaction (that is the first local peak). The localization points in all test back analysis are very close to the first local peaks where deformation bands are assumed to form with the exception of the test back analysis of the triaxial experiment performed at 5 MPa confining pressure, where the onset of the compaction band is predicted quite pre-peak.

Conventional triaxial and K-constant experiments were also performed to elucidate the stress dependence of permeability. The effective mean

stresses were sufficiently high that the sample failed by cataclastic flow. The critical stress levels C^* (onsets of shear-enhanced compaction) mark the onset of considerable permeability reduction due to the coupling effect of the deviatoric and hydrostatic stresses. Before the onset of shear-enhanced compaction, permeability is primarily controlled by the effective mean stress, independent of the deviatoric stresses.

Acknowledgements

The first author thanks Jørn Stenebråten for his crucial help in the experimental work. This work was conducted at SINTEF Petroleum Research, and received financial support from the EU project 'Degradation and Instabilities in Geomaterials with Application to Hazard Mitigation' (DIGA-HPRN-CT-2002-00220) in the framework of the Human Potential Program, Research Training Networks.

References

1. Baud, P., E. Klein, and T.-f. Wong (2004) Compaction localization in porous sandstones: spatial evolution of damage and acoustic emission activity, *Journal of Structural Geology*, 26: 603-624.
2. Borja, R.I. (2002) Bifurcation of elastoplastic solids to shear band mode at finite strain, *Comput. Methods Mech. Engrg.*, 191: 5287-5314.
3. Borja, R.I. and A. Aydin (2004), Computational modeling of deformation bands in granular media. I. Geological and Mathematical framework, *Comput. Methods Mech. Engrg.*, 193: 2667-2698
4. Borja, R.I. (2004), Computational modeling of deformation bands in granular media. II. Numerical simulations, *Comput. Methods Mech. Engrg.*, 193: 2699-2718
5. Haimson, B.C. (2003) Borehole breakouts in Berea Sandstone reveal a new fracture mechanism, *Pure and Applied Geophysics* 160: 813-831.
6. Haimson, B.C. and I. Song (1998), Borehole Breakouts in Berea Sandstone: Two Porosity-Dependent Distinct Shapes and Mechanisms of Formation, *SPE/ISRM*, 229-238
7. Haimson, B.C. and H. Lee (2004), Borehole breakouts and compaction bands in two high-porosity sandstones, *International Journal of Rock Mechanics & Mining Sciences* 41: 287-301.
8. Holcomb, D. and W. Olsson (2003), Compaction localization and fluid flow, *J Geophys Res* 108 (B6): 2290-2303, doi:10.1029/2001JB000813.
9. Holt, R.M. (1989) Permeability reduction induced by a nonhydrostatic stress field, paper SPE19595 presented at 64th Annual Technical Conference, Soc. Of Petr. Eng., San Antonio, TX.

10. Issen, K.A., and J.W. Rudnicki (2000) Conditions for compaction bands in porous rocks, *J. Geophysical Res.*, 105: 21529-21536.
11. Issen, K.A., and J.W. Rudnicki (2001) Theory of compaction bands in porous rock, *Phys. Chem. Earth (A)*, 26: 95-100.
12. Issen, K.A. (2002) The influence of constitutive models on localization conditions for porous rock, *Eng. Fract. Mech.*, 69: 1891-1906.
13. Kim, M.K., and P.V. Lade (1984) Modeling rock strength in three dimensions, *Int. J. Rock Mech. Min. Sci. and Geomech. Abstr.*, 21, No 1: 21-33.
14. Kim¹, M.K., and P.V. Lade (1988) Single hardening constitutive model for frictional materials. I. Plastic potential function, *Comput. Geotech.*, 5: 307-324.
15. Kim², M.K., and P.V. Lade (1988) Single hardening constitutive model for frictional materials. II. Yield criterion and plastic work contours, *Comput. Geotech.*, 6: 13-29.
16. Klein, E., P. Baud, T. Reuschle and T.-f. Wong (2001) Mechanical behavior and failure mode of Bentheim sandstone under triaxial compression, *Phys. Chem. Earth (A)*, 26: 21-25.
17. Lade, P.V. and M.K. Kim (1988) Single hardening constitutive model for frictional materials. III. Comparisons with experimental data, *Comput. Geotech.*, 6: 31-47.
18. Lajtai, E. Z. (1974) Brittle fracture in compression, *Int. J. Fract.*, 10: 525-536.
19. Molemma, P.N. and M.A. Antonellini (1996) Compaction bands: a structural analog for anti-mode I cracks in Aeolian sandstone, *Tectonophysics*, 267: 209- 228.
20. Olsson, W.A. (1999) Theoretical and experimental investigation of compaction bands, *J. Geophys. Res.*, 104: 7219-7228.
21. Olsson, W.A., and D.J. Holcomb (2000) Compaction localization in porous rock, *Geophys. Res. Lett.*, 27: 3537-3540.
22. Papka, S.D., and S. Kyriakides (1998) In plane crushing of a polycarbonate honeycombs, *Int. J. Solids Struct.*, 35: 239-267.
23. Park, C., and S.R. Nutt (2001) Anisotropy and strain localization in steel foam, *Mat. Sci. Eng.*, A299: 69-74.
24. Rhett, D.V., and L.W. Teufel (1992) Stress path dependence of matrix permeability of north Sea sandstone reservoir rock, *Proc. U.S. Rock Mech. Symp.*, 33: 345-354.
25. Rudnicki, J.W., and L.R. Rice (1975) Conditions for the localization of deformation in pressure-sensitive dilatant materials, *J. Mech. Phys. Solids*, 23: 371-94.
26. Somerton, W.H., I.M. Solemnization, and R.C. Duddy (1975) Effect of stress on permeability of coal, *Int. J. Rock Mech. Min. Sci.*, 12: 129-145.
27. Sternlof, K. and D.D. Pollard (2001), Deformation bands as linear elastic fractures: progress in theory and observation, *Eos Transactions American Geophysical Union* 82(47): F1222.

28. Sternlof, K.R., J.W. Rudnicki, and D.D. Pollard (2005), Anticrack-inclusion model for compaction bands in sandstone. *Journal of Geophysical Research* 110:B11403, doi:10.11029/12005JB003764.
29. Vajdova, V., P. Baud, and T. Wong (2004), Compaction, dilatancy, and failure in porous carbonate rocks, *J. Geophys. Res.*, 109: 1029-, doi:10.1029/2003JB002508.
30. Wong, T.-f., P. Baud, and E. Clein (2001) Localized failure modes in a compactant porous rock. *Geophys. Res. Lett.*, 28: 2521-2524.
31. Zhu,W., and T.-f. Wong (1996) Permeability reduction in a dilating rock: Network modeling of damage and tortuosity, *Geophys. Res. Lett.*, 23: 3099-3102.

Local Second Gradient Models and Damage Mechanics: 1D Post-Localization Studies in Concrete Specimens

P. Kotronis¹, F. Collin², P. Bésuelle¹, R. Chambon¹ and J. Mazars¹

¹Laboratoire Sols, Solides, Structures (3S)
UJF/INPG/CNRS,
Domaine Universitaire,
BP 53, 38041 Grenoble cedex 9,
France
E-mail: Panagiotis.Kotronis@inpg.fr

²Département Géomac,
FNRS-ULG,
Liège,
Belgium,
E-mail: f.collin@ulg.ac.be

1 Introduction

Continuum damage mechanics is often used as a framework for describing the variations of the elastic properties of due to micro-structural degradations. Experimentally, concrete specimens exhibit a network of microscopic cracks that nucleate sub-parallel to the axis of loading. Due to the presence of heterogeneities in the material (aggregates surrounded by a cement matrix), tensile transverse strains generate a self-equilibrated stress field orthogonal to the loading direction, a pure mode I (extension) is thus considered to describe the behaviour even in compression. This rupture mode must be reproduced numerically. This is the reason why the failure criterion of the chosen constitutive law is expressed in terms of the principal extensions and that a tension test is modelled at the end of this paper. The influence of micro-cracking due to the external loads is introduced via damage variables, ranging from 0 for the undamaged material to 1 for a completely damaged material.

This approach, however, is known to be inadequate for studies where strain softening appears. Calculations performed with a local classical continuum model - which does not incorporate an internal length variable -

are unable to objectively model intrinsic failure zones. Spurious mesh dependence appears and also cases of failure without any energy dissipation. In order to improve computational performance the nonlocal damage approach is often used in the literature. A different solution is investigated within this work. Local second gradient models are chosen to include a meso scale in the continuous. This approach differs from the nonlocal one in the sense that it is a local theory with higher order stresses depending only on the local kinematic history.

A brief presentation of a classical damage mechanics constitutive law used for the calculations is given at the first part of the paper. The second gradient local approach for a 1D medium is then introduced. Finally, different numerical computations with 1D specimens in traction are presented. Using a random initialization of the iterative solver of the equilibrium equation we search the existence of various solutions and we show that the second gradient term regularize the problem giving results that are mesh insensitive and objective.

2 Scalar Damage Model

Introduced in 1958 by Kachanov [1] for creep-related problems, continuum damage mechanics has been applied in the 1980s for simulating the non linear behaviour of concrete [2], [3], [4]. Thermodynamics of irreversible processes gave the framework to formulate the adapted constitutive laws [5], [6]. Considering the material as a system described by a set of variables and a thermodynamic potential, constitutive laws are systematically derived along with conditions on the evolution of damage. However, an adequate choice of the potential and of the damage variable (scalar or tensor) remains to be made. Several anisotropic damage models have already been proposed [7], [8], [9], [10]. Possible applications cover also dynamic problems [11], [12], porous materials [13] and chemical damage [14]. Recent literature reviews on damage mechanics and concrete can be found in [15], [16], [17].

The outlines of a local scalar 3D damage mechanics law for concrete are presented hereafter [18], [19]. In this model, the material is supposed to behave elastically and to remain isotropic. The loading surface takes the following form:

$$f(D) = \varepsilon_{eq} - K(D) \quad (2.1)$$

with ε_{eq} the equivalent strain defined as:

$$\varepsilon_{eq} = \sqrt{\sum_{i=1}^3 \langle \varepsilon_i \rangle_+^2} \quad (2.2)$$

being ε_i the principal strains with (+ for traction)

$$\langle \varepsilon_i \rangle_+ = \varepsilon_i \quad \text{if} \quad \varepsilon_i \geq 0 \quad \text{and} \quad \langle \varepsilon_i \rangle_+ = 0 \quad \text{if} \quad \varepsilon_i < 0 \quad (2.3)$$

The choice of the previous definition of the equivalent strain ε_{eq} is guided by the fact that tensile transverse strains are considered to describe the behaviour even in compression (see section 1). D is a scalar whose value is in the domain $[0, 1]$. The hardening-softening parameter $K(D)$ takes the largest value of the equivalent strain ever reached by the material at the considered point. In that way it retains the previous loading history. Initially $K(0)$ equals a given threshold ε_{D0} . Evolution laws for damage are used to describe the response in tension or compression - index j refers either to tension (t) or compression (c):

$$D_j = 1 - \frac{\varepsilon_{D0}(1 - A_j)}{\varepsilon_{eq}} - A_j \exp\left[-B_j(\varepsilon_{eq} - \varepsilon_{D0})\right] \quad (2.4)$$

A_j and B_j are material parameters identified independently from compression tests on cylinders and bending tests on beams. The scalar damage variable D , that has to be introduced in the constitutive equation, is a weighted sum of D_t and D_c .

$$D = \alpha_t^\beta D_t + \alpha_c^\beta D_c \quad (2.5)$$

β is a parameter that has been added to the original version of the model in order to reproduce more accurately the behaviour of under shear. It is usually taken equal to 1.06. We call σ_+ and σ_- ($\sigma = \sigma_+ + \sigma_-$) the tensors in which appear only the positive and negative principal stress respectively, and ε_t and ε_c the strain tensors defined as:

$$\varepsilon_t = \Lambda^{-1} : \sigma_+ \quad \text{and} \quad \varepsilon_c = \Lambda^{-1} : \sigma_- \quad (2.6)$$

$\Lambda(D)$ is a fourth-order symmetric tensor interpreted as the secant stiffness matrix and it is a function of damage. The weights α_t and α_c are defined by the following expressions:

$$a_t = \sum_{i=1}^3 H_i \frac{\varepsilon_{ii}(\varepsilon_{ii} + \varepsilon_{ci})}{\varepsilon_{eq}^2} \quad (2.7)$$

$$a_c = \sum_{i=1}^3 H_i \frac{\varepsilon_{ci}(\varepsilon_{ii} + \varepsilon_{ci})}{\varepsilon_{eq}^2} \quad (2.8)$$

$H_i = 1$ if $\varepsilon_i = \varepsilon_{ci} + \varepsilon_{ii} \geq 0$, otherwise $H_i = 0$. a_c and a_t are the coefficients defining the contribution of each type of damage for general loading. From (2.7) and (2.8) it can be verified that for uniaxial tension $a_t = 1, a_c = 0, D = D_t$, and vice versa for compression. Responses under uniaxial compression and tension of this model are presented in figure 2.1.

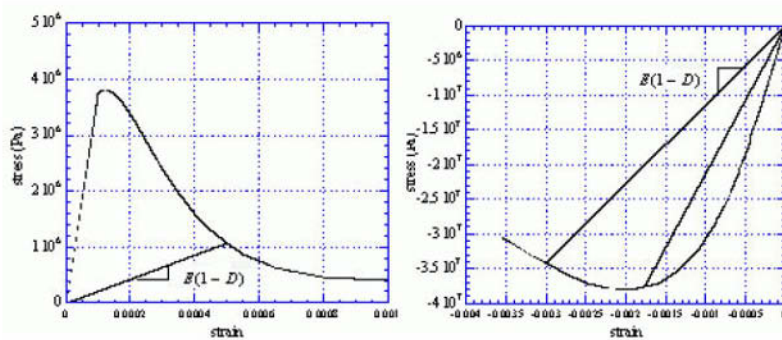


Fig. 2.1. Response of the Mazars damage model for concrete in uniaxial tension (left) and compression (right), (E being the Young modulus)

3 Local Second Gradient Model

It is today well established that strain softening induces bifurcation, strain localization, and that the numerical codes often predict failure without any energy dissipation [20],[21]. One of the possible remedies is to use classical damage mechanics constitutive laws based on the nonlocal damage theory (e.g., [22], [23], [24]) or nonlocal second within the flow theory of plasticity. The latter involve the second gradient of the plastic strain in the consistency condition and/or the flow rule, while the kinematic and equilibrium equations remain unchanged (e.g., [25], [26], [27]). For these models the constitutive equation in its incremental form is

itself a partial differential equation. Peerlings [28], [29] and Fremond [30] have also studied second gradient models within the theory of damage mechanics. Zervos et al. [31] proposed a mixed type model that can be interpreted as a strain-gradient theory with softening law enriched by the second gradient on an internal variable.

A different approach is investigated within this work consisting of using second gradient local models to introduce a meso scale in continuous models [32], [33], [34]. The word local means that the constitutive equation is a relation only between local quantities. Strain gradients are considered as additional observable state variables and are conjugate to higher order stresses that enter the equilibrium equations. This local model is a direct extension of microstructured or micromorphic continua proposed in [35] and [36]. Its general formulation follows.

For a 1D medium the internal virtual power P_{in}^* for the domain $\Omega = [a, b]$ is a linear form in \dot{u}^{*} and \dot{u}^{**} , the first and second derivatives with respect to the space variable x of the virtual velocity field \dot{u}^* ($\dot{}$ is the symbol used for the derivatives with respect to the time and ' with respect to the space variable x). It takes the following form:

$$P_{in}^* = - \int_a^b (N\dot{u}^{*} + M\dot{u}^{**}) dx \tag{3.1}$$

N being the usual normal stress in 1D continuum, M is a double stress.

In order to calculate the external virtual power P_{ex}^* , additional external forces μ , associated to the second gradient terms, have to be added to the classical external forces v , associated to the first gradient terms (no distributed forces are taken into consideration, so the only forces are those acting on the two ends a and b). The virtual power of the external forces is then:

$$P_{ex}^* = v_b\dot{u}_b^* + v_a\dot{u}_a^* + \mu_b\dot{u}_b^{**} + \mu_a\dot{u}_a^{**} \tag{3.2}$$

The virtual power formulation of the equilibrium equation of the continuum is for all kinematically admissible field \dot{u}^* :

$$P_{ex}^* + P_{in}^* = 0 \tag{3.3}$$

Integrating by parts twice shows that equation (3.3) is equivalent to:

$$N' - M'' = 0 \tag{3.4}$$

and

$$\begin{aligned} M(a) &= -\mu_a; M(b) = \mu_b; \\ N(a) - M'(a) &= -v_a; N(b) - M'(b) = -v_b \end{aligned} \quad (3.5)$$

The next step is to choose the constitutive laws linked with the first and the second gradient part of the model.

$$\dot{N} = f(\dot{u}') \quad (3.6)$$

$$\dot{M} = g(\dot{u}'') \quad (3.7)$$

For large strain computations, there is a difference between the time derivative of the strains ε and \dot{u}' , the derivative of the velocity with respect to the actual space variable. ε is a Lagrangian measure and u' , \dot{u}' are Eulerian ones. When small strains are assumed $\varepsilon = u'$ and both models can be written in an integral manner as follows:

$$N = f(\varepsilon) \quad (3.8)$$

$$M = g(\varepsilon') \quad (3.9)$$

The balance equation (3.4) can be integrated as:

$$N - M' = \text{constant} = N_1 \quad (3.10)$$

Substituting N and M given by equations (3.8) and (3.9) in equation (3.10), yields a differential equation which has to be met by the function u of x . This equation can be solved analytically under certain conditions. Assuming that there is no coupling between those f and g , various types of constitutive relations can be studied. In the original papers [32], [33], a classical elastoplastic bilinear model (or a CLoE family model [37], [38]) exhibiting softening has been chosen for f and a linear relation for g . The authors have proven analytically that for a given problem the solutions have to be built using patches of different fundamental solutions, consisted of ‘hard parts’ corresponding to the unloading pieces and ‘soft parts’ for the loading pieces of the media. In that way, different solutions are possible (an inner hard solution, a hard-soft solution, a soft-hard-soft solution... see figure 3.1). In order to build a patch solution, one has to equate the values of the displacements u , strains u' and of the two internal forces $N - M'$ and M at the ends of the different pieces in order to meet the virtual power equation, and then to check that $u' < e_{\text{lim}}$ in hard pieces and

$u' > e_{lim}$ in soft pieces (e_{lim} being a threshold of the constitutive law, for example $e_{lim} = \varepsilon_{D0}$ for the Mazars law).

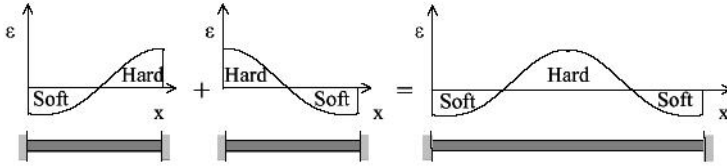


Fig. 3.1. Patches of different fundamental solutions

A 2D second gradient element has been developed [39], [40] and implemented in the finite element code LAGAMINE (Université de Liège). The formulation of the element and the corresponding constitutive equations use a mathematical constraint between the micro kinematics description and the usual macro deformation gradient field. They are valid for large strains. This constraint is enforced in a weak sense by using Lagrange multipliers in order to avoid difficulties with the C1 continuity (second involving the first and the second derivatives of the displacement field).

In the following section, the feasibility of this local approach with constitutive laws based on damage mechanics is proven numerically using 1D simulations. The Mazars damage mechanics law is used for the function f and some remarks about the uniqueness of solution, the objectivity of the calculations and the influence of a possible coupling between the functions f and g are drawn.

4 1D Numerical Simulations

A 1D concrete bar submitted to traction is studied hereafter and the length of the localization zone is compared with the analytical solutions provided in [32], [33]. The bar is modelled using the 2D second gradient element of the finite element code LAGAMINE (Université de Liège, [39], [40]) under plane deformations. In order to avoid any 2D effects, a zero vertical displacement is applied at the upper and lower boundaries along the bar ($u_2 = 0$, figure 4.1). The right end of the bar is fixed ($u_1 = u_2 = 0$) and the external traction displacement is applied at the left end. The additional external forces v_b, v_a, μ_b, μ_a are assumed to be zero at both ends. The section of the bar is $0.1 \times 1m^2$ and its length $1m$.

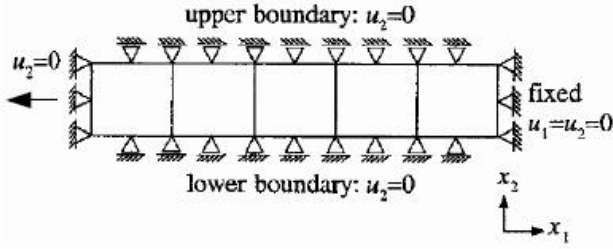


Fig. 4.1. Boundary conditions for simulating 1D traction in a 2D FE code

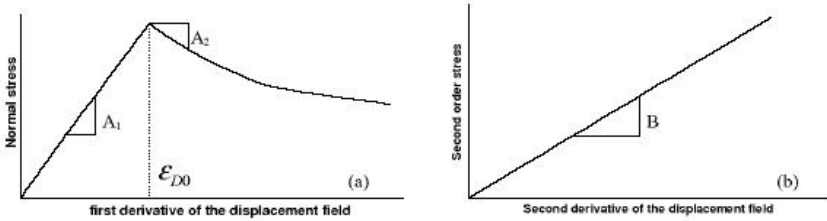


Fig. 4.2. Constitutive models: (a) first gradient part, (b) second gradient part

For the calculations presented hereafter it is assumed that there is no coupling between the first and the second gradient part of the model (functions f and g). The constitutive relations are the Mazars damage law for the first gradient part and a linear relation for the second gradient part (Figure 4.2). The parameters chosen for the damage law correspond to that of a typical specimen ($A_1 = 30.E + 09Pa, \epsilon_{D0} = 1.E - 04, A_2 = 0.5, B_1 = 2E + 04$, Poisson’s ratio 0.2, parameters that provide $A_2 \approx -16.7E + 09Pa$).

The second gradient local approach defines implicitly two internal lengths, the first (namely $\sqrt{B/A_1}$) corresponding to the unloading regime of the first gradient part of the model, and the second (namely $\sqrt{B/(-A_2)}$) corresponding to the softening loading regime just after the peak (B being the slope of the linear relation of the second gradient part, see figure 4.2). A way to define the order of magnitude used for B , is to use the criteria proposed in [32], [33] - valid under the small strain assumption and for a bilinear plastic law - in order to have possible analytical solutions and to avoid snap-back phenomena for the corresponding differential equation.

Assuming a two-part solution is possible (built with a patch of a hard part and a soft one) and considering $B = 0.37E + 09N$, one finds analytically that under small strains and for a bilinear law with $A_1 = 30.E + 09Pa$ and $A_2 = -16.7E + 09Pa$ the length of the soft part is equal approximately to $0.37m$. For the case of a three-part solution (hard - soft - hard) the length of the soft part equals approximately $0.78m$.

As soon as the peak is reached the problem exhibits a loss of uniqueness. In order to determine numerically bifurcation thresholds, an algorithm of random initialization of the iterative solver of the equilibrium equation is used just after the peak (at $\varepsilon_{D0} = 1.2E - 04$, [41], [42]). For every step, a full Newton-Raphson method under displacement control, involving a numerical consistent tangent stiffness operator for the complete model (i.e. the second gradient terms as well as the classical ones) is used [39]. The results of two meshes with 14 and 50 elements are presented hereafter [43]. Figure 4.3 shows the global force displacement curve for both meshes. Figure 4.4 presents the distribution of the damage variable D just after the peak ($\varepsilon_{D0} = 1.2E - 04$), and figure 4.5 at the end of the loading ($\varepsilon_{D0} = 2.9E - 04$).

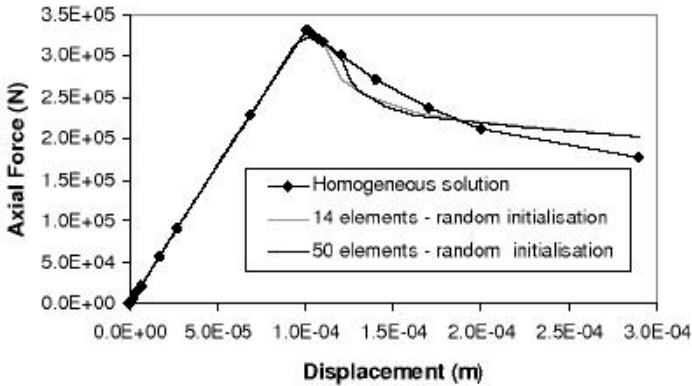


Fig. 4.3. 1D traction: Force - displacement curves for the two meshes

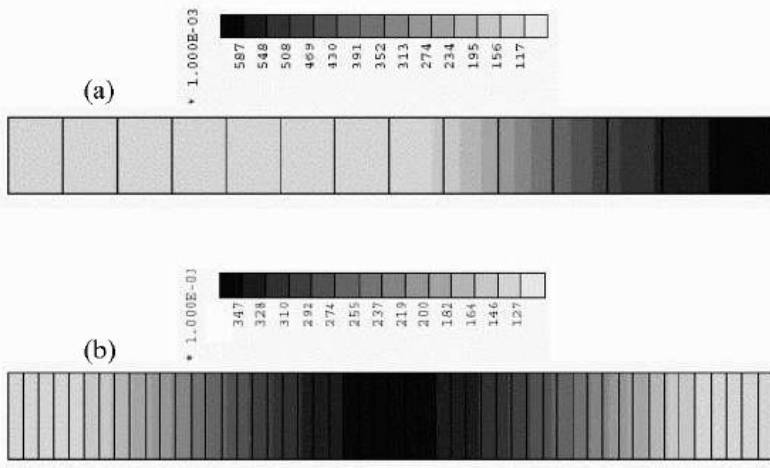


Fig. 4.4. Localization patterns (distribution of damage variable D) just after the peak ($\varepsilon_{D0} = 1.2E - 04$): (a) 14-element mesh, (b) 50-element mesh

Both meshes reproduce the homogeneous solution when no random initialization of the iterative solver is used. When random initialization of the velocities is used just after the peak, differences in the global curves appear. This is due to the different corresponding localization patterns. The mesh with 14 elements has converged to a solution with two patches (a hard part and a soft one with a length equal approximately to the length calculated analytically). The mesh with 50 elements has converged to a three-part solution (hard - soft - hard) with the length of the soft part again very similar to the analytical value (Figure 4.4). One can also notice that the maximum values of the damage variable D are different (0.587 for the 14 element mesh and 0.347 for the 50 element mesh). Of course, other random initialization can converge to different solutions, independently of the mesh discretization.

The 50-element mesh switches after to the two-part solution (Figure 4.5), thus the localization pattern and the global curves become identical. This is also seen in [44]. The maximum values of the damage variable D for both meshes are almost the same (approximately equal to 0.876).

From the previous results, it is obvious that the use of local second with damage mechanics laws provide internal lengths, and consequently solutions that do not depend on the spatial discretization. Finite element meshes with different number of elements provide the same solutions

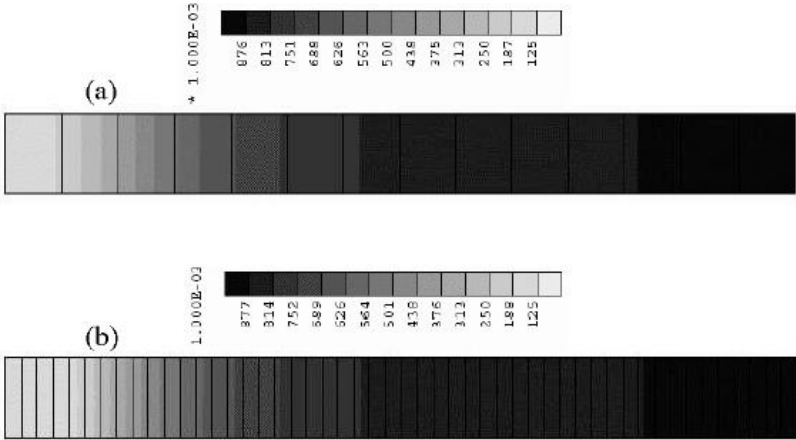


Fig. 4.5. Localization patterns (distribution of damage variable D) at the end of the loading ($\varepsilon_{D0} = 2.9E - 04$): (a) 14-element mesh, (b) 50-element mesh

(Figures 4.3 and 4.5 at the end of the loading). However, this approach does not restore the uniqueness properties for the corresponding boundary value problem. Different converged solutions can appear (Figures 4.3 and 4.4 just after the peak). Nevertheless, all these solutions are correct and possible to happen, contrary to the parasitic solutions obtained with a classical medium [20], [21].

5 Expansion of the Plastic Region

The previous results show that when the magnitude of the softening modulus decreases during the softening process, the plastic region is expanding. Some limited expansion of the plastic region is acceptable. However, as the softening modulus tends to zero, the size of the plastic region can grow without any bounds. This, as mentioned in [45], is a spurious, non physical effect which can be accompanied by stress locking, manifested by a non vanishing residual resistance of the structure even at very large elongations. The total work needed to completely break the bar (given by the area under the load-displacement diagram) is larger than in the absence of localization. In other words, the bar cannot fail by yielding of its limited segments, but every section must sooner or later start yielding. This is in

contradiction with the observed failure of concrete specimens, typically localized in regions having a limited length.

A way to deal with this problem is to abandon the hypothesis of the non coupling between the first and the second gradient part of the model (functions f and g). Assuming an anelastic relation also for the function g (inducing a decrease of the tangent modulus with the loading), one can expect that the structure will not present any residual resistance at very large elongations, and that the spurious stress locking will disappear. The function g could be such that the internal length corresponding to the softening loading regime after the peak stays constant throughout the whole loading history or is a function of the damage variable D . In that way we could control the evolution of the localization zone, that can now increase, stay constant or even decrease depending on the form of the chosen function.

For the following simulation the functions f and g are considered coupled. The Mazars damage mechanics law is used for the function f and the material parameters are kept the same as before. However, this time the second order stress M is calculated as a function of the damage variable D . Figure 5.1 shows the global force - displacement curves using the second gradient model with or without coupling. Figure 5.2 presents the distribution of the damage variable D during the whole loading when f and g are coupled.

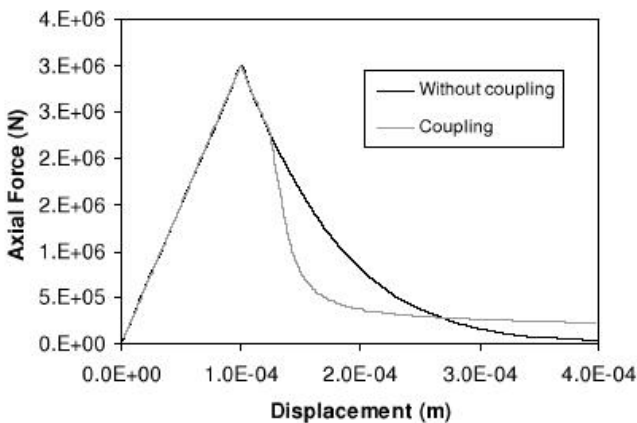


Fig. 5.1. 1D traction: Force - displacement curves considering or not coupling between the first and the second gradient part

In figure 5.1, one can observe that although the global curve presents a non-zero stress for large elongations, the localization zones in figure 5.2 do not expand. At the beginning and for the first displacement increments the

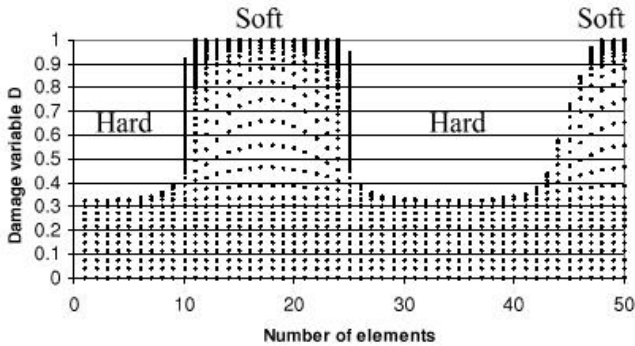


Fig. 5.2. 1D traction: Evolution of the localization pattern for the whole loading history considering coupling between the first and the second gradient part

damage variable has the same value all along the bar. However, a hard soft hard soft solution soon appears and the localization zone does not increase although the damage variable D approaches to 1. This behaviour is more realistic. The results of this first simulation seem to indicate that the coupling of the first and the second gradient part of the model could provide a solution in order to correctly predict complete failure.

6 Conclusions

The feasibility of using local second gradient models with constitutive laws based on damage mechanics is proved throughout this work. 1D numerical computations with concrete specimens and the relevant post-localization studies are presented. Using a random initialization of the iterative solver of the equilibrium equations it is shown once again that the second gradient term regularizes the problem providing results that are mesh insensitive and objective. However, as expected, it does not restore uniqueness properties for the corresponding boundary value problem. Numerical results considering coupling of the first and the second gradient part of the model indicate that the length of the localization zone can stay constant, property that could be useful in order to reproduce correctly the complete failure of concrete specimens.

Work in progress concerns the implementation of advanced following path techniques into the finite element code LAGAMINE to reproduce correctly snap-back phenomena [46], and various studies on the boundary conditions to use within a second gradient medium. Numerical simulations of biaxial tests will also be performed and comparisons with experimental 2D failure schemes of various concrete specimens.

References

1. Kachanov LM (1958) Time of rupture process under creep conditions. *Izvestia akademii nauk, USSR*, (in Russian), (8):26–31.
2. Krajcinovic D (1983) Constitutive equations for damaging material. *Journal of Applied Mechanics ASME*, 50:355–360.
3. Lemaitre J, Mazars J (1982) Application de la théorie de l'endommagement au comportement non linéaire et à la rupture du béton de structures. *Annales de l'ITBTP*, 4010.
4. Ladevéze P (1983) Sur une théorie de l'endommagement anisotrope. Report n. 34, Laboratoire de Mécanique et Technologie, Cachan, France.
5. Lemaitre J, Chaboche JL (1985) *Mécanique des matériaux solides*. Dunod-Bordas Ed. Paris, France.
6. Lemaitre J, Chaboche JL (1994) *Mechanics of Materials*. Cambridge University Press, Cambridge, pp. 556.
7. Dragon A, Mroz Z (1979) A continuum model for plastic-brittle behaviour of rock and concrete. *International Journal of Engineering Science*, 17:121–137.
8. Fichant S, Pijaudier-Cabot G, La Borderie C (1997) Continuum damage modelling: approximation of crack induced anisotropy. *Mech. Res. Comm.*, 24:109–114.
9. Fichant S, La Borderie C, Pijaudier-Cabot G (1999) Isotropic and anisotropic descriptions of damage in concrete structures. *Mechanics Cohesive Frictional Materials*, 4:339–359.
10. Mazars J, Pijaudier-Cabot G (1989) Continuum damage theory – application to concrete. *Journal of Engineering Mechanics ASCE*, 115:345–365.
11. La Borderie CL (1991) Phénomènes unilatéraux dans un matériau endommageable: modélisation et application à l'analyse des structures en béton. Thèse de doctorat, Université Paris 6.
12. Ragueneau F, La Borderie C, Mazars J (2000) Damage Model for Concrete Like Materials Coupling Cracking and Friction, Contribution towards Structural Damping: First Uniaxial Application. *Mechanics Cohesive Frictional Materials*, 5:607–625.
13. Pijaudier-Cabot G, Burlion N (1996) Damage and localisation in elastic materials with voids. *Mechanics Cohesive Frictional Materials*, 1:129–144.

14. Gérard B, Pijaudier-Cabot G, La Borderie C (1998) Coupled Diffusion-Damage Modelling and the Implications on Failure due to Strain Localisation. *International Journal of Solids Structures*, 35:4107–4120.
15. Pijaudier-Cabot G (2000) Continuum damage modelling. *Revue Française de Génie Civil*, 4(5):33–57. Numéro spécial, Ecole d'été ALERT, Constitutive Modelling of Geomaterials. Cambou, Di Prisco (eds).
16. Pijaudier-Cabot G, Mazars J (2001) Damage models for concrete. In *Handbook of Materials Behaviour Models*. Lemaitre J (ed.) Chapter 6-Damage models. Academic Press: New York, 500-513.
17. Jirasek M, Bažant ZP (2001) *Inelastic Analysis of Structures*. John Wiley and Sons (eds), 758 pages, Chichester, November.
18. Mazars J (1984) Application de la mécanique de l'endommagement au comportement non linéaire et à la rupture du béton de structure. Thèse de Doctorat d'Etat des Sciences Physiques, Université Pierre et Marie Curie Paris 6, France.
19. Mazars J (1986) A description of micro and macroscale damage of concrete structures. *Engineering Fracture Mechanics*, 25(5/6):729–737.
20. Bažant ZP (1976) Instability, ductility and size effect in strain softening concrete. *Journal of Engineering Mechanics ASCE*, 102:331–344.
21. Bažant ZP (1984) Continuum theory for strain softening *Journal of Engineering Mechanics ASCE*, 110:1666–1692.
21. Pijaudier-Cabot G, Bažant ZP (1987) Nonlocal damage theory. *Journal of Engineering Mechanics ASCE*, 113:1512–1533.
22. Pijaudier-Cabot G, Haidar K, Dubé JF (2004) Non-local damage model with evolving internal length. *International Journal for Numerical and Analytical Methods in Geomechanics*, 28:633–652.
23. Jirásek M (2004) Non-local damage mechanics with application to concrete. *Revue française de Génie Civil*, 8:683–707.
24. Aifantis E (1984) On the microstructural origin of certain inelastic models. *Transaction of ASME, J. Mat. Engng. Tech.* 106:326–330.
25. Vardoulakis I, Aifantis E (1991) A gradient flow theory of plasticity for granular materials. *Acta Mech.*, 87:197–217.
26. De Borst R, Mühlhaus H (1992) Gradient dependent plasticity: formulation and algorithmic aspects. *International Journal of Numerical Methods in Engineering*, 35:521–539.
27. Peerlings RHJ, de Borst R, Brekelmans WAM, de Vree JHP (1996) Gradient enhanced damage for quasi-brittle materials. *International Journal of Numerical Methods in Engineering*, 39:3391–3403.
28. Peerlings RHJ, Geers MGD, de Borst R, Brekelmans WAM (2001) A critical comparison of nonlocal and gradient-enhanced softening continua. *International Journal of Solids Structures*, 38:7723–7746.
29. Fremond M, Nedjar B (1996) Damage gradient of damage and principle of virtual work. *International Journal of Solids Structures*, 33(8):1083–1103.
30. Zervos A, Papanastasiou P, Vardoulakis I (2001) A finite element displacement formulation for gradient elastoplasticity. *International Journal of Numerical Methods in Engineering*, 50:1369–1388.

31. Chambon R, Caillerie D, El Hassan N (1996) Etude de la localisation unidimensionnelle à l'aide d'un modèle de second gradient. *C.R.A.S-Série IIb*, 323:231–238.
32. Chambon R, Caillerie D, El Hassan N (1998) One dimensional localisation studied with a second grade model. *European Journal of Mechanics A/Solids*, 17(4):637–656.
33. Chambon R, Caillerie D, Matsushima T (2001) Plastic continuum with microstructure, local second gradient theories for geomaterials: localization studies. *International Journal of Solids and Structures*, 38:8503–8527.
34. Mindlin RD (1964) Micro-structure in linear elasticity. *Arch. Ration. Mech. Anal.*, 16:51–78.
35. Germain P (1973) The method of virtual power in continuum mechanics. Part 2 : Microstructure. *SIAM J. Appl. Math.*, 25:556–575.
36. Chambon R (1989) Une classe de lois de comportement incrémentalement non linéaires pour les sols, résolution de quelques problèmes de cohérence. *C.R.A.S. Série II*, 308:1571–1576.
37. Chambon R, Desrues J, Charlier R, Hammad W (1994) CLoE, A new rate type constitutive model for geomaterials: Theoretical basis and implementation. *International Journal for Numerical and Analytical Methods in Geomechanics*, 18(4):253–278.
38. Matsushima T, Chambon R, Caillerie D (2000) Second gradient models as a particular case of microstructured models: a large strain finite element analysis. *C.R.A.S-Série II b*, 328:179–186.
39. Bésuelle P (2003) Implémentation d'un nouveau type d'élément fini dans le code LAGAMINE pour une classe de lois à longueur interne. Rapport d'activité pour le FNRS, Belgique, mai.
40. Chambon R, Crochepeyre S, Charlier R (2001) An algorithm and a method to search bifurcation points in nonlinear problems. *International Journal of Numerical Methods in Engineering*, 51:315–332.
41. Chambon R, Moullet JC (2004) Uniqueness studies in boundary value problems involving some second gradient models. *Computer methods in applied mechanics and engineering*, 193:2771–2796.
42. Kotronis P, Chambon R, Mazars J, Collin F (2005) Local second gradient models and damage mechanics: Application to concrete. 11th International Conference on Fracture, Turin, Italy, Org. ICF, cd paper no 5712, 20-25 March.
43. Bésuelle P, Chambon R, Collin F (2006) Switching mode of deformation in post-localization solutions with quasi brittle material. *Journal of mechanics of materials and structures* in print.
44. Rolshoven S (2003) Nonlocal plasticity models for localised fracture. Thèse N° 2887, Ecole Polytechnique Fédérale de Lausanne.
45. Kotronis P, Collin F (2005) Implementation of following path techniques into the finite element code LAGAMINE. Rapport Interne G'eomac/3S, septembre.

Part II

Micromechanical Aspects

Entropy and Material Instability in the Quasi-Static Mechanics of Granular Media

J. D. Goddard

Department of Aerospace & Mechanical Engineering,
University of California,
San Diego,
U.S.A.,
E-mail: jgoddard@ucsd.edu

Summary

Starting from a maximum-entropy model of granular statics, this brief note explores a possible material instability in the form of a “stress localization” anticipated in previous work (Goddard, 2002). After a brief review of the maximum-entropy model, it is shown that a special case allows for non-convex pressure-volume response of a kind that could lead to heterogeneous stress states in an isotropically compressed granular packing.

1 Statistics of Kinematics and Stress

Maximum-entropy estimates for the quasi-static mechanics of granular media date back at least to the pioneering work of Kanatani (1980) on the voidage of 2D granular packings. Recent works (Bagi, 1997; Kruyt & Rothenburg, 2002; Kruyt, 2003; Goddard, 2004a) treat both stress and infinitesimal strain, the latter pointing out the necessity of some specification of *a priori* probability in the relevant state space. This fact is already recognized in the work of Kanatani (1980), who refers to it as the “density of states” (a term also employed in quantum mechanics).

1.1 Delaunay Triangulation, Deformation and Stress

Following previous works, Kanatani (1980); Satake (1992); Bagi (1996), we assign to a granular assembly a (Satake) graph, which we associate with a Delaunay triangulation. The graph consists of a network of vertices

or nodes, representing particle centroids, connected by edges or “bonds”, representing nearest-neighbor pairs. The latter correspond to real and latent mechanical contacts and define the edges of an elementary space-filling volume known as Delaunay simplices. In space dimension d the Delaunay simplex represents the minimal cluster of particles for which a d -volume can be assigned, with $d + 1$ vertices connected $d(d + 1)/2$ edges, defining triangles in 2D, tetrahedral (Fig. 1.1) in 3D, etc. The Delaunay triangulation in any dimension d suffices to define the global stress and kinematics of a granular assembly.

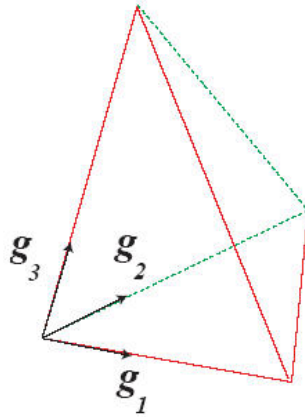


Fig. 1.1. Delaunay simplex (tetrahedron) in 3D, with vertices representing grain centroids and edges representing contacts, actual (solid lines) and latent (dotted lines). Basis vectors \mathbf{g}_i , foreshortened for clarity, have length of Delaunay edges

Stress and deformation for an assembly of rigid grains involve contributions from the forces and relative motion between particles. We restrict attention to globally homogeneous deformations, where the difference between particle rotation and mean material rotation (Cosserat effect) is negligible. Hence, we can focus on the kinematics and stress associated with Delaunay edges.

As in Goddard (2004b), the global or effective velocity gradient $L = (\nabla v)^T$ of a granular assembly is provisionally taken to be the volume-weighted average over simplexes $s = 1, 2, \dots$

$$L = \langle L \rangle_s := \frac{1}{V} \sum_s V_s L_s \quad (1.1)$$

where V_s is the volume of simplex s and

$$V = \sum_s V_s \tag{1.2}$$

is that of the assembly. For statistically homogeneous assemblies, averages of the type (1.1) can be identified with ensemble averages based on an appropriate probability measure.

The relation (1.1) written in terms of a given edge, say $i = 1$ in simplex s as

$$L_{1,s} = \frac{1}{V_s} u_1 \otimes a_{1,s} \tag{1.3}$$

where $u_1 \equiv \dot{g}_1$ is the difference in velocity at the vertices connected by this edge, and

$$a_{1,s} = V_s g_1 = \frac{1}{2} g_2 \times g_3, \quad V_s = \frac{1}{2} g_1 \bullet g_2 \times g_3 \tag{1.4}$$

are, respectively, the area vector of the opposite face and the volume of the simplex.

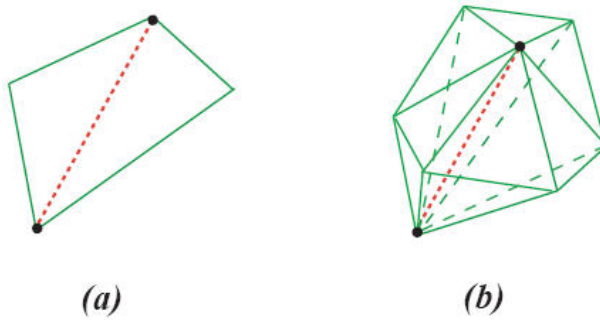


Fig. 1.2. Edge (contact) complexes in (a) 2D, (b) 3D

As illustrated in Fig 1.2, we identify the simplicial edge complex $c(e)$ for a given edge e as the set of simplices having e as common edge. Replacing subscript 1 in (1.3) by e , we obtain the contribution of an arbitrary edge e to the global velocity gradient:

$$L_e = \frac{1}{V_e} \sum_{s \in c(e)} V_s L_{e,s} = \frac{1}{V_e} u_e \otimes a_e \quad (1.5)$$

where

$$a_e = \sum_{s \in c(e)} a_{e,s}, \quad 1_e \cdot a_e = \sum_{s \in c(e)} V_s = V_e \quad (1.6)$$

The corresponding volume-average velocity gradient is given by

$$\langle L \rangle = \frac{1}{V} \sum_e V_e L_e = \frac{1}{V} \sum_e u_e \otimes a_e \quad (1.7)$$

1.2 Stress and Stress Power

The conventional expression for granular (Cauchy) stress as dipolar force density can be expressed in terms of edge contributions as

$$T = \frac{1}{V} \sum_e V_e T_e, \text{ where } T_e = \frac{f_e \otimes 1_e}{V_e} \quad (1.8)$$

where f_e is interparticle force at particle contact represented by edge e . At this level, (1.5) and (1.8) provide the correct expression for stress-power:

$$T_e : L_e = \frac{f_e \cdot u_e}{V_e}, \text{ where } A : B = \text{tr}(AB^T) = A_a^\beta B_\beta^a \quad (1.9)$$

By contrast, it is generally recognized that the corresponding expression $\mathbf{T}:\mathbf{L}$, with \mathbf{T} defined by (1.8) and \mathbf{L} by (1.7), does *not* represent global stress power, owing essentially to micro-level heterogeneity. The latter requires additional work terms to account higher-order moment stresses and gradients (Goddard, 2006), reconsidered briefly below.

2 Maximum Entropy & Virtual Thermodynamics

Following Goddard (2004a), letting $\mathbf{z} \in \Omega$ denote a representative point in the relevant state (or phase) space Ω , having probability measure $P(\mathbf{z})d\Omega(\mathbf{z})$, where $d\Omega(\mathbf{z})$ is an elemental state-space measure that remains to be specified. $P(\mathbf{z})$ may depend on time, but we restrict attention here to spatially homogeneous systems, such that $P(\mathbf{z})$ and $d\Omega(\mathbf{z})$ are independent

of spatial position. Statistical averages of arbitrary mechanical variables $A(\mathbf{z})$ are then given by

$$\langle A \rangle = \int_{\Omega} A(\mathbf{z})P(\mathbf{z})d\Omega(\mathbf{z}) \tag{2.1}$$

with relation between probability densities

$$\begin{aligned} P(\mathbf{z})d\Omega(\mathbf{z}) &= \rho(\mathbf{z})dV(\mathbf{z}), \text{ with } dV(\mathbf{z}) := dz_1dz_2\dots dz_n, \\ d\omega(\mathbf{z}) &= J(\mathbf{z})dV(\mathbf{z}), \text{ and } \rho(\mathbf{z}) = J(\mathbf{z})P(\mathbf{z}) \end{aligned} \tag{2.2}$$

connecting P and the probability density ρ in $dV(\mathbf{z})$. Specification of J , the “density of states” (Kanatani, 1980), is essential to the determination of $\rho(\mathbf{z})$. Several examples are considered elsewhere (Goddard, 2004a), where it is conjectured that J generally should represent a dynamically invariant measure determined by the micromechanics.

The standard statistical-thermodynamical estimate for the unknown probability distribution $P(\mathbf{z})$ is based on maximization of the entropy functional:

$$S[P] = -\langle \log P \rangle = - \int_{\Omega} P(\mathbf{z}) \log P(\mathbf{z})d\Omega(\mathbf{z}) \tag{2.3}$$

subject to a discrete set of constraints of the form $\langle \Lambda(\mathbf{z}) \rangle = \text{const.}$

For either constrained stress or constrained kinematics, the expressions (1.7) and (1.8) can be put into the common form Goddard (2004b)

$$A = n_c \langle M(x, y) \rangle, \text{ with } M(x, y) := x \otimes y \tag{2.4}$$

with sums interpreted in terms of ensemble averages $\langle \ \ \rangle$ over contacts or edges, and with n_c denoting contact-number density.

With state space is now defined by $z = x \oplus y$, the maximization of (2.3) subject to stationarity of A yields the canonical distribution

$$P(x, y) = Z^{-1} \exp\{-\beta\Lambda : M\} = Z^{-1} \exp\{-\beta x \cdot \Lambda \cdot y\} \tag{2.5}$$

where Z is the partition function:

$$Z(\Lambda) = \int_{\Omega} \exp\{-\beta x \cdot \Lambda y\}d\Omega(x, y) \tag{2.6}$$

a function of a tensor-valued Lagrange multiplier $\beta\Lambda$. The arbitrary constant β , having units of inverse energy or power, plays the role of temperature in the usual thermodynamic formalism (Goddard, 2004b). This same formalism dictates that all macroscopic properties be derivable from Z , in particular

$$A = \partial_{\Lambda} x, \text{ with } x(\beta, \Lambda) = -n_c \beta^{-1} \log Z(\beta, \Lambda) \quad (2.7)$$

with x assuming the role of potential-energy function and ∂_{Λ} denoting partial derivative at constant β .

Table 2.1. Constraints and variables

Constraint	x	y	A	A	χ
Stress	f	l	L	$T(\beta, \Lambda)$	$\psi(\beta, L)$
deformation	u	a	T	$L(\beta, T)$	$\phi(\beta, T)$

Table 2.1, from Goddard (2004b), summarizes the complementary relations between stress \mathbf{T} and velocity or displacement gradient \mathbf{L} . With a further restriction to infinitesimal deformation, one may interpret \mathbf{L} as displacement gradient. The relation (2.7) represents a *virtual* thermomechanics, with ψ serving as analog of Helmholtz free energy and ϕ as its complementary energy. The standard thermodynamic interpretation of Table 2.1 would require that the measures $d\Omega(f, l)$ and $d\Omega(u, a)$ be such as to satisfy the (Legendre) relation:

$$\psi(\beta, L) + \phi(\beta, T) = T : L \quad (2.8)$$

As also pointed out by Goddard (2004b), the general validity of (2.7) appears to hinge on the possibility of capturing both elastic and frictional effects (conservative and non-conservative forces) via an elastic-plastic decomposition of the type employed in well-known incremental plasticity theories. However, such decompositions impose severe restrictions on particle-level statistical mechanics and need further micromechanical justification.

3 Material Instability

As the main contribution of the present article, we consider the possible non-convexity (Goddard, 2002, 2004b) of the functions ψ or φ as a condition for material instability, with non-unique relation between stress and deformation. The analog of thermodynamic phase transition, this could allow for the well-known strain localization or its less familiar counterpart, stress localization.

To illustrate the latter, we consider the simplest case of a static isotropic compression, with $\mathbf{T} = -p\mathbf{1}$ as constraint and $t = -n_c u \cdot a$ as local compressive volumetric strain, which we shall allow to take on values in $[0, \infty)$. Then, by means of (2.7) and the second row of Table 2.1, the nondimensional pressure $s = \beta p/n_c$ is given as implicit function of global volumetric strain ε_V by:

$$\varepsilon_V = \frac{\int_0^\infty e^{-st} J(t) dt}{\int_0^\infty e^{-st} J(t) dt} \tag{3.1}$$

To make further progress, we assume a local density of states $J(t)$ of the general form

$$J(t) = t^\nu [J_0 + J_1 t + \dots + J_n t^n], \nu > -1, n = 0, 1, \dots \tag{3.2}$$

which gives an $(n+1)$ th-degree polynomial for s :

$$P_0 s^{n+1} + P_1 s^n + \dots + P_{n+1} = 0 \tag{3.3}$$

where

$$P_k = (\nu + k) \dots (\nu + 1) (J_{k-1} - J_k \varepsilon_V), k = 0, \dots, n + 1, J_{-1} = J_{n+1} = 0 \tag{3.4}$$

By Descartes' rule of sign, one can readily predict the number of real positive roots $s = \beta p/n_c$, and this prediction is independent of the exponent ν in (3.2).

For example, with $n = 2$ and $J(t) > 0$ for $t \geq 0$, then $J_0 > 0$, and we obtain three positive roots for $J_2 > 0, J_1 < J_2 \varepsilon_V, J_0 > J_1 \varepsilon_V$. If $J_1 > 0$, this reduces to

$$J_k > 0, k = 0, 1, 2, \text{ with } J_1 / J_2 < \varepsilon_V < J_0 / J_1 \tag{3.5}$$

a situation depicted schematically in Fig. 3.1 (Goddard, 2002).

Presumably, the above multiplicity could lead to a two-phase granular structure such as that found in the numerical simulations of Radjai et al.

(1998), consisting of an isotropic high-pressure network of force chains, supported laterally by an amorphous granular phase having much smaller contact forces and pressure.

Although not pursued here, the simplicity of the above construct suggests a similar construct for multiple stress states involving shear stress with anisotropic two-phase structures like those of Radjai et al. (1998). Of course, a more fundamental micromechanical analysis is needed to justify phenomenological models like (3.2) for the density of states. In the author's opinion, a particle-chain buckling instability with local densification represents a plausible mechanism.

In closing, we note that there is a further interesting question as to length scales of the conjectured two-phase structures. While a micromechanical analysis is obviously needed to establish the implied spatial correlations, one can anticipate that these must signal the emergence of moment stresses $T^{\alpha\beta\gamma}, \dots$ and conjugate kinematic quantities $L_{\alpha\beta\gamma}, \dots$ (Goddard, 2006).

One can further anticipate that the maximum entropy principal would add terms $T^{\alpha\beta\gamma} u_{\alpha} \alpha_{\beta} \alpha_{\gamma}, \dots$ or $L_{\alpha\beta\gamma} l^{\alpha} l^{\beta} l^{\gamma}, \dots$ to the canonical exponential form (2.5). However, it is not clear how the corresponding constraints are to be imposed in a granular medium with nominally homogeneous stress or deformation.

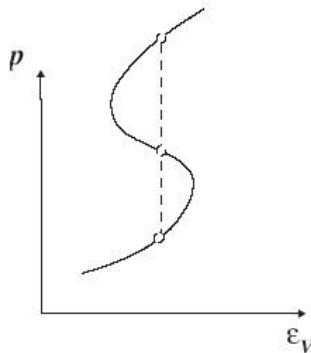


Fig. 3.1. Schematic of pressure vs. volumetric compressive strain for conditions in (3.5)

4 Conclusions

The preceding analysis suggests that maximum-entropy estimates of quasi-static granular stress and kinematics, together with a relatively simple phe-

nomenological model for the density of states, can provide a model of material instability with two-phase structure. Further micromechanical modeling is required to justify the purely phenomenological forms assumed above and to determine the relevant mesoscopic length scales.

Acknowledgements

This work is an outgrowth of research supported in part by National Aeronautics and Space Administration Grant NAG3-2465.

References

1. K. Bagi (1996). 'Stress and strain in granular assemblies.' *Mech. Mater.* 22(3):165–177.
2. K. Bagi (1997). 'Analysis of micro-variables through entropy principle.' In R. Behringer & J. T. Jenkins (eds.), *Powders and Grains*, pp. 251–4. Balkema, Rotterdam.
3. J. D. Goddard (2002). 'Material instability with stress localization.' In J. Labuz & A. Drescher (eds.), *Bifurcations and Instabilities in Geomechanics*, pp. 57–64. Balkema, Lisse.
4. J. D. Goddard (2004a). 'On entropy estimates of contact forces in static granular assemblies.' *Int. J. Solids Struct.* 41(21):5851–61.
5. J. D. Goddard (2004b). 'On maximum-entropy estimates for granular statics.' In J. Vermeer et al. (eds.), *2nd Intl. Symp. on Continuous and Discontinuous Modelling of Cohesive Frictional Materials*. Balkema, Lisse, University of Stuttgart, Germany, September 27-28, 2004.
6. J. D. Goddard (2006). 'From granular matter to generalized continuum.' In P. Mariano, G. Capriz, & P. Giovine (eds.), *Lecture Notes in Mathematics*, pp. 22pp., to appear. Springer, Berlin.
7. K.-I. Kanatani (1980). 'An entropy model for shear deformation of granular materials.' *Lett. Appl. Engng. Sci. (Int. J. Eng. Sci.)* 18:989–998.
8. N. P. Krut (2003). 'Contact forces in anisotropic frictional granular materials.' *Int. J. Solids Struct.* 40(13-14):3537–3556.
9. N. P. Krut & L. Rothenburg (2002). 'Probability density functions of contact forces for cohesionless frictional granular materials.' *Int. J. Solids Struct.* 39(3):571–583.
10. F. Radjai, D. E. Wolf, M. Jean, & J. J. Moreau (1998). 'Bimodal character of stress transmission in granular packings.' *Phys. Rev. Lett.* 80(1):61–4.
11. M. Satake (1992). 'Discrete-mechanical approach to granular materials.' *Int. J. Eng. Sci.* 30(10):1525–1533.

A DEM Study of Compaction Band Formation

G. Marketos and M. D. Bolton

Centre of Geotechnical Process and Construction Modelling,
Cambridge University Engineering Department,
Cambridge,
U.K.

Summary

Thin zones of localised compaction have been observed in the field and were associated with regions of severe grain crushing or microcracking. They were found to occur inside cemented granular materials and have been successfully reproduced in experiments. This is a relatively new form of localised feature for which the mechanics is not yet clearly understood. In addition, compaction bands form as thin impermeable structures that could therefore severely decrease the permeability of a soil. The implications this might have for the recovery of oil from a reservoir are immense. A thorough understanding of the micromechanical processes involved in their triggering and propagation is therefore needed.

Discrete Element Modelling of the specific phenomenon has been carried out. The discrete element sample has been slightly modified so as to ensure that compaction bands do not form near the boundaries (as happens in the laboratory). Compaction bands were observed as forming inside the bulk of the material, in a direction sub-perpendicular to the maximum principal stress in the sample. This implies that their direction might be controllable. It was observed that such instabilities due to particle crushing might form in unbonded granular materials as well, something that has not been fully investigated by experiments on sand. The effects of inter-particle bond breakage and grain breakage will be contrasted.

The initiation of grain crushing or bond cracking is seen in relation to the joint probability density function of contact forces exceeding grain crushing or bond strengths. The propagation of crushing or cracking after the initial event will be seen in relation to the perturbation of the local stress-carrying network inside the simulated rock. An insight into the conditions and micromechanical parameters which will lead to a crushing / cracking avalanche will be sought.

1 Introduction

Certain high-porosity sandstones have been seen to depart from the condition of homogeneous compaction throughout their volume and to favour localisation when subjected to certain stress paths (e.g. Baud et al. 2004, Olsson et al. 2002). They then form zones of low porosity and localised compaction, called compaction bands. They have been seen to form in directions sub-perpendicular to the major principal stress direction in the parent rock. Compaction bands are similar in appearance to shear bands as observed in loose sands, the significant difference being that there is no observed offset (shear) of the top relative to the bottom layer. Another difference is that they come about by a different micromechanism; this however has not been fully understood.

Inside all compaction bands a loss of pore space is observed through particle (and particle fragment) rearrangement to a locally denser structure. It should be noted that depending on the material tested, compaction bands can come about by very different micromechanisms. The main focus of this investigation is compaction bands forming in sandstones with quartz grains, a common oil-reservoir rock, which we might term 'crushing compaction bands'. Here intense particle crushing and closer packing of the products of fragmentation is occurring inside a band (as observed by Baud et al. 2004 in experiments). Therefore we will be examining the phenomenon of crushing localisation inside a sample.

One should note that compaction bands have been observed in other materials as well. Of particular relevance to this work is the experimental observation of crushing localisation inside an unbonded sample of mono-disperse glass beads as made by Garbrecht (1973) and reproduced by Vardoulakis and Sulem (1995). In addition, Papamichos et al. (2005) report features similar to compaction bands in calcarenite, and Arroyo et al. (2005) in artificial conchiliades (a bonded material made of silica sand, fragmented shells and lime).

The importance of compaction bands in sandstone is that they are relatively impermeable structures that might trap, or channel pore-fluid between them. As they have been found in sandstone which is an oil-reservoir rock, their significance as barriers to oil extraction is of great importance. Existing compaction bands will be picked up by oil companies' site investigation. However, new compaction bands might also form if the reservoir pore pressure is lowered, inducing significant effective stress increases due to oil extraction. By carefully controlling the pore pressure inside the rock (and hence the effective stress field) the formation of bands might be controlled to specific directions perpendicular to the major prin-

cipal stress, thus creating advantageous flow paths (channels) for the oil. Furthermore, Haimson (2003) suggests that compaction bands are one of the mechanisms responsible for borehole breakouts in high-porosity sandstones.

It might be therefore advantageous to understand in which rocks compaction bands will form, and how exactly they form and propagate. A micromechanical study of the phenomenon of crushing localisation using Discrete Element Modelling is therefore thought essential. Results of relevant computer simulations and the insight they have provided will be presented here.

2 The Discrete Element Method

The simulations reported here were conducted using the three-dimensional discrete element code PFC^{3D} developed by Itasca Inc. A concise description of this code can be found in the PFC^{3D} manual (Itasca Inc. 2003). Two different sets of simulations were conducted, one on a bonded material with infinitely strong grains and one on unbonded material consisting of crushable particles. These are considered to be analogous materials to a sandstone and a sand respectively. In order to produce comparable results the same sample was used for both. The reason why simulations on both sand and sandstone were conducted was to assess the relative significance of particle crushing and bond cracking in the production of significant porosity reduction and compaction bands.

The sample used was cuboidal having a porosity of 44.8% and initial dimensions of 6 cm x 6 cm x 7.2 cm. It consisted of 8943 spherical particles of radii uniformly distributed between 1 and 2 mm. In selecting 25 as the ratio of the size of the sample to the diameter of the typical particle, the intention was to provide sufficient volume remote from any boundary effects, within which localisation could occur. The sample was prepared by a simulated 'numerical dry pluviation' and was bounded by frictionless walls on all sides. It should be noted that no gravity forces were included in this model and a soft contact approach was used. The side-walls were kept stationary while a constant axial shortening rate of 0.1 m/s was applied. The micromechanical parameters used in these simulations can be found in Table 2.1. Care was taken when choosing the parameters so that their values were of the same order of magnitude as those inferred from single crushing tests on quartz particles reported by Nakata et al. (1999).

Table 2.1. Micromechanical parameters used for the simulation

Parameter	Numerical Value
normal and shear stiffness of balls	4×10^6 N/m
normal and shear stiffness of walls	4×10^6 N/m
particle friction coefficient, μ_b	0.5
wall friction coefficient, μ_w	0.0
density of spheres	2650 kg/m^3
coefficient of local damping	0.7
sample shortening rate	0.1 m/s
particle 'crushing strength'	40MPa
cementation bond radius / particle radius	0.4
bond normal and shear strength	40MPa
normal and shear bond stiffness	5000 N/mm^3

2.1 Simulations on Sandstone

In the computer modelling of sandstone the cementation bond between two particles was represented by a disk around the contact. This is a standard procedure in PFC3D and is described in the relevant user's manual (Itasca Inc. 2003). The cementation bond is put in as both a normal and tangential spring acting in parallel to the ones representing the contact. The full parameters associated with the bond can be found in Table 2.1. The bond was allowed to break at a limiting value of the relevant stress in the bond, both in tension, compression and shear (40MPa). After a bond breakage normal frictional behaviour is imposed at the contact. In these sandstone simulations no individual particle crushing was allowed.

2.2 Simulations on Sand

Sand simulations were conducted on unbonded particles. Crushing events were simulated as follows. A characteristic crushing stress parameter was assigned to each particle (here uniform, set as 40MPa). The characteristic stress inside a particle, defined as the maximum normal contact force divided by the square of the diameter (following Nakata et al. 1999) was monitored throughout the simulation. A particle was then completely removed, so as to simulate crushing, when its characteristic stress exceeded its characteristic strength. This is thought to represent adequately the process by which small fragments, produced by crushing, fall into the pore space and lose their force-carrying capacity. This is certainly true for small strain increments and sufficient for our case where the characteristics of the localisation itself and not the post-localisation behaviour are sought.

Extra care is needed when considering what boundary to use for the simulations. A flat boundary will impose a local disruption to the fabric defined in terms of contact orientations (seen in Fig. 2.1a) that extends up to a maximum distance of three particle diameters away from it, and a more local density variation (see Fig. 2.1b). The particle density in the boundary region is smaller than in other planes inside the element. As force needs to be transmitted from the top to the bottom platen of the sample the decreased density means that boundary particles see a local increase in force, which will favour particle crushing here. Very similar simulations using a flat boundary were observed to produce localisation exactly at the boundary (Marketos and Bolton (2005)). This is no artefact of the specific simulation; it should also be observed in experiments using flat boundaries, and might be the reason why Olsson et al. (2002) report crushing localisation initiating at the top of their sample.

In order to suppress the unwanted localisation at the boundary an internal element was used that excluded the region 3 mean particle diameters away from the top and bottom platens. Particles in the outside region were not allowed to crush in the sand simulations and cementation bonds were not allowed to break in the sandstone simulations. This method is thought to be a good way of creating a representative element for a discrete material as it allows for the behaviour of the bulk of the material to be investigated. Its main advantage over periodic boundaries is that no artificial reflections of localised features are observed and there is no distortion of sample space.

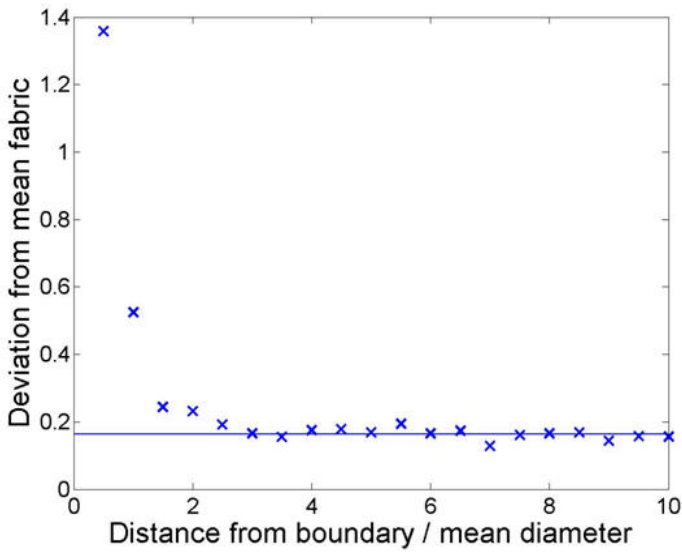


Fig. 2.1a. A plot of the deviation from the mean fabric versus distance from the flat boundary (as non-dimensionalised by the mean particle diameter)

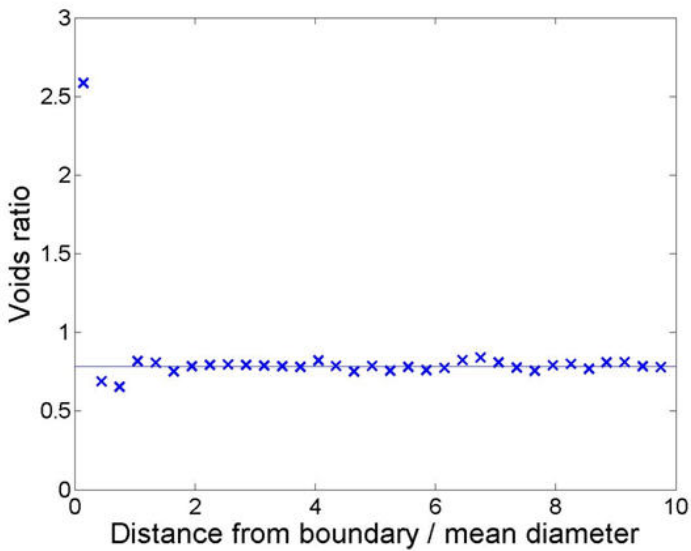


Fig. 2.1b. A plot of the local voids ratio versus distance from the flat boundary (as non-dimensionalised by the mean particle diameter)

3 Results

3.1 Sand Simulations

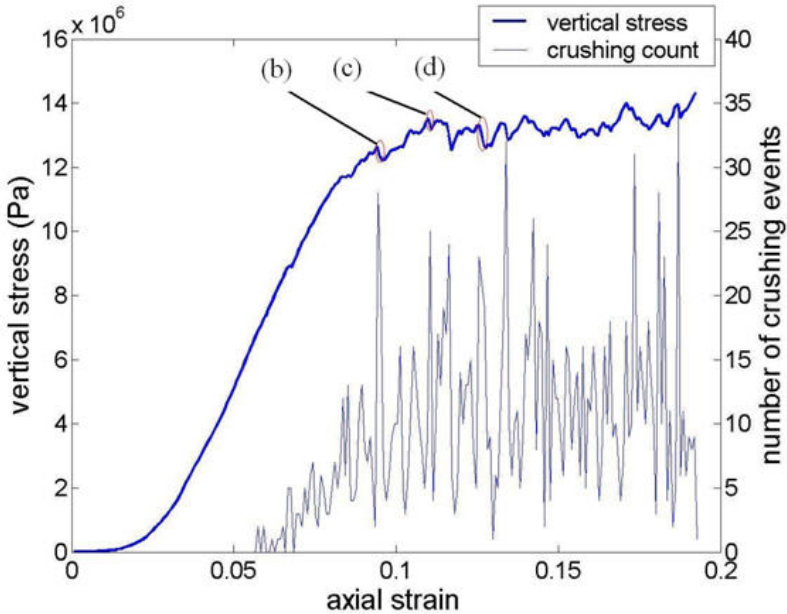


Fig. 3.1. A plot of the vertical stress and number of crushing events (similar to acoustic emission data) versus strain

The simulations on unbonded crushable particles yielded the stress-strain curve of Fig. 3.1. This plot includes a history of crushing events similar to acoustic emission data reported in experiments (e.g. Baud et al. 2004). One can observe two phases of behaviour of the sample. Initially and up to 0.06 strain, contraction is due mostly to particles rearranging and to a lesser extent elastic shortening at the contacts. Crushing of particles is initiated at this point and finally a constant mean level of crushing of about 100 events per 0.007 strain interval is reached. Sample shortening is dominated by particle crushing after a strain of roughly 0.10. It is this last regime of behaviour, where the stress-strain curve is flatter in which one might observe compaction bands.

As one can see on Fig. 3.1 the stress-strain curve exhibits instabilities. Its peaks and drops can be associated with peaks and drops in the number of crushing events observed. The locations of the crushing events corre-

sponding with these drops (i.e. points marked (b), (c) and (d) on Fig. 3.1) are plotted in Fig. 3.2. One can see that at each stress drop particle crushing, and therefore pore collapse, is fairly localised within a region that we might call a compaction band. A plot of all the particle crushing events is included in Fig. 3a. We can observe here that overall crushing is homogeneously distributed through the sample. As a stronger boundary region was imposed on the specimen (see section above), these compaction bands were observed to form inside the specimen. Here there is no density or contact anisotropy variation due to the boundary and these features are thought to be representative of the sort of localisation that would affect the bulk behaviour of the material.

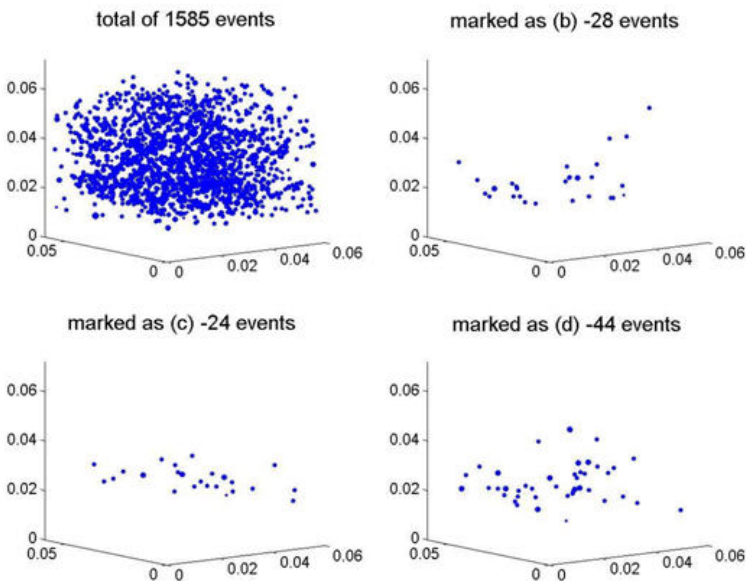


Fig. 3.2. A 3D plot of the location of crushing events inside the cubical element for a strain increment of (a) the whole run and (b), (c), (d) as marked on Fig. 3.1

An inspection of individual compaction bands reveals that they correspond to a surge in the number of crushing events and a stress drop, as observed in experiments (see Fig. 3.1). The first particle-crushing event

causes a severe disruption to the stress-carrying network of the sample, by removing the highest-stressed link in the strong-force network. The force carried by the crushed particle will need to redistribute itself to neighbouring particles (neighbouring links in the stress network). This might cause a crushing avalanche by locally removing links lying roughly on the same plane normal to the major principal compressive stress. The observation of a crushing localisation will be dependent on the particle structure and density (packing), the stress level, and the coefficient of variation of particle crushing strengths. The rate at which crushing will pulverise particles in a compaction band might be larger than the strain rate in a strain-controlled test. This will severely damage the stress-carrying ability of the sample, thus producing a stress drop, as observed. The stress-drops interpreted as instabilities and seen in Fig. 3.1 occur over very small displacement increments (of the order of 0.2% of sample size, which corresponds to approximately 0.05 particle diameters). This supports the use of particle removal to simulate the propagation effect of grain breakage. Although a real grain may fragment into pieces that later pick up loads themselves, this could only occur after much larger compressions, perhaps of the order of 0.3 particle diameters. Of course, it would be necessary to replace broken fragments if the post-localisation stiffening of the sample was the focus of the investigation. It is however not expected that the inclusion of fragments can have a significant effect on the magnitude of such small-strain stress drops. Compaction bands in stress-controlled experiments (or simulations) will appear as jumps in the strain rate. As in nature most events are stress-controlled this might prove catastrophic in the vicinity of structures such as oil wells.

3.2 Sandstone Simulations

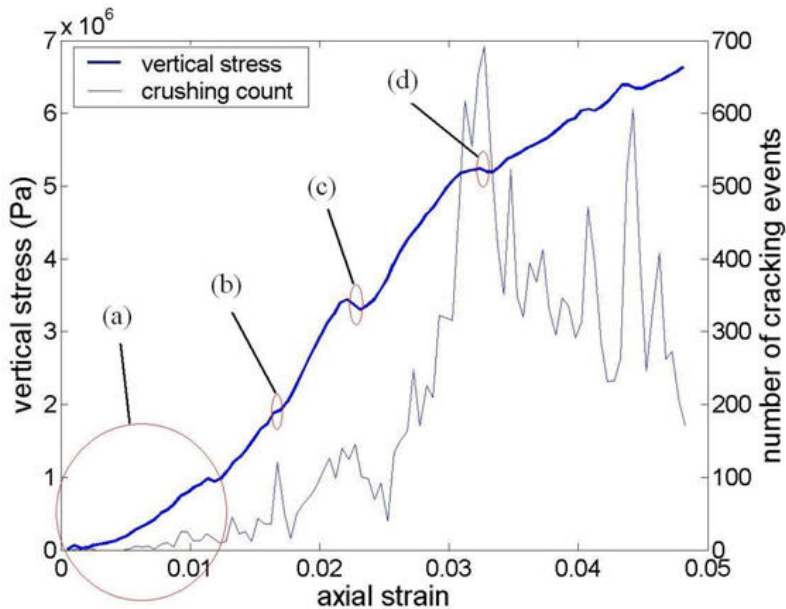


Fig. 3.3. A plot of the vertical stress and number of cracking events (similar to acoustic emission data) versus strain

The simulations with infinitely strong particles held together by breakable cementation bonds yielded the stress-strain curve of Fig. 3.3. As for the sand simulations a plot of the history of bond cracking events (similar to acoustic emission) is plotted on the same diagram. One should note here the difference between the crushing and cracking rates. The cracking rate is overall 50 times larger than the crushing rate even though the shortening rate of the specimen is the same. This can be explained by the fact that crushing, as it pulverises the grains, is associated with a larger volume contraction as compared to cracking of bonds in sandstones, where the initial particles are still there. One can note that instability (a stress drop in strain-controlled simulations) can be observed in Fig. 3.3. Plots for the bond cracking locations for the strain increments annotated as a b c and d on the plot of Fig. 3.3 are shown on Fig 3.4.

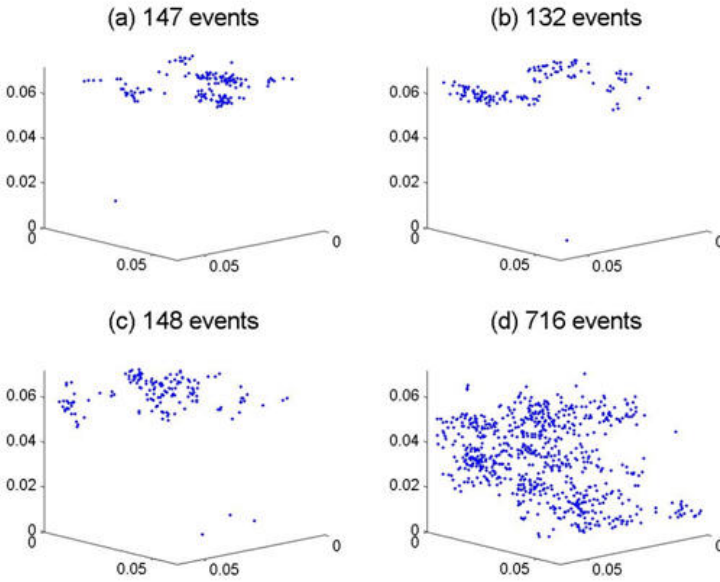


Fig. 3.4. 3D plots of the location of cracking events inside the cubical element for the strain increments (a), (b), (c) and (d) as marked on Fig. 3.3

On Figs. 3.4a, 3.4b and 3.4c one can see that cracking might also be interpreted as local. However, one can say that on its own, cementation bond cracking is not responsible for compaction bands, as it cannot produce the large porosity and permeability reductions for sandstones with common grain structures. When bond cracking occurs, particles still have to rearrange in denser structures, something that involves extensive grain movement. It is improbable for common material grain structures that this micromechanism alone, with no crushing, will produce so big a porosity reduction as observed in a compaction band.

A comparison of the results of the sand and sandstone simulations has allowed us to assess the relative importance of grain crushing and bond cracking in compaction banding of rocks. Having realised the importance of grain crushing in this phenomenon, future work will focus on the better understanding of crushing localisations from a micromechanics point of view. In particular, a probabilistic analysis of crushing and a statistical analysis of the crushing locations might hold the key to this phenomenon.

4 Proposed Statistical Approach

The force inside a granular material is distributed in a highly inhomogeneous manner with some researchers speaking of the separation of the force network into a sparse strong force network carrying the majority of force and a weak force network which has relatively low importance (Thornton 1997). In order to quantify the variability in the force network we have conducted a set of simulations for the sample where no bonding and no crushing is present, so that the only mechanism responsible for deformation is particle rearrangement. Fig. 4.1 shows the resultant probability density of normal contact force at 3 different stress levels, both on linear (a) and semi-logarithmic scales (b). This plot is essentially a histogram plot where the y value has been divided by the histogram interval width so as to ensure that the area under the curve has a value of 1.

It is interesting to observe that when the force is non-dimensionalised by the mean force the plots for different stress levels collapse to the same curve. This is very promising as it allows for an easy mathematical description of the force variability in terms of the mean force and therefore the stress-level. This curve was fitted using the expression $(x+A)^B e^{-Cx+D}$ (with $A = 1.15$, $B = 4.75$, $C = 2.92$, $D = -1.41$). The semi-logarithmic plot of Fig. 3.5b shows that the force exhibits an approximately exponential tail. If only large force is important (as in our case where these forces will cause crushing) a single exponential of the form $a e^{-bx}$ might be used to describe the strong force network (for $F > F_{\text{mean}}$, with $a = 6.6$ and $b = 1.8$). This last observation agrees well with simulation results reported by (Thornton 1997, Radjai et al. 1996).

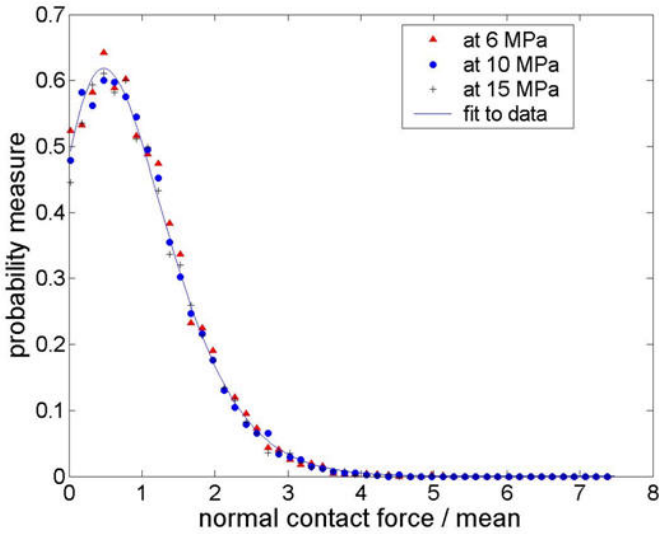


Fig. 4.1a. A plot of the probability density function of the normal contact force (as non-dimensionalised by the mean force) for three different stress levels. A fit to the data of the functional form $(x+A)^B e^{-Cx+D}$ has also been plotted

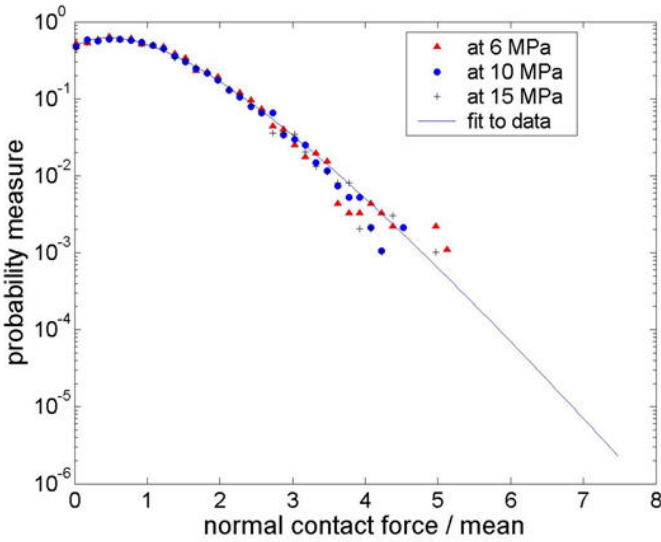


Fig. 4.1b. A semi-logarithmic plot of the probability density function of the normal contact force (as non-dimensionalised by the mean force) for three different stress levels. A fit to the data of the functional form $(x+A)^B e^{-Cx+D}$ has also been plotted

In our case one can imagine the following sequence of events: Particles with strengths given by a certain distribution (e.g. Weibull) are randomly distributed in the sample. As the sample is stressed and the mean force is increased the weakest particles under a strong force chain will be the first to crush. Further increase of force will mean that a greater number of grains will crush and a probabilistic analysis could be used to quantify the amount of crushing inside a sample. Work in this direction is in progress, and results from a simple statistical analysis are presented in Marketos and Bolton (2006).

However if our main aim is to understand localisation a more sophisticated approach is needed. Central to this approach is the understanding of the effect one crushing event has on the force distribution around it. For this reason, a set of 72 particle-crushing simulations were performed starting from the same initial sample stressed at 6 MPa. The force network was probed both before and after the crush and the difference in the magnitude of force was plotted versus the distance from the crushed particle. This has yielded the plot of Fig. 4.2.

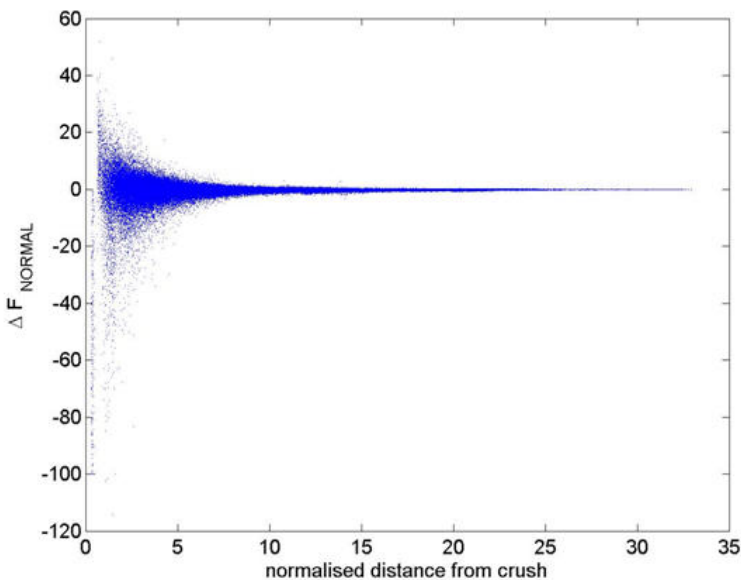


Fig. 4.2 A plot of the difference in the magnitude of force (non-dimensionalised by the maximum force on the particle that crushed and expressed as a percentage) versus the distance from the crushed particle (non-dimensionalised by the mean particle diameter)

It should be noted that this plot is again in terms of non-dimensional quantities, which in this case are distance normalised by the mean particle diameter and difference in the force magnitude normalised by the maximum force on the particle that crushed and expressed as a percentage. One can immediately note from Fig. 4.2 that the force network is disturbed significantly up to a distance of 5 particle diameters. Plotting again probability density functions in each R-range will produce the plot of Fig. 4.3 below.

An approach using the spatial information on the effect of crushing might predict where a subsequent crush will occur. Two crushing events close to each other will create a larger force perturbation in the sample, creating larger stress concentrations in their vicinity. A compaction band, which is essentially the unstable propagation of crushing might be initiated and a method taking into account the force perturbation due to crushing might be able to predict its location. This is the main focus of future work.

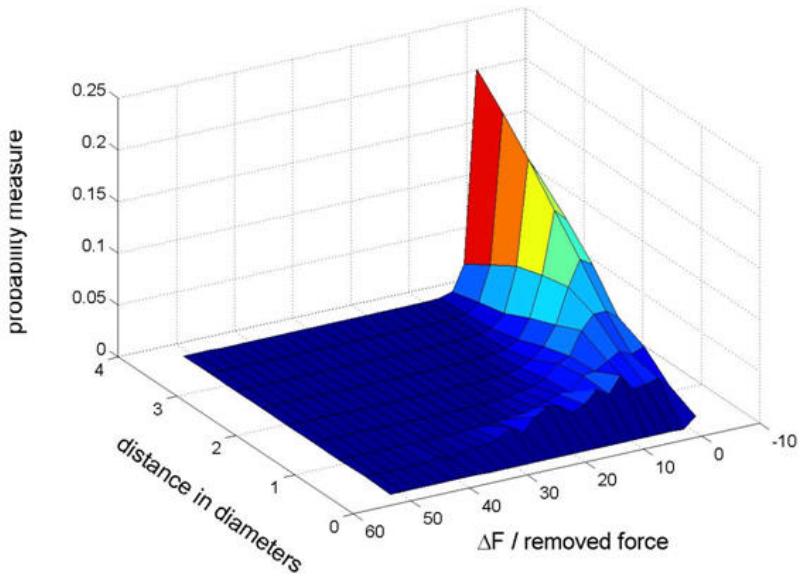


Fig. 4.3. A 3D plot of the probability density functions in each R-range as a function of the normalised distance from the crushed particle and the percentage of normalised force increase. Note that only positive force magnitude differences are plotted

5 Conclusions

The simulations reported here were performed in order to contrast two micromechanisms potentially responsible for compaction band formation, grain crushing and inter-particle bond cracking. We have observed localisation of crushing in sand and to a lesser extent localisation of cracking in sandstone, related with the unstable propagation of cracks for relatively low bond strengths. However, given the porosity reduction reported by Mollema and Antonellini (1996), from 20-25% to a few %, we have concluded that for common initial grain structures of sandstones only grain crushing can produce significant permeability decrease. This is consistent with Baud et al. (2004) observations that report compaction bands due to crushing in the laboratory.

We therefore decided to focus on simulations of crushing. The strain-controlled simulations exhibit significant drops in the stress-strain curve. These instabilities can be attributed to the localisation of crushing. Inside the sample a crushing event occurs. This event locally disturbs the force distribution inside the specimen, meaning that neighbouring particles see an increase in stress for equilibrium to be conserved. This might cause a second particle to crush, increasing the local force disturbance, and under certain conditions crushing might propagate in an unstable fashion through the sample. This is what we call a compaction band.

From the above it becomes apparent that a micromechanical analysis of this type of localisation is needed. We have seen that useful insight into grain crushing can be obtained by using statistics and probabilistic arguments. We have seen that a crush creates a local disturbance of force that extends roughly 5 particles away from the crush. Future work will make use of statistics in this direction. We are hoping to relate the parameters in the probability density functions involved to measurable quantities inside a real sand sample. This might allow us to use a few simple physical tests to predict whether compaction banding is possible or not, without the conduction of a triaxial test.

Acknowledgements

The authors would like to thank the A.S. Onassis Foundation and the A.G. Leventis Foundation for their generous financial support.

References

1. Arroyo M, Castellanza R, Nova R (2005) Compaction bands and oedometric testing in cemented soils. *Soils and Foundations*, 45, (2):181
2. Baud P, Klein E, Wong T-F (2004) Compaction localization in porous sandstones: spatial evolution of damage and acoustic emission activity, *Journal of Structural Geology*, 26, (3): 603–624.
3. Garbrecht D (1973) Kornbruch in irregulären Haufwerken aus elastisch-spröden Kugeln. Dissertation, Universität Karlsruhe, Germany.
4. Haimson BC (2003) Borehole breakouts in Berea Sandstone reveal a new fracture mechanism. *Pure and Applied Geophysics*, 160: 813-831.
5. Itasca Consulting Group, Inc. (2003) PFC^{3D}: Particle Flow Code in 3 Dimensions, Version 3.0, Minneapolis, U.S.A.
6. Marketos G, Bolton MD (2005) Compaction bands as observed in DEM simulations. *Powders and Grains*, Proceedings of the 5th international Conference on Micromechanics of Granular Media, Eds. Garcia-Rojo R., Herrmann H. J., McNamara S. 2: 1405-1409
7. Marketos G, Bolton MD (2006) A statistical investigation of particle crushing in sand. Proceedings of the IS-Yamaguchi 06 Symposium on Geomechanics and Geotechnics of Particulate Media, Ube, Japan.
8. Mollema PN, Antonellini MA (1996) Compaction bands: a structural analog for anti-mode I cracks in Aeolian sandstone. *Tectonophysics*, 267: 209-228.
9. Nakata Y, Hyde AFL, Hyodo M, Murata H (1999) A probabilistic approach to sand particle crushing in the triaxial test, *Geotechnique*, 49 (5): 567-583.
10. Olsson WA, Holcomb DJ, Rudnicki JW (2002) Compaction Localization in Porous Sandstone: Implications for Reservoir Mechanics. *Oil and Gas Science Technology*, Revue de l' Institut Français du Pétrole, 57: 591-599.
11. Papamichos E, Baxevanis T, Larsen I (2005) Compaction localisation in calcarenite. 7th International Workshop on Bifurcation, Instabilities and Degradation in Geomechanics, Chania, Greece
12. Radjai F, Jean M, Moreau J-J, Roux S (1996) Force distributions in dense two-dimensional granular systems, *Physical Review Letters*, 77 (2): 274-277.
13. Sternlof KR, Rudnicki JW, Pollard DD (2005) Anticrack inclusion model for compaction bands in sandstone, *Journal of Geophysical Research*, 110: B11403
14. Thornton C (1997) Force transmission in granular media, *KONA*, 15: 81-90.
15. Vardoulakis I and Sulem J (1995) *Bifurcation Analysis in Geomechanics*. Blackie Academic & Professional, Glasgow, U.K.

Shear Zone Formation in 2D Random Granular Specimens within Enhanced Hypoplasticity

Jacek Tejchman

Gdansk University of Technology,
Faculty for Civil and Environmental Engineering,
80-952 Gdansk - Wrzeszcz, Narutowicza 11/12,
Poland,
E-mail:tejchmk@pg.gda.pl

Summary

The paper focuses on the effect of different spatially correlated stochastic distributions of the initial void ratio on the formation of shear localization within a granular specimen during a conventional plane strain compression test. For a simulation of the mechanical behavior of a sand specimen during a monotonous deformation path, a hypoplastic constitutive enhanced by a characteristic length of micro-structure within a micro-polar, non-local and second-gradient continuum was used. The random fields of the initial void ratio were generated in a granular specimen using a conditional rejection method.

1 Introduction

Localization of deformation in the form of narrow zones of intense shearing is a fundamental phenomenon in granular materials and can appear under both drained and undrained conditions [9], [15], [20], [35], [40], [49], [51]. Localization can appear as a spontaneous one inside of granular materials or as an induced one at interfaces between granulates and structure members. An understanding of the mechanism of the formation of shear zones is important since they usually act as a precursor to ultimate soils failure.

To model the mechanical behaviour of granular bodies based on continuum mechanics, two different approaches are usually used: elastoplastic [18], [31], [50] and hypoplastic [2], [10], [12], [17], [19], [21], [46], [47]. To describe the properly the shear zone formation in a quasi-static regime,

the approaches have to be enriched by a characteristic length of micro-structure by means of a micro-polar [23], [34], [43], non-local [3], [7], [21] and second-gradient theory [1], [5], [29]. The approaches regularize the ill-posedness (i.e. preserve the well-posedness) of the underlying incremental boundary value problem caused by strain-softening material behaviour and localization formation (differential equations of motion do not change their elliptic type during quasi-static calculations and hyperbolic type during dynamic calculations) and prevent pathological discretization sensitivity [6]. Thus, objective and properly convergent numerical solutions for localized deformation (mesh-insensitive load-displacement diagram and mesh-insensitive deformation pattern) are achieved. The presence of a characteristic length allows also to take into account microscopic inhomogeneities triggering shear localization (e.g. grain size, size of micro-defects) and to capture the size effect of a specimen [37] (dependence of strength and other mechanical properties on the size of the specimen) observed experimentally on softening granular specimens.

Laboratory experiments [9], [49] and FE-studies [4], [8], [11], [14], [25], [26], [33], [37] show that the distribution of microscopic inhomogeneities inherently present in granular materials and triggering shear localization seems to be an influential factor. In the paper, the shear zone formation during monotonic plane strain compression with a cohesionless non-homogeneous granular material under constant lateral pressure was investigated. The analysis was performed with the finite element method and a hypoplastic constitutive model enhanced by a characteristic length of micro-structure (with the aid of micro-polar, non-local and second-gradient terms [21], [37]) which is able to describe the essential properties of granular bodies during shear localization in a wide range of pressures and densities during monotonous deformation paths. The FE-calculations of a plane strain compression test for granular materials [37] have demonstrated that the mesh dependence inherent in classical plasticity and hypoplasticity is remedied using the enhanced approaches. In those calculations (similarly as in other FE-analyses), the distribution of the initial void ratio was assumed to be uniform (with exception of one element with a higher initial void ratio to induce shear localization). In the calculations presented in this paper, the distribution of an initial void ratio was assumed to be more realistic, i.e. it was taken stochastically with a spatially correlated distribution [32], [44]. The random fields of the initial void ratio were generated in a granular specimen using a conditional rejection method proposed by Walukiewicz et al. [44]. The quasi-static 2D calculations were carried out with the same random field of the mean initial void ratio for different characteristic lengths of micro-structure within enhanced hypo-

plastic models. The effect of different stochastic parameters on the shear zone formation was investigated only with a micro-polar hypoplastic law.

The FE-simulations of the influence of the initial void ratio (with a spatially correlated distribution) on the shear zone formation have not been performed yet.

2 Hypoplasticity

Hypoplastic constitutive laws [2], [12], [17], [21], [24], [46] formulated at the Karlsruhe University are an alternative to elasto-plastic formulations [18], [31], [50] for continuum modeling of granular materials. They describe the evolution of effective stress components with the evolution of strain components by a differential equation including isotropic linear and non-linear tensorial functions according to the representation theorem by Wang [45]. In contrast to elasto-plastic models, the decomposition of deformation components into elastic and plastic parts, yield surface, plastic potential, flow rule and hardening rule are not needed. The hypoplastic models describe the behaviour of so-called simple grain skeletons which are characterized by the following properties [12]:

- the state is fully defined through the skeleton pressure and the void ratio (inherent anisotropy of contact forces between grains is not considered and vanishing principal stresses are not allowed),
- deformation of the skeleton is due to grain rearrangements (e.g. small deformations $<10^{-5}$ due to an elastic behaviour of grain contacts are negligible),
- grains are permanent (abrasion and crushing are excluded in order to keep the granulometric properties unchanged),
- three various void ratios decreasing exponentially with pressure are distinguished (minimum, maximum and critical),
- the material manifests an asymptotic behaviour for monotonous and cyclic shearing or SOM-states (swept-out-of-memory) for proportional compression,
- rate effects are negligible,
- physico-chemical effects (capillary and osmotic pressure) and cementation of grain contacts are not taken into account.

The hypoplastic constitutive laws are of the rate type. Due to the incremental non-linearity with the deformation rate, they are able to describe both a non-linear stress-strain and volumetric behaviour of granular bodies during shearing up to and after the peak with a single tensorial equation. They include also: barotropy (dependence on pressure level), pycnotropy

(dependence on density), dependence on the direction of deformation rate, dilatancy and contractancy during shearing with a constant pressure, increase and release of pressure during shearing with a constant volume, and material softening during shearing of a dense material. They are apt to describe stationary states, i.e. states in which a grain aggregate can continuously be deformed at a constant stress and a constant volume under a certain rate of deformation. Although, the hypoplastic models are developed without recourse to concepts of the theory of plasticity, a failure surface, flow rule and plastic potential are obtained as natural outcomes [24]. The feature of the model is a simple formulation and procedure for determination of material parameters with standard laboratory experiments [16]. The parameters are directly related to granulometric properties encompassing grain size distribution curve, shape, angularity and hardness of grains [16]. Owing to that only one set of material parameters is valid within a large range of pressures and densities. The constitutive law can be summarized as follows:

$$\overset{o}{\sigma}_{ij} = f_s [L_{ij}(\overset{\wedge}{\sigma}_{kl}) + f_d N_{ij}(\overset{\wedge}{\sigma}_{ij}) \sqrt{d_{kl} d_{kl}}], \quad (2.1)$$

$$L_{ij} = a_I^2 d_{ij} + \overset{\wedge}{\sigma}_{ij} \overset{\wedge}{\sigma}_{kl} d_{kl}, \quad (2.2)$$

$$N_{ij} = a_I (\overset{\wedge}{\sigma}_{ij} + \overset{\wedge}{\sigma}_{ij}^*), \quad (2.3)$$

$$\overset{\wedge}{\sigma}_{ij} = \frac{\sigma_{ij}}{\sigma_{kk}}, \quad (2.4)$$

$$\overset{o}{\sigma}_{ij} = \overset{\bullet}{\sigma}_{ij} - w_{ik} \sigma_{kj} + \sigma_{ik} w_{kj}, \quad (2.5)$$

$$d_{ij} = (v_{i,j} + v_{j,i})/2, \quad w_{ij} = (v_{i,j} - v_{j,i})/2, \quad (2.6)$$

$$\overset{\bullet}{e} = (1 + e) d_{kk}, \quad (2.7)$$

$$e_i = e_{i0} \exp[-(-\sigma_{kk}/h_s)^n], \quad (2.8)$$

$$e_d = e_{d0} \exp[-(-\sigma_{kk}/h_s)^n], \quad (2.9)$$

$$e_c = e_{c0} \exp[-(-\sigma_{kk} / h_s)^n], \quad (2.10)$$

$$f_s = \frac{h_s}{nh_i} \left(\frac{1+e_i}{e_i} \right) \left(\frac{e_i}{e} \right)^\beta \left(-\frac{\sigma_{kk}}{h_s} \right)^{1-n}, \quad (2.11)$$

$$h_i = \frac{1}{c_1^2} + \frac{1}{3} - \left(\frac{e_{i0} - e_{d0}}{e_{c0} - e_{d0}} \right)^\alpha \frac{1}{c_1 \sqrt{3}}, \quad (2.12)$$

$$f_d = \left(\frac{e - e_d}{e_c - e_d} \right)^\alpha, \quad (2.13)$$

$$a_1^{-1} = c_1 + c_2 \sqrt{\hat{\sigma}_{kl}^* \hat{\sigma}_{kl}^*} [1 + \cos(3\theta)], \quad (2.14)$$

$$\cos(3\theta) = -\frac{\sqrt{6}}{[\hat{\sigma}_{kl}^* \hat{\sigma}_{kl}^*]^{1.5}} (\hat{\sigma}_{kl}^* \hat{\sigma}_{lm}^* \hat{\sigma}_{mk}^*), \quad (2.15)$$

$$c_1 = \sqrt{\frac{3}{8}} \frac{(3 - \sin \phi_c)}{\sin \phi_c}, \quad c_2 = \frac{3}{8} \frac{(3 + \sin \phi_c)}{\sin \phi_c}, \quad (2.16)$$

wherein

- σ_{ij} - Cauchy stress tensor,
- σ_{ij}^* - deviatoric part of σ_{ij} ,
- $\overset{o}{\sigma}_{ij}$ - Jaumann stress rate tensor (objective stress rate tensor),
- e - current void ratio,
- \dot{e} - changes of the current void ratio,
- d_{kl} - rate of deformation tensor (stretching tensor),
- w_{ij} - spin tensor,
- v - material velocity,
- f_s - stiffness factor,
- h_s - granular hardness,
- σ_{kk} - mean stress,
- f_d - density factor,
- e_c - critical void ratio (e_{c0} - value of e_c for $\sigma_{kk}=0$),
- e_d - void ratio at maximum densification (e_{d0} - value of e_d for $\sigma_{kk}=0$),

- e_i - maximum void ratio (e_{i0} - value of e_i for $\sigma_{kk}=0$),
- α - pycnotropy coefficient,
- n - compression coefficient,
- β - stiffness coefficient,
- a_1 - parameter representing the deviatoric part of the normalized stress in critical states,
- ϕ_c - critical angle of internal friction during stationary flow,
- θ - Lode angle.

In case of sand, the hypoplastic constitutive relation is approximately valid in a pressure range $1 \text{ kPa} < -\sigma_{kk}/3 < 1000 \text{ kPa}$. Below it, additional capillary forces due to the air humidity and van der Waals forces may become important, and above it, grain crushing. The first term in Eq. 2.1 is linear in d_{kl} , and the second one is non-linear in d_{kl} . The constitutive relationship requires 8 material constants: e_{i0} , e_{d0} , e_{c0} , ϕ_c , h_s , n , β and α . The FE-analyses were carried out with the following material constants (for so-called Karlsruhe sand): $e_{i0}=1.3$, $e_{d0}=0.51$, $e_{c0}=0.82$, $\phi_c=30^\circ$, $h_s=190 \text{ MPa}$, $n=0.5$, $\beta=1.0$ and $\alpha=0.3$ [2]. The parameters h_s and n are estimated from a single oedometric compression test with an initially loose specimen (h_s reflects the slope of the curve in a semi-logarithmic representation, and n its curvature). The constants α and β are found from a triaxial test with a dense specimen (they reflect the height and position of the peak value of the stress-strain curve). The angle ϕ_c is determined from the angle of repose (inclination angle of a free granular heap) or measured in a triaxial test with a loose specimen. The values of e_{i0} , e_{d0} and e_{c0} are obtained with conventional index tests ($e_{c0} \approx e_{max}$, $e_{d0} \approx e_{min}$, $e_{i0} \approx (1.1-1.5)e_{max}$).

A hypoplastic constitutive law cannot describe realistically the thickness of shear localization since it does not include a characteristic length of micro-structure. The characteristic length can be taken into account by means of a polar, non-local and second-gradient theory [37].

3 Micro-Polar Hypoplastic Law

The micro-polar terms were introduced in a hypoplastic law with the aid of a polar (Cosserat) continuum [23]. In a Cosserat continuum, each material point has for the case of plane strain three degrees of freedom: two translational degrees of freedom and one independent rotational degree of freedom (Fig.3.1a). The gradients of the rotation are connected to curvatures which are associated with couple stresses (Fig.3.1b). It leads to a non-symmetry of the stress tensor and a presence of a characteristic length

directly related to a mean grain diameter. The polar extension of the hypo-elastic constitutive law [37], [42] was achieved analogously to Mühlhaus's formulation [23] (for details, the reader is referred to [42]). Its other advantages are: it takes into account Cosserat rotations (resultant grain rotations from a certain region of the granular specimen) and couple stresses which are significant during shearing [27], [28], the characteristic length l_c is directly related to the mean grain diameter d_{50} [37], and realistic wall boundary conditions at the interface of granulate with a structure (with consideration of the wall roughness) can be derived [41]. Pasternak and Mühlhaus [30] have demonstrated that the additional rotational degree of freedom of a Cosserat continuum arises naturally by mathematical homogenization of an originally discrete system of spherical grains with contact forces and contact moments. The Cosserat model is only suitable for shear dominated problems.

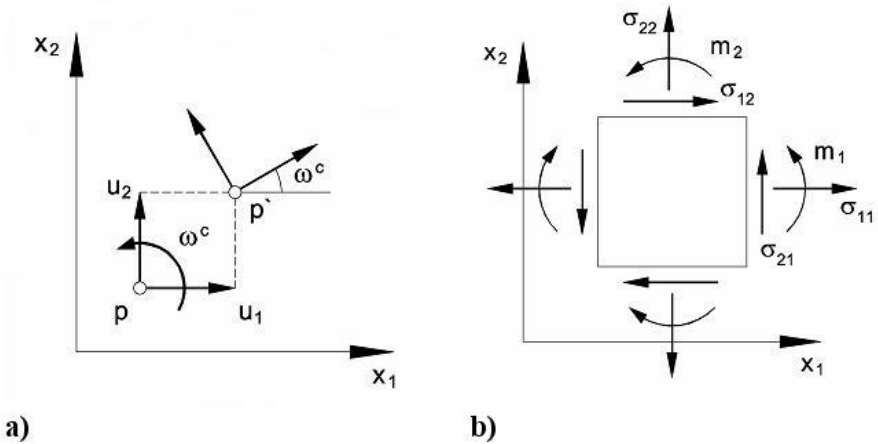


Fig. 3.1. Plane strain Cosserat continuum: **a)** degrees of freedom (u_1 - horizontal displacement, u_2 - vertical displacement, ω^c - Cosserat rotation), **b)** stresses σ_{ij} and couple stresses m_i at an element

The constitutive law can be summarized for plane strain as follows [37], [42]:

$$\begin{aligned} \overset{o}{\sigma}_{ij} = & f_s [L_{ij}(\overset{\wedge}{\sigma}_{kl}, \hat{m}_k, \hat{d}_{kl}^c, k_k d_{50}^c) + \\ & f_d N_{ij}(\overset{\wedge}{\sigma}_{ij}) \sqrt{\hat{d}_{kl}^c \hat{d}_{kl}^c + k_k k_k d_{50}^2} J, \end{aligned} \tag{3.1}$$

$$\overset{o}{m}_i / d_{50} = f_s [L_i^c (\overset{\wedge}{\sigma}_{kl}, \hat{m}_k, d_{kl}^c, k_k d_{50}) + f_d N_i^c (\hat{m}_i) \sqrt{d_{kl}^c d_{kl}^c + k_k k_k d_{50}^2}], \quad (3.2)$$

$$L_{ij} = a_I^2 d_{ij}^c + \overset{\wedge}{\sigma}_{ij}^c (\overset{\wedge}{\sigma}_{kl} d_{kl}^c + \hat{m}_k k_k d_{50}), \quad (3.3)$$

$$L_i^c = a_I^2 k_i d_{50} + a_I^2 \hat{m}_i (\overset{\wedge}{\sigma}_{kl} d_{kl}^c + \hat{m}_k k_k d_{50}), \quad (3.4)$$

$$N_i^c = a_I^2 a_c \hat{m}_i, \quad (3.5)$$

$$\overset{o}{m}_i = \overset{\bullet}{m}_i - 0.5 w_{ik} m_k + 0.5 m_k w_{ki}, \quad (3.6)$$

$$\hat{m}_k = \frac{m_k}{\sigma_{kk} d_{50}}, \quad (3.7)$$

$$d_{ij}^c = d_{ij} + w_{ij} - w_{ij}^c, \quad (3.8)$$

$$k_i = w_{,i}^c, \quad (3.9)$$

$$w_{kk}^c = 0, \quad w_{21}^c = -w_{12}^c = w^c, \quad (3.10)$$

wherein

- m_i - Cauchy couple stress vector,
- $\overset{o}{m}_i$ - Jaumann couple stress rate vector,
- d_{ij}^c - polar rate of deformation tensor,
- k_i - rate of curvature vector,
- w^c - rate of Cosserat rotation,
- a_c - micro-polar constant,
- d_{50} - mean grain diameter of sand ($d_{50}=0.5$ mm).

A micro-polar constant a_c can be correlated with the grain roughness and estimated with a numerical analysis for shearing of a narrow granular strip between two very rough boundaries (e.g. $a_c = a_I^{-1}$ [42]). The micro-polar hypoplastic model has 10 material constants.

4 Non-Local Hypoplastic Law

A non-local approach can take into account shear zones and cracks. It is based on spatial averaging of tensor or scalar state variables in a certain neighbourhood of a given point (i.e. material response at a point depends both on the state of its neighbourhood and the state of the point itself). It is sufficient to treat non-locally only one internal constitutive variable (e.g. equivalent plastic strain in an elasto-plastic formulation [7] or modulus of the deformation rate or density factor in a hypoplastic approach [21], [37]) whereas the others can retain their local definitions.

In the FE-calculations, the modulus of the deformation rate of Eq. 2.1 expressed by

$$d = \sqrt{d_{kl}d_{kl}} \tag{4.1}$$

was treated non-locally. It was assumed as

$$d^*(x) = \frac{1}{A} \int_{-\infty}^{\infty} w(r) d(x+r) dV, \tag{4.2}$$

where r is the distance from the material point considered to other integration points of the entire material body, w is the weighting function and A is the weighted body volume. The error density function (normal Gaussian distribution function) was chosen as a weighting function w [37]:

$$w(r) = \frac{1}{l_c \sqrt{\pi}} e^{-\left(\frac{r}{l_c}\right)^2} \tag{4.3}$$

The parameter l_c denotes a characteristic length (it determines the size of the neighbourhood influencing the state at a given point). At the distance of $3 \times l_c$, the function w is almost equal to zero. Generally, the characteristic length l_c in Eq. 4.3 is not directly related to the mean grain diameter of the granulate. It can be determined from an inverse identification process of experimental data [21].

5 Second-Gradient Hypoplastic Law

In the FE-calculations, the second gradient of the Euclidean norm of the deformation rate (Eq. 3.10) was taken into account [37]. Thus, the enhan-

ced modulus of the deformation rate d^* was calculated for two-dimensional problems in the following way

$$d^*(x, y) = d + \frac{l_c^2}{4} \left(\frac{\partial^2 d}{\partial x^2} + \frac{\partial^2 d}{\partial y^2} + 2 \frac{\partial^2 d}{\partial x \partial y} \right). \tag{5.1}$$

Instead of using complex shape functions to describe the evolution of the second gradient of d [29], [52], a central difference scheme was applied. The advantages of such approach are: simplicity of computation, little effort to modify each commercial FE-code and high computation efficiency. To take into account the effect of not only adjacent elements (as in the standard difference method), one assumed a polynomial inter-polation of the function d of the fourth order in both directions [37]. The second derivatives of the variable d can be approximated in each triangular element of the same quadrilateral, e.g. in the element 13 of Fig.5.1 (for the mesh regular in the vertical and horizontal direction) as [37]:

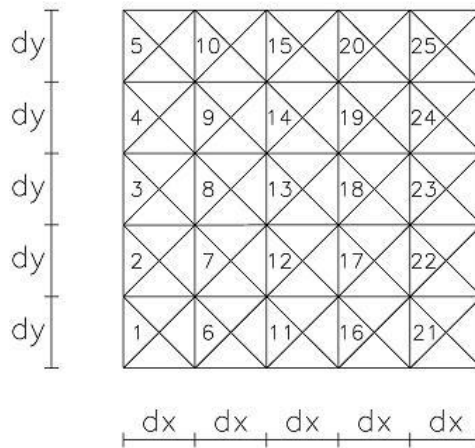


Fig. 5.1. Diagram for determination of the gradient of the constitutive variable d in triangular elements using a central difference method

$$\frac{\partial^2 d_{13}}{\partial x^2} = \frac{1}{dx^2} \left[-\frac{1}{12} d_3 + \frac{16}{12} d_8 - \frac{30}{12} d_{13} + \frac{16}{12} d_{18} - \frac{1}{12} d_{23} \right], \tag{5.2}$$

$$\frac{\partial^2 d_{13}}{\partial y^2} = \frac{1}{dy^2} \left[-\frac{1}{12} d_{11} + \frac{16}{12} d_{12} - \frac{30}{12} d_{13} + \frac{16}{12} d_{14} - \frac{1}{12} d_{15} \right], \tag{5.3}$$

$$\begin{aligned} \frac{\partial^2 d_{13}}{\partial x \partial y} = & \frac{1}{dxdy} \left[\frac{1}{12} \left(\frac{1}{12} d_1 - \frac{8}{12} d_2 + \frac{8}{12} d_4 - \frac{1}{12} d_5 \right) - \right. \\ & \frac{8}{12} \left(\frac{1}{12} d_6 - \frac{8}{12} d_7 + \frac{8}{12} d_9 - \frac{1}{12} d_{10} \right) + \\ & \frac{8}{12} \left(\frac{1}{12} d_{16} - \frac{8}{12} d_{17} + \frac{8}{12} d_{19} - \frac{1}{12} d_{20} \right) - \\ & \left. \frac{1}{12} \left(\frac{1}{12} d_{21} - \frac{8}{12} d_{22} + \frac{8}{12} d_{24} - \frac{1}{12} d_{25} \right) \right], \end{aligned} \tag{5.4}$$

where the lower subscript at the variable d denotes the number of any triangular element in the specified quadrilateral (Fig.5.1), and dx and dy are the distances between the triangle centers in the neighboring quadrilaterals in a horizontal and vertical direction, respectively. Thus, the effect of neighboring elements near each element is taken into account. The advantage of a second-gradient approach is that it is suitable for both shear and tension dominated applications, and the computation time is shorter as compared to micro-polar and non-local hypoplasticity [37]. The disadvantages is (similarly as in a non-local continuum) that the characteristic length can be only determined from an inverse identification process of experimental data [21].

6 FE-Input Data

FE-calculations of plane strain compression tests were performed with a sand specimen which was $h_o=14$ cm high and $b=4$ cm wide (as in the experiments [48], [49]). Only quadrilateral finite elements composed of four diagonally crossed triangles were applied to avoid volumetric locking. In total, 896 quadrilateral elements (0.25×0.25 cm²) divided into 3584 triangular elements with linear shape functions for displacements were used. The dimensions of finite elements were $5 \times d_{50}$ to obtain the thickness of shear zones independent of the mesh size within an enhanced hypoplasticity [21], [37]. The integration was performed with one sampling point placed in the middle of each element. The calculations were carried out with large deformations (non-local and gradient model) or large deformations and curvatures (micro-polar model) using the so-called Updated Lagrangian formulation [37]. The second gradient terms and non-local terms of the modulus of the deformation rate d were calculated in each triangular element on the basis of the previous iteration step (explicit scheme).

As the initial stress state, a K_0 -state with $\sigma_{22}=\gamma_d x_2$ and $\sigma_{11}=K_0 \gamma_d x_2$ was assumed in the specimen where, x_2 is the vertical coordinate measured from the top of the specimen, $\gamma_d=16.5 \text{ kN/m}^3$ denotes the initial volume weight of medium dense sand and $K_0=0.47$ is the earth pressure coefficient at rest [2] (σ_{11} - horizontal normal stress, σ_{22} - vertical normal stress). Next, a confining pressure of $\sigma_c=200 \text{ kPa}$ was prescribed.

A quasi-static deformation in sand was imposed through a constant vertical displacement increment prescribed at nodes along the upper edge of the specimen. The boundary conditions of the sand specimen implied no shear stress at the smooth top and smooth bottom edge. To preserve the stability of the specimen against horizontal sliding, one node in the middle of the top edge was kept fixed. To simulate a movable roller bearing in the experiment [49], the horizontal displacements along the specimen bottom were constrained to move by the same amount. Other calculations have shown that the effect of the boundary condition along a smooth bottom is insignificant on the results [36]. The derivatives of the modulus of the deformation rate $\partial^2 d / \partial x^2$ were set to zero along vertical boundaries and the derivatives $\partial^2 d / \partial y^2$ were set to zero along horizontal boundaries within a second-gradient approach [37] (similarly as in elasto-plasticity [29]). The mixed derivatives were zero along all boundaries.

Different distributions of the initial void ratio can be assumed in granular specimens [11], [13], [22], [25]. However, it is not easy to assume a realistic spatial stochastic distribution of the initial void ratio due to the lack of experimental data. In the paper, a spatially correlated distribution of the initial void ratio e_o was assumed in the form of a two-dimensional Gaussian random field. Randomness of the initial void ratio was described by the following correlation function [32], [44]

$$K(x, y) = s_d^2 \times e^{-\lambda_{x_1} \Delta x_1} (1 + \lambda_{x_1} \Delta x_1) \times e^{-\lambda_{x_2} \Delta x_2} (1 + \lambda_{x_2} \Delta x_2), \quad (6.1)$$

where Δx_1 and Δx_2 are the distances between two field points along the axis x_1 and x_2 , λ_{x_1} and λ_{x_2} are the decay coefficients characterizing spatial variability of the specimen properties while the standard deviation s_d represents its scattering. The random fields were generated using a conditional rejection method proposed by Walukiewicz et al. [44], where a superior role plays a propagation scheme consisting of a growing number of points covering sequentially the nodes of the mesh. A discrete random field was described by multidimensional random variables defined at mesh nodes. The field was represented by the random vector $\mathbf{x}(m \times 1)$, and its mean value $\bar{\mathbf{x}}(m \times 1)$. The covariance function was replaced by the sym-

metric and positively defined covariance matrix $K(m \times m)$. The random variable vector $\mathbf{x}(m \times 1)$ was divided into blocks consisting of the unknown $\mathbf{x}_u(n \times 1)$ and the known $x_k(p \times 1)$ elements ($n + p = m$). The covariance matrix $K(m \times m)$ and the expected values vector $\bar{\mathbf{x}}(m \times 1)$ were also appropriately cut:

$$\mathbf{x} = \begin{Bmatrix} \mathbf{x}_u \\ \mathbf{x}_k \end{Bmatrix} \begin{matrix} n \\ p \end{matrix}, \quad \mathbf{K} = \begin{bmatrix} \mathbf{K}_{11} & \mathbf{K}_{12} \\ \mathbf{K}_{21} & \mathbf{K}_{22} \end{bmatrix} \begin{matrix} n \\ p \end{matrix}, \quad \bar{\mathbf{x}} = \begin{Bmatrix} \bar{\mathbf{x}}_u \\ \bar{\mathbf{x}}_k \end{Bmatrix} \begin{matrix} n \\ p \end{matrix} \quad (6.2)$$

The unknown vector x_u was estimated from the following conditional truncated distribution [44].

$$f_i(x_u / x_k) = (1-t)^{\frac{m}{2}} (\det K_c)^{-\frac{1}{2}} (2\pi)^{-\frac{m}{2}} \exp\left(-\frac{1}{2(1-t)} \begin{pmatrix} x_u - \bar{x}_c \end{pmatrix}^T K_c^{-1} \begin{pmatrix} x_u - \bar{x}_c \end{pmatrix}\right) \quad (6.3)$$

where K_c and \bar{x}_c are described as the conditional covariance matrix and conditional expected value vector:

$$K_c = K_{11} - K_{12} K_{22}^{-1} K_{21}, \quad (6.4)$$

$$\bar{x}_c = \bar{x}_u + K_{12} K_{22}^{-1} (x_k - \bar{x}_k). \quad (6.5)$$

The constant t is the truncation parameter

$$t = \frac{s_d \cdot \exp(-s_d^2/2)}{\sqrt{2\pi} \operatorname{erf}(s_d)} \quad (6.6)$$

with

$$\operatorname{erf}(s_d) = \frac{1}{\sqrt{2\pi}} \int_0^{s_d} \exp\left(-\frac{x^2}{2}\right) dx \quad (6.7)$$

The single variable was determined in accordance with the random field boundaries

$$x_i = a_i + (b_i - a_i) u_i, \quad i = 1, \dots, m \quad (6.8)$$

where u_i are the random variables uniformly distributed in the interval $[0,1]$, and (a_i, b_i) , $i = 1, 2, \dots, m$ are intervals of the reals (an envelope of the random field). The simulation process was divided into three stages. First, the four-corner random values were generated. Next, a propagation scheme with a growing number of points covered a defined base scheme of

the field mesh. In the third stage, the base scheme was appropriately shifted, and the next group of unknown random values was simulated (Fig.6.1). The base scheme was translated so as to cover all the field nodes. The following random fields for the initial void ratio were introduced by means of 2000 realizations: $\bar{e}_o \pm 6s_d$ (\bar{e}_o - mean initial void ratio). The void ratio scattering in the specimen was also limited by the pressure dependent void ratios e_{d0} and e_{i0} (Eqs. 2.8 and 2.9). For the sake of simplicity, only realizations of the random correlated fields with $\bar{e}_o = 0.65$ (medium dense sand) were performed. To compare FE-results of shear localization within a micro-polar, non-local and second-gradient continuum, the same random field for e_o with $s_d = 0.1$ and $\lambda_{x1} = \lambda_{x2} = 1$ (strongly correlated entire field) was assumed (Fig.6.2). In addition, the FE-calculations were carried out for different combinations of decay coefficients λ_{x1} and λ_{x2} assuming a smaller standard deviation ($s_d = 0.05$) within a micro-polar continuum. One random field was also generated with consideration of the rotation of the axis x_1 or x_2 by the angle $\delta = 30^\circ$.

For the solution of a non-linear system, a modified Newton-Raphson scheme with line search was used with a global stiffness matrix calculated with only linear terms. The stiffness matrix was updated every 100 steps. To accelerate the calculations in the softening regime, the initial increments of displacements (non-local and gradient approach) or displacements and rotations (micro-polar approach) in each calculation step were assumed to be equal to the final increments in the previous step [37].

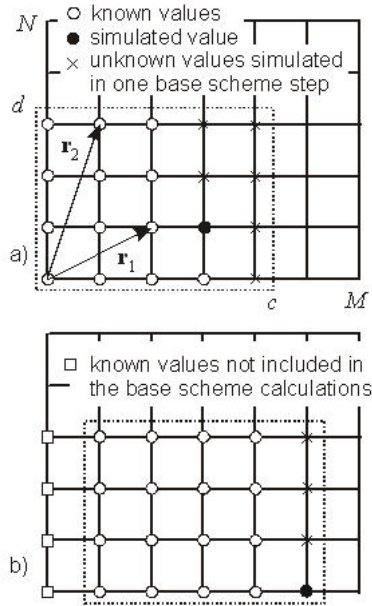


Fig. 6.1. Coverage of the field points with the moving propagation scheme during a generation process [44]

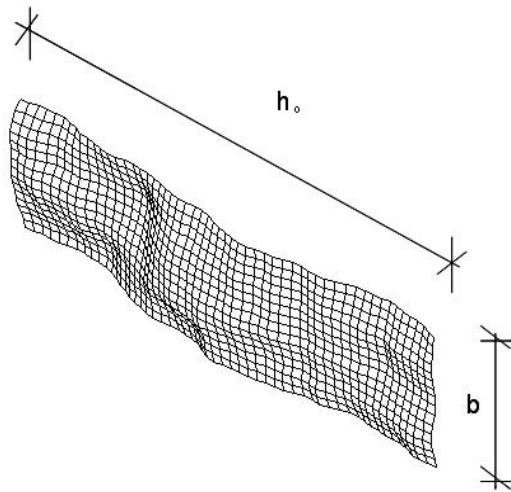


Fig. 6.2. Distribution of the initial void ratio in the random granular specimen for decay coefficients $\lambda_{x1}=1$, $\lambda_{x2}=1$, standard deviation $s_d=0.1$ and mean initial void ratio $\bar{e}_o=0.65$ (h_o – specimen height, b – specimen width)

The iteration steps were performed using translational convergence criteria (non-local and gradient approach) or translational and rotational convergence criteria (micro-polar approach).

7 FE-Results

Figures 7.1-7.6 present the results of the plane strain compression test for medium-dense sand ($e_o=0.65$, $\gamma_d=16.50$ kN/m³) within the micro-polar continuum (Figs.7.1 and 7.2), second-gradient continuum (Figs.7.3 and 7.4) and non-local continuum (Figs.7.5 and 7.6) under confining pressure $\sigma_c=0.2$ MPa using characteristic lengths in the range of $l_c=0.5-2.0$ mm. The normalized load-displacement curves are depicted in Figs.7.1, 7.3 and 7.5 (P – vertical force, σ_c – confining pressure, b - specimen width, u_2^t – vertical displacement of the top, h_o – initial height of the sand body). The specimen length is $l=1.0$ m due to two-dimensional calculations. In turn, Figures 7.2, 7.4 and 7.6 show the deformed FE-mesh with the distribution of void ratio (Eq.2.2) (the darker the region, the higher the void ratio). The results of the overall internal friction angle at the peak and at residual state ($u_2^t/h_o=0.10$) are given in Table 7.1. In addition, the vertical normal strain corresponding to the maximum force and the thickness of the shear zone at residual state are presented. The overall mobilized angle of internal friction for the sand specimen was calculated with the aid of principal stresses from the Mohr's formula

$$\phi = \arcsin \frac{\sigma_1 - \sigma_3}{\sigma_1 + \sigma_3}, \quad (7.1)$$

where $\sigma_1=P/(bl)$ denotes the vertical principal stress and $\sigma_3=\sigma_c$ is the horizontal principal stress ($l=1.0$ m).

The resultant vertical force in the specimen P increases first, shows a pronounced peak, drops later and approaches a residual state. The maximum vertical force P_{max} and the vertical displacement of the top boundary corresponding to P_{max} increase with increasing l_c . The material becomes more ductile after the peak with increasing l_c . The reason is that the enriched continua are stiffer than the conventional one since their work is augmented by additional terms which depend upon the characteristic length of microstructure. Thus, the shear resistance and material ductility increases always with increasing ratio l_c/L (L – specimen size).

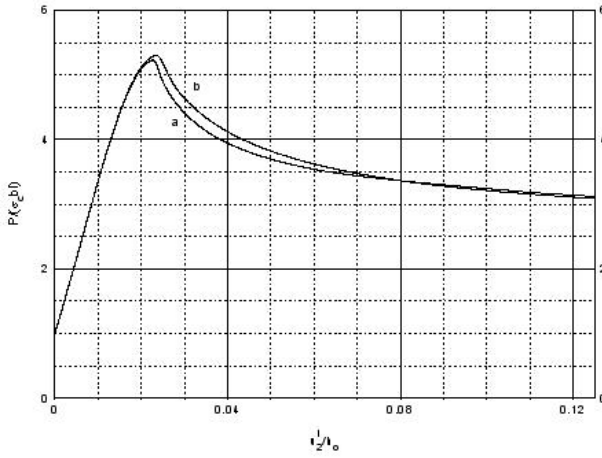


Fig. 7.1. Normalized load-displacement curve within a micro-polar hypoplastic continuum ($\bar{e}_o = 0.65$): a) $l_c = d_{50} = 0.5$ mm, b) $l_c = d_{50} = 1.0$ mm

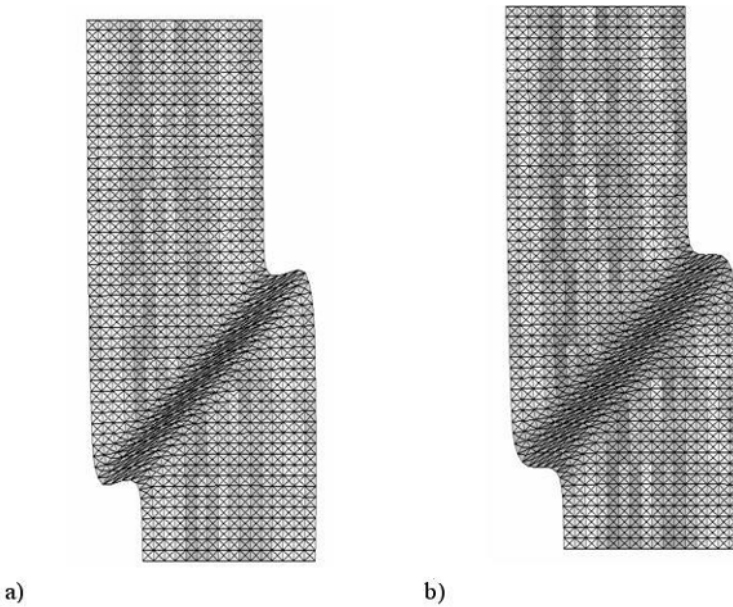


Fig. 7.2. Deformed FE-mesh with the distribution of void ratio in the residual state within a micro-polar hypoplastic continuum ($\bar{e}_o = 0.65$): a) $l_c = d_{50} = 0.5$ mm, b) $l_c = d_{50} = 1.0$ mm

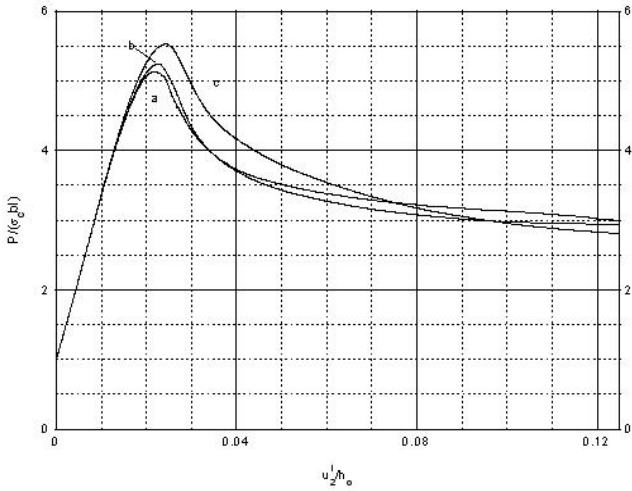


Fig. 7.3. Normalized load-displacement curve within a within a second-gradient hypoplastic continuum ($\bar{e}_o = 0.65$): a) $l_c = 0.5$ mm, b) $l_c = 1.0$ mm, c) $l_c = 2.0$ mm

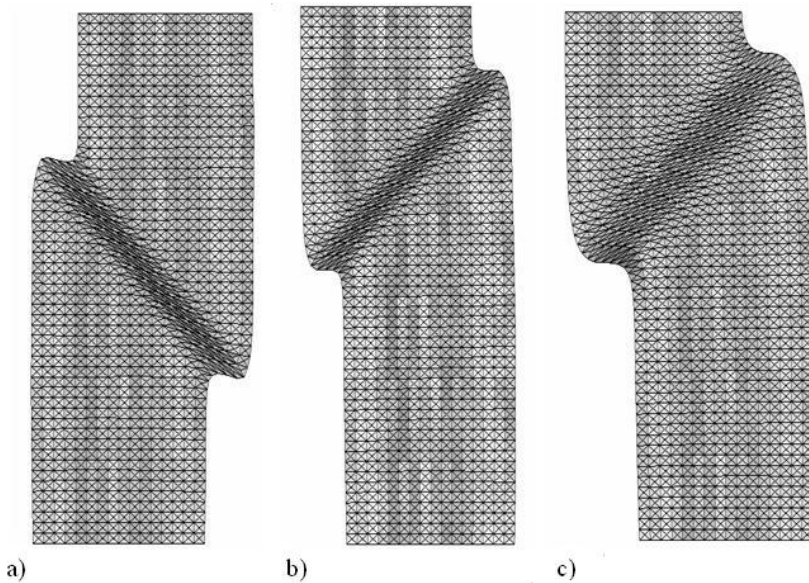


Fig. 7.4. Deformed FE-mesh with the distribution of void ratio in the residual state within a second-gradient hypoplastic continuum ($\bar{e}_o = 0.65$): a) $l_c = 0.5$ mm, b) $l_c = 1.0$ mm, c) $l_c = 2.0$ mm

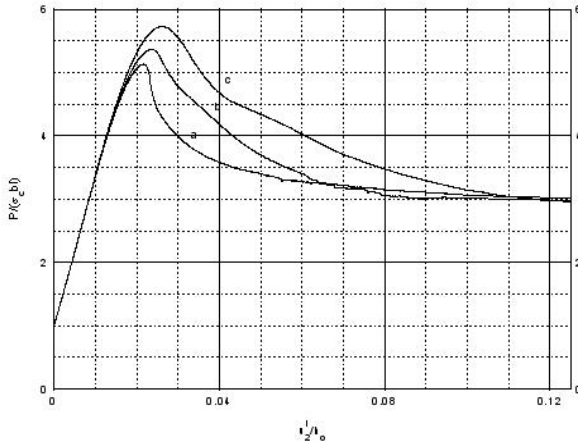


Fig. 7.5. Normalized load-displacement curve within a non-local hypoplastic continuum ($\bar{e}_o = 0.65$): a) $l_c = 0.5$ mm, b) $l_c = 1.0$ mm, c) $l_c = 2.0$ mm

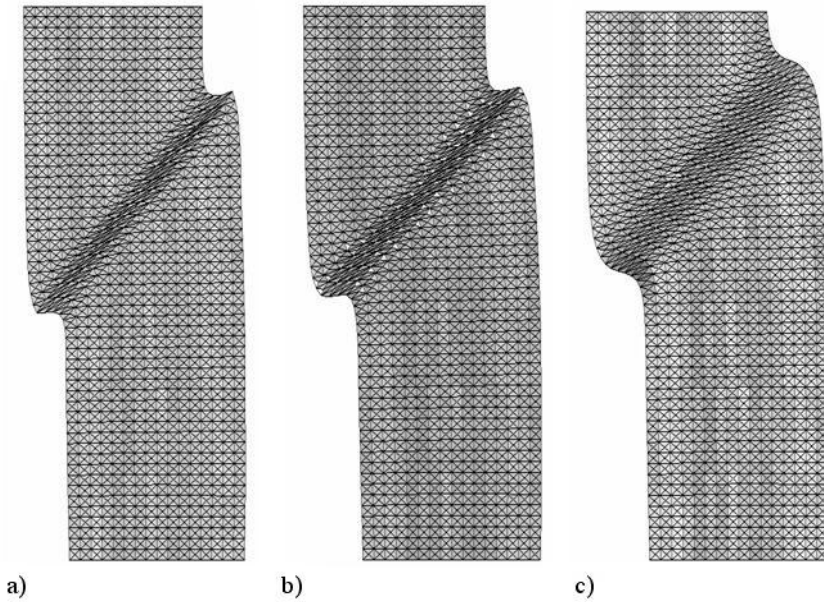


Fig. 7.6. Deformed FE-mesh with the distribution of void ratio in the residual state within a non-local hypoplastic continuum ($\bar{e}_o = 0.65$): a) $l_c = 0.5$ mm, b) $l_c = 1.0$ mm, c) $l_c = 2.0$ mm

Table 7.1. Results of mobilized internal friction angle at peak ϕ^p and residual state ϕ_{res} , vertical normal strain corresponding to ϕ^p and shear zone thickness t_s for different characteristic lengths l_c within a micro-polar, second-gradient and non-local hypoplastic continuum ($\bar{e}_o=0.65$, $\sigma_c=0.2$ MPa)

Enhanced hypoplastic constitutive model ($e_o=0.65$, $\sigma_c=0.2$ MPa)	ϕ^p [$^\circ$]	u_2^t/h_o [-] at peak	ϕ_{res} [$^\circ$] at $u_2^t/h_o=0.125$	t_s [mm] at residual state for $u_2^t/h_o=0.10$
l_c [mm]				
Micro-polar model				
$l_c=0.5$ mm	42.8	0.023	31.4	8.2 (16.4 $\times l_c$)
$l_c=1.0$ mm	43.0	0.024	31.4	10.3 (10.3 $\times l_c$)
Gradient model				
$l_c=0.5$ mm	42.4	0.022	30.8	6.5 (13.0 $\times l_c$)
$l_c=1.0$ mm	42.8	0.023	29.8	7.7 (7.7 $\times l_c$)
$l_c=2.0$ mm	43.9	0.024	29.0	10.6 (5.3 $\times l_c$)
Non-local model				
$l_c=0.5$ mm	42.4	0.022	30.8	5.5 (11 $\times l_c$)
$l_c=1.0$ mm	43.3	0.024	30.1	6.6 (6.6 $\times l_c$)
$l_c=2.0$ mm	44.7	0.026	30.5	10.6 (5.4 $\times l_c$)

The overall internal friction angle at peak is in the range $\phi^p=42.4^\circ$ - 44.7° and at residual state $\phi_{res}=29.0^\circ$ - 31.4° (at $u_2^t/h_o=0.125$) with 3 different enhanced hypoplastic models. The evolution of the vertical force on the top after the peak is dependent upon the enhanced model used. The material is the most ductile within a non-local continuum and the most brittle within a second-gradient continuum.

The obtained results of internal friction angles at the peak and in the residual state in medium dense sand, and the corresponding vertical displacements of the sand specimen compare well with experimental results with Karlsruhe sand ($d_{50}=0.5$ mm) carried out by Vardoulakis [49]

and Vardoulakis and Goldscheider [48], where the dimensions of the sand specimen were: $h_0=140$ mm, $b=40$ mm and $l=80$ mm.

The experiments with dense sand ($e_o=0.55-0.60$) resulted in the following values of $\phi^p=45^\circ-48^\circ$ and $\phi_{res}=32^\circ-33^\circ$ at $\sigma_c=200$ kPa. In turn, the experiments with loose sand ($e_o=0.70-0.75$) resulted in the following values of $\phi^p=37^\circ$ and $\phi_{res}=33^\circ-34^\circ$ at $\sigma_c=200$ kPa. The calculated values of ϕ^p for medium dense sand lie between the experimental results. In turn, the calculated values of ϕ_{res} are slightly smaller than the experimental ones. The shape of the calculated load-displacement curves is close to the experimental one [48]. However, the calculated stiffness is too high before the peak (in the hardening region).

During deformation, first, a pattern of shear zones can be observed due to a stochastic distribution of the initial void ratio [13], [38]. Next, strain localization continues to localize within one dominant single zone inside of the specimen. The complete shear zone is already noticeable shortly after the peak. It is characterized both by a concentration of shear deformations, and a significant increase of the void ratio and modulus of the deformation rate [37]. The thickness of the internal shear zone grows with increasing l_c (Tab.7.1) and is about (on the basis of shear deformation): 8.2-10.3 mm (micro-polar continuum, $l_c=0.5-1.0$ mm), 6.5-10.6 mm (second-gradient continuum, $l_c=0.5-2.0$ mm) and 5.5-10.6 mm (non-local continuum, $l_c=0.5-2.0$ mm). The calculated thickness of the shear zone with $l_c=d_{50}=0.5$ mm within a micro-polar continuum and $l_c=1.0$ mm within a second-gradient and non-local continuum is similar. It is in satisfactory accordance with the observed thickness, $t_s=(10-15)\times d_{50}$, during plane strain compression tests with dense sand at $\sigma_c=200$ kPa [48], [49]. The calculated inclination of the shear zone is about 50° . The location of the shear zone is the same for $l_c=d_{50}=0.5-1.0$ mm (micro-polar continuum) and $l_c=1.0-2.0$ mm (second-gradient and non-local continuum).

Figures 7.7 and 7.8 present the calculated load-displacement curves for different coefficients λ and s_d as compared to the solution with the uniform initial void ratio using one weak element within a micro-polar continuum.

The effect of the initial void ratio distribution on the load-displacement diagram can be observed up to the residual state where all forces are almost the same. The highest vertical force on the top appears for the case of $\lambda_{x1}=1$, $\lambda_{x2}=3$ and $s_d=0.1$ (curve 'g' in Fig.7.8) and the lowest one for $\lambda_{x1}=1$, $\lambda_{x2}=3$, $s_d=0.05$ (curve 'c' in Fig.7.7) and $\lambda_{x1}=3$, $\lambda_{x2}=1$, $s_d=0.1$ (curve 'h' in Fig.7.8). The maximum vertical forces for stochastic distributions of e_o can be larger than this for the uniform distribution of e_o (curve 'a' in Figs.7.7 and 7.8). The vertical strain corresponding to the maximum vertical force is always smaller than this for the uniform distri-

bution of e_o . The highest difference between the maximum vertical forces for various distributions of e_o is about 15%. Thus, the weakest link principle does not apply. The fact that the spatial fluctuation of the void ratio can make the material stronger is caused by the fact that at the early stage of deformation, initially several shear zones propagate starting from the weakest spots (Fig.7.9). Thus, the weakest cross-section cannot be chosen at the beginning of deformation.

The effect of different fields of the initial void ratio on the shear zone formation (thickness and inclination) was found to be insignificant. The location of the shear zone in the granular specimen was influenced only.

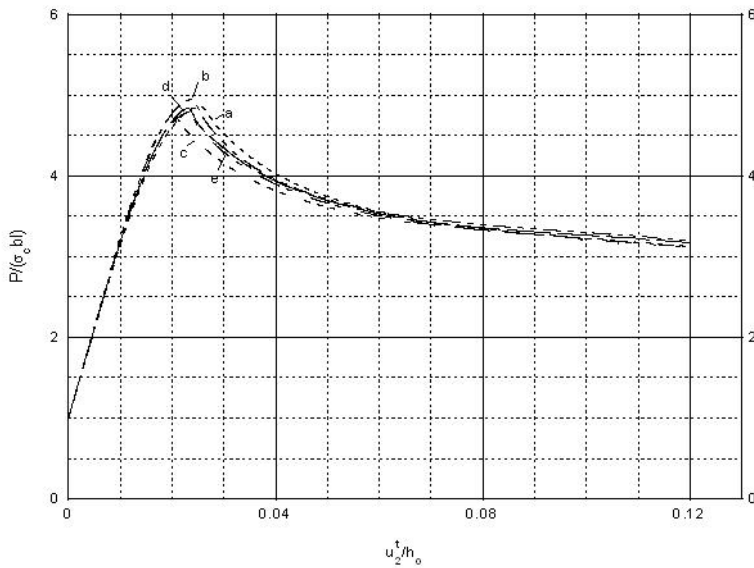


Fig. 7.7. Load-displacement curves during plane strain compression with a medium dense specimen for the uniform distribution (a) and spatially correlated distribution of the initial void ratio ($s_d=0.05$): b) $\lambda_{x1}=1, \lambda_{x2}=1$, c) $\lambda_{x1}=1, \lambda_{x2}=3$, d) $\lambda_{x1}=3, \lambda_{x2}=1$, e) $\lambda_{x1}=3, \lambda_{x2}=3$

8 Conclusions

The FE-calculations of a plane strain compression test for a random granular material with a spatially correlated distribution of the initial void ratio demonstrate that the internal friction angle at peak and the thickness of the

localized shear zone increase with increasing characteristic length within the enhanced continuums.

The characteristic length of micro-structure for the second-gradient continuum and non-local continuum corresponds approximately to two mean grain diameters of the granulate within the micro-polar continuum.

The granular material becomes the most ductile within the non-local continuum and the most brittle within the second-gradient continuum.

The material strength can be larger for the stochastic field of the initial void ratio than for the uniform one due to the appearance of several shear zones at the beginning of deformation.

The stochastic distribution of the initial void ratio does not affect the load-displacement curve at residual state and shear zone formation (its thickness and inclination).

The vertical strain corresponding to the maximum vertical force is always smaller in the case of a stochastic distribution of the initial void ratio.

The void ratio in the shear zone always approaches the critical pressure-dependent void ratio.

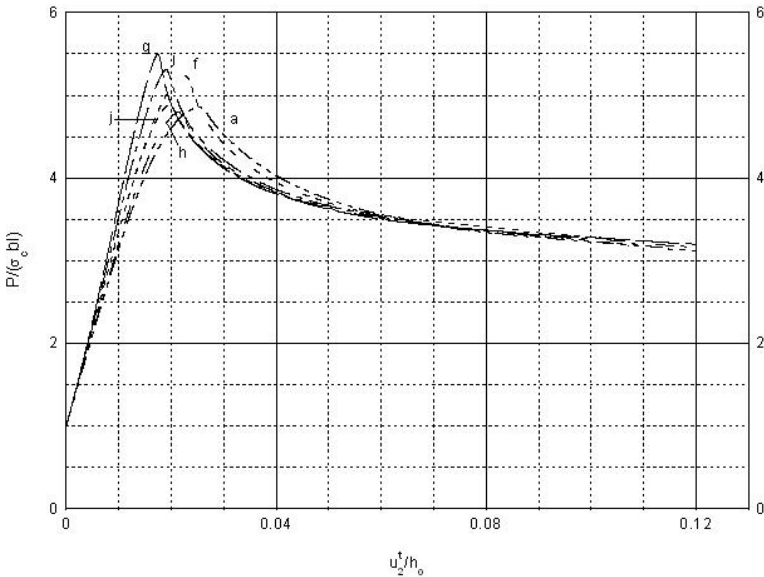


Fig. 7.8. Load-displacement curves during plane strain compression with a medium dense specimen for the uniform distribution (a) and spatially correlated distribution of the initial void ratio ($s_d=0.1$): f) $\lambda_{x1}=1, \lambda_{x2}=1$, g) $\lambda_{x1}=1, \lambda_{x2}=3$, h) $\lambda_{x1}=3, \lambda_{x2}=1$, i) $\lambda_{x1}=3, \lambda_{x2}=3$, j) $\lambda_{x1}=3, \lambda_{x2}=1, \delta=30^\circ$

The numerical calculations of the shear zone formation in a 2D random granular specimen will be continued for other boundary value problems. The choice of the representative samples will be governed by the Latin hypercube sampling method.

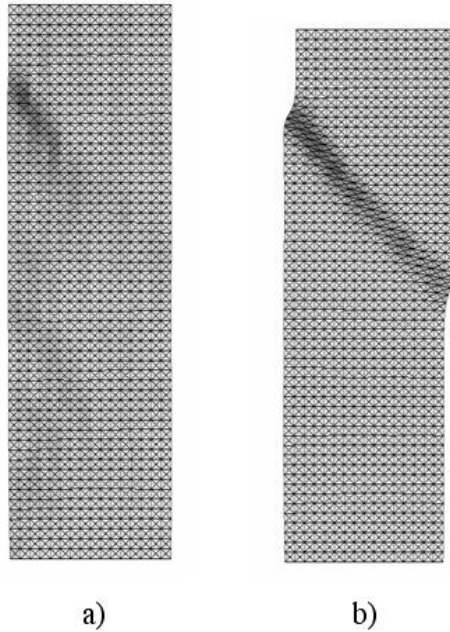


Fig. 7.9. FE-mesh with distribution of strain measure $\bar{\varepsilon} = \sqrt{\varepsilon_{ij}\varepsilon_{ij}}$ at different vertical deformation: a) $u_2^t/h_0=0.018$, b) $u_2^t/h_0=0.036$ ($\lambda_{x1}=1$, $\lambda_{x2}=3$, $s_d=0.1$)

References

1. Aifantis E (1984) On the microstructural origin of certain inelastic models. Trans. ASME J. Mat. Engng. Technol. 6:326-330
2. Bauer E (1996) Calibration of a comprehensive hypoplastic model for granular materials. Soils and Foundations, 36, 1:13-26
3. Bazant Z, Lin F, Pijaudier-Cabot G (1987) Yield limit degradation: non-local continuum model with local strain. In: Owen DRJ (ed) Proc. Int. Conf. Computational Plasticity, Barcelona, pp 1757-1780
4. Belytschko T, Chiang H, Plaskacz E (1994) High resolution two dimensional shear band computations: imperfections and mesh dependence. Com. Meth. Appl. Mech. Engng., 119:1-15

5. De Borst R, Mühlhaus HB (1992) Gradient dependent plasticity: formulation and algorithmic aspects. *Int. J. Numer. Methods Engng.* 35:521-539
6. De Borst R, Mühlhaus HB, Pamin J, Sluys L (1992) Computational modelling of localization of deformation. In: D. R. J. Owen DRJ, Onate H, Hinton e (eds) *Proc. of the 3rd Int. Conf. Comp. Plasticity*, Swansea, Pineridge Press, pp 483-508
7. Brinkgreve R (1994) Geomaterial models and numerical analysis of softening. Dissertation, Delft University, 1-153
8. Chambon R, Caillerie D, El Hassan N (1998) One-dimensional localization studied with a second grade model. *European Journal of Mechanics*, 17, 4:637-656
9. Desrues J, Chambon R, Mokni M, Mazerolle F (1996) Void ratio evolution inside shear bands in triaxial sand specimens studied by computed tomography. *Géotechnique* 46(3):529-546
10. Desrues J, Chambon R (1989) Shear band analysis for granular materials – the question of incremental linearity. *Ingenieur Archiv*, 59:187-196
11. Fenton GA, Griffiths DV (2002) Probabilistic foundation settlement on spatially random soil. *J. Geotech. Geoenvironment. Eng.* 128, 5:381-389
12. Gudehus G (1996) A comprehensive constitutive equation for granular materials. *Soils and Foundations*, 36, 1:1-12
13. Gudehus G, Nübel K (2004) Evolution of shear bands in sand. *Geotechnique* 54, 3:187-201
14. Gutierrez MA, de Borst R (1998) Energy dissipation, internal length scale and localization patterning – a probabilistic approach. In: Idelsohn, S, Onate E, Dvorkin, E (eds) *Computational Mechanics*, CIMNE, Barcelona, pp 1-9
15. Han C, Vardoulakis I (1991) Plane strain compression experiments on water saturated fine-grained sand. *Geotechnique* 41:49-78
16. Herle I, Gudehus G (1999) Determination of parameters of a hypoplastic constitutive model from grain properties. *Mechanics of Cohesive-Frictional Materials* 4,5:461-486
17. Kolymbas D (1977) A rate-dependent constitutive equation for soils. *Mech. Res. Comm.*, 6:367-372
18. Lade PV (1997) Elasto-plastic stress-strain theory for cohesionless soil with curved yield surfaces. *Int. J. Solid Structures* 13:1019-1035
19. Lanier J, Caillerie D, Chambon R (2004) A general formulation of hypoplasticity. *Int. J. Numer. Anal. Methods in Geomech.* 28, 15:1461-1478
20. Leśniewska D, Mróz Z (2003) Shear bands in soil deformation processes. In: Labuz J., Drescher A (eds) *Bifurcations and Instabilities in Geomechanics*, Swets and Zeitlinger, pp 109-119
21. Maier T (2002) Numerische Modellierung der Entfestigung im Rahmen der Hypoplastizität. PhD Thesis, University of Dortmund
22. Matthies H, Brenner CE, Bucher CG, Soares C (1997) Uncertainties in probabilistic numerical analysis of structures and solids – stochastic finite elements. *Structural Safety*, 19, 3:283-336

23. Mühlhaus HB (1989) Application of Cosserat theory in numerical solutions of limit load problems. *Ing. Arch.* 59:124-137
24. Niemunis A (2003) Extended hypoplastic models for soils. Habilitation Monography. Gdansk University of Technology
25. Niemunis A, Wichtmann T, Petryna Y, Triantafyllidis T (2005) Stochastic modeling of settlements due to cyclic loading for soil-structure interaction. *Proc. Int. Conf. Structural Damage and Lifetime Assessment, Rome*, pp 1-8
26. Nübel K, Karcher C (1998) FE simulations of granular material with a given frequency distribution of voids as initial condition. *Granular Matter*, 1, 3:105-112
27. Oda M, Konishi J, Nemat-Nasser S (1982) Experimental micromechanical evaluation of strength of granular materials, effects of particle rolling. *Mechanics of Materials, North-Holland Publishing Comp.* 1:269-283
28. Oda M (1993) Micro-fabric and couple stress in shear bands of granular materials. In: Thornton C (ed). *Powders and Grains, Rotterdam, Balkema*, pp 161-167
29. Pamin J (1994) Gradient dependent plasticity in numerical simulation of localisation phenomena. PhD Thesis, Delft University
30. Pasternak E, Mühlhaus H-B (2001) Cosserat continuum modelling of granulate materials. In: Valliappan S., Khalili, N (eds) *Computational Mechanics – New Frontiers for New Millennium, Elsevier Science*, pp 1189-1194
31. Pestana J M, Whittle AJ (1999) Formulation of a unified constitutive model for clays and sands. *Int. J. Num. Anal. Meth. Geomech.* 23:1215-1243
32. Przewlocki J, Gorski J (2001) Strip foundation on 2-D and 3-D random subsoil. *Probabilistic Engineering Mechanics*, 16:121-136
33. Shi Q, Chang CS (2003) Numerical analysis for the effect of heterogeneity on shear band formation. *Proc. 16th ASCE Engineering Mechanics Conference, University of Washington, Seattle*, pp 1-11
34. Sluys L (1992) Wave propagation, localisation and dispersion in softening solids. PhD Thesis, Delft University of Technology
35. Tatsuoka F, Siddiquee MS, Yoshida T, Park CS, Kamegai Y, Goto, Kohata SY (1994) Testing methods and results of element tests and testing conditions of plane strain model bearing capacity tests using air-dried dense Silver Buzzard Sand. Internal Report, University of Tokyo, pp 1-129
36. Tejchman J (2006) Effect of fluctuation of current void ratio on the shear zone formation in granular bodies within micro-polar hypoplasticity. *Computers and Geotechnics* 33, 1:29-46
37. Tejchman J (2004) Influence of a characteristic length on shear zone formation in hypoplasticity with different enhancements. *Computers and Geotechnics* 31, 8:595-611
38. Tejchman J (2005) Investigations of shear localization in granular bodies within an anisotropic micro-polar hypoplasticity. *Archives of Hydro-Engineering and Environmental Mechanics* 52, 4:85-102
39. Tejchman J (2002) Patterns of shear zones in granular materials within a polar hypoplastic continuum. *Acta Mechanica*, 155, 1-2, 71-95

40. Tejchman J (1989) Scherzonenbildung und Verspannungseffekte in Granulaten unter Berücksichtigung von Korndrehungen. Publication Series of the Institute of Soil and Rock Mechanics, University Karlsruhe 117
41. Tejchman J (2001) Shearing of an infinite narrow granular layer between two boundaries. In: Mühlhaus HB (ed) Bifurcation and Localisation Theory in Geomechanics, Swets and Zeitlinger, Lisse, pp 95-102
42. Tejchman J, Gudehus G (2001) Shearing of a narrow granular strip with polar quantities. *J. Num. and Anal. Methods in Geomechanics*, 25:1-28
43. Tejchman J, Wu W (1993) Numerical study on shear band patterning in a Cosserat continuum. *Acta Mechanica* 99:61-74
44. Walukiewicz H, Bielewicz E, Gorski J (1997) Simulation of nonhomogeneous random fields for structural applications. *Computers and Structures*, 64, 1-4:491-498
45. Wang CC (1970) A new representation theorem for isotropic functions. *J. Rat. Mech. Anal.* 36:166-223
46. Von Wolffersdorff, PA (1996) A hypoplastic relation for granular materials with a predefined limit state surface. *Mechanics Cohesive-Frictional Materials*, 1: 251-271
47. Wu W (1992) Hypoplastizität als mathematisches Modell zum mechanischen Verhalten granularer Stoffe. Publication Series of the Institute of Soil and Rock Mechanics, University Karlsruhe, 129
48. Vardoulakis I and Goldscheider M (1981) Biaxial apparatus for testing shear bands in soils. *Proc. 10th Conf. Soil Mech. Found. Engng.*, Stockholm, pp 819-824
49. Vardoulakis I (1980) Shear band inclination and shear modulus in biaxial tests. *Int. J. Num. Anal. Meth. Geomech.* 4:103-119
50. Vermeer P (1982) A five-constant model unifying well-established concepts. In: Gudehus G, Darve F, Vardoulakis I (eds) *Proc. Int. Workshop on Constitutive Relations for Soils*, Balkema, pp 175-197
51. Yoshida T, Tatsuoka F, Siddiquee MS (1994) Shear banding in sands observed in plane strain compression. In: R. Chambon, J. Desrues and I. Vardoulakis, editors. *Localisation and Bifurcation Theory for Soils and Rocks*. Balkema, Rotterdam, pp 165-181
52. Zervos E, Papanastasiou O, Vardoulakis I (2001) A finite element displacement formulation for gradient plasticity. *Int. J. Numer. Methods in Engineering*, 50:1369-1388

A Rational Approach to Stress-Dilatancy Modelling Using an Explicit Micromechanical Formulation

Peijun Guo¹ and Richard Wan²

¹Assistant Professor
Department of Civil Engineering
Mc Master University
Hamilton, ONT L8S 4L7,
Canada.

²Professor,
Civil Engineering Department,
University of Calgary,
2500 University Dr. NW,
Calgary, Alberta, T2N 1N4, Canada
E-mail: wan@ucalgary.ca
Phone: +1 (403) 220-5504
Fax: +1 (403) 282-7026

Summary

This paper presents a theoretical approach for deriving a stress-dilatancy formulation for granular materials. We first revisit Rowe's stress-dilatancy relation by investigating two-dimensional granular assemblies with various regular particle arrangements. It is found that the energy ratio during deformation varies with particle arrangements (or fabric) with its minimum value corresponding to a particular deformation state. As such, Rowe's stress-dilatancy equation is seen to be the lower bound of all possible dilatancy states the material can assume at various particle arrangements. Furthermore, we demonstrate that Rowe's hypothesis of minimum energy ratio can be lifted, if we work out rigorously the local sliding planes through micromechanical analysis. Such a micromechanical approach yields a more accurate description of the dilatancy behaviour of sand. More importantly, this new approach can be readily extended to describe the dilatancy behaviour of sand under general stress conditions.

1 Introduction

Shear induced volume change, or dilatancy, distinguishes granular materials from most of other engineering materials. The phenomenon of dilatancy was first revealed by Osborne Reynolds (1885) and has fascinated researchers over centuries with pioneering works from Caquot (1934), Taylor (1948), Newland and Alley (1957), Rowe (1962) and Horne (1965), to name a few. Dilatancy is important since any successful description of the stress/strain/strength behaviour of granular materials, particularly for dense sand, crucially depends on an appropriate account of accurate volumetric changes. It has been recognized physically that dilatancy is the manifestation of an internal kinematical constraint, involving both particle shape and particle arrangement with operative inter-particle friction, against applied stresses.

Early studies on dilatancy primarily focused on the increased shear strength due to dilatancy based on energy principles; *see*, for example, Taylor (1948), Newland and Alley (1957), Roscoe *et al.* (1963), and Schofield and Wroth (1968) among others. Based on a purely frictional deformation mechanism and the hypothesis of minimum energy ratio (work input to work output), Rowe (1962) related dilatancy to the principal stress ratio and developed a conceptual stress-dilatancy relation. However, even though Rowe recognized that dilatancy is due to an internal geometry constraint of granular particles with sliding occurring on a global plane different from local inter-granular contact planes, this notion of packing (fabric) is ultimately lost when making the hypothesis of minimum energy ratio. As such, there seems to be a contradiction in reasoning.

According to the modern theory of internally constrained continua, Goddard and Bashir (1990) argued that Reynolds dilatancy represents a kinematic constraint imposed by internal grain geometry during macroscopic deformations. As stated in Goddard (1999), “Reynolds dilatancy represents a strict kinematic coupling between shape and volume for assemblies of rigid particles, such that, in the limit of frictionless granules envisaged by Reynolds, the plastic yield locus is tantamount to a purely reactive (work-free) stress”. Stress-dilatancy relations have been developed along this line; *see*, e.g., Matsuoka (1974), Tokue (1979), Nemat-Nasser (1980), Houlsby (1993), and Goddard and Didwania (1998). The microstructure (fabric) of granular materials acts as an internal kinematic constraint against applied stresses, giving rise to volume dilation with a concomitant constraining stress (in particular, dissipative). Kanatani (1982) further argued that if this additional constraining stress is subtracted from the total effective stress, Drucker’s postulate may still apply. On the

other hand, the applied stress and interparticle friction control the force network developed at particle contacts. Hence, the connectivity of particles and grain geometry necessarily imply a kinematic constraint to global deformations. In other words, dilatancy has to be related to applied stress, interparticle friction as well as fabric, which in general is in agreement with the recent work of Collins and Muhunthan (2003). The latter demonstrated according to thermodynamics that, when internal constraint is defined as a deformation in which the applied pressure dissipates no energy, the dilation and friction angles can be related by Taylor's formula (Taylor, 1948).

The micromechanics of granular materials along with the discrete element method provide alternate approaches towards the development of dilatancy formulations. For example, based on a micromechanical analysis, Christoffersen *et al.* (1981) proposed a dilatancy formulation, which has almost the same features as Rowe's model. The notion of fabric, however, is lost in the final expression of the dilatancy formulation, even though it was developed by accounting for particle arrangement. Kruyt and Rothenburg (2004) showed that the rate of dilatancy can be uniquely determined from particle arrangement quantified by the distribution of contact normals, while the applied stress and interparticle friction are not explicitly involved. Obviously, dilatancy formulations of this type may not be easily incorporated into continuum constitutive models.

The above issues motivate the present paper, whose primary goal is to develop a new approach for describing stress-dilatancy of granular soils explicitly in terms of fabric by invoking a micromechanical analysis. The latter offers the possibility to express micro-parameters (inter-particle forces, relative displacements and rotations) to macro-parameters ("average" stresses and strains) through a so-called fabric tensor describing particle connectivity. By revisiting Rowe's stress-dilatancy formulation and investigating two-dimensional granular assemblies with various regular particle arrangements, we first explore the variation of energy ratio during deformation with respect to particle arrangements (or fabric) to examine Rowe's hypothesis of minimum energy ratio. Then, we demonstrate that the hypothesis of minimum energy ratio can be lifted, if we work out rigorously the local sliding planes through micromechanical analysis. As such, the resulting micromechanically based approach yields a more accurate description of the dilatancy behaviour of sand. Finally, the dilatancy formulation derived from the new approach is simplified so that it can be easily implemented into an elasto-plasticity model via a flow rule. More importantly, this new approach can be readily extended to describe the dilatancy behaviour of sand under general stress conditions.

2 Rowe's Stress-Dilatancy Formulation Revisited

As a prelude we recall various experimental observations that highlight the roles of dilatancy and fabric on the shear strength of a granular material.

Considering a biaxial compression stress state with the principal effective stresses $\sigma_1 > \sigma_2 > 0$, Rowe (1962) showed that the ratio between the incremental plastic work due to the principal stresses could be expressed as

$$E = -\frac{\sigma_1 \dot{\epsilon}_1^p}{\sigma_2 \dot{\epsilon}_2^p} = \frac{\tan(\varphi_\mu + \beta)}{\tan \beta} \quad (2.1)$$

where $\dot{\epsilon}_1^p$ and $\dot{\epsilon}_2^p$ = major and minor plastic strain increment, respectively; φ_μ = interparticle friction angle; and β = angle of inclination of the grain-to-grain sliding contact plane with the direction of σ_1 . Rowe showed that when $\beta = \pi/4 - \varphi_\mu/2$, the work increment ratio E reaches its minimum, yielding

$$-\frac{\sigma_1 \dot{\epsilon}_1^p}{\sigma_2 \dot{\epsilon}_2^p} = \tan^2 \left(\frac{\pi}{4} + \frac{\varphi_\mu}{2} \right) \quad (2.2)$$

When defining the angle of dilation ψ as

$$\sin \psi = -\frac{\dot{\epsilon}_v^p}{\dot{\gamma}^p} = -\frac{\dot{\epsilon}_1^p + \dot{\epsilon}_2^p}{\dot{\epsilon}_1^p - \dot{\epsilon}_2^p} \quad (2.3)$$

and invoking the mobilized friction angle φ_m via Mohr-Coulomb criterion such that $\sin \varphi_m = (\sigma_1 - \sigma_2)/(\sigma_1 + \sigma_2)$, Eq. (2.2) becomes

$$\sin \psi = \frac{\sin \varphi_m - \sin \varphi_\mu}{1 - \sin \varphi_m \sin \varphi_\mu} \quad (2.4)$$

In order to accommodate for the behaviour of both loose and dense sand, and to account for the influence of sliding, rolling and rearrangement of particles, Rowe suggested using the critical state friction angle φ_{cv} to replace φ_μ in Eq. (2.4). Even though Eq. (2.1) is based on recognizing that dilatancy is due to an internal geometry constraint of granular particles with sliding occurring on a global plane different from local inter-granular contact planes, when making the hypothesis of minimum energy ratio, the notion of packing (fabric) is ultimately lost in Eqs. (2.2) and (2.4).

The principles involved in Rowe's stress-dilatancy theory were more rigorously substantiated by Horne (1965), who showed that, for triaxial

compression, the geometrical anisotropy could be characterized by the ratio between m_1 and m_3 that are the numbers of contacts at incipient slip in the direction of σ_1 and σ_3 respectively. Horne further argued that the principal stress ratio σ_1/σ_3 and the corresponding strain increment ratio can both be related to changes of geometrical anisotropy such that

$$\frac{\sigma_1}{\sigma_3} = \frac{4m_1}{\pi m_3} \tan\left(\frac{\pi}{4} + \frac{\varphi_\mu}{2}\right); \quad \frac{\dot{\epsilon}_1}{\dot{\epsilon}_3} = -\frac{2m_1}{\pi m_3} \tan\left(\frac{\pi}{4} - \frac{\varphi_\mu}{2}\right) \quad (2.5)$$

These relations result in a stress-dilatancy equation

$$-\frac{\sigma_1 \dot{\epsilon}_1}{2\sigma_3 \dot{\epsilon}_3} = \tan^2\left(\frac{\pi}{4} + \frac{\varphi_\mu}{2}\right) \quad (2.6)$$

which is identical to Rowe's stress-dilatancy formulation for triaxial stress conditions. It should be noted that Horne's approach provided a conceptual method to describe the relation between dilatancy of granular materials and anisotropy, which is assumed to be a cross-anisotropy under axisymmetric stress conditions.

Oda (1972) introduced a fabric parameter S based on the directional distribution of contact normal to account for the effect of fabric on strength and dilatancy behaviour of sand. He demonstrated that, for triaxial compression, the principal stress and strain increment ratios can be related to S in the principal stress directions through

$$\frac{\sigma_1}{\sigma_3} = k_1 \frac{S_z}{S_x} + k_2; \quad -\frac{\dot{\epsilon}_v}{\dot{\epsilon}_1} = k_3 \frac{S_z}{S_x} + k_4 \quad (2.7)$$

which yields a stress-dilatancy formulation in the form of

$$\frac{\sigma_1}{\sigma_3} = k_5 \frac{\dot{\epsilon}_v}{\dot{\epsilon}_1} + k_6 \quad (2.8)$$

where $\dot{\epsilon}_v$ is the volumetric strain increment, k_1 through k_6 are constants, while S_z and S_x , which are the components of S in the direction of σ_1 and σ_3 respectively, can be regarded as the projected area of contacts in the directions of σ_1 and σ_3 with the ratio S_z/S_x reflecting the fabric characteristics of granular materials.

In general, approaches proposed by Horne (1965) and Oda (1972) are more rigorous than Rowe's method. However, the resulting stress-dilatancy relations given in Eqs. (2.6) and (2.8) still do not explicitly include the influence of fabric. In other words, all these dilatancy formations, in

which the notion of packing (fabric) is lost, imply that the rate of dilation only depends on the applied stress ratio, which is inconsistent with numerous experimental results (e.g., Miyamori 1976, Tokue 1979, Miura and Toki 1984, and Nakai 1987). As a result, it is necessary to re-examine the effect of fabric on dilatancy of granular materials.

3 Effect of Fabric on Stress-Dilatancy Relations

3.1 Simple Cases: Regular Packing

Let us consider three packings of monodisperse and polydisperse rigid granular materials, as illustrated in Fig. 3.1. For all of these regular packings subjected to uniformly distributed stress σ_1 and σ_2 , the ratio of external forces and incremental displacements in the vertical and horizontal directions can be found from an equilibrium and kinematic analysis as

$$\frac{F_v}{F_h} = \frac{\sin \beta + \mu \cos \beta}{\sin \beta - \mu \cos \beta} = \tan(\varphi_\mu + \beta) \quad (3.1)$$

$$\frac{\dot{u}_v}{\dot{u}_h} = -\cot \beta \quad (3.2)$$

where β is the inclination angle of contact normals, or the angle between the sliding plane and the direction of major principal stress σ_1 , and $\mu = \tan \varphi_\mu$ with φ_μ being the interparticle friction angle. By means of Eqs. (3.1) and (3.2), the work increment ratio can be expressed as

$$E = -\frac{F_v \dot{u}_v}{F_h \dot{u}_h} = -\frac{\sigma_1 \dot{\epsilon}_1^p}{\sigma_2 \dot{\epsilon}_2^p} = \frac{\tan(\varphi_\mu + \beta)}{\tan \beta} \quad (3.3)$$

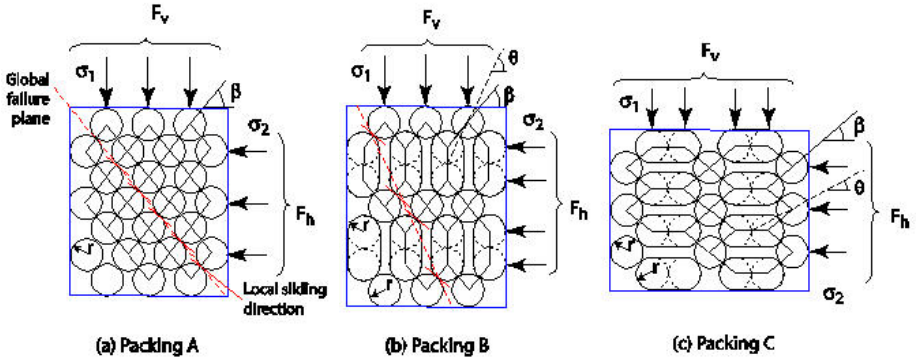


Fig. 3.1. Typical regular packings for 2D granular particles

which leads to the following stress-dilatancy relation

$$\frac{\sigma_1}{\sigma_2} = \frac{\tan(\varphi_\mu + \beta)}{\tan \beta} \left(-\frac{\dot{\epsilon}_2^p}{\dot{\epsilon}_1^p} \right) \quad (3.4)$$

One observes that Eq. (3.3) is identical to Rowe's work increment ratio given in Eq. (2.1). Referring to Fig. 1, the angle β , which has a clear physical meaning, reflects the mode of particle arrangement (or fabric) and varies with deformation or the applied stresses. Moreover, β does not have to take the value of $\beta = \pi/4 - \varphi_\mu/2$ as derived from Rowe's minimum energy ratio hypothesis.

The variation of work increment ratio E during deformation can be determined as follows. For all of the three cases shown in Fig. 1, the principal stress ratios can be derived from equilibrium conditions as

$$\frac{\sigma_1}{\sigma_2} = \frac{F_v/(4r \cos \beta)}{F_h/(4r \sin \beta)} = \tan(\varphi_\mu + \beta) \tan \beta \quad \text{for Packing A} \quad (3.5)$$

$$\frac{\sigma_1}{\sigma_2} = \frac{F_v/(4r \cos \beta)}{F_h/(2r + 4r \sin \beta)} = \tan(\varphi_\mu + \beta) \frac{1 + 2 \sin \beta}{2 \cos \beta} \quad \text{for Packing B} \quad (3.6)$$

$$\frac{\sigma_1}{\sigma_2} = \frac{F_v/(2r + 4r \cos \beta)}{F_h/(4r \sin \beta)} = \tan(\varphi_\mu + \beta) \frac{2 \sin \beta}{1 + 2 \cos \beta} \quad \text{for Packing C} \quad (3.7)$$

respectively. Herein r is defined in Fig. 3.1 to characterize the size of individual grains. The corresponding incremental plastic strain ratios are readily obtained from the stress-dilatancy relation given in Eq. (3.4):

$$\frac{\dot{\varepsilon}_1^p}{\dot{\varepsilon}_2^p} = \begin{cases} -\cot^2 \beta & \text{for Packing A} \\ -\frac{2 \cos \beta}{(1 + 2 \sin \beta) \tan \beta} & \text{for Packing B} \\ -\frac{1 + 2 \cos \beta}{2 \sin \beta \tan \beta} & \text{for Packing C} \end{cases} \quad (3.8)$$

which are identical to those derived by considering the kinematic constraints and connectivity of particles during deformation. For any given value of β , one can determine the stress ratio and work increment ratio, and hence the variation of E with respect to σ_1/σ_2 , as shown in Fig. 3.2 plotted for $\varphi_\mu = 20^\circ$. One observes that the energy ratio E changes in the course of deformation and reaches the same minimum value $E_{\min} = \tan^2(\pi/4 + \varphi_\mu/2)$ at a particular deformation state (stress ratio) for each case; see Fig. 2a. In contrast, Rowe's major assumption was that at any given time during deformation, the energy ratio is the minimum, regardless of the packing. The dilatancy plots for Packing A, B and C shown in Fig. 3.22b further confirm that the dilatancy characteristics of granular materials may deviate substantially from Rowe's equation. The closest agreement with Rowe's equation seems to be Packing B for which the energy ratio changes moderately during deformation, as shown in Fig. 3.2a.

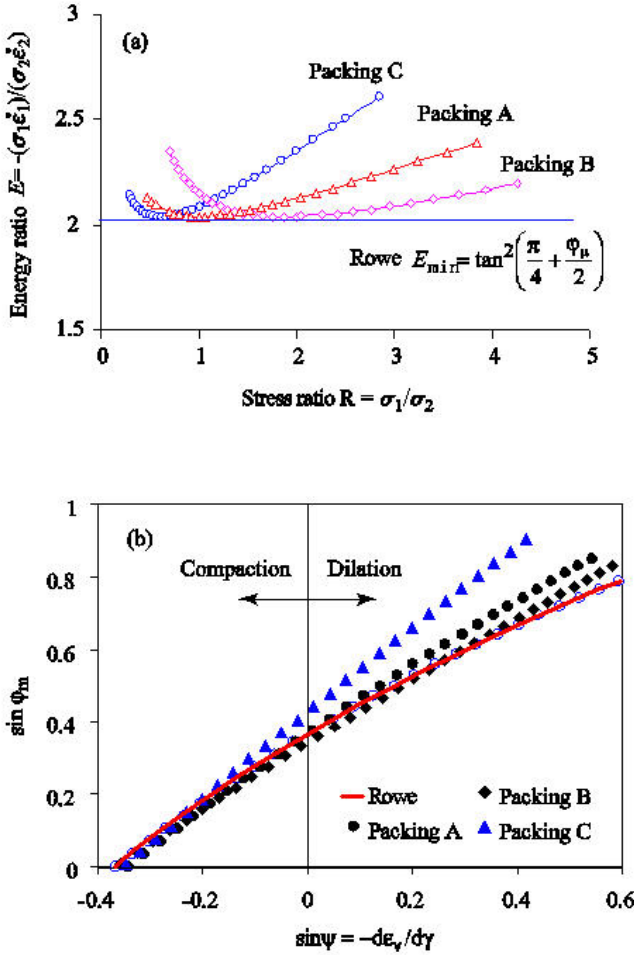


Fig. 3.2(a) Energy ratio and (b) dilatancy characteristics of granular assemblies with regular packing

It should be noted that the deformation of the regular granulate packings shown in Fig. 3.1 might be unstable in biaxial compression, since axial compression of each packing reduces the angle β , which in turn requires a decrease in the principal stress ratio σ_1 / σ_2 according to Eqs. (3.5) to (3.7). Fig. 3.3 presents the variation of σ_1 / σ_2 with angle β and axial strain for Packings A and B. For a given initial value of β , before Eq. (3.5) is

satisfied, the initial increase of σ_1/σ_2 does not induce any deformation of the granular assembly. Once sliding is triggered, the stress ratio σ_1/σ_2 decreases with axial strains as a result of variation in angle β during deformation as illustrated in Fig. 3.3.

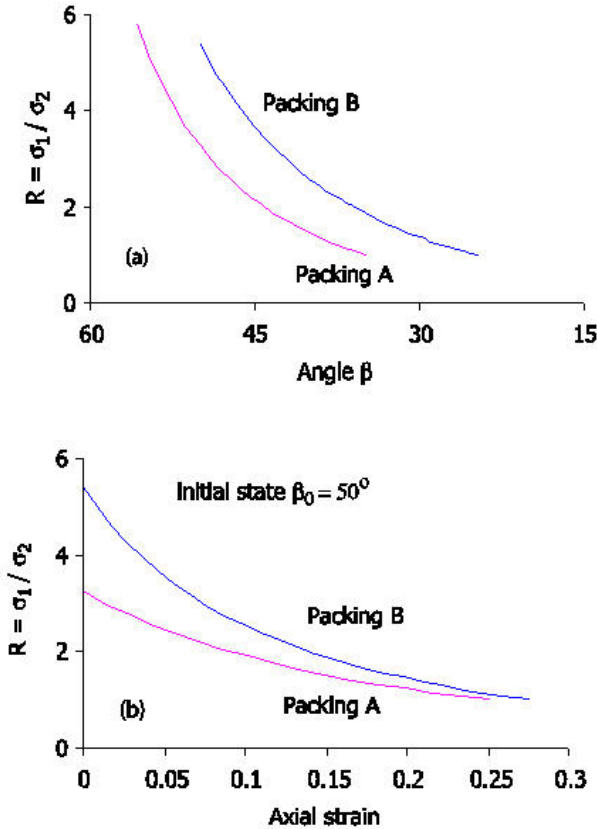


Fig. 3.3. Unstable deformation for regular packings A and B

For the random packing of granular particles that will be discussed in the following section, stable deformation is expected. Since β for any contact particles varies between -90° and 90° in a random packing of particles, sliding may first take place at contacts of large β angles. The number of sliding contacts, however, may only be a small fraction of the total. Moreover, the rearrangement of sliding particles tends to produce more

stable structures, resulting in an increase in the vertical stress with continuing deformation.

3.2 Random Packing

Now let us extend the above analysis meant for regular packing to granular assemblies of random packing shown in Fig. 3.4. Assume that global failure takes place on plane ab , while local sliding occurs along a zigzag slide path with the mean sliding direction making an angle $\bar{\beta}$ relative to the direction of major principle stress σ_1 (i.e., the vertical direction). On a segment AB in the mean sliding direction, however, individual particles may move in different directions (as shown in Figs. 3.4b and c). For any two particles at a sliding contact k on AB , given the angle $\beta^{(k)}$ that defines the orientation of local contact plane, the vertical and horizontal components of the contact force at k are related by

$$f_v^{(k)} = f_h^{(k)} \tan(\varphi_\mu + \beta^{(k)}) \quad (3.9)$$

The ratio between the vertical and horizontal components of the total force on ab is then

$$\frac{F_v}{F_h} = \frac{\sum f_v^{(k)}}{\sum f_h^{(k)}} = \frac{\sum f_h^{(k)} \tan(\varphi_\mu + \beta^{(k)})}{\sum f_h^{(k)}} = \frac{\sum (f_h + \tilde{f}_h^{(k)}) \tan(\varphi_\mu + \bar{\beta} + \tilde{\beta}^{(k)})}{\sum (f_h + \tilde{f}_h^{(k)})} \quad (3.10)$$

where $\bar{\beta}$ and f_h are the average values of the contact angle and the horizontal contact force component, with $\tilde{\beta}^{(k)}$ and $\tilde{f}_h^{(k)}$ being the local fluctuations at contact k . When $\tilde{\beta}^{(k)}$ varying over a limited range, Eq. (3.10) may be approximated to

$$\frac{F_v}{F_h} \approx \tan(\varphi_\mu + \bar{\beta}) + \frac{[1 + \tan^2(\varphi_\mu + \bar{\beta})] \sum \tilde{f}_h^{(k)} \tan \tilde{\beta}^{(k)} + \tan(\varphi_\mu + \bar{\beta}) \sum \tilde{f}_h^{(k)} \tan^2 \tilde{\beta}^{(k)}}{\sum f_h^{(k)}} \quad (3.11)$$

which may be further simplified as

$$\frac{F_v}{F_h} \approx \tan(\varphi_f + \bar{\beta}) \quad (3.12)$$

where φ_f , which is different from the interparticle friction angle φ_μ , should be considered as an equivalent friction angle in terms of the normal and tangential forces along the mean sliding direction AB . By applying the same reasoning to the kinematical analysis, one obtains the relation

between incremental displacements in the horizontal and vertical directions:

$$\frac{\dot{u}_h}{\dot{u}_v} \approx -\tan \bar{\beta} \tag{3.13}$$

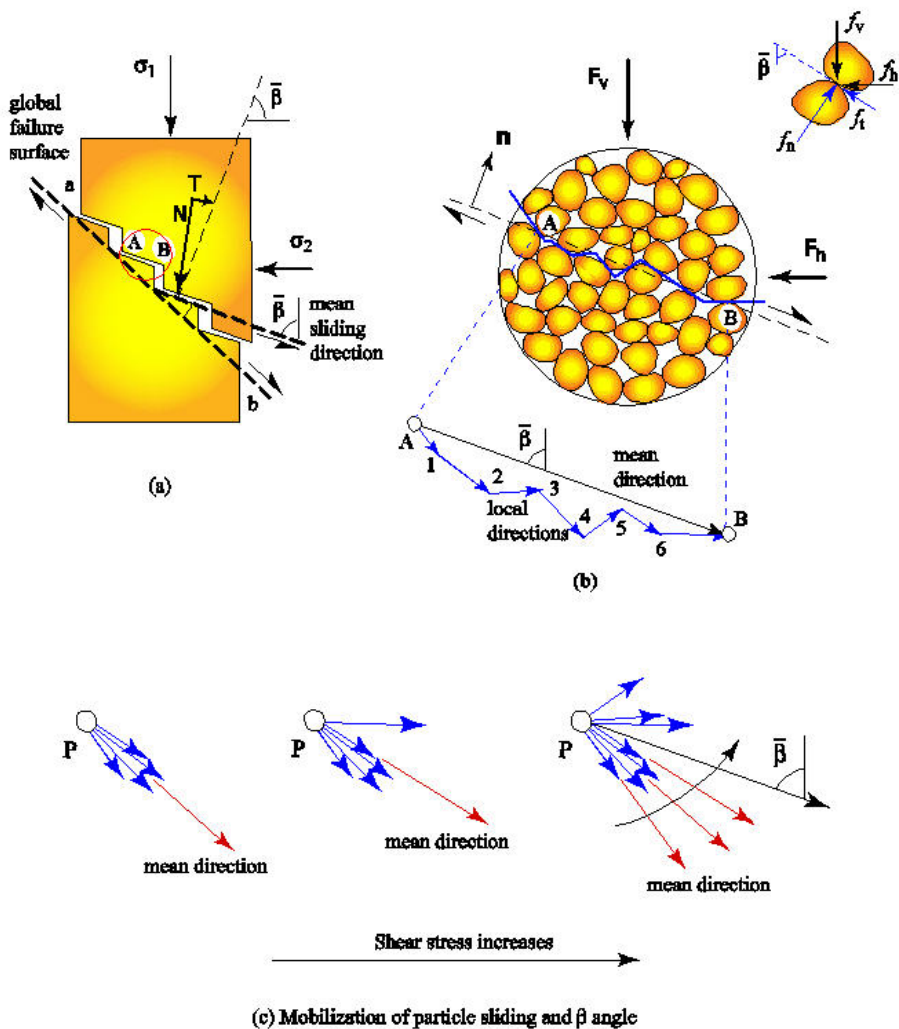


Fig. 3.4. Granular assembly for a random packing

Eqs. (3.12) and (3.13) yield the energy ratio

$$E = -\frac{\sigma_1 \dot{\epsilon}_1^p}{\sigma_2 \dot{\epsilon}_2^p} = -\frac{F_v \dot{u}_v}{F_h \dot{u}_h} \square \frac{\tan(\varphi_f + \bar{\beta})}{\tan \bar{\beta}} \quad (3.14)$$

It follows that

$$\frac{\sigma_1}{\sigma_2} = \frac{\tan(\varphi_f + \bar{\beta})}{\tan \bar{\beta}} \left(-\frac{\dot{\epsilon}_2^p}{\dot{\epsilon}_1^p} \right) \quad (3.15)$$

Eq. (3.15) takes the same form as Eq. (3.3), given that $\bar{\beta}$ represents the angle between the average particle sliding direction and the major principal stress σ_1 . One may conclude that Eq. (3.15) can be regarded as a general expression of stress-dilatancy relation for granular materials, however, $\bar{\beta}$ and φ_f are yet to be determined. As illustrated in Fig. 3.4c, the mean sliding direction $\bar{\beta}$ varies with mobilization of particle sliding or the increase of shear stresses. In other words, $\beta = \pi/4 - \varphi_\mu/2$, a condition required by the minimum energy ratio hypothesis in Rowe's dilatancy formulation is not a necessary condition for dilation to occur. Consequently, the minimum energy ratio hypothesis may be lifted.

In the following sections, an alternative approach for the determination of $\bar{\beta}$ is proposed based on micromechanical analysis to incorporate microstructural aspects into the formulation of stress-dilatancy relations.

4 Stress-Dilatancy Formulation with Micromechanical Considerations

4.1 Stress-Dilatancy Formulation: Generalities

According to the micromechanics of granular materials, for a representative elementary volume (REV), micro-variables can be averaged and expressed in terms of macro-variables and *vice versa*. Fig. 4.1 shows a cluster of rigid particles chosen in a REV with particle connectivity represented by a graph of branch vectors l that connect the gravity centres of contacting particles. As a result of volume averaging, Cauchy stress, σ , can be determined from contact forces f between particles and the local branch vector l via

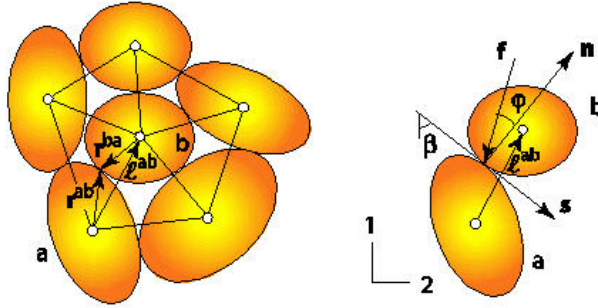


Fig. 4.1. Granular assembly in REV and graph representation of contact topology

$$\sigma_{ij} = \frac{1}{V} \sum f_i l_j \tag{4.1}$$

A so-called fabric tensor, F , that describes the geometrical arrangement of particles, can be essentially represented by a second order tensor formed of the dyadic product of local branch vectors such as

$$F_{ij} = \frac{1}{V} \sum l_i l_j = \frac{N_0}{N} \sum l_i l_j \tag{4.2}$$

where N_0 is the number of contacts per unit volume and $N = N_0 V$ is the total number of contacts in volume V . Via a so-called "localization" operation (Emeriault and Chang 1997) that is opposite to averaging, the contact forces f_i between particles can be expressed in terms of Cauchy stress, σ , and the fabric tensor, F , as

$$f_i = \sigma_{ij} F_{jm}^{-1} l_m \tag{4.3}$$

Details can be found in Guo (2000), Emeriault and Chang (1997) and Chang and Ma (1991) among others.

For a granular assembly of random packing with a given interparticle friction angle φ_μ , the tangential and normal components of contact forces, T and N , satisfy $T \leq N \tan \varphi_\mu$. Sliding only occurs at a fraction of contacts at which T reaches the maximum

$$T = N \tan \varphi_\mu \tag{4.4}$$

For a contact with contact normal \mathbf{n} , N and T can be computed from

$$N = -f_i n_i = -\sigma_{ij} F_{jm}^{-1} l_m n_i; \quad T = f_i s_i = \sigma_{ij} F_{jm}^{-1} l_m s_i \quad (4.5)$$

with s being the tangent of the contact plane. It should be noted that s and n are both unit vectors with

$$s_i n_i = 0, \quad s_i s_i = 1, \quad n_i n_i = 1 \quad (4.6)$$

Consequently, the direction of local sliding planes can be determined from

$$\frac{T}{N} = -\frac{\sigma_{ij} F_{jm}^{-1} l_m s_i}{\sigma_{ij} F_{jm}^{-1} l_m n_i} = \tan \varphi_\mu \quad (4.7)$$

Introducing the Lagrangian formulation for constraints in Eq. (4.6), Eq. (4.7) may be more generally expressed as the *minimization* of

$$\Delta = \left(\sigma_{ij} F_{jm}^{-1} l_m s_i + \mu \sigma_{ij} F_{jm}^{-1} l_m n_i \right)^2 + \lambda_1 (n_i n_i - 1) + \lambda_2 (s_i s_i - 1) + \lambda_3 n_i s_i \quad (4.8)$$

in which λ_1 , λ_2 and λ_3 are the Lagrangian multipliers. The stationary conditions of Δ with respect to λ 's recover constraint conditions (4.6), whereas the stationary conditions with respect to n_i and s_i yield

$$\frac{\partial \Delta}{\partial n_k} = 2 \left(\sigma_{ij} F_{jm}^{-1} l_m s_i + \mu \sigma_{ij} F_{jm}^{-1} l_m n_i \right) \left(\sigma_{ij} F_{jm}^{-1} s_i \frac{\partial l_m}{\partial n_k} + \mu \sigma_{ij} F_{jm}^{-1} n_i \frac{\partial l_m}{\partial n_k} + \mu \sigma_{kj} F_{jm}^{-1} l_m \right) + 2\lambda_1 n_k + \lambda_3 s_k = 0 \quad (4.9)$$

and

$$\frac{\partial \Delta}{\partial s_k} = 2 \left(\sigma_{ij} F_{jm}^{-1} l_m s_i + \mu \sigma_{ij} F_{jm}^{-1} l_m n_i \right) \left(\sigma_{kj} F_{jm}^{-1} n_m \right) + 2\lambda_2 s_k + \lambda_3 n_k = 0 \quad (4.10)$$

which with Eq. (4.6) provide a set of equations that can be solved for the Lagrangian multipliers as well as the directions n_i and s_i . It should be noted that n_i and s_i represent the directions of critical contacts at which sliding is just triggered by the current stress σ_{ij} , with particles mobilized previously continuing to slide (as illustrated in Fig. 3.4). For a random packing with the contact normal distribution described by a density function $p(\mathbf{n})$, the normal of the average sliding direction can be expressed as

$$\bar{\mathbf{n}}_s = \int_{\Omega_s} p(\mathbf{n}) \mathbf{n}_s d\Omega \quad (4.11)$$

with \mathbf{n}_s being the normal of a sliding contact and Ω_s the domain in which sliding takes place. Referring to Fig. 3.4, the inclination angle $\bar{\beta}$ of the average sliding plane can be readily obtained from $\bar{\mathbf{n}}_s$.

It is noted from Eqs. (4.8) to (4.10) that the distributions of both the contact normal and branch vectors are required to determine the average sliding direction or $\bar{\beta}$. However, since the directions of the branch vector \mathbf{l} and the contact normal \mathbf{n} at a contact may be different, particularly for non-spherical particles (as illustrated in Fig. 4.2), the density functions describing the directional distribution of \mathbf{l} and \mathbf{n} are generally required. Alternatively, one may decompose the branch vector \mathbf{l} in the directions of \mathbf{n} and \mathbf{s} ; i.e.,

$$\mathbf{l} = \mathbf{l}^{(n)} + \mathbf{l}^{(s)} = l^{(n)}\mathbf{n} + l^{(s)}\mathbf{s} \tag{4.12}$$

with $l^{(n)}$ and $l^{(s)}$ being the length of branch vector projected in the directions of \mathbf{n} and \mathbf{s} , respectively (see Fig. 6). By introducing the ratio of $l^{(s)}$ and $l^{(n)}$ associated to a contact normal \mathbf{n}

$$\tilde{n}(\mathbf{n}) = \frac{l^{(s)}}{l^{(n)}} \tag{4.13}$$

the corresponding expressions for contact forces become

$$N = -\sigma_{ij}F_{jm}^{-1}l^{(n)}(n_m + \tilde{n}s_m)n_i, \quad T = \sigma_{ij}F_{jm}^{-1}l^{(n)}(n_m + \tilde{n}s_m)s_i \tag{4.14}$$

As can be seen, whether sliding takes place at a contact is determined by not only the applied stresses and the contact normal, but the non-coaxiality between the branch vector \mathbf{l} and the contact normal \mathbf{n} .

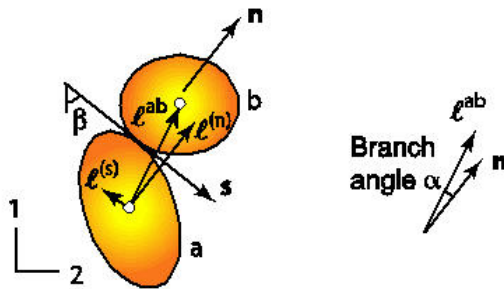


Fig. 4.2. Decomposition of a branch vector

As a special case, the procedure described above can be simplified for a regular packing of spherical particles with a single size, such as packing A in Fig. 3.1a. In this case, the length of branch vector is constant and the

direction of a branch vector is identical to the contact normal at any contact point; i.e., $\mathbf{l} = \bar{\mathbf{l}} \mathbf{n}$. As a result, Eq. (4.14) is simplified into

$$\mathbf{N} = -f_i \mathbf{n}_i = -\bar{\mathbf{l}} \sigma_{ij} F_{jm}^{-1} \mathbf{n}_m \mathbf{n}_i; \quad \mathbf{T} = f_i \mathbf{s}_i = \bar{\mathbf{l}} \sigma_{ij} F_{jm}^{-1} \mathbf{n}_m \mathbf{s}_i \quad (4.15)$$

The stationary conditions in Eqs. (4.9) and (4.10) become

$$\frac{\partial \Delta}{\partial n_k} = 2(\sigma_{ij} F_{jm}^{-1} \mathbf{n}_m \mathbf{s}_i + \mu \sigma_{ij} F_{jm}^{-1} \mathbf{n}_m \mathbf{n}_i) (\sigma_{ij} F_{jk}^{-1} \mathbf{s}_i + \mu \sigma_{ij} F_{jk}^{-1} \mathbf{n}_i + \mu \sigma_{kj} F_{jm}^{-1} \mathbf{n}_m) + 2\lambda_1 n_k + \lambda_3 s_k = 0 \quad (4.16)$$

$$\frac{\partial \Delta}{\partial s_k} = 2(\sigma_{ij} F_{jm}^{-1} \mathbf{n}_m \mathbf{s}_i + \mu \sigma_{ij} F_{jm}^{-1} \mathbf{n}_m \mathbf{n}_i) (\sigma_{kj} F_{jm}^{-1} \mathbf{n}_m) + 2\lambda_2 s_k + \lambda_3 n_k = 0 \quad (4.17)$$

It should be noted that for this regular packing, sliding occurs in the same direction at all sliding contacts; i.e. $\bar{\mathbf{n}} = \mathbf{n}$.

4.2 Nominal Friction Angle φ_f on Sliding Plane and Critical State Friction Angle φ_{cv}

After the mean sliding direction is determined, the nominal friction angle φ_f on the average sliding plane is still required to complete the stress-dilatancy formulation. For any regular packing given in Fig. 3.1, it can be shown $\varphi_f = \varphi_\mu$ since sliding occurs in the same direction at all sliding contacts. For a random packing of particles, however, the nominal friction angle φ_f along the mean sliding plane varies with the progressive mobilization of sliding particles. Referring to Eq. (3.12) and Fig. 3.4, φ_f by definition can be calculated from

$$\bar{\mu} = \tan \varphi_f = \frac{T}{N} = -\frac{\sum (f_j^{(k)} n_j^{(k)} \tan \varphi_\mu s_i^{(k)}) (\bar{s}_i)}{\sum (f_m^{(k)} n_m^{(k)} n_i^{(k)}) (\bar{n}_i)} = -\frac{\sigma_{jp} F_{pq}^{-1} \sum (l_q^{(k)} n_j^{(k)} s_i^{(k)}) (\bar{s}_i)}{\sigma_{ms} F_{st}^{-1} \sum (l_i^{(k)} n_m^{(k)} n_i^{(k)}) (\bar{n}_i)} \tan \varphi_\mu \quad (4.18)$$

where T and N are the tangential and normal components of the total contact force on the average sliding plane. By taking into account the directional distribution of contact normals using the density function $p(\mathbf{n})$, Eq. (4.18) may be rewritten as

$$\bar{\mu} = \tan \varphi_f = \frac{\sigma_{jp} F_{pq}^{-1} \bar{s}_i \int_{\Omega_s} p(\mathbf{n}) l_q n_j s_i d\Omega}{\sigma_{ms} F_{st}^{-1} \bar{n}_l \int_{\Omega_s} p(\mathbf{n}) l_l n_m n_l d\Omega} \tan \varphi_\mu \quad (4.19)$$

where Ω_s is the domain in which sliding takes place (see Fig. 3.4c) and it has been determined based on the local sliding criterion as discussed in the

previous section. One observes from Eq. (4.19) that φ_f , which is a function of fabric and the applied stresses, tends to vary with the mobilization of sliding among particles. When sliding occurs at all contacts in the same direction, $\bar{\mu} = \tan \varphi_\mu$ is recovered from Eq. (4.19).

It should be noted that when an equivalent friction angle $\bar{\varphi}_f$ is defined such that

$$K^* = \tan^2 \left(\frac{\pi}{4} + \frac{\bar{\varphi}_f}{2} \right) = \frac{\tan(\varphi_f + \bar{\beta})}{\tan \bar{\beta}} \quad (4.20)$$

the dilatancy formulation in Eq. (3.15) takes the same form as Rowe's equation in Eq. (2.2) with the interparticle friction angle φ_μ being replaced by $\bar{\varphi}_f$.

5 Verification

This section verifies the new approach for the derivation of dilatancy formulation for granular assemblies of regular packing as shown in Fig. 3.1. The procedure to find the orientation of local sliding plane can be significantly simplified as follows.

According to Eq. (4.2), the fabric tensor and its inverse for packing A are

$$F_{ij} = N_0 \begin{bmatrix} \sin^2 \beta & 0 \\ 0 & \cos^2 \beta \end{bmatrix}; F_{ij}^{-1} = \frac{1}{N_0 \sin^2 \beta \cos^2 \beta} \begin{bmatrix} \cos^2 \beta & 0 \\ 0 & \sin^2 \beta \end{bmatrix} \quad (5.1)$$

where $N_0 = N/V$ is the number of contact in a unit volume of the specimen, β is the inclination angle of the contact normal, which is the same as the associated branch vector. The components of the contact force at a given contact according to Eqs. (4.3) and (4.5) are

$$f_1 = \sigma_1 F_{11}^{-1} \sin \beta; f_2 = \sigma_{22} F_{22}^{-1} \cos \beta \quad (5.2)$$

$$N = f_1 \sin \beta + f_2 \cos \beta, T = f_1 \cos \beta - f_2 \sin \beta \quad (5.3)$$

When applying the sliding criterion given in Eq. (4.7), one has

$$\tan(\varphi_\mu + \beta) = \frac{\sum \sigma_1 F_{11}^{-1} l_1}{\sum \sigma_2 F_{22}^{-1} l_2} = \frac{\sigma_1}{\sigma_2} \frac{1}{\tan \beta} \quad (5.4)$$

The stress-dilatancy formulation in Eq. (3.15) yields the strain increment ratio as

$$\frac{\dot{\epsilon}_1^p}{\dot{\epsilon}_2^p} = -\frac{1}{\tan^2 \beta} \quad (5.5)$$

which is identical to the first equation of Eq. (3.8).

For the particle assembly of Packing B shown in Fig. 3.1(b), the directions of the contact normal and the branch vectors are different, with the inclination angles being β and θ , respectively. Given the fabric tensor and its inverse

$$F_{ij} = N_0 \begin{bmatrix} \sin^2 \theta & 0 \\ 0 & \cos^2 \theta \end{bmatrix}; F_{ij}^{-1} = \frac{1}{N_0 \sin^2 \theta \cos^2 \theta} \begin{bmatrix} \cos^2 \theta & 0 \\ 0 & \sin^2 \theta \end{bmatrix} \quad (5.6)$$

with β and θ being related by

$$\tan \theta = \frac{1 + 2 \sin \beta}{2 \cos \beta} \quad (5.7)$$

the sliding condition for this case is expressed as

$$\tan(\varphi_\mu + \beta) = \frac{\sum \sigma_{11} F_{11}^{-1} l_1}{\sum \sigma_{22} F_{22}^{-1} l_2} = \frac{\sigma_1}{\sigma_2} \frac{2 \cos \beta}{1 + 2 \sin \beta} \quad (5.8)$$

When applying the stress-dilatancy formulation to Eq. (3.15), the second equation of Eq. (3.8) is recovered.

By drawing a parallel to Packings A and B, it can be shown that the combination of the sliding criterion and the stress-dilatancy formulation in Eq. (3.15) also recovers, for Packing C, the strain increment ratio given in the last equation of Eq. (3.8).

6 Simplified Procedure and Modified Rowe's Stress-Dilatancy Relation

Even though the fundamentals for the derivation of dilatancy formulation are given in Section 4 already, including the determination of the mean sliding direction $\bar{\beta}$ and the nominal friction angle φ_f , the resulting dilatancy equation is not given in an explicit form. This section discusses a simplified procedure to obtain an easy to implement stress-dilatancy formulation.

6.1 Mean Sliding Direction and Nominal Friction Angle φ_f

It is expected that sliding does not occur at a contact k with the mobilized coefficient of friction $\mu_{mob}^{(k)} = T^{(k)}/N^{(k)} < \mu$. According to Eq. (4.5), $\mu_{mob}^{(k)}$ is calculated as

$$\mu_{mob}^{(k)} = \frac{T^{(k)}}{N^{(k)}} = \frac{f_1^{(k)} \cos \beta^{(k)} - f_2^{(k)} \sin \beta^{(k)}}{f_1^{(k)} \sin \beta^{(k)} + f_2^{(k)} \cos \beta^{(k)}} = \frac{\sigma_{11} F_{11}^{-1} l_1^{(k)} \cos \beta^{(k)} - \sigma_{22} F_{22}^{-1} l_2^{(k)} \sin \beta^{(k)}}{\sigma_{11} F_{11}^{-1} l_1^{(k)} \sin \beta^{(k)} + \sigma_{22} F_{22}^{-1} l_2^{(k)} \cos \beta^{(k)}} \quad (6.1)$$

The superscript k , which represents quantities at an individual contact, will be dropped in the following discussions for simplicity. When the branch vector is different from the associated contact normal with an inclination angle of θ , μ_{mob} can be rewritten as

$$\mu_{mob} = \frac{\sin \bar{\varphi}_m^* \sin 2\beta}{1 - \sin \bar{\varphi}_m^* \cos 2\beta} \quad (6.2)$$

where $\sin \bar{\varphi}_m^*$, which is a local parameter at a specific contact point, is expressed as

$$\sin \bar{\varphi}_m^* = \frac{\sigma_{11}^* \sin \theta \cos \beta - \sigma_{22}^* \cos \theta \sin \beta}{\sigma_{11}^* \sin \theta \cos \beta + \sigma_{22}^* \cos \theta \sin \beta} \quad (6.3)$$

and

$$\sigma_{11}^* = \sigma_{11} F_{11}^{-1}, \quad \sigma_{22}^* = \sigma_{22} F_{22}^{-1} \quad (6.4)$$

It can be shown that the non-sliding condition $\mu_{mob} < \mu$ can be rewritten as

$$\sin(2\beta + \varphi_\mu) < \frac{\sin \varphi_\mu}{\sin \bar{\varphi}_m^*} \quad (6.5)$$

Consequently, one concludes that sliding occurs at contacts with the inclination angle β satisfying

$$\sin^{-1} \left(\frac{\sin \varphi_\mu}{\sin \bar{\varphi}_m^*} \right) \leq 2\beta + \varphi_\mu \leq \pi - \sin^{-1} \left(\frac{\sin \varphi_\mu}{\sin \bar{\varphi}_m^*} \right) \quad (6.6)$$

which defines the range of sliding contacts as $\beta_{\min} \leq \beta \leq \beta_{\max}$ with

$$\beta_{\min} = \frac{1}{2} \sin^{-1} \left(\frac{\sin \varphi_\mu}{\sin \bar{\varphi}_m^*} \right) - \frac{\varphi_\mu}{2}; \quad \beta_{\max} = \frac{\pi}{2} - \frac{1}{2} \sin^{-1} \left(\frac{\sin \varphi_\mu}{\sin \bar{\varphi}_m^*} \right) - \frac{\varphi_\mu}{2} \quad (6.7)$$

One observes that sliding first takes place at contacts with $\beta = \pi/4 - \varphi_\mu/2$ when $\bar{\varphi}_m^* = \varphi_\mu$. When the mobilized friction $\bar{\varphi}_m^*$ exceeds φ_μ owing to the increase of shear stress, more sliding is activated and the difference between β_{\max} and β_{\min} is

$$\delta_\beta = \beta_{\max} - \beta_{\min} = \frac{\pi}{2} - \sin^{-1} \left(\frac{\sin \varphi_\mu}{\sin \bar{\varphi}_m^*} \right) \tag{6.8}$$

The value of δ_β varies between 0 (when sliding starts at $\bar{\varphi}_m^* = \varphi_\mu$) and $\pi/2 - \varphi_\mu$ (when $\sin \bar{\varphi}_m^* = 1$).

Without loss of generality, one may assume that the mean sliding direction to be

$$\bar{\beta} = \frac{1}{2}(\beta_{\max} + \beta_{\min}) = \frac{\pi}{4} - \frac{\varphi_\mu}{2} \tag{6.9}$$

The nominal friction along the mean sliding direction may be considered as the average of the friction on all planes with $\beta_{\min} \leq \beta \leq \beta_{\max}$. When introducing a density function describing the directional distribution of contact normal (Emeriault and Chang 1997)

$$E(\mathbf{n}) = 1 + \varpi \cos 2(\beta - \beta_0) \tag{6.10}$$

with ϖ defining the degree of anisotropy and β_0 representing the orientation of the greatest density of the contact normals, φ_f can be calculated as

$$\begin{aligned} \mu_f = \tan \varphi_f & \square \frac{1}{\delta_\beta} \int_{-\delta_\beta/2}^{\delta_\beta/2} \tan(\varphi_\mu + \beta) [1 + \varpi \cos 2(\beta - \beta_0)] d\beta \\ & \square \frac{1}{\delta_\beta} \ln \frac{\cos(\varphi_\mu - \delta_\beta/2)}{\cos(\varphi_\mu + \delta_\beta/2)} + \frac{\varpi}{6} \left[\tan \left(\varphi_\mu + \frac{\delta_\beta}{2} \right) \cos(\delta_\beta - 2\beta_0) \right. \\ & \left. + \tan \left(\varphi_\mu - \frac{\delta_\beta}{2} \right) \cos(\delta_\beta + 2\beta_0) + 4 \tan \varphi_\mu \cos 2\beta_0 \right] \end{aligned} \tag{6.11}$$

Herein, Simpson’s three-point method is used to evaluate the integral. When $\delta_\beta = 0$ and $\pi/2 - \varphi_\mu$, φ_f reaches its minimum and maximum values, which are given as follows:

$$\tan \varphi_{f \min} = \lim_{\delta_\mu \rightarrow 0} \tan \varphi_f \square (1 + \varpi \cos 2\beta_0) \tan \varphi_\mu \tag{6.12}$$

$$\tan \varphi_{f \max} \square \frac{1}{\frac{\pi}{2} - \varphi_\mu} \ln \frac{\cos(\frac{\pi}{4} - \frac{3\varphi_\mu}{2})}{\cos(\frac{\pi}{4} + \frac{\varphi_\mu}{2})} + \frac{\xi \sin 2\beta_0 + 2(\xi \sin \varphi_\mu + 1) \tan \varphi_\mu \cos 2\beta_0}{3} \varpi \tag{6.13}$$

with $\xi = \cos^2 \varphi_\mu / (\sin \varphi_\mu + \cos 2\varphi_\mu)$. Finally, the stress dilatancy formulation is expressed as

$$-\frac{\sigma_1 \dot{\epsilon}_1^p}{\sigma_2 \dot{\epsilon}_2^p} = \frac{\tan(\varphi_f + \bar{\beta})}{\tan \bar{\beta}} = K^*, \quad \bar{\beta} = \frac{\pi}{4} - \frac{\varphi_\mu}{2} \tag{6.14}$$

One may further define an equivalent friction angle $\bar{\varphi}_f$ such that

$$K^* = \tan^2 \left(\frac{\pi}{4} + \frac{\bar{\varphi}_f}{2} \right) = \frac{\tan(\varphi_f + \pi/4 - \varphi_\mu/2)}{\tan(\pi/4 - \varphi_\mu/2)} \tag{6.15}$$

As a result, the dilatancy equation in Eq. (6.14) will have the same form as Rowe’s formulation with φ_{cv} being replaced by $\bar{\varphi}_f$ such that

$$\sin \psi = \frac{\sin \varphi_m - \sin \bar{\varphi}_f}{1 - \sin \varphi_m \sin \bar{\varphi}_f} \tag{6.16}$$

According to Eqs. (6.12) and (6.15), the minimum values of $\sin \bar{\varphi}_{f \min}$ can be approximated to

$$\sin \bar{\varphi}_{f \min} = (1 + 0.85\varpi \cos 2\beta_0) \sin \varphi_\mu \tag{6.17}$$

When turning to $\bar{\varphi}_{f \max}$, let us check a special case of $\beta_0 = \pi/2$ when the orientation of the greatest density of the contact normal is aligned in the direction of the major principal stress σ_1 . Fig. 6.1 shows the variation of $\bar{\varphi}_{f \max}$ with respect to φ_μ at different degrees of anisotropy. Though $\bar{\varphi}_{f \max}$ tends to decrease with increased degree of anisotropy, a comparison of $\bar{\varphi}_{f \max}$ with experimental data for critical state friction angles φ_{cv} (Moroto 1988, and Hardin 1985) reveals that $\bar{\varphi}_{f \max}$ calculated from Eq. (6.13) is very close to φ_{cv} for materials of weak to medium anisotropy. In other words, the critical state friction angle φ_{cv} can be regarded as the upper bound of $\bar{\varphi}_f$. This conclusion is consistent with Rowe’s experimental

data. Without loss of accuracy, one may argue that $\bar{\varphi}_f$ varies over a range of $(1 + 0.82\varpi \cos 2\beta_0) \sin \varphi_\mu \leq \sin \bar{\varphi}_f \leq \sin \varphi_{cv}$.

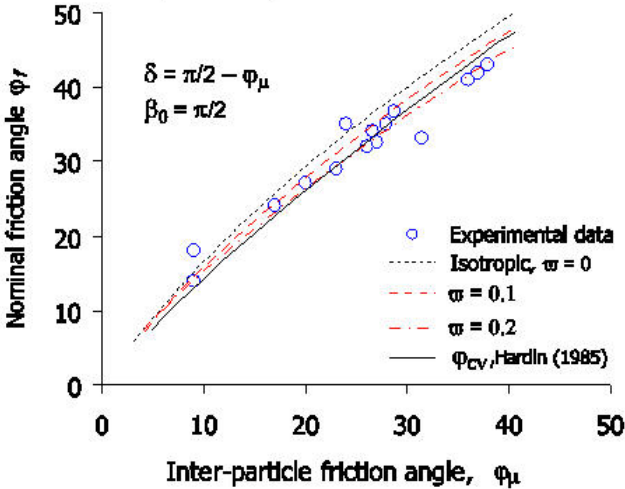


Fig. 6.1. Dependency of $\bar{\varphi}_{f \max}$ on interparticle friction angle φ_μ

As for the evolution of $\bar{\varphi}_f$ during deformation, referring to Eq. (6.11), φ_f and hence $\bar{\varphi}_f$ both increase with δ_β , which describes the range of contact normal orientation at sliding contacts. Moreover, $\bar{\varphi}_f$ is meaningful only when relatively displacements occur between soil particles, implying that $\bar{\varphi}_f$ is a function of plastic deformation. Consequently, it is reasonable to assume an evolution law for $\bar{\varphi}_f$ in the form of

$$\sin \bar{\varphi}_f = \frac{X(1 + 0.85\varpi \cos 2\beta_0) + \gamma^p}{a + \gamma^p} \sin \varphi_{cv} \tag{6.18}$$

By adopting $X = \sin \varphi_\mu / \sin \varphi_{cv}$, $\sin \bar{\varphi}_{f \max} = \sin \varphi_{cv}$ and $\sin \bar{\varphi}_{f \min}$ given in Eq. (6.17) are both recovered.

According to Cambou *et al.* (1995), the degree of anisotropy ϖ can be related to the principal components of the fabric tensor via

$$\varpi = \frac{F_1 - F_2}{F_1 + F_2} \tag{6.19}$$

When the fabric and stress tensors are non-coaxial, one has

$$\frac{F_{11} - F_{22}}{F_{11} + F_{22}} = -\frac{F_1 - F_2}{F_1 + F_2} \cos 2\beta_0 = -\varpi \cos 2\beta_0 \tag{6.20}$$

with β_0 being the angle the major principal fabric direction makes with respect to the horizontal (i.e., the direction of σ_2 in biaxial compression shown in Fig. 3.4). By applying Eq. (6.20), the minimum value of $\sin \bar{\varphi}_f$ can be approximately expressed as

$$\sin \bar{\varphi}_{f \min} = \frac{1}{2} \left(1 + \frac{F_{22}}{F_{11}} \right) \sin \varphi_\mu \tag{6.21}$$

which yields an alternative expression for Eq. (6.18):

$$\sin \bar{\varphi}_f = \frac{X(1 + F_{22}/F_{11})/2 + \gamma^p}{a + \gamma^p} \sin \varphi_{cv} \tag{6.22}$$

For weakly anisotropic materials with $F_{22}/F_{11} \rightarrow 1$, the above equation can be further simplified into

$$\sin \bar{\varphi}_f \square \frac{XF_{22}/F_{11} + \gamma^p}{a + \gamma^p} \sin \varphi_{cv} \tag{6.23}$$

which is consistent with the expression proposed by Wan and Guo (2001) in the following form

$$\sin \bar{\varphi}_f = \frac{XF_{22}/F_{11} + \gamma^p}{a + \gamma^p} \left(\frac{e}{e_{cr}} \right)^\alpha \sin \varphi_{cv} \tag{6.24}$$

in which the effect of void ratio is taken into account by the $(e/e_{cr})^\alpha$ factor.

6.2 Comments on $\bar{\varphi}_m^*$ and δ_β

Even though $\bar{\varphi}_m^*$ is introduced in Eq. (6.3) as a friction angle of some stress measure, its physical meaning is not clear at this point. For an

ensemble of spherical particles, $\bar{\varphi}_m^*$ is the friction angle associated with the modified stress σ_{ij}^* defined in Eq. (6.4). According to Oda (1993), the modified stress σ_{ij}^* can be considered as the “true” stress in terms of effective contact area between particles. It has been known that during the deformation process of granular materials, contact normals gradually concentrate towards the major principal stress direction and form particle columns or force chains; between the columns, particle may carry little or even no load. Usually sliding does not occur at contacts comprising the major force chains. Instead, slip takes place predominantly in the regions between the major force chains. The deformation consists of a series of buckling of these major force chains, resulting into fewer contacts between particles in the minor principal stress direction. When the steady-state is reached, new columns are created at the same rate that old columns collapse and vanish: the total number of contacts remains more or less constant. More generally, when taking into account the discrete feature of contact forces and forces chain, the true stress σ_{ij}^* used for determining contact forces should be considered as a “local” measurement of stresses. For a small domain along the major columns, one may expect that the local value of σ_{ij}^* in the direction of the column is much higher than that in the orthonormal direction, yielding high $\sigma_{11}^*/\sigma_{22}^*$ ratios. As a result, the value of $\bar{\varphi}_m^*$ is likely to be much higher than the friction angle based on the average stress σ_{ij} .

One can also check the possible value of $\bar{\varphi}_m^*$ by exploring the variation of δ_β , i.e., the range of the sliding contact orientations. Oda *et al.* (1982) and Konishi *et al.* (1983) observed in a series of biaxial compression tests on assemblies of oval cross-sectional rods that the disappearing and generated contacts were limited in a certain range. It is plausible that relative sliding (or rolling) occurs, but not limited to disappearing contacts and new contacts are generated during deformation. As shown in Fig. 6.2, the orientation of disappearing contacts varies over a range of $0 \leq \beta \leq \pi/2 - \varphi_\mu$, which is consistent with Eq. (6.7). Closer examinations of particle movement (Oda and Kazama 1998) reveal that the buckling of particle columns at the residual stress state is induced by particle movement in the direction of $\pi/2 - \varphi_\mu$, which corresponds to $\beta_{\max} = \pi/2 - \varphi_\mu$. More experimental evidence which confirms that relative

particle sliding occurs at $0 \leq \beta \leq \pi/2 - \varphi_\mu$ can be found in Calvetti *et al.* (1997).

Discrete element simulations for biaxial compression tests can also be used to examine the range of sliding contact orientation. Fig. 6.3 shows the directional distribution of the sliding contacts at different shear stress levels (Alonso-Marroquin *et al.* 2004). It can be seen from the figure that the range of sliding contact orientation increases with shearing and β_{\max} gradually approaches $\pi/2 - \varphi_\mu$. As a result, one may conclude that results shown in Figs. 8 and 9 provide the physical bases for the reasoning presented in the previous section.

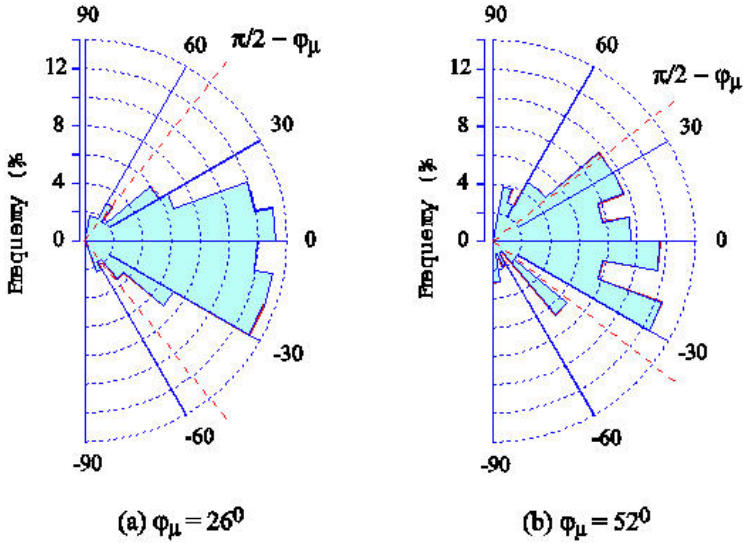


Fig. 6.2. Disappearing contacts: from initial state to peak, rods of oval cross-section (data after Oda *et al.* 1982 and Konishi *et al.* 1983)

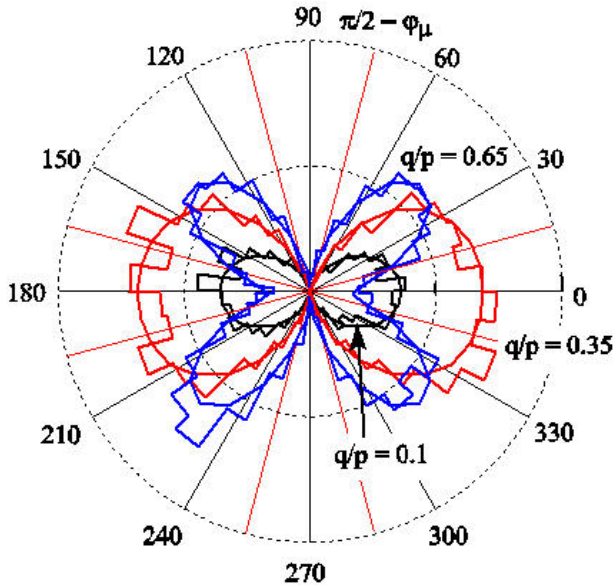


Fig. 6.3. Directional distribution of sliding contacts at various shear stress levels

7 Closing Remarks

Based on the investigation of two-dimensional granular assemblies with various regular particle arrangements, it is demonstrated that Rowe's hypothesis of minimum energy ratio is not necessary for granular material deformation. Rowe's stress-dilatancy equation is in fact the lower bound of all possible dilatancy states the material can assume at various particle arrangements. When working out rigorously the local sliding planes through principles of the micromechanics of granular materials, a theoretical dilatancy formulation is derived with Rowe's hypothesis of minimum energy being lifted. The resulting micromechanically based approach, with the effect of fabric embedded in the analysis, yields a more accurate description of the dilatancy behaviour of granular materials; it can also be readily extended to describe the dilatancy behaviour of sand under general stress conditions. When simplified, the new dilatancy formulation reverts to the basic form that was proposed by the authors in previous publications, see Wan and Guo (1998, 2001, 2004).

Acknowledgements

Funding provided by the Natural Science and Engineering Research Council of Canada is gratefully acknowledged.

References

1. Alonso-Marroquin F, Herrmann HJ and Vardoulakis I (2004) Micromechanical Investigation of soil plasticity: An investigation using a discrete model of polygonal particles. Proc. 2nd Int. Symp. Continuous and Discontinuous Modeling of Cohesive-Frictional Materials, Stuttgart, Germany
2. Calvetti F, Combe G and Lanier J (1997) Experimental micromechanical analysis of a 2D granular material: relation between structure evolution and loading path. *Mechanics of Cohesive-Frictional Materials*, 2: 121-163
3. Cambou B, Dubujet P, Emeriault F and Sidoroff F (1995) Homogenization for granular materials. *Eur. J. Mech., A/Solids*, 14(2): 255-276
4. Caquot A (1934) *Équilibre des massifs à frottement interne. Stabilité des terres pulvérents et cohérentes*. Gauthier Villars, Paris
5. Christoffersen J, Mehrabadi MM, Nemat-Nasser S (1981) A micromechanical description of granular material behaviour. *J. Appl. Mech.* 48: 339-344
6. Collins IF and Muhunthan B (2003) On the relationship between stress-dilatancy, anisotropy, and plastic dissipation for granular materials. *Géotechnique* 53(7): 611-618
7. Dafalias Y and Manzari MT (2004) Simple plasticity sand model accounting for fabric change effects. *J. Eng. Mech., ASCE*, 130(6): 635-645
8. Davis EH (1968) *Theories of plasticity and the failure of soil masses*. Soil mechanics, selected topics (ed. Lee IK). Butterworth
9. De Josselin de Jong G (1976) Rowe's stress-dilatancy relation based on friction. *Géotechnique* 26(3): 527-534
10. Drescher A and de Josselin de Jong G (1972) Photoelastic verification of a mechanical model for the flow of a granular material. *J. Mech. Phys. Solids* 20: 337-351
11. Emeriault F and Chang CS (1997) Intersurface forces and displacements in granular materials. *Computers and Geotechnic* 20(3-4): 223-244
12. Goddard JD (1999) Granular dilatancy and plasticity of glassy lubricants. *Ind. Eng. Chem. Res.* 38: 820-822
13. Goddard JD and Bashir YM (1990) On Reynolds dilatancy. In *Recent Developments in Structured Continua* (eds DeKee D and Kaloni PN), vol. 2, pp. 23-35. New York: Longman
14. Goddard JD and Didwania AK (1998) Computations of dilatancy and yield surfaces for assemblies of rigid frictional spheres. *Q. J. Mech. Appl. Math.* 51: 16-44

15. Gudehus G (1996) A comprehensive constitutive equation for granular materials. *Soils and Foundations* 36 (1): 1-12
16. Hardin BO (1985) Strength of soils in terms of effective stress. In: *Richart Commemorative Lectures* (ed. Wood RD), pp. 1-77
17. Houlsby GT (1993) Interpretation of dilation as a kinematic constraint. In *Modern Approaches to Plasticity* (ed. Kolymbas D), pp. 119-138. New York: Elsevier
18. Kanatani KI (1982) Mechanical foundation of the plastic deformation of granular materials. *Proc. IUTAM Conf. on Deformation and Failure of Granular Materials, Delft*, pp. 119-127
19. Konishi J, Oda M, and Nemat-Nasser S (1983) Induced anisotropy in assemblies of oval cross-sectional rods in biaxial compression. In: *Mechanics of Granular Materials: New Models and Constitutive Relations* (eds. Jenkins JT and Satake M), Elsevier, Amsterdam, pp. 31-39
20. Kruyt NP and Rothenburg L (2004) Kinematic and static assumptions for homogenization in micromechanics of granular materials. *Mech. Mater.* 36: 1157-1173
21. Li XS, and Dafalias YF (2000) Dilatancy for cohesionless soils. *Géotechnique* 50(4): 449-460
22. Miura S and Toki S (1984) Elasto-plastic stress-strain relationship for loose sands with anisotropic fabric under three-dimensional stress conditions. *Soils and Foundations* 24(2): 43-57
23. Miyamori T (1976) Deformation and strength of a sand in three-dimensional stress state. *Proc. JSCE*, 225, 81-91 (in Japanese)
24. Moroto N (1988) Some consideration on shearing resistance angles of sands. In: *Micromechanics of Granular Materials* (eds. Satake M and Jenkins JT), Elsevier Science Publishers B.V., Amsterdam, 47-54
25. Nakai T (1987) A unified mechanical quantity for granular materials in three-dimensional stresses. In: *Micromechanics mechanics of granular materials, Proc. U.S./Japan Seminar on the Micromechanics of Granular Materials* (eds. Satake M and Jenkins JT), Sendai-Zao, Japan, Oct. 26-30, 1987, pp. 297-307
26. Ng T-T (2002) Fabric evolution of ellipsoidal arrays with different particle shapes. *J. Eng. Mech.* 127(10): 994-999
27. Oda M (1972) Initial fabrics and their relations to mechanical properties of granular material. *Soils and Foundations* 12(1): 17-36
28. Oda M (1993) Inherent and induced anisotropy in plasticity of granular soils. *Mech. Mater.* 16: 35-45
29. Oda M, Konish J, Nemat-Nasser S (1982) Experimental micromechanical evaluation of strength of granular materials: effects of particle rolling. *Mech. Mater.* 1: 269-283
30. Oda M and Kazama H (1998) Microstructure of shear bands and its relation to the mechanisms of dilatancy and failure of dense granular soils. *Géotechnique* 48(4): 465-481
31. Rowe PW (1969) The relation between the shear strength of sands in triaxial compression, plane strain and direct shear. *Géotechnique* 19(1): 75-86

32. Tokue T (1979) A stress-dilatancy model of granular material under general stress condition. *Soils and Foundations* 19(1): 63-80
33. Wan R and Guo PJ (2004). Stress Dilatancy and Fabric Dependencies on Sand Behavior. *Journal of Engineering Mechanics* 130(6): 635-645
34. Wan R and Guo PJ (2001) Effect of microstructure on undrained behaviour of sands, *Canadian Geotechnical Journal* 38: 16-28
35. Wan R and Guo PJ (1998) A simple constitutive model for granular soils: Modified stress-dilatancy approach. *Computers and Geotechnics* 22(2): 109-133
36. Wood DM (1990) *Soil behaviour and critical soil mechanics*. Cambridge University Press, Cambridge

Micro-Fracture Instabilities in Granular Solids

G. Bilbie, C. Dascalu, R. Chambon and D. Caillerie

Laboratoire Sols Solides Structures,
Université J. Fourier,
BP 53, 38041 Grenoble Cedex 9,
France,

E-mail: bilbie@geo.hmg.inpg.fr, Cristian.Dascalu@hmg.inpg.fr,
Rene.Chambon@hmg.inpg.fr, Denis.Caillerie@hmg.inpg.fr

Summary

We study the appearance of instable behaviors (like strain localization bands) in elastic solids, as a consequence of micro-fracture. A two-scale approach of computational homogenization is considered. The macroscopic behavior is obtained by unit cell finite element computations. On the micro-level, we consider a granular structure with each grain made of a large strain elastic material. Inter-granular boundaries are modeled with cohesive laws, friction and unilateral contact. We show that decohesion between grains give rise to macro-instabilities, indicated by the loss of ellipticity, typical for deformation localization bands. The relation between the microscopic softening on inter-granular boundaries and the onset of macro-instabilities is pointed out on some numerical examples. The influence of the cohesive law and friction parameters is analyzed.

1 Introduction

This contribution aims at establishing a link between inter-granular micro-fracture and the onset of macro-instabilities in granular solids.

A two-scale framework of computational homogenization (e.g. Kouznetsova *et al.* [1], Miehe [2]) is considered. The macroscopic response is obtained by localization/homogenization exchanges with a representative volume element (RVE). Linear deformation boundary conditions are assumed for the elementary cell. The microstructure is composed of deformable grains separated by cohesive interfaces. Large strain hyper-elastic St. Venant-Kirchhoff material is considered for grains and traction-

displacement cohesive laws for the inter-granular interfaces. A Coulomb-type friction law is also considered on these interfaces. We show that a microscopic origin of the loss of ellipticity for the homogenized equilibrium can be the granular decohesion, the inside-grain equilibrium equations remaining elliptic.

Two particular geometries of the RVE are studied. First, we consider a RVE made of two grains, separated by an interface. This simple morphology provides an elementary deformation pattern which will be reproduced in more complex geometries. We show that the unstable macroscopic behavior may appear when a critical length of interface zones in softening regime is reached. This behavior depends very much on the values of the friction and cohesive parameters. Zones of stability/instability and curves of complete decohesion are identified in the plane of macroscopic bi-axial loading.

Then, we illustrate the case of more complex granular structures by an unit cell composed of 15 grains. In this case, the successive decohesion on different inter-granular interfaces is resulting as a composition of elementary modes described previously. The homogenized response appears as a sequence of alternating stable/unstable regions.

These two examples allow us to understand the case of more realistic microstructures, with a large number of grains. It can be easily seen that a macroscopic unstable response is appearing as a limit of the alternating stable/unstable regions observed on our examples.

The paper is structured as follows. In section 3 we describe the microscopic problem and the homogenization procedure. Section 4 is devoted to the macroscopic stability analysis. Numerical examples and discussions are given in Section 5.

2 RVE Problem

The macroscopic response is obtained through numerical homogenization on elementary cells representing granular microstructures. We focus on the behavior in a macroscopic point by performing a unit cell analysis. A mean kinematics is applied through boundary conditions and the mean stress is recovered from the computed microscopic solution.

Let V_0 a two-dimensional representative volume of the undeformed configuration of the body (Fig. 2.2). We denote by $\varphi(\mathbf{X})$ the deformation application and by $\mathbf{F}(\mathbf{X})$ its gradient. The microscopic stress is described

by the first Piola-Kirchhoff tensor $\mathbf{P}(\mathbf{X})$. At the macroscopic level we have the deformation gradient $\bar{\mathbf{F}}(\mathbf{X})$ and the stress $\bar{\mathbf{P}}(\mathbf{X})$.

Given a macro-deformation gradient $\bar{\mathbf{F}}$, linear deformations boundary conditions are applied on the cell boundary :

$$\varphi(\mathbf{X}) = \bar{\mathbf{F}} \cdot \mathbf{X} \tag{2.1}$$

We have two types of internal boundaries: cohesive interfaces and traction-free boundaries around the holes at intersections of interfaces or at the intersection of one interface with an external boundary. In the first case, we consider an interface traction-separation law (e.g. Tvergaard [3]) of the form:

$$\mathbf{P}^+ \mathbf{N} = \mathbf{P}^- \mathbf{N} = \mathbf{T}; \quad \mathbf{T} = \mathbf{T}(\Delta) \tag{2.2}$$

where $\mathbf{T} = [T_n \ T_t]$ are the normal and tangential tractions and $\Delta = [\Delta_n \ \Delta_t]$, respectively, the normal and tangent relative displacements on the interface.

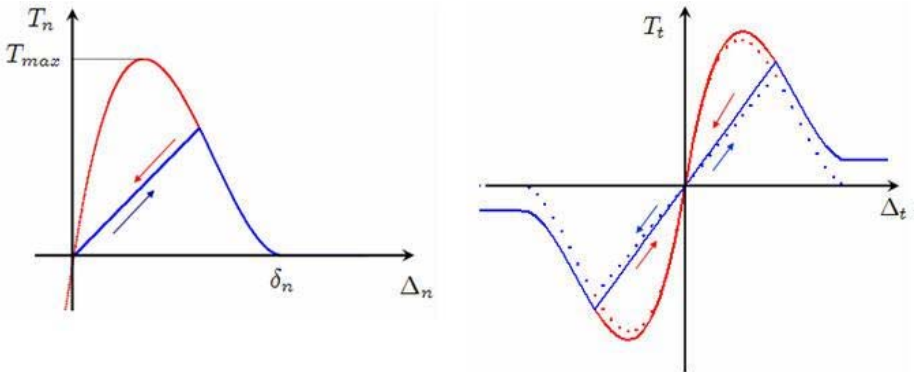


Fig. 2.1. Traction-separation and contact relations in normal and tangential direction on a cohesive interface. The continuous curves also incorporate friction behavior

By introducing the non-dimensional parameter

$$\lambda = \begin{cases} \sqrt{\left(\frac{\Delta_n}{\delta_n}\right)^2 + \left(\frac{\Delta_t}{\delta_t}\right)^2}, & \Delta_n > 0, \\ \left|\frac{\Delta_t}{\delta_t}\right|, & \Delta_n \leq 0. \end{cases} \quad (2.3)$$

and the function

$$F(\lambda) = \frac{27}{4} T_{\max} (1 - 2\lambda + \lambda^2), \text{ for } 0 \leq \lambda \leq 1 \quad (2.4)$$

one defines the separation/contact laws

$$T_n(X) = \begin{cases} \left(\frac{\Delta_n}{\delta_n}\right) F(\lambda), & \Delta_n > 0, \dot{\lambda} \geq 0 \\ \left(\frac{\Delta_n}{\delta_n}\right) F(\lambda_{\max}), & \Delta_n > 0, \dot{\lambda} < 0, \\ \kappa_n \Delta_n, & \Delta_n < 0. \end{cases}$$

$$T_t(X) = \begin{cases} \alpha \left(\frac{\Delta_t}{\delta_t}\right) F(\lambda), & \Delta_n > 0, \dot{\lambda} \geq 0, \\ \alpha \left(\frac{\Delta_t}{\delta_t}\right) F(\lambda_{\max}), & \Delta_n > 0, \dot{\lambda} < 0, \\ \alpha \left(\frac{\Delta_t}{\delta_t}\right) F(\lambda) - \text{sign}(\Delta_t) \mu_f T_n, & \Delta_n < 0, \dot{\lambda} \geq 0, \\ \alpha \left(\frac{\Delta_t}{\delta_t}\right) F(\lambda_{\max}) - \text{sign}(\Delta_t) \mu_f T_n, & \Delta_n < 0, \dot{\lambda} < 0 \end{cases} \quad (2.5)$$

$$\mu_f = \begin{cases} \mu_0 \frac{|\Delta_t|}{\delta_t}, & \lambda < 1 \\ \mu_0, & \text{otherwise} \end{cases} \quad (2.6)$$

where δ_n, δ_t are the total separation values in the purely normal and, respectively, purely tangential modes. The unilateral contact in normal compression is implemented through the penalty condition with the constant κ_n . The superimposed dot represents the time derivative in the quasistatic deformation process. For decreasing λ elastic unloading holds, with $\lambda = \lambda_{\max}$, on the partially damaged interface. The friction acts

progressively during decohesion and completely after, with μ_0 the friction coefficient. The above relations are illustrated in Fig. 2.1, for the normal and tangential directions.

For every grain subdomain we consider a Saint-Venant Kirchhoff material:

$$\mathbf{S} = \lambda \text{tr}(\mathbf{E})\mathbf{I} + 2\mu'\mathbf{E} \tag{2.7}$$

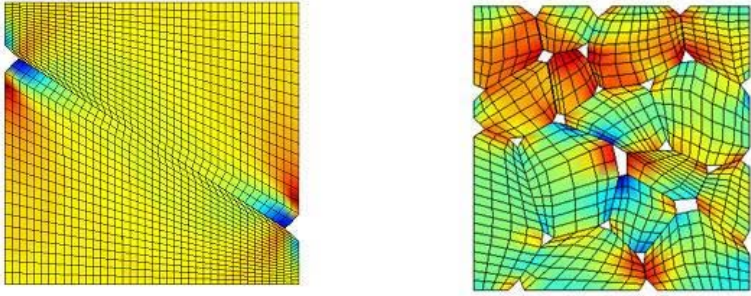


Fig. 2.2. Elementary volumes with 2 and respectively 15 grains

where $\mathbf{S} = \mathbf{F}^{-1}\mathbf{P}$ is the second Piola-Kirchhoff stress tensor and $\mathbf{E} = \frac{1}{2}(\mathbf{F}^T\mathbf{F} - \mathbf{I})$ is the Green-Lagrange deformation tensor.

The equilibrium equation reads

$$\text{div}(\mathbf{P}) = 0 \tag{2.8}$$

The numerical solution of the above boundary value problem allow us to obtain the mean stress as

$$\bar{\mathbf{P}} = \frac{1}{|V_0|} \int_{V_0} \mathbf{P} dV_0 \tag{2.9}$$

Here $|V_0|$ represents the area occupied by the solid in the RVE and the integral is considered on this region. In this way we get the mechanical response of the RVE in the form of a numerical constitutive law. For an increasing macroscopic loading, this equation can be written as $\bar{\mathbf{P}} = \bar{\mathbf{P}}(\bar{\mathbf{F}})$. This relation allows us to perform a macro-stability analysis based on the loss of ellipticity of the homogenized equilibrium equation.

3 Macroscopic Loss of Ellipticity

Let us consider a quasi-static deformation process. If \bar{X}_i represents the position of a macroscopic point in the reference configuration and \bar{x}_i its position in the deformed configuration, then the macro-deformation gradient is $\bar{F}_{kL} = \frac{\partial \bar{x}_k}{\partial \bar{X}_L}$ and the equilibrium equation is

$$\frac{\partial \bar{P}_{ij}}{\partial \bar{X}_j} = 0 \tag{3.1}$$

The homogenized constitutive law can be written in the incremental form, in the vicinity of a direction of the gradient of deformation gradient:

$$\dot{\bar{P}}_{ij} = B_{ijkl} \dot{\bar{F}}_{kl} \tag{3.2}$$

This rate constitutive law is certainly nonlinear, with the modulus B depending on the direction on the deformation gradient. Due to the complexity of the geometry of the representative volume it may not be simple to define a global unloading in connection with the local unloading on interfaces.

The tangent modulus, depending only on the above-mentioned direction, is given by

$$B_{ijkl} = \frac{\partial \bar{P}_{ij}}{\partial \bar{F}_{kl}} \approx \frac{\Delta \bar{P}_{ij}}{\Delta \bar{F}_{kl}} \tag{3.3}$$

The last expression is a finite-difference approximation for the computation of the tangent modulus with the cell solutions.

The macroscopic stability is defined by the ellipticity of the equilibrium equation (3.1). It can be shown ([4]) that localization modes are possible if

$$\det(\mathbf{Q}) \leq 0 \tag{3.4}$$

where we have introduced the acoustic tensor $Q_{ik} = n_j (B_{ijkl}) n_L$, with \mathbf{n} is the normal to the localisation band. This condition corresponds to the loss of ellipticity of the homogenized equilibrium equations (3.1).

The loss of ellipticity expressed by (3.4) it the instability concept adopted in this paper. Different instability modes may occur, especially due to the presence of friction. Further analysis should be carried out in order to completely describe the onset of macro-instabilities.

The ellipticity condition is an indicator of the stability of the deformation process. Its violation describes the onset of macro-instabilities, like the localized deformation bands. In what follows we'll check the conditions (3.4) for the homogenized constitutive law.

The stability question may be also formulated at the microscopic level. We can show (e.g. [5]) that, for $\lambda' + 2\mu' > 0$, $\mu' > 0$ and the Poisson ratio $0 < \nu < 0.5$, the relation (2.5) assures the strong ellipticity of the microscopic equilibrium. This means that the macroscopic instabilities are exclusively the result of decohesion fracture on inter-granular boundaries.

4 Numerical Examples and Discussion

Two examples of micro structural geometry will be considered in this section. In both cases the RVE is a square of 1.0 mm. The Lamé constants for the St-Venant Kirchhoff material are $\lambda' = 1442.3 \text{ MPa}$, $\mu' = 961.5 \text{ MPa}$.

A total Lagrangian finite element formulation is implemented to obtain the solution of the cell problem. The interfaces between grains are modelled using cohesive finite elements (see, for instance [6], [7]). All the computations are performed for applied macro-deformation gradients of the form $\bar{\mathbf{F}} = \mathbf{I} + \alpha \mathbf{G}^0$ where \mathbf{G}^0 is a fixed macroscopic load and α is a load factor running from 0 to 1.

The first geometry, represented in Fig. 2.2, consists of two grains separated by an interface. This simple microstructure will provide an elementary mode for the onset of macro-instabilities due to inter-granular decohesion.

Fig. 4.1 clearly shows the hierarchy of unstable behaviours for our model. A lag between the occurrence of softening on the interface (step (1)) and the loss of macro-ellipticity (step (2)) is observed. The other numerical results given in this section will show the dependence of the step of loss of macro-ellipticity and the corresponding micro-modes for different parameters of the cohesive law. The next step (3), in Fig. 4.1, corresponds to the first occurrence of total decohesion at the micro-level. One can remark that the loss of macro-stability corresponds to some length of the softening zone on the interface. This result is similar to that obtained in [8] where we have proved that a critical length of the softening region on an interface is necessary to activate instability modes.

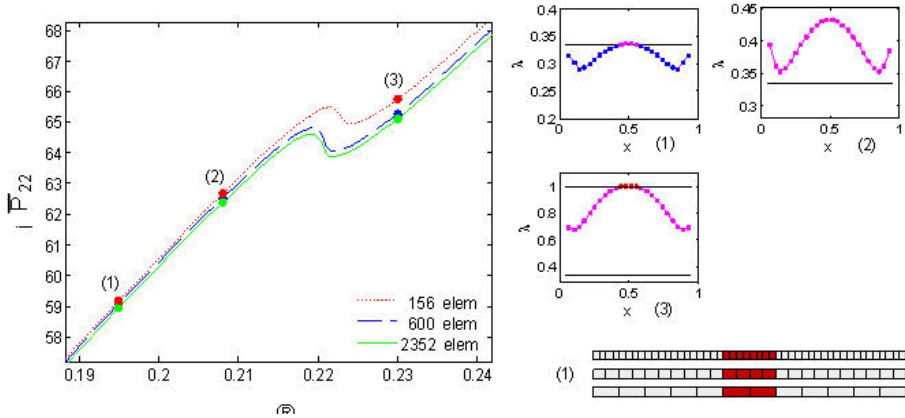


Fig. 4.1. Left: homogenized stress (MPa) versus loading factor α , for the values of $\delta_n = \delta_t = 0.01$, $T_{\max} = 10$ MPa, for 3 different meshes. The point (1) is the first step in which micro-softening points occur on the interface. (2) is the step in which macroscopic loss of ellipticity occurs, while the step (3) represents the first occurrence of some complete decohesion points on the interface. The corresponding values of λ , for the three steps, are plotted at the right. For the step (1) we also represented the softening region for the three cohesive element discretisations of the interface, corresponding to the three meshes in the bulk.

Let's consider now the question of the mesh dependence of our results. All the numerical tests we have performed showed independence of the mesh. One can easily see in the Figure 4.1 (left) that all the instability points, obtained with three different meshes, correspond to the same loading steps. We have also represented in Fig. 4.1 the softening region for the loading (1), as obtained with the three meshes. One can remark that the three regions coincide. We believe that the mesh independence is due to the stability inside the grains and the fact that softening microscopic behaviours occur only on sets of measure zero (2D curves).

For the representation in Figure 4.2 we have taken the compressive load $\mathbf{G}^0 = [0 \ 0; 0 \ -0.1]$, for different values of $\delta_n = \delta_t$ and $T_{\max} = 30$ MPa.

The numerical results show that the onset of macro-instabilities may correspond to different lengths of the interface micro-instability zones, depending on the cohesive law parameters.

A similar connection between micro-macro instability is illustrated in Fig. 4.3, for different values of T_{\max} . For large values of T_{\max} , only a few instable interface elements are necessary for the loss of ellipticity at the

macro level, while for small values of T_{max} all the interface elements should be in the softening regime.

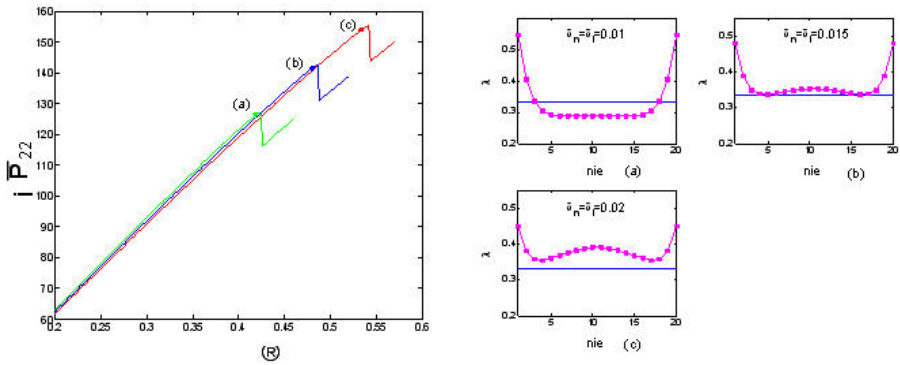


Fig. 4.2. Homogenized stress (MPa) versus loading factor α , for different values of $\delta_n = \delta_t$ and the corresponding values of the decohesion parameter λ . nie = number of the interface element and the interface softening regime corresponds to $\lambda > 1/3$ (horizontal lines).

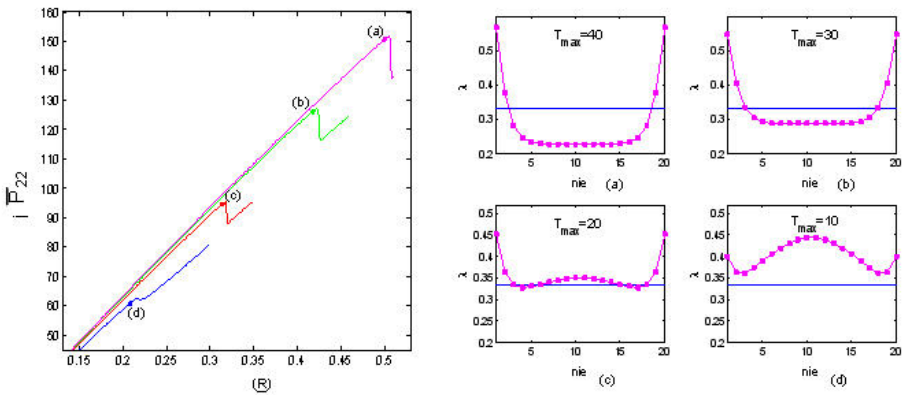


Fig. 4.3. Homogenized stress (MPa) versus loading factor α , for different values of T_{max} and the corresponding values of the decohesion parameter λ .

The influence of the friction parameter μ_0 is analyzed in Figure 4.4. It can be seen that the presence of friction has an impeding effect on the initiation of macro-instabilities.

In Figure 4.5 we represented the regions of stability/instability in the macroscopic loading plane $\bar{F}_{11} - \bar{F}_{22}$, with and without friction on the interface. One can remark the difference between tension and compression as concerns the macro-stability domain and the fact that in some directions we didn't find that ellipticity is lost.

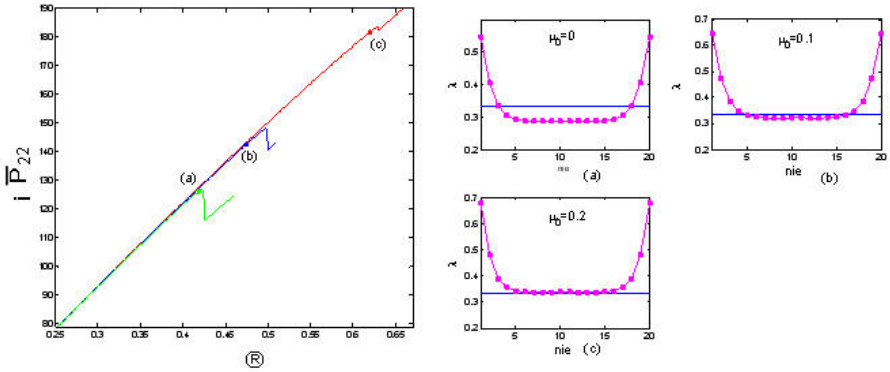


Fig. 4.4. Homogenized stress (MPa) versus loading factor α , for different values of the friction coefficient μ_0 and the corresponding values of λ .

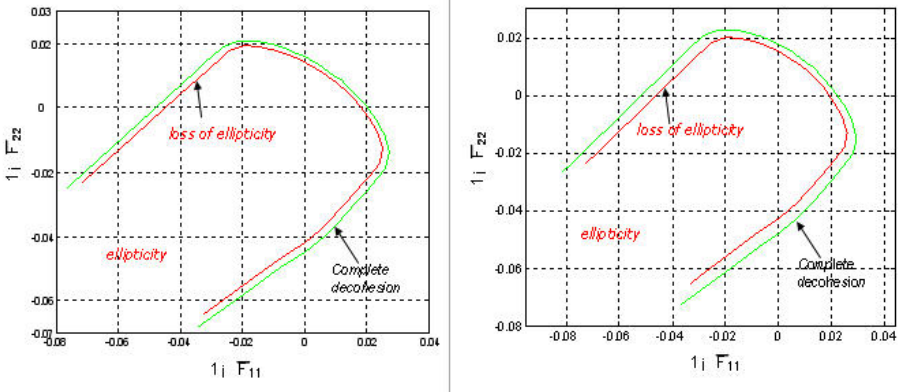


Fig. 4.5. Zones of (non) ellipticity in the macroscopic loading plane with (right) and without (left) friction on the interface ($\mu_0=0.1$). We represent the curves of loss of ellipticity and of decohesion in all points of the interface.

The complete decohesion curve, corresponding to total rupture of the elementary volume, is also represented. Comparison between the two cases confirms that friction has a retarding effect on macro-instability onset.

The second RVE geometry is the granular structure illustrated in Fig 2.2b. The cell dimension and the material constants are the same as before.

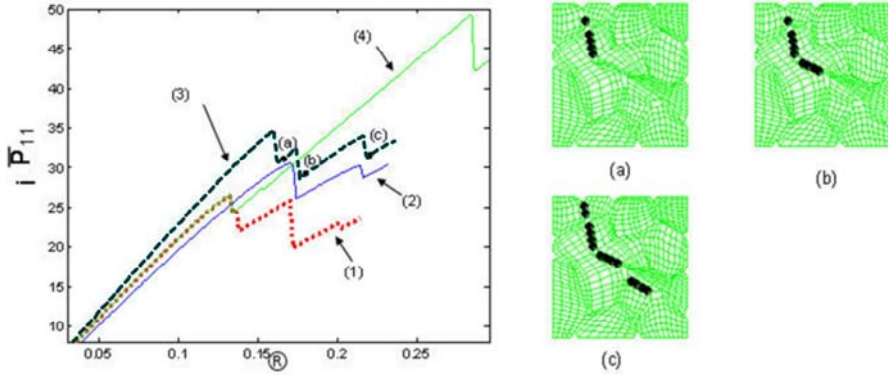


Fig. 4.6. Homogenized stress P_{11} (MPa) versus loading factor α for different sets of parameters 1) $T_{max}=20$, $\delta_t = \delta_n = 0.01$, $\mu_0=0$; 2) $T_{max}=20$, $\delta_t = \delta_n = 0.015$, $\mu_0=0$; 3) $T_{max}=30$, $\delta_t = \delta_n = 0.01$, $\mu_0=0$; 4) $T_{max}=20$, $\delta_t = \delta_n = 0.01$, $\mu_0=0.1$. In the case 3) we show three successive configurations of RVE and the corresponding zones of complete decohesion on inter-granular boundaries.

We consider the compressive loading $\mathbf{G}^0 = [-0.1 \ 0; 0 \ 0]$ and different variations of the parameters T_{max} , δ_n , δ_t and μ_0 , as described in the legend of Fig. 4.6. Successive ruptures, of the type described before, are here present. This is illustrated by the three RVE configurations shown. This stepwise decohesion leads to a combination of stable/instable zones in the macroscopic response. The influences of the different parameters pointed out before are here recovered.

We finally remark that in a more realistic situation, for a RVE with a large number of grains, the “discrete” alternated stable/instable behaviour obtained in the last example will approach a smooth instable curve, as can be observed for the mean response, in a region after the first peak on the curves in Fig 4.4. In this case, successive decohesions take place on a large number of interfaces leading to a macro-instability region in the homogenized response. The influences of cohesion and friction

parameters, illustrated in the simple cases considered in this paper, will remain true for more complex micro-structural geometries.

References

1. Kouznetsova, V., Geers, M. G., and Brekelmans, W. A. M., Multi-scale constitutive modelling of heterogeneous materials with a gradient-enhanced computational homogenization scheme *Int. J. Numer. Meth. Engng.*, 54 (2002) 1235-1260.
2. Miehe C., Computational Micro-to-Macro Transition for Discretized Micro-Structures of Heterogeneous Materials at Finite Strains Based on the Minimization of Averaged Incremental Energy. *Comput. Methods Appl. Mech. Engng.*, 192 (2003), 559-591.
3. Tvergaard V., Cohesive zone representations of failure between elastic or rigid solids and ductile solids *Engineering Fracture Mechanics* 70 (2003) 1859-1868.
4. Rice J.R., The Localization of Plastic Deformation. In: *Theoretical and Applied Mechanics* (ed. W.T. Koiter), North-Holland Amsterdam (1976) 207-220.
5. Knowles J. K. and Sternberg E., On the Failure of Ellipticity of the Equations for Finite Elastostatic Plane Strain. *Arch. Rat. Mech. Anal.*, 63 (1977) 321-336.
6. Xu XP, Needleman A. Numerical simulations of fast crack growth in brittle solids. *J. Mech. Phys. Solids* 42 (1994) 1397-1434.
7. [7] Ortiz M, Pandolfi A. Finite-deformation irreversible cohesive elements for three-dimensional crack-propagation analysis. *Int. J. Num. Meth. Engng.* 44 (1999) 1267-1282.
8. [8] Dascalu C., Ionescu I.R. and Campillo M. "Fault Finiteness and Initiation of Dynamic Shear Instability» *Earth and Planetary Science Letters*, 177 (2000), p.163-176.

Part III

Constitutive Aspects

Entropy and Material Instability in the Quasi-Static Mechanics of Granular Media

Bernhard Pichler^{1,2}, Christian Hellmich¹ and Luc Dormieux²

¹Institute for Mechanics of Materials and Structures,
Vienna University of Technology (TU Wien),
Karlsplatz 13/202,
A-1040, Vienna,
Austria.

E-mail: Bernhard.Pichler@tuwien.ac.at, Christian.Hellmich@tuwien.ac.at

²Laboratory for Materials and Structures (LMSGC),
National School of Civil Engineering (ENPC),
Avenue Blaise Pascal 2 et 4,
77455 Marne-la-Vallée,
France.

E-mail: Luc.Dormieux@lmsgc.enpc.fr

Summary

We here investigate potentials and limitations of Griffith's energy release rate criterion to describe effective stress-strain behavior of brittle materials damaged by mode I type propagating microcracks. For this purpose stiffness estimates for representative volume elements (RVEs) of a microcracked material (based on continuum micromechanics) are combined with the energy release rate criterion for the behavior of one single penny-shaped crack embedded in an infinite matrix subjected to remote uniform stresses (taken from linear-elastic fracture mechanics). This combination allows for studying the effect of stable (quasi-static) mode I propagation of open microcracks on the macroscopic behavior of microcracked material volumes subjected to different types of macroscopic loading. As regards uniaxial tension, the combined fracture-micromechanics approach predicts macroscopic strain-softening, resulting from propagation of cracks perpendicular to the loading direction. As regards uniaxial compression, consideration of non-zero crack openings is mandatory in order to predict a typical relation between tensile and compressive strengths, amounting to about 1:12. Thereby, uniaxial compressive failure is related to axial splitting, i.e. to propagation of open cracks in the loading direction. As regards

axial splitting caused by confined compression, additional strength increase because of lateral confinement can be represented at least qualitatively. However, it turns out to be necessary to combine Griffith's energy release rate criterion with a stress criterion taking into account the sign of the microstresses in the vicinity of the crack edge.

1 Statistics of Kinematics and Stress

Microcracking is the dominant failure mechanism of brittle materials. Specific types of macroscopic loading lead to propagation of microcracks along their planes, while the relative displacement between the two crack surfaces is perpendicular to the crack growth direction. This type of crack propagation, referred to as cracking mode I, is observed under macroscopic uniaxial tension, macroscopic uniaxial compression, and macroscopic axial compression with lateral confinement. It is the central issue of the present paper.

Uniaxial tension experiments on brittle materials are very sensitive to imperfections [33]. Therefore, such experiments require very accurate and experienced handling of the specimen, the loading machine, and the measurement equipment [33]. In the post-peak regime of a uniaxial tension experiment, strain-softening is observed. Thereby, crack propagation is concentrated in a localization zone, i.e. to a narrow crack band [1]. The crack propagation direction is perpendicular to the direction of the applied tension. At the end of a uniaxial tension test on a brittle specimen, the sample splits up into two parts.

In uniaxial compression experiments with carefully lubricated interfaces between load platens and specimen, characterized by approximately uniform stress states within the tested sample, open cracks propagate in the direction of axial loading, through a predominantly mode I cracking mechanism [37]. In the post-peak regime of such a test, crack propagation is accompanied by strain-softening. Thereby, the number of cracks developing within a certain volume is rather large [36]. At the end of a uniaxial compression test on a brittle specimen, the sample splits up into many slender "columns", and final failure is due to buckling and bending, or tilting and sliding of these columns [37].

Complementing uniaxial compression experiments by lateral confinement pressure results in different failure mechanisms, related to different levels of confinement pressure:

- At small confinements, strain-softening is observed after the onset of axial splitting, and the final failure mode is the same as in unconfined uniaxial compression experiments.
- At moderate confinements, axial splitting is first associated with strain hardening, i.e. an increase of stress with increasing strain. Subsequently, strain softening and final failure is caused by shear-mode propagation of closed cracks which are inclined to the axis of uniaxial loading. This type of failure is referred to as faulting [19].
- At large confinements a transition from brittle failure to ductile material behavior is observed [19].

In this paper, we investigate whether effective macroscopic stress-strain behavior under uniaxial tension, uniaxial compression, and axial compression with lateral confinement, respectively, can be predicted by combining Griffith's energy release rate criterion for mode I crack propagation (taken from linear-elastic fracture mechanics) with the Mori-Tanaka stiffness estimate specified for microcracked materials (taken from continuum micromechanics). In Section 2, we shortly revisit Griffith's energy release rate criterion and determine, in the framework of the equivalent inclusion method, the energy release associated with the growth of a single crack embedded in an infinite matrix subjected to remote uniform stress states, namely uniaxial tensile stresses acting perpendicular to the crack plane, uniaxial compressive stresses acting parallel to the crack plane, and triaxial compressive stresses acting both parallel and perpendicular to the crack plane. Section 3 deals with continuum micromechanics. There, we give details on the Mori-Tanaka estimation of the effective stiffness of a representative material volume damaged by microcracks. Employing the simple concentration procedure proposed by Zaoui [39, 40, 41], we recall how these estimates can be derived on the basis of the strain state in a single penny-shaped crack surrounded by an infinite matrix subjected to fictitious remote (uniform) strains. The explicit consideration of these fictitious remote strains provides the link between continuum micromechanics and classical fracture mechanics, i.e. the link between the crack propagation criteria at the level of a single crack and the damage evolution at the level of the microcracked (“damaged”) material. This link is worked out in detail for macroscopic uniaxial tension, uniaxial compression, and axial compression with lateral confinement in Section 4: Through the aforementioned upscaling technique, we study the effect of stable (quasi-static) mode I propagation of open microcracks on the macroscopic behavior of a microcracked material volume.

2 Single Crack Mechanics

2.1 Short Review of Griffith’s Crack Propagation Criterion

Linear-elastic fracture mechanics deals with the behavior of a single crack embedded in an infinite matrix subjected to remote uniform stresses Σ^∞ (Fig. 2.1). Griffith [12] and Irwin [21] related crack propagation to the energy

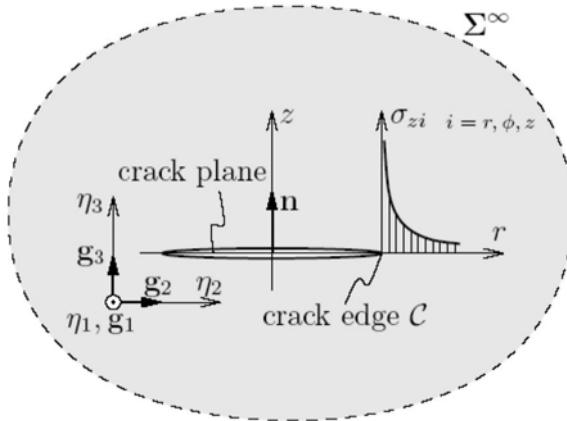


Fig. 2.1. Problem of linear-elastic fracture mechanics: A single penny-shaped crack (Fig. 2.2) is embedded in an infinite matrix subjected to remote uniform stresses Σ^∞

ε released upon an increase of the crack area A from zero to its current size, $\varepsilon = \varepsilon(\Sigma^\infty, A)$. The driving force for crack propagation is the energy release rate \mathbf{G} , which is obtained by derivation of ε with respect to A .

$$G(\Sigma^\infty, A) = \frac{\partial \varepsilon(\Sigma^\infty, A)}{\partial A} \tag{2.1}$$

The material resistance against crack propagation is referred to as \mathbf{G}_c . Comparison of $\mathbf{G}(\Sigma^\infty, A)$ with \mathbf{G}_c allows for identifying different types of crack behavior:

- a crack is stationary, i.e. it does not propagate, if

$$G(\Sigma^\infty, A) < G_c \tag{2.2}$$

- onset of cracking occurs, if

$$G(\Sigma^\infty, A) = G_c \quad (2.3)$$

- stable (quasi-static) crack propagation occurs, if (2.3) is satisfied and if

$$dG = \frac{\partial G}{\partial \Sigma^\infty} d\Sigma^\infty + \frac{\partial G}{\partial A} dA = 0 \quad \text{and} \quad dA > 0 \quad (2.4)$$

- and instable (dynamic) crack growth is associated with

$$G(\Sigma^\infty, A) > G_c \quad (2.5)$$

Since we restrict our considerations throughout the paper to penny-shaped cracks with crack radius a and crack half-opening c (Fig. 2.2), it is convenient to reformulate the expression of the energy release rate (2.1) as [26]

$$G = \frac{\partial \varepsilon}{\partial \alpha} \frac{\partial \alpha}{\partial A} = \frac{1}{2\alpha\pi} \frac{\partial \varepsilon}{\partial \alpha} \quad (2.6)$$

where, instead of the crack area $A = a^2\pi$, the crack radius a is introduced as the parameter describing the size of the crack.

2.2 Energy Released by Penny-Shaped Cracks Propagating in Mode I under Uniaxial and Triaxial Stress States

The energy ε , released upon crack growth from zero to its current size, can be determined in the framework of the equivalent inclusion method [9, 27, 18]. This method deals with two different types of subdomains within an infinite, linear-elastic matrix: inhomogeneities and inclusions (see, e.g., [27]). An inhomogeneity has an elastic stiffness C_i differing from the matrix stiffness C_m (Fig. 2.3a); whereas an inclusion has the same stiffness as the matrix, but exhibits eigenstrains ε^* [27] (Fig. 2.3b), also called stress-free strains [9].

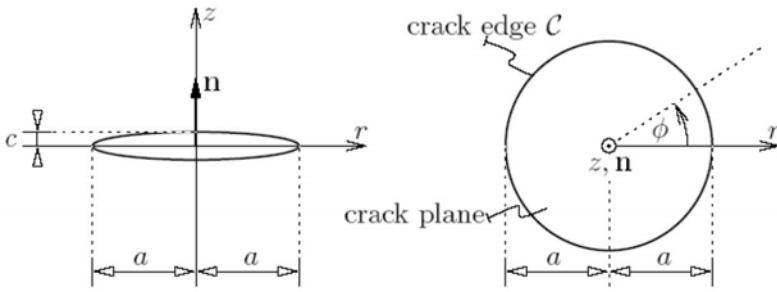


Fig. 2.2. Spatial dimensions of a penny-shaped crack (inhomogeneity) with unit normal to the crack plane \mathbf{n} , and definition of the crack coordinate system (r, ϕ, z)

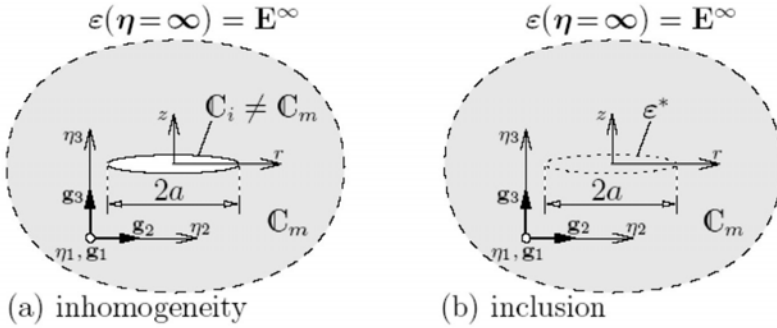


Fig. 2.3. Eshelby's equivalent inclusion problem: the behavior of (a) a single ellipsoidal inhomogeneity with stiffness C_i , embedded in a 3D infinite matrix of stiffness C_m , which is subject to remote uniform strain E^∞ , is modeled by (b) an ellipsoidal inclusion with equivalent eigenstrain ϵ^* , embedded in a homogeneous infinite body of stiffness C_m , which is subject to remote uniform strain E^∞

In case of remote uniform loading, either in terms of strains E^∞ or of stresses

$$\Sigma^\infty = C_m : E^\infty \tag{2.7}$$

the mechanical behavior of an infinite matrix containing a single ellipsoidal inhomogeneity is equivalent to that of an infinite matrix containing an

equally-shaped inclusion with eigenstrains ε^* [9] (Figs. 2.3a and 2.3b), reading as [13].

$$\varepsilon^* = -[\mathbb{S}_i^m + (C_i - C_m)^{-1} : C_m]^{-1} : E^\infty \quad (2.8)$$

where \mathbb{S}_i^m denotes the so-called Eshelby tensor, relating the eigenstrains ε^* to the difference between the total inclusion strains ε^i (eigenstrains plus elastic strains resulting from constraints of the inclusion by the surrounding matrix) and the remote uniform strains E^∞ [39].

$$\varepsilon^i = -E^\infty = \mathbb{S}_i^m : \varepsilon^* \quad (2.9)$$

ε^* enters the expression for the difference between the potential energy W of a Σ^∞ -loaded matrix with an inhomogeneity and that of the same matrix without any inhomogeneity, W_0 , [27].

$$\Delta W = W - W_0 = \frac{1}{2} V_i \Sigma^\infty : \varepsilon^* \quad (2.10)$$

where V_i denotes the volume of the inhomogeneity. The energy difference ΔW is called interaction energy.

For an open crack, represented as an ellipsoidal inclusion with vanishing stiffness $C_i = 0$, the equivalent eigenstrains follow from (2.8) as

$$\varepsilon^* = (\mathbf{I} - \mathbb{S}_c^m)^{-1} : E^\infty \quad (2.11)$$

where \mathbf{I} denotes the fourth-order unity tensor, $I_{ijkl} = 1/2 (\delta_{ik}\delta_{jl} + \delta_{il}\delta_{kj})$, with δ_{ij} denoting the Kronecker delta. For a penny-shaped crack (Fig. 2.2) with unit normal \mathbf{n} pointing in the x_3 direction ($\theta=0$, Fig. 2.4), embedded in an isotropic matrix, the non-zero components of \mathbb{S}_c^m read as [18, 27].

$$\begin{aligned}
 S_{1111} &= \frac{13-8\nu_m}{32(1-\nu_m)} \pi \frac{c}{a} + O\left(\frac{c}{a}\right)^2, & S_{2222} &= S_{1111}, \\
 S_{1122} &= \frac{8\nu_m-1}{32(1-\nu_m)} \pi \frac{c}{a} + O\left(\frac{c}{a}\right)^2, & S_{2211} &= S_{1122}, \\
 S_{1133} &= \frac{2\nu_m-1}{8(1-\nu_m)} \pi \frac{c}{a} + O\left(\frac{c}{a}\right)^2, & S_{2233} &= S_{1133}, \\
 S_{3311} &= \frac{\nu_m}{1-\nu_m} \left(1 - \frac{4\nu_m+1}{8\nu_m} \pi \frac{c}{a}\right) + O\left(\frac{c}{a}\right)^2, & S_{3322} &= S_{3311}, \\
 S_{2323} &= \frac{1}{2} \left(1 + \frac{\nu_m-2}{1-\nu_m} \frac{\pi c}{4a}\right) + O\left(\frac{c}{a}\right)^2, & S_{3131} &= S_{2323}, \\
 S_{1212} &= \frac{7-8\nu_m}{32(1-\nu_m)} \pi \frac{c}{a} + O\left(\frac{c}{a}\right)^2, \\
 S_{3333} &= 1 - \frac{1-2\nu_m}{1-\nu_m} \frac{\pi c}{4a} + O\left(\frac{c}{a}\right)^2, \text{ with } S_{ijkl} = S_{jikl} = S_{ijlk}
 \end{aligned} \tag{2.12}$$

and with ν_m as the Poisson's ratio of the matrix. The crack interaction energy ΔW i.e. the change in potential energy because of the presence of the crack, is identical to Griffith's energy \mathcal{E} released upon an increase of the crack radius a from zero to its current size, so that [compare (10)]

$$\mathcal{E} = \frac{1}{2} V_c \Sigma^\infty \varepsilon^* \tag{2.13}$$

where V_c denotes the volume of the crack:

$$V_c = \frac{4\pi}{3} a^2 c \tag{2.14}$$

In the following, we consider three specific remote uniform stress states Σ^∞ (i) uniaxial tension acting orthogonal to the crack plane, (ii) uniaxial

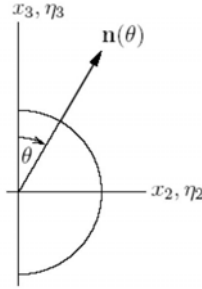


Fig. 2.4. Definition of the unit vector \mathbf{n} as a function of the angular coordinate θ

compression acting parallel to the crack plane, and (iii) a triaxial stress state where compressive stresses act both orthogonal as well as parallel to the crack plane.

For remote uniaxial tensile stress acting perpendicular to the crack plane (Fig. 2.1).

$$\Sigma^\infty = \Sigma_{33}^\infty \mathbf{g}_3 \otimes \mathbf{g}_3, \quad \Sigma_{33}^\infty \geq 0 \quad (2.15)$$

\mathcal{E} follows from specification of (2.13) for (2.14), (2.15), (2.11), (2.12), and (2.7) as

$$\mathcal{E} = \frac{8a^3 (\Sigma_{33}^\infty)^2}{3} \frac{1 - \nu_m^2}{E_m} + \frac{\pi a^3 (\Sigma_{33}^\infty)^2}{3} \frac{1 + 3\nu_m - 4\nu_m^3}{E_m} \left(\frac{c}{a}\right) + O\left(\frac{c}{a}\right)^2 \quad (2.16)$$

and the energy release rate follows from insertion of (2.16) into (2.6) as

$$G_I = \frac{4a (\Sigma_{33}^\infty)^2}{\pi} \frac{1 - \nu_m^2}{E_m} + \frac{a (\Sigma_{33}^\infty)^2}{3} \frac{1 + 3\nu_m - 4\nu_m^3}{E_m} \left(\frac{c}{a}\right) + O\left(\frac{c}{a}\right)^2 \quad (2.17)$$

In case of $(c/a) \ll 1$, the first term of (2.17) is significantly larger than the following terms, such that the energy released by a slightly opened crack ($a \gg c \neq 0$) can be approximated by that released by a sharp crack ($c=0$).

For remote uniaxial compressive stress acting parallel to the crack plane (Fig. 2.1).

$$\Sigma^\infty = \Sigma_{11}^\infty \mathbf{g}_1 \otimes \mathbf{g}_1, \quad \Sigma_{11}^\infty \leq 0 \quad (2.18)$$

\mathcal{E} follows from specification of (2.13) for (2.14), (2.18), (2.11), (2.12), and (2.7) as

$$\mathcal{E} = \frac{2\pi a^3 (\Sigma_{11}^\infty)^2}{3E_m} \left(\frac{c}{a} \right) + O\left(\frac{c}{a} \right)^2 \quad (2.19)$$

and the energy release rate follows from insertion of (2.19) into (2.6) as

$$\mathcal{G} = \frac{2a (\Sigma_{11}^\infty)^2}{3E_m} \left(\frac{c}{a} \right) + O\left(\frac{c}{a} \right)^2 \quad (2.20)$$

Hence, energy release requires at least slight opening of the crack; and *no* energy is released if a sharp crack ($c = 0$) propagates.

For remote triaxial stress states in the form of compressive stress Σ_{11}^∞ acting parallel to the crack plane and confinement stress Σ_{33}^∞ acting both parallel and perpendicular to the crack plane (Fig. 2.1).

$$\Sigma^\infty = \Sigma_{11}^\infty g_1 \otimes g_1 + \Sigma_{33}^\infty (g_2 \otimes g_2 + g_3 \otimes g_3), \quad \Sigma_{11}^\infty \leq 0, \Sigma_{33}^\infty \leq 0 \quad (2.21)$$

\mathcal{E} follows from specification of (2.13) for (2.14), (2.21), (2.11), (2.12), and (2.7) as

$$\begin{aligned} \mathcal{E} = & \frac{8a^3 (\Sigma_{33}^\infty)^2}{3} \frac{1 - \nu_m^2}{E_m} + \frac{\pi a^3}{3} \left[\frac{(\Sigma_{33}^\infty)^2 (1 + \nu_m + 4\nu_m^2 - 4\nu_m^3)}{E_m} + \right. \\ & \left. + \frac{2(\Sigma_{11}^\infty)^2 - 2\Sigma_{11}^\infty \Sigma_{33}^\infty (1 + 3\nu_m - 2\nu_m^2)}{E_m} \right] \left(\frac{c}{a} \right) + O\left(\frac{c}{a} \right)^2 \end{aligned} \quad (2.22)$$

and the energy release rate follows from insertion of (2.22) into (2.6) as

$$\begin{aligned} \mathcal{G}_I = & \frac{4a (\Sigma_{33}^\infty)^2}{\pi} \frac{1 - \nu_m^2}{E_m} + \frac{a}{3} \left[\frac{(\Sigma_{33}^\infty)^2 (1 + \nu_m + 4\nu_m^2 - 4\nu_m^3)}{E_m} + \right. \\ & \left. + \frac{2(\Sigma_{11}^\infty)^2 - 2\Sigma_{11}^\infty \Sigma_{33}^\infty (1 + 3\nu_m - 2\nu_m^2)}{E_m} \right] \left(\frac{c}{a} \right) + O\left(\frac{c}{a} \right)^2 \end{aligned} \quad (2.23)$$

For very small confinements $\Sigma_{33}^\infty \ll \Sigma_{11}^\infty$, the first two terms on the right-hand side in (2.23), containing as factors $(c/a)^0 = 1$ and $(c/a)^1$, respectively, are of the same magnitude; otherwise the confinement pressure Σ_{33}^∞ governs the energy release rate in (2.23).

3 Representative Volume Elements Damaged by many Interacting Microcracks

3.1 Representative Volume Element (RVE) and Material Phases [17, 40, 31]

To study the mechanical behavior of a deformable solid with the help of continuum (micro)mechanics, constitutive material elements must be labeled and their geometrical evolution must be followed [40, 31]. A representative volume element (RVE) of a micro-heterogeneous material must be homogeneous on a macroscopic scale [17], which implies that the characteristic length l of a RVE satisfies the condition

$$l \gg b \quad (3.1)$$

where b denotes the characteristic length of heterogeneities within the RVE, see Figs. 5b, 6b, and 6c for RVEs containing penny-shaped microcracks. Furthermore, in order to render differential calculus applicable in continuum mechanics, the condition

$$\{L, P\} \gg l \quad (3.2)$$

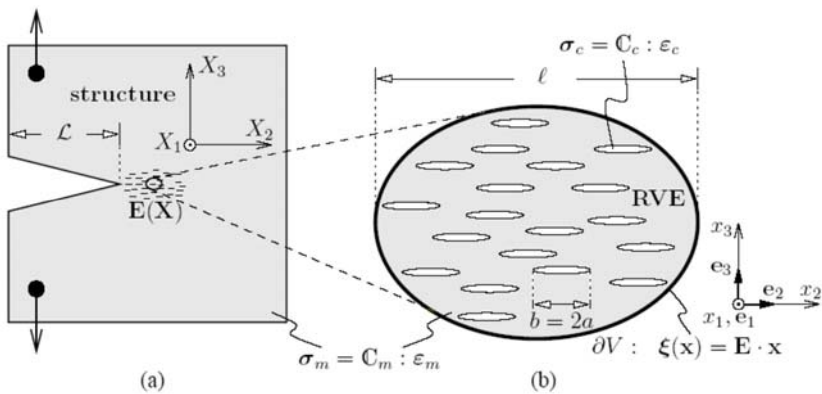


Fig. 3.1. Separation of scales: (a) Structure containing a fracture process zone ahead of a macrocrack and (b) RVE of a microcracked (damaged) material with cracks of identical size and orientation, subjected to displacements ξ related to “homogeneous strains” E at the boundary

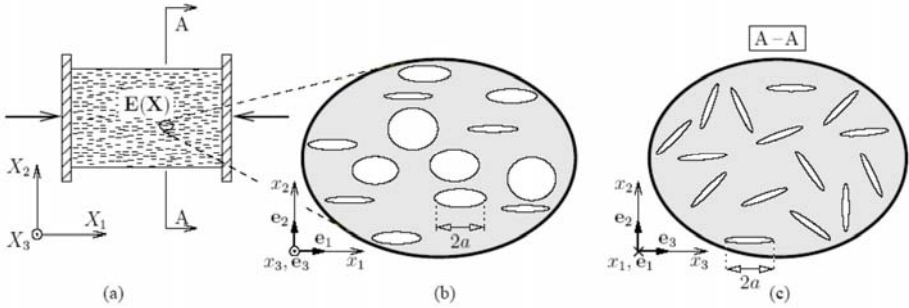


Fig. 3.2. (a) Microcracked sample tested in a uniaxial compression device, (b) and (c) sections through a RVE of a microcracked (damaged) material with equally-sized penny-shaped cracks, axisymmetrically distributed with respect to the x_1 axis

must be satisfied, where L denotes the characteristic length of the structure containing the RVE, and P stands for the characteristic length of structure excitations such as, e.g., surface-loads or wave lengths (Figs. 3.1a and 3.2a).

In general, the microstructure within each RVE is so complicated that it cannot be described in complete detail. Therefore, quasi-homogeneous sub-domains with known physical quantities (such as volume fractions and elastic properties) are reasonably chosen. They are called material phases. As regards microcracked (damaged) media, the introduction of two phases is most common in the open literature [5, 13, 23, 29, 30, 32]: (1) the sane (uncracked) matrix, and (2) the cracks in form of penny-shaped inhomogeneities.

For the sake of simplicity, we deal with RVEs comprising penny-shaped cracks with identical size. In case of uniaxial tension, we consider cracks of identical orientation where the crack normal \mathbf{n} is aligned with the direction of tensile loading. Notably, the problem of strain localization, as observed, e.g., in a uniaxial tension test on a brittle material, is beyond the scope of this paper. Moreover, we do not deal with macrocracking, and in particular not with the influence of many microcracks on the behavior of a macrocrack, such as done in [10, 20, 28, 8]. We rather describe the behavior of a material volume element (Fig. 3.1b) inside the localization zone (narrow crack band [1]) observed in a uniaxial tension experiment or *inside* the fracture process zone ahead of a macrocrack (Fig. 3.1). In case of axial compression (with and without lateral confinement), we consider axisymmetrically distributed cracks with normals \mathbf{n} orthogonal to the direction of the predominant axial compressive loading (Fig. 3.2).

3.2 Stress / Strain Averaging and Concentration [17, 39, 40, 41]

For studying deformation states of the RVE, a position vector \mathbf{x} is introduced. It labels, with resolution b , locations within the RVE and on its boundary. Subjecting the boundary ∂V of the RVE to displacements

$$\xi(x) = E \cdot x \quad \text{on} \quad \partial V \quad (3.3)$$

(Hashin boundary condition [15]), implies

$$E = \langle \varepsilon \rangle = \frac{1}{V} \int_V \varepsilon(x) dV = f_c \frac{1}{\theta^*} \int_0^{\theta^*} \varepsilon_c[n(\theta)] d\theta + f_m \varepsilon_m \quad (3.4)$$

with $\langle \bullet \rangle := (1/V) \int \bullet dV$ as the volume average. f_m and f_c denote the volume fraction of the matrix and of the cracks, respectively. ε_m and $\varepsilon_c[n(\theta)]$ denote the (average) strains of the matrix and of cracks with normals \mathbf{n} defined by the angular coordinate θ (Fig. 2.4), respectively. The integral over $d\theta$ in (3.4) accounts for different crack orientations. Cracks of identical orientation, as observed under uniaxial tension (Fig. 3.1b), correspond to $\theta^* \rightarrow 0$. An axisymmetrical distribution of cracks, as observed under axial compression with and without lateral confinement (Figs. 3.2b and 3.2c), refers to $\theta^* = \pi$.

Linear-elastic behavior of the cracks and of the matrix is considered

$$\sigma_c = C_c : \varepsilon_c \quad \text{and} \quad \sigma_m = C_m : \varepsilon_m \quad (3.5)$$

with C_c and C_m as the stiffness of the cracks and of the matrix, respectively. Consequently, the superposition principle implies the existence of a linear relationship between macroscopic strains E and (“microscopic”) strains ε_m and $\varepsilon_c(\theta)$ [17].

$$\varepsilon_c[n(\theta)] = A_c[n(\theta)] : E \quad \text{and} \quad \varepsilon_m = A_m : E \quad (3.6)$$

with A_m as the fourth-order concentration tensors of the matrix and $A_c[n(\theta)]$ as the fourth-order concentration tensors of the cracks with normal \mathbf{n} defined by θ . (3.4) and (3.6) imply that

$$f_c \frac{1}{\theta^*} \int_0^{\theta^*} A_c[n(\theta)] d\theta + f_m A_m = I \quad (3.7)$$

Insertion of (3.6) into (3.5), averaging over the resulting expressions for $\sigma_c[n(\theta)]$ and σ_m according to

$$\Sigma = \langle \sigma \rangle = f_c \frac{1}{\theta^*} \int_0^{\theta^*} \sigma_c [n(\theta)] d\theta + f_m \sigma_m \tag{3.8}$$

(with Σ as the macroscopic stress tensor), and accounting for (3.7) yields the macroscopic constitutive law

$$\Sigma = C_{\text{hom}} : E \tag{3.9}$$

with

$$C_{\text{hom}} = C_m + f_c \frac{1}{\theta^*} \int_0^{\theta^*} (C_c - C_m) : A_c [n(\theta)] d\theta \tag{3.10}$$

as the homogenized (macroscopic) elasticity tensor. We are left with the determination of the strain concentration tensors $A_c[n(\theta)]$, which are unknown so far. However, they can be estimated from Eshelby's matrix-inclusion problem.

3.3 Stiffness Estimation on the Basis of Eshelby's Matrix - Inclusion Problem [39, 40, 41]

The concentration tensors $A_c[n(\theta)]$ can be estimated on the basis of matrix-inclusion problems [39, 40, 41], such as the ones of Eshelby [9] or Laws [24, 25]. The stiffness of the sane matrix of the (microcracked) RVE, C_m , is introduced as the stiffness of the matrix in the Eshelby problem (Figs. 3.1b and 2.3). Following Zaoui's concentration procedure [39, 40, 41], the average strains of each phase, $\varepsilon_c[n(\theta)]$ and ε_m , are set equal to the strains in a single ellipsoidal inclusion (with stiffness C_c and C_m , respectively) embedded in an infinite matrix of stiffness C_m , subjected to fictitious (uniform) strains E^∞ at infinity [39, 40, 41]. Accordingly, the average strains of penny-shaped microcracks embedded in a RVE follow as [39, 13].

$$\varepsilon_c [n(\theta)] = [I + S_c^m [n(\theta)] : C_m^{-1} : (C_c - C_m)]^{-1} : E^\infty \tag{3.11}$$

as can be shown from (2.8) and (2.9). In the same sense, the average strains of the matrix phase of the RVE are set equal to those prevailing in an inclusion of stiffness C_m , resulting in the trivial relation [39, 40, 41].

$$\varepsilon_m = E^\infty \tag{3.12}$$

The strains \mathbf{E}^∞ , prescribed at infinity to a matrix surrounding a single crack, must be related appropriately to the macroscopic strains \mathbf{E} , imposed as uniform boundary condition onto the RVE.

Assuming the case of a non-dilute concentration of cracks, their interaction needs to be considered. The simplest consideration of crack interaction consists of defining the fictitious remote strains \mathbf{E}^∞ such that the strain average rule (3.4) is satisfied [39, 40, 41], i.e. by insertion of (3.11) and (3.12) into (3.4).

$$\mathbf{E}^\infty = \left\{ f_m \mathbf{I} + f_c \frac{1}{\theta^*} \int_0^{\theta^*} [\mathbf{I} + \mathbb{S}_c^m[n(\theta)]: \mathbf{C}_m^{-1} : (\mathbf{C}_c - \mathbf{C}_m)]^{-1} d\theta \right\}^{-1} : \mathbf{E} \quad (3.13)$$

Back-substitution of (3.12) into (3.10), while considering (3.6.1), yields the Mori-Tanaka estimate for the concentration tensors $\mathbf{A}_c[n(\theta)]$.

$$\begin{aligned} \mathbf{A}_c^{(MT)}[n(\theta)] &= [\mathbf{I} + \mathbb{S}_c^m[n(\theta)]: \mathbf{C}_m^{-1} : (\mathbf{C}_c - \mathbf{C}_m)]^{-1} : \\ &: \left\{ f_m \mathbf{I} + f_c \frac{1}{\theta^*} \int_0^{\theta^*} [\mathbf{I} + \mathbb{S}_c^m[n(\theta)]: \mathbf{C}_m^{-1} : (\mathbf{C}_c - \mathbf{C}_m)]^{-1} d\theta \right\}^{-1} \end{aligned} \quad (3.14)$$

Finally, insertion of (3.14) into (3.10) yields the Mori-Tanaka stiffness estimate of a material with microcracks [2, 3, 4, 11]

$$\begin{aligned} \mathbf{C}_{\text{hom}}^{(MT)} &= \mathbf{C}_m + f_c \frac{1}{\theta^*} \int_0^{\theta^*} (\mathbf{C}_c - \mathbf{C}_m) : [\mathbf{I} + \mathbb{S}_c^m[n(\theta)]: \mathbf{C}_m^{-1} : (\mathbf{C}_c - \mathbf{C}_m)]^{-1} d\theta : \\ &: \left\{ f_m \mathbf{I} + f_c \frac{1}{\theta^*} \int_0^{\theta^*} [\mathbf{I} + \mathbb{S}_c^m[n(\theta)]: \mathbf{C}_m^{-1} : (\mathbf{C}_c - \mathbf{C}_m)]^{-1} d\theta \right\}^{-1} \end{aligned} \quad (3.15)$$

Evidence for the suitability of considering crack interaction through (3.15) was gained in 2D, see [22]. There, it is shown that the 2D equivalent to the 3D Mori-Tanaka stiffness estimate used in this paper is quasi-identical to effective stiffnesses determined from a series of full structural computations (computer experiments [22]) of solids with different crack configurations (Fig. 3.3). These numerical analyses precisely accounted for (i) the load-carrying behavior of the matrix between the cracks and, hence, for (ii) crack interaction. The self consistent scheme and the differential scheme (for the latter see also [16]), however, overestimate the stiffness decrease with increasing crack density parameter (Fig. 3.3). This is the motivation to restrict our considerations to the Mori-Tanaka scheme.

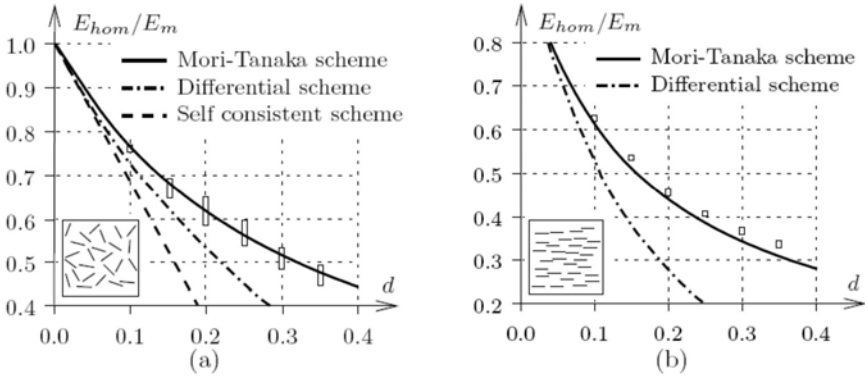


Fig. 3.3. Illustration of results of [22]: Young's modulus of a microcracked material over Young's modulus of the uncracked (sane) matrix, as a function of the (2D) crack density parameter; for (a) randomly orientated cracks and (b) parallel cracks. The vertical bars refer to the scatter interval of computed effective stiffnesses obtained from 15 numerical simulations with the same crack density, but with different, randomly generated configurations of interacting cracks.

3.4 Open and Empty Penny-Shaped Cracks

Specification of (3.15) for open and empty penny-shaped cracks, characterized by $\mathbf{C}_c = 0$, yields

$$C_{\text{hom}}^{(MT)} = f_m C_m \left\{ f_m \mathbf{I} + f_c \frac{1}{\theta^*} \int_0^{\theta^*} [\mathbf{I} - \mathcal{S}_c^m [n(\theta)]]^{-1} d\theta \right\}^{-1} \quad (3.16)$$

Based on (2.14), the crack volume fraction reads as

$$f_c = NV_c = N \frac{4\pi}{3} a^2 c \quad (3.17)$$

with N denoting the number of cracks per unit volume.

As regards microcracking under uniaxial tension, we deal with RVEs comprising penny-shaped cracks of identical orientation (Fig. 3.1b) with $\mathbf{n} = \mathbf{n}$ ($\theta=0$). The corresponding stiffness estimate is obtained from specification of (3.16) for the limit case $\theta^* \rightarrow 0$. When also considering (3.17) and $f_m = 1 - f_c$, it reads as

$$C_{\text{hom}}^{(MT)} = (1 - f_c) C_m \left\{ (1 - f_c) \mathbf{I} + f_c [\mathbf{I} - \mathcal{S}_c^m [n(\theta=0)]]^{-1} \right\}^{-1} \quad (3.18)$$

where the non-vanishing components of $\mathbb{S}_c^m[n(\theta=0)]$, which are function of the crack aspect ratio c/α , are given in (2.12). For the limit case of sharp open cracks, characterized by the crack aspect ratio tending to zero: $c/\alpha \rightarrow 0$, the stiffness estimate (3.18) reduces to [6, 7]

$$\mathbf{C}_{\text{hom}}^{(MT)} = \mathbf{C}_m \left(\mathbf{I} + \frac{4\pi}{3} Na^3 \mathbf{T} \right)^{-1} \quad (3.19)$$

Thereby, the tensor \mathbf{T} , introduced by Dormieux and Kondo [6, 7], is defined as

$$\mathbf{T} = \lim_{c/\alpha \rightarrow 0} \left\{ \frac{c}{a} \left[\mathbf{I} - \mathbb{S}_c^m[n(\theta=0)] \right]^{-1} \right\} \quad (3.20)$$

The non-vanishing components of \mathbf{T} , exhibiting the symmetries $\mathbf{T}_{ijkl} = \mathbf{T}_{jikl} = \mathbf{T}_{ijlk}$, read as [6, 7]

$$\begin{aligned} T_{3311} = T_{3322} &= \frac{4v_m(1-v_m)}{(1-2v_m)\pi}, & T_{3333} &= \frac{4(1-v_m)^2}{(1-2v_m)\pi}, \\ T_{1313} = T_{2323} &= \frac{2(1-v_m)}{(2-v_m)\pi}, \end{aligned} \quad (3.21)$$

As regards microcracking under axial compression (with and without lateral confinement), we consider cracks with normals \mathbf{n} , oriented perpendicular to the direction of loading, i.e. $\mathbf{n} \perp \mathbf{e}_1$. The corresponding stiffness estimate is obtained from specification of (3.16) for $\theta^* = \pi$. When also considering (3.17) and $f_m = 1 - f_c$, this yields

$$\mathbf{C}_{\text{hom}}^{(MT)} = (1-f_c) \mathbf{C}_m \left\{ (1-f_c) \mathbf{I} + f_c \frac{1}{\pi} \int_0^\pi \left[\mathbf{I} - \mathbb{S}_c^m[n(\theta)] \right]^{-1} d\theta \right\}^{-1} \quad (3.22)$$

The secant-stiffness estimates of (3.19) and (3.22) depend on the actual degree of damage within the RVE, described by the crack volume fraction f_c [see (3.22)] or Budiansky's crack density parameter Na^3 [see (3.19)], respectively. For $f_c = \text{const}$ or $Na^3 = \text{const}$, respectively, they describe the behavior of stationary (non-propagating) cracks. Estimation of the homogenized stiffness during microcrack propagation requires quantification of the evolution of f_c or Na^3 , respectively, i.e. a damage evolution law is needed, which is derived subsequently. To end up with a fully micromechanics-based damage model for brittle materials, we will consider onset of

cracking and crack propagation of every *single microcrack* embedded in a RVE containing many such cracks.

3.5 Linking Macroscopic Stresses to Single-Crack Related Crack Propagation Criteria

In the following, we describe a link between the single-crack related crack propagation criteria of Section 2 and the macroscopic stresses Σ imposed as uniform boundary conditions on a microcracked RVE. This link allows for investigation of the influence of the propagation of single cracks on the progressive reduction of the effective stiffness of a material comprising numerous propagating cracks. The key to this link is that both micro-mechanics and fracture-mechanics rely on matrix-inclusion problems (Figs. 2.3 and 2.1) dealing with a single crack embedded in an infinite matrix subjected to remote uniform loading: Zaoui's concentration procedure [39, 40, 41] provides a relation between the macroscopic strains \mathbf{E} (Fig. 3.1b) acting on the boundary of the RVE of a damaged material with numerous microcracks and the strains \mathbf{E}^∞ (Fig. 2.3) imposed (at infinity) on a matrix surrounding a single microcrack:

$$\mathbf{E}^\infty = \left[f_m \mathbf{I} + f_c \frac{1}{\theta^*} \int_0^{\theta^*} (\mathbf{I} + S_c^m [n(\theta)])^{-1} d\theta \right]^{-1} : \mathbf{E} \quad (3.23)$$

as follows from specification of (3.13) for $\mathbf{C}_c=0$. Setting the fictitious strains \mathbf{E}^∞ equal to the ones caused by Σ^∞ in the fracture mechanics problem of Fig. 2.1, i.e.

$$\mathbf{E}^\infty = \mathbf{C}_m^{-1} : \Sigma^\infty \quad (3.24)$$

establishes the aforementioned link between micromechanics and fracture-mechanics: (3.24), together with (3.23), allow for relating the remote stresses Σ^∞ “felt” by one single microcrack to the macroscopic strains \mathbf{E} prevailing on the RVE of the material with numerous microcracks. Additional consideration of (3.9) delivers the relation between Σ^∞ and the macroscopic stresses Σ acting on the RVE, reading, with $\mathbf{C}_{\text{hom}} = \mathbf{C}_{\text{hom}}^{(MT)}$ from (3.16), as

$$\Sigma^\infty = \frac{\Sigma}{f_m} = \frac{\Sigma}{1-f_c} \quad (3.25)$$

Particularly, (3.25) provides the link between the RVE-related quantity Σ and the fracture-mechanics related quantity Σ^∞ , playing the governing role in the criteria for single-crack propagation (2.2)-(2.5), see also (2.17), (2.20), and (2.23).

4 Effective Stress-Strain Behavior of Microcracked Brittle Materials – Assessment of Griffith’s Energy Release Rate Criterion

While the stiffness estimates (3.19) and (3.22) define the effective stress-strain behavior in the elastic regime, the link (3.25), together with single-crack related propagation criteria (2.2)-(2.4) mark the limit of this regime, and give access to the effective stress-strain behavior during stable mode-I-type propagation of the microcracks; i.e. during evolving damage of the material defined on the RVE. Thereby, they relate the macroscopic stress imposed on the RVE to the characteristics of the microcracks inside the RVE (i.e. α , c , and N).

Comparison of model predictions with the behavior of brittle materials observed in corresponding experiments will allow for assessing the performance of Griffith's energy release rate criterion in the framework of mode I type microcracking in brittle materials.

4.1 Uniaxial Macroscopic Tension – Tensile Mode I Micro-cracking

To study tensile microcracking, we consider a RVE (Fig. 3.1b) subjected to the macroscopic uniaxial tensile stress state

$$\Sigma = \Sigma_{33} e_3 \otimes e_3, \quad \Sigma_{33} > 0 \quad (4.1)$$

In order to represent the crack patterns observed in corresponding experiments [33, 34], we consider cracks of identical orientation with normals \mathbf{n} (Fig. 2.2) pointing in the direction of loading ($\mathbf{n} = e_3$ in Fig. 3.1b). Consideration of sharp cracks ($c = 0$), as relevant approximation for slightly opened cracks under tensile mode-I-type loading (see (2.17) and discussion below), implies $f_c = 0$ [see (3.17)], and, hence, $\Sigma^\infty = \Sigma$ [see (3.25)]. Therefore, the expression of G_I for every single of the many microcracks embedded in the considered RVE follows from replacing Σ_{33}^∞ by Σ_{33} in (2.17), i.e.

$$G_I = \frac{4\Sigma_{33}^2 a}{\pi} \left(\frac{1 - \nu_m^2}{E_m} \right) \quad (4.2)$$

The relation (4.2), together with the crack propagation criteria (2.2)-(2.4), allows for testing whether or not macroscopic loading Σ_{33} on the RVE of the microcracked material leads to propagation of the individual microcracks in the material. If the criterion (2.2) is satisfied:

$$G_I = \frac{4\Sigma_{33}^2 a}{\pi} \left(\frac{1 - \nu_m^2}{E_m} \right) < G_c \quad (4.3)$$

the microcracks do not propagate, i.e. $a = a_{ini} = \text{const.}$, where a_{ini} denotes the initial radius of the penny-shaped cracks. The damaged material behaves linear elastically, according to the specification of (3.9) for (3.19) and (4.1)

$$\Sigma_{33} = E_m \left[1 + \frac{16}{3} N a^3 (1 - \nu_m^2) \right]^{-1} E_{33} \quad (4.4)$$

If, however, (2.3) and (2.4) are satisfied:

$$G_I = \frac{4\Sigma_{33}^2 a}{\pi} \left(\frac{1 - \nu_m^2}{E_m} \right) = G_c \quad (4.5)$$

the cracks propagate such that the crack radius increases ($da > 0$) while the equality (4.5) remains satisfied. This renders the uniaxial macroscopic stress Σ_{33} as a function of the crack radius a .

$$\Sigma_{33}(a) = \sqrt{\frac{G_c E_m \pi}{4a(1 - \nu_m^2)}} \quad (4.6)$$

When assuming that $N = \text{const.}$ during crack propagation, the corresponding strain $E_{33} = E_{33}(a)$ follows from substitution of (4.6) into the stress-strain relation (4.4),

$$E_{33}(a) = \sqrt{\frac{G_c \pi}{4a E_m (1 - \nu_m^2)}} \left[1 + \frac{16}{3} N a^3 (1 - \nu_m^2) \right] \quad (4.7)$$

(4.6) and (4.7) describe stress-strain relations in parameter form, with the crack radius a as the parameter, see descending crack propagation paths in Fig. 4.1a and 4.2b.

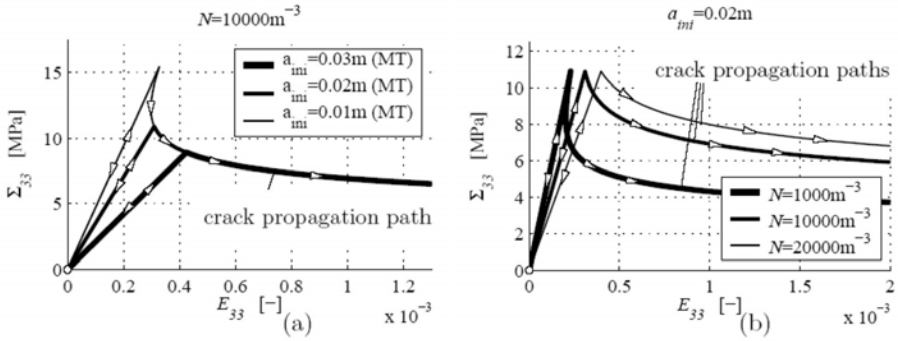


Fig. 4.1. Effective stress-strain behavior in uniaxial tension of a microcracked brittle material (Fig. 3.1b), predicted by combined fracture-micromechanics model on the basis of material constants of Silurian sedimentary rock (Table 4.1): (a) effect of initial crack radius α_{ini} and (b) effect of number of cracks per unit volume, N

Table 4.1. Material constants, uniaxial tensile strength, and uniaxial compressive strength of Silurian sedimentary rock [14]

E_m [GPa]	ν_m [-]	K_{Ic} [MPa \sqrt{m}]	G_c [J/m ²]	Σ_{tu} [MPa]	$ \Sigma_{cu} $ [MPa]
49.4	0.24	1.74	57.76	13.6	158

(4.6) and (4.7) propose that materials *with the same number of differently sized* microcracks exhibit identical softening paths in the Σ_{33} - E_{33} space (Fig. 4.1a). However, the peak stresses (theoretical tensile strengths) of such materials decrease with increasing initial crack radius α_{ini} (Fig. 4.1a). On the other hand, materials *with different numbers of equally sized* microcracks exhibit identical peak stresses (Fig. 4.1b). Related softening paths are, however, the steeper the fewer cracks are contained in the RVE (Fig. 4.1b). Summarizing these results, effective strain-softening under uniaxial tension can be, at least qualitatively, predicted by a combined fracture micromechanics model based on Griffith's energy release rate criterion.

4.2 Uniaxial Macroscopic Compression – Axial Splitting

To study axial splitting, we consider a RVE subjected to the macroscopic uniaxial compressive stress state

$$\Sigma = \Sigma_{11} e_1 \otimes e_1, \quad \Sigma_{11} < 0 \quad (4.8)$$

In order to represent the crack patterns observed in corresponding experiments [35, 36, 37], we consider cracks with normals \mathbf{n} (Fig. 2.2) perpendicular to the direction of loading ($\mathbf{n}(\theta) \perp e_1 \Leftrightarrow \theta \in [0, \pi]$ in Fig. 2.4), i.e. we introduce microcracks with orientations axisymmetrically distributed with respect to the axis of loading, the x_1 axis in Fig. 3.2. Opposed to the situation in Subsection 4.1, consideration of the crack opening ($c \neq 0$) is mandatory for appropriate determination of the energy release (see (2.20) and discussion below), even if the crack is only slightly opened. Accordingly, the released energy \mathcal{E} for every single of many axisymmetrically distributed microcracks embedded in the considered RVE follows from insertion of (3.25), relating Σ_{11}^∞ to $\Sigma_{11}/(1-f_c)$, into (2.19), yielding

$$\mathcal{E} = \frac{2\pi a^3 \Sigma_{11}^2}{3(1-f_c)^2 E_m} \left(\frac{c}{a}\right) + \mathcal{O}\left(\frac{c}{a}\right)^2 \quad (4.9)$$

Calculation of G_I requires derivation of \mathcal{E} with respect to α [see (2.6)]. Thereby, the dependence of f_c on α [see (3.17)] must be taken into account, which yields

$$G_I = \frac{2a \Sigma_{11}^2}{3E_m} \left(\frac{c}{a}\right) + \mathcal{O}\left(\frac{c}{a}\right)^2 \quad (4.10)$$

Since $c/\alpha \ll 1$, quadratic and higher-order terms in c/α may be neglected, rendering G_I as

$$G_I = \frac{2c \Sigma_{11}^2}{3E_m} \quad (4.11)$$

The relation (4.11), together with the crack propagation criteria (2.2)-(2.4), allows for testing whether or not macroscopic loading Σ_{11} on the RVE of the microcracked material leads to propagation of the individual microcracks in the material. If the criterion (2.2) is satisfied:

$$G_I = \frac{2c \Sigma_{11}^2}{3E_m} < G_c \quad (4.12)$$

the cracks do not propagate, i.e. $\alpha = \alpha_{ini} = \text{const.}$, and the damaged material behaves linear elastically, according to the specification of (3.9) for (3.22) and (4.8):

$$\Sigma_{11} = E_m \left(1 + \frac{4\pi}{3} N a^2 c \right)^{-1} E_{11} \quad (4.13)$$

If, however, (2.3) and (2.4) are satisfied:

$$G_I = \frac{2c\Sigma_{11}^2}{3E_m} = G_c \quad (4.14)$$

the cracks propagate such that the crack radius increases ($da > 0$) while the equality (4.14) remains satisfied. Since (4.14) does not depend on α , it follows that stable crack propagation (increase of α) requires a constant macroscopic stress: $\Sigma_{11} = \text{const.}$ (Fig. 4.2). This is a remarkable difference to macroscopic uniaxial tension where stable microcrack propagation requires a decreasing loading of the RVE (Figs. 4.1a and 4.1b). (4.14) delivers the macroscopic stress Σ_{11} associated to microcrack propagation as

$$\Sigma_{11}(a) = -\sqrt{\frac{3G_c E_m}{2c}} = \text{const.} \quad (4.15)$$

When assuming that $N = \text{const}$ during crack propagation, the corresponding strain $E_{11} = E_{11}(a)$ follows from substitution of (4.15) into the stress-strain relation (4.13),

$$E_{11}(a) = -\sqrt{\frac{3G_c E_m}{2c}} \left(1 + \frac{4\pi N a^2 c}{3} \right) \quad (4.16)$$

(4.15) and (4.16) describe stress-strain relations in parameter form, with the crack radius α as the parameter. Related crack propagation paths yield a stress plateau in the Σ_{11} - E_{11} space (Fig. 4.2). Thereby, the absolute value of the bearable compressive stress increases with decreasing crack half opening width (Fig. 4.2). However, Griffith's energy release rate criterion does not predict strain-softening under uniaxial compression. In this line, the experimentally observed strain-softening behavior [36] would have to be caused by failure effects after the sample has split up into many slender "columns", i.e. by buckling and bending and/or tilting and sliding of these columns. Experimental observations of [38] foster this argumentation: The characteristic stress strain curve referring to unconfined axial compression shows, before the stress drop beyond the peak load, a region of almost vanishing inclination of the stress strain curve, i.e. a quasi-plateau, such as predicted by our model. In this region of the stress strain curve, a *large*

number of isolated fractures are formed, and fracturing clearly predominates along the direction of loading [38].

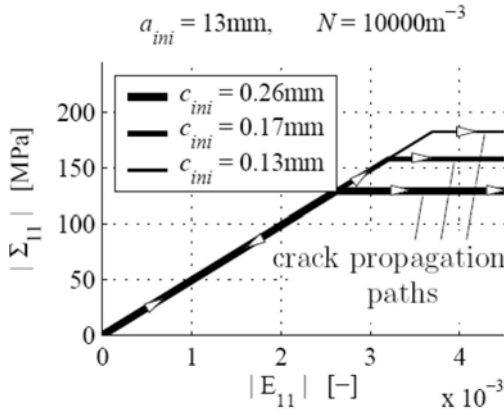


Fig. 4.2. Effective stress-strain behavior in uniaxial compression of a microcracked brittle material (Figs. 3.2b and 3.2c), predicted by combined fracture-micromechanics model on the basis of material constants of Silurian sedimentary rock (Table 4.1): effect of initial crack half opening width c_{ini}

4.3 Determination of the Initial Microcrack Radius and of the Initial Microcrack Half-Opening from the Uniaxial Tensile Strength and the Uniaxial Compressive Strength

By example of brittle Silurian sedimentary rock [14] (Table 4.1), experimentally determined uniaxial strength values in tension and compression, Σ_{tu} and Σ_{cu} , will be used for identification of the (initial) geometric properties of the microcracks: The initial crack radius a_{ini} follows from setting $\Sigma_{33} \equiv \Sigma_{tu}$ and in (4.5) and solving the resulting expression for a , yielding

$$a_{ini} = \frac{\pi E_m G_c}{4 \Sigma_{tu}^2 (1 - \nu_m^2)} = 12.86 \text{ mm} \tag{4.17}$$

according to the material constants listed in Table 4.1. The initial crack half-opening c_{ini} follows from setting the stress $\Sigma_{11} \equiv \Sigma_{cu}$ in (4.14) and solving the resulting expression for c , yielding

$$c_{ini} = \frac{3 E_m G_c}{2 \Sigma_{cu}^2} = 0.17 \text{ mm} \tag{4.18}$$

according to the material constants listed in Table 4.1. Remarkably, (4.17) and (4.18) imply that the ratio between the uniaxial compressive strength and the uniaxial tensile strength depends on the Poisson's ratio of the matrix and on the initial crack aspect ratio c_{ini}/a_{ini} (Fig. 4.3).

$$\frac{\Sigma_{cu}}{\Sigma_{tu}} = -\sqrt{\frac{6(1-v_m^2)}{\pi} \left(\frac{c_{ini}}{a_{ini}}\right)^{-1}} \quad (4.19)$$

This is a key result of the combined fracture-micromechanics approach of Subsection 3.5. According to (4.17) and (4.18), the Silurian sedimentary rock, described in [14], is characterized by an initial microcrack aspect ratio equal to $c_{ini}/a_{ini} = 1/75$.

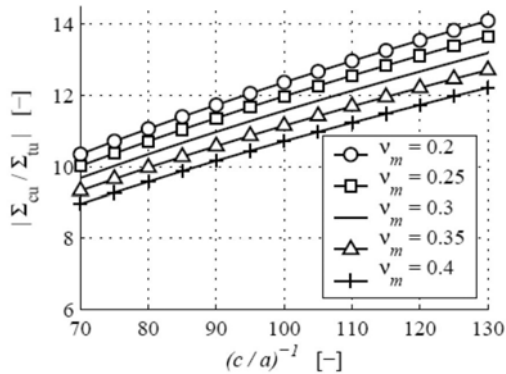


Fig. 4.3. Ratio between the uniaxial compressive strength Σ_{cu} and the uniaxial tensile strength Σ_{tu} as a function of the crack aspect ratio c/α and Poisson's ratio of the matrix, v_m , predicted by the combined fracture-micromechanics approach

$c_{ini} = 0.17\text{mm}$ may appear as quite large, however, one should take into account that c_{ini} is the half opening of an *equivalent penny-shaped crack*. Real crack surfaces in rocks are not plane but have some kind of micro-roughness (Fig. 4.4), and the initial opening of real cracks might be well below 0.17mm. If such a crack is modeled by an equivalent (ideal) penny-shaped microcrack, the initial opening of the latter accounts for both the microroughness and the initial opening of the real crack (Fig. 4.4). Therefore, modeled crack openings are always larger than the real ones.



Fig. 4.4. Representation of (a) a realistic crack shape with microroughness by (b) an equivalent elliptic crack

4.4 Confined Macroscopic Compression – Axial Splitting

To study axial splitting under confined compression, we consider a RVE subjected to the macroscopic triaxial compressive stress state

$$\Sigma = \Sigma_{11}e_1 \otimes e_1 + \Sigma_{33}(e_2 \otimes e_2 + e_3 \otimes e_3), \quad \Sigma_{11} \leq 0, \quad \Sigma_{33} \leq 0 \quad (4.20)$$

where Σ_{11} is the predominant axial compressive stress and Σ_{33} is the lateral confinement pressure. In order to represent the crack patterns observed in corresponding experiments [35, 36, 37], we again consider cracks with axisymmetric orientation and non-vanishing crack half-opening widths, $c \neq 0$, as in Subsection 4.2 (Fig. 3.2). The released energy \mathcal{E} for every single of many axisymmetrically distributed microcracks embedded in the considered RVE follows from insertion of (3.25), relating Σ_{11}^∞ to $\Sigma_{11}/(1-f_c)$ and $\Sigma_{33}/(1-f_c)$, into (2.22), yielding

$$\begin{aligned} \mathcal{E} = & \frac{8a^3\Sigma_{33}^2}{3(1-f_c)^2} \frac{1-v_m^2}{E_m} + \frac{\pi a^3}{3} \left[\frac{\Sigma_{33}^2(1+v_m+4v_m^2-4v_m^3)}{E_m} + \right. \\ & \left. + \frac{2\Sigma_{11}^2 - 2\Sigma_{11}\Sigma_{33}(1+3v_m-2v_m^2)}{E_m(1-f_c)^2} \right] \left(\frac{c}{a} \right) + O\left(\frac{c}{a} \right)^2 \end{aligned} \quad (4.21)$$

Calculation of G_I requires derivation of \mathcal{E} with respect to a [see (2.6)]. Thereby, the dependence of f_c on a [see (3.17)] must be taken into account:

$$\begin{aligned} \mathcal{G} = & \frac{4\Sigma_{33}^2 a}{\pi} \frac{1-v_m^2}{E_m} \left[1 + \frac{40\pi N a^3}{9} \left(\frac{c}{a} \right) \right] + \frac{a}{3} \left[\frac{\Sigma_{33}^2(1+v_m+4v_m^2-4v_m^3)}{E_m} + \right. \\ & \left. + \frac{2\Sigma_{11}^2 - 2\Sigma_{11}\Sigma_{33}(1+3v_m-2v_m^2)}{E_m} \right] \left(\frac{c}{a} \right) + O\left(\frac{c}{a} \right)^2 \end{aligned} \quad (4.22)$$

In order to assess whether or not Griffith's energy release rate criterion has the potential to satisfactorily predict material damage under confined

compression, it is useful to consider onset of microcracking, by inserting G_I from (4.22) into the condition (2.3), yielding

$$\begin{aligned} \mathbb{G} = & \frac{4\Sigma_{33}^2 a}{\pi} \frac{1-v_m^2}{E_m} \left[1 + \frac{40\pi N a^3}{9} \left(\frac{c}{a} \right) \right] + \frac{a}{3} \left[\frac{\Sigma_{33}^2 (1+v_m+4v_m^2-4v_m^3)}{E_m} + \right. \\ & \left. + \frac{2\Sigma_{11}^2 - 2\Sigma_{11}\Sigma_{33} (1+3v_m-2v_m^2)}{E_m} \right] \left(\frac{c}{a} \right) = \mathbb{G}_c \end{aligned} \quad (4.23)$$

when having neglected the higher-order terms $O(c/a)^2$ in (4.22). Solving (4.23) for Σ_{11} delivers the predominant axial compressive stress at onset of microcracking, denoted by Σ_{11}^{cr} , as a function of the lateral confinement pressure Σ_{33} .

$$\Sigma_{11}^{cr} = -\sqrt{\frac{3G_c E_m}{2a} - \frac{6\Sigma_{33}(1-v_m^2)}{\pi} \left(\frac{c}{a} \right)^{\frac{1}{2}} + \frac{\Sigma_{33}(1+3v_m-2v_m^2)}{2}} + O\left(\frac{c}{a} \right)^{\frac{1}{2}} \quad (4.24)$$

Evaluation of (4.24) for the material parameters of Table 4.1 and for α_{ini} and c_{ini} according to (4.17) and (4.18), proposes that an increase of lateral confinement pressure from zero up to 1% of Σ_{cu} increases the predominant axial compressive stress at onset of axial splitting, but only by less than 1% (Fig. 4.5). Further increase of the confinement pressure is predicted to *decrease* the predominant axial compressive stress at onset of axial splitting, which contradicts experimental findings.

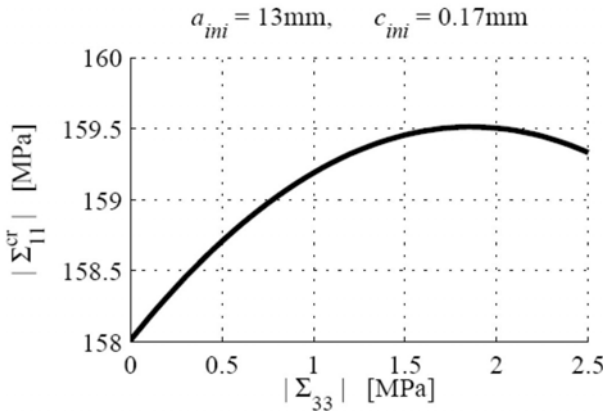


Fig. 4.5. Predominant axial compressive stress at onset of microcracking as a function of the lateral confinement pressure, predicted by combined fracture-micro-

mechanics model on the basis of material constants of Silurian sedimentary rock (Table 4.1)

This contradiction is due to the fact that we do not account for the sign of the microstress component σ_{zz} in the vicinity of the crack edge (Fig. 2.1). In case of uniaxial compression parallel to the crack plane, these stresses are tensile. If confinement stresses orthogonal to the crack plane are additionally applied, the initially tensile stresses σ_{zz} become compressive, already at very small confinement pressures. Consequently, crack propagation becomes impossible and (4.23) as well as (4.24) are no longer valid. Hence, the presented approach proposes that, under such confinements, brittle failure is not associated with mode I propagation of cracks in the direction of predominant compressive axial loading, but with propagation of closed, inclined cracks. This shear mode type of crack propagation, however, is not the topic of the present paper. Summarizing these results, Griffith's crack propagation criterion based on energy release rate is seen to be applicable also to compressive stress states, but it is mandatory to account for the sign of the normal stresses in the vicinity of the crack edge, acting in the crack normal direction.

5 Conclusions

The aim of this paper was to assess the potentials and the limitations of Griffith's energy release rate criterion to predict effective stress-strain behavior of brittle materials damaged by microcracks propagating in cracking mode I. For this purpose, Griffith's energy release rate criterion, related to a single penny-shaped crack embedded in an infinite matrix subjected to remote uniform stresses, was combined with stiffness estimates for RVEs of damaged (microcracked) materials taken from continuum micromechanics. As regards uniaxial tension, this combination allows for modeling macroscopic strain-softening as a result of propagation of microcracks, i.e. as a microstructural effect. Hence, Griffith's energy release rate criterion has the potential to predict, at least qualitatively, the behavior of microcracked materials under uniaxial tension. Thereby, the microcracks may be modeled as sharp cracks (as commonly introduced in fracture mechanics), since sharp cracks release (during tensile crack propagation) an amount of energy similar to that released by slightly opened cracks. As for uniaxial compression, however, the non-vanishing opening width of the microcracks must be taken into account, even though it is commonly by orders of magnitude smaller than the in-plane crack

diameter. There, the described combination of fracture and micromechanics proposes that macroscopic axial splitting under uniaxial compression is characterized by a constant stress level. Remarkably, the proposed model reveals that the ratio between the uniaxial tensile strength and the uniaxial compressive strength is a function of the crack aspect ratio, i.e. the ratio between the crack half-opening width and the crack radius. Therefore, the combined fracture-micromechanics approach accounts for the basic strength properties of brittle materials simply by introducing geometric properties of the microcracks within the RVE. However, Griffith's energy release rate criterion does not have the potential to predict effective strain-softening under uniaxial compression. The latter would have to be explained by buckling or tilting of slender columns after disintegration of the material. As a further limitation, Griffith's energy release rate criterion alone was found to be insufficient for prediction of axial splitting caused by confined compression: A complementary stress criterion accounting for the sign of the microstresses in the vicinity of the crack edge would be necessary.

References

1. Z.P. Bažant and J. Planas. *Fracture and Size Effect in Concrete and Other Quasibrittle Materials*. CRC Press, Boca Raton and London, 1998.
2. Y. Benveniste. A new approach to the application of Mori-Tanaka's theory in composite materials. *Mechanics of Materials*, 6(2):147{157, 1987.
3. Y. Benveniste, G.J. Dvorak, and T. Chen. On diagonal and elastic symmetry of the approximate effective stiffness tensor of heterogeneous media. *Journal of the Mechanics and Physics of Solids*, 39(7):927{946, 1991.
4. R.D. Bradshaw, F.T. Fisher, and L.C. Brinson. Fiber waviness in nanotube-reinforced polymer composites - ii: modeling via numerical approximation of the dilute strain concentration tensor. *Composites Science and Technology*, 63(11):1705-1722, 2003.
5. V. Deudé, L. Dormieux, D. Kondo, and S. Maghous. Micromechanical approach to nonlinear poroelasticity: application to cracked rock. *Journal of Engineering Mechanics (ASCE)*, 128(8):848{855, 2002.
6. L. Dormieux and D. Kondo. Approche micromécanique du couplage perméabilité-endommagement [Micromechanical approach to the coupling between permeability and damage]. *C. R. Mécanique*, 332(2):135{140, 2004. In French.
7. L. Dormieux and D. Kondo. Poroelasticity and damage theory for saturated cracked media. In L. Dormieux and F.-J. Ulm, editors, *Applied micromechanics of porous media*, volume 480 of *CISM Course and Lecture Notes*, pages 153-186. Springer Wien New York, 2005.

8. A.V. Dyskin. Self-similar crack patterns induced by spatial stress fluctuations. *Fatigue and Fracture of Engineering Materials and Structures*, 25(2):187-200, 2002.
9. J.D. Eshelby. The determination of the elastic field of an ellipsoidal inclusion, and related problems. *Proceedings of the Royal Society of London A*, 241:376-396, 1957.
10. A.G. Evans and Y. Fu. Some effects of microcracks on the mechanical properties of brittle solids - II. Microcrack toughening. *Acta Metallurgica*, 33(8):1515-1523, 1985.
11. F.T. Fisher, R.D. Bradshaw, and L.C. Brinson. Fiber waviness in nanotube-reinforced polymer composites - i: Modulus predictions using effective nanotube properties. *Composites Science and Technology*, 63(11):1689-1703, 2003.
12. A.A. Griffith. The phenomena of rupture and flow in solids. *Philosophical Transactions, Series A*, 221:163-198, 1920.
13. D. Gross and Th. Seelig. *Bruchmechanik mit einer Einführung in die Mikro-mechanik [Fracture mechanics with an introduction to micromechanics]*. Springer, Berlin, 3rd edition, 2001. In German.
14. K.L. Gunsallus and F.H. Kulhawy. A comparative evaluation of rock strength measures. *International Journal of Rock Mechanics and Mining Sciences*, 21(5):233-248, 1984.
15. Z. Hashin. Analysis of composite materials - a survey. *Journal of Applied Mechanics*, 50(3):481-505, 1983.
16. Z. Hashin. The differential scheme and its application to cracked materials. *Journal of the Mechanics and Physics of Solids*, 36(6):719-734, 1988.
17. R. Hill. Elastic properties of reinforced solids. *Journal of the Mechanics and Physics of Solids*, 11(5):357-372, 1963.
18. H. Horii and S. Nemat-Nasser. Overall moduli of solids with microcracks: load-induced anisotropy. *Journal of the Mechanics and Physics of Solids*, 31(2):155-171, 1983.
19. H. Horii and S. Nemat-Nasser. Brittle failure in compression: splitting, faulting and brittle-ductile transition. *Philosophical Transactions of the Royal Society of London, Series A*, 319:337-374, 1986.
20. J.W. Hutchinson. Crack tip shielding by micro-cracking in brittle solids. *Acta Metallurgica*, 35(7):1605-1619, 1987.
21. G.R. Irwin. Onset of fast crack propagation in high strength steel and aluminum alloys. *Segamore Research Conference Proceedings*, 2:289-305, 1956.
22. M. Kachanov. Effective elastic properties of cracked solids: critical review of some basic concepts. *Applied Mechanics Reviews (ASME)*, 45(8):304-335, 1992.
23. M. Kachanov and I. Sevostianov. On quantitative characterization of microstructures and effective properties. *International Journal of Solids and Structures*, 42(2):309-336, 2005.
24. N. Laws. On interfacial discontinuities in elastic composites. *Journal of Elasticity*, 5(3-4):227-335, 1975.

25. N. Laws. A note on penny-shaped cracks in transversely isotropic materials. *Mechanics of Materials*, 4(2):209-212, 1985.
26. N. Laws and G.J. Dvorak. The effect of fiber breaks and aligned penny-shaped cracks on the stiffness and energy release rates in unidirectional composites. *International Journal of Solids and Structures*, 23(9):1269-1283, 1987.
27. T. Mura. *Micromechanics of defects in solids*. Martinus Nijhoff Publishers, Dordrecht, 1987.
28. M. Ortiz. Microcrack coalescence and macroscopic crack growth initiation in brittle solids. *International Journal of Solids and Structures*, 24(3):231-250, 1988.
29. V. Pensée, D. Kondo, and L. Dormieux. Micromechanical analysis of anisotropic damage in brittle materials. *Journal of Engineering Mechanics (ASCE)*, 128(8):889-897, 2002.
30. J.R. Ponte Castañeda, P. Willis. The effect of spatial distribution on the effective behavior of composite materials and cracked media. *Journal of the Mechanics and Physics of Solids*, 43(12):1919-1951, 1995.
31. J. Salençon. *Handbook of Continuum Mechanics*. Springer Berlin Heidelberg, 2001.
32. V.P. Smyshlyaev and J.R. Willis. Effective relations for nonlinear dynamics of cracked solids. *Journal of the Mechanics and Physics of Solids*, 44(1):49-75, 1996.
33. J.G.M. van Mier and M.R.A. van Vliet. Uniaxial tension tests for the determination of fracture parameters of concrete: state of the art. *Engineering Fracture Mechanics*, 69(2):235-247, 2002.
34. J.G.M. van Mier and M.R.A. van Vliet. Influence of microstructure of concrete on size/scale effects in tensile fracture. *Engineering Fracture Mechanics*, 79(16):2281-2306, 2003.
35. M.R.A. van Vliet and J.G.M. van Mier. Experimental investigation of concrete fracture under uniaxial compression. *Mechanics of Cohesive-Frictional Materials*, 1:115-127, 1996.
36. J. Vardoulakis, J.F. Labuz, E. Papamichos, and J. Tronvoll. Continuum fracture mechanics of uniaxial compression on brittle materials. *International Journal of Solids and Structures*, 35(31-32):4313-4335, 1998.
37. E.Z. Wang and N.G. Shrive. Brittle fracture in compression: mechanisms, models, criteria. *Engineering Fracture Mechanics*, 52(6):1107-1126, 1995.
38. W.R. Wawersik and C. Fairhurst. A study of brittle rock fracture in laboratory compression experiments. *International Journal of Rock Mechanics and Mining Science & Geomechanics Abstract*, 7(5):561-575, 1970.
39. A. Zaoui. *Matériaux hétérogènes et composites [Heterogeneous materials and composites]*. Lecture Notes. Ecole Polytechnique, Paris, France, 1997. In French.
40. A. Zaoui. Structural morphology and constitutive behavior of microheterogeneous materials. In P. Suquet, editor, *Continuum Micromechanics*, pages 291-347, Wien, 1997. Springer.

41. A. Zaoui. Continuum micromechanics: Survey. *Journal of Engineering Mechanics*, ASCE, 128(8):808-816, 2002.

Modeling the Influence of Pressure and Moisture Content on the Disintegration of Weathered Rockfill Materials

E. Bauer¹, K. Kast², S.F. Tanton¹, W. Cen³

¹ Institute of Applied Mechanics,
Graz University of Technology,
Graz, Austria

² Consulting Geotechnical Engineering ICOLD,
Germany

³ Institute of Hydraulic Engineering,
Hohai University,
Nanjing,
P.R. China

Summary

In this paper the essential mechanical behavior of rockfill materials is modeled using a hypoplastic continuum approach. Critical states are included in the model for large shearing. With respect to a pressure dependent relative density the model can capture the essential mechanical properties of initially loose and dense granular materials with a single set of constants. While the calibration and application of hypoplastic models has already been extensively investigated for fine-grained materials like sand and powders, the present application to weathered rockfill materials is a first attempt to describe coarse-grained materials with a low and decreasing grain hardness. Particular attention is paid to modeling the influence of the initial density, the pressure and the moisture content of weathered broken rock on the incremental stiffness. An increase of the compressibility and a decrease of the limit void ratios with an increase of the moisture content of the grains is modeled in a simplified manner using only a moisture dependent granular hardness. The comparison of the numerical simulations of isotropic compression tests and triaxial compression test with experiments shows that the model captures the essential properties of weathered rockfill materials for both dry and water saturated grains. The

possibility of spontaneous shear band bifurcation under plane strain compression is analyzed and discussed for different initial densities.

1 Introduction

The mechanical behavior of rockfill materials is mainly determined by the grain hardness, the grain shape, the grain size distribution, the packing density, the orientation of contact planes, the stress state and the loading history. Stiffness and shear strength are influenced by the pressure level, the packing density and the rate of deformation and are therefore not material constants, e.g. [12]. The mechanical behavior of broken rock is different for unweathered or weathered grains. The degree of geological disintegration, i.e. by chemical weathering or by the intensity and the orientation of micro-cracks, has a significant influence on the granular hardness and as a consequence on the evolution of grain abrasion, grain breakage and grain size distribution. Depending on the state of weathering the propagation of micro-cracks due to water-induced stress corrosion can be strongly influenced by the moisture content of the grains [24]. Under higher stress levels the disintegration of grains can be accelerated by moisture, which leads to a reduction of the resistance to compaction and shearing [19, 20, 23].

The focus of the present paper is on modeling the mechanical behavior of broken rock materials using a hypoplastic continuum approach. In hypoplasticity the evolution equation for the stress tensor is formulated with a nonlinear isotropic tensor-valued function depending on the current state quantities and the rate of deformation. Unlike the classical concept of elasto-plasticity no decomposition of the deformation into elastic and plastic parts is needed in hypoplasticity [13, 21]. In order to model inelastic material properties the rate of deformation tensor is incorporated in the constitutive equation in a nonlinear formulation. With a pressure dependent density factor the influence of pressure and density on the incremental stiffness, the peak friction angle and the dilatancy can be modeled for an initially loose or dense state using a single set of constants [2, 15, 33, 34]. Limit states or so-called critical states are included in the constitutive equation for a simultaneous vanishing of the stress rate and volume strain rate. Originally hypoplastic material models were developed and calibrated for dry and cohesionless granular materials like sand. A comprehensive historical review can be found for instance in Wu and Kolymbas [37], Bauer and Herle [6].

While in the hypoplastic model by Gudehus [15] and Bauer [2] for granular materials with unweathered grains the so-called granular hardness is assumed to be constant, an extension of this version with a granular hardness depending on the moisture content is discussed for applications to weathered broken rock materials in the present paper. Herein the granular hardness is related to the grain assembly in the sense of a continuum description and does not mean the hardness of an individual grain. It is demonstrated that with the moisture content as an additional state variable the extended model captures the essential properties of weathered rockfill materials with a single set of constants for both dry and moisture grains. The model is calibrated for a weathered broken granite and the results obtained from the numerical simulation of element tests are compared with experiments. Finally the possibility of a spontaneous shear band bifurcation under plane strain compression is analyzed for different initial densities and for dry and wet conditions.

Throughout the paper compression stresses and strains are defined as negative. Bold lower case, bold upper case and calligraphic letters denote vectors, tensors of second order and of fourth order, respectively. In particular, the identity tensor of second order is denoted by \mathbf{I} and the identity tensor of fourth order is denoted by \mathcal{I} . For vector and tensor components indices notation with respect to a rectangular Cartesian basis e_i ($i=1, 2, 3$) is used. Operations and symbols are defined as: $\mathbf{ab} = a_i b_i$, $\mathbf{Ab} = A_{ij} b_j \mathbf{e}_i$, $\mathbf{a} \otimes \mathbf{b} = a_i b_j \mathbf{e}_i \otimes \mathbf{e}_j$, $\mathbf{I} = \delta_{ij} \mathbf{e}_i \otimes \mathbf{e}_j$, $\mathcal{I} = \delta_{ik} \delta_{jl} \mathbf{e}_i \otimes \mathbf{e}_j \otimes \mathbf{e}_k \otimes \mathbf{e}_l$, $\mathbf{A} \otimes \mathbf{B} = A_{ij} B_{kl} \mathbf{e}_i \otimes \mathbf{e}_j \otimes \mathbf{e}_k \otimes \mathbf{e}_l$, $\mathbf{AB} = A_{ik} B_{kj} \mathbf{e}_i \otimes \mathbf{e}_j$, $\mathbf{I} : \mathbf{A} = A_{ii}$, and $\mathbf{A} : \mathbf{B} = A_{ijkl} B_{kl} \mathbf{e}_i \otimes \mathbf{e}_j$. Herein δ_{ik} denotes the Kronecker delta and the summation convention over repeated indices is employed. A superimposed dot indicates a time derivatives, i.e. $\dot{\mathbf{A}} = d\mathbf{A}/dt$, and the symbol $\llbracket \mathbf{A} \rrbracket$ denotes the jump of the field quantity \mathbf{A} at the discontinuity.

2 Granular Hardness and Pressure Dependent Limit Void Ratios

It is experimentally evident that for weathered rockfill materials the compressibility is higher for a wet than for a dry material as illustrated in Fig. (2.1). For a pre-compressed material under dry conditions (path A-B) a following wetting leads to an additional settlement along the path B-C. For a continuing loading the load-displacement curve (path C-D) follows the curve A-D obtained for an initially wet material, i.e. the memory of the

material of the pre-compaction under dry conditions is swept out if the load-displacement curve obtained for the wet material (path A-D) starts from the same initial density. In this context it is important to note that for different initial densities the compression curves are different for both dry and wet states of the material [20].

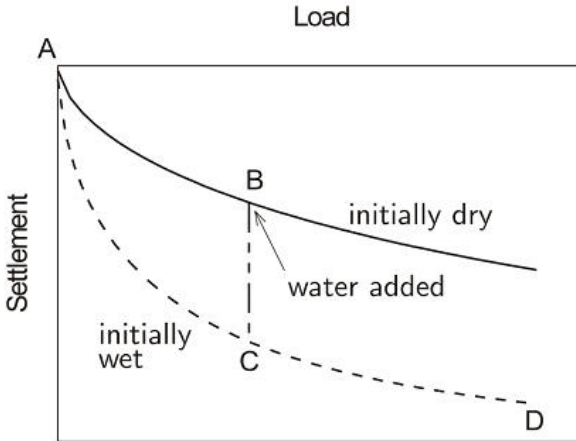


Fig. 2.1. Compression behavior of weathered broken rock in dry and wet states

In the following the compression behavior is first discussed for a dry granular material and modeled using a relation between the void ratio e and the mean pressure $p = -\mathbf{I}:\mathbf{T}/3$ where \mathbf{T} denotes the Cauchy stress tensor. The evaluation of numerous tests has shown that the compression behavior of various cohesionless materials can be approximated with the following exponential function [1]:

$$e = e_0 \exp \left[- \left(\frac{3p}{h_s} \right)^n \right]. \quad (2.1)$$

Herein the constant e_0 denotes the void ratio for $p \approx 0$, h_s has the dimension of stress and n is a dimensionless constant. The quantity of h_s is called granular hardness [15] which is related to the grain aggregate under isotropic compression and different from the hardness of an individual grain. Experimental investigations show that the quantity of h_s reflects the isotropic pressure where grain crushing becomes dominant.

More precisely, h_s represents the isotropic pressure $3p$ at which the compression curve in a semi-logarithmic representation shows the point of inflection while the exponent n is related to the inclination of the corresponding tangent (Figure 2.2a). For high pressures the void ratio in Eq. (2.1) tends to zero, which can be explained by grain plastification and grain crushing. Relation (2.1) is consistent within a very wide pressure range with the exception of states $p \rightarrow \infty$, which are characterized by a phase transition of the material.

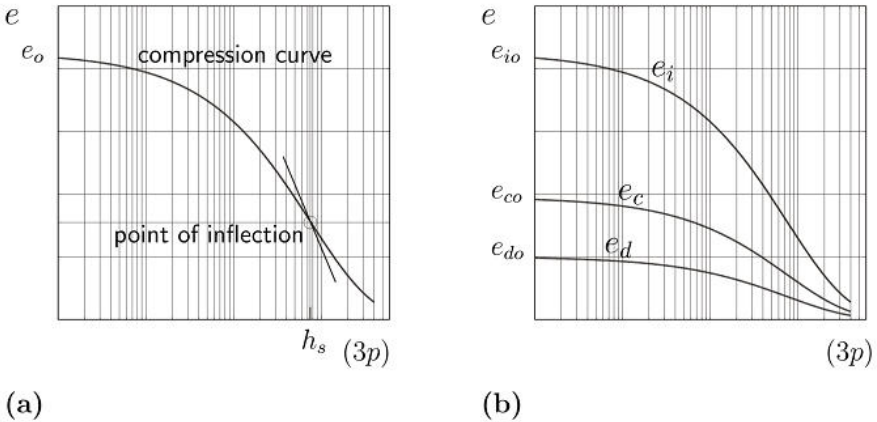


Fig. 2.2. (a) Isotropic compression relation (1) in a semi-logarithmic representation, (b) Pressure dependence of the maximum void ratio e_i , minimum void ratio e_d and critical void ratio e_c

For the evolution of the current void ratio e the assumption is made that the volume change of the solid material can be neglected. To this end, the rate of the void ratio can be directly derived from the mass balance, which yields:

$$\dot{e} = (1 + e) \mathbf{I} : \mathbf{D}. \tag{2.2}$$

Herein the rate of deformation \mathbf{D} is defined as the symmetric part of the velocity gradient of the grain skeleton. It can be noted that relation (2) is not restricted to granular materials with permanent rigid grains because the requirement of a constant solid volume is also fulfilled for a volume constant deformation of individual grains, grain crushing and abrasion.

Under the same pressure cohesionless granular materials can show different packing densities of the grain assembly so that the void ratio can range between a maximum void ratio e_i and a minimum void ratio e_d . In order to represent the range of possible void ratios for a given granular material it is convenient to consider the so-called phase diagram of grain skeletons [16] as sketched in Figure (2.2b). Herein the limit void ratios e_i and e_d are pressure dependent and they decrease with an increase of the mean pressure p . The upper bound, e_i , can be related to an isotropic compression starting from the loosest possible skeleton with grain contacts, i.e. there exists no homogeneous deformation which goes beyond $e = e_i$. Values of e_d will be achieved by cyclic shearing with very low amplitudes and nearly fixed mean pressure. By contrast, large monotonic shearing leads to a stationary state, which is characterized by a constant stress and constant void ratio. The void ratio in such a limit state, which is called critical void ratio, e_c , is not a material constant. Experimental observations with sand specimens (e.g. [8]) indicate that the critical void ratio decreases with the pressure p . It was suggested by Gudehus [15] to postulate that the maximum void ratio e_i , the minimum void ratio e_d and the critical void ratio e_c decrease with the mean pressure according to

$$\frac{e_i}{e_{io}} = \frac{e_d}{e_{do}} = \frac{e_c}{e_{co}} = \exp\left[-\left(\frac{3p}{h_s}\right)^n\right], \quad (2.3)$$

where e_{io} , e_{do} , and e_{co} are the corresponding values for $p \approx 0$ as shown in Figure (2.2b).

In order to model the influence of disintegration of a stressed rockfill by a reaction with water a degradation of the granular hardness with an increase of the moisture content ω of the solid material is assumed in the following. To this end the constant granular hardness h_s in Eq.(2.3) is replaced by the moisture dependent quantity h_s^* , i.e. [7]

$$h_s^* = h_{so}\psi(\omega). \quad (2.4)$$

Herein h_{so} is the value of the granular hardness obtained for the dry material, i.e. h_{so} is related to $\psi = 1$, and $\psi(\omega) \leq 1$ denotes the disintegration factor depending on the moisture content ω of the grain

material. A lower value of h_s^* means a higher compressibility of the material as illustrated in Fig. (2.3a).

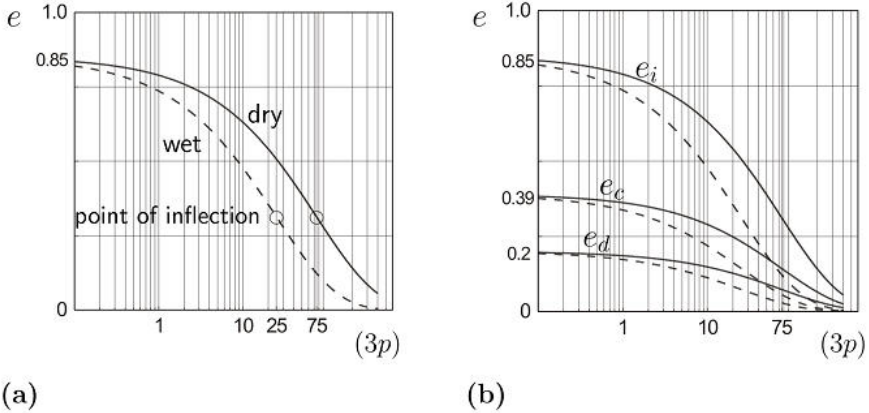


Fig. 2.3. Influence of the moisture content (solid curves: dry state, dashed curve: wet state) on (a) compression behavior, (b) limit void ratios

A specific representation of the scalar function $\psi(\omega)$ can be obtained by curve fitting experimental data. Due to the lack of experimental data for states with intermediary moisture contents, only a distinction between the granular hardness in the dry and the water-saturated state will be considered in the present paper. Then the disintegration factor $\psi(\omega)$ can be obtained by comparing the compression behavior for the dry material with the water saturated material using the compression relation (2.3) for the maximum void ratio e_i , i.e. $\psi(\omega)=1$ for the dry state and the value obtained for the water-saturated state must be $\psi(\omega)\leq 1$. It is obvious that with a degradation of the granular hardness according to relation (2.4) the pressure dependent limit void ratios and the critical void ratio obtained from relation (2.3) are lower for $\psi(\omega)\leq 1$ as illustrated in Fig. (2.3b).

3 Hypoplastic Model

3.1 Inelastic Material Properties

In hypoplasticity inelastic material properties are modeled with a constitutive equation of the rate type where the objective stress rate $\dot{\mathbf{T}}$ is expressed by an isotropic tensor-valued function consisting of the sum of the tensor function $\mathbf{A}:\mathbf{D}$, which is linear in the rate of deformation \mathbf{D} , and the tensor function $\mathbf{B}\sqrt{\mathbf{D}:\mathbf{D}}$, which is nonlinear in \mathbf{D} , i.e.

$$\dot{\mathbf{T}} = \mathbf{A}:\mathbf{D} + \mathbf{B}\sqrt{\mathbf{D}:\mathbf{D}} \quad (3.1)$$

Herein \mathbf{A} and \mathbf{B} are tensor-valued functions of the fourth order and second order, respectively. In the simplest case \mathbf{A} and \mathbf{B} only depend on the current Cauchy stress tensor \mathbf{T} , i.e. $\mathbf{A} = \mathbf{A}(\mathbf{T})$ and $\mathbf{B} = \mathbf{B}(\mathbf{T})$, but for a refined modeling of the material behavior it may also depend on additional state quantities as outlined in the following sections. The constitutive equation (3.1) is positively homogeneous of the first order in \mathbf{D} , thus the material behavior to be described is rate independent. With the nonlinearity in \mathbf{D} an inelastic material behavior is modeled in hypoplasticity with a single constitutive equation and there is no need to distinguish between elastic and plastic parts of the deformation explicitly [21]. Limit states are included in the constitutive equation for states in which $\mathbf{D} \neq 0$ and $\dot{\mathbf{T}} = 0$. In particular for a vanishing stress rate $\dot{\mathbf{T}}$ it follows from the constitutive equation (3.1) that \mathbf{T} and \mathbf{D} in the limit state satisfy the relation

$$\mathbf{A}:\mathbf{D} + \mathbf{B}\sqrt{\mathbf{D}:\mathbf{D}} = 0. \quad (3.2)$$

The normalized rate of deformation, $\hat{\mathbf{D}}$, can be obtained from Eq.(3.2) to:

$$\hat{\mathbf{D}} = \frac{\mathbf{D}}{\sqrt{\mathbf{D}:\mathbf{D}}} = -\mathbf{A}^{-1}:\mathbf{B}. \quad (3.3)$$

Inserting Eq.(3.3) into the identity $\hat{\mathbf{D}}:\hat{\mathbf{D}} = 1$ leads to the stress limit condition [10]:

$$(\mathbf{A}^{-1}:\mathbf{B}):(\mathbf{A}^{-1}:\mathbf{B}) - 1 = 0 \quad (3.4)$$

The set of all stresses which fulfill this condition can be represented by a surface in the stress space which is called limit stress surface, e.g. [35]. It

is worth noting that Eq.(3.4) first fulfills only the requirement for a vanishing stress rate and it is only related to critical stress states if the second requirement for a vanishing volume strain rate is also fulfilled, i.e.

$$\mathbf{I} : \hat{\mathbf{D}} = \mathbf{I} : (\mathbf{A}^{-1} : \mathbf{B}) = 0. \quad (3.5)$$

In order to model critical states for any deviatoric stress direction Eqs. (3.4) and (3.5) are necessary conditions for specific representations of \mathbf{A} and \mathbf{B} as firstly discussed by Bauer [1] and von Wolffersdorff [30]. Furthermore in a stationary state the right-hand side of Eq. (3.3) must be homogeneous of degree zero in \mathbf{T} , otherwise the critical stress ratio would not be invariant with regard to the stress level.

3.2 Density, Pressure and Moisture Dependent Properties

In order to take into account the influence of the density, the pressure and the disintegration of the granular hardness on the incremental stiffness the state quantities of the tensor functions \mathbf{A} and \mathbf{B} of the constitutive Eq. (3.1) are extended with the current void ratio e and the moisture dependent granular hardness h_s^* , i.e. $\mathbf{A} = \mathbf{A}(e, h_s^*, p, \mathbf{T})$ and $\mathbf{B} = \mathbf{B}(e, h_s^*, p, \mathbf{T})$. Herein the mean pressure is defined as $p = -\mathbf{I} : \mathbf{T} / 3$. To specify these tensor functions a factorized representation is used in a way similar to those proposed by Gudehus [15] and Bauer [2]. In particular with $\mathbf{A} = f_s(e, h_s^*, p) L(\hat{\mathbf{T}})$ and $\mathbf{B} = f_s(e, h_s^*, p) f_d(e, h_s^*, p) \mathbf{N}(\hat{\mathbf{T}})$ the extended constitutive equation can be written as:

$$\dot{\mathbf{T}} = f_s(e, h_s^*, p) \left[L(\hat{\mathbf{T}}) : \mathbf{D} + f_d(e, h_s^*, p) \mathbf{N}(\hat{\mathbf{T}}) \sqrt{\mathbf{D} : \mathbf{D}} \right] \quad (3.6)$$

In Eq. (10) the scalar factors f_s and f_d are called stiffness factor and density factor, respectively. The fourth order tensor $L(\hat{\mathbf{T}})$ and the second order tensor $\mathbf{N}(\hat{\mathbf{T}})$ are isotropic tensor-valued functions of the normalized stress tensor $\hat{\mathbf{T}} = \mathbf{T} / (\mathbf{I} : \mathbf{T})$ and the corresponding deviatoric part $\hat{\mathbf{T}}^* = \hat{\mathbf{T}} - \mathbf{I} / 3$. The requirements (3.4) and (3.5) for modeling critical states are satisfied for the following specific functions [5]:

$$L(\hat{\mathbf{T}}) = \hat{a}^2 \mathbf{I} + \hat{\mathbf{T}} \otimes \hat{\mathbf{T}}, \quad (3.7)$$

$$\mathbf{N}(\hat{\mathbf{T}}) = \hat{a}^2 (\hat{\mathbf{T}} + \hat{\mathbf{T}}^*). \quad (3.8)$$

$$f_s = \left(\frac{e_i}{e}\right)^\beta \frac{1}{\hat{\mathbf{T}}:\hat{\mathbf{T}}} f_b, \tag{3.9}$$

$$f_d = \left(\frac{e - e_d}{e_c - e_d}\right)^\alpha. \tag{3.10}$$

Herein \hat{a} is related to the stress limit condition in critical states as outlined later on and $\alpha < 0.5$ and $\beta > 1$ are constitutive constants. In relations (3.9) and (3.10) the current void ratio e is related to the maximum void ratio e_i , the minimum void ratio e_d and the critical void ratio e_c . According to the relations (2.3) and (2.4) the quantities e_i , e_d and e_c decrease with the mean pressure p and they are lower for a smaller granular hardness h_s^* (Fig. 2.3b). Factor f_s models the influence of the pressure, density and granular hardness on the incremental stiffness while factor f_d triggers the dilatancy behavior and the peak friction angle. Under shearing a stress peak is defined for a vanishing stress rate and for $f_d \neq 1$. A closer inspection shows that for an initially dense material, i.e. $e < e_c$ and $f_d < 1$, the part $f_d(e, h_s^*, p) \mathbf{N}(\hat{\mathbf{T}}) \|\mathbf{D}\|$ in (3.6) decreases and a higher peak friction angle is obtained. As a consequence of dilatancy the void ratio increases after the peak and it tends towards the critical void ratio e_c . Shearing of an initially loose material, i.e. $e > e_c$ and consequently $f_d > 1$, leads a densification towards the critical void ratio, but no stress peak appears. In a critical state, $e = e_c$, the value of the density factor $f_d = 1$ and it is independent of the initial void ratio, the pressure level and the granular hardness. It can be proved that for unlimited monotonic shearing a stationary stress state \mathbf{T}_c and void ratio e_c is reached asymptotically both for an initially dense and for an initially loose state [1]. By substituting the conditions for critical states, i.e. $\hat{\mathbf{T}}_c = \mathbf{0}$, $\dot{\mathbf{e}}_c = \mathbf{I}:\mathbf{D}_c = 0$ and $f_d = 1$, into the constitutive equation (3.6) the following relation for the stress limit condition in critical states is obtained [1,5]:

$$\hat{a}_c - \sqrt{\hat{\mathbf{T}}_c^*:\hat{\mathbf{T}}_c^*} = 0. \tag{3.11}$$

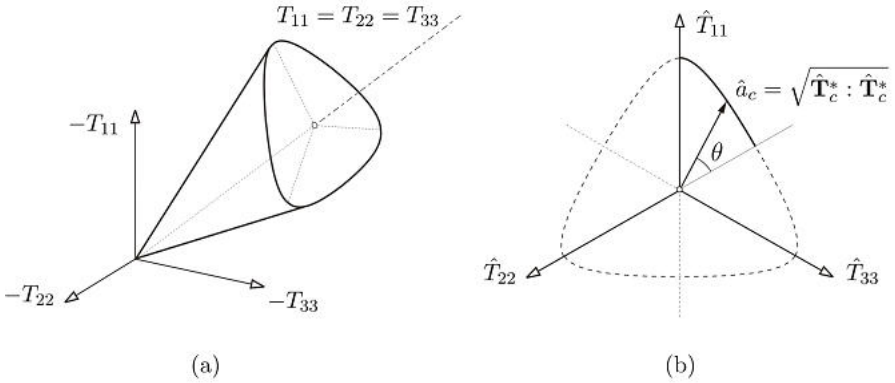


Fig. 3.1. (a) Critical stress surface in the space of principal stress component, (b) contour of the stress limit condition in the π -plane

By substituting the identity $\hat{\mathbf{T}}_c^* = \hat{\mathbf{T}} - \mathbf{I}/3$ into (3.11) it is obvious that in the space of principal stress components the stress limit condition represents a conical surface with its apex at the origin of the stress space (Fig. 3.1a). The scalar \hat{a}_c in (3.11) can be interpreted as the radius of the trace of the critical stress surface in the π -plane, i.e. \hat{a}_c is equal to the Euclidean norm of the normalized stress deviator (Fig. 3.1b). Apparently the size and shape of the critical stress surface is fully determined by factor \hat{a} of the constitutive equation. By choosing suitable representations for \hat{a} the reproduction of various conical limit surfaces is possible without loss of the general form of the constitutive equation (3.6) as outlined in detail by Bauer [5]. In the present paper the stress limit condition given by Matsuoka and Nakai [22] is considered, which can be modeled by factor \hat{a} as:

$$\hat{a} = \frac{\sin \varphi}{3 - \sin \varphi} \left[\sqrt{b} - \sqrt{\hat{\mathbf{T}}^* : \hat{\mathbf{T}}^*} \right], \tag{3.12}$$

$$\text{with } b = \frac{(8/3) - 3(\hat{\mathbf{T}}^* : \hat{\mathbf{T}}^*) + \sqrt{3/2}(\hat{\mathbf{T}}^* : \hat{\mathbf{T}}^*)^{3/2} \cos(3\theta)}{1 + \sqrt{3/2}(\hat{\mathbf{T}}^* : \hat{\mathbf{T}}^*)^{1/2} \cos(3\theta)}.$$

Herein φ denotes the critical friction angle and θ is the Lode-angle, which is defined as:

$$\cos(3\theta) = -\sqrt{6} \frac{\mathbf{I} : \hat{\mathbf{T}}^{*3}}{[\mathbf{I} : \hat{\mathbf{T}}^{*2}]^{3/2}}. \tag{3.13}$$

Since \hat{a} is embedded in the constitutive equation (3.6) it is always effective and only for cases where $\hat{\mathbf{T}}^* = \hat{\mathbf{T}}_c^*$ the value of \hat{a} obtained from Eq. (3.12) is equal to the limit condition given by Matsuoka and Nakai, i.e. $\hat{a}(\hat{\mathbf{T}}^* = \hat{\mathbf{T}}_c^*) = \hat{a}_c = \sqrt{\hat{\mathbf{T}}_c^* : \hat{\mathbf{T}}_c^*}$.

In order to link Eq. (3.6) with Eq.(2.1) it was postulated by Gudehus [15] that the response of the constitutive equation (3.6) for an isotropic compression starting from the loosest state, i.e. $e = e_{io}$, must coincide with the proposed compression law (2.1). This condition permits the direct determination of factor f_b in (3.9), yielding:

$$f_b = \frac{h_s^*}{n h_i} \frac{1 + e_i}{e_i} \left(\frac{3p}{h_s^*} \right)^{1-n}, \tag{3.14}$$

$$\text{with } h_i = \frac{8 \sin^2 \varphi}{(3 - \sin \varphi)^2} + 1 - \frac{2\sqrt{2} \sin \varphi}{3 - \sin \varphi} \left(\frac{e_{io} - e_{do}}{e_{co} - e_{do}} \right)^\alpha.$$

It follows from relation (3.14) that the stiffness factor f_s in (3.9) is proportional to the moisture dependent granular hardness h_s^* . Therefore the moisture content of the solid material is not only taken into account for the isotropic compression behavior and the pressure dependent limit void ratios in relation (2.3), it generally influences the incremental stiffness modeled by the constitutive equation (3.6).

The present hypoplastic model for cohesionless granular materials includes 9 constants which can be determined from simple index and element tests [2, 18]. In particular h_{so} and n can be determined from the compression behavior of the dry material, ψ depends on the moisture content ω . The quantities φ and e_{co} are related to the critical state in triaxial compression, α and β depend on the peak friction angle, and e_{io} and e_{do} are the limit void ratios for a nearly stress free state. Since the current void ratio e is related to the pressure dependent limit void ratios by the functions f_s and f_d , the constitutive constants are not restricted to a certain initial density. In the present paper the calibration of the constants is based on the experiments carried out by Kast [20] with weathered

broken granite. The following values were obtained: $\varphi = 42^\circ$, $h_{so} = 75 \text{ MPa}$, $\psi = 1$ for dry states and $\psi = 0.34$ for the water saturated state of the solid material, $n = 0.6$, $e_{io} = 0.85$, $e_{co} = 0.39$, $e_{do} = 0.2$, $\alpha = 0.125$ and $\beta = 1.05$. It should be noted that in the present model the critical friction angle φ is assumed to be a constant because the experiments used for the present calibration did not show a clear influence of the moisture content on the critical friction angle.

3.3 Comparison of Numerical Simulations with Experiments

The results obtained from the numerical simulation of homogeneous element tests are compared with experiments carried out by Kast [20] for isotropic compression (Fig. 3.2) and triaxial compression (Fig. 3.3 and Fig. 3.4). Under isotropic compression starting from an initial void ratio of $e_0 = 0.46$ the densification is significantly higher for the water-saturated state of the solid material (Fig. 3.2b) than for the dry state (Fig. 3.2a).

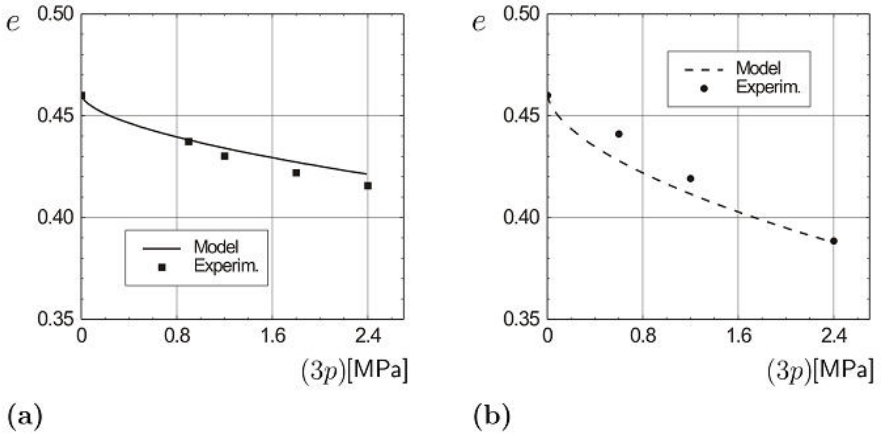


Fig. 3.2. Isotropic compression starting from an initial void ratio of $e_0 = 0.46$: (a) dry state ($\psi = 1$), (b) saturated state ($\psi = 0.34$)

For a mean pressure of $p = 0.8 \text{ MPa}$ the corresponding void ratios are $e = 0.418$ for the dry material and $e = 0.378$ for the saturated solid material. These are the initial states for the triaxial compression under a

constant mean pressure of $p = 0.8\text{MPa}$ as shown in Fig.(3.3). As the initial void ratio is higher than the corresponding pressure dependent critical one, i.e. for $p = 0.8\text{MPa} \rightarrow e_c = 0.34$ for the dry material and $e_c = 0.31$ for the saturated material, the triaxial compression leads to a further densification for both the dry material and the saturated material.

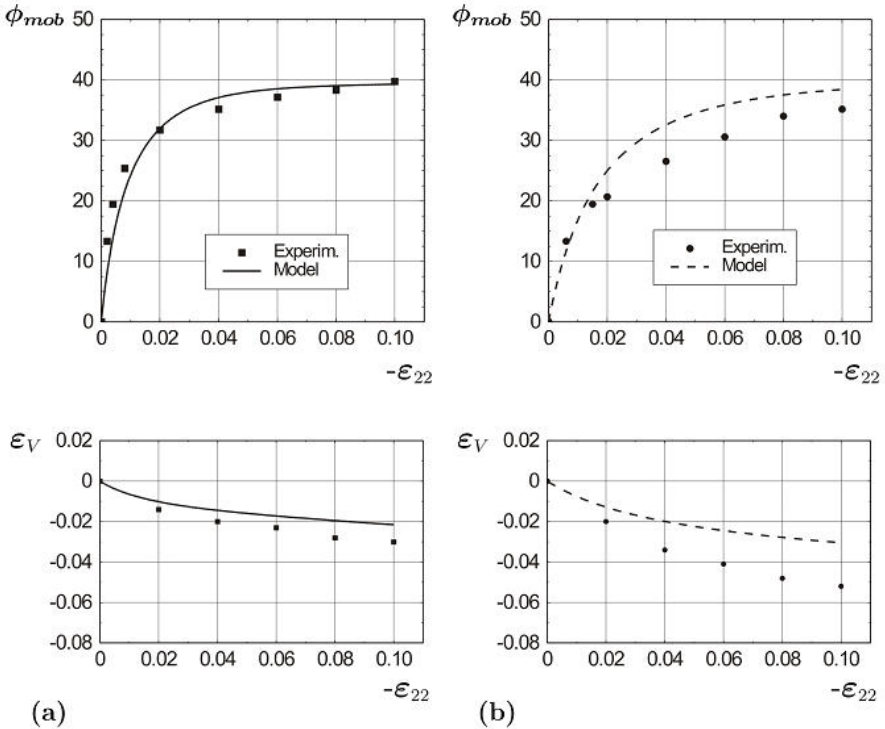


Fig. 3.3. Triaxial compression under constant mean pressure starting from an initial void ratio of: (a) $e_0 = 0.418$ for the dry state ($\psi = 1$), (b) $e_0 = 0.387$ for the saturated state ($\psi = 0.34$)

The increase of the mobilized friction angle ϕ_{mob} with the vertical strain ϵ_{22} is more pronounced for the dry material (Fig. 3.3a) than for the saturated one (Fig. 3.3b), which is also in agreement with the experiments. In order to study the influence of an initially dense material the experiments for triaxial compression under a constant mean pressure of $p = 0.8\text{MPa}$

starting from $e = 0.29$ for the dry material and $e = 0.285$ for the saturated solid material are compared with the prediction of the hypoplastic model in Fig.(3.4).

A comparison of Fig. (3.3) with Fig. (3.4) shows that the volume-strain behavior is strongly influenced by the initial density and it differs for the dry and saturated states of the solid material. The additional densification is less pronounced and the maximum mobilized friction angle is higher for the initially dense material. A clear peak state for ϕ_{mob} can only be detected for the dry and initially dense material (Fig. 3.4a). After the peak the value of ϕ_{mob} slightly decreases with advanced vertical compression and it is accompanied by dilatancy. For the saturated and initially dense state of the material the dilatancy is less pronounced.

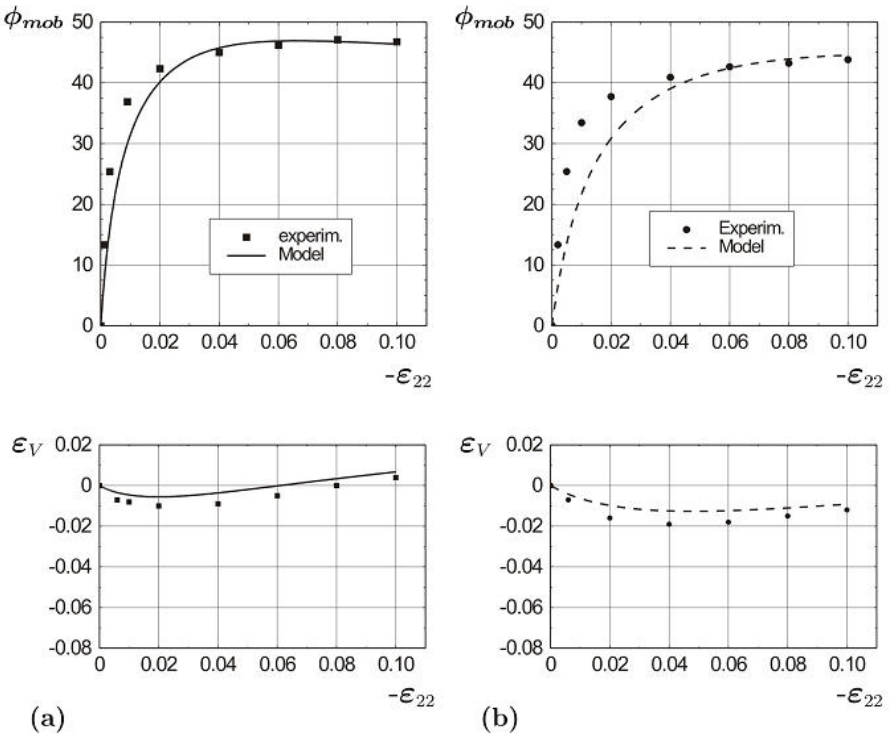


Fig. 3.4. Triaxial compression under constant mean pressure starting from an initial void ratio of: (a) $e_0 = 0.29$ for the dry state ($\psi = 1$), (b) $e_0 = 0.285$ for the saturated state ($\psi = 0.34$)

4 Shear Band Analysis or Plane Strain Compression

In this section the possibility of a spontaneous shear band formation under plane strain compression at a constant lateral pressure is studied. Of particular interest is the influence of the density, pressure level and granular hardness on the lowest stress ratio and the inclination angle of the shear band at the onset of shear band formation. The present investigation is based on the general bifurcation theory [17, 25, 26, 29]. The bifurcation condition is derived in a way similar to the ones outlined for hypoplastic models in earlier publications (e.g. [3, 4, 9, 10, 11, 14, 31, 32, 36]). A comprehensive historical review of the individual contributions can be found for instance in Tamagnini et al. [27, 28].

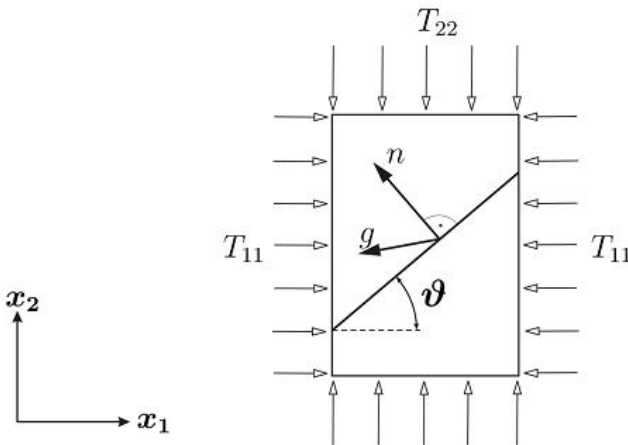


Fig. 4.1. Orientation ϑ of the shear band under plane strain compression

In the following the possibility of a spontaneous formation of a shear band is studied for discrete states (e, h_s^*, \mathbf{T}) with respect to a fixed Cartesian co-ordinate system as sketched in Fig. (4.1). The shear plane or so-called discontinuity plane is characterized by a different velocity gradient $\nabla \mathbf{v}$ on either side of this plane. The jump of the velocity gradient can be represented by the dyadic product of the unit normal \mathbf{n} of the discontinuity plane and a vector \mathbf{g} defining the discontinuity mode of the velocity gradient [4], i.e.

$$[[\nabla \mathbf{v}]] = \mathbf{g} \otimes \mathbf{n} \neq 0. \quad (4.1)$$

The condition for a continuing equilibrium across the discontinuity requires the jump of the stress rate normal to the discontinuity plane to be zero [25]:

$$[[\dot{\mathbf{T}}]] \mathbf{n} = 0. \quad (4.2)$$

Herein the jump of the stress rate can be related to the jump of the Jaumann stress rate, i.e.

$$[[\dot{\mathbf{T}}]] = [[\dot{\mathbf{T}}]] + [[\mathbf{W}]] \mathbf{T} - \mathbf{T} [[\mathbf{W}]]. \quad (4.3)$$

where $\dot{\mathbf{T}}$ is the response of the hypoplastic model (3.6) and \mathbf{W} denotes the antisymmetric part of the velocity gradient. Inserting the Jaumann stress rate into Eq.(4.2) leads to the relation:

$$f_s (L : [[\mathbf{D}]]) \mathbf{n} + \lambda f_s f_d \mathbf{N} \mathbf{n} + [[\mathbf{W}]] \mathbf{T} \mathbf{n} - \mathbf{T} [[\mathbf{W}]] \mathbf{n} = 0,$$

with:

$$[[\mathbf{D}]] = \frac{\mathbf{g} \otimes \mathbf{n} + \mathbf{n} \otimes \mathbf{g}}{2}, \quad [[\mathbf{W}]] = \frac{\mathbf{g} \otimes \mathbf{n} - \mathbf{n} \otimes \mathbf{g}}{2}, \quad (4.4)$$

$$\lambda = [[\sqrt{\mathbf{D} : \mathbf{D}}]].$$

At the onset of a shear band bifurcation the quantities f_s , f_d , L and \mathbf{N} of Eq.(3.6) are the same on either side of the discontinuity plane and they are independent of the velocity gradient. It is a peculiarity in hypoplasticity that the possibility of different incremental stiffnesses due to a different velocity gradient on either side of the discontinuity is taken into account by the single relation (4.4) and there is no need to distinguish whether the material outside the shear band undergoes loading or unloading (e.g. [3, 9, 31]). Relation (4.4) can be rewritten as $\mathbf{K} \mathbf{g} = \lambda \mathbf{r}$ or:

$$\mathbf{g} = \lambda \mathbf{K}^{-1} \mathbf{r}, \quad (4.5)$$

with:

$$\begin{aligned} \mathbf{K} &= f_s \mathbf{b}_1 + \frac{1}{2} \mathbf{b}_2, \\ \mathbf{b}_1 &= \hat{a}^2 \frac{1}{2} (\mathbf{I} + \mathbf{n} \otimes \mathbf{n}) + (\hat{\mathbf{T}} (\mathbf{n} \otimes \mathbf{n})) \hat{\mathbf{T}}, \\ \mathbf{b}_2 &= (\mathbf{n} (\mathbf{T} \mathbf{n})) \mathbf{I} - (\mathbf{n} \otimes \mathbf{n}) \mathbf{T} - \mathbf{T} + \mathbf{T} (\mathbf{n} \otimes \mathbf{n}) \end{aligned} \quad (4.6)$$

and

$$\mathbf{r} = -f_s f_d \hat{a} (\hat{\mathbf{T}} + \hat{\mathbf{T}}^*) \mathbf{n}. \quad (4.7)$$

Inserting relation (4.5) for \mathbf{g} into the norm of $[[\mathbf{D}]]$, i.e.

$$\sqrt{[[\mathbf{D}]]: [[\mathbf{D}]]} = \sqrt{\frac{(\mathbf{g} \mathbf{g}) + (\mathbf{g} \mathbf{n})^2}{2}} = \gamma \quad (4.8)$$

leads to the bifurcation condition:

$$f(\theta) = \sqrt{\frac{(\mathbf{K}^{-1} \mathbf{r})(\mathbf{K}^{-1} \mathbf{r}) + [(\mathbf{K}^{-1} \mathbf{r}) \mathbf{n}]^2}{2}} - \frac{\gamma}{|\lambda|} = 0. \quad (4.9)$$

The components of the unit normal \mathbf{n} of the discontinuity plane are related to the unknown shear band inclination angle ϑ , i.e. $\mathbf{n} = [-\sin \vartheta, \cos \vartheta, 0]^T$ with respect to the co-ordinate system in Fig. (4.1).

\mathbf{K} and \mathbf{r} depend on the current state quantities: e , h_s^* , and \mathbf{T} . In order to find the lowest possible bifurcation stress ratio the value of $\gamma/|\lambda|$ can be set equal to 1 as discussed for instance by Wu et al. [32] and Bauer [4]. Thus, relation (4.9) represents an equation for the unknown ϑ , whereby only real solutions to (4.9) indicate the possibility of a shear band bifurcation.

For a homogeneous plane strain compression under a constant lateral stress of $T_{11} = -0.8 \text{ MPa}$ the results are shown for an initial loose material (Fig. 4.2a) and an initially dense material (Fig. 4.2b) for both dry state ($\psi = 1$) and water saturated state ($\psi = 0.34$) of the solid material. In all the tests an initially isotropic stress state was assumed. The stress-strain curves and volume-strain curves show a strong influence of the initial void ratio and they are different for the dry and the water saturated material. In particular the incremental stiffness at the beginning of compression is higher for an initially dense material and a dry state. The densification is more pronounced in the case of an initially looser material and for saturated states. Dilatancy can only be detected for the initially dense and dry material.

Starting from the isotropic state the bifurcation criterion (4.9) was examined for the individual stress paths. In Fig. (4.2) the first possibility where a shear band can appear is marked with a dot. Therefore the bold part of the curves denotes states in which a spontaneous shear band bifurcation is not possible. But states above the first bifurcation point

(dotted curves) again fulfill criterion (4.9) also for $\gamma > |\lambda|$ as discussed in detail for an inherently isotropic material by Bauer [4]. It can clearly be seen that the smallest stress ratio for a possible shear band bifurcation occurs before the peak state. The stress ratio is lower for the initially higher void ratio and for the saturated state of the material. But for the same initial density the difference of the predicted stress ratio for the dry state and the saturated state of the material is not very pronounced. The shear band inclination ϑ is higher for the initially denser material and the dry state.

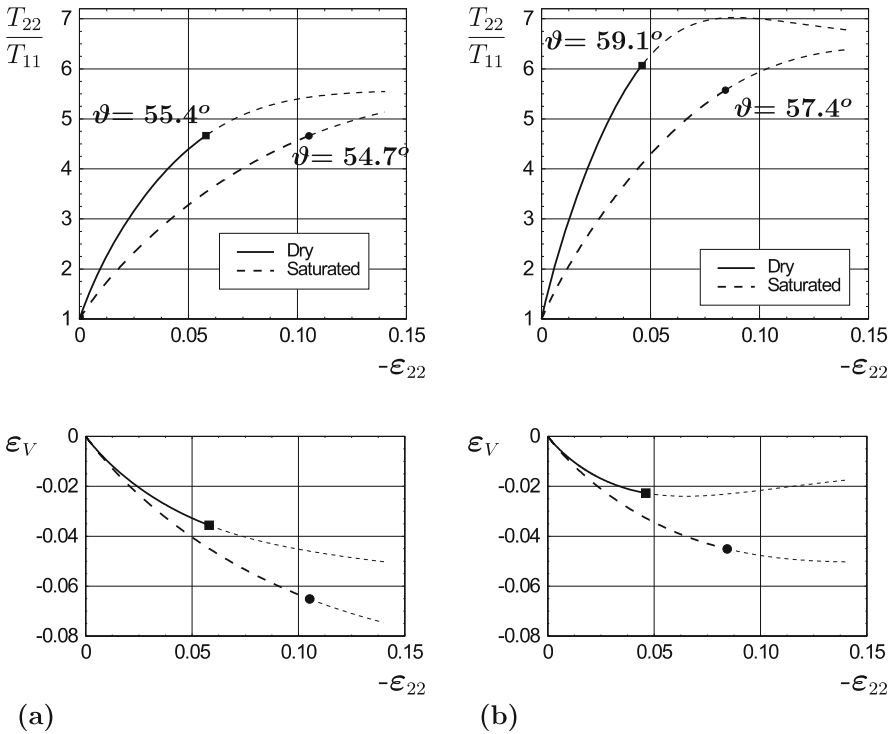


Fig. 4.2. Onset of shear band bifurcation under plane strain compression starting from an initial void ratio of: (a) $e_0 = 0.418$ for the dry state ($\psi = 1$), $e_0 = 0.387$ for the saturated state ($\psi = 0.34$), (b) $e_0 = 0.29$ for the dry state ($\psi = 1$), $e_0 = 0.285$ for the saturated state ($\psi = 0.34$)

5 Conclusions

A hypoplastic continuum model is presented to describe the essential properties of weathered rockfill materials. In particular an increase of the compressibility and a decrease of the limit void ratios with an increase of the moisture content of the solid material is modeled in a simplified manner using only a moisture dependent granular hardness. The constitutive equation for the evolution of the stress is based on nonlinear tensor-valued functions depending on the current void ratio, the stress, a moisture dependent granular hardness and the rate of deformation. As the hypoplastic concept does not need to distinguish between elastic and plastic deformation the calibration of the constitutive constants is rather easy. The calibration is carried out based on experiments for a weathered broken granite. It is demonstrated in this paper that the mechanical behavior of an initially loose and dense material can be captured with a single set of constants. The comparison of the numerical simulations of isotropic compression and triaxial compression with experiments shows that the model captures the essential properties of weathered rockfill materials for both dry and water saturated grains. For a homogeneous plane strain compression under a constant lateral stress the possibility of spontaneous shear band bifurcation is analyzed for different initial states. It can be concluded that the lowest possible bifurcation stress ratio occurs before the peak and the stress ratio and shear band inclination is higher for dry and an initially dense state of the material.

Acknowledgements

Support from the Ministry for Science and Technology in China and the Federal Ministry of Education, Science and Culture in Austria for the bilateral scientific- technological co-operation between Hohai University in Nanjing and Graz University of Technology is greatly acknowledged.

References

1. Bauer E. (1995) Constitutive modeling of critical states in hypoplasticity. In: Proceedings of the Fifth International Symposium on Numerical Models in Geomechanics, Pande and Pietruszczak (eds). Balkema press, pp. 15-20
2. Bauer E. (1996) Calibration of a comprehensive hypoplastic model for granular materials. *Solis and Foundations*, vol 36(1), pp13-26
3. Bauer E, Huang W (1998) The dependence of shear banding on pressure and density in hypoplasticity. In: Proc. of the 4th Int. Workshop on Localization

- and Bifurcation Theory for Soils and Rocks, Adachi, Oka and Yashima (eds). Balkema, pp. 81-90
4. Bauer E (1999) Analysis of shear band bifurcation with a hypoplastic model for a pressure and density sensitive granular material. *Mechanics of Materials*, vol 31, pp. 597-609
 5. Bauer E (2000) Conditions for embedding Casagrande's critical states into hypoplasticity. *Mechanics of Cohesive-Frictional Materials*, vol 5, pp. 125-148
 6. Bauer E, Herle I (2000) Stationary states in hypoplasticity. In: *Constitutive Modelling of Granular Materials*, Kolymbas (ed). Springer-Verlag, pp. 167-192
 7. Bauer E, Zhu Y (2004) Constitutive modeling of the influence of pressure, density and moisture content on the mechanical behavior of rockfill materials. In: *Proc. of the 4th Int. Conference on Dam Engineering*, Wieland, Rena and Tan (eds). Balkema Publisher, Nanjing, pp. 139-146
 8. Bouvard D, Stutz P (1986) Experimental study of rheological properties of sand using a special triaxial apparatus. *Geotechnical Testing Journal*, vol 9(1), pp. 10-18
 9. Chambon R, Desrues J (1985) Bifurcation par localisation et non linearite incrementale: un exemple heuristique d'analyse complete. In: *Plastic Instability*, Presses de l'ENPC (eds). Paris, pp. 101-113
 10. Chambon R (1989) Bases theoriques d'une loi de comportement incrementale consistante pour les sols. Groupe C.O.S.M. Rapport de Recherche
 11. Charlier R, Chambon R, Desrues J, Hammad W (1991) Shear band bifurcation and soil modeling: a rate type constitutive law for explicit localization analysis. In: *3rd Int. Conf. on Constitutive Laws for Engineering Materials*, Desai and Krempl (eds). ASME Press: Tucson, pp. 1-4
 12. Charles J A and Watts K S (1980) The influence of confining pressure on the shear strength of compacted rockfill. *Geotechnique*, vol 30(4), pp. 353-367
 13. Darve F (1991) Incrementally non-linear constitutive relationships. In: *Geomaterials: Constitutive Equations and Modelling*, Darve (ed). Elsevier press, pp. 213-237
 14. Desrues J, Chambon R (2000) Shear band analysis and shear moduli calibration. *International Journal of Solids and Structures*, vol 39, pp. 3757-3776
 15. Gudehus G (1996) A comprehensive constitutive equation for granular materials. *Soils and Foundations*, vol 36(1), pp. 1-12
 16. Gudehus G (1997) Attractors, percolation thresholds and phase limits of granular soils. In: *Powders and grains*, Behringer and Jenkins (eds). Balkema, pp. 169-183
 17. Hill R (1962) Acceleration waves in solids. *Journal of the Mechanics and Physics of Solids*, vol 10, pp. 1-16
 18. Herle I, Gudehus G (1999) Determination of parameters of a hypoplastic constitutive model from properties of grain assemblies. *Mechanics of Cohesive-Frictional Materials*, vol 4, pp. 461-486
 19. Kast K, Blinde A, Brauns J (1985) Verdichtungs-, Verformungs- und Saettigungsverhalten von Schüttungen in Abhaengigkeit von der

- geologischen Gesteinsentfestigung. In: Ingenieurgeologische Probleme im Grenzbereich zwischen Locker- und Festgesteinen. Springer-Verlag: Berlin Heidelberg
20. Kast K (1992) Mechanisches Verhalten von Granitschuttungen. In: Veröffentlichungen des Institutes fuer Bodenmechanik und Felsmechanik der Universitaet Fridericiana in Karlsruhe, Heft 125
 21. Kolymbas D (1991) An outline of hypoplasticity. *Archive of Applied Mechanics*, vol 3, pp. 143-151
 22. Matsuoka H and Nakai T (1977) Stress-strain relationship of soil based on the 'SMP'. In: Proc. of Specialty Session 9, IX Int. Conf. Soil Mech. Found. Eng., Tokyo, pp. 153-162
 23. Nobari E S, Duncan J M (1972) Effect of reservoir filling on stress and movements in earth and rockfill dams. U.S.Army Engineers Waterways Experiment Station
 24. Rzadkowski B, Zurek J (1970) Influence de l'Eau sur la Deformabilites des Roches Broyees et sur le Tassement des Barrages en Enrochement. In: Proc. Xth Congr. on Large Dams, Montreal, vol 1, pp. 857-867
 25. Rice J, Rudnicki J W (1980) A note on some features on the theory of localization of deformation. *International Journal of Solids and Structures*, vol 16, pp. 597-605
 26. Rudnicki J W, Rice J (1975) Conditions for the localization of deformation in pressure sensitive dilatant materials. *Journal of the Mechanics and Physics of Solids*, vol 23, pp. 371-394
 27. Tamagnini C, Viggiani G, Chambon R (2000) A review of two different approaches to hypoplasticity. In: *Constitutive Modelling of Granular Materials*, Kolymbas (eds). Springer press, pp. 107-145
 28. Tamagnini C, Viggiani G, Chambon R (2001) Some remarks on shear band analysis in hypoplasticity. In: 5th Int. Workshop on Localisation and Bifurcation Theory in Geomechanics, Muehlhaus, Dyskin and Pasternak (eds). Balkema Publisher: Perth, pp. 85-93
 29. Vardoulakis I and Sulem J (1995) *Bifurcation Analysis in Geomechanics*. Blackie Academic & Professional, London
 30. von Wolffersdorff P -A (1996) A hypoplastic relation for granular materials with a predefined limit state surface. *Mechanics of Cohesive-Frictional Materials*, vol 1, pp. 251-271
 31. Wu W, Sikora Z (1991) Localized bifurcation in hypoplasticity. *International Journal of Engineering Science*, vol 29(2), pp. 195-201
 32. Wu W, Sikora Z (1992) Localized bifurcation in pressure sensitive dilatant granular materials. *Mechanics Research Communications*, vol 19, pp. 289-299
 33. Wu W, Bauer E (1993) A hypoplastic model for barotropy and pyknotropy of granular soils. In: Proc. of the Int. Workshop on Modern Approaches to Plasticity, Kolymbas (eds). Elsevier, pp. 225-245
 34. Wu W, Bauer E and Kolymbas D (1996) Hypoplastic constitutive model with critical state for granular materials. *Mechanics of Materials*, vol 23, pp. 45-69

35. Wu W and Niemunis A (1996) Failure criterion, flow rule and dissipation function derived from hypoplasticity. *Mechanics of Cohesive-Frictional Materials*, vol 1, pp. 145-163
36. Wu W (2000) Nonlinear analysis of shear band formation in sand. *International Journal for Numerical and Analytical Methods in Geomechanics*, vol 24, pp. 245-263
37. Wu W and Kolymbas D (2000) Hypoplasticity then and now. In: *Constitutive Modelling of Granular Materials*, Kolymbas (eds). Springer press, pp. 57-105

Shear Zone Formation in 2D Random Granular Specimens within Enhanced Hypoplasticity

A. V. Dyskin¹ and E. Pasternak²

¹School of Civil and Resource Engineering,
University of Western Australia,
Australia,
E-mail: adyskin@cyllene.uwa.edu.au

²School of Mathematics and Statistics,
University of Western Australia,
Australia.

Summary

We consider a mechanism of macroscopic crack growth and failure in rock and rock mass in compression based on three-dimensional patterns of stress non-uniformity associated with generation of multitudes of wing cracks. In 3D each wing crack has a limiting ability to grow and hence cannot produce sample failure on its own. Neither the crack coalescence can form 3D patterns that can evolve into a macroscopic crack. Instead opening and shearing of the wing cracks produce additional stress disturbance. The combined effect of the stress disturbances from all wing cracks results in a non-uniform stress field spatially varying in a random fashion. The main feature of such a field is that any plane running through the sample can potentially have parts subjected to tensile stress alongside with the parts under compression (the average stress equal to the applied external load acting on this plane). As the load increases, these stress variations become stronger and, eventually, produce a macroscopic tensile crack at the place where the tension was maximal. Further growth of the macrocrack proceeds by initiating new segments, offset from the main crack plane in order to avoid the places under compression. This apparently en-echelon fracture is formed through a specific mechanism of tensile crack growth rather than coalescence. The macroscopic crack is inclined to the direction of axial compression at the angle maximising the average magnitude of the tensile parts of the stress field. This angle depend upon the ratio between total normal opening (dilatancy) and shear of the wing cracks, which in its own term depends upon the material micro-

structure and the confining pressure. When this ratio is above a certain threshold, the macrocrack will be parallel to the direction of axial compression producing splitting. When the ratio is below the threshold, the macrocrack will be inclined and look like shear fracture.

1 Introduction

Failure in compression of heterogeneous materials such as rocks and, at large scales the Earth's crust, is characterised by two major modes (see Germanovich et al. 1994 and the literature cited there): (1) splitting or columnar failure, predominantly observed in uniaxial compression; (2) shear or oblique failure observed in triaxial compression and, often in uniaxial compression. In the latter case the sample is broken by what appears as shear cracks.

The most popular approach to describe shear failure is to use the Mohr-Coulomb theory or its various modifications, which adequately represent experimental data related to the oblique failure. In this theory, as well known, the direction of the future fracture is determined as the one at which the shear stress reaches the friction stress at the least load magnitude the latter being referred to as the compressive strength. The drawbacks of this theory are also well known. Firstly, it has a contradiction in itself since it is based on friction properties of a not yet existing interface. This immediately turns the Mohr-Coulomb criterion into an empirical one in which the friction parameters are treated as internal material parameters to be back calculated from the results of compressive tests. Subsequently, the application of the criterion becomes limited to the cases allowing direct testing, which often excludes *in-situ* characterisation since direct transfer of laboratory data to large-scale situations is precluded by the scale effect. The second drawback is the inability of the Mohr-Coulomb theory to explain the splitting. In view of these drawbacks a considerable effort was devoted to developing micromechanical models of failure.

The majority of models developed to explain splitting are based on the concept of wing crack – the crack generated by a local stress concentrator (a pre-existing shear crack or pore or a certain type of grain contact) assuming that the wing crack can grow extensively at least under uniaxial compression as observed in 2D experiments (e.g., Brace and Bombolakis 1986, Horii and Nemat-Nasser 1986). The failure is attributed either to the growth of one of the wing cracks throughout the whole sample or to unstable crack growth caused by interaction between the cracks (e.g., Ashby and Hallam 1986, Germanovich and Dyskin 1988, Kemeny 1991).

These 2D models fail however to recognise the fact that the real three dimensional wing cracks have an intrinsic limitation to the growth preventing the wing elongation beyond the size of the initial shear crack even in the most favourable case of uniaxial compression, Fig. 1.1.

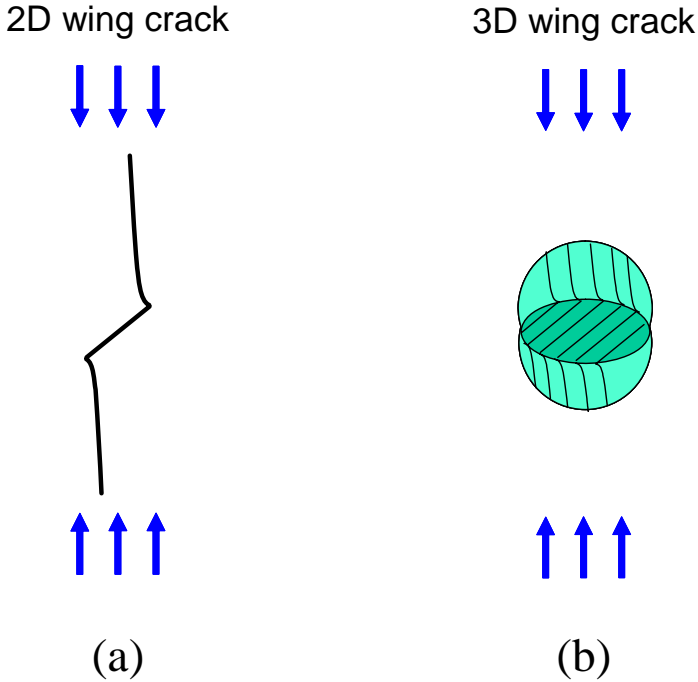


Fig. 1.1. Wing crack growth in uniaxial compression: (a) 2D wing crack growth. The wings are capable of extensive growth and can reach lengths macroscopic as compared to the length of the initial crack; (b) 3D wing crack growth. The wings have intrinsic limitations to their growth. Their maximum dimensions are comparable with the size of the initial crack, Dyskin et al. (2003).

Modelling of shear failure in compression, that takes into account the fact that the shear cracks do not propagate in their own plane, but rather kink, is based on considering various mechanisms of wing crack coalescence (e.g., Wittmann 1981, Stavrogin and Tarasov 2001) or en-echelon formation (e.g., Horii and Nemat-Nasser 1986, Schulson 1990, Reches and Lockner 1994). A typical model of en-echelon crack is shown in Fig. 1.2a. The main feature of models of this kind is that they are two-

dimensional. As soon as one returns to a real 3D situation the picture becomes complicated. Indeed, a direct three-dimensional analogue of the en-echelon model is an arrangement sketched in Fig. 1.2b. Two conditions should be satisfied to make such an arrangement possible. Firstly, all wing cracks or the corresponding parts of the wings participating in the formation of the en-echelon crack should be more or less parallel to each other. Secondly, since the wings are more or less equiaxial, the ones forming the en-echelon crack should have suitable spatial arrangement.

In order to make the idea of en-echelon crack formation viable, it is therefore necessary to identify the mechanism(s) ensuring these arrangements. If one hypothesises that the cracks forming en-echelon constitute only a portion of all cracks then, inevitably, extremely high concentrations of such cracks should be assumed. In particular, given that the dimensions of the wing cracks in rocks are often of the order of the grain size, the first of the above conditions demands that the grains happened to be in the place of future en-echelon crack be already separated from the rest of the rock volume. Indeed, while the wings separate the grain from the sides, the initial crack that initiated the wings separates the grain from above or below (the compression direction being vertical). This obviously contradicts the experimental observations according to which the formation of macroscopic shear fracture does not yet lead to full rock separation.

The above consideration suggests that the cracks forming en-echelon were not there initially, but rather were formed in the process of propagation of the macrocrack.

Direct finite element simulations of failure in heterogeneous materials are based on specifying failure criteria for each finite element (e.g., Zou et al. 1996). In essence, these criteria are usually chosen similar to the ones deduced from the tests on macroscopic samples. Therefore, the question of the failure criterion is simply shifted from macroscopic to microscopic scale without actually producing the relevant failure mechanism. Models treating the shear cracks as planes of strain localisation (e.g., Rudnicki and Rice 1975) face the same problem: the material behaviour at the micro level should resemble the macroscopic behaviour the model is set to explain. To complicate the matter further, the direct numerical simulations suffer from mesh-dependence which renders the simulations unusable.

Dyskin (1999) noticed that the wing cracks create considerable stress non-uniformity (spatial stress fluctuations) with the material in some places subjected to tensile stresses and therefore capable of generating tensile cracks. Based on this idea a 3D model of splitting crack formation and propagation was proposed. In this paper we extend this idea to model

the formation and propagation of inclined tensile cracks which produce oblique (shear-like) failure.

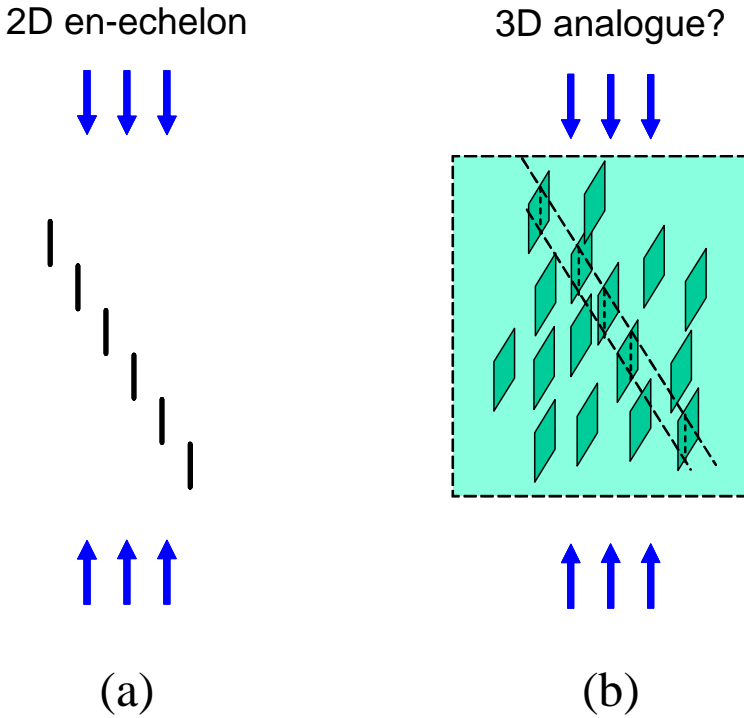


Fig. 1.2. ‘En-echelon’ crack: (a) 2D en-echelon crack as depicted following cross-section observations in rock samples or the Earth’s crust; (b) a schematics of possible 3D analogue of en-echelon crack. It is assumed that the vertical fractures being parts of wing cracks are approximately equiaxial, as shown in Fig. 1.1. The broken line shaded area signifies a cross-section of observation, while two inclined broken lines indicate the position of traces of the en-echelon crack in the cross-section.

2 Mechanism of Crack Propagation in Non-Uniform Stress Fields

The stress field generated by wing cracks as well as other heterogeneities is non-uniform and random owing to their random locations, orientations, shapes and dimensions. In the parts of the sample where the stress variations become tensile new cracks can be generated and grown to

macrocracks, Dyskin (1999). Fig. 2.1 explains a possible mechanism of tensile macrocrack formation and propagation. Fig. 2.1a shows a possible realisation of random field of a normal stress component σ_{33} ; the stress increasing from dark to white, such that the dark areas correspond to compression, while the white areas correspond to tension. For the illustration purpose, only a section parallel to the (x_2, x_3) plane is shown. Obviously, the first crack (crack 1) is generated at the area with the maximum tensile stress. This crack will propagate until it is arrested in the areas subjected to compression. As the applied load increases, so does the amplitude of the stress variations. Further propagation of crack 1 will however be prevented by similarly increased compression; instead a new crack (crack 2) will be generated where the original stress distribution showed no compression. This will result in a discontinuous offset-type trajectory of crack growth, which in the real 3D case will look like the one shown in Fig. 2.1b. Essentially, the crack segments will be situated at places where no compressive stresses acted. On average, the magnitude of these stresses is equal to the mathematical expectation of positive (tensile) values

$$\sigma_+ = \int \max(\sigma, 0) f(\sigma) d\sigma \quad (2.1)$$

where σ denotes the relevant stress component, $f(\sigma)$ is the probability density function.

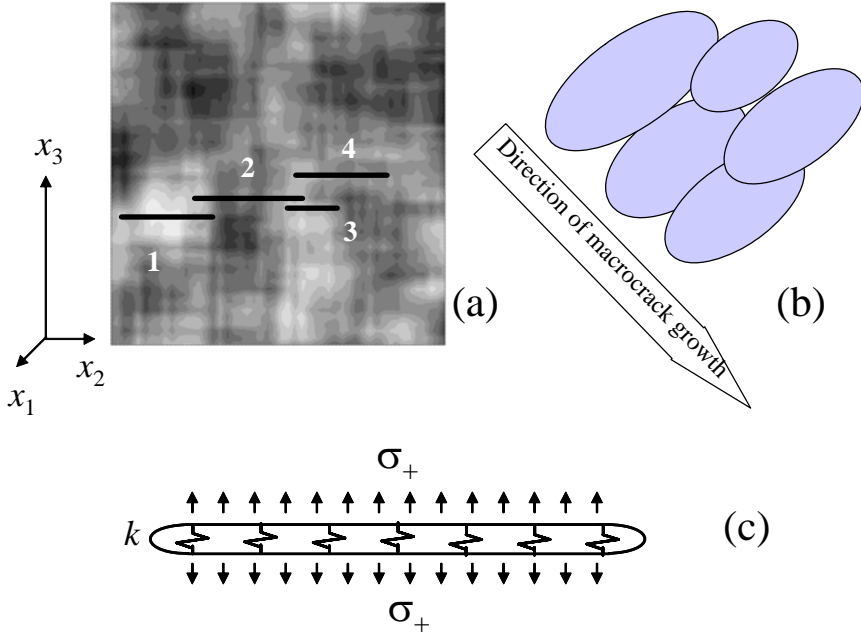


Fig. 2.1. Macroscopic crack formation and growth under spatially random stress field: (a) a realisation of the random stress field σ_{33} ; the maximum compression is shown in black, the tension - in white. The first crack segment (crack 1) appears at the place of maximum tension. Crack 2 is then generated at the closest place where the compressive stress is minimal (whitish spot), then other segments (cracks 3 and 4) are generated in the same fashion; (b) a 3D structure of the compound (en-echelon) macrocrack; (c) the macrocrack is modelled as a crack (a cross-section is shown) with Winkler layer of stiffness k that depends upon the size and the density of the segment cracks

We will model such a complex compound (en-echelon) crack, macroscopically, as a planar crack with Winkler layer, i.e. we will assume that opening of the crack is resisted by linear links between the faces, Fig. 2.1c. These linear links model the action of intact material between the crack segments. The Winkler layer is characterised by stiffness k that locally relate the mutual normal displacement of the crack faces Δv and the normal stress σ , $\sigma = k\Delta v$, the stiffness k being dependent upon the crack segment sizes and concentration. We will also assume that the faces of the macroscopic crack are subjected to a uniform load σ_+ associated with the action of stress fluctuations. We assume further that the macro-crack is

disk-like of a radius R . We will characterise the conditions of its growth using the macroscopic scale, where we can employ the conventional criterion of crack propagation $K_I = K_{Ic}$. Here K_{Ic} is the macroscopic fracture toughness which characterise the conditions of creation of the new crack segments.

Since the macrocrack is much larger than the characteristic size of the Winkler layer, E/k , where E is the Young's modulus of the rock, the stress intensity factor has the following form, Shifrin (1988)

$$K_I = \sigma_+ \sqrt{\frac{E}{\pi k(1 - \nu^2)}} \quad (2.2)$$

One can see that the stress intensity factor is independent of the macrocrack size, i.e. the macrocrack can support its own growth without an increase in the load.

A remark should be made with respect to the concept introduced. Macroscopically, the considered crack grows as an open tensile crack. However, it is also subjected to shear stress. The corresponding shear component of the relative displacement of the crack faces creates tensile stresses on one side of the macrocrack contour and compressive on the other. In the process of the macrocrack growth the tensile stress concentration leads to the appearance of small tensile cracks approximately oriented in the vertical direction and predominantly located on one side of the macrocrack, Fig. 2.2. It is these cracks that create impression of en-echelon nature of the macrocrack. It has also been observed on sample cross-sections by Moore and Lockner (1995) that these vertical cracks are biased to one side of the macrocrack.

We shall now introduce a method for estimating the fluctuation-induced stress σ_+ . Suppose the random stress is Gaussian with the uniform mathematical expectation, σ_{av} and standard deviation, Σ . Then direct calculations give:

$$\sigma_+ = \Sigma \left\{ \xi \left[\frac{1}{2} - \Phi(-\xi) \right] + \frac{1}{\sqrt{2\pi}} e^{-\frac{\xi^2}{2}} \right\} \quad (2.3)$$

$$\xi = \frac{\sigma_{av}}{\Sigma}, \quad \Phi(x) = \frac{1}{\sqrt{2\pi}} \int_0^x e^{-\frac{x^2}{2}} dx$$

Therefore, in order to determine the fluctuation-induced stress one needs to know the statistical properties of the Gaussian stress fluctuations. These will be determined in the following section.

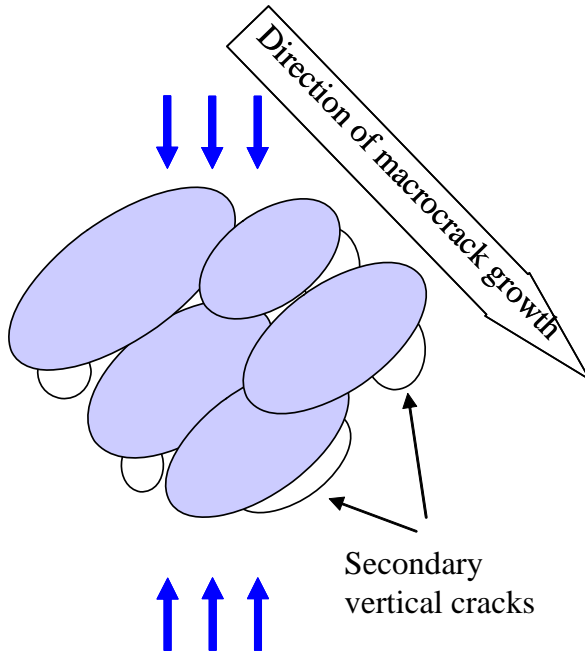


Fig. 2.2. Formation of secondary tensile cracks in the process of macrocrack growth. These secondary cracks may be responsible for the en-echelon appearance.

3 Statistical Properties of Non-Uniform Stress Field Created by Many Wing Cracks

In order to quantify the mechanism by which this field produces and drives macrocracks we need to determine the mathematical expectation and variance of this field.

Suppose that the rock volume is loaded such that in a similar homogeneous volume a uniform stress field σ_{ik}^0 ($i, k=1, 2, 3$) would be produced. In the case of compression of magnitude p in x_3 direction (see the coordinate frame on Fig. 3.1) and confining pressure of magnitude q in the normal directions

$$\sigma_{11}^0 = \sigma_{22}^0 = -q, \quad \sigma_{33}^0 = -p, \quad \sigma_{12}^0 = \sigma_{13}^0 = \sigma_{21}^0 = 0 \quad (3.1)$$

The actual stress field σ_{ik} is of course different from the uniform one, predominantly owing to the effect of wing cracks with some contribution from other heterogeneities. Nevertheless its volumetric average over the whole sample, $\langle \sigma_{ij} \rangle$, is equal to σ_{ij}^0 . Indeed, suppose a volume V is loaded at its external surface S by tractions $\sigma_{ij}^0 n_j$, where n_i is the external normal vector to S , while its internal surfaces (e.g., pores or cracks) are free from external load (only contact forces can act there). We will also neglect the body forces.

We use the following identity which is based on the divergence theorem

$$\int_{S_0} \sigma_{ik}(\mathbf{x}) x_j n_k dS = \int_V (\sigma_{ik}(\mathbf{x}) x_j)_{,k} dV_{\mathbf{x}} = \int_V \sigma_{ik,k}(\mathbf{x}) x_j dV_{\mathbf{x}} + \int_V \sigma_{ik}(\mathbf{x}) \delta_{jk} dV_{\mathbf{x}} \quad (3.2)$$

The first integral in the right-hand part is equal to zero because of the equations of equilibrium with zero body forces. Because the actual and uniform stress fields corresponds to the same tractions at S , one obtains

$$\begin{aligned} \langle \sigma_{ij} \rangle &= \frac{1}{V} \int_V \sigma_{ij}(\mathbf{x}) dV_{\mathbf{x}} = \frac{1}{V} \int_{S_0} \sigma_{ik}(\mathbf{x}) x_j n_k dS \\ &= \frac{1}{V} \int_{S_0} \sigma_{ik}^0(\mathbf{x}) x_j n_k dS = \langle \sigma_{ij}^0 \rangle = \sigma_{ij}^0 \end{aligned} \quad (3.3)$$

Furthermore, assuming ergodicity, the mathematical expectation of this random stress field can be found

$$\overline{\sigma_{ik}} = \langle \sigma_{ik} \rangle = \sigma_{ik}^0 \quad (3.4)$$

In order to estimate the variance of the stress field generated by the wing cracks we model each crack by a dislocation loop, Fig. 3.1, with the shear component of the Burgers vector, b_t , directed parallel to the axial load and the normal component, b_n , directed perpendicular to the axial load. The shear component reflects the contribution of the wing crack to the non-linear part of axial strain, while the normal component reflects the wing crack contribution to dilatancy. As further simplification, in order to account for the collective effect of the wing cracks while neglecting the peculiarities of the shape of each crack, we replace the dislocation loops with point defects. It will be done by limiting transition of the loop area, A , to zero keeping the corresponding volumes, $U_t = b_t A$, $U_n = b_n A$, constant.

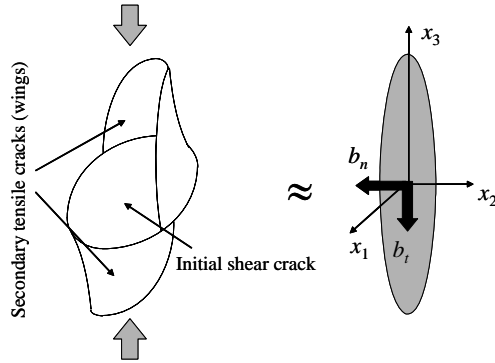


Fig. 3.1. Wing crack evolved form an initial inclined shear crack (left) and its model as a dislocation loop (right) with Burgers vector (b_t, b_n) .

We represent, following Landau and Lifshitz (1959), the dislocation loop through equivalent body forces

$$f_i = \frac{1}{2} \lambda_{iklm} [(n_l b_m + n_m b_l) \delta(\zeta)]_{,k}, \quad (3.5)$$

where n_m and b_m are the components of unit normal vector to the loop and the Burgers vector respectively, $\delta(\zeta)$ is the delta-function of coordinate ζ along the normal vector, $(\cdot)_{,k}$ denotes differentiation with respect to x_k (summation is presumed over repeated indexes) and λ_{iklm} is the tensor of elastic moduli. For isotropic rock with the Young's modulus E and Poisson's ratio ν it has the form:

$$\lambda_{iklm} = \frac{E}{1 + \nu} \left[\frac{1}{2} (\delta_{il} \delta_{km} + \delta_{im} \delta_{kl}) + \frac{\nu}{1 - 2\nu} \delta_{ik} \delta_{lm} \right] \quad (3.6)$$

We now represent the crack as a point defect located at a point \mathbf{x}_μ , $\mu = 1, \dots, M$, where M is the number of wing cracks in the rock volume and take into account that in this representation the Burgers vectors are constant

$$b_i = U_n n_i + U_t \delta_{i3}. \quad (3.7)$$

Here we considered that the normal vector, according to Fig. 3.1 is always perpendicular to the x_3 axis. As a result, we come up with the

following expression for the body forces through the volumes of crack opening/shear

$$f_i = \frac{1}{2} \lambda_{iklm} (n_l b_m + n_m b_l) \delta(\mathbf{x} - \mathbf{x}_\mu)_{,k} \quad (3.8)$$

Now, using identity (3.2) and the equilibrium equations

$$\sigma_{ij,i} + f_j = 0, \quad (3.9)$$

with the body forces (3.8) one can express the volumetric average of the stress field generated by these point defects, which is the average stress field *outside* the wing cracks. It reads

$$\begin{aligned} \langle \sigma_{ik}^{dist} \rangle &= \sigma_{ik}^0 \\ &+ \frac{E}{1+\nu} \frac{1}{V} \sum_{\mu=1}^M \left[U_n^\mu \left(n_i^\mu n_k^\mu + \frac{\nu}{1-2\nu} \delta_{ik} \right) + \frac{1}{2} U_t^\mu \left(n_i^\mu \delta_{k3} + n_k^\mu \delta_{i3} \right) \right] \end{aligned} \quad (3.10)$$

where σ_{ik}^0 is the applied load, V is the rock volume, M is the number of wing cracks in the volume (this number can grow as loading progresses), the superscript index μ refers to a particular wing crack. It is important to distinguish between this stress field which essentially represents the stresses generated at a distance from the wing cracks (since this approximation relates to the scale from which the wing cracks are seen as point defects) with the full stress field (that includes stresses in immediate neighbourhoods of the wing cracks) which volumetric average is given by equation (3.4).

Direct computations of the correlation function for the stress fields in the point defect approximation, Dyskin (1999), suggested that the correlation length is of the order of the wing crack size. Based on this observation, we break the sample volume V into M parts V_λ , $\lambda=1, \dots, M$ such that the averages over V_λ , $\langle \sigma_{ik} \rangle_\lambda$ are approximately independent from each other. Then from the ergodicity, the variance $\text{Var}(\langle \sigma_{ik} \rangle_\lambda)$ can be expressed through the variance of the full volumetric average, $\text{Var}(\langle \sigma_{ik} \rangle)$. We assume that the latter is adequately represented by the variance of (3.10). For wing cracks uniformly oriented in the (x_1, x_2) plane, assuming that the average values of shear ‘volume’ U_t and volume of opening of wing cracks U_n are independent, one obtains

$$\begin{aligned} \text{Var}(\langle \sigma_{ik} \rangle_\lambda) &= \frac{t^2}{2} \left[\kappa^2 (1 - \delta_{i3} \delta_{k3}) + (\delta_{i3} + \delta_{k3} - 2\delta_{i3} \delta_{k3}) \right] \\ t &= \frac{NEU_t}{2(1+\nu)}, \quad \kappa t = \frac{NEU_n}{2(1+\nu)} \end{aligned} \quad (3.11)$$

where N is the number of wing cracks per unit volume, κ has the meaning of the ratio between dilatancy and inelastic part of the axial strain.

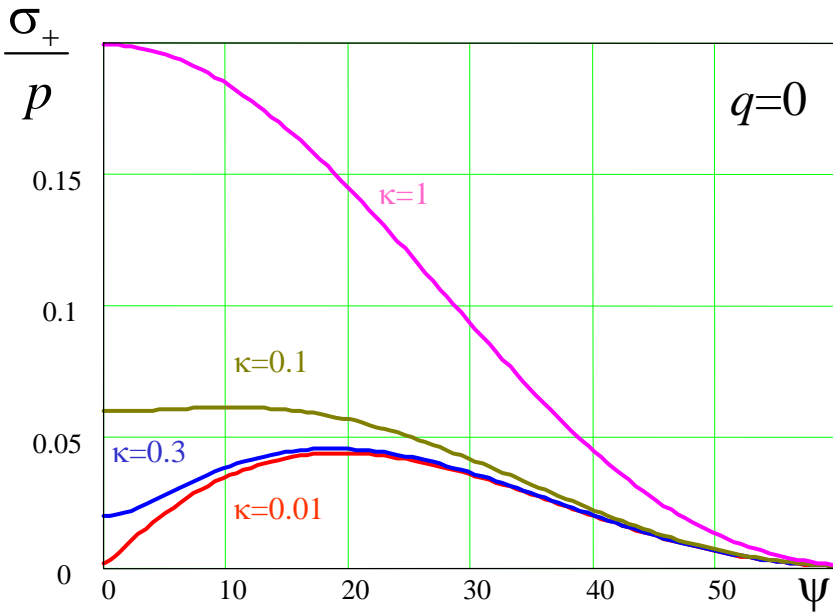
4 A Mechanism of Splitting and Oblique Failure in Compression

Consider a plane inclined at an angle ψ to the x_3 axis and determine the average tensile stress σ_+ acting on that plane. Substituting (3.1), (3.11) into (2.3) one obtains

$$\sigma_+ = \frac{t}{2\sqrt{2\pi}} e^{-\frac{\xi^2}{2}} \cos^2 \psi \sqrt{\kappa^2 + 2 \tan^2 \psi} - (p \sin^2 \psi + q \cos^2 \psi) \left[\frac{1}{2} - \Phi(-\xi) \right]$$

$$\xi = -\frac{2(q + p \tan^2 \psi)}{t \sqrt{\kappa^2 + 2 \tan^2 \psi}} \tag{4.1}$$

Fig. 4.1 shows stress (4.1) for $t=p$ and for different q and κ . It is seen that for $\kappa=1$ stress σ_+ reaches maximum at $\psi=0$, which corresponds to splitting. Small values of κ lead to oblique failure. Since for $q>0$ mainly oblique failure is observed, κ should be small as compared to $\tan(\psi)$.



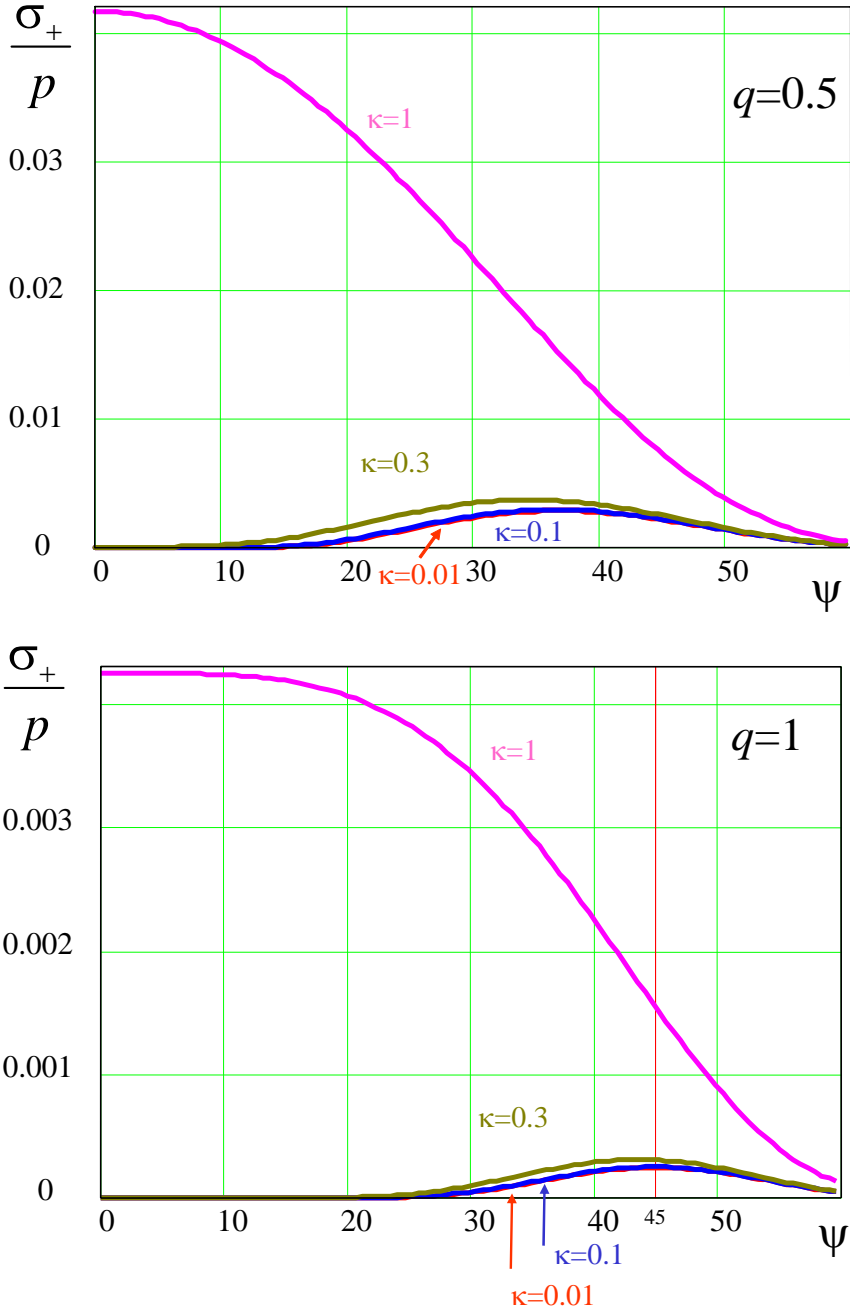


Fig. 4.1. Dependence of average tensile stress acting on a plane vs. the angle of its inclination for various values of the lateral compression q

For uniaxial compression the critical value of κ has the form

$$\kappa_{cr} = -\frac{p\sqrt{2\pi}}{t} + \sqrt{\frac{2\pi p^2}{t^2} + 1} \quad (4.2)$$

Subsequently, $\kappa > \kappa_{cr}$ corresponds to splitting, while $\kappa < \kappa_{cr}$ corresponds to oblique or ‘shear’ failure.

We now assume that the opening of the wing cracks is mainly controlled by sliding of their shear part and for that reason the average opening is proportional to the deviatoric stress acting on them such that $t = \eta(p - q)$, where η is a factor. We also assume that the macrocrack start propagating when the positive component of stress fluctuations acting in its plane reaches a certain critical value: $\sigma_+ = \sigma_{cr}$. For the case of low values of κ , such that $\sqrt{\kappa^2 + 2 \tan^2 \psi} \approx \sqrt{2} \tan \psi$, we can rearrange expression (4.1) in the following way:

$$(p - q) \sin \psi \cos \psi = c + (p \sin^2 \psi + q \cos^2 \psi) \tan \varphi \quad (4.3)$$

where

$$c = \frac{2\sqrt{\pi}\sigma_{cr}}{\eta} e^{\frac{\xi^2}{2}}, \quad \tan \varphi = \left[\frac{1}{2} - \Phi(-\xi) \right] \frac{2\sqrt{\pi}\sigma_{cr}}{\eta} e^{\frac{\xi^2}{2}} \quad (4.4)$$

This is an expression similar to Coulomb-Mohr criterion. In general its parameters are not independent of p and q . If, in addition, $t \gg p$ the Coulomb-Mohr parameters will change little and can be considered independent of the loads p and q .

The values of parameters depend upon the factors associated with the wing cracks, their sizes and distributions. However, the mechanism itself is scale-independent.

5 Conclusions

It is demonstrated that the random stress non-uniformity created by the multitude of wing cracks is sufficient to induce tensile cracks and then make them grow as a macroscopic tensile fracture. Its structure – a set of crack-segments as well as vertical cracks induced by shear stresses in the process of its growth create an appearance of en-echelon fracture. The macroscopic fracture is inclined to the direction of axial compression at the angle maximising the average magnitude of the tensile parts of the stress field. This angle depends upon the ratio between total normal opening

(dilatancy) and shear of the wing cracks. When this ratio is above a certain threshold, the macrocrack will be parallel to the direction of axial compression producing splitting. When the ratio is below the threshold, the macrocrack will be inclined and look like shear fracture.

Acknowledgements

The first author acknowledges the financial support through the University of Western Australia Research Grant 2004 and the Australian Research Council Discovery Grant DP0559737 (2005-2007), the second author acknowledges the support of the Australian Research Council Australian Postdoctoral Fellowship and Discovery Grant, DP0346148 (2003-2006).

References

1. Ashby MF, Hallam SD (1986) The failure of brittle solids containing small cracks under compressive stress states. *Acta Metallurgica* 34:497-510.
2. Brace WF, Bombolakis EG (1963) A note of brittle crack growth in compression. *J. Geophys. Res.* 68:3,709-3,713.
3. Dyskin AV (1999) On the role of stress fluctuations in brittle fracture. *Intern. J. Fracture* 100:29-53.
4. Dyskin AV, Jewell R.J, Joer H, Sahouryeh, E Ustinov KB (2003) Influence of shape and locations of initial 3-D cracks on their growth in uniaxial compression. *Engg. Fracture Mechanics* 70:2115-2136.
5. Germanovich LN, Dyskin AV (1988) A model of brittle failure for materials with cracks in uniaxial loading. *Mechanics of Solids* 23(2):111-123.
6. Germanovich LN, Salganik RL, Dyskin AV, Lee KK (1994) Mechanisms of brittle fracture of rock with multiple pre-existing cracks in compression. *Pure and Applied Geophys.* 143(1/2/3):117-149.
7. Horii H, Nemat-Nasser S (1986) Brittle failure in compression: splitting, faulting, and brittle-ductile transition. *Phil. Trans. R. Soc. Lond., A*319:337-374.
8. Kemeny JM (1991) A model for non-linear rock deformation under compression due to sub-critical crack growth. *Int. J. Rock Mech. Min. Sci. & Geomech. Abstr.* 28:459-467.
9. Landau LD, Lifshitz EM (1959) *Theory of Elasticity.* Oxford, London Edinburgh New York Toronto Sydney Paris Braunschweig.
10. Moore DE, Lockner DA. (1995). The role of microcracking in shear fracture propagation in granite. *J. Struct. Geol.* 17:95-114.
11. Reches Z, Lockner DA (1994) Nucleation and growth of faults in brittle rocks. *J. Geophys. Res.* B99:18,159-18,173.
12. Rudnicki JW, Rice JR (1975) Conditions for the localization of deformation in pressure-sensitive dilatant materials. *J. Mech. Phys. Solids* 23:371-394,.

13. Schulson EM (1990) The brittle compressive fracture of ice. *Acta Metall. Mater.* 38:1963-1976.
14. Stavrogin AN, Tarasov BG (2001) *Experimental Physics and Rock Mechanics*. Balkema, Rotterdam.
15. Shifrin EI (1988) The I-Mode crack whose sides interact according to a linear law. *Mechanics of Solids* 23, No. 5:91-97.
16. Wittmann FH (1981) Mechanisms and mechanics of fracture of concrete. In: Francois D (ed.) *Advances in Fracture Research*. Pergamon Press, Oxford New York Toronto Sydney Paris Frankfurt, pp. 1467-1487.
17. Zou Y, Taylor WEG, Heath DJ (1996) A numerical model for borehole breakouts. *Int. J. Rock Mech. Min. Sci. & Geomech. Abstr.* 33:103-109.

A Rational Approach to Stress-Dilatancy Modelling Using an Explicit Micromechanical Formulation

J. Bobiński and J. Tejchman

Faculty of Civil and Environmental Engineering,
Gdansk University of Technology,
80-952, Gdansk, Narutowicza 11/12,
Poland.
E-mail: tejchmk@pg.gda.pl

Summary

The paper presents results of numerical simulations of the behaviour of quasi-brittle materials (like concrete) under plane strain conditions. Two boundary value problems with a dominating failure mode I were simulated: uniaxial tension and a three-point bending test for concrete beams with a different size. To model the material behaviour, two different continuum approaches were used: elasto-plastic and an isotropic damage constitutive model with non-local softening. Attention was focused of the effect of a characteristic length on the width of strain localization and load-displacement curve, and an identification of a characteristic length on the basis of the load-displacement curves only from size effect tests.

1 Introduction

The analysis of concrete elements is complex due to occurrence of strain localization which is a fundamental phenomenon under both quasi-static and dynamic conditions [5], [9], [17], [48], [50]. It can occur in the form of cracks (if cohesive properties are dominant) or shear zones (if frictional properties prevail). The determination of the width and spacing of strain localization is crucial to evaluate the material strength at peak and in the post-peak regime. The concrete behaviour can be modeled within continuum mechanics models using, e.g.: non-linear elasticity [34], fracture [4], [24], endochronic theory [3], [8], micro-plane theory [7], [27], plasticity [11], [33], [38], [48], damage theory [11], [16], [20], [37] and coupled plastic-damage approach [14], [26], [32], [42], and discrete models using a lattice approach [23], [30], [43], [49] and DEM [18], [19],

[41]. To describe properly strain localization within continuum mechanics, the models should be enhanced by a characteristic length of microstructure [13]. There are several approaches within continuum mechanics to include a characteristic length and to preserve the well-posedness of the underlying incremental boundary value problem in engineering materials as: second-gradient [17], [35], [36], [37], non-local [2], [10], [16], [39] and viscous ones [13], [45]. Owing to them, objective and properly convergent numerical solutions for localized deformation (mesh-insensitive load-displacement diagram and mesh-insensitive deformation pattern) are achieved. Otherwise, FE-results are completely controlled by the size and orientation of the mesh and thus produce unreliable results, i.e. strain localization becomes narrower upon mesh refinement (element size becomes the characteristic length) and computed force-displacement curves change considerably depending on the width of the calculated localization. In addition, a premature divergence of incremental FE-calculations is often met.

The aim of the present paper is to compare the FE-results of the width of strain localization in concrete elements (characterized by a failure mode I) during uniaxial tension and three-point bending using two different continuum models enhanced by an internal length of microstructure: isotropic elasto-plastic model and isotropic damage model both with non-local softening. The FE-results with respect to the load-displacement curves were compared to some laboratory experiments and the size effect law by Bazant [5]. Attention was focused of the effect of a characteristic length on the width of strain localization and load-displacement curve, and an identification of a characteristic length on the basis of the measured load-displacement curves only.

2 Constitutive Models for Concrete

2.1 Elasto-Plastic Model

An elasto-plastic model with isotropic hardening and softening using two yield conditions was assumed. In a compression regime, a Drucker-Prager criterion was defined as [1]

$$f_1 = q + p \tan \varphi - \left(1 - \frac{1}{3} \tan \varphi \right) \sigma_c (\kappa_1), \quad (2.1)$$

where q – von Mises equivalent stress, p – mean stress, φ – the internal friction angle, σ_c – uniaxial compression yield stress and κ_1 – hardening (softening) parameter equal to plastic vertical strain in uniaxial compression ε_{11}^p . The invariants p and q were defined as

$$p = \frac{1}{3} \sigma_{kk} \quad \text{and} \quad q = \sqrt{\frac{3}{2} s_{ij} s_{ji}}, \quad (2.2)$$

where σ_{ij} is the stress tensor and s_{ij} stands for the deviatoric stress tensor. The flow potential function was taken as

$$g_1 = q + p \tan \psi, \quad (2.3)$$

where ψ is the dilatancy angle. In a tensile regime, a Rankine criterion was assumed with the yield function

$$f_2 = \max \{ \sigma_1, \sigma_2, \sigma_3 \} - \sigma_t (\kappa_2), \quad (2.4)$$

where σ_1, σ_2 and σ_3 – principal stresses, σ_t – the tensile yield stress and κ_2 – softening parameter (equal to the maximum principal plastic strain ε_1^p). The associated flow rule was assumed.

2.2 Damage Model

An isotropic damage continuum model describes the degradation of the material due to micro-cracking with the aid of a single scalar damage parameter D growing from zero (undamaged state) to one (completely damaged state). The stress-strain function is represented by the following relationship

$$\sigma_{ij} = (1 - D) C_{ijkl}^e \varepsilon_{kl}, \quad (2.5)$$

where C_{ijkl}^e – linear elastic material stiffness matrix and ε_{kl} – strain tensor. The damage parameter D acts as a stiffness reduction factor (the Poisson ratio ν is not affected by damage). The growth of the damage variable is controlled by a damage threshold parameter κ which is defined as a maximum of the equivalent strain measure $\tilde{\varepsilon}$ reached during the load history up to time t . The loading function of damage is

$$f(\tilde{\varepsilon}, \kappa) = \tilde{\varepsilon} - \max \{ \kappa, \kappa_0 \} \quad (2.6)$$

where κ_0 – initial value of κ when damage begins. If the loading function f is negative, damage does not develop. During monotonic loading, the parameter κ grows (it coincides with $\tilde{\varepsilon}$) and during unloading and reloading it remains constant. To define the equivalent strain measure $\tilde{\varepsilon}$, two different criteria were assumed: a) a von Mises failure criterion in terms of strains [37] and b) Rankine failure type criterion [28]. In the first case $\tilde{\varepsilon}$ was [37]

$$\tilde{\varepsilon} = \frac{k-1}{2k(1-2\nu)} I_1 + \frac{1}{2k} \sqrt{\frac{(k-1)^2}{(1-2\nu)^2} I_1^2 + \frac{12k}{(1+\nu)^2} J_2}, \quad (2.7)$$

where ν is the Poisson's ratio, and I_1 and J_2 are the first invariant of the strain tensor and the second invariant of the deviatoric strain tensor, respectively:

$$I_1 = \varepsilon_{11} + \varepsilon_{22} + \varepsilon_{33} \quad \text{and} \quad J_2 = \frac{1}{2} \varepsilon_{ij} \varepsilon_{ij} - \frac{1}{6} I_1^2, \quad (2.8)$$

The parameter k in Eq.2.7 denotes the ratio between the compressive and tensile strength of the material. In the second case, the equivalent strain measure $\tilde{\varepsilon}$ was [28]

$$\tilde{\varepsilon} = \frac{1}{E} \max \{ \sigma_i^{eff} \}, \quad (2.9)$$

where E denotes the Young modulus and σ_i^{eff} are the principal values of the effective stress σ_{ij}^{eff}

$$\sigma_{ij}^{eff} = C_{ijkl}^e \varepsilon_{kl} \quad (2.10)$$

To describe the evolution of the damage parameter D , an exponential softening law was used [37]

$$D = 1 - \frac{\kappa}{\kappa_0} \left(1 - \alpha + \alpha e^{-\beta(\kappa - \kappa_0)} \right), \quad (2.11)$$

where α and β are the material parameters.

3 Non-Local Approach

To describe strain localization, to preserve the well-posedness of the boundary value problem and to obtain mesh-independent FE-results, a non-local theory was used as a regularization technique [6], [39]. Usually, it is sufficient to treat non-locally only variable controlling material softening [15], [39] (whereas stresses and strains remain local). It was assumed in elasto-plasticity that the softening parameter κ was non-local

$$\bar{\kappa}(x_k) = \frac{1}{A} \int \omega(r) \kappa(x_k + r) dV, \quad (3.1)$$

where x_k – coordinates of the considered (actual) point, r – distance measured from the point x_k to other material points, ω – weighting function and A – weighted volume. As a weighting function ω , the Gauss distribution function for 2D problems was used

$$\omega(r) = \frac{1}{l_c \sqrt{\pi}} e^{-\left(\frac{r}{l_c}\right)^2}, \quad (3.2)$$

where l_c denotes a characteristic (internal) length connected to microstructure of the material. The averaging in Eqs.3.1 and 3.2 is restricted to a small representative area around each material point. The influence of the points at the distance of $r=3l_c$ is only about 0.1%. The softening rates $d\kappa_i$ were assumed according to the Brinkreave modified formula [15] (independently for both yield surfaces)

$$d\bar{\kappa}_i(x_k) = (1-m) d\kappa_i(x_k) + \frac{m}{A} \int \omega(r) d\kappa_i(x_k + r) dV, \quad (3.3)$$

where m is the non-local parameter which should be greater than 1 to obtain mesh-independent results [10]. Equation 3.3 can be rewritten as [15]

$$d\bar{\kappa}_i(x_k) = d\kappa_i(x_k) + m \left(\frac{1}{A} \int \omega(r) d\kappa_i(x_k + r) dV - d\kappa_i(x_k) \right), \quad (3.4)$$

Since the rates of the hardening parameter are not known at the beginning of each iteration, the extra sub-iterations are required to solve Eq.3.4. To simplify the calculations, the non-local rates were replaced by their approximations $d\kappa_i^{est}$ calculated on the basis of the known total strain rates [15].

$$d\bar{\kappa}_i(x_k) \approx d\kappa_i(x_k) + m \left(\frac{1}{A} \int \omega(r) d\kappa_i^{est}(x_k + r) dV - d\kappa_i^{est}(x_k) \right), \quad (3.5)$$

In the damage mechanics model, the equivalent strain measure $\tilde{\varepsilon}$ was replaced in Eqs. 2.7 and 2.9 by its non-local definition $\bar{\varepsilon}$

$$\bar{\varepsilon}(x_k) = \frac{1}{A} \int \omega(r) \tilde{\varepsilon}(x_k + r) dV, \quad (3.6)$$

Both models enhanced by non-local terms were implemented in the Abaqus Standard program [1] with the aid of the subroutine UMAT (user constitutive law definition) and UEL (user element definition) [10]. The FE-simulations were performed under plane strain conditions. The geometric nonlinearity was taken into account. The non-local averaging was performed in the current configuration. The quadrilateral elements composed of four diagonally crossed triangles were used to avoid volumetric locking [42].

4 FE - Simulations

4.1 Uniaxial Tension

4.1.1 Elasto-Plastic Model

To study the size effect, the calculations were carried out with 3 different concrete specimens with one notch whose dimensions (from Fe-simulations by Gutierrez and de Borst [22]) and boundary conditions are given in Fig.4.1. The lower and upper edge of the specimen were smooth (no shear stress). The nodes along the bottom edge were fixed in vertical direction. To preserve the stability of the specimen, the node in the middle of the bottom was fixed in the horizontal direction. The deformation was imposed by prescribing a vertical displacement u along the upper edge. To introduce a non-homogenous strain field, a small notch at the left side at mid-height was assumed. Three different meshes were used with 1500, 2620 and 5100 triangular elements for the small, medium and large specimens, respectively. When calculating non-local quantities close to the notch, the so-called “shading effect” was considered (i.e. the averaging procedure considers the notch as an internal barrier that is shading the non-local interaction [29]). In the elastic region, the modulus of elasticity was taken as $E=30$ GPa and Poisson’s ratio as $\nu=0.20$. The diagram describing

the tensile stress σ_t versus the softening parameter κ_2 is shown in Fig.4.2. To simplify calculations, a linear relationship $\sigma_t=f(\kappa_2)$ was assumed with the softening modulus in tension equal to $H_t=3.0/(3.0\times 10^{-3})=1000$ MPa. The tensile strength was equal $f_t=3.0$ MPa. The non-locality parameter $m=2$ was chosen on the basis of initial own FE-studies [10] and other studies [29]. Higher values of m resulted in unrealistic large shear zone widths. The characteristic length was taken as $l_c=15$ mm.

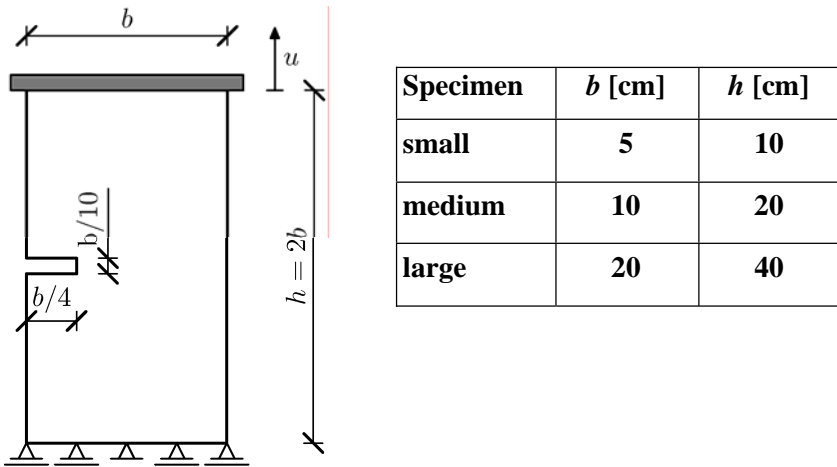


Fig. 4.1. Geometry and boundary conditions of the specimen subjected to uniaxial tension ([22])

Fig.4.3 presents the normalized load-displacement curves for different sizes of the concrete specimen of Fig.4.1 (P – resultant vertical force, u – vertical displacement of the top edge).

The size effect is significant, i.e. the smaller the specimen, the larger the normalized strength and the larger the material ductility. The plots of the non-local softening parameter $\bar{\kappa}_2$ in the neighborhood of the notch for 3 different specimens are shown in Fig. 4.4.

The calculated height of the localized zone increases with the specimen size and is equal to 5.0 cm ($3.3\times l_c$), 6.0 cm ($4\times l_c$) and 7.0 cm ($4.6\times l_c$) for the small, medium and large specimens, respectively. The results are qualitatively similar to those obtained with the second-gradient elastoplastic constitutive model by Gutierrez and de Borst [22].

The maximum loads obtained from FE-simulations for concrete were compared with the energetic size effect law given by Bazant [5], [9] which is valid for structures with pre-existing notches or large cracks:

$$\sigma = \frac{Bf_t}{\sqrt{1-D/D_0}}, \quad (4.1)$$

where σ - nominal strength, B - dimensionless geometry-dependent parameter which depends on the geometry of the structure and of the crack, D - specimen size (equal to the specimen height h) and D_0 - size-dependent parameter called the transitional size.

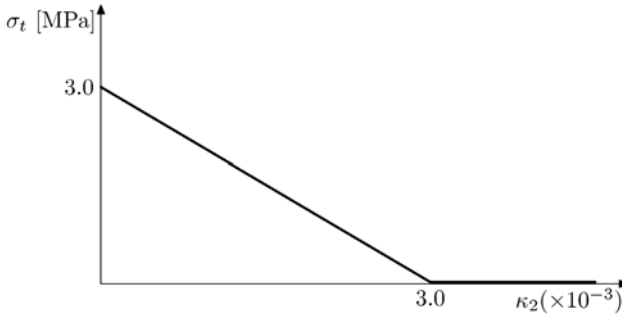


Fig. 4.2. Assumed curve $\sigma_t=f(\kappa_2)$ in tensile regime using the elasto-plastic model for uniaxial tension (σ_t - tensile stress, κ_2 - softening parameter)

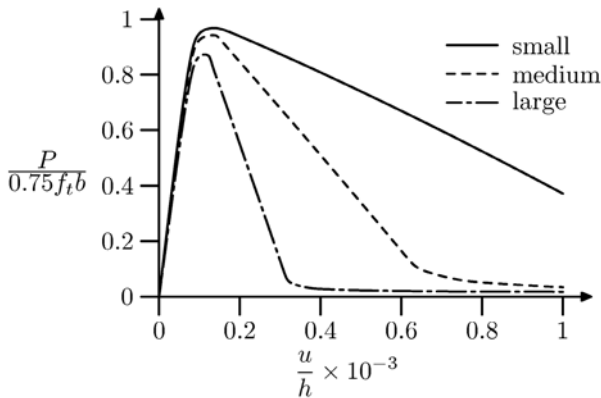


Fig. 4.3. Calculated normalized load-displacement curves for uniaxial tension (elasto-plastic model with non-local softening)

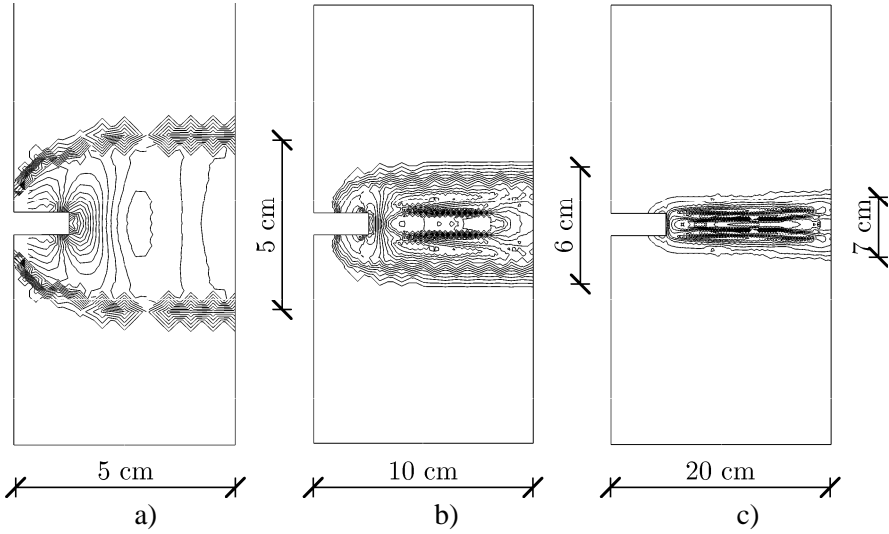


Fig. 4.4. Calculated contours of the nonlocal softening parameter \bar{k}_2 for uniaxial tension of a large (a), medium (b) and small (c) specimen within elasto-plasticity with non-local softening) (different scale is used in 3 specimens)

Eq.4.1 can be rewritten as:

$$\frac{1}{\sigma^2} = \alpha D + c \quad \text{with} \quad \alpha = c/D_0 \quad \text{and} \quad Bf = 1/\sqrt{c}, \quad (4.2)$$

To find parameters B and D_0 from the FE-analysis, a linear regression was used. Fig.4.5 present the differences between stresses σ from the FE-calculations ($\sigma = P/(0.75bt)$, b - element width, $t=1.0$ m – size in the third direction) and those obtained from Eq. 4.2. A good agreement with Bazant's size effect law [9] was obtained. The normalized strength decreases almost linearly with the size ratio h/l_c in the considered range.

4.1.2 Damage Model

The problem of a double notched specimen under uniaxial tension was experimentally investigated by Hordijk [25]. The geometry of the concrete specimen (width $b=60$ mm, height $h=125$ mm, thickness in the out-of-plane direction $t=50$ mm) and boundary conditions (similar as in Fig.4.1) are presented in Fig.4.6. Two symmetric notches 5×5 mm² were located at the mid-point of both sides of the specimen. The modulus of elasticity was equal to $E=18$ GPa and the Poisson's ratio was $\nu=0.2$. The following

parameters of the damage model were chosen (using Eqs.2.7 and 2.11): $\kappa_0 = 2.1 \times 10^{-4}$, $\alpha=0.96$, $\beta=500$ and $k=10$. The characteristic length l_c was assumed to be 5 mm. Three different FE-meshes were used: coarse (1192 triangular elements), medium (1912 triangular elements) and fine (4168 triangular elements), Fig.4.7.

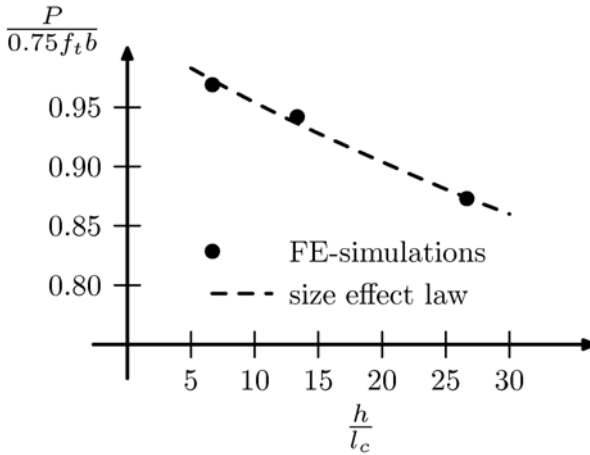


Fig. 4.5. Relationship between calculated normalized concrete strength $\sigma=P/(0.75bt)$ from uniaxial tension and ratio h/l_c (elasto-plastic model with non-local softening) compared to the size effect law by Bazant [5]

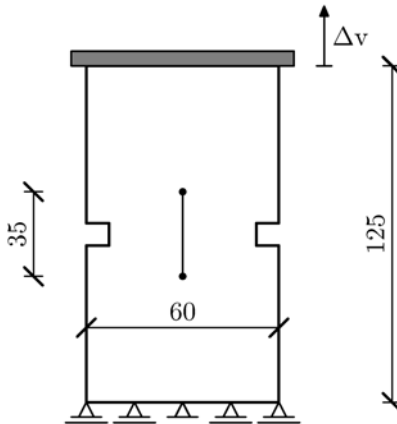


Fig. 4.6. Geometry and boundary conditions of a specimen with a notch under uniaxial tension (dimensions are given in mm)

The calculated contours of the damage parameter κ in the specimen are shown in Fig.4.8 at residual state. The results are mesh-independent since the width of the damage region in the mid-region of the specimen is always the same. The width of the localization zone is approximately 22 mm ($4.4 \times l_c$).

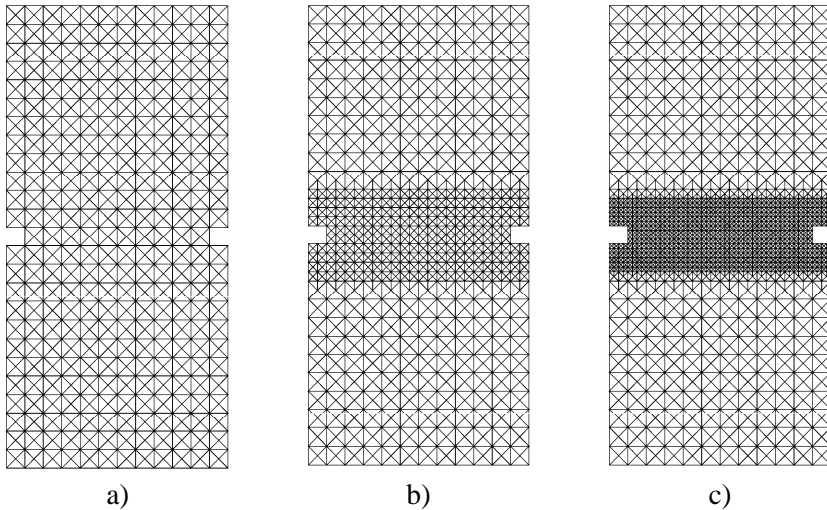


Fig. 4.7. FE-meshes used for calculations of uniaxial tension: a) coarse, b) medium, c) fine

Fig.4.9 presents the nominal stress–elongation tensile curves for all meshes as compared to the experimental curve [25]. The elongation δ in Fig.4.9 denotes the elongation of the specimen above and below both notches at the height of 35 mm (Fig.4.7). It was measured experimentally by 4 pairs of extensometers with a gauge length of 35 mm. The vertical normal stress was calculated by dividing the calculated resultant vertical force along the upper edge by the specimen cross-section of $50 \times 50 \text{ mm}^2$. The calculated load-displacement curves of Fig. 4.9 practically coincide for the different meshes. They are also in a satisfactory agreement with the experimental curve [25], although a small deviation between the theory and the experiment (in particular after the peak) takes place.

In addition, the influence of the characteristic length l_c of micro-structure on the specimen behaviour was investigated. The FE-calculations were performed with l_c in the range from 2.5 mm up to 10.0 mm. The obtained

load-displacement curves are presented in Fig. 4.10. The larger the characteristic length, the higher the maximum tensile stress. The inclination of all curves to the horizontal after the peak becomes smaller with increasing l_c (the material becomes more ductile). The width of the localized zone was 12 mm ($4.8 \times l_c$ for $l_c=2.5$ mm), 22 mm ($4.4 \times l_c$ for $l_c=5$ mm), 34 mm ($4.5 \times l_c$ for $l_c=7.5$ mm) and 44 mm ($4.4 \times l_c$ for $l_c=10$ mm), Fig. 4.11.

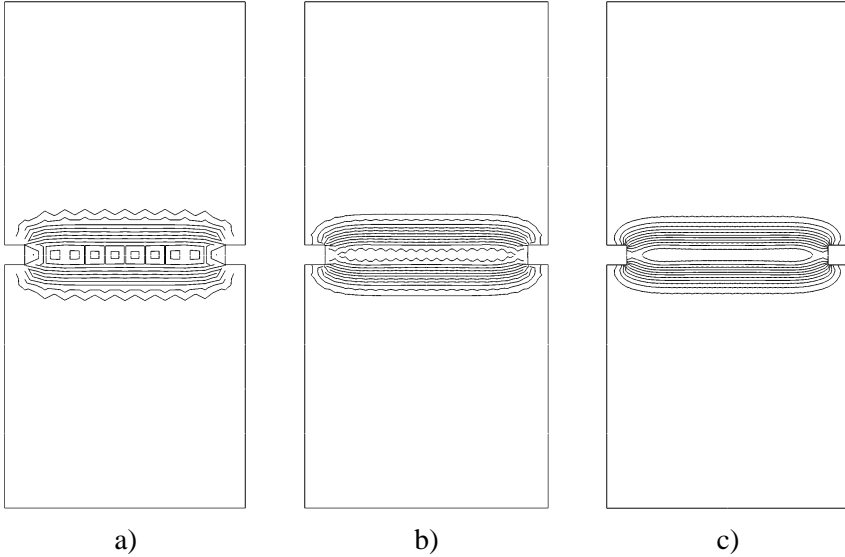


Fig. 4.8. Calculated contours of the damage parameter κ in a specimen under uniaxial tension for: a) coarse, b) medium and c) fine mesh (damage model with non-local softening)

The results are in a good accordance with the FE-results by Pamin [36] and Peerlings et al. [37] using a second-gradient damage continuum model.

4.2 Three-Point Bending

The behaviour of the concrete beam with a notch at the bottom at mid-span and free ends during three-point bending was simulated. This behaviour was experimentally investigated by Le Bellego et al. [31], and later numerically simulated by Le Bellego et al. [31] and Rodriguez-Ferran et al

[40] with a non-local damage approach. Three different beams were used in laboratory tests: small ($h=8$ cm), medium ($h=16$ cm) and large one ($h=32$ cm). The beam length was $L=3h$. The geometry and boundary conditions of the beam are presented in Fig.4.12. The loading was prescribed at the top edge in the mid-span via displacement. Three different FE-meshes were assumed: with 1534, 2478 and 4566 triangular elements for a small, medium and large specimen, respectively. Due to the symmetry of the problem, only half of the beam was modeled. In the simulations, the modulus of elasticity was taken as $E=38.5$ GPa and the Poisson ratio as $\nu=0.2$.

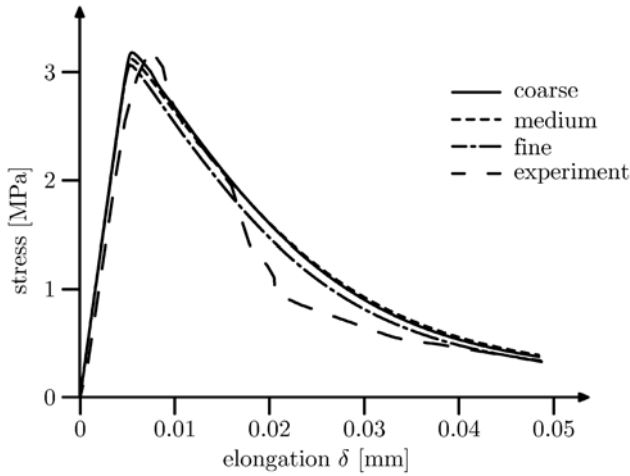


Fig. 4.9. Calculated stress–elongation diagrams for a specimen under uniaxial tension (damage model with non-local softening) with different FE-meshes compared to the experimental diagram [25]

4.2.1 Elasto-Plastic Model

In the tensile regime, the Rankine criterion (Eq.2.4) using the exponential curve in the softening regime proposed by Hordijk [25] was defined

$$\sigma_t(\kappa_2) = f_t \left\{ \left[1 + \left(c_1 \frac{\kappa_2}{\kappa_u} \right)^3 \right] \exp\left(-c_2 \frac{\kappa_2}{\kappa_u} \right) - \frac{\kappa_2}{\kappa_u} (1 + c_1^3) \exp(-c_2) \right\}, \quad (4.3)$$

where σ_t – tensile stress, f_t – tensile strength of the concrete, κ_u – ultimate value of the softening parameter and c_1, c_2 – constants equal to 3 and 6.93,

respectively. Two different characteristic lengths were assumed in the FE-analyses, namely $l_c=5$ mm and $l_c=10$ mm. For each characteristic length, the following material parameters were chosen: $f_i=3.6$ MPa, $\kappa_i=0.005$ ($l_c=5$ mm), and $f_i=3.3$ MPa, $\kappa_i=0.003$ ($l_c=10$ mm) with $m=2$. They were adopted to obtain the best agreement between the load-displacement diagrams from FE-analyses and laboratory tests [31]. The internal friction angle was equal to $\varphi=10^\circ$ [1] and the dilatancy angle $\psi=5^\circ$. The compressive strength was equal to $f_c=40$ MPa. The softening modulus in compression was $H_c=0.8$ MPa. The material parameters in the compressive regime did not influence the FE-results.

Fig. 4.13 presents the load-displacement curves for all beams obtained from FE-calculations with the characteristic length of $l_c=5$ mm and $l_c=10$ mm compared with experiments. A satisfactory agreement was obtained. The FE-results overestimate slightly the load bearing capacity of the small and medium beam and underestimate the maximum load for the large beam. The results demonstrate that a characteristic length can be only determined on the basis of the measured width of strain localization (from an inverse identification process) but not from the measured load-displacement curves.

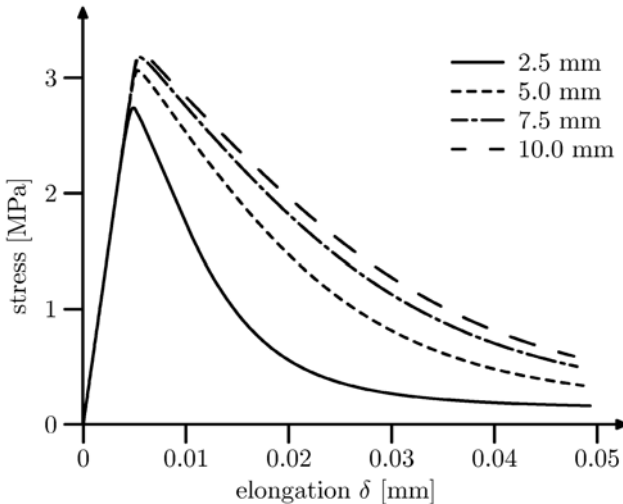


Fig. 4.10. Calculated stress–elongation diagrams using different characteristic lengths l_c for a specimen under uniaxial tension (damage model with non-local softening)

The width of the calculated localization zone was about 20 mm ($4 \times l_c$) for $l_c=5$ mm (Fig.4.13), and 45 mm ($4.5 \times l_c$) (small beam), 40 mm ($4 \times l_c$) (medium beam, Fig.4.13) and 35 mm ($3.5 \times l_c$) (large beam) for $l_c=10$ mm, respectively. It did not depend on the mesh size.

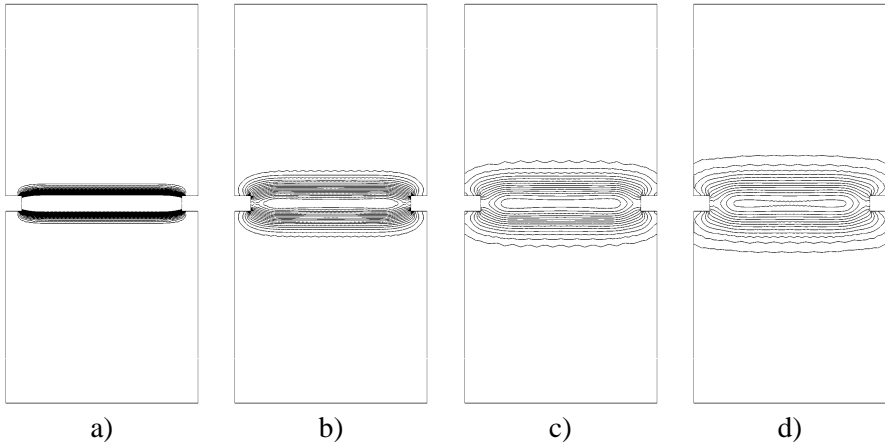


Fig. 4.11. Calculated contours of the damage parameter κ in a specimen under uniaxial tension: a) $l_c=2.5$ mm, b) $l_c=5$ mm, c) $l_c=7.5$ mm, d) $l_c=10$ mm (damage model with non-local softening, fine mesh)

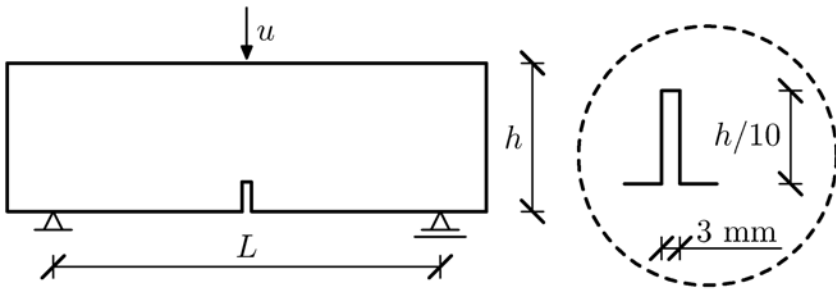


Fig. 4.12. Geometry of the beam and boundary conditions [31]

4.2.2 Damage model

Two different characteristic lengths were again assumed, namely $l_c=5$ mm and $l_c=10$ mm. For each l_c , the following material parameters were chosen: $\kappa_0=7\cdot 10^{-5}$, $\alpha=0.99$, $\beta=600$ ($l_c=5$ mm), and $\kappa_0=6.25\cdot 10^{-5}$, $\alpha=0.99$, $\beta=1000$ ($l_c=10$ mm) (using Eqs.2.9 and 2.11). A satisfactory agreement between FE-results and experimental ones was achieved in both cases (Fig. 4.14).

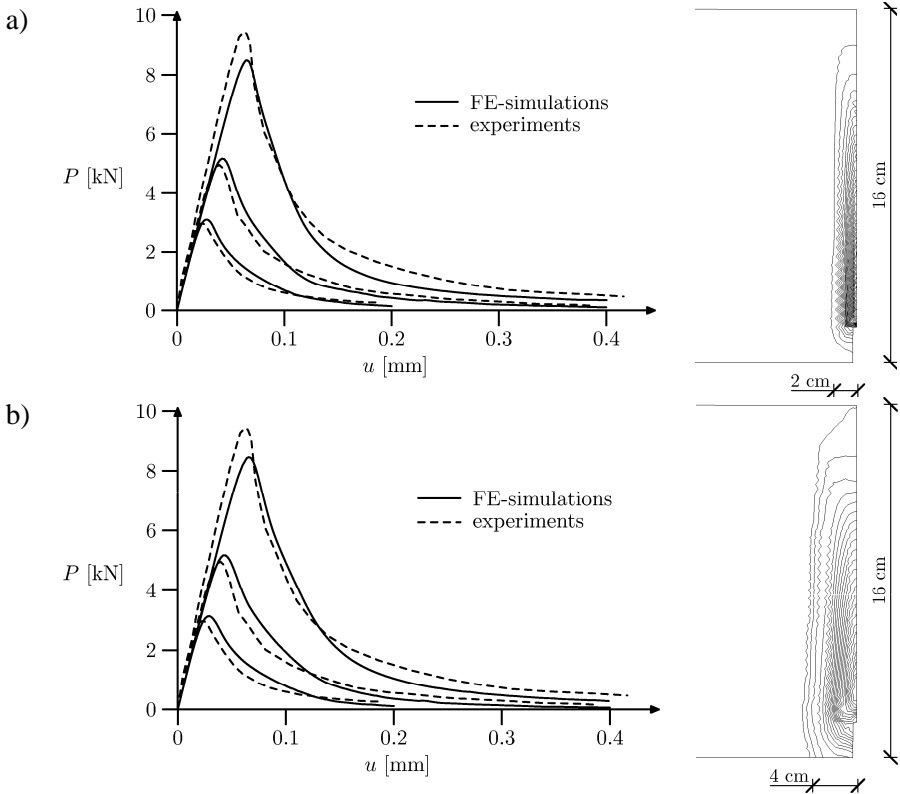


Fig. 4.13. Load-displacement curves from experiments [31] and FE-simulations, and calculated contours of the non-local parameter: a) $l_c=5$ mm, b) $l_c=10$ mm (elasto-plastic model with non-local softening, beam height $h=160$ mm)

The width of the localization zone at the end of the loading process was equal to 40 mm ($8\times l_c$) (small beam), 35 mm ($7\times l_c$) (medium beam, Fig.4.14) and 40 mm ($8\times l_c$) (large beam) for $l_c=5$ mm, and 50 mm ($5\times l_c$) (small beam), 60 mm ($6\times l_c$) (medium beam, Fig.4.14) and 80 mm ($8\times l_c$)

(large beam) for $l_c=10$ mm, respectively. It did not depend on the mesh size. The width of the localization zone was not constant and it increased during loading [36]. Similarly as in elasto-plasticity, the FE-calculations overestimate slightly the load bearing capacity for the small and medium beam and underestimate the maximum load for the large beam. The same conclusions were drawn by Le Bellego et al. [31] and Rodriguez-Ferran et al. [40] from their simulations, although they used different definitions of the equivalent strain $\tilde{\epsilon}$ and evolution laws.

The maximum loads obtained from FE-simulations were compared again with the energetic size effect law given by Bazant (Eq.4.1) (Fig.4.15). A good match was achieved. The normalized strength decreases almost linearly with increasing size ratio h/l_c in the considered range.

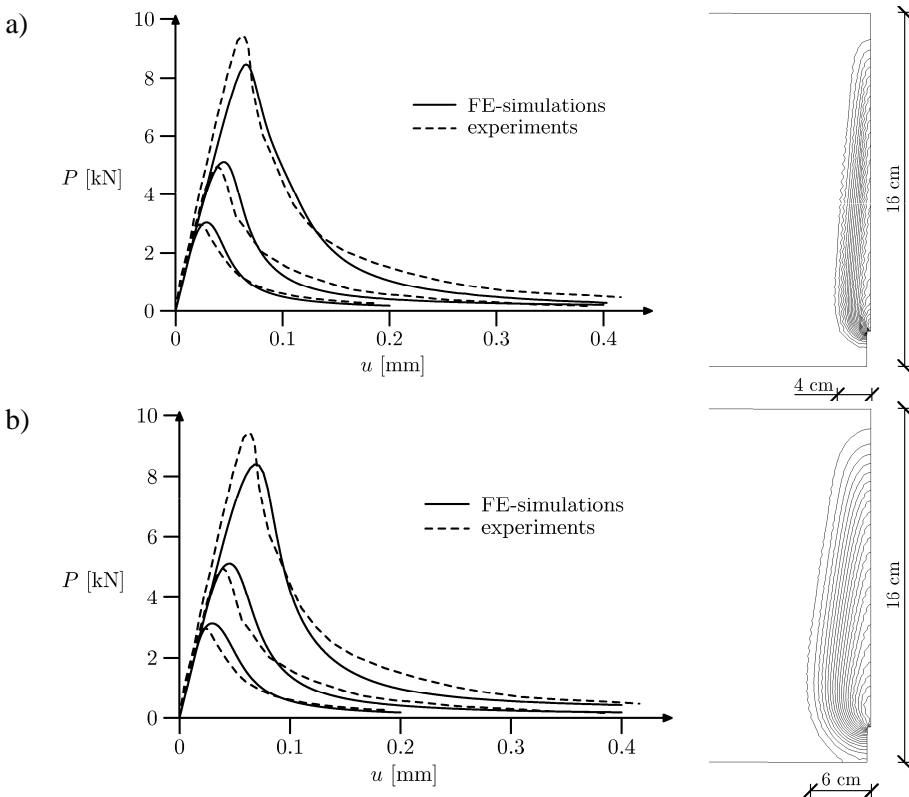


Fig. 4.14. Load-displacement curves from experiments [31] and FE-simulations and calculated contours of the non-local parameter for beam height $h=160$ mm: a) $l_c=5$ mm, b) $l_c=10$ mm (damage model with non-local softening)

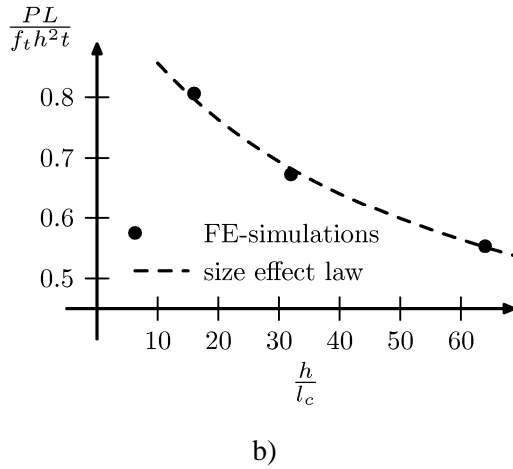
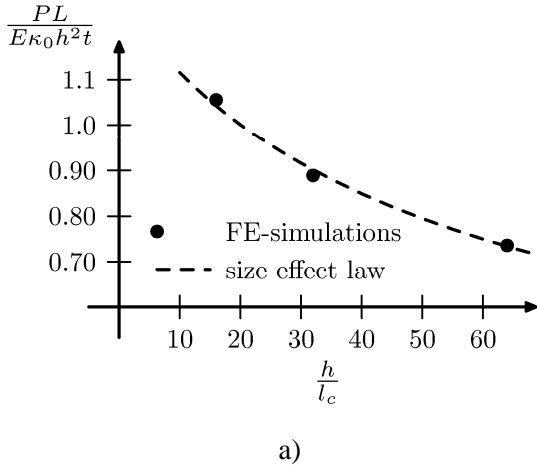


Fig. 4.15. Relationship between the calculated normalized loads: $(PL)/(E\kappa_0 h^2 t)$ and $(PL)/(f_t h^2 t)$ during bending (with $l_c=5\text{mm}$) and the ratio h/l_c as compared to the size effect law by Bazant [5] within: a) damage mechanics, b) elasto-plasticity

5 Conclusions

The FE-calculations have shown that both constitutive models: elasto-plastic and damage with non-local softening are able to capture strain localization and related size effect in problems characterized by the failure mode I. The obtained FE-results did not suffer from the mesh sensitivity.

A satisfactory agreement between numerical simulations and laboratory experiments with respect to the load-displacement curves was achieved.

The larger the ratio between the characteristic length of micro-structure and the specimen size, the higher both the material strength and ductility of the specimen.

The width of the localized strain zone in concrete specimens increases with increasing ratio between the characteristic length of micro-structure and the specimen size.

The width of the localized strain zone is for uniaxial tension about $(3.3-4.5) \times l_c$ within elasto-plasticity and $(4.5-5.0) \times l_c$ damage mechanics. The width of the localized zone in beams was larger in FE-analyses with a damage model (about $(5-8) \times l_c$) than with an elasto-plastic model (about $(3.5-4.5) \times l_c$). It was similar in beams for the characteristic length of 5 mm, and decreased in elasto-plasticity and increased in damage mechanics with increasing beam size for the characteristic length of 10 mm.

The size effect decreases almost linearly with decreasing ratio between the specimen size and characteristic length. It is in agreement with the size effect law by Bazant.

A characteristic length of micro-structure can be only identified on the basis of measurements of strain localization.

The calculations on strain localization in concrete will be continued. To include plastic deformation and hardening, the damage model will be combined with an elasto-plastic model [12]. Afterwards, the model will be enriched by anisotropy [51]. To describe a statistical size effect, a spatially correlated distribution of the tensile strength will be assumed [46]. In addition, laboratory tests will be performed wherein the width of strain localization will be measured using a DIC technique.

Acknowledgements

The numerical calculations were performed on supercomputers of the Academic Computer Centre in Gdansk TASK.

References

1. Abaqus (1998) Theory Manual, Version 5.8, Hibbit, Karlsson & Sorensen Inc.
2. Akkermann J (2000) Rotationsverhalten von Stahlbeton-Rahmenecken, Dissertation, Universitat Fridericiana zu Karlsruhe, Karlsruhe

3. Bazant ZP, Bhat PD (1976) Endochronic theory of inelasticity and failure of concrete, *J. Engng. Mech. Div. ASCE*, 102:701-722
4. Bazant ZP, Cedolin L (1979) Blunt crackband propagation in finite element analysis, *J. Engng. Mech. Div. ASCE*, 105, 2:297-315
5. Bazant ZP (1984) Size effect in blunt fracture: concrete, rock, metal. *J. Engng. Mech. ASCE* 110:518-535
6. Bazant ZP, Lin FB, Pijaudier-Cabot G (1987) Yield limit degradation; nonlocal continuum model with local strain. *Proceedings of the International Conference on Computational Plasticity. Barcelona pp 1757-1780*
7. Bazant ZP, Ozbolt J. (1990) Non-local microplane model for fracture, damage and size effect in structures. *J. Engng. Mech. ASCE*, 116:2485-2505
8. Bazant ZP, Shieh CL (1978) Endochronic model for nonlinear triaxial behaviour of concrete, *Nucl. Engng. Des.*, 47:305-315
9. Bazant ZP (2003) *Scaling of Structural Strength*. Hermes-Penton, London
10. Bobinski J, Tejchman J (2004) Numerical simulations of localization of deformation in quasi-brittle materials within non-local softening plasticity, *Computers and Concrete*, 4:433-455
11. Bobinski J, Tejchman J (2005) Modelling of concrete behaviour with a non-local continuum damage approach. *Archives of Hydro-Engineering and Environmental Mechanics, Polish Academy of Sciences*, 1, 52, 2:85-102
12. Bobinski J, Tejchman J (2006) Modelling of strain localization in quasi-brittle materials with nonlocal continuum models. In: Bicanic N, de Borst R, Mang H (eds) *Proc. Euro-C 2006*, pp 301-307
13. de Borst R, Mühlhaus H-B, Pamin J, Sluys L (1992) Computational modelling of localization of deformation. In: Owen DRJ, Onate H, Hinton, E (eds). *Proc. of the 3rd Int. Conf. Comp. Plasticity*, Swansea, Pineridge Press pp 483-508
14. de Borst R, Pamin J, Geers M (1999) On coupled gradient-dependent plasticity and damage theories with a view to localization analysis. *Eur. J. Mech. A/Solids* 18, 6:939-962
15. Brinkgreve RBJ (1994) *Geomaterial models and numerical analysis of softening*. PhD Thesis. Delft University of Technology
16. Chen E (1999) Non-local effects on dynamic damage accumulation in brittle solids, *I. J. Num. Anal. Meth. Geomech.* 23:1-21
17. Chen J, Yuan H, Kalkhof D (2001) A nonlocal damage model for elastoplastic materials based on gradient plasticity theory. Report Nr.01-13, Paul Scherrer Institut, pp 1-130
18. D'Addetta GA, Kun F, Ramm E (2002) In the application of a discrete model to the fracture process of cohesive granular materials. *Granular Matter* 4:77-90
19. Donze FV, Magnier SA, Daudeville L, Mariotti C, Davenne L (1999) Numerical study of compressive behaviour of concrete at high strain rates, *Journal Engineering Mechanics* 1154-1163
20. Dragon A, Mroz Z (1979) A continuum model for plastic-brittle behaviour of rock and concrete, *Int. Journal Eng. Science* 17

21. Groen AE (1997) Three-dimensional elasto-plastic analysis of soils. PhD Thesis, Delft University, pp 1-114
22. Gutierrez MA, de Borst R (2003) Simulation of size-effect behaviour through sensitivity analysis, *Engineering Fracture Mechanics*, 70:2269-2279
23. Herrmann HJ, Hansen A, Roux S (1989) Fracture of disordered elastic lattices in two dimensions. *Physical Rev. B*, 39:637-647
24. Hilleborg A (1985) The theoretical basis of a method to determine the fracture energy of concrete, *Materials and Structures*, 18:291-296
25. Hordijk DA (1991) Local approach to fatigue of concrete, PhD dissertation, Delft University of Technology
26. Ibrahimbegovic A, Markovic D, Gatuing F (2003) Constitutive model of coupled damage-plasticity and its finite element implementation, *Eur. J. Finite Elem.* 12, 4:381-405
27. Jirasek M (1999) Comments on microplane theory. *Mechanics of quasi-brittle materials and structures*. In: Pijaudier-Cabot, G, Bittnar Z, and Gerard B (eds), Hermes Science Publications, pp 55-77
28. Jirasek M (2004) Non-local damage mechanics with application to concrete. *Revue Francaise de Genie Civil*. 8:683-707
29. Jirasek M, Rolshoven S (2003) Comparison of integral-type nonlocal plasticity models for strain-softening materials. *Int. J. Engineering Science*, 41:1553-1602
30. Kozicki J, Tejchman J (2006) 2D lattice model for fracture in brittle materials. *Archives of Hydro-Engineering and Environmental Mechanics*, Polish Academy of Sciences, 53, 2: 71-88
31. Le Bellego C, Dube JF, Pijaudier-Cabot G, Gerard B (2003) Calibration of nonlocal damage model from size effect tests. *European Journal of Mechanics A/Solids*, 22:33-46
32. Lemaitre J (1985) Coupled elasto-plasticity and damage constitutive equations, *Computer Methods Appl. Mech. Eng.*, 51:31-49
33. Menetrey P, Willam K J (1995) Triaxial failure criterion for concrete and its generalization, *ACI Structural Journal* 311-318
34. Palaniswamy R, Shah SP (1974) Fracture and stress-strain relationship of concrete under triaxial compression, *J. Struct. Div. ASCE*, 100:901-916
35. Pamin J, de Borst R (1998) Simulation of crack spacing using a reinforced concrete model with an internal length parameter. *Arch. App. Mech.*, 68, 9:613-625
36. Pamin J (2004) Gradient-enhanced continuum models: formulation, discretization and applications, *Habilitation Monography*, Cracow University of Technology, Cracow
37. Peerlings RHJ, de Borst R, Brekelmans WAM, Geers MGD (1998) Gradient enhanced damage modelling of concrete fracture, *Mech. Cohesion.-Friction. Materials*, 3:323-342
38. Pietruszczak D, Jiang J, Mirza FA (1988) An elastoplastic constitutive model for concrete, *Int. J. Solids Structures*, 24, 7:705-722
39. Pijaudier-Cabot G, Bazant ZP (1987) Nonlocal damage theory. *ASCE J. Eng. Mech.*, 113:1512 -1533

40. Rodriguez-Ferran A, Morata I, Huerta A (2002) Numerical modelling of notched specimens. Proc. WCCM V, Vienna Austria
41. Sakaguchi H, Mühlhaus HB (1997) Mesh free modelling of failure and localisation in brittle materials. In: Asaoka A, Adachi T, Oka F (eds), Deformation and Progressive Failure in Geomechanics, Pergamon, pp 15-21
42. Salari MR, Saeb S, Willam K, Patchet SJ, Carrasco RC (2004) A coupled elastoplastic damage model for geomaterials. Computers Methods in Applied Mechanics and Engineering, 193:2625-2643
43. Schlangen E, Garboczi EJ (1997) Fracture simulations of concrete using lattice models: computational aspects. Engineering Fracture Mechanics 57:319-332
44. Sluys L (1992) Wave propagation, localisation and dispersion in softening solids. PhD Thesis, Delft University of Technology
45. Sluys LJ, de Borst R (1994) Dispersive properties of gradient and rate-dependent media, Mech. Mater. 183:131-149
46. Tejchman J (2006) Effect of fluctuation of current void ratio on the shear zone formation in granular bodies within micro-polar hypoplasticity, *Computers and Geotechnics* 33, 1:29-46
47. Willam KJ, Warnke EP (1975) Constitutive model for the triaxial behaviour of concrete, IABSE Seminar on concrete structures subjected to triaxial stress, Bergamo, Italy, 1-31
48. Wittmann FH, Mihashi H, Nomura N (1992) Size effect on fracture energy using three-point bend tests. Materials and Structures, 25:327-334
49. Vervuurt A, van Mier JGM, Schlangen E (1994) Lattice model for analyzing steel-concrete interactions. In: Siriwardane, Zaman (eds) Comp. Methods and Advances in Geomechanics, Balkema, Rotterdam, pp 713-718
50. Van Vliet MRA, van Mier JGM (1996) Experimental investigation of concrete fracture under uniaxial compression. Mechanics of Cohesive-Frictional Materials, 1:115-127
51. Zhou W, Zhao J, Liu Y, Yang Q (2002) Simulation of localization failure with strain-gradient-enhanced damage mechanics, Int. J. Numer. Anal. Meth. Geomech. 26:793-813

Kinematics of Shear Zone Deformation in Soft Sensitive Clays

V. Thakur¹, S. Nordal¹, H. P. Jostad² and L. Andresen²

¹Geotechnical Division,
NTNU,
Norway.

²Geo-Mechanics Division,
NGI,
Norway.

Summary

Sensitive clays, exhibits softening, are characterized by a response in which shear stress increases monotonically up to a peak value, and decreases with further increase of shear strain i.e. second order work becomes negative, during the shear deformation and will therefore develop excess pore pressure in the shear bands. Due to the low permeability of clays in combination with a generally high deformation rate, the failure process is often considered being undrained and analyzed using a total stress approach. However, if thin localized shear zones develop, local pore-water dissipation will take place. This diffusion process may be important to define the shear bands. To study this process an effective stress based soil model is needed. The model must incorporate a formulation for how excess pore pressures accompany the softening process. Keeping in view, a simple direct shear sample (DSS) test and one dimensional soil column is simulated to analyze the coupled strain softening pore water mechanism. This study is initiated to test the hypothesis that a finite shear band thickness may result for a given deformation rate.

Key words: strain softening, sensitive clays, finite element analyses, shear band

1 Introduction

Since Biot (1941, 1965) have derived the general theory of three dimensional consolidations and initiated research on material instability, much effort has been devoted to the study of multi-phase media (Bardet 1992; Bowen 1982; Schrefler et al. 1990) and solid instability (Bardet 1991; Hill and Hutchinson 1975; Vardoulakis 1981; Bardet, 1990).

The mechanical response of multiphase (solid, air and water) system like geomaterials is of great importance in engineering practice. For instance uneven settlement of underlying soil deposits due to time dependent pore water pressure dissipation from foundation loading, shear creep are the most comely recognized examples. Since the end of 70's several authors have studied strain localization in multiphase materials. Rudnicki (1984) analyzed a fluid saturated rock mass with an embedded weakened layer. Rice (1985) studied the effect of material dilatancy on strain localization in fully saturated frictional material. In recent years, much effort has been developed to devise regularization strategies to simulate the development of shear band in multiphase material without mesh dependency. Rice (1985) and Vardoulakis (1985) extended the instability analyses from single phase to multiphase materials. (Liu, 2003)

According to studies e.g. Schrefler et al (1995), Schrefler et al.(1996), Liu et al. (2001) and Liu (2003), numerical simulation of strain localization in a multiphase material have evidenced that mesh dependency is not severe as in single phase material. The reason is that the governing field eq.s a gradient term is included through Darcy's law, an internal length scale is introduced naturally, resulting thus a regularization for strain localization (Loret and Prevost, 1991 and Schrefler et al. 1995). This internal length scale depends on several material parameters and in particular on the permeability, applied strain rates.

A numerical simulation of biaxial test by Liu (2003) reports the importance of permeability, boundary roughness and excess pore water pressure in strain localization phenomenon for granular material under undrained condition.

This paper presents some initial numerical examples using the finite element simulation to demonstrate the kinematics of shear zone deformation governed by the coupled mechanism.

2 Governing Equation for Coupled Flow

A coupled formulation for the description of deformation and motion of a multiphase media are carried out on the basis of modern mixture theory, see Bowen (1982) Ehlers (1989), Lewis and Schrefler (1998) and Liu (2003). In this study, soil is considered as two phase media, solid and water, sighting the assumption of a fully saturated state.

The equilibrium equation for the soil solid skeleton can be written as

$$\begin{aligned}
 & \int_V N^T \cdot \rho \cdot \alpha \cdot dV + \int_V B^T \cdot \left(\int_{t-\Delta t}^t \beta \cdot \delta \cdot \dot{p}_w \cdot dt \right) dV \\
 & + \int_V B^T \cdot \int_{t-\Delta t}^t \sigma' \cdot dt \cdot dV \tag{2.1} \\
 & = \int_{\Omega} N^T \cdot s \cdot d\Omega - \int_V B^T \cdot \sigma'_t \cdot dV + \int_V N^T \cdot \rho \cdot g \cdot dV
 \end{aligned}$$

where \mathbf{N} is the shape function, \mathbf{a} is the acceleration, \mathbf{B} is the displacement vector, β is the Biot's constant, δ is the Kronecker's delta, p_w is pore water pressure, t is the time, V represents the volume, σ' is the effective stresses which represents the stress associated with the total deformation of the multiphase media, s is the surface traction and \mathbf{g} is the gravity.

In wide sense, in finite element analyses by using multidimensional incremental springs, the element stiffness matrix for soil skeleton can also be written as

$$\mathbf{D} \cdot \Delta v = \Delta f \tag{2.2}$$

where \mathbf{D} is fourth order tensor that characterizes the material behavior, Δv is nodal displacements and Δf is corresponding nodal forces. By adding for all elements gives the global increment stiffness matrix.

By including the time derivative of \dot{p}_w , eq. (2.1) can also be written as

$$\tilde{C} \cdot \Delta V + E \cdot \Delta p = \Delta f \tag{2.3}$$

$$\tilde{C} = K_o \cdot A + C \tag{2.4}$$

$$A = \int_V N^T \cdot \rho \cdot N \cdot dV \tag{2.5}$$

$$C = \int_V B^T \cdot t^{-\Delta t} D \cdot B \cdot dV \tag{2.6}$$

$$E = \int_V B^T \cdot \beta \cdot \delta \cdot N \cdot S_w dV + \int_V B^T \cdot \beta \cdot \delta \cdot N \frac{W_s}{n} \cdot N \cdot p dV \tag{2.7}$$

$$F_t = \int_{\Omega} N^T \cdot s \cdot d\Omega + \int_V N^T \cdot \rho \cdot g \cdot dV \tag{2.8}$$

$$\Delta f = T_f - f_t^{int} \tag{2.9}$$

$$T = F_t + A(K_1 \cdot \dot{v} + K_2 \cdot \ddot{v}) \tag{2.10}$$

$$f_t^{int} = \int_V B^T \cdot \sigma'_t \cdot dV \tag{2.11}$$

and, the continuity eq. of the pore fluid can be as following

$$\int_{\Omega} (N_p)^T \cdot \hat{q} \cdot d\Omega - \int_V (\nabla N_p)^T \cdot k \frac{k_{rp}}{\mu_p} \nabla N_p \cdot p dV - \int_V (\nabla N_p)^T + \int_V (\nabla N_p)^T \cdot Q^w \cdot N_p \cdot \dot{p} dV + \int_V (\nabla N_p)^T \cdot \beta \cdot \delta^T \cdot \dot{v} dV = 0 \tag{2.12}$$

Also, for two dimensional flow cases, Darcy’s law can be written as

$$\begin{bmatrix} q_x \\ q_y \end{bmatrix} = \begin{bmatrix} k_x & 0 \\ 0 & k_y \end{bmatrix} \begin{bmatrix} \frac{1}{\gamma_w} & \frac{\partial p_w}{\partial x} \\ \frac{1}{\gamma_w} & \frac{\partial p_w}{\partial y} \end{bmatrix} \tag{2.13}$$

Here p_w is the pore pressure and q designated to nodal flow in x and y directions respectively. Pore water flow follows the Darcy’s law which can be rewritten from eq. (2.12)

$$J^T \cdot v + M \cdot p + R \cdot p = q_p \tag{2.14}$$

$$J^T = \int_V N^T \cdot \beta \cdot \delta^T \cdot B \cdot \dot{v} dV \tag{2.15}$$

$$M = \int_V N^T \cdot Q^p \cdot N \cdot dV \tag{2.16}$$

$$R = \int_V (\nabla N)^T \cdot k \frac{k_{rp}}{\mu_p} \nabla N \cdot dV \tag{2.17}$$

$$q_p = \int_V \nabla N^T \cdot k \frac{k_{rp}}{\mu_p} \nabla \rho_p g dV - \int_{\Omega} N^T \cdot \hat{q} \cdot d\Omega \tag{2.18}$$

After rearranging above esq., can be combined in matrix form as

$$\begin{bmatrix} \tilde{C} & E \\ J^T & (M' + \beta^*) \end{bmatrix} \cdot \begin{bmatrix} \Delta v \\ \Delta p \end{bmatrix} = \begin{bmatrix} \Delta f \\ \Delta q_p \end{bmatrix} \tag{2.19}$$

$$M' = \frac{M\beta}{\gamma} \tag{2.20}$$

$$\beta^* = R \cdot \Delta t \frac{\beta}{\gamma} \tag{2.21}$$

3 Pore Water Pressure Generation Dissipation Equation

Considering a one dimensional consolidation situation, a classical eq. of flux flow can be written as

$$\frac{\partial P_w}{\partial t} = c^2 \frac{\partial^2 P_w}{\partial z^2} \tag{3.1}$$

Assuming that drainage path is of infinite length on both sides (and laterally impermeable surface). Then there will not be any boundary conditions, but only the initial condition

$$P_w(z,0) = f(z) \tag{3.2}$$

where $f(z)$ is the given initial pore water pressure of the bar. By substituting $P_w(z,t)=F(z)G(t)$, we obtained two ordinary differential eq.

$$\frac{\partial^2 F}{\partial z^2} + \psi^2 F = 0 \tag{3.3}$$

$$\frac{\partial G}{\partial t} + c^2 \psi^2 G = 0 \tag{3.4}$$

A complete solution can be written as

$$P_w(z, t; \psi) FG = (A \cos \psi z + B \sin \psi z) e^{-c^2 \psi^2 t} \tag{3.5}$$

Since $f(x)$ is not assumed to be periodic, it is natural to use Fourier integral instead of Fourier series. Also, A and B in eq. (3.5) are arbitrary and re-garded as the function of ψ , can be determined from initial condition.

$$P_w(z, 0) = \int_0^\infty [A(\psi) \cos \psi z + B(\psi) \sin \psi z] d\psi = f(z) \tag{3.6}$$

$$A(\psi) = \frac{1}{\pi} \int_{-\infty}^\infty f(v) \cos \psi v dv \tag{3.7}$$

$$B(\psi) = \frac{1}{\pi} \int_{-\infty}^\infty f(v) \sin \psi v dv \tag{3.8}$$

and hence $u(x, 0)$ can be written as

$$P_w(z, 0) = \frac{1}{\pi} \int_0^\infty \left[\int_{-\infty}^\infty f(v) \cos(\psi z - \psi v) dv \right] d\psi \tag{3.9}$$

Finally, eq. (3.9) becomes

$$P_w(z, t) = \frac{1}{\pi} \int_{-\infty}^\infty f(v) \left[\int_0^\infty e^{-c^2 \psi^2 t} \cos(\psi z - \psi v) d\psi \right] dv \tag{3.10}$$

The above eq. can be simplified to

$$P_w(z, t) = \frac{1}{2c\sqrt{\pi t}} \int_{-\infty}^\infty f(v) \exp\left\{-\frac{(z-v)^2}{4c^2 t}\right\} dv \tag{3.11}$$

In order to demonstrate characteristic of eq. (3.11), a one dimensional soil column is of length (z) with an embedded shear band thickness (v). In this example, refer Fig. 3.1, the ratio between length of soil column to the shear band thickness is assumed as 10. Soft clays have coefficient of diffusion (c) equals to $0.24 \text{ m}^2/\text{year}$.

A globally undrained soil column is subjected to shear at different strain rates such that the local undrained to a partial drainage situation can be obtained. Excess pore pressure is maximum within contracting shear band due to incompressibility of pore water. At significantly higher strain rate, distribution of excess pore pressure is quasi-static. This also represents a situation where no pore water flow from shear band to the outside body and hence softening can be very rapid due to drastic reduction in effective stress. This situation is recognized as locally undrained condition.

A smooth transition of pore water is observed with decreasing applied strain rates.

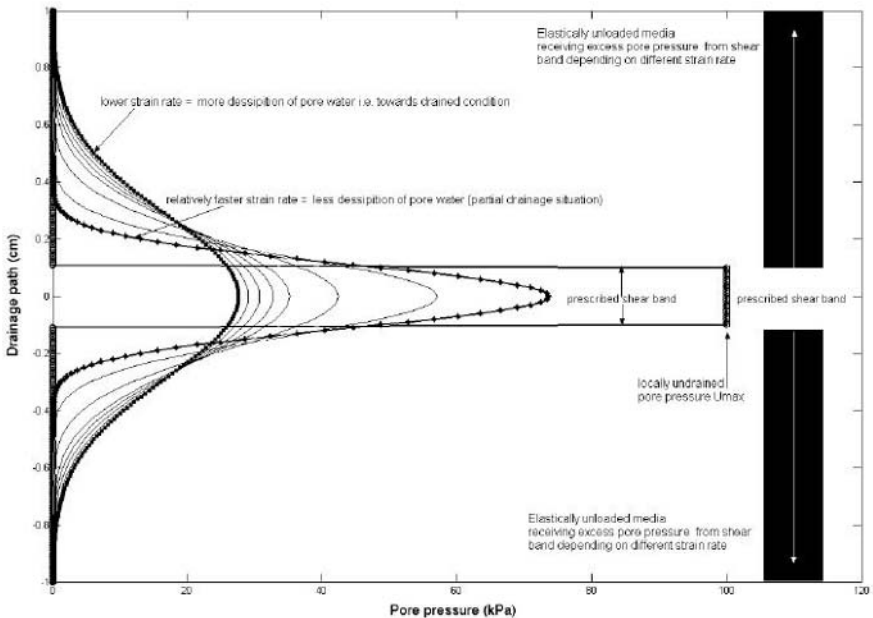


Fig. 3.1. Strain localized pore water diffusion from shear column

4 Finite Element Simulation of Coupled Pore Water and Strain Localization

A finite element model is simulated and practiced for different strain rates. A long natural slope in soft soil shown in Fig. 4.1 is utilized for modeling purpose, however due to specific nature of this study; only a small portion of the slope is modeled.

At the onset of localization, plastic deformation is only concentrated in the shear band zone and rest of the non-localized body have a rigid body motion, which means it is more important to simulate a local model which has embedded shear band and neighborhood explicitly. It is not a very useful to consider complete non-localized elastically deforming slope, because influence of localization will decrease with the increasing distance from the shear band. This statement is true only for the present case.

For simplicity, referring to a local co-ordinate (n, s) system, a direct simple shear model is simulated in finite element code using poro-elastic element in order to have a coupled tangent stiffness matrix where pore water and soil skeleton contributes simultaneously.

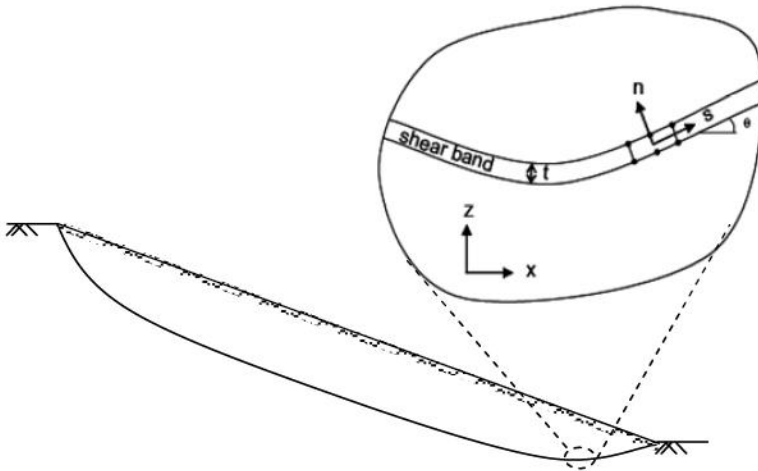


Fig. 4.1 Shear band in a natural slope

Simple elastic perfectly plastic with negative dilatancy material model is considered. Experimentally affiliated parameters have been selected for the modeling purpose, a typical soft and sensitive clay, for example the Norwegian quick clays have shear modulus of 5000 kPa, Poisson's ratio

equal to 0.25, frictional angle 30 degrees, dilatancy of minus 1 degree and horizontal and vertical permeability equal to 1×10^{-6} m/day.

In order to trigger localization, a weak perturbation is embedded within model. Fig. 4.2 represents (a) the DSS model after deformation; (b) localized zone and (c) consequently developed excess pore pressure and pore water flow. A different mesh size and different strain rates were practiced in order to study the model widely.

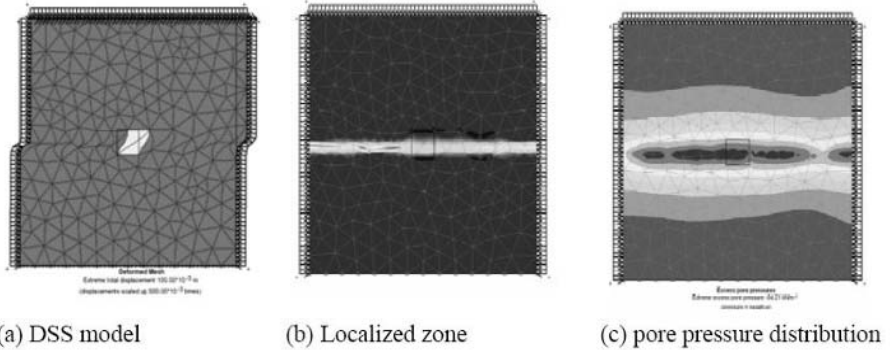


Fig. 4.2 Direct simple shear model

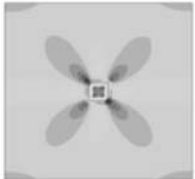

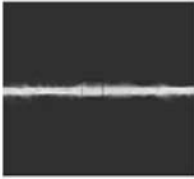

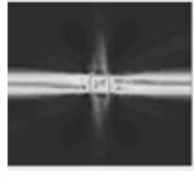

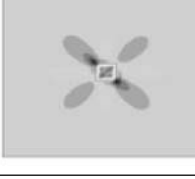
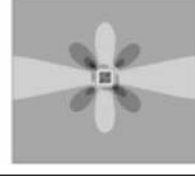

5 Results and Discussion

Phenomenological characteristics of coupled localization obtained from DSS model is discussed pedagogically. Results are presented in different sub-sections, as follows.

5.1 Evaluation of Strain Localization

Strain localization occurs when the deformation in a continuum is localized in well defined but narrow zones of intense straining. In order to illustrate, DSS model has been simulated and studied for different displacement rates to observe time dependent pore water flow and localization. Results are presented in Table 1.

Table 5.1. Evaluation of strain localization at different strain rates

Shear strain level	0.7%	1.2%	2%
→			
Displacement rate			
0.07 mm/min (fastest)			
0.007 mm/min (medium)			
0.014 mm/min (slowest)			

An embedded weak element initiates the localization process and gradually progresses in neighborhood horizontally (by virtue of direct shear). At the onset of localization shear band can propagate in any critical direction (horizontally or vertically) due to symmetric model. But in this case, a guided shear band development in the direction of globally applied displacement is achieved.

For sake of brevity, only three cases are considered where globally applied displacement rates are equal to 0.07mm/min, 0.007mm/min and 0.0014mm/min. In other words, the first two displacement rates are 50 times (0.07mm/min) and 5 times (0.007mm/min) faster than the slowest displacement rate i.e. 0.0014mm/min. Table 1 represents the growth of shear band at three different shear strain level e.g. 0.7%, 1.2% and 2%, for these displacement rates.

The slowest (0.0014mm/min) deformation rate delays the localization occurrence; refer Table 5.1, on other hand fastest deformation rate (0.07mm/min) can cause a rapid localization. In order to justify this statement, for instance, choose a strain level of 1.2 % and compare the

localization pattern for all three deformation rates. At higher rate, shear band developed more dominating and distinct, on other hand, at the slowest rate is plastic strain distribution is more diffused in behaviour and yet to localized in a well defined state.

Excess drainage of pore water from shear band at slower rate causes less reduction in effective stresses and hence post peak stress strain response is not as severe as in case of faster deformation rate. However, end result is same for all the cases, apart from different magnitude of plastic strain within shear band. The same time it must also be noted that finite element analysis is certainly suffer from mesh dependency. However, coupled analyses helps to make well posed situation up to a certain extent but at the higher strain, hydraulic gradient between two gauss point becomes very high, plastic strain distribution also becomes irregular, as shown in Fig. 5.1, and mesh dependent result yields.

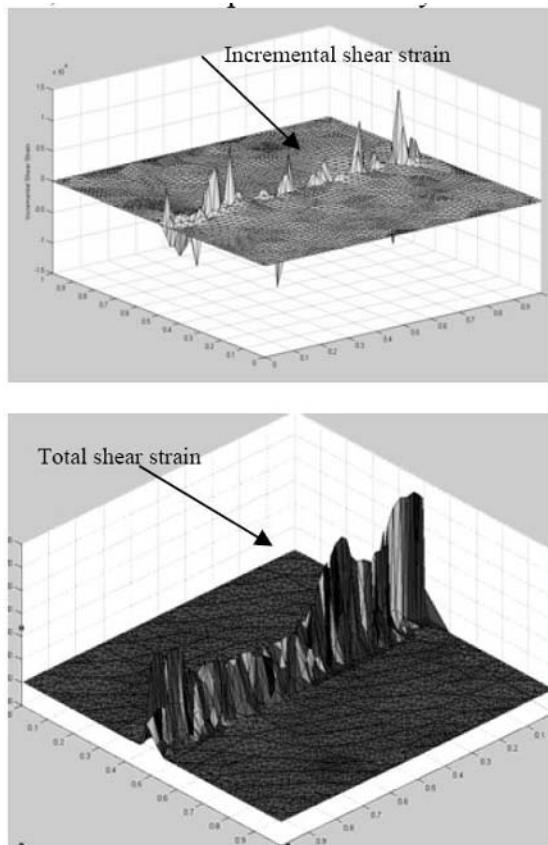


Fig. 5.1. Incremental and total shear strains along the shear band at higher strain

5.2 Effect of Excess Pore Water Pressure

According to laboratory observation, in drained test, depending on the stress level, material exhibits a dilating or contracting behavior. In the undrained test due to incompressibility of pore water will induced pore water pressure changes (Liu 2003).

Desrues (2004) describes that the low over consolidated clays have tendency of local drainage within a global undrained boundary of specimen. By finite element simulation and analytical solution proposed by Thakur et al (2005) shows that generation of excess pore pressure is one of the major reasons for localization in soft and sensitive clays. A rate dependent partial drainage characteristics coupled with localization not only influences the strain softening behavior but also affect the shear band thick-ness. Clays have a global undrained boundary and so global volumetric change must be zero, however internal exchange between contracting zones i.e. shear bands and swelling zone i.e. elastically unloading body is possible.

From Fig. 5.2, at higher deformation rate, high excess pore pressure develops within shear band and vice versa. Higher deformation rate also represent a more undrained situation where pore pressure is accumulated within shear band and thus stain softening is more pronounce. In case of slower rate of deformation, there is sufficient time for pore water to escape and hence accumulated pore water pressure within shear band is also less which ultimately causes a reduction in rate of softening and hence results are less mesh sensitive.

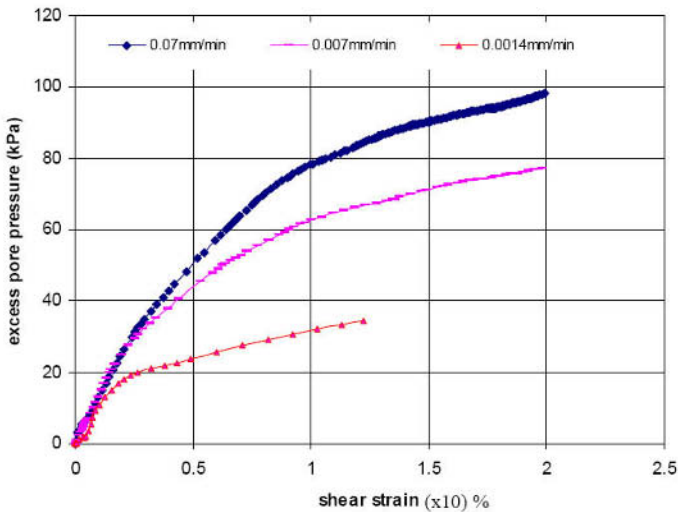


Fig. 5.2. Rate dependent pore water pressure accumulated inside shear band

Sufficient drained condition can also be responsible for a steady state situation, rate of pore water pressure generation and dissipation is constant, that can lead to a definite thickness of shear band. Smooth transition of pore water diffusion is observed at lower strain rates. At higher strain rate, due to lack of sufficient time to reach a steady state situation, pore water distribution profile along and across the shear band is abrupt, refer Fig.5.3.

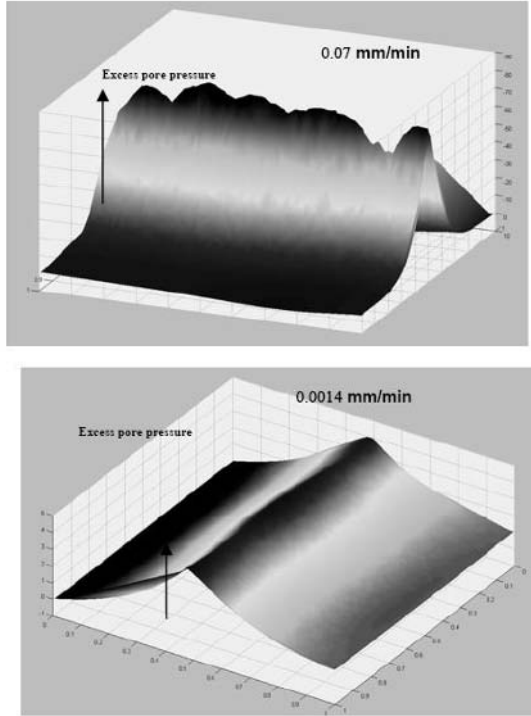


Fig. 5.3. Pore water pressure profile

5.3 Material Behavior

Well known that at the onset of localization domain divide in two parts i.e. localized and elastically unloaded part. Localized part, so called shear band emerges at low displacement and contracts as the strain concentration increases. Due to incompressibility of pore water, excess pore pressure develops and cause reduction in effective stress and so the mobilization. This statement is valid for post peak condition within the perspective of the model used for this study.

Once the partial drainage occurs, there will be a local volume change however global volume of the body remains constant. Shear band reduces to an equal volume replaced by the elastically swollen media. Change in volume depends how fast pore water is transported from shear band. If a situation when the rate of pore water pressure dissipation equal to the rate of pore water pressure generation, i.e. a steady state condition, the contraction in shear band will also stop because effective stresses will not decrease anymore. In such a situation, a definite thickness of shear band can be expected. Fig. 5.4, represents a rate dependent stress strain characteristics, with the decrease in strain rate, strain softening is also reducing.

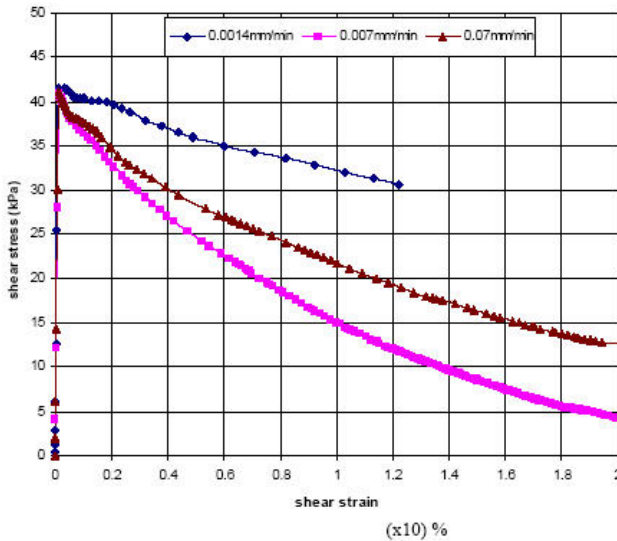


Fig. 5.4. Stress strain curve

From the present study, it is also understandable that simple material models can only predict the real characteristics of localization within a limited gamut. One of the important reasons to obtain mesh sensitive results is due to insufficient loading and unloading criterion in constitutive modeling. This becomes more severe with over simplified simple material models.

Fig. 5.5 shows a typical effective stress path for the DSS model analyses, five different gauss points has been chosen, A,B,C,D and E. Point A of the material and with equally increasing distance (in vertical direction) from shear band respectively. In the beginning A, B localizes, however C, D, E

never reaches to yield and starts unloading. Gauss point A always retains in localization state and hence passes along the failure line. On other hands, point B travel in failure line for some distance and than unloaded due to contracting shear band but parallel to failure line, due to decrease of effective stress caused by gain of high excess pore pressure from the neighborhood. Similarly, point C, D, and E also violate the constitutive rule where elastically unloading must be a rigid body motion without changing its effective stress state.

Especially point B which receives a high excess pore pressure from the shear band (point A) must also develop some plastic strain due to change in mobilization and a mesh independent result can be expected. Since the present model is not robust enough to take in account such type of facts and hence only one gauss point A remain under softening branch and mesh dependent results achieved. In sort, if proper criteria must utilize then a finite element analyses can also be well posed up to certain extent within the contrast of coupled analyses.

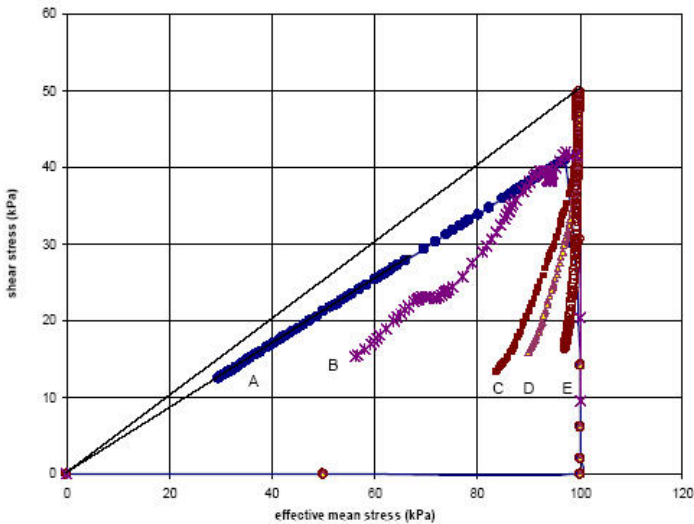


Fig. 5.5. The effective stress path

6 Conclusions

This study brings out the importance of solid fluid interaction within the perspective of strain localization in soft clays. An introductory exercise is chosen to demonstrate the mechanism of shear band and pore water flow using a simple constitutive model in finite element analyses. Rate dependent pore water diffusion from shear band and consequently, strain softening rate are analogously discussed. Inherence regularization in a form of hydraulic gradient helps to handle post peak softening. Elasto-plastic frame work with fluid coupling can also be a sufficient tool to handle strain softening problem. However, in order to validate this statement, a robust model must be utilized and practiced for complete boundary value problems. In short, contracting behavior of shear bands and pore water diffusion not only a complementary characteristics in porous media but also opens a new technique to regularize the ill posed boundary value problem.

Acknowledgements

International Centre for Geohazards, Norwegian University of science and Technology and Norwegian Geotechnical Institute is gratefully acknowledged for their financial support and assistance.

References

1. Bardet JP (1990) Finite element analysis of plane strain bifurcation within compressible solids. *Computers and Structures* 36(6) pp.993-1007.
2. Bowen RM (1982) Compressible porous media models by use of the theory of mixtures. *International Journal of Engineering Science* 20(6) pp.697-735.
3. Desrues J (1996) Strain localization in geomaterials: experimental basis. 8th European autumn school in bifurcation and localization in geomaterials ALERT/Geomaterials, Grenoble, pp.31-32.
4. Ehlers W (1989) On thermodynamics of elasto-plastic porous media. *Arch of Mech.* 41(1) pp.73-99.
5. Lewis RW, Schrefler BA (1998) *The finite element method in the deformation and consolidation of porous media.* John Wiley & Sons.
6. Liu X (2003) Numerical modeling of porous media response. PhD Thesis, TU Delft, the Netherlands.
7. Liu X., Scarpas A. and Blaauwendraad J. (2001) Finite element investigation of localization in porous media. 10th IACMAG, pp.559-564.

8. Loret B, Prevost JH (1991) Dynamics strain localization in fluid saturated porous media. *ASCE Journal of Engineering Mechanics* 11 pp.907-922.
9. Rice JR (1985) On the stability of dilating hardening for saturated rock masses. *Journal of Geophysics research* 80 pp.1531-1536.
10. Rudnicki JW (1984) Effect of dilatant hardening on the development of concentrated shear deformation in fissured rock masses. *Journal of geophysics Research* 89(B11) pp.9259-9270.
11. Schrefler BA, Sanavia L, Majorana CE (1996) A multiphase medium model for localization and post-localization simulation in geomaterials, *Mech. Cohes-Fric. Materials and structures* 1 pp.95-114.
12. Schrefler BA, Majorana CE, Sanavia L (1995) Shear band localization in saturated porous media. *Arch. Mech.* 47 pp.577-599.
13. Thakur V, Nordal S, Jostad HP, Andresen L (2005) Study on generation dissipation of pore water during shear banding in sensitive clays. 11th IACMAG Turin, Italy, 4 pp. 289-296.
14. Vardoulakis I (1986) Dynamics stability analysis of undrained simple shear on water saturated granular soils. *International Journal of Numerical and Analytical Methods in Geomechanics* 10 pp.177-190.

Part IV

Numerical Aspects

Numerical Analysis of Deformation of Methane Hydrated Contained Soil due to the Dissociation of Gas Hydrate

Sayuri Kimoto¹, Fusao Oka¹, Masaya Fujiwaki¹ and Yuji Fujita²

¹Kyoto University,
Japan.

²Former student of Kyoto University,
Japan.

Summary

We have developed a simulation method to predict the ground deformation due to the dissociation of methane hydrate. In the dissociation process, the phase change from solid to fluids leads to the change in partial stresses in the porous media, which will cause the ground deformation. The simulations are based on the chemo-thermo-mechanical coupled finite element analysis, in which the phase change, the flow of pore fluids, the mechanical behavior of solid skeleton, and heat transfer are simultaneously solved. We treat the ground as unsaturated soils, and apply an elasto-viscoplastic constitutive model to the soil skeleton. Using the proposed method, we have numerically analyzed the dissociation process for heating methods. Ground deformation has been predicted which is caused by water and gas generation during the dissociation.

1 Introduction

Hydrates are treated as a potential energy resource for the 21st century because a large amount of methane gas is contained in hydrate reservoirs. The impact of gas hydrate dissociation on the ground stability is important for evaluating the safety of offshore structures as well as for understanding environmental effect. From an environmental point of view it is necessary to predict the long-term behavior of reservoir and surrounding ground due to the dissociation. In order to accurately predict the behavior of sea ground due to the dissociation of natural gas hydrate, it is necessary to

develop a powerful simulator considering soil deformation as well as gas production. In the past few years, some numerical simulators to evaluate gas production values have been developed. Masuda et al. (2002) and Ahmadi et al. (2004) have developed a numerical model by using finite difference method for predicting gas and water flow with hydrate dissociation. They consider fluid transfer and heat transfer, however, solid phases are assumed to be immobile. Some other simulators have been developed, however, in most of them the solid phases are assumed to be rigid (e.g., Bejan et al. 2002; Tsyarkin 2000; Bondarev and Kapitonova 1999). Klar and Soga (2005) presented flow-deformation analysis of methane hydrate extraction problems using finite difference code. They treat hydrate-solid mixture as plastic material which strength is a function of hydrate saturation. Heat transfer has not been considered in the model. Therefore the powerful simulator which can consider chemo-thermo-mechanical coupling behavior needs to be developed in order to investigate the ground stability during gas production.

The proposed analysis in the present paper is based on the fundamental concept of theory of porous media (e.g. Ehlers 2003) and the extended Biot's theory (1956). Materials are assumed to be composed of solid, water, and gas, which are continuously distributed over the space. In the simulation, dissociation occurs when hydrated pass out the stability zone which is described by pressure and temperature (Bejan et al. 2002). In order to consider phase change caused by dissociation, the mass increasing ratio of water, gas and dissociation heat ratio is introduced in the mass conservation law and the energy conservation law. Water and gas flows are assumed to be controlled by Darcy's type law.

In the dissociation process, the generated gas pressure cannot be neglected, and hence soil mechanics under unsaturated state becomes important to predict the ground deformation. In the modeling of mechanical behavior for unsaturated soil, it is necessary to choose appropriate stress variables which control the mechanical behavior. Furthermore, the effect of suction has to be described in the model. In the present study the average skeleton stress, which is determined from the difference between the total stress and the average pore fluid pressure, is used as the stress variables in the constitutive model. The effect of suction is expressed in the constitutive equation, as shrinkage or expansion of the yield surface. An elasto-viscoplastic constitutive model is adopted for the soil skeleton, since the hydrate reservoir around Japan archipelago is laminated with sand, clay, and silt. Several material parameters were determined considering the results obtained by the field research at Nankai Ocean.

2 Simulation Method

2.1 Multiphase Mixture Theory

Geomaterials generally fall into the category of multiphase materials. They are basically composed of soil particles, water, and air. The behavior of multiphase materials can be described within the framework of a macroscopic continuum mechanical approach through the use of the theory of porous media (Boer 1998). The theory is considered to be a generalization of Biot's two-phase mixture theory for saturated soil (Biot 1941; Biot 1955; Biot 1956).

Proceeding from the general geometrically non-linear formulation, governing balance relations for the multiphase materials can be obtained (e.g., Boer 1998; Loret and Khalili 2000; Ehlers 2003; Ehlers et al. 2004). Mass conservation laws for the gas phase as well as for the liquid phase are considered in those analyses. In the field of geotechnics, air pressure is assumed to be zero in many research works (e.g., Sheng et al. 2003), since geomaterials usually exist in an unsaturated state near the ground surface. Considering the hydrate dissociation, however, we have to deal with a high level of gas pressure under the deep ground; this means that the mass balance for both phases has to be considered.

Furthermore, the conservation of energy is required when there is a considerable change in temperature during the deformation process. Vardoulakis (2002) has shown that the temperature in saturated clay rises with plastic deformation. Oka et al. (2004) has simulated the thermal consolidation process. Hydrate dissociation is an endothermic reaction, and heat transfer plays an important role in gas production and in ground deformation.

2.2 General Setting

Materials are composed of four phases, namely, solid (S), water (W), gas (G) which are continuously distributed over space, and hydrates (H). For simplicity, we assume that hydrates (H) move with the solid phase before dissociation. Total volume V is obtained from the sum of the partial volumes of the constituents, namely,

$$\sum_a V^a = V \quad (a = S, W, G, H) \quad (2.1)$$

The volume of the void V^v , which is composed of water, gas, and hydrates is given in the following:

$$\sum_{\beta} V^{\beta} = V^v \quad (\beta = W, G, H) \quad (2.2)$$

Volume fraction n^{α} is defined as the local ratio of the volume element with respect to the total volume, in other words,

$$n^{\alpha} = \frac{V^{\alpha}}{V} \quad (2.3)$$

$$\sum_{\alpha} n^{\alpha} = 1 \quad (\alpha = S, W, G, H) \quad (2.4)$$

The volume fraction of the void, n , is written as

$$n = \sum_{\beta} n^{\beta} = \frac{V^v}{V} = \frac{V - V^s}{V} = 1 - n^s \quad (\beta = W, G, H) \quad (2.5)$$

The volume fraction of the fluid, n^F , is given by

$$n^F = \sum_{\gamma} n^{\gamma} = n - n^H \quad (\gamma = W, G) \quad (2.6)$$

In addition, water saturation is required in the triphasic model, namely,

$$s_r = \frac{V^W}{V^W + V^G} = \frac{n^W}{n^W + n^G} = \frac{n^W}{n^F} \quad (2.7)$$

2.3 Conservations of Mass

The conservations of mass for phase $\beta (=W, G)$ are given in the following equation as:

$$\frac{\partial}{\partial t} (\rho^{\beta} n^{\beta}) = -q_{Mi,i}^{\beta} + \dot{m}^{\beta} \quad (\beta = W, G) \quad (2.8)$$

in which ρ^{β} is the material density, q_{Mi}^{β} is the flux vector of the fluid and \dot{m}^{β} is the mass rate of phase per unit volume generated by dissociation. The flux vector is expressed with the relative velocity of flow, V_i^{β} , namely,

$$V_i^{\beta} = n^{\beta} (v_i^{\beta} - v_i^s) \quad (\beta = W, G) \quad (2.9)$$

$$q_{Mi,i}^{\beta} = \rho^{\beta} V_i^{\beta} \quad (\beta = W, G) \quad (2.10)$$

where V_i^β is the velocity of phase β . The conservation laws in Eq. (2.8) for the water and the gas phases are expressed with water saturation s_r and the volume fraction of the void, n as:

$$s_r \dot{n}^F + \dot{s}_r n^F = -V_{i,i}^W + \frac{\dot{m}^W}{\rho^W} \tag{2.11}$$

$$(1 - s_r) \dot{n}^F - \dot{s}_r n^F + (1 - s_r) n^F \frac{\dot{\rho}^G}{\rho^G} = -\frac{(\rho^G V_{i,i}^G)}{\rho^G} + \frac{\dot{m}^G}{\rho^G} \tag{2.12}$$

The water density is assumed to be constant in Eq. (2.11). The volume fraction changing rate of hydrates is given by

$$\dot{n}^H = \frac{\dot{V}^H}{V} = \frac{\dot{m}^H}{\rho^H} \tag{2.13}$$

where $\dot{n}^H < 0$ when dissociation occurs, and \dot{m}^H is a mass decreasing ratio of hydrates.

2.4 Skeleton Stress

In the theory of porous media, the concept of the effective stress tensor, which is related to the deformation of the soil skeleton, plays an important role. The effective stress tensor has been defined by Terzaghi (1943) for water saturated soil; however, the effective stress needs to be redefined if the fluid is made of compressible materials. In the present study, the skeleton stress σ'_{ij} is defined, which is used as the stress variables in the constitutive relation for the soil skeleton (Jommi 2000; Gallipoli et al. 2003).

$$\sigma'_{ij} = \sigma_{ij} - P^F \delta_{ij} \tag{2.14}$$

σ_{ij} is the total stress and P^F is the average pressure of the fluids surrounding the grain (Schrefler 1996) expressed by

$$P^F = s_r P^W + (1 - s_r) P^G \tag{2.15}$$

in which P^W is the pore water pressure and P^G is the pore gas pressure.

2.5 Conservation of Momentum

The momentum balance is required for each phase, namely,

$$n^\alpha \rho^\alpha \dot{v}_i^\alpha = \sigma_{ij,j}^\alpha + \rho^\alpha n^\alpha \bar{F}_i - \tilde{P}_i^\alpha \quad (\alpha = S, W, G) \tag{2.16}$$

in which \bar{F}_i is the gravity force and \tilde{P}_i^α is related to the interaction term given by

$$\tilde{P}_i^\alpha = \sum_\gamma D^{\alpha\beta} (v_i^\alpha - v_i^\gamma), \quad D^{\alpha\gamma} = D^{\gamma\alpha} \quad (\alpha = S, W, G) \tag{2.17}$$

where $D^{\alpha\beta}$ are parameters which describe the interaction with each phase. The momentum balance equation for each phase is obtained in the following equations when the acceleration is disregarded as:

$$\sigma'_{ji,j} + (n^S P^F)_{,j} + \rho^S n^S \bar{F}_i - D^{SW} (v_i^S - v_i^W) - D^{SG} (v_i^S - v_i^G) = 0 \tag{2.18}$$

$$(n^W P^W)_{,j} + \rho^W n^W \bar{F}_i - D^{WS} (v_i^W - v_i^S) - D^{WG} (v_i^W - v_i^G) = 0 \tag{2.19}$$

$$(n^G P^G)_{,j} + \rho^G n^G \bar{F}_i - D^{GS} (v_i^G - v_i^S) - D^{GW} (v_i^G - v_i^W) = 0 \tag{2.20}$$

where $D^{\alpha\beta}$ is given in the following:

$$D^{WS} = \frac{(n^W)^2 \rho^W g}{k^W}, \quad D^{GS} = \frac{(n^G)^2 \rho^G g}{k^G} \tag{2.21}$$

in which k^W and k^G are the permeability coefficients for the water and the gas phases, g is the acceleration of gravity.

When we assume that the space derivative of volume fraction $n_{,i}^\alpha$, is negligible and the interaction between water and gas phases D^{GW} and D^{WG} is zero, Darcy's type laws for the water phase and the gas phase are obtained from Eqs. (2.19) and (2.20) as:

$$V_i^W = n^W (v_i^W - v_i^S) = \frac{k^W}{\rho^W g} (P_{,i}^W + \rho^W \bar{F}_i) \tag{2.22}$$

$$V_i^G = n^G (v_i^G - v_i^S) = \frac{k^G}{\rho^G g} (P_{,i}^G + \rho^G \bar{F}_i) \tag{2.23}$$

In the analysis, the gravity force of the gas phase is neglected. The sum of Eqs. (2.18) – (2.20) leads to

$$\sigma'_{ji,j} + \rho^E \bar{F}_i = 0 \tag{2.24}$$

$$\rho^E = \sum_\alpha n^\alpha \rho^\alpha \quad (\alpha = S, W, G) \tag{2.25}$$

The rate type of conservation of momentum is given by

$$\dot{S}_{ji,j} = 0 \quad (2.26)$$

where $\dot{S}_{ji,j}$ is the total nominal stress rate tensor defined as

$$\dot{S}_{ji,j} = \dot{\sigma}_{ij} + L_{pp}\sigma_{ij} - \sigma_{qj}L_{qi} \quad (2.27)$$

where σ_{ij} is the Cauchy stress tensor, $\dot{\sigma}_{ij}$ is the time rate of stress, and L_{ij} is the velocity gradient tensor. The relations between Cauchy stress tensor and the skeleton Cauchy stress tensor is given in Eq. (2.14) as

$$\sigma_{ij} = \sigma'_{ij} + P^F \delta_{ij} \quad (2.28)$$

From the above equations, we obtain

$$\dot{S}_{ij} = \dot{S}'_{ij} + \dot{P}^F \delta_{ij} + L_{kk}P^F \delta_{ij} - P^F \delta_{ik}L_{jk} \quad (2.29)$$

in which, \dot{S}'_{ij} is the skeleton nominal stress rate tensor.

2.6 Conservation of Energy

The following energy conservation equation is applied for considering the heat conductivity and the heat sink rate with hydrate dissociation:

$$(\rho c)^E \dot{\theta} = D_{ij}^{vp} \sigma'_{ij} - h_{i,i} + \dot{Q}^H \quad (2.30)$$

$$(\rho c)^E = \sum_{\alpha} n^{\alpha} \rho^{\alpha} c^{\alpha} \quad (\alpha = S, W, G, H) \quad (2.31)$$

where c^{α} is the specific heat, $\theta(K)$ is the temperature for all the phases, D_{ij}^{vp} is viscoplastic stretching tensor and \dot{Q}^H is the dissociation heat rate per unit volume by hydrate dissociation.

$$\dot{Q}^H = \frac{\dot{N}^H Q}{V} \quad (2.32)$$

where Q (kJ/kmol) is the dissociation heat per unit kilo mole (Kuustaa et al. 1983), and it changes with temperature:

$$Q = 56599 - 16.744\theta \quad (2.33)$$

h_i denotes heat flux defined as

$$h_i = -\lambda^E \theta_{,i}, \quad \lambda^E = \sum_{\alpha} n^{\alpha} \lambda^{\alpha} \quad (\alpha = W, G) \quad (2.34)$$

in which λ^{α} is the thermal conductivity.

2.7 Suction-Saturation Relation

The relation between suction and saturation is given in the following equation proposed by van Genuchten (1980).

$$s_{re} = \left\{ 1 + (\alpha P^C)^n \right\}^{-m} \quad (2.35)$$

in which α , m and n are the material parameters, and $m = 1 - 1/n$ is assumed. $P^C (=P^G - P^W)$ is the suction and s_{re} is the effective saturation as

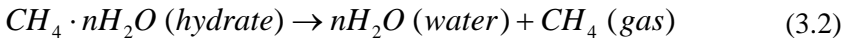
$$s_{re} = \frac{s_r - s_{r \min}}{s_{r \max} - s_{r \min}} \quad (2.36)$$

where $s_{r \max}$ and $s_{r \min}$ are the maximum and the minimum values of suction, respectively.

3 Dissociation of Hydrates

If the conditions for pore pressure and temperature shift to the unstable region given in the following equation (Bejan et al. 2002) as schematically shown in Fig. 5.1, gas hydrates dissociate into water and gas with the reaction expressed in Eq. (3.2). The average pressure of fluids P^f is regarded as pore pressure P in the analysis.

$$P \leq c \exp\left(\alpha - \frac{b}{T}\right) \quad (\text{Unstable region}) \quad (3.1)$$



where a , b and c are material parameters. n is a hydrate number and is assumed to be 5.75. Dissociation ratio \dot{N}^H (kmol/s) is given by following Kim-Bishnoi's equation (Kim et al., 1987):

$$\dot{N}^H = -0.585 \times 10^{10} \times \exp\left(\frac{9400}{\theta}\right) (P^e - P) N^{H_0^{\frac{1}{3}}} N^{H^{\frac{2}{3}}} \quad (3.3)$$

in which N^H (kmol) is moles of hydrates in volume V (m^3), N^{H_0} (kmol) is moles of hydrates at initial state, P (kPa) is average pore pressure P^e is equilibrium pressure at temperature θ (K). $\dot{N}^H < 0$ when dissociation occurs. Water and gas generating ratios are given by

$$\dot{N}^W = -5.75 \dot{N}^H \quad (3.4)$$

$$\dot{N}^G = -\dot{N}^H \quad (3.5)$$

The mass increasing ratio (t/sec/m³) for hydrates, water, and gas phase required in mass conservation law Eqs. (2.11), (2.12), and (2.13) is given as follows:

$$\dot{m}^H = \dot{N}^H M^H / V \times 10^{-3} \tag{3.6}$$

$$\dot{m}^W = \dot{N}^W M^W / V \times 10^{-3} \tag{3.7}$$

$$\dot{m}^G = \dot{N}^G M^G / V \times 10^{-3} \tag{3.8}$$

in which M^H , M^W , M^G (kg/kmol) are the molecular weights for each material.

4 Constitutive Model for Soil

4.1 Elasto-Viscoplastic Model for Unsaturated Soil

Natural hydrates exist between soil particles and are considered to have a bonding effect which makes the solid phase hard. From this point of view, we assume that the soil is a rigid elastic material before dissociation, and that the soil is an elasto-viscoplastic material after dissociation. An elasto-viscoplastic model for the overstress-type of viscoplasticity with soil structure degradation for saturated soil (Kimoto et al. 2004) has been extended to unsaturated soil using the skeleton stress and the newly introduced suction effect within the constitutive model (Kim et al. 2005).

It is assumed that the strain rate tensor consists of elastic stretching tensor D_{ij}^e and viscoplastic stretching tensor D_{ij}^{vp} as:

$$D_{ij} = D_{ij}^e + D_{ij}^{vp} \tag{4.1}$$

The elastic stretching is given by a generalized Hooke type of law, namely,

$$D_{ij}^e = \frac{1}{2G} \dot{S}_{ij} + \frac{\kappa}{3(1+e)} \frac{\dot{\sigma}'_m}{\sigma'_m} \delta_{ij} \tag{4.2}$$

where S_{ij} is the deviatoric stress tensor, σ'_m is the mean skeleton stress, G is the elastic shear coefficient, e is the initial void ratio, κ is the swelling index, and the superimposed dot denotes the time differentiation.

4.2 Overconsolidation Boundary Surface

In this model, it is assumed that there is an overconsolidation (OC) boundary surface that delineates the normally consolidated (NC) region, $f_b \geq 0$, and the overconsolidated region, $f_b < 0$ as follows:

$$f_b = \bar{\eta}_{(0)}^* + M_m^* \ln \left(\frac{\sigma'_m}{\sigma'_{mb}} \right) = 0 \quad (4.3)$$

$$\bar{\eta}_{(0)}^* = \left\{ (\eta_{ij}^* - \eta_{ij(0)}^*) (\eta_{ij}^* - \eta_{ij(0)}^*) \right\}^{\frac{1}{2}}, \quad \eta_{ij}^* = S_{ij} / \sigma'_m \quad (4.4)$$

$$\sigma'_{mb} = \sigma'_{ma} (P^C, z) \exp \left(\frac{1+e}{\lambda - \kappa} \varepsilon_v^{vp} \right) \quad (4.5)$$

where M_m^* is the value of $\eta^* = \sqrt{\eta_{ij}^* \eta_{ij}^*}$ when the volumetric strain increment changes from compression to dilating, which is equal to the ratio M_f^* at the critical state, σ'_{mb} is the hardening parameter, λ is the compression index, κ is the swelling index, and b is a material parameter which is determined by the σ'_m -axis intercept of the critical state line. $\eta_{ij(0)}^*$ is the stress ratio at the end of the anisotropic consolidation. In the value of $\sigma'_{ma} (P^C, z)$, which controls the size of the surface, suction effect is introduced (Kim et al. 2005).

$$\sigma'_{ma} (P^C, z) = \sigma'_{ma} \left[1 + S_I \left\{ \exp \left(-s_d \left(\frac{P_i^C}{P^C} - 1 \right) \right) \right\} \right] \quad (4.6)$$

where P_i^C is the initial value of suction, P^C is the present value of suction, S_I denotes the material parameter which denotes the strength ratio to the saturated soil when the suction is P_i^C . s_d is the parameter which controls the rate of the increasing or decreasing strength. In the initial state of P_i^C , the strength ratio of the unsaturated soil to the saturated soil is $1 + S_I$, and it decreases with a decrease in suction. σ'_{ma} is a strain softening parameter used to describe the degradation of the material caused by structural changes, namely,

$$\sigma'_{ma} = \sigma'_{maf} + (\sigma'_{mai} - \sigma'_{maf}) \exp(-\beta z) \quad (4.7)$$

$$z = \int_0^t \dot{z} dt, \quad \dot{z} = \sqrt{\dot{\varepsilon}_{ij}^{vp} \dot{\varepsilon}_{ij}^{vp}} \tag{4.8}$$

in which σ'_{mai} and σ'_{maf} are the initial and the final values of σ'_{ma} , β is a material parameter which controls the rate of structural changes, and z is an accumulation of the second invariant of viscoplastic strain rate $\dot{\varepsilon}_{ij}^{vp}$. Details of the constitutive model with soil structure degradation are given by Kimoto et al. (2004).

4.3 Static Yield Surface

The static yield function is given by Eq. (4.9).

$$f_y = \bar{\eta}_{(0)}^* + \tilde{M}^* \ln \left(\frac{\sigma'_m}{\sigma'_{my}^{(s)}} \right) = 0 \tag{4.9}$$

In the same way as the overconsolidation boundary surface, the suction effect is introduced in the value of $\sigma'_{my}^{(s)}$.

$$\sigma'_{my}^{(s)} = \frac{\sigma'_{ma}(P^C, z)}{\sigma'_{mai}} \sigma'_{myi}^{(s)} \exp \left(\frac{1+e}{\lambda - \kappa} \varepsilon_{kk}^{vp} \right) \tag{4.10}$$

The value of $\sigma'_{my}^{(s)}$ changes with changes in $\sigma'_{ma}(P^C, z)$ when suction increases or decreases.

4.4 Viscoplastic Potential Surface

The plastic potential surface is described as:

$$f_p = \bar{\eta}_{(0)}^* + \tilde{M}^* \ln \left(\frac{\sigma'_m}{\sigma'_{mp}} \right) = 0 \tag{4.11}$$

where \tilde{M}^* is assumed to be constant in the NC region and varies with the current stress in the OC region as

$$\tilde{M}^* = \begin{cases} M_m^* & : NC \text{ region} \\ -\frac{\sqrt{\eta_{ij}^* \eta_{ij}^*}}{\ln(\sigma'_m / \sigma'_{mc})} & : OC \text{ region} \end{cases} \tag{4.12}$$

where \tilde{M}^* is the value of $\sqrt{\eta_{ij}^* \eta_{ij}^*} / \sigma'_m$ at the critical state, and σ'_{mc} denotes the mean skeleton stress at the intersection of the overconsolidation boundary surface and the σ'_m axis as:

$$\sigma'_{mc} = \sigma'_{mb} \exp \frac{\sqrt{\eta_{ij(0)}^* \eta_{ij(0)}^*}}{M_m^*} \tag{4.13}$$

4.5 Viscoplastic Flow Rule

The viscoplastic stretching tensor is given as the following equation based on Perzyna's type of viscoplastic theory (Oka 1982; Oka et al. 2004) as:

$$D_{ij}^{vp} = C_{ijkl} \langle \Phi_1(f_y) \rangle \frac{\partial f_p}{\partial \sigma'_{ij}} \tag{4.14}$$

$$C_{ijkl} = \alpha \delta_{ij} \delta_{kl} + b(\delta_{ik} \delta_{jl} + \delta_{il} \delta_{jk}), \quad C_1 = 2b, \quad C_2 = 3\alpha + 2b \tag{4.15}$$

in which $\langle \ \rangle$ are Macaulay's brackets; $\langle f(x) \rangle = f(x)$, if $x > 0$, =0 if $x \leq 0$. C_1 and C_2 are the viscoplastic parameters for the deviatoric component and the volumetric component respectively. Φ_1 indicates the strain rate sensitivity. Based on the experimental data from the strain rate constant triaxial tests, material function Φ_1 is given as:

$$\begin{aligned} \gamma \Phi_1(f_y) &= C' \sigma'_m \exp \left\{ m' \left(\bar{\eta}^* + \tilde{M}^* \ln \frac{\sigma'_m}{\sigma'_{my(s)}} \right) \right\} \\ &= C \sigma'_m \exp \left\{ m' \left(\bar{\eta}^* + \tilde{M}^* \ln \frac{\sigma'_m}{\sigma'_{mb}} \right) \right\} \end{aligned} \tag{4.16}$$

$$C = C' \exp \left(m' \tilde{M}^* \ln \frac{\sigma'_{mai}}{\sigma'_{myi(s)}} \right) \tag{4.17}$$

Finally the viscoplastic stretching tensor is given in the following equation as:

$$D_{ij}^{vp} = C_{ijkl} \exp \left\{ m' \left(\bar{\eta}_{(0)}^* + \tilde{M}^* \ln \left(\frac{\sigma'_m}{\sigma'_{mb}} \right) \right) \right\} \frac{\partial f_p}{\partial \sigma'_{kl}} \tag{4.18}$$

5 Simulation Examples

The weak forms of Eqs. (2.11), (2.12), (2.26), and (2.30) are discretized in space and solved by a finite element method. The independent variables are nodal velocity, pore water pressure, pore gas pressure, and temperature. In the finite-element formulation, an eight-node quadrilateral element with a reduced Gaussian integration is used for the displacement, and four corner nodes are used for the pore pressures, and the temperature. For the time discretization, the backward finite difference method is used. An eight-node quadrilateral isoparametric element with a reduced Gaussian four points integration is used for the displacement, and the pore water pressure, the pore gas pressure, and the temperature are defined by four node quadrilateral isoparametric element.

We have simulated dissociation by heating in the seabed ground. Finite element meshes and boundary conditions are shown in Fig. 5.2, and Table 5.1. All elements are initially in a stable state, that is, they have a pressure level of 11 MPa and a temperature of 282 K, as shown in Fig. 5.2. The bottom edge is heated to promote dissociation, and water and gas can flow out from the bottom edge. The initial conditions are listed in Table 5.2. Material parameters for soil listed in Table 5.3 are determined considering the results obtained by the field research at Nankai Ocean. The parameters for the suction-saturation relation are listed in Table 5.4. The initial water permeability set to be 1.0×10^{-9} m/s, and the gas permeability is set to be 1.0×10^{-8} m/s. Notice that the gas permeability is equal to zero before dissociation, whereas it takes constant value and gas can flow out after dissociation.

Changes in moles of hydrates in each element are shown in Fig. 5.4. The dissociation progresses from the bottom to the top of the elements, and it takes longer time for dissociation for the upper element. From Fig. 5.5, temperature takes constant value around 286 kPa in the elements during dissociation. It means that the obtained all of the heat is consumed for dissociation and the temperature-pressure relation is on the equilibrium curve in Fig. 5.1. Fig. 5.6 shows generated gas pressure at nodes. The gas is generated at each node when the dissociation takes place and then it flows out. In contrast, the water pressure decreases during the dissociation as shown in Fig. 5.7, which results in the increases of skeleton stress. Compressive deformation takes place as shown in Fig. 5.8. In this case, viscoplastic deformation is small and deformation recovers after dissociation. One of the reasons for the behavior is that we do not consider the structural change caused by dissociation, namely, strength dependency on hydrates saturation and thermal softening.

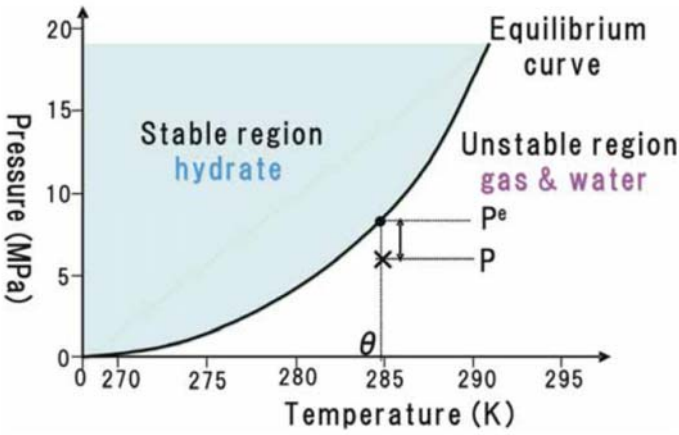


Fig. 5.1. Stable zone of hydrates

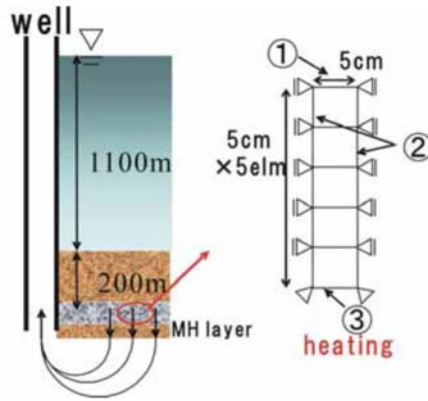


Fig. 5.2. Simulation model

Table 5.1. Boundary conditions

	displacement	pore water	pore gas	heat
1	fixed in x-direction	permeable (11MPa)	impermeable	zero heat flux
2	fixed in x-direction	impermeable	impermeable	zero heat flux
3	fixed in x,y-direction	permeable (11MPa)	permeable (11MPa)	fixed (322K)

Table 5.2. Initial conditions

Initial void ratio	$n = 0.5$
Initial volume ratio of hydrate	$n^H = 0.3$
Initial vertical stress	$\sigma'_{v0} = 1725.0(kPa)$
Earth pressure at rest	$K_0 = 0.5$
Initial saturation	$s_0 = 1.0$
Initial pore pressure	$P_{s0} = 11000.0(kPa)$
Initial temperature	$\theta_0 = 282.0(K)$

Table 5.3. Material parameters for soil

Elastic shear modulus	$G = 53800.0(kPa)$
Compression index	$\lambda = 0.169$
Swelling index	$\kappa = 0.017$
Consolidation yield stress	$\sigma'_{mbi} = 1150.0(kPa)$
Stress ratio at maximum compression	$M_m^* = 1.08$
Viscoplastic parameter	$m' = 23.0$
Viscoplastic parameter	$C_0 = 1.0 \times 10^{-12} (1/s)$
Structural parameter	$\beta = 0$
Suction parameter	$P_i^C = 200(kPa)$
Suction parameter	$S_l = 0.8$
Suction parameter	$s_d = 5.0$

Table 5.4. Parameters for suction-saturation relations

van Genuchten parameter	$\alpha = 0.0025$
van Genuchten parameter	$n = 10.0$
maximum saturation	$s_{\max} = 1.0$
minimum saturation	$s_{\min} = 0.0$

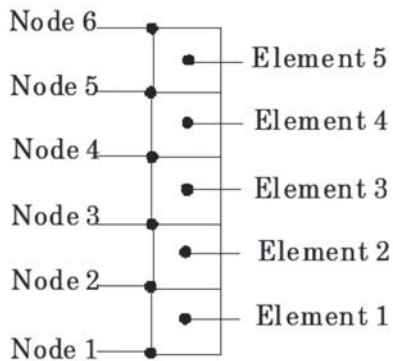


Fig. 5.3. Numbers of elements and nodes

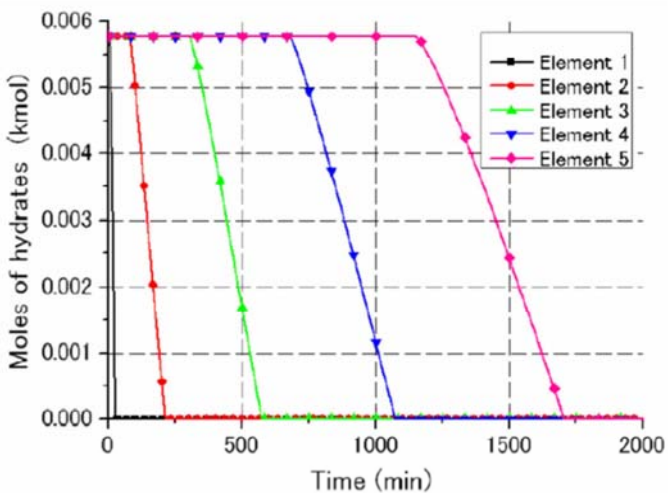


Fig. 5.4. Moles of hydrates-time relations

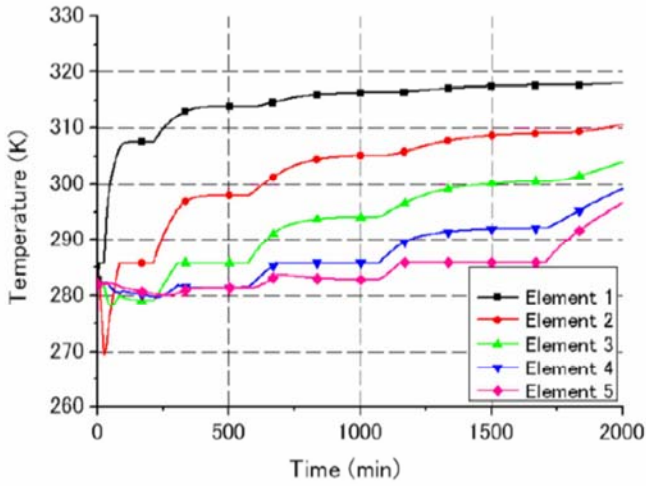
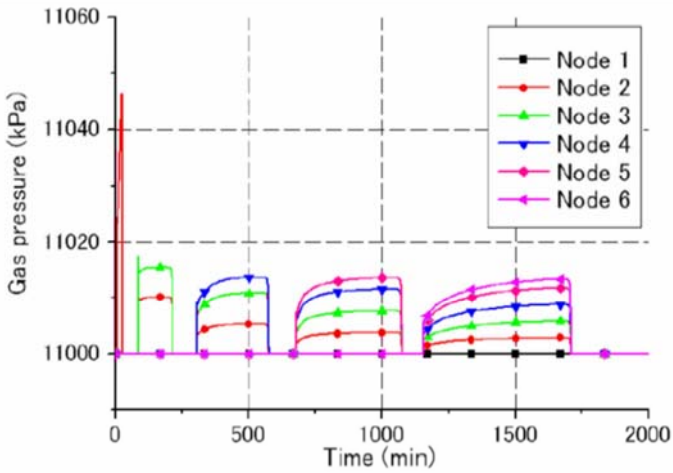


Fig. 5.5. Temperature-time relations



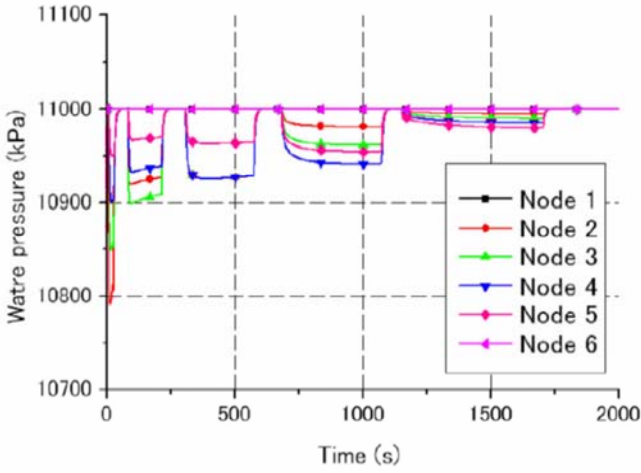


Fig. 5.7. Water pressure-time relations

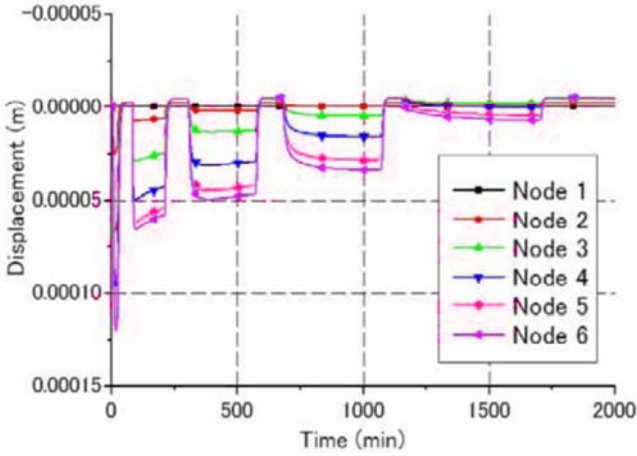


Fig. 5.8. Displacement-time relations

6 Conclusions

We have developed a chemo-thermo-mechanical coupled simulation method to predict the ground stability during hydrate dissociation. From the simulations, the ground deformation can be predicted due to the ejection of pore fluid and change in pore pressure. To predict actual mechanical behavior, saturation dependency of permeability, and strength degradation caused by loss of hydrates have to be introduced in the future work.

References

1. Ahmadi G, Ji C, Smith D (2004). Numerical solution for natural gas production from methane hydrate dissociation. *J. Petroleum Science and Engineering*, vol 41, pp 269-285
2. Bejan A, Rocha LAO, Cherry RS (2002) Methane hydrates in porous layers: Gas formation and convection. *Transport Phenomena in Porous Media*, Ingham B.D. and Pop I. eds., Pergamon
3. Biot MA (1941) Three dimensional theory of consolidation. *J. Appl. Physics*, vol 12, pp 155-164
4. Biot MA (1955) Theory of elasticity and consolidation for a porous anisotropic media. *J. Appl. Phys.*, vol 27, pp 459-467
5. Biot MA (1956) Theory of propagation of elastic waves in a fluid saturated porous solid. I: Low frequency range, *Int. J. Acoust. Soc. Am.*, vol 28, pp 168-178
6. Boer RD (1998) Theory of porous media -past and present. *Z. Angew. Math. Tech*, vol 78 (7), pp 441-466
7. Bondarev EA and Kapitonova TA (1999) Simulation of multiphase flow in porous media accompanied by gas hydrate formation and dissociation. *Russ. J. Eng. Thermophy*, vol 9 (1) (2)
8. Ehlers W (2003) Continuum and numerical simulation of porous materials in science and technology. *Modeling and mechanics of granular and porous materials*, Chapter 9, G. Capriz, V.N. Ghionna, P. Giovine, eds, Birkhauser
9. Ehlers W, Graf T, Ammann M (2004) Deformation and localization analysis of partially saturated soil. *Compt. Methods Appl. Mech. Engrg.*, vol 193, pp 2885-2910
10. Gallipoli D, Gens A, Sharma R, Vaunat J (2003) An elasto-plastic model for unsaturated soil incorporating the effects of suction and degree of saturation on mechanical behaviour. *Geotechnique*, vol 53 (1), pp 123-135
11. Jommi C (2000) Remarks on the constitutive modelling of unsaturated soils. *Experimental Evidence and Theoretical Approaches in Unsaturated Soils*, Tarantino & Mancuso eds., Balkema, pp 139-153
12. Kim HC, Bishnoi PR, Heidemann RA, Rizvi SSH (1987) Kinetics of methane hydrate decomposition, *Chemical Engineering Science*, vol 42 (7), pp 1645-1653

13. Kim Y-S, Kimoto S, Oka F, Kodaka T (2005) Numerical simulation of the triaxial compression behaviour of unsaturated silt using an elasto-viscoplastic model. Proc. 11th IACMAG, June 19-24, 2005, Torino, Italy, vol 1, pp 361-367
14. Kimoto S, Oka F, Higo Y (2004) Strain localization analysis of elasto-viscoplastic soil considering structural degradation, *Comput. Methods Appl. Mech. Engrg.*, vol 193, pp 2854-2866
15. Klar A, Soga K (2005) Coupled deformation-flow analysis for methane hydrate production by depressurized wells. *Poromechanics -Biot Centennial-Abousleiman, Cheng, and Ulm eds.*, Taylor & Francis Group, London, pp 653-659
16. Kuustraa VA, Hammershaimb EC, Holder GD, Sloan ED (1983) Handbook of gas hydrate properties and occurrence, DOE/MC/19239-1546, 94
17. Loret B, Khalili N (2000) A three-phase model for unsaturated soils. *Int. J. Numer. Anal. Meth. Geomech.* vol 24, pp 893-927
18. Masuda Y, Kurihara M, Ohuchi H, Sato T (2002) A field-scale simulation study on gas productivity of formations containing gas hydrates. Proc. 4th Int. Conf. on Gas Hydrates, Yokohama, Japan, May, pp 19-23
19. Oka F (1982) Elasto-viscoplastic constitutive equation for over-consolidated clay. Proc. 1st International Symposium on Numerical Models in Geomechanics, Zurich, Dungar, R., Pande, G. N. and Studer, J. A., eds., Balkema, pp 147-156
20. Oka F, Higo Y, Kim Y-S, Imura Y, Kimoto S (2004) Thermo-Hydro-Mechanically Coupled Finite Element Analysis of Cohesive Soil using an Elasto-Viscoplastic Model. *Computational Mechanics (Abstracts), WCCM 4 in conjunction with APCOM'04*, Sept. 5-10, Beijing, China, 266
21. Sheng D, Sloan W, Gens A, Smith DW (2003) Finite element formulation and algorithms for unsaturated soils. Part 1: Theory. *Int. J. Numer. Anal. Meth. Geomech.*, vol 27, pp 745-765
22. Schrefler BA, Gawin D (1996) The effective stress principle: incremental or finite form. *Int. J. Numer. Anal. Meth. Geomech.*, vol 20 (11), pp 785-814
23. Terzaghi K (1943) *Theoretical soil mechanics*. John Wiley & Sons
24. Tsyppkin GG (2000) Mathematical models of gas hydrates dissociation in porous media. *Annals New York Ac. Sci.* vol 912, pp 428-436
25. van Genuchten M. Th. (1980) A closed-form equation for predicting the hydraulic conductivity of unsaturated soils. *Soil Sci. Soc. Am. J.*, 44, pp 892-899
26. Vardoulakis I (2002) Dynamic thermo-poro-mechanical analysis of catastrophic landslides. *Geotechnique*, vol 52 (3), pp 157-171

Numerical Prediction of Impact Force of Geomaterial Flow against Retaining Structure using CIP Method

S. Moriguchi¹, A. Yashima¹, K. Sawada¹, M. Ito¹, S. Hadush² and S. Inoue¹

¹Gifu University,
Japan.

²Addis Ababa University,
Ethiopia

Summary

This study presents numerical framework for predicting impact force of geomaterial flow against a retaining structure. The numerical scheme used in this study is CCUP method that is based on fluid dynamics. In order to describe behavior of geomaterials, the Mohr-Coulomb failure criterion is introduced into the Bingham plastic fluid model. To validate the numerical framework, a series of laboratory experiments related to impact force of geomaterial flow against a retaining structure were conducted, and then simulations of the experiments were carried out. In this paper, the numerical framework, the laboratory experiments and numerical simulations are explained, and effectiveness of the numerical framework is discussed.

1 Introduction

Slope disasters, such as landslide, slope failure and soil avalanche have caused loss of many lives and huge damage to important infrastructures. Especially, in Japan, the disasters have occurred year after year. For example, during the 1995 Hyogoken-Nanbu earthquake, a large-scale landslide occurred at Nishinomiya city in Hyogo Prefecture (Sabo Technical Center, 1995). Other reported incidents, which caused many casualties, include a soil avalanche that occurred at Izumi City, Kagoshima Prefecture in 1997 (Kitamura et al., 1998, Iwamatsu, 1997) and another

soil avalanche that took place at Minamata City, Kumamoto Prefecture in 2003 (Iwao, 2003, Taniguchi, 2003).

In order to reduce damages from slope disasters, it is important to predict the behavior of geomaterial flow, such as traveling distance and impact force against a retaining structure. As far as traveling distance concerned, some methods have been proposed, and can be classified into two categories. One group is the methods based on statistical processing (Scheidegger (1973), Moriwaki (1987)). And the other group is based on numerical calculation using physical model (Ashida et al. (1983)). Although these methods can predict traveling distance of sediment simply, it is difficult to reflect the influence of an important factor, the slope configuration. In addition, the methods cannot describe precisely the behavior of the sediment during flow, such as the speed of the flow and configuration of flow sediment. It is necessary to conduct numerical simulation to know detail behavior of geomaterial flow. It is, however, difficult to simulate geomaterial flow using traditional methods based on continuum mechanics with lagrangean mesh framework, such as the Finite Element Method (FEM). Although, the Arbitrary Lagrangian-Eulerian (ALE) method (Hughes et al., 1981) has been applied to deformation analysis of geomaterials, it is still incapable of treating extreme large deformation problems.

There is different way to simulate behavior of geomaterials at large deformation region. Trunk and Dent (1986), Sousa and Voight (1991), Uzuoka et al. (1998), Hadush et al. (2001) and Moriguchi et al. (2005) proposed numerical methods based on fluid dynamics with non-Newtonian fluid models for the deformation analysis of geomaterials. In these works, geomaterials are assumed to be viscous fluids. The proposed methods can treat large deformation of geomaterials in the framework of Eulerian mesh. Uzuoka et al. (1998) and Moriguchi et al. (2005) conducted simulation of real geomaterial flow to validate the proposed methods. According to the simulated results, it was confirmed that the methods are effective to predict flow behavior and traveling distance of sediment. Additionally, Moriguchi et al (2005) proposed fluid model with the Mohr-Coulomb failure criterion, and it was confirmed that deformation of geomaterials can be described using the friction angle and the cohesion in the framework of fluid dynamics.

It is important to know traveling distance of sediment for predicting damage from slope disasters. As mentioned above, it can be considered that the methods based on fluid dynamics with non-Newtonian fluid models are effective for predicting traveling distance. The effectiveness of the methods for impact force against a retaining structure, however, has not been confirmed in previous study. In this study, a series of laboratory

experiments are conducted, and numerical simulations of the experiments are carried out using a method based on fluid dynamics to validate the numerical framework based on fluid dynamics.

2 Numerical Framework

2.1 Constitutive Model

In this study, geomaterial is assumed to be a special fluid that has the shear strength. Chen and Ling (1996, 1998) proposed generalized visco-plastic fluid models to describe the behavior of granular flow. In their models, the shear rate is used as the most important parameter among other parameters such as grain concentration and grain size. Although we can predict rheological behavior of geomaterials with granular characteristics by those models, it is still difficult to express the real phenomena in simulations with many parameters. In this study, a simplified fluid model is used to describe behavior of geomaterial. The fluid model used in this study is obtained by modifying the Bingham plastic fluid model. The behavior of the Bingham fluid can be expressed in one-dimensional condition as follow,

$$\tau = \eta_0 \dot{\gamma} + \tau_y \quad (2.1)$$

where τ is the shear stress, η_0 is viscosity after yield, $\dot{\gamma}$ is the shear strain rate and τ_y is shear strength. From Equation 1, an equivalent Newtonian viscosity of the Bingham fluid can be obtained. The equivalent viscosity η' is expressed by following equation.

$$\eta' = \frac{\tau}{\dot{\gamma}} = \eta_0 + \frac{\tau_y}{\dot{\gamma}} \quad (2.2)$$

Figure 2.1 shows behavior of the Bingham fluid and the concept of the equivalent viscosity. As shown in Equation 2.1, the shear stress of the Bingham fluid is described as a linear function of shear strain rate. Shear strength of the Bingham fluid is expressed as intercept of the liner function. In Figure 2.1, a solid line describes the behavior of the Bingham fluid, and a dashed line expresses the behavior of an equivalent Newtonian fluid. The equivalent viscosity η' is described as the gradient of the dashed line. In other words, η' is an apparent viscosity of the Bingham

fluid. If the shear strain rate increases, the dashed line moves in the direction of (A) as shown in Figure 2.1, and the equivalent viscosity coefficient becomes smaller. Likewise, when the shear strain decreases and the dashed line moves in the direction of (B) then the equivalent viscosity coefficient becomes larger. An infinite value of the equivalent viscosity arises when shear strain rate equals to zero. It is impossible to treat such infinite value in numerical calculations. In order to avoid the numerical difficulty, the maximum value for the equivalent viscosity is defined as below,

$$\begin{aligned} \eta' &= \eta_0 \dot{\gamma} + \frac{\tau_y}{\dot{\gamma}} & \text{if } \eta' < \eta_{\max} \\ \eta' &= \eta_{\max} & \text{if } \eta' < \eta_{\max} \end{aligned} \quad (2.3)$$

where η_{\max} is maximum equivalent viscosity. Using this concept, the Bingham model is described as a bi-linear model as shown in Figure. 2.2. The relationship between the equivalent viscosity and the shear strain rate is described in Figure 2.3. As shown in Figure 2.3, η_{\max} and η_o defines the maximum and minimum value of the equivalent viscosity. In the simulation conducted in this study, the equivalent viscosity η' is constant value in one calculation step, and η' is updated step by step. In the calculation for η' in two and three-dimensional condition, the shear strain rate $\dot{\gamma}$ is defined using second invariant of shear strain tensor V_{ij} as follow,

$$\dot{\gamma} = \sqrt{\frac{1}{2} V_{ij} V_{ij}} \quad (2.4)$$

in which,

$$V_{ij} = \frac{1}{2} \left(\frac{\partial u_i}{\partial x_j} + \frac{\partial u_j}{\partial x_i} \right) \quad (2.5)$$

where u_i is the velocity vector.

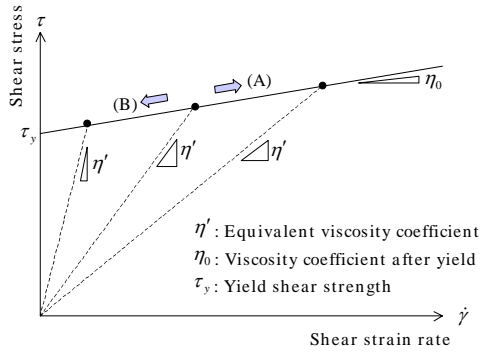


Fig. 2.1. Equivalent viscosity of the Bingham model

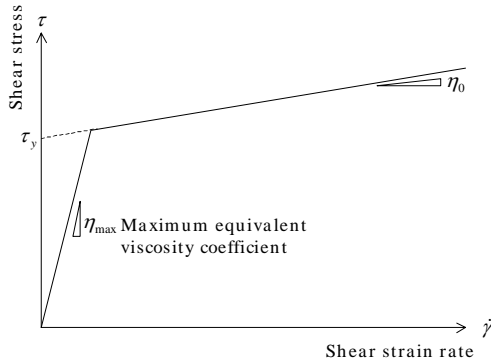


Fig. 2.2. Newtonian viscosity at small shear strain region

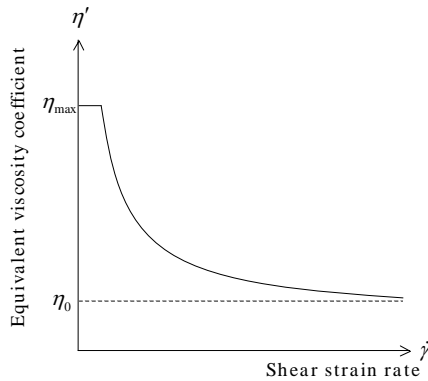


Fig. 2.3. Relation between equivalent viscosity coefficient and shear strain rate

Using the equivalent Newtonian viscosity, the behavior of the Bingham model can be expressed in the numerical analysis. The original Bingham model, however, cannot describe deformation behavior of geomaterials perfectly. In order to express the shear strength of geomaterial, Moriguchi et al (2005) introduced the Mohr-Coulomb failure criterion into the Bingham model. The Mohr-Coulomb failure criterion is described as follows,

$$\tau_y = \sigma_n \tan \phi + c \quad (2.6)$$

where τ_y is the shear strength of geomaterial, σ_n is the effective stress, ϕ is the internal friction angle and c is the cohesion. Substituting the shear strength derived from Equation 2.6 into Equation 2.1, the modified Bingham model with shear strength of geomaterial is given as below,

$$\tau = \eta_0 \dot{\gamma} + \sigma_n \tan \phi + c \quad (2.7)$$

In this study, as numerical simulations are conducted based on fluid dynamics, there is no concept of the effective stress. Therefore, the hydrostatic pressure p is used as a substitute for the normal stress σ_n as follows,

$$\tau = \eta_0 \dot{\gamma} + p \tan \phi + c \quad (2.8)$$

Using the modified Bingham model in Equation 2.8, the equivalent viscosity is described as follow,

$$\begin{aligned} \eta' &= \eta_0 \dot{\gamma} + \frac{p \tan \phi + c}{\dot{\gamma}} \quad \text{if } \eta' < \eta_{\max} \\ \eta' &= \eta_{\max} \quad \text{if } \eta' > \eta_{\max} \end{aligned} \quad (2.9)$$

The equivalent viscosity is used to describe deformation behavior of geomaterials in this study.

The stress tensor for a Newtonian fluid is described by the following equation.

$$\sigma_{ij} = -p \delta_{ij} + \xi V_{kk} \delta_{ij} + 2\eta V_{ij} \quad (2.10)$$

where σ_{ij} is the stress tensor, p is the hydraulic pressure, δ_{ij} is the Kronecker delta, V_{ij} is the shear strain rate tensor, ξ is the second coefficient of viscosity and η is the viscosity coefficient. Here, the following hypothesis is introduced.

$$\xi + \frac{2}{3}\eta = 0 \tag{2.11}$$

Above equation describes the relationship between the second coefficient of viscosity ξ and the viscosity coefficient η , and is called as Stokes hypothesis. Based on this hypothesis, Equation 2.10 can be rewritten as below,

$$\sigma_{ij} = -p\delta_{ij} - \frac{2}{3}\eta V_{kk}\delta_{ij} + 2\eta V_{ij} \tag{2.12}$$

By substituting the equivalent viscosity η' for η , the constitutive model used in this study is given as below,

$$\sigma_{ij} = -p\delta_{ij} - \frac{2}{3}\eta' V_{kk}\delta_{ij} + 2\eta' V_{ij} \tag{2.13}$$

2.2 Governing Equations

In this study, following equations are used as governing equations.

$$\frac{\partial \rho}{\partial t} + u_j \frac{\partial \rho}{\partial x_j} = -\rho \left(\frac{\partial u_k}{\partial x_k} \right) \tag{2.14}$$

$$\frac{\partial p}{\partial t} + u_j \frac{\partial p}{\partial x_j} = -\rho C_s^2 \left(\frac{\partial u_k}{\partial x_k} \right) \tag{2.15}$$

$$\frac{\partial u_i}{\partial t} + u_j \frac{\partial u_i}{\partial x_j} = \frac{1}{\rho} \frac{\partial \sigma_{ij}}{\partial x_j} + b_i \tag{2.16}$$

where u_i is the velocity vector ρ is the density, C_s is the sound speed and b_i is the body force vector. Equation 2.14 shows the continuity equation, Equation 2.15 shows the equation related to the pressure, and equation 2.16 shows the law of linear conservation of momentum. By using the constitutive model shown in equation 2.13, the law of linear conservation of momentum is described as follow.

$$\frac{\partial u_i}{\partial t} + u_j \frac{\partial u_i}{\partial x_j} = -\frac{1}{\rho} \frac{\partial p}{\partial x_i} - \frac{2}{3} \frac{1}{\rho} \frac{\partial}{\partial x_i} (\eta' V_{kk}) + 2 \frac{1}{\rho} \frac{\partial}{\partial x_j} (\eta' V_{ij}) + b_i \quad (2.17)$$

For Newtonian fluid, generally, the spatial derivative of viscosity is not considered. The value of the equivalent viscosity, however, depends on the distribution of velocity and pressure as shown in Equation 2.9. This means that the equivalent viscosity η' has the spatial derivative. Therefore, the spatial derivative of η' is considered in Equation 2.15.

2.3 Numerical Scheme

In this study, CCUP (CIP and Combined, Unified Procedure) method (Yabe and Wang, 1991) is used as the numerical scheme. In the numerical schemes, the governing equations are split into two parts, called the advection phase and the non-advection phase by using the time splitting technique.

Advection phase

$$\frac{\partial \rho}{\partial t} + u_j \frac{\partial \rho}{\partial x_j} = 0 \quad (2.18)$$

$$\frac{\partial p}{\partial t} + u_j \frac{\partial p}{\partial x_j} = 0 \quad (2.19)$$

$$\frac{\partial u_i}{\partial t} + u_j \frac{\partial u_i}{\partial x_j} = 0 \quad (2.20)$$

Non advection phase

$$\frac{\partial \rho}{\partial t} = -\rho \left(\frac{\partial u_k}{\partial x_k} \right) \quad (2.21)$$

$$\frac{\partial p}{\partial t} = -\rho C_s^2 \left(\frac{\partial u_k}{\partial x_k} \right) \quad (2.22)$$

$$\frac{\partial u_i}{\partial t} = -\frac{1}{\rho} \frac{\partial p}{\partial x_i} - \frac{2}{3} \frac{1}{\rho} \frac{\partial}{\partial x_i} (\eta' V_{kk}) + 2 \frac{1}{\rho} \frac{\partial}{\partial x_j} (\eta' V_{ij}) + b_i \tag{2.23}$$

By solving the advection phase and the non-advection phase alternately, quantities such as pressure, density and velocity, are updated. In this study, the non-advection phases are calculated firstly, and then the advection phases are calculated. At the current time step, we have the quantities at the previous time step (u_i^n, ρ^n, p^n) . After the non-advection calculation, the tentative quantities (u_i^*, ρ^*, p^*) are obtained, and the quantities at current time step $(u_i^{n+1}, \rho^{n+1}, p^{n+1})$ are given by solving the advection phases. The Eulerian type finite difference scheme is used to solve non-advection phases as follows,

$$\frac{\rho^* - \rho^n}{\Delta t} = -\rho^n \left(\frac{\partial u_k^*}{\partial x_k} \right) \tag{2.24}$$

$$\frac{p^* - p^n}{\Delta t} = -\rho^n C_s^2 \left(\frac{\partial u_k^{**}}{\partial x_k} \right) \tag{2.25}$$

$$\frac{u_i^{**} - u_i^n}{\Delta t} = -\frac{1}{\rho^n} \frac{\partial p^*}{\partial x_i} + b_i \tag{2.26}$$

$$\frac{u_i^* - u_i^{**}}{\Delta t} = \frac{1}{3} \frac{1}{\rho^n} \frac{\partial}{\partial x_i} \left(\eta' \frac{\partial u_k^*}{\partial x_k} \right) + \frac{\eta}{\rho^n} \frac{\partial}{\partial x_j} \left(\eta' \frac{\partial u_i^*}{\partial x_j} \right) \tag{2.27}$$

Generally, the pressure term of the Equation 2.18 is solved implicitly, and the viscous term is solved explicitly. However, the equivalent viscosity η' changes greatly with time and space step by step, so that numerical instability arises when the viscous term is solved explicitly. Therefore, the viscous term is treated implicitly in this study.

Considering the divergence of Equation 2.26 the following equation is given.

$$\frac{\partial u_i^{**}}{\partial x_i} = -\Delta t \frac{\partial}{\partial x_i} \left(\frac{1}{\rho^n} \frac{\partial p^*}{\partial x_i} \right) + \frac{\partial u_i^n}{\partial x_i} \tag{2.28}$$

By using the concept of fractional step method (Chorin, 1969), the following Poisson equation of pressure is obtained from Equations 2.25 and 2.28.

$$\frac{\partial}{\partial x_i} \left(\frac{1}{\rho^n} \frac{\partial p^*}{\partial x_i} \right) = \frac{p^* - p^n}{\Delta t^2 \rho^n C_s^2} + \frac{1}{\Delta t} \frac{\partial u_i^n}{\partial x_i} \quad (2.29)$$

By solving the above Poisson equation, the tentative pressure p^* is obtained, and then u_i^{**} is given from Equation 2.26. Finally, u_i^* and ρ^* are obtained from Equations 2.24 and 2.27. The matrix derived from Equations 2.27 and 2.29 is computed using the Preconditioned Conjugate Gradient Squared method (PCGS) (Zhang et al. 1996) with the Incomplete LU (ILU) pre-conditioner. In the CCUP method, the sound speed is used as a numerical parameter. Thus, it is possible to treat two or more different materials with different respective densities in a same calculation domain. By using the CCUP method, we can calculate behavior of air and geomaterial together, therefore it is not necessary to give a special boundary condition for surface of geomaterial.

After the calculation of the non-advection phase, advection phase is solved to get the quantities at current time step ($u_i^{n+1}, \rho^{n+1}, p^{n+1}$). In the CCUP method, the Constrained Interpolated Profile (CIP) method (Yabe et al., 1991, Yabe and Aoki, 1991) is adopted to solve the advection phase. The CIP method has some advantages over other methods. Here, a one-dimensional advection equation is used to simplify the explanation of CIP method. One dimensional advection equation is described as below,

$$\frac{\partial f}{\partial t} + u \frac{\partial f}{\partial x} = 0 \quad (2.30)$$

where f stands for physical quantities such as velocity, density and pressure. The approximate solution of the above equation is given as:

$$f(x_i, t + \Delta t) \cong f(x_i - u\Delta t, t) \quad (2.31)$$

where x_i is the coordinates of calculation grid. The above equation indicates that a specific profile of f at time $t + \Delta t$ is obtained by shifting the profile at time t with a distance $u\Delta t$. Therefore, if the spatial profile of f at time t can be obtained, the value of f at each point can be predicted. In the numerical analysis, however, the value of f is kept at only grid points, so that it is necessary to interpolate spatial profile between grid points. The simplest way for the interpolation is to use linear

function. In this case, great difference arises between the interpolated profile and exact solution. There is the ways to use high order function to overcome this problem. In this case, it is necessary to be careful about numerical undershooting and overshooting. On the other hand, in the CIP method, a spatial profile between grid points is interpolated considering the continuity of spatial derivative of f . Differentiating Equation 2.25 with a spatial variable x gives:

$$\frac{\partial g}{\partial t} + u \frac{\partial g}{\partial x} = -g \frac{\partial u}{\partial x} \tag{2.32}$$

where g stands for the spatial derivative of f ($g = \partial f / \partial x$). By solving Equations 2.25 and 2.27 simultaneously, not only value of f but also its spatial derivative g can be obtained at each grid points. Therefore, High order function can be adapted by using information of a small number of grid points. Additionally, the spatial profile can be given without the numerical undershooting and overshooting.

Changes of velocity, density and pressure can be expressed by the governing equations. However, changes of viscosity and sound speed are not expressed. Especially, value of viscosity and sound speed should be given with good accuracy in multi-phase flow analysis. For this purpose, density functions (color functions) φ_i are used to distinguish different kinds of materials. Density functions are defined in each element. If $\varphi_i=1$, the element is filled up with the material i , and if $\varphi_i=0$, there is no material i in the mesh. Using the density functions, the viscosity coefficient and the sound speed in each element are calculated as follows,

$$\eta = \sum \varphi_i \eta_i \quad (0 \leq \varphi_i \leq 1) \tag{2.33}$$

$$C_s = \sum \varphi_i C_{s_i} \quad (0 \leq \varphi_i \leq 1) \tag{2.34}$$

The change of density functions is calculated using following advection equation.

$$\frac{\partial \varphi_i}{\partial t} + u_k \frac{\partial \varphi_i}{\partial x_k} = 0 \tag{2.35}$$

In this study, the equivalent viscosity is used to describe the behavior of geomaterials, so that it is necessary to pay much attention to the interface treatment. For this proposes, a tangent transformation method (Yabe et al.

1993) is applied. In the method, density functions are transformed using a tangent function as below,

$$H(\varphi) = \tan[\pi(\varphi - 0.5)] \quad (2.36)$$

where H is the transformed density function. In the calculation, this transformation is applied before advection calculation, and following inverse transformation is applied after advection calculation.

$$\varphi = \frac{\arctan[H(\varphi)]}{\pi} + 0.5 \quad (2.37)$$

Using this technique, the interface of different materials can be kept sharply. In this study, the transformation method is applied for the treatment of interface of geomaterial. The aforementioned method for treatment of boundary surface is similar to the method in the level set (Osher and Sethian, 1988, Sussman et al., 1994), however, there is a big difference between two methods. In the CIP method, the advection equation with a transformed density function H is solved. Thus, it is possible to describe boundary surface sharply, so that it is not necessary to conduct re-initialization, which is employed in the level set method.

3 Laboratory Experiment

In order to obtain detailed data about the impact force of geomaterial flow against a retaining structure, a laboratory experiment, namely sand flow experiment, is conducted using a model slope. Figure 3.1 shows the photo of the model slope, and Figure 3.2 shows an illustrative figure of the model slope. The length of the model slope is 1.8m, and the width is 30 cm. Different slope angles, 45, 50, 55, 60 and 65 degree, are used in the experiment. Vertical wall is set at the end of the model slope against the flow. A transparent acrylic board is used for the side wall of the model slope to see whole flow process. The flow process is recorded by a video camera. A wooden box, namely sand box, which has a side door, is fixed at the upstream side of the model slope. In the experiment, Toyoura sand is filled into the box, and the flow is initiated by quickly opening of the door of the sand box. Figures 3.3 and 3.4 show the photo and an illustrated figure of the sand box, respectively. The total weight of the sand in the box is 500N and the average density of the sand is 13.80 kN/m³. The impact forces due to the sand flow on the vertical wall are measured using an instrument with load cells set in front of the wall. Figures 3.5 and 3.6 show a photo and an illustrated figure of the instrument. As shown in Figure 3.6,

rollers are used to transfer the impact forces from the surface to the load cells. The surface of the model slope is coated with Toyoura sand in order to consider friction at the bottom part.



Fig. 3.1. Photo of the model slope

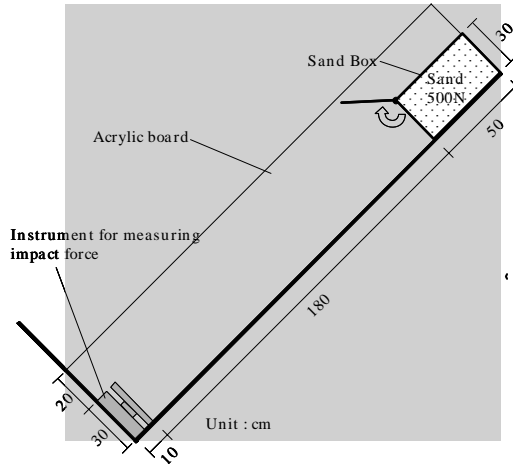


Fig. 3.2. Illustrated figure of the model slope



Fig. 3.3. Photo of sand box

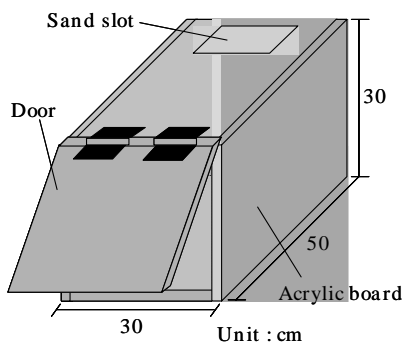


Fig. 3.4. Photo of sand box



Fig. 3.5. Photo of instrument for measuring the impact force

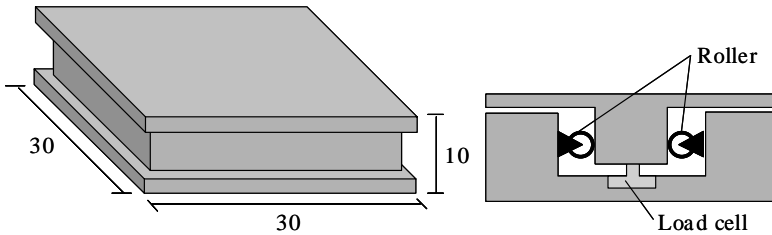


Fig. 3.6. Illustration of instrument for measuring the impact force

In the experiment, five different slope angles are used to investigate influence of slope angle. Besides, the same experiment is repeated five times for each slope angle to investigate reproducibility of the experiment. Figure 3.7 shows the time histories of the impact force for each slope angle measured in this experiment. These time histories are selected from five ones in each case and can be regarded as a typical history for each slope angle. Table 3.1 shows the maximum impact force obtained in the experiment. Additionally, the average and standard deviation of the obtained maximum impact forces are shown in Table 3.1. As shown in Table 3.1, the experimental data show no much scattering. Therefore, it can be considered that the experimental results are quite convincing.

Two-dimensional simulations of the sand flow experiment are carried out using the numerical framework mentioned before. Figure 3.8 shows the numerical model used in this simulation. The numerical model is prepared based on the experimental condition. A sand column of 30 cm high and 50 cm wide is set at the upstream side of the slope. Gravity is the only external force considered in this simulation and the slope angle is described by the gravity forces in the x and y directions as shown in Figure 3.8. The impact force due to the flowing sand on the downstream wall is calculated by the contacted area multiplied with average pressures on the wall. The area of the wall is assumed to be 30 cm high as shown in Figure 3.8. The size of the area is corresponds to the size of the instrument for measuring impact force used in the experiment. Table 3.2 shows the parameters used in this simulation. In the simulation, sand is assumed to be pure granular material, so that the value of cohesion is 0. To determine the internal friction angle of the sand, the box shear test was carried out, and the value of internal friction angle obtained from the box shear test ($\phi=41.0$) is used in the simulation.

As is the same in the experiment, five different slope angle cases are considered in the simulations. Figure 3.9 shows simulated time histories of

the impact force for each slope angle obtained from the simulations. Figure 3.9 shows the relationship between the slope angles and maximum impact force obtained from both the simulations and the experiments. By comparing Figure 3.7 and Figure 3.9, it is found that simulated impact forces are smaller than the impact forces obtained from the experiment, and there are big difference between simulated data and experimental data. It can be also seen from Figure 3.10. The reason of this difference can be considered that the value of internal friction angle used in the simulations is not suitable. The value of internal friction angle obtained from the box shear test corresponds to the static friction angle, but it is necessary to use the kinetic friction angle in the simulation. In order to investigate the effect of internal friction angle, parametric study was carried out. Based on the numerical investigation, it is found that most suitable numerical results are obtained when ϕ equal to 30 degree. The simulated results in the case of $\phi=30$ degree are described in Figure 3.11 and 3.12. These figure show simulated time histories of the impact force for each slope angle and the relationship between the slope angles and maximum impact force, respectively. As shown in these figure, there is a good agreement with experimental results and simulated results.

Figures 3.13(a)-(d), 3.14(a)-(d) and 3.15(a)-(d), show surface configurations of the flowing sand at different time steps obtained from experiment and simulations in the cases of $\phi=41.0$ and $\phi=30.0$. In Figure 3.13 (experimental result), lines are made at interface of sand to get a better view. As is the same about value of impact force, the simulated surface configuration in the case of $\phi=41.0$ dose not correspond with the experimental result. On the other hand, there is a good agreement between the simulated result in the case of $\phi=30.0$ and the experimental result.

Based on the results mentioned above, it is found that the numerical method can describe behavior of geomaterial flow including impact force and configuration during flow. It is, however, also found that it is important to use kinetic friction angle in the numerical simulation, so that a way to determine the parameter still remains as unsolved problem.

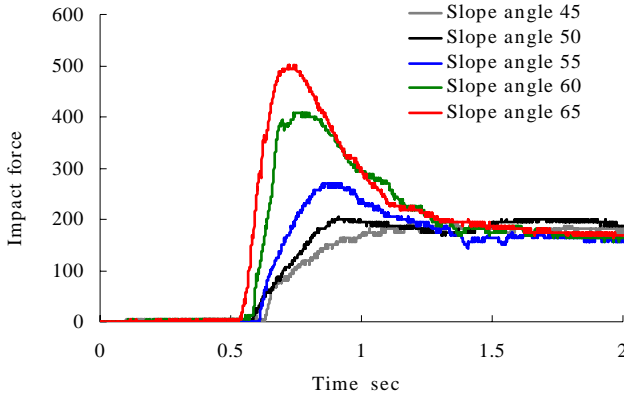


Fig. 3.7. Time history of impact forces from experiment

Table 3.1. Maximum impact force

Slope angle (degree)	Maximum impact force (N)				
	45	50	55	60	65
Trial 1	168.9	212.7	269.0	394.1	500.4
Trial 2	200.2	193.9	262.7	369.1	487.8
Trial 3	187.7	200.4	265.5	406.6	512.9
Trial 4	193.9	200.2	294.0	444.1	469.1
Trial 5	212.7	206.4	300.2	337.7	512.9
Average	192.7	202.7	276.5	390.3	469.7
Standard deviation	14.5	6.4	17.4	35.7	16.6

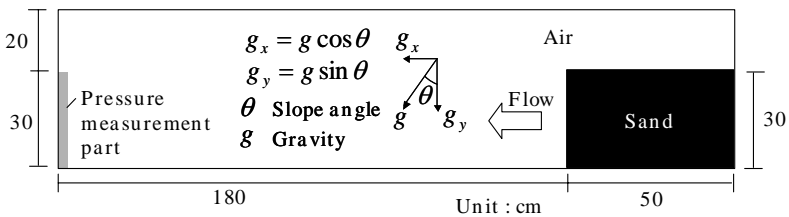


Fig. 3.8. Numerical model for simulation of sand flow experiment

Table 3.2. Parameters used for simulation of sand flow experiment

	Air	Granular Material
Density (kN/m ³)	0.0125	13.80
Sound speed (m/s)	340.0	1500.0
Viscosity coefficient (Pa s)	0.00002	
Cohesion (Pa)		0.0
Internal friction angle (degree)		41.0
Mesh size dx,dy (m)	dx=0.02 dy=0.02	
Number of mesh Nx×Ny	115×50	

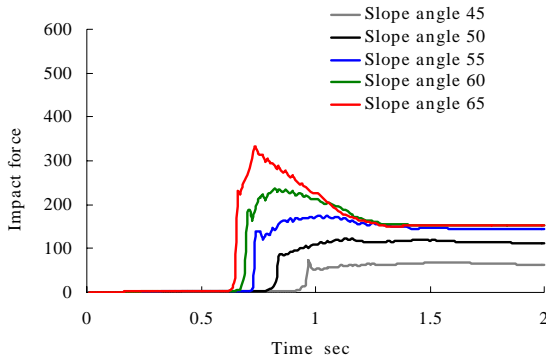


Fig. 3.9. Simulated time histories of impact force ($\phi=41.0$)

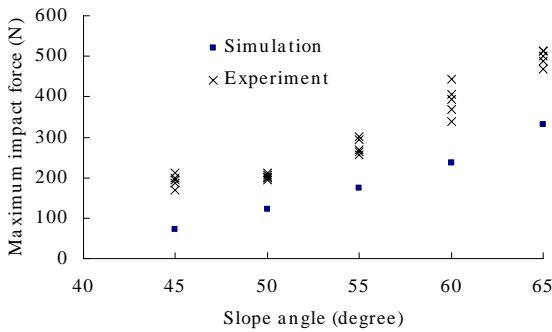


Fig. 3.10. Relationship between slope angle and maximum impact force ($\phi=41.0$)

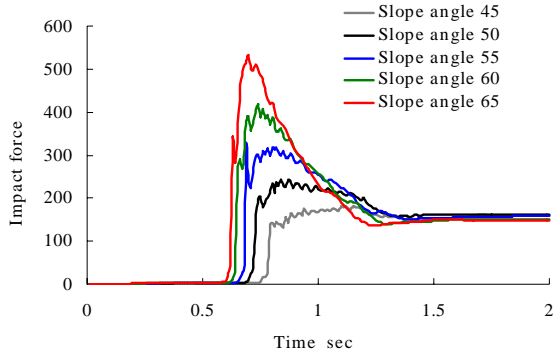


Fig. 3.11. Simulated time histories of impact force ($\phi=30.0$)

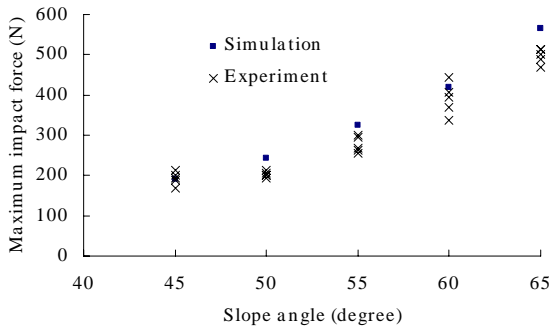


Fig. 3.12. Relationship between slope angle and maximum impact force ($\phi=30.0$)

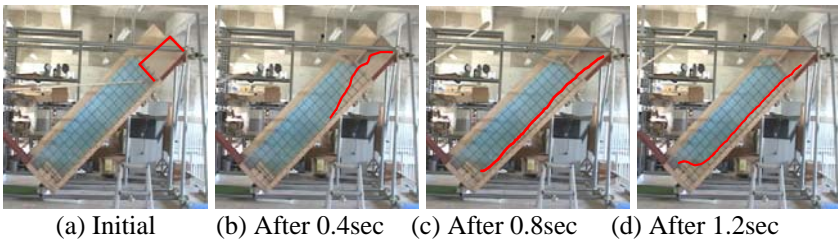


Fig. 3.13. Surface configurations of sand (from experiment)

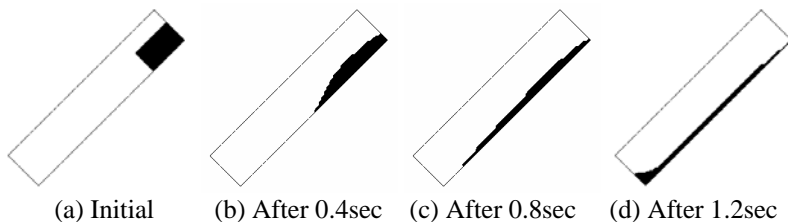


Fig. 3.14. Surface configurations of sand (from simulation with $\phi=41.0$)

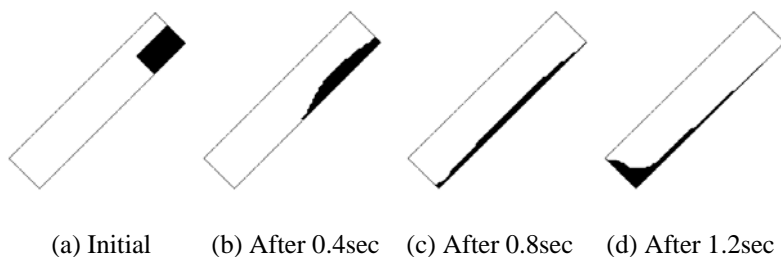


Fig. 3.15. Surface configurations of sand (from simulation with $\phi=30.0$)

4 Conclusions

This work presents experiments related to impact force of geomaterial flow and its simulations. The Bingham fluid model with the Mohr-Coulomb failure criterion was used to describe the behavior of geomaterial, and the CCUP method was used as a numerical scheme. The results from this work are summarized as follows.

1. In order to reproduce experimental results, we have to use much smaller friction angle in simulations than that obtained by usual direct shear tests.
2. It is supposed that the appropriate kinetic friction angle used in the simulation depends on the shear strain rate. It is necessary to examine the relationship between the value of kinetic friction angle and shear strain rate for better simulations.

References

1. Ashida, K., Egashira, S., Ohtsuki H., Dynamic behavior of a soil mass produced by slope failure, Annual report of Disaster Prevention Research Institute, Kyoto University, **26**, B-2, 1-3, 1983.
2. Chen, C. L., and Ling, C. H., Granular-flow rheology: Role of shear rate number in transition regime., *J. Engrg. Mech., ASCE*, **122**-5, 469-480, 1996
3. Chen, C. L., and Ling, C. H., Rheological Equations in asymptotic regimes of granular flow, *J. Engrg. Mech., ASCE*, **124**-3, 301-310, 1998
4. Chorin, A. J., On the Convergence of discrete approximations to the Navier-Stokes Equations, *Math. Comput.*, **23**, 341-353, 1969
5. Hadush, S., Yashima, A., Uzuoka, R., Moriguchi, S. and Sawada, K., Liquefaction Induced Lateral Spread Analysis Using the CIP Method. *Computers and Geotechnics*, **28**, 549-574, 2001
6. Hughes, T. J. R., Liu, W. K. and Zimmermann, T. K., Lagrangian-Eulerian finite element formulation for incompressible viscous flows, *Comput. Methods Appl. Mech. Engrg.*, **29**, 329-349, 1981.
7. Iwamatsu A., 1997 Debris Flow Disaster along the Harihara River, Izumi City, Kagoshima Prefecture, *Journal of Japan Society for Natural Disaster Science*, **16**-2, 107-111, 1997 (in Japanese).
8. Iwao, Y., Slope hazard induced by heavy rain in 2003, Minamata city, Kumamoto, *Journal of the Japanese Landslide Society*, **40**-3, 239, 65-66, 2003 (in Japanese).
9. Kitamura, R., Ochiai, H., Yakabe, H. and Takada M., Natural disaster due to debris flow and its countermeasures in Kagoshima Prefecture, *The Japanese Geotechnical Society*, **46**-7, 486, 24-26, July, 1998 (in Japanese).
10. Moriguchi, S., Yashima, A., Sawada, K., Uzuoka, R. and Ito, M., Numerical simulation of flow failure of Geomaterials based on fluid dynamics, *Soils & Foundations*, **45**-2, 155-166, 2005
11. Moriwaki, H., A prediction of the runout distance of a debris flow, *Journal of the Japanese Landslide Society*, **24**-2, 10-16, 1987 (in Japanese).
12. Osher, S. and Sethian, J. A., Front propagating with curvature dependent speed: Algorithms based on Hamilton-Jacobi formulations, *J. Comput. Phys.* **79**, 12-49, 1988
13. Sabo Technical Center, Realities of sediment-related disaster 2002, 2002 (in Japanese).
14. Scheidegger, A. E., On the prediction of the reach and velocity of catastrophic landslide, *Rock Mechanics*, **5**, 231-236, 1973.
15. Sousa, J. and Voigt, B., Continuum simulation of the flow failure, *Geotechnique*, **41**, 4, 515-538, 1991.
16. Sussman, M., Smereka, P., and Osher S., A level set approach for computing solutions to incompressible two-phase flow, *J. Comput. Phys.* **114**, 146-159, 1994
17. Taniguch, Y., Debris disaster caused by local heavy rain in Kyushu area on July 20th, 2003, *Japan Society Erosion Control Engineering*, **56**-3, 31-35, 2003 (in Japanese).

18. Trunk F.J., Dent D.J. and Lang T.E., Computer modeling of large rockslides, *Journal of the Geotechnical Division, ASCE*, **112** (GE 3), 348-360, 1986
19. Uzuoka R., Yashima A., Kawakami T. and Konrad J-M., Fluid dynamics based prediction of liquefaction induced lateral spreading, *Computers and Geotechnics*, **22** 3/4, 234-282, 1998
20. Yabe, T., Wang, P. Y., Unified Numerical Procedure for Compressible and incompressible fluid, *J. Phys. Soc., Japan*, **60**-7, 2105-2108, 1991.
21. Yabe, T. and Aoki, T., A Universal Solver for Hyperbolic Equations by Cubic Polynomial Interpolation. *Comput. Phys. Commn.* **66**, 219-232, 1991
22. Yabe T., Ishikawa T., Wang P. Y., Aoki T., Kodata Y. and Ikeda F., A universal solver for hyperbolic equations by cubic-polynomial interpolation, two- and three-dimensional solvers. *Comput. Phys. Commun.* **66**, 233-242, 1991.
23. Yabe, T. and Xiao, F., Description of Complex and Sharp Interface During Shock Wave Interaction with Liquid Drop. *J. Phys. Soc. Japan* **62**, 2537-2540, 1993
24. Zhang, S. L., NEC Corp. and Fujino, S., *Mathematics in iteration schemes.* Asakura, 1996 (in Japanese).

Numerical Simulation of the Cracked Brazilian Disc under Diametral Compression

E. Sarris¹, Z. Agioutantis¹, K. Kaklis¹ and S. K. Kourkoulis²

¹Department of Mineral Resources Engineering,
Technical University of Crete,
Chania, Crete,
Greece.
E-mail: zach@mred.tuc.gr

²Department of Mechanics,
National Technical University of Athens,
Athens,
Greece.

Summary

This paper focuses on the diametral compression of a disc with an “almost mathematical” central crack (Centrally Cracked Brazilian Disc - CCBD). A 2D finite element methodology is used to study the stress field and the Stress Intensity Factors K_I and K_{II} at the tips of the crack for different values of the crack length, $2L$ and the crack inclination angle, φ . By changing the crack inclination angle the mode of fracture was varied from mode I (tensile) to mixed mode (tension-shear and compression-shear). The dimensions of the models fitted those of the specimens (as suggested by the international standards), in order to check the numerical results by standardized experiments that are planned in the future

Keywords: Cracked Brazilian test, indirect tensile test, stress intensity factors, finite element analysis, caustics.

1 Introduction

The conventional method of measuring the tensile strength of rocks is the direct tension test, which, however, presents experimental difficulties and is not commonly conducted in Rock Mechanics laboratories. This is due to

both the bending or torsion moments (developed due to the eccentricity of the applied axial loads) and the localized concentrated stresses (caused by improper gripping of the specimens) ^[5, 24].

Because of these experimental difficulties, alternative techniques were developed to determine the tensile strength of rocks. The Brazilian test was developed to measure indirectly the tensile strength of brittle materials like rocks and concrete ^[6]. In this test, the specimen preparation and the experimental setup are simple when compared to other methods. This method was also suggested by the I.S.R.M ^[16] and it uses a circular solid disc, which is compressed to failure across the loading diameter. In principle, the stress field, which induces tensile failure when the disc is compressed diametrically, can be fully determined, provided that the material maintains a perfect linear elastic behavior up to the point of failure.

The Brazilian test has been under investigation and continuous development in rock mechanics since the very first publication on the subject. The theoretical fundamentals (i.e. the stress solutions), as they are thoroughly discussed by Timoshenko and Goodier ^[29], were originally proposed by Hertz in 1883 and by Mitchell some years later (in 1900). Hondros ^[15] proposed a solution for the Brazilian test configuration for the case of isotropic rocks along the loading diameter and the horizontal diameter. Fairhurst ^[12] and Collback ^[10], have set the basic issue of the validity of the Brazilian test. Their studies showed that the failure meets the Griffith failure criterion ^[13], and for very small loading angles, failure may occur away from the center of the specimen. Addinall and Hackett^[1], have proved experimentally that the fracture initiation under specific loading conditions is a function of the contact area. They also showed that fracturing does not always initiate at the center of the disk. Mellor and Hawkes ^[22], proved that in a successful test fracturing does not initiate under the steel platens. They studied the contact stresses under the applied loads and as a result, they designed a system of metal jigs with curved contact areas. The distributions of the contact forces are still under investigation in the rock mechanics community, but in general the test with metal jigs provides adequate results for Griffith materials. In 1993, Guo and his colleagues proposed the Brazilian test as a method to determine the fracture toughness ($K_{ic, i=I,II}$) ^[14]. Samples with a center notch were utilised to examine the fracture mode in Brazilian tests by Jia et al. ^[17]. By changing the notch inclination angle, with respect to the loading direction, the mode fracture was varied from mode I to mixed mode (I+II). A theoretical treatment of tangential loading effects on the Brazilian test stress distribution was presented by Lavrov and Vervoort ^[20]. Wang et al. improved Guo's work on the fracture toughness ($K_{ic, i=I,II}$) ^[31]. It was made clear that the key

problem of center crack initiation must be addressed properly. Wang suggested the modification of the circular disk by introducing two flat ends at the disk. This modification changes the circumferential loading to uniform distributed at the flat ends of the disk. This type of loading is assumed to guarantee the center crack initiation.

Concerning the anisotropic material properties, Pinto ^[27] extended Hondros's method to anisotropic rocks and checked the validity of his methodology on schisteous rock. Recent investigations have led to a closed form solution for an anisotropic disc ^[2,3], a series of charts for the determination of the stress concentration factors at the center of an anisotropic disc ^[9] and explicit representations of stresses and strains at characteristic points of an anisotropic circular disc compressed diametrically ^[11,18].

Although rocks with pre-existing cracks are a common occurrence, the theoretical solutions to these problems find limited application in engineering practice and when an analytical solution is available it is quite a challenge to deal with. Hence, many researchers have turned to numerical approaches to study the Brazilian test such as the boundary element and the finite element methods. Bouchard et al. ^[7] have used the finite element method to study the fracture propagation in the Brazilian test. Remeshing techniques are used to update the mesh following the crack extension. This technique becomes computationally inefficient when multiple cracks propagate simultaneously. The advantage of the finite element method over the boundary element method is that the former can model the material anisotropy more easily and computationally effective. Recently, Cai and Kaiser ^[8] used the distinct element method (micro-mechanical models) to simulate the Brazilian disk with anisotropic material properties as well as to simulate the fracture propagation of pre-existing cracks.

In this paper, section 2 details the configuration of a Brazilian Disc test where an "almost mathematical" crack (almost zero width) is introduced passing through the center of the disc. The geometry and boundary conditions of the models used in the numerical analysis are also presented. In Section 3, the distributions of the stress components σ_θ and σ_r along the crack diameter as well as the equivalent stress σ_G are presented in order to investigate the center crack initiation. The Stress Intensity Factors K_I and K_{II} calculated from the numerical models are also illustrated. In Section 4, the numerical results for the stress components are discussed and the calculated K_I and K_{II} are compared with those presented by Atkinson et al. ^[4].

2 The Problem

2.1 The Scope

The purpose of the present work is to investigate how a single pre-existing crack (of varying length and orientation) affects the stress field a) at the center of a Brazilian disc and b) at the crack tip, during diametral compression. This study focuses on two distinct areas:

- The numerical calculation of the stress components at each point of the disc and especially in the critical regimes, i.e. the disc center and the crack tip.
- The numerical determination of the Stress Intensity Factors K_I and K_{II} at the crack tips and the determination of the inclination angle φ , at which the crack is under pure mode II loading.

2.2 The Intact Brazilian Disc

For the elastic equilibrium of a homogeneous, continuous, isotropic disc with diameter $D=2R$ and thickness, t , subjected to a uniform radial pressure, p acting along an arc which corresponds to a loading angle, 2α (original Brazilian test, see Figure 2.1), the exact stress solution on the loading diameter is given by the following relationships ^[11, 15].

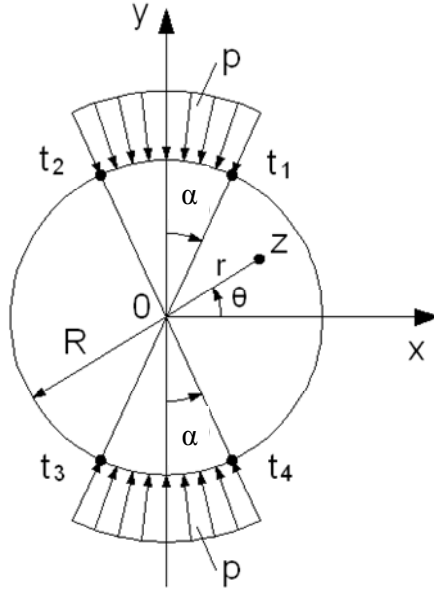


Fig. 2.1. The intact Brazilian Disc specimen under uniform diametral compression

$$\sigma_{\theta} = \frac{2p}{\pi} \left\{ \frac{\sin 2\alpha}{1 - 2\left(\frac{r}{R}\right)^2 \cos 2\alpha + \left(\frac{r}{R}\right)^4} \left[1 - \left(\frac{r}{R}\right)^2 \right] - \arctan \left[\frac{\left(\frac{r}{R}\right)^2 \sin 2\alpha}{1 - \left(\frac{r}{R}\right)^2 \cos 2\alpha} \right] - \alpha \right\} \quad (2.1)$$

$$\sigma_r = \frac{2p}{\pi} \left\{ \frac{\sin 2\alpha}{1 - 2\left(\frac{r}{R}\right)^2 \cos 2\alpha + \left(\frac{r}{R}\right)^4} \left[\left(\frac{r}{R}\right)^2 - 1 \right] - \arctan \left[\frac{\left(\frac{r}{R}\right)^2 \sin 2\alpha}{1 - \left(\frac{r}{R}\right)^2 \cos 2\alpha} \right] - \alpha \right\}$$

At the center of the disc these stresses become:

$$\sigma_{\theta} = \frac{2P}{\pi Dt} \quad (2.2)$$

$$\sigma_r = -\frac{6P}{\pi Dt}$$

where $P = \int_{t_1}^{t_2} -p dt$ is the total external force.

Recently a full field solution has been presented ^[21] according to which the stress components at any point of the disc are given by the following relationships:

$$\sigma_r = \frac{p}{\pi} \left\{ 2\alpha + \arg(t_1 - z) + \arg(t_3 - z) - \arg(t_2 - z) - \arg(t_4 - z) + \right. \\ \left. + R^2 (r^2 - R^2) \left[\frac{\sin 2(\varphi - \alpha)}{R^4 + 2r^2 R^2 \cos 2(\varphi - \alpha) + r^4} - \frac{\sin 2(\varphi + \alpha)}{R^4 + 2r^2 R^2 \cos 2(\varphi + \alpha) + r^4} \right] \right\} \quad (2.3a)$$

$$\sigma_\theta = \frac{p}{\pi} \left\{ 2\alpha + \arg(t_1 - z) + \arg(t_3 - z) - \arg(t_2 - z) - \arg(t_4 - z) - \right. \\ \left. - R^2 (r^2 - R^2) \left[\frac{\sin 2(\varphi - \alpha)}{R^4 + 2r^2 R^2 \cos 2(\varphi - \alpha) + r^4} - \frac{\sin 2(\varphi + \alpha)}{R^4 + 2r^2 R^2 \cos 2(\varphi + \alpha) + r^4} \right] \right\} \quad (2.3b)$$

$$\sigma_{r\theta} = -\frac{p}{\pi} (r^2 - R^2) \left[\frac{R^2 \cos 2(\varphi + \alpha) + r^2}{R^4 + 2r^2 R^2 \cos 2(\varphi + \alpha) + r^4} - \frac{R^2 \cos 2(\varphi - \alpha) + r^2}{R^4 + 2r^2 R^2 \cos 2(\varphi - \alpha) + r^4} \right] \quad (2.3c)$$

where $z=x+iy=re^{i\theta}$ and t_1, t_2, t_3 and t_4 are the points of the physical plane at which the externally applied uniform loading begins and ends (Figure 2.1).

However, for the cracked Brazilian disc (Figure 2.2) similar closed-form solutions are not yet available so a Finite Element Analysis program is used here for the calculation of the tangential σ_θ and the radial σ_r stresses along the vertical axis of symmetry for different central crack lengths $2L$ and orientation angles, φ .

2.3 The Cracked Brazilian Disc

The proposed configuration of the cracked Brazilian test is presented in Figure 2.2. The elastic, homogeneous, continuous and isotropic disc of diameter D and thickness t with a central through crack of length $2L$ and orientation angle, φ , is subjected to a uniform pressure, p acting over a strip of the circumference at each end of the diameter which corresponds to the loading angle 2α .

Throughout this paper (unless stated otherwise) tensile stresses and strains are considered to be positive quantities and consequently compressive stresses and strains are taken as negative quantities.

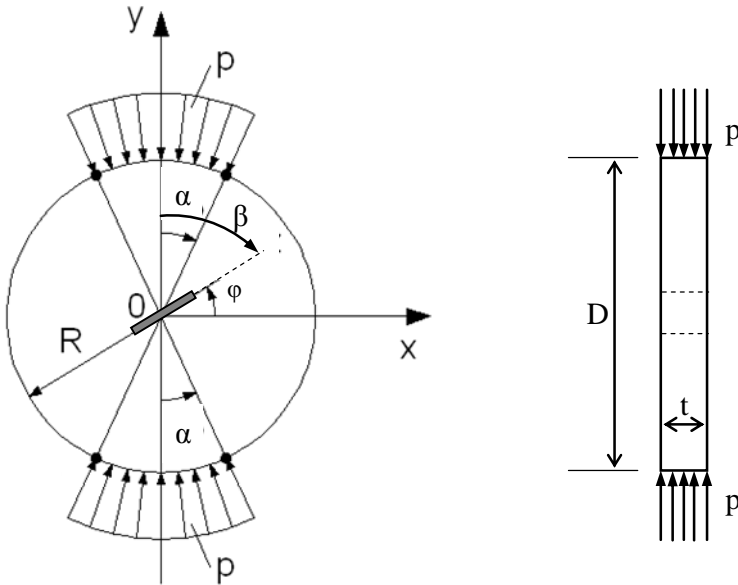


Fig. 2.2. The cracked Brazilian Disc specimen under uniform diametral compression

2.4 Geometry

The test was modeled in 2-D space in the MSC.Mentat front-end program, and was solved by the MSC.Marc Finite Element Analysis program^[23]. To fully simulate the behavior of the material during diametral compression, both the specimen and the steel jigs used to apply the load were modeled

Models were created for six different orientation angles φ (15° , 30° , 45° , 60° , 75° , 90°) and four different crack lengths $2L$ (10 mm, 20 mm, 30 mm, 40 mm). All models were in actual experimental dimensions, i.e. corresponding to the full laboratory specimen and the metal jigs setup. A number of these models are presented in Figure 2.3.

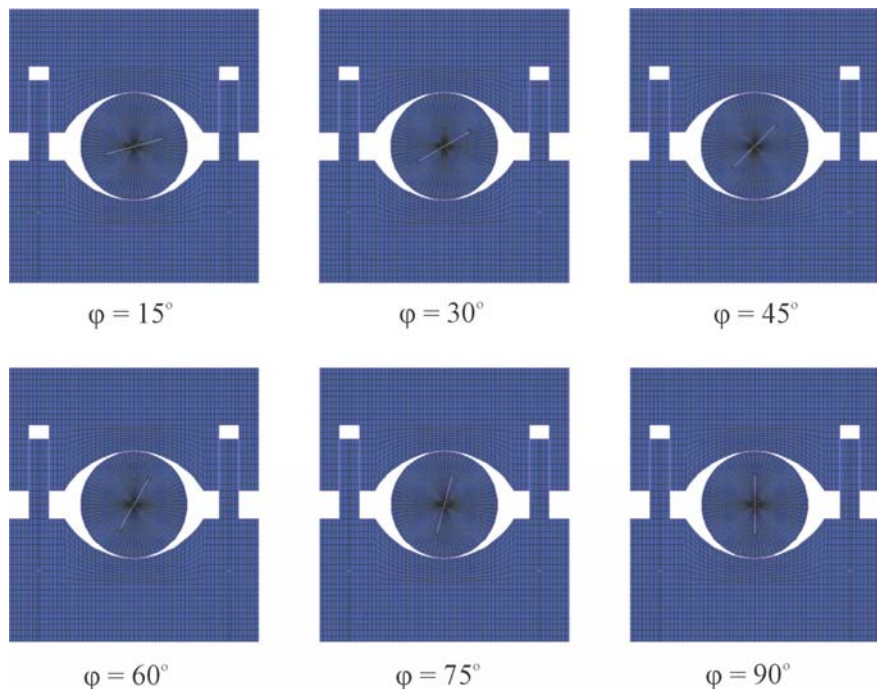


Fig. 2.3. A series of CCBD models with diametral crack length $2L=30$ mm and diameter $D=54$ mm with the steel jigs and six different orientation angles φ .

2.5 Material Models and Boundary Conditions

The steel jigs and the specimen were modeled as linearly elastic isotropic materials with elastic constants $E=210$ GPa, $\nu=0.3$, and $E=80$ GPa, $\nu=0.25$ respectively (E denotes the modulus of elasticity and ν the Poisson's ratio). Note that these are typical values for Dionysos marble ^[19,30]. The boundary conditions were as follows (Figure 2.4):

1. A maximum pressure of 4.5 MPa was applied on the upper and lower flat edge of the jigs in twenty linear loading. The total applied load corresponds to the estimated failure load.
2. For the jigs, the left and right vertical boundary line of nodes for each model was fixed for horizontal displacement ($dx=0$) in order to ensure the perfect vertical motion of the metal jigs towards the specimen.
3. For the specimen, the two boundary nodes along the vertical diameter of the disc, at the upper and lower end of the specimen, were fixed for horizontal displacement ($dx=0$) as well as the two boundary nodes along

the horizontal diameter of the disc, at the left and right end of the specimen, were fixed for vertical displacement ($dy=0$).

A uniformly distributed traction was applied in the vertical direction on the flat ends of the jigs. Contact elements with friction coefficient $\mu = 0.4$ were used to model the crack lips as well as the interface between steel platens and specimen in order to avoid element overlapping. No symmetry was taken into consideration due to the existence of a “mathematical crack” of varying orientation.

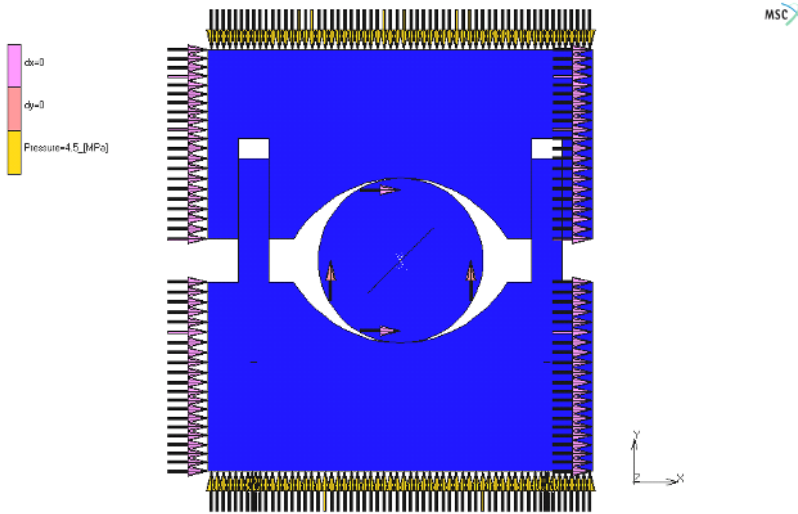


Fig. 2.4. Typical boundary conditions for all models. Model with crack length $2L=30$ mm and orientation angle $\varphi=45^\circ$

3 Numerical Analysis and Results

3.1 Stress Distributions

Figure 3.1 presents a typical distribution of the σ_{xx} stress component for CCBD models with a crack length $2L=20$ mm and an orientation angle $\varphi=45^\circ$ (Figure 4a) and $\varphi=90^\circ$ (Figure 4b). Similar results were obtained for all models.

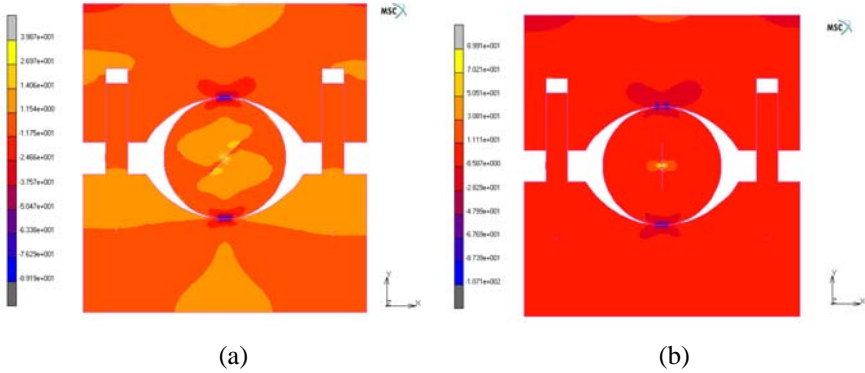
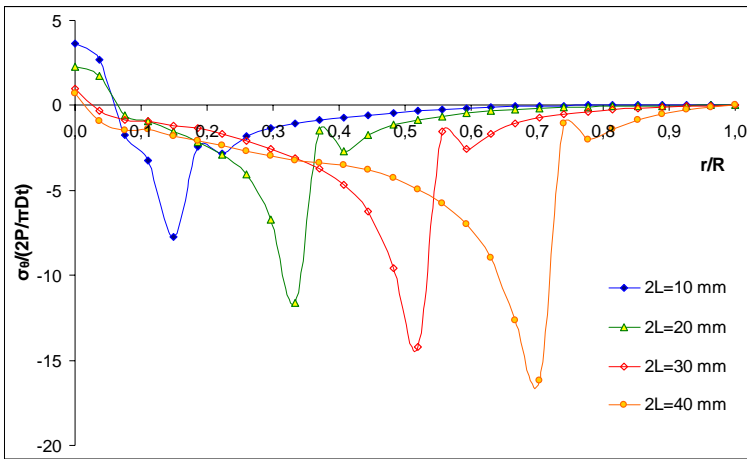
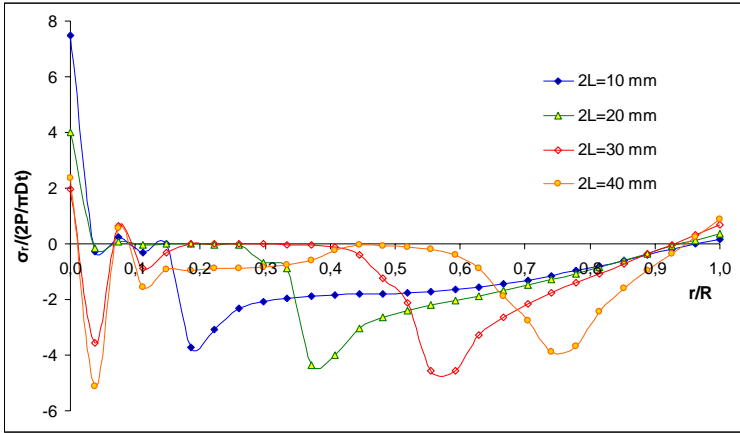


Fig. 3.1. Distribution of the σ_{xx} stress component on CCB models with crack length $2L=20$ mm and orientation angle $\varphi=45^\circ$ (a) and $\varphi=90^\circ$ (b)

Figs. 3.2 and 3.3 present the variation of the dimensionless $\sigma_\theta/[2P/\pi Dt]$ and $\sigma_r/[2P/\pi Dt]$ along the crack diameter for the models with an inclination angle $\varphi=45^\circ$ and $\varphi=90^\circ$ respectively, while Figure 3.4 presents the same variation for the model with a crack length $2L=20$ mm.

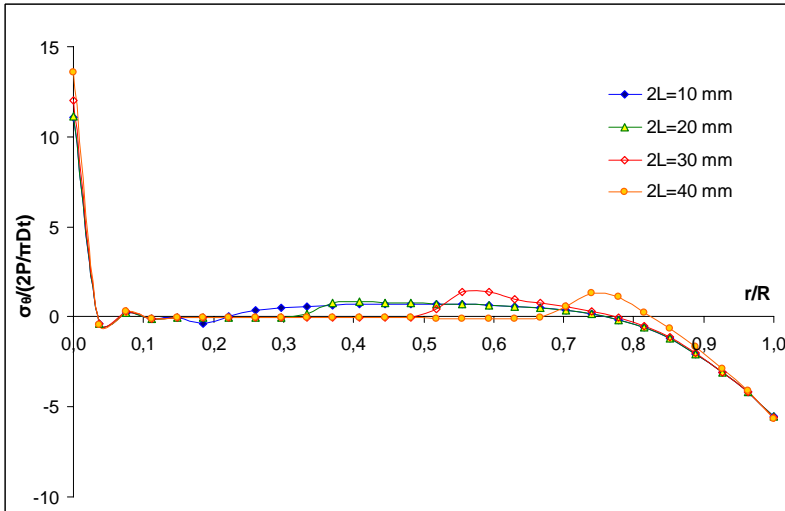


(a)

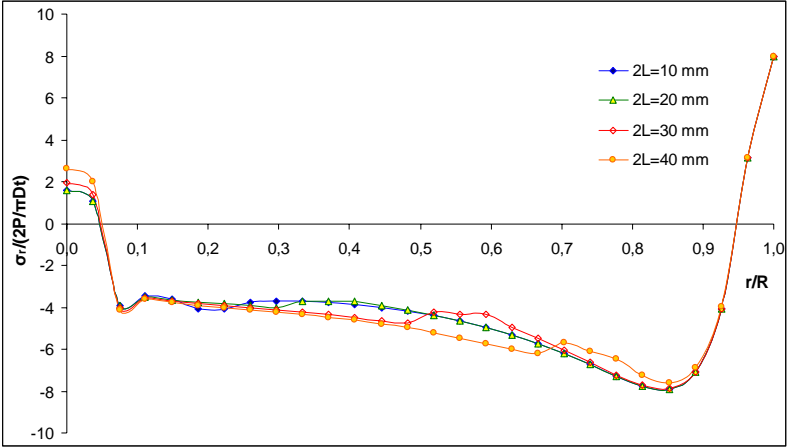


(b)

Fig. 3.2. Variation of the reduced σ_θ (a) and σ_r (b) along the crack diameter, for a crack inclination angle $\varphi=45^\circ$

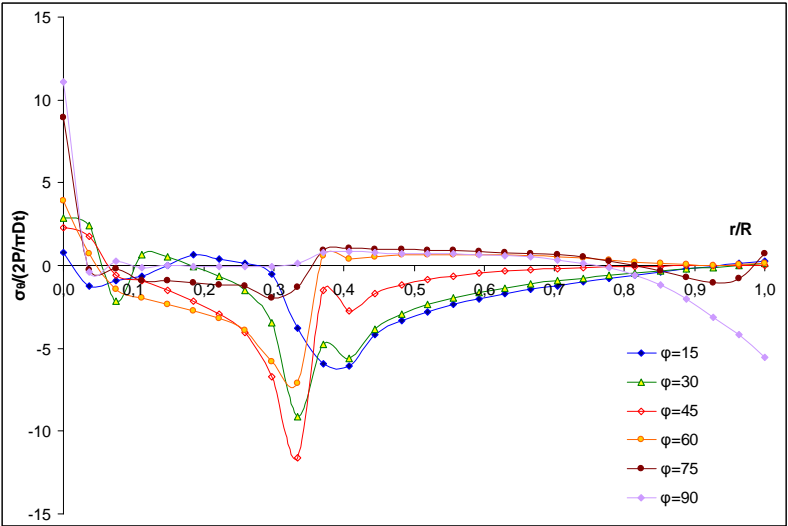


(a)

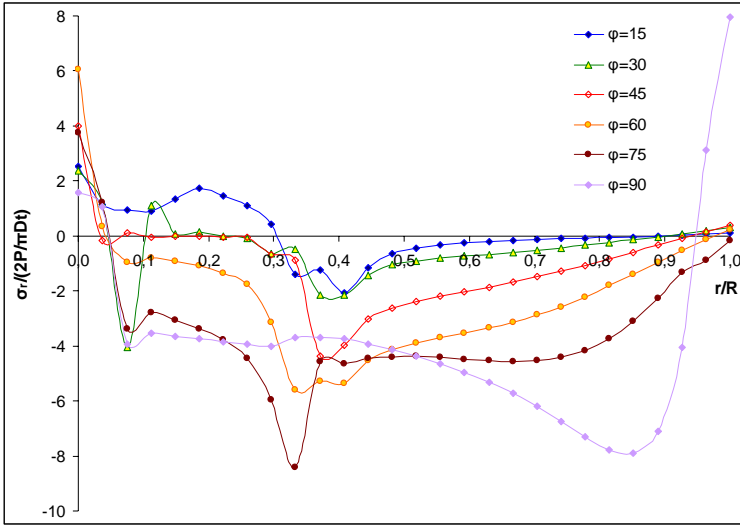


(b)

Fig. 3.3. Variation of the reduced σ_θ (a) and σ_r (b) along the crack diameter, for a crack inclination angle $\varphi=90^\circ$



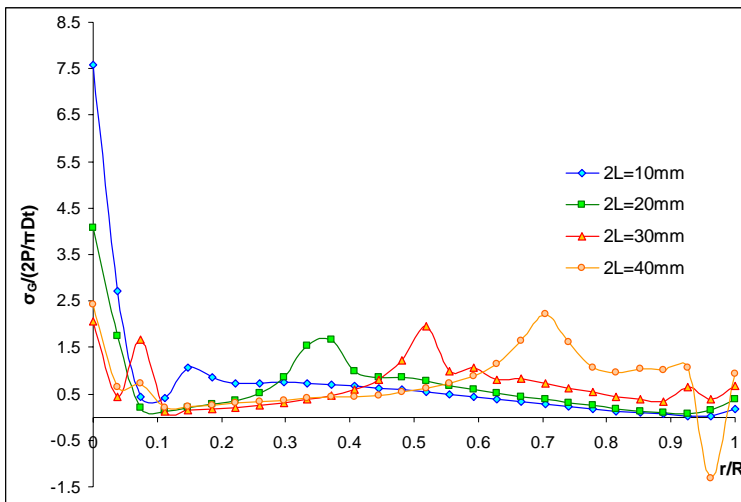
(a)



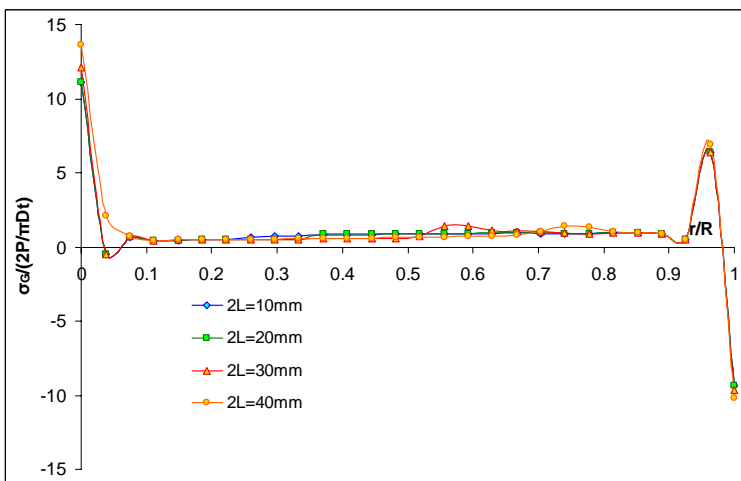
(b)

Fig. 3.4. Variation of the reduced σ_θ (a) and σ_r (b) along the crack diameter, for $2L=20$ mm

Figure 3.5 presents the variation of the dimensionless quantity $\sigma_G/[2P/\pi Dt]$ along the crack diameter for the models with an inclination angle $\varphi=45^\circ$ (Figure 3.5a) and $\varphi=90^\circ$ (Figure 3.5b) respectively, while Figure 3.6 presents the variation of the same quantity for the model with a crack length $2L=20$ mm. Note that σ_G is the equivalent Griffith stress as defined in Section 4.1.



(a)



(b)

Fig. 3.5. Variation of the reduced σ_G along the crack diameter, for $\varphi=45^\circ$ (a) and $\varphi=90^\circ$

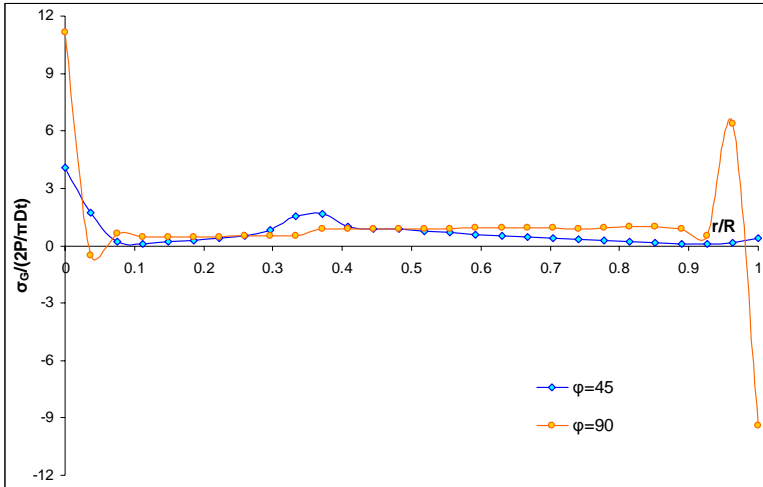
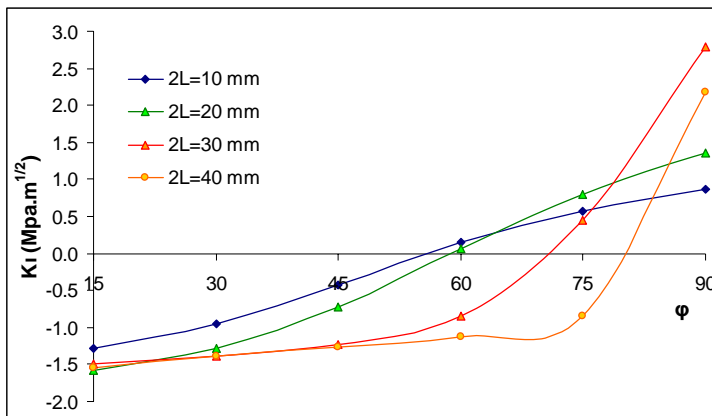


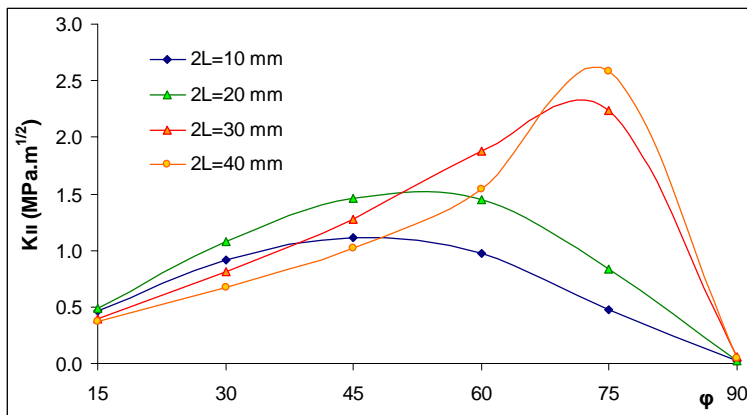
Fig. 3.6. Variation of the reduced σ_G along the crack diameter for $2L=20$ mm

3.2 Distributions of Stress Intensity Factors

Figure 3.7 presents the variation of the Stress Intensity Factors K_I and K_{II} , at the crack tip for all crack lengths with varying inclination angle. Similarly Figure 3.8 presents the variation of the Stress Intensity Factors K_I and K_{II} at the crack tip for all inclination angles as a function of crack length.

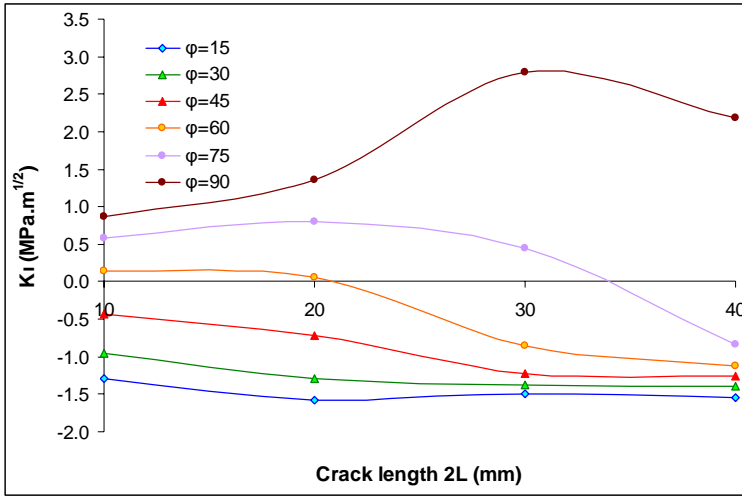


(a)

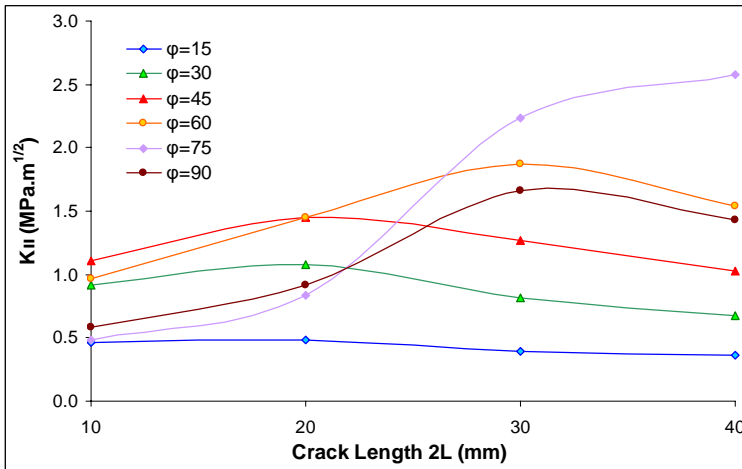


(b)

Fig. 3.7. Variation of the Stress Intensity Factor K_{I} (a) and K_{II} (b) at the crack tips



(a)



(b)

Fig. 3.8. Variation of the Stress Intensity Factor K_I (a) and K_{II} (b) at the crack tips

4. Discussion

The discussion focuses on two subjects. The stress distribution on the specimen and how the distribution compares to the Griffith strength criterion and the comparison of the Stress Intensity Factors obtained numerically to analytical values proposed by other researchers.

4.1 Stress - Griffith Strength Criterion

As expected the stress distribution varies with the inclination angle of the assumed “mathematical” crack. For example, for the case with $\varphi=45^\circ$, the peak stresses (both tangential and radial) are compressive and appear at the crack tip for all crack lengths (Figure 3.2) (note that the peaks for radial stresses occurring close to crack center for longer cracks need to be further investigated). Similar results are obtained for angles less than 45° , were crack closure is observed at the crack tip as well.

For the case where $\varphi=90^\circ$ (vertical crack) the maximum tangential stresses are tensile and occur at the center of the disc (Figure 3.3a). The high radial stresses observed for the longer cracks may be attributed to the proximity of the crack tip to the loaded area. Figure 3.4 shows that the peak tangential stress appear at the crack tip for a given crack length for low inclination angles, while high stresses appear around the crack center for higher inclination angles. Table 4.1 summarizes the nature (compressive or tensile) of the expected stress regimes at the crack tip for all inclination angles and crack lengths.

Table 4.1. Summary of the nature of the expected stress regimes

	$\varphi = 15^\circ$	$\varphi = 30^\circ$	$\varphi = 45^\circ$	$\varphi = 60^\circ$	$\varphi = 75^\circ$	$\varphi = 90^\circ$
2L=10mm	compression	compression	compression	tension	tension	tension
2L=20mm	compression	compression	compression	tension	tension	tension
2L=30mm	compression	compression	compression	compression	tension	tension
2L=40mm	compression	compression	compression	compression	compression	tension

From Figure 3.7b, it follows that shear stresses are developed at the crack tip for all crack inclinations and lengths with the exception of $\varphi=90^\circ$. It should be noted again that the high shear stresses observed for higher

crack lengths could be attributed to the interaction of the crack process zone with the disc loading area.

Figures 3.7a,b support the notion that for $\varphi=90^\circ$ cracking is under pure mode I while for the other cracked inclinations, cracking can be considered as mixed mode (I+II).

When considering the Griffith strength criterion^[13], the equivalent stress σ_G is calculated as follows (assuming that the tensile stress is considered positive and $\sigma_1 \geq \sigma_2 \geq \sigma_3$):

$$\begin{aligned} &\text{when } 3\sigma_1 + \sigma_3 \geq 0, \sigma_G = \sigma_1 \\ &\text{when } 3\sigma_1 + \sigma_3 < 0, \sigma_G = -\frac{(\sigma_1 - \sigma_3)^2}{8(\sigma_1 + \sigma_3)} \end{aligned} \tag{4.1}$$

Applying Eq.(4.1) for the case of the CCBD test the equivalent stress σ_G can be calculated by setting $\sigma_1 = \sigma_\theta$, $\sigma_3 = \sigma_r$. This was accomplished for all studied inclination angles and crack lengths (Figures 3.5 and 3.6). It is evident from these figures that the largest value of σ_G is calculated for the disc center than for any point elsewhere on the loading diameter. Hence the crack is most likely to initiate at the centre of the disc.

4.2 Stress Intensity Factors

Atkinson et al.^[4], have calculated the Stress Intensity Factors for the Brazilian disc containing a central straight-through crack. The numerical solutions for the Stress Intensity Factors, K_I and K_{II} , can be expressed by the following relationships:

$$K_I = \frac{P\sqrt{2L}}{\sqrt{\pi R t}} N_I \tag{4.2}$$

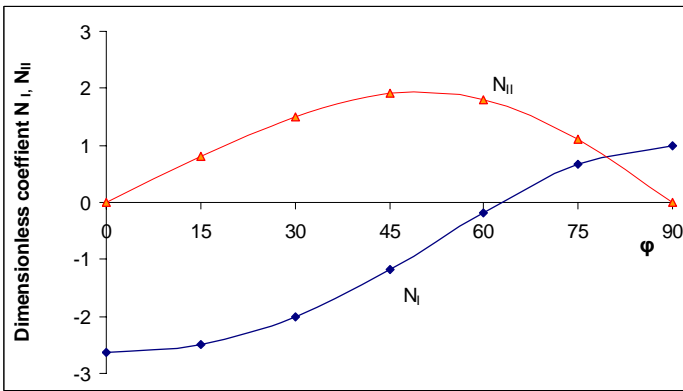
$$K_{II} = \frac{P\sqrt{2L}}{\sqrt{\pi R t}} N_{II} \tag{4.3}$$

where N_I and N_{II} are dimensionless coefficients depending on the dimensionless crack length ($2L/R$) and the crack inclination angle φ . For small crack lengths ($2L/R \leq 0.3$) N_I and N_{II} are given by the following expressions:

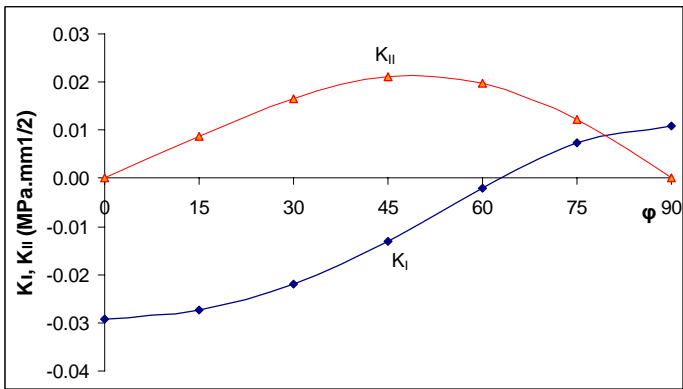
$$N_I = 1 - 4\sin^2\left(\frac{\pi}{2} - j\right) + 4\sin^2\left(\frac{\pi}{2} - j\right)\left[1 - 4\cos^2\left(\frac{\pi}{2} - j\right)\right]\left(\frac{2L}{R}\right) \quad (4.4)$$

$$N_{II} = \left[2 + \left(-5 + 4\cos^2\left(\frac{\pi}{2} - j\right)\right)\left(\frac{2L}{R}\right)^2\right]\sin\left[2\left(\frac{\pi}{2} - j\right)\right] \quad (4.5)$$

For $2L/R=0.3 \Rightarrow 2L/(27 \text{ mm})=0.3 \Rightarrow 2L=8.1 \text{ mm}$, the variations of N_I and N_{II} with the inclination angle φ are presented in Figure 4.1.a. Also the corresponding variations of K_I and K_{II} are presented in Figure 4.1.b.



(a)



(b)

Fig. 4.1. Variation of the dimensionless coefficients N_I and N_{II} (a) and the Stress Intensity Factors K_I and K_{II} (Atkinson et al.)

From equation (4.4) an equation may be obtained for the inclination angle at which the crack is under pure mode II loading. The angle φ can be determined by equating $N_I = 0$, i.e.

$$1 - 4\sin^2\left(\frac{\pi}{2} - j\right) + 4\sin^2\left(\frac{\pi}{2} - j\right)\left[1 - 4\cos^2\left(\frac{\pi}{2} - j\right)\right]\left(\frac{2L}{R}\right) = 0 \quad (4.6)$$

Equation (4.6) clearly shows that the angle φ is a function of the dimensionless crack length, $2L/R$. In Table 4.2 the crack inclination angles φ for pure mode II loadings obtained by the relationship (4.4) for the values L/R used in the numerical study are presented. The numerical results are also presented in the same table.

Table 4.2. Crack inclination angle for pure mode II loadings for various crack lengths.

L (mm)	L/R	φ (degrees) (Atkinson et al.)	φ (degrees) (numerical results)	Deviations with respect to Atkinson et al. (%)
5	0.185	61.11	56	8.4
10	0.370	64.06	58.5	8.7
15	0.555	67.79	71	4.7
20	0.741	71.25	80	12.3

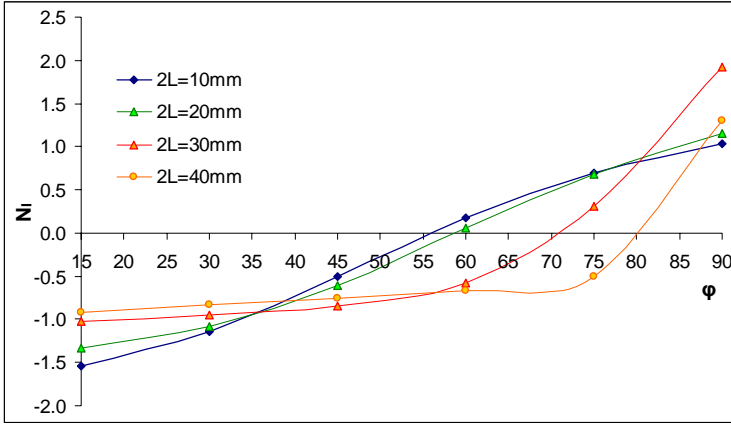


Fig. 4.2. Variation of the dimensionless coefficient N_I obtained by the numerical analysis.

It is observed that the numerical results are in good agreement with the corresponding values presented by Atkinson et al. [4] especially for crack length values under 0.3. Fig. 4.2 presents the variation of the dimensionless coefficient N_I versus the inclination angle ϕ , for different crack length values. The corresponding values of ϕ for pure mode II loading are presented in Table 4.1.

As it is concluded from Table 4.1 and Figure 4.2, crack closure is possible since the specific combinations of y and L , the mode I Stress Intensity Factor becomes negative. The problem of the partial closure of the lips of a crack (natural or artificial) concerns the scientific community already from the late sixties since it imposes a change of the boundary conditions rendering the analytic solution extremely difficult.

According to the classical elasticity solution, the displacement field (u,v) for a plane body with an internal crack of length $2a$, along axis x (the inclination angle with respect to the vertical direction is denoted by β) loaded bi-axially with $\sigma_{\infty, \text{horizontal}}/\sigma_{\infty, \text{vertical}}=k$, is given by the following Muskhelishvili - Kolossov relations in terms of the complex potentials $\Phi(z)$ and $\Omega(z)$:

$$\begin{aligned}
 \sigma_{xx} + \sigma_{yy} &= 2(\Phi(z) + \overline{\Phi(z)}) \\
 \sigma_{xx} - i\sigma_{yy} &= \Phi(z) + \Omega(\bar{z}) + (z - \bar{z})\overline{\Phi(z)} \\
 2G(u + iv) &= \kappa\phi(z) - \omega(\bar{z}) - (z - \bar{z})\overline{\Phi(z)}
 \end{aligned}
 \tag{4.7}$$

where the over-bar designates the complex conjugate, G is the shear modulus, ν is Poisson's ratio while $\kappa=(3-\nu)/(1+\nu)$ for plane stress and $\kappa=3-4\nu$ for plane strain. Regarding the holomorphic functions $\Phi(z)$ and $\Omega(z)$ the following are true ^[28]:

$$\begin{aligned} \Phi(z) = \phi'(z) &= \frac{1}{2}(2\Gamma + \bar{\Gamma}') \frac{z}{\sqrt{z^2 - a}} - \frac{1}{2}\bar{\Gamma}' \\ \Omega(z) = \omega'(z) &= \frac{1}{2}(2\Gamma + \bar{\Gamma}') \frac{z}{\sqrt{z^2 - a}} + \frac{1}{2}\bar{\Gamma}' \end{aligned} \tag{4.8}$$

with:

$$\begin{aligned} \frac{1}{2}\bar{\Gamma}' &= -\frac{1}{4}\sigma_0(1-k)e^{2i\beta} \\ \frac{1}{2}(2\Gamma + \bar{\Gamma}') &= \frac{1}{4}\sigma_0\left[\left(1 - e^{2i\beta}\right) + k\left(1 + e^{2i\beta}\right)\right] \end{aligned} \tag{4.9}$$

The displacement field is obtained from the above relations as ^[26]:

$$\begin{aligned} u_{\pm}(x) &= \frac{\kappa+1}{2G} \operatorname{Re}\phi(z)\Big|_{z=x} = \\ &= \frac{\sigma_0(\kappa+1)}{8G} \left[(1-k)(\cos 2\beta)x \pm (1-k)(\sin 2\beta)\sqrt{a^2 - x^2} \right] \\ v_{\pm}(x) &= \frac{\kappa+1}{2G} \operatorname{Im}\phi(z)\Big|_{z=x} = \\ &= \frac{\sigma_0(\kappa+1)}{8G} \left\{ (1-k)(\sin 2\beta)x \pm \left[(1+k) - (1-k)(\cos 2\beta) \right] \sqrt{a^2 - x^2} \right\} \end{aligned} \tag{4.10}$$

The index $[+]$ or $[-]$ indicates the displacements of the upper or lower crack lip, respectively of the analytic equations. The above relations represent the exact form of the displacements of the crack lips and they allow the calculation of the exact shape of the deformed crack.

It should be noted that, for a given material, specific combinations of geometry and loading exist which yield overlapping lips for various values of parameter $c=\sigma_{\infty}(1+\kappa)/G$, violating the stress free crack lips condition. These combinations are presented in Figure 4.3.

The general touching lips condition in terms of k (loading), β (geometry) and c (material) is given by:

$$c\left[(1+k) - (1-k)\cos 2\beta - c(1-k)^2 + c(1-k^2)\cos 2\beta\right] = 0 \tag{4.11}$$

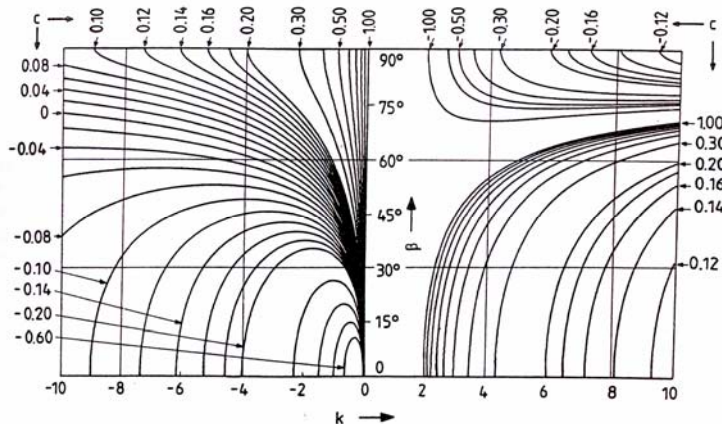


Fig. 4.3. Combinations of β (geometry) and k (loading) leading to overlapping of the crack lips for various values of the material parameter $c = \sigma_{\infty}(1+k)/G$ [26]

For the Brazilian disc (uniaxial external field of compressive nature) the crack closure, for a natural crack, is avoided only when the crack is parallel to the load direction. In any other configuration the Stress Intensity Factors calculated numerically deviate significantly from the experimentally obtained ones. This is due to the friction forces developed between the lips of the crack, which are now under mutual compression. These forces “prohibit” the displacement field along the crack flanks from reaching the tip of the natural crack and, thus, the crack tip appears to be unloaded.

The above observation has been verified experimentally using the optical method of caustics [25]. Indeed, for most tests a caustic does not appear, until a certain load level was reached, equal to almost half of the failure load. Then if this limit is exceeded the friction forces are overcome and the displacement field appears “propagating” under constant load towards the crack tip. Upon reaching it, the caustic suddenly appears. In Figure 4.4 a series of three photographs is displayed, corresponding exactly to the instant at which the load reached the above mentioned critical level, and the displacement field started “propagating” towards the tip of the natural crack. It is emphasized that *all three photographs of Figure 16 correspond to the same load level*. It is concluded, thus, that at least for natural cracks the influence of the friction forces cannot be ignored in case the critical Stress Intensity Factors are to be calculated, because the results obtained are erroneous.

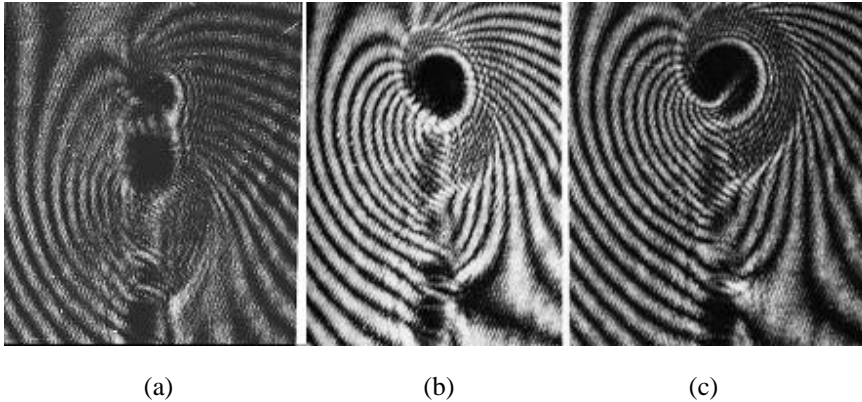


Fig. 4.4. A series of photographs indicating the evolution of the caustic at the tip of a natural crack, at a constant load $P=0.68P_{\text{fracture}}$, from the almost load free state (a) to the preliminary mixed-mode caustic (b) up to the almost pure mode-II caustic (c) ^[25]

Regarding the case of artificial cracks it is again possible to observe contact of the lips as it was verified experimentally by the method of caustics ^[25], however the critical parameter is now the width of the crack. For this problem there are not any closed form solutions and therefore the numerical approximations, like the one discussed previously, become extremely valuable.

5 Conclusions

The present work, verifies that the presence of pre-existing cracks in the specimens, with different lengths and orientations affect the determination of the overall tensile strength of the rocks. From the simulations conducted it was shown that the presence of pre-existing cracks does not affect the stress field developing at the center of the disk. Stress concentrations of high magnitude also develop at the crack tips but depending on the crack orientations, they may be either compressive or tensile. This is also shown by applying the Griffith fracture criterion for the case of the open crack situation at a compressive stress field. The results indicate that that initial failure will primarily occur at the center of the disk and secondly at the crack tips.

As far as the Stress Intensity Factors are concerned, it has been verified that for crack orientation $\varphi=90^\circ$, the crack is under mode I loading. For all the other cases of crack orientation, the crack is under mixed mode loading

conditions. In such cases, if the crack is considered as natural, crack-lips contact cannot be avoided unless the crack is parallel to the loading direction. Otherwise the results are meaningless since the friction forces render the initial formulation of the problem unacceptable from a mathematical point of view and only numerical simulations can provide estimations of the Stress Intensity Factors. The results obtained from the numerical simulation of the present paper are in good agreement with the corresponding values presented by Atkinson et al. ^[4].

References

1. Addinall E, Hackett P. "The effect of platen conditions on the tensile strengths of rock-like materials", *Civ. Eng. Public Works Rev.* 59, 1964.
2. Amadei, B., J.D Rogers, R.E Goodman, "Elastic constants and tensile strength of anisotropic rocks", *Proceedings of the 5th ISRM Congress, Melbourne, A189-A196, 1983.*
3. Amadei B., "Importance of anisotropy when estimating and measuring in situ stresses in rock", *Int. J. Rock Mech. Min. Sci and Geomech. Abstr.*, Vol.33, pp. 293-325, 1996.
4. Atkinson, C., R.E Smelser, Sanchez, J., "Combined mode fracture via the cracked Brazilian disk test", *Int. J. Fract.* 18, No. 4, pp. 279-291, 1982.
5. Barla, G., L. Goffi, "Direct tensile testing of anisotropic rocks", *Proceedings of the Third International Congress of Rock Mechanics, Denver, Vol. 2, Part A, pp.93-98, 1974.*
6. Berenbaum R., I Brodie, "Measurement of tensile strength of brittle materials", *Br. J. Appl. Phys.*, Vol. 10, pp.281-286, 1959.
7. Bouchard P.O., F. Bay, Y. Chastel, I. Tovená, "Crack propagation modeling using an advance remeshing technique", *Computer methods in applied mechanics and engineering*, Vol. 189, pp. 723-742, 2000.
8. Cai, M, P.K Kaiser, "Numerical simulation of the Brazilian test and the tensile strength of anisotropic rocks and rocks with pre-existing cracks", *Int. J. Rock Mech. Min. Sci*, Vol. 41, 2B03, *sinorock2004 symposium*, 2004.
9. Chen, C.S., E. Pan, B. Amadei, "Determination of deformability and tensile strength of anisotropic rock using Brazilian tests", *Int. J. Rock Mech. Min. Sci and Geomech. Abstr.*, Vol. 35, pp.43-61, 1998.
10. Collback PSB, "An analysis of brittle fracture initiation and propagation in the Brazilian test", In: *Proceedings of the first congress of the international society of rock mechanics, Lisbon.* pp. 385-391, 1966.
11. Exadaktylos G.E., K.N. Kaklis, "Applications of an explicit solution for the transversely isotropic circular disc compressed diametrically", *Int. J. Rock Mech. Min. Sci and Geomech. Abstr.*, Vol. 38, pp. 227-343, 2001.
12. Fairhurst C. "On the validity of the Brazilian test for brittle materials", *Int. J. Rock Mech. Min. Sci and Geomech. Abstr.*, Vol.1, pp. 515-546, 1964.

13. Griffith A.A. "Theory of rupture", Proceedings of the First International Congress on Applied Mechanics, pp. 55-63, 1924.
14. Guo, H., N.I. Aziz, "A simple Method of Measuring rock Fracture Toughness Using the Brazilian Test Method", Proceedings of the 11th International Conference on Ground Control in Mining, University of Wollongong, NSW, Australia, 1993.
15. Hondros, G., "The evaluation of Poisson's ratio and the modulus of materials of a low tensile resistance by the Brazilian (indirect tensile) test with particular reference to concrete", Aust. J. Appl. Sci., Vol.10, pp. 243-264, 1959.
16. ISRM, "Suggested methods for determining tensile strength of rock materials", *Int. J. Rock Mech. Min. Sci and Geomech. Abstr.*, Vol.15, pp. 99-103, 1978.
17. Jia Z., A. Castro-Montero, S.P Shah, "Observation of mixed mode fracture with center notched disk specimens", Cement and Concrete research, Vol. 26, pp.125-137, 1996.
18. Kaklis K.N., "Characterization of rock anisotropy and tensile strength using the Brazilian test", PhD thesis, Technical University of Crete, Hania, Greece, 2003.
19. Kourkoulis S. K., Exadaktylos G. E. and Vardoulakis I., "The Influence of Notch Geometry and Non-linearity on the SIF in Case of 3PB Marble Specimens", *Proc. 14th European Conf. on Fracture*, Krakow, Poland, Eds. A. Neimitz, I.V. Rokach, D. Kocanda, K. Golos, EMAS Publishing, United Kingdom, Vol. II, pp. 243-250 (2002).
20. Lavrov A., A. Vervoort, "Theoretical treatment of tangential loading effects on the Brazilian test stress distribution", *Int. J. Rock Mech. Min. Sci and Geomech. Abstr.*, Vol. 39, pp. 275-283, 2002.
21. Markides Ch., Sarris E., Pazis D.N., Agioutantis Z. and Kourkoulis S. K., "Marble discs under distributed loading: theoretical, numerical and experimental study", 16th European Conference on Fracture, Alexandroupolis, Hellas, 3-7 July, 2006, accepted for presentation.
22. Mellor M., I. Hawkes, "Measurement of Tensile Strength by Diametral Compression of Discs and Annuli", *Engineering Geology*, Vol. 5, pp. 173-225, 1971.
23. Msc. Marc-Mentat, "User's guide", 2000.
24. Nova, R., A. Zaninetti, "An investigation into the tensile behavior of a schistose rock", *Int. J. Rock Mech. Min. Sci and Geomech. Abstr.*, Vol. 27, pp. 231-242, 1990.
25. Pazis, D. and Kourkoulis S.K., 'Determination of SIFs and crack-tip position in mixed mode problems by caustics: An alternative approach', *Proc. International Conference on Advanced Experimental Technology (ATEM '99)*, Ube, Yamaguchi, Japan, The Japan Society of Mechanical Engineers 99-294, Vol. 1, pp. 75-80, July 1999.
26. Pazis D.N., Theocaris P.S. and Konstantellos V., "Elastic overlapping of the crack flanks under mixed-mode loading", *Int. J. Fracture*, 37(1988), 303-319.

27. Pinto, J.L., "Determination of the elastic constants of anisotropic bodies by diametral compression tests", *Proceedings of the Fourth ISRM Congress*, Montreux, Vol. 2, pp. 359-363, 1979.
28. Theocaris P.S. and Michopoulos J.G., *Engineering Fracture Mechanics*, 17 (1983) 97-123.
29. Timoshenko, S.P., J.N. Goodier, "*Theory of Elasticity*", 3rd Edition, International Students Edition, 1970.
30. Vardoulakis I., Kourkoulis S. K., Exadaktylos G. E. and Rosakis A., Mechanical Properties and Compatibility of Natural Building Stones of Ancient Monuments: Dionysos marble", *Proc. of the Interdisciplinary Workshop "The building stone in monuments"*, Athens, IGME Publishing, Eds. M. Varti-Mataranga and Y. Katsikis, 187-210, (2002).
31. Wang Q.Z., X.M. Jia, S.Q. Kou, Z.X. Zhang, P.A. Lindqvist, "The flattened Brazilian disc specimen used for testing elastic modulus, tensile strength and fracture toughness of brittle rocks: analytical and numerical results", *Int. J. Rock Mech. Min. Sci and Geomech. Abstr.*, Vol. 4

Stress Analysis of Multiply Fractured Porous Rocks

P. Liolios and G. Exadaktylos

Department of Mineral Resources Engineering,
Technical University of Crete,
Chania, Crete,
Greece.
E-mail: exadakty@mred.tuc.gr

Summary

The present work is essentially a continuation of a previous study (Liolios and Exadaktylos, 2006) aiming at the investigation of the stress-deformation state of a porous body under the influence of mechanical and fluid flow fields, in the regions where stress singularities (e.g. cracks, thin strip inclusions, holes etc.) exist. For the solution of the problem the theories of complex variables and Cauchy-type singular integral equations are employed, since these methods are the most suitable for the calculation of the Stress Intensity Factors (SIFs) at crack tips. A fast solver has been developed for the stress analysis of multiply fractured porous media.

1 Introduction

A class of important geomechanical problems involves the quantification of critical conditions for crack initiation in the vicinity of singularities and stress concentrators in geomaterials (e.g. fractures, faults, joints, interface cracks, corners in slopes and foundations, rectangular underground excavations in rocks etc.). It is apparent that this class of problems may be significantly extended if the diffusion of pore pressure and/or heat in the porous saturated geomaterial is also considered.

The study of fluid flow and stresses in rocks has many significant practical applications such as: hydraulic fracturing in boreholes in petroleum or geothermal reservoirs in order to increase the permeability of the formation, pore pressure influence on fracture propagation and in situ stress measurements with the hydraulic fracturing technique, estimation of the permeability of fluid reservoirs (e.g. petroleum, water), hydro-mechanical erosion of rocks around wellbores, rock fracturing with thermal fatigue,

applications involving the injection or withdrawal of fluids from porous subsurface formations that are transected by compaction bands, such as aquifer management, energy recovery and storage, waste disposal etc. In the laboratory as well as in many theoretical studies, the length of material discontinuities is limited to the width of specimen or of the modeled domain, respectively, but in the field finite lengths of faults, joints and cracks that exhibit stress singularities at their tips, are observed. Even if the failure mechanism cannot, in many cases, be completely described only by the propagation of cracks, the investigation of the conditions which trigger the initiation of a crack or a system of cracks from the pre-existing defects in the material (cracks, inclusions, cavities etc.) is of great theoretical and technological importance.

There are also two other areas of application that came into the authors attention during this Conference, namely: (a) the influence of stress non-uniformity produced by many interacting cracks under a given stress field on the strength of brittle rocks proposed by Dyskin and Pasternak (2006) (in this volume), and (b) the validation of continuum micromechanical models such as that proposed by Pichler et al. (2006) in this volume.

The approach, which is followed here, is based on the Theories of Complex Variables and Singular Integral Equations (SIE) developed by Muskhelishvili (1953) and on the numerical solution of the SIE's. The present solution can be applied for the general case of multiple non-intersecting curvilinear cracks where the shape of each crack may not be reduced to a known equation. Furthermore, it is demonstrated that the proposed solution converges rapidly to an estimation. Hence, it may be used to test the accuracy of a numerical code (such as Finite Elements, Finite Differences or Boundary Elements), as a tool for quick back analysis of in situ fluid flow or pore pressure measurements, and as a supplement to another numerical code dedicated for coupled thermo-hydro-mechanical problems.

2 Formulation of the (a) Short-Term and (b) Long-Term Problems

The variability of properties and the complexity of a porous, granular medium make it impossible to mathematically characterize it on a microscopic scale which identifies each constituent boundary. An average material element can be introduced in place of a detailed point description, provided that the Representative Element Volume (REV) is large enough to remove microscopic inhomogeneities of the constituent interfaces but

small enough to ensure that large-scale discontinuities in the porous media are not included. Since our interest is to model material behavior on a macroscopic scale, grid blocks, which define elementary volumes in simulations, will be assumed to be large enough to treat porosity and other material properties as well-defined continuum variables. The following assumptions are made in this study:

1. Infinitesimal displacements
2. Linear elastic behavior
3. Saturated porous medium
4. Isotropic, homogeneous medium
5. Isothermal conditions
6. Body forces are discarded
7. Plane strain conditions
8. Terzaghi's effective stress principle holds true
9. The cracks are open

Terzaghi's effective stress principle has as follows

$$\sigma_{ij} = \sigma'_{ij} + \delta_{ij}p \Leftrightarrow \sigma'_{ij} = \sigma_{ij} - \delta_{ij}p \tag{2.1}$$

where σ_{ij} is the stress tensor of the total stresses, σ'_{ij} is the effective stress tensor and p is the pore pressure. The basic state variables of the problem are the total stress and pore pressure. Herein, unless otherwise stated, we follow the geomechanics convention, namely that compressive stresses are positive. The solution must satisfy equilibrium, compatibility and Hooke's equations, as well as the boundary conditions.

In plane strain equilibrium, the combination of compatibility and elasticity equations gives

$$\left(\frac{\partial^2}{\partial x^2} + \frac{\partial^2}{\partial y^2} \right) (\sigma'_{xx} + \sigma'_{yy}) + \frac{1}{1-\nu} \left(\frac{\partial^2}{\partial x^2} + \frac{\partial^2}{\partial y^2} \right) p = 0 \tag{2.2}$$

The field equation for flow in the porous medium in plane strain is

$$\frac{EK}{(1+\nu)(1-2\nu)\gamma_w} \left(\frac{\partial^2}{\partial x^2} + \frac{\partial^2}{\partial y^2} \right) p = -\frac{\partial}{\partial t} (\sigma'_{xx} + \sigma'_{yy}) \tag{2.3}$$

where E, ν are the elasticity constants of the isotropic medium, K is the permeability of the porous medium and γ_w is the unit weight of the pore

fluid. Note that (2.1), (2.2) and (2.3) are coupled equations that must be solved simultaneously.

However, in steady state conditions where no more changes occur with time $\partial/\partial t = 0$, hence (2.3) simplifies to the Laplace's equation

$$\left(\frac{\partial^2}{\partial x^2} + \frac{\partial^2}{\partial y^2} \right) p = 0 \quad (2.4a)$$

Also (2.2) takes the form

$$\left(\frac{\partial^2}{\partial x^2} + \frac{\partial^2}{\partial y^2} \right) (\sigma'_{xx} + \sigma'_{yy}) = 0 \quad (2.4b)$$

Since from (2.1)

$$\left(\frac{\partial^2}{\partial x^2} + \frac{\partial^2}{\partial y^2} \right) (\sigma_{xx} + \sigma_{yy}) = \left(\frac{\partial^2}{\partial x^2} + \frac{\partial^2}{\partial y^2} \right) (\sigma'_{xx} + \sigma'_{yy}) + 2 \left(\frac{\partial^2}{\partial x^2} + \frac{\partial^2}{\partial y^2} \right) p \quad (2.4c)$$

then (2.4b) is equivalent to

$$\left(\frac{\partial^2}{\partial x^2} + \frac{\partial^2}{\partial y^2} \right) (\sigma_{xx} + \sigma_{yy}) = 0 \quad (2.4d)$$

Thus, the problem may be formulated in terms of total stresses, instead of (2.4b) that is expressed in terms of effective stresses. The end result remains the same, namely that the partial differential eqs for stresses (either total or effective) and for the pore pressure are decoupled in long term.

In short term (t tends to zero or the phenomenon occurs over a period of time that is very short compared to the permeability of the medium) it is known from poroelasticity that the volumetric strain is zero (that is to say there is no change in volume)

$$\varepsilon_{vol} = \frac{(1-2\nu)(1+\nu)}{E} (\sigma'_{xx} + \sigma'_{yy}) = 0 \quad (2.5)$$

This essentially means that the effective hydrostatic stress is zero everywhere in the domain

$$\sigma'_{xx} + \sigma'_{yy} = 0 \quad \Leftrightarrow \quad \sigma'_{yy} = -\sigma'_{xx} \quad (2.6)$$

Thus, the effective stresses and pore pressure are related with total stresses through the formulae

$$\sigma'_{xx} = -\sigma'_{yy} = \frac{1}{2}(\sigma_{xx} - \sigma_{yy}) \quad (2.7a)$$

$$\sigma_{xx} + \sigma_{yy} = 2p \quad \Leftrightarrow \quad p = \frac{1}{2}(\sigma_{xx} + \sigma_{yy}) \quad (2.7b)$$

Hence by solving only the stress problem governed by pde (2.4d), the effective stresses and pore pressure are found from eqs (2.7a,b), respectively. This solution corresponds to the short term or *undrained conditions*.

For example based on the above arguments the state of affairs close to the crack tip in the short term will be as follows

$$\begin{aligned} \sigma_{xx} &= \frac{K_I}{\sqrt{2\pi r}} \cos \frac{\theta}{2} \left[1 - \sin \frac{\theta}{2} \sin \frac{3\theta}{2} \right] - \frac{K_{II}}{\sqrt{2\pi r}} \sin \frac{\theta}{2} \left[2 + \cos \frac{\theta}{2} \cos \frac{3\theta}{2} \right], \\ \sigma_{yy} &= \frac{K_I}{\sqrt{2\pi r}} \cos \frac{\theta}{2} \left[1 + \sin \frac{\theta}{2} \sin \frac{3\theta}{2} \right] + \frac{K_{II}}{\sqrt{2\pi r}} \cos \frac{\theta}{2} \sin \frac{\theta}{2} \cos \frac{3\theta}{2}, \\ \tau_{xy} &= \frac{K_I}{\sqrt{2\pi r}} \cos \frac{\theta}{2} \sin \theta \sin \frac{3\theta}{2} + \frac{K_{II}}{\sqrt{2\pi r}} \cos \frac{\theta}{2} \left[1 - \sin \frac{\theta}{2} \sin \frac{3\theta}{2} \right], \\ \sigma'_{xx} = -\sigma'_{yy} &= \frac{1}{2}(\sigma_{xx} - \sigma_{yy}) = -\frac{K_I}{\sqrt{2\pi r}} \cos \frac{\theta}{2} \sin \frac{\theta}{2} \sin \frac{3\theta}{2} - \frac{K_{II}}{\sqrt{2\pi r}} \sin \frac{\theta}{2} \left[1 + \cos \frac{\theta}{2} \cos \frac{3\theta}{2} \right], \\ p &= \frac{1}{2}(\sigma_{xx} + \sigma_{yy}) = \frac{K_I}{\sqrt{2\pi r}} \cos \frac{\theta}{2} - \frac{K_{II}}{\sqrt{2\pi r}} \sin \frac{\theta}{2} \end{aligned} \quad (2.8)$$

wherein K_I, K_{II} denote the stress intensity factors in mode-I and mode-II, respectively, and r, θ are the polar coordinates with their origin to be seated on the crack tip.

3 The First Fundamental Boundary Value Problem of the Cracked Body (Prescribed Normal and Tangential Stresses on Cracks)

The total stresses in an isotropic linear elastic solid transected by a system of cracks, holes and thin inclusions (e.g. Fig. 3.1) that obey the equilibrium and strain compatibility equations (2.4d), may be given as expressions of two complex potentials $\Phi_0(z), \Psi_0(z)$ of the complex coordinate $z = x + iy$ as follows (Muskhelishvili, 1953).

$$\begin{aligned} \sigma_x + \sigma_y &= 2[\Phi_0(z) + \overline{\Phi_0(z)}] = 4 \operatorname{Re}[\Phi_0(z)] \\ (\sigma_y - \sigma_x) + 2i\tau_{xy} &= 2[\overline{z}\Phi_0'(z) + \Psi_0(z)] \end{aligned} \quad (3.1)$$

where we have set

$$\begin{aligned} \Phi_0(z) &= \Gamma + \Phi(z) \\ \Psi_0(z) &= \Gamma' + \Psi(z) \end{aligned} \tag{3.2}$$

and

$$\begin{aligned} \Gamma &= \frac{1}{4}(N_1 + N_2) \\ \Gamma' &= \frac{1}{2}(N_1 - N_2)e^{-2i\alpha} \end{aligned} \tag{3.3}$$

N_1, N_2 are the principal stresses at infinity, α is the angle subtended between the vector of principal stress N_1 and the Ox axis (Fig. 3.1), and the bar over a symbol denotes complex conjugate.

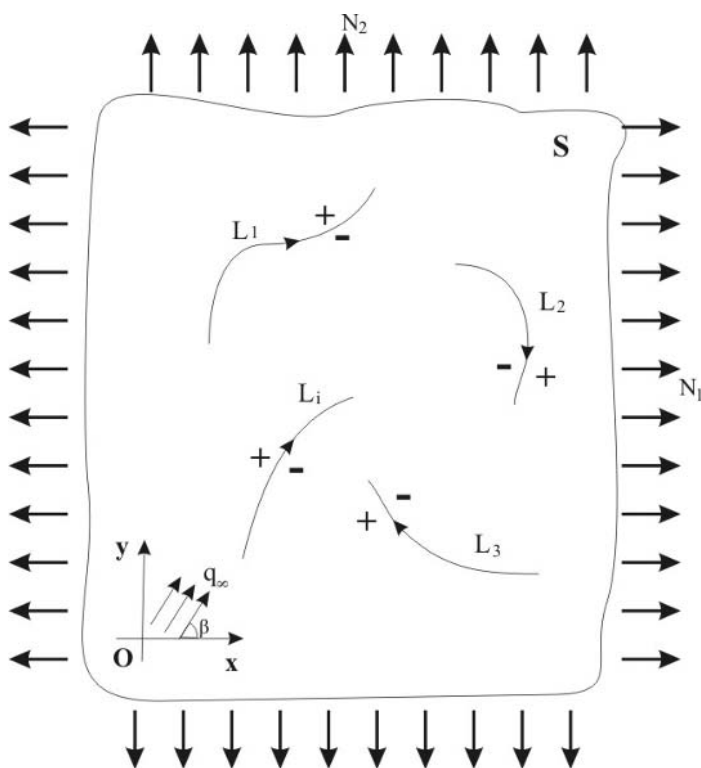


Fig. 3.1. A plane elastic body containing cracks L_i ($i = 1, k_1$) subjected to a homogeneous fluid flow q_∞ and to principal stresses N_1, N_2 at infinity

3.1 Formulation for a Single Crack

The first fundamental problem refers to the calculation of the two complex potentials subject to the following boundary conditions of prescribed tractions along the lips of the crack (Muskhelishvili, 1953) (Fig. 3.2).

$$\sigma_n^\pm - i\sigma_t^\pm = \Phi_0^\pm(t_0) + \overline{\Phi_0^\pm(t_0)} + \frac{dt_0}{dt_0} \left[\overline{t_0} \Phi_0^\pm(t_0) + \Psi_0^\pm(t_0) \right] \quad (3.4)$$

where $t_0 \in L$ and σ_n, σ_t are the total normal and the tangential stresses acting on the crack, respectively. By adding and subtracting by parts equations (3.4) the following system of equations is obtained.

$$\begin{aligned} & [\Phi^+(t_0) + \Phi^-(t_0)] + [\overline{\Phi^+(t_0)} + \overline{\Phi^-(t_0)}] + \frac{dt_0}{dt_0} \left\{ \overline{t_0} [\Phi^+(t_0) + \Phi^-(t_0)] + \right. \\ & \left. + [\Psi^+(t_0) + \Psi^-(t_0)] \right\} = 2\overline{p_1(t_0)} \end{aligned} \quad (3.5a)$$

and

$$\begin{aligned} & [\Phi^+(t_0) - \Phi^-(t_0)] + [\overline{\Phi^+(t_0)} - \overline{\Phi^-(t_0)}] + \frac{dt_0}{dt_0} \left\{ \overline{t_0} [\Phi^+(t_0) - \Phi^-(t_0)] + \right. \\ & \left. + [\Psi^+(t_0) - \Psi^-(t_0)] \right\} = 2\overline{q_1(t_0)} \end{aligned} \quad (3.5b)$$

where we have set

$$2p_1(t_0) = (\sigma_n^+ + \sigma_n^-) + i(\sigma_t^+ + \sigma_t^-) - 2(\Gamma + \overline{\Gamma}) - 2\overline{\Gamma} \frac{dt_0}{dt_0} \quad (3.6a)$$

and

$$2q_1(t_0) = (\sigma_n^+ - \sigma_n^-) + i(\sigma_t^+ - \sigma_t^-) \quad (3.6b)$$

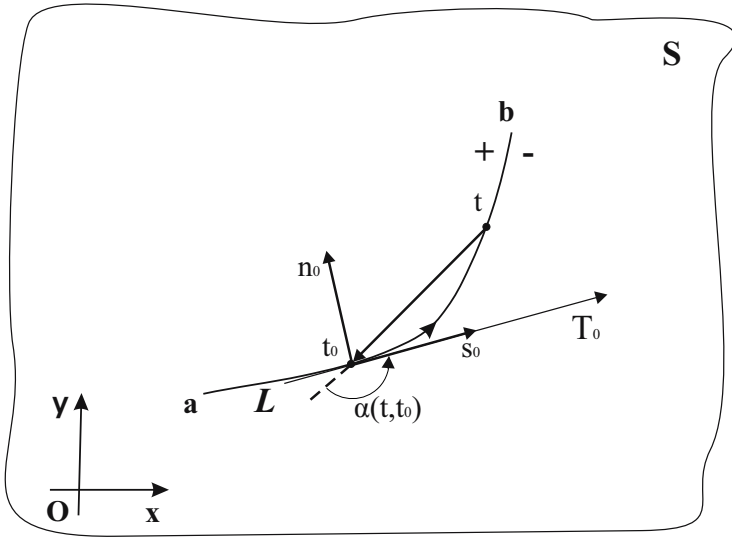


Fig.3.2. Single curvilinear crack L in the body S and global as well local systems of coordinates

We assume that the function $\Phi(z)$ is holomorphic in the entire plane except on the crack, thus it is partially holomorphic, and at the infinity its behavior as well as the behavior of $\Psi(z)$, is as follows

$$\Phi(z)\Big|_{z \rightarrow \infty} = O\left(\frac{1}{z}\right), \quad \Psi(z)\Big|_{z \rightarrow \infty} = O\left(\frac{1}{z}\right) \tag{3.7}$$

For this purpose, we assume that $\Phi(z)$ is given by a Cauchy integral:

$$\Phi(z) = \frac{1}{2\pi i} \int_L \frac{\varphi(t)}{t - z} dt \tag{3.8}$$

without having poles either at infinity or at any specific point of the plane (except of the tips of the crack) and the principal stresses at infinity do not affect $\Phi(z)$. We assume that the functions σ_n^\pm , σ_t^\pm and consequently the functions $p_1(t_0)$, $q_1(t_0)$ and the density $\varphi(t)$ satisfy the Hölder condition which is also assumed for the density function $\varphi(t)$.

The Plemelj's formulae due to (3.8) may be expressed as follows

$$\Phi^+(t_0) - \Phi^-(t_0) = \varphi(t_0) \tag{3.9a}$$

$$\Phi^+(t_0) + \Phi^-(t_0) = \frac{1}{\pi i} \int_L \frac{\varphi(t)}{t - t_0} dt \tag{3.9b}$$

Also, by taking the derivatives of (3.9a) and (3.9b) with respect to t_0 we get:

$$\Phi'^+(t_0) - \Phi'^-(t_0) = \varphi'(t_0) \tag{3.10a}$$

$$\Phi'^+(t_0) + \Phi'^-(t_0) = \frac{1}{\pi i} \int_L \frac{\varphi(t)}{(t - t_0)^2} dt \tag{3.10b}$$

By combining equations (3.8), (3.10) and (3.5b) we get:

$$\Psi^+(t_0) - \Psi^-(t_0) = \frac{dt_0}{dt_0} [2\overline{q_1(t_0)} - \varphi(t_0) - \overline{\varphi(t_0)}] - \overline{t_0} \varphi'(t_0) \tag{3.11}$$

From equation (3.11) it is derived that the function $\Psi(z)$, which is sectionally holomorphic on the entire plane except on the crack L and its behavior at the infinity is described by equation (3.7), can be expressed as a function of the density $\varphi(t_0)$ and $q_1(t_0)$, as follows

$$\Psi(z) = \frac{1}{\pi i} \int_L \frac{\overline{q_1(t)}}{t - z} \overline{dt} - \frac{1}{2\pi i} \int_L \frac{\overline{\varphi(t)}}{t - z} \overline{dt} - \frac{1}{2\pi i} \int_L \frac{\overline{t\varphi(t)}}{(t - z)^2} dt \tag{3.12}$$

By applying Plemelj's formula to (3.12), for the expression $\Psi^+(t_0) - \Psi^-(t_0)$ we get equation (3.11) while for the expression $\Psi^+(t_0) + \Psi^-(t_0)$ the following result is obtained

$$\Psi^+(t_0) + \Psi^-(t_0) = \frac{2}{\pi i} \int_L \frac{\overline{q_1(t)}}{t - t_0} \overline{dt} - \frac{1}{\pi i} \int_L \frac{\overline{\varphi(t)}}{t - t_0} \overline{dt} - \frac{1}{\pi i} \int_L \frac{\overline{t\varphi(t)}}{(t - t_0)^2} dt \tag{3.13}$$

By substituting the expressions (3.9b), (3.10b) and (3.13) into the boundary condition (3.5a) we get the following singular integral equation

$$\begin{aligned} & \frac{1}{\pi i} \int_L \frac{\varphi(t)}{t - t_0} dt - \frac{1}{\pi i} \int_L \frac{\overline{\varphi(t)}}{\overline{t - t_0}} \overline{dt} - \frac{dt_0}{dt_0} \left\{ \frac{1}{\pi i} \int_L \frac{\overline{\varphi(t)}}{t - t_0} \overline{dt} + \right. \\ & \left. + \frac{1}{\pi i} \int_L \varphi(t) \frac{\overline{t - t_0}}{(t - t_0)^2} dt \right\} = 2\overline{p_1(t_0)} - \frac{2}{\pi i} \frac{dt_0}{dt_0} \int_L \frac{\overline{q_1(t)}}{t - t_0} \overline{dt} \end{aligned} \tag{3.14}$$

The unknown function in equation (3.14) is the density function $\varphi(t)$. The determination of $\varphi(t)$ leads to the calculation of the potentials $\Phi(z)$

and $\Psi(z)$, hence to the solution of the problem. The determination of the density function $\varphi(t)$ in closed form is impossible except for some special very simple cases. However, the density can be calculated approximately by numerical integration that will be presented in a subsequent paragraph.

In the case the loading on the lips of the crack are equal and opposite, then equation (3.14) takes the form

$$\frac{1}{\pi i} \int \frac{\varphi(t)}{t-t_0} dt - \frac{1}{\pi i} \int \frac{\overline{\varphi(t)}}{t-t_0} dt - \frac{dt_0}{dt_0} \left\{ \frac{1}{\pi i} \int \frac{\overline{\varphi(t)}}{t-t_0} dt + \frac{1}{\pi i} \int \varphi(t) \frac{\overline{t-t_0}}{(t-t_0)^2} dt \right\} = 2\overline{p_1(t_0)} \tag{3.15}$$

Next, the complex singular integral equation (3.15) is further reduced into a system of two real singular integral equations by introducing two functions $h_1(s)$ and $h_2(s)$ with respect to the variable s which is the arc length of the crack as follows

$$h(s) = h_1(s) + ih_2(s) = \varphi(t) \frac{dt}{ds} = \varphi(t) e^{i\theta(t)} \tag{3.16}$$

where $\theta(t)$ is the angle enclosed by the tangent at the point t and the Ox -axis (measured counterclockwise). By solving (3.16) with respect to $\varphi(t)$ we get:

$$\varphi(t) = [h_1(s) + h_2(s)] e^{-i\theta(t)} \tag{3.17}$$

Substitution of (3.17) into (3.15) leads to the following form of the complex singular integral equation:

$$\frac{1}{\pi} \operatorname{Re} \int \frac{h_2(s) - ih_1(s)}{t(s) - t_0(\sigma)} ds + \frac{i}{\pi} e^{2i\theta(\sigma)} \int \frac{h_2(s) \operatorname{Im}[t(s) - t_0(\sigma)] + h_1(s) \operatorname{Re}[t(s) - t_0(\sigma)]}{[t(s) - t_0(\sigma)]^2} ds = \overline{p_1(\sigma)} \tag{3.18}$$

where $\theta(\sigma)$ is the angle subtended by the tangent at the point t_0 and the Ox -axis (measured counterclockwise), and s, σ are real arc length coordinates at t and t_0 respectively. In addition we set

$$\begin{aligned} t &= x(s) + iy(s) \\ t_0 &= x'(\sigma) + iy'(\sigma) \end{aligned} \tag{3.19}$$

and

$$p_1(\sigma) = p_{11}(\sigma) + ip_{12}(\sigma) \tag{3.20}$$

By taking into consideration the following relationship

$$e^{2i\theta(\sigma)} = \cos 2\theta(\sigma) + i \sin 2\theta(\sigma) \tag{3.21}$$

and substituting equations (3.19), (3.20) and (3.21) into (3.18) we derive the following system of real singular integral equations

$$\begin{aligned} & \frac{1}{\pi} \int_{\mathcal{L}} \frac{h_2(s)x_*(s) - h_1(s)y_*(s)}{x_*^2(s) + y_*^2(s)} ds - \\ & - \frac{1}{\pi} \int_{\mathcal{L}} \frac{h_2(s)y_*(s) + h_1(s)x_*(s)}{[x_*^2(s) + y_*^2(s)]^2} [x_*^2(s) - y_*^2(s)] \sin 2\theta(\sigma) ds + \\ & + \frac{1}{\pi} \int_{\mathcal{L}} \frac{h_2(s)y_*(s) + h_1(s)x_*(s)}{[x_*^2(s) + y_*^2(s)]^2} 2x_*(s)y_*(s) \cos 2\theta(\sigma) ds = p_{11}(\sigma) \end{aligned} \tag{3.22}$$

and

$$\begin{aligned} & \frac{1}{\pi} \int_{\mathcal{L}} \frac{h_2(s)y_*(s) + h_1(s)x_*(s)}{[x_*^2(s) + y_*^2(s)]^2} [x_*^2(s) - y_*^2(s)] \cos 2\theta(\sigma) ds + \\ & + \frac{1}{\pi} \int_{\mathcal{L}} \frac{h_2(s)y_*(s) + h_1(s)x_*(s)}{[x_*^2(s) + y_*^2(s)]^2} 2x_*(s)y_*(s) \sin 2\theta(\sigma) ds = -p_{12}(\sigma) \end{aligned} \tag{3.23}$$

wherein

$$\begin{aligned} x_*(s) &= x(s) - x'(\sigma) \\ y_*(s) &= y(s) - y'(\sigma) \end{aligned} \tag{3.24}$$

Additionally, the system of real singular equations (3.22) and (3.23) is subjected to the following condition which is derived from the condition of single-valuedness of displacements

$$\int_{\mathcal{L}} \varphi(t) dt = 0 \tag{3.25}$$

which is finally equivalent to the following set of real integral equations

$$\begin{aligned} \int_{\mathcal{L}} h_1(s) ds &= 0 \\ \int_{\mathcal{L}} h_2(s) ds &= 0 \end{aligned} \tag{3.26}$$

3.2 Formulation for a System of Non-Intersecting Cracks

In the case of a system of k non-intersecting cracks, it can be proven that at a point t_0 that belongs to a crack L_c the following system of real singular integral equations holds true:

$$\begin{aligned}
 & \frac{1}{\pi} \int_{L_c} \frac{h_{2c}(s)x_*(s) - h_{1c}(s)y_*(s)}{x_*^2(s) + y_*^2(s)} ds - \\
 & - \frac{1}{\pi} \int_{L_c} \frac{h_{2c}(s)y_*(s) + h_{1c}(s)x_*(s)}{[x_*^2(s) + y_*^2(s)]^2} [x_*^2(s) - y_*^2(s)] \sin 2\theta(\sigma) ds + \\
 & + \frac{1}{\pi} \int_{L_c} \frac{h_{2c}(s)y_*(s) + h_{1c}(s)x_*(s)}{[x_*^2(s) + y_*^2(s)]^2} 2x_*(s)y_*(s) \cos 2\theta(\sigma) ds + \\
 & + \sum_{\substack{i=1 \\ i \neq c}}^k \left\{ \frac{1}{\pi} \int_{L_i} \frac{h_{2i}(s)x_*(s) - h_{1i}(s)y_*(s)}{x_*^2(s) + y_*^2(s)} ds - \right. \\
 & - \frac{1}{\pi} \int_{L_i} \frac{h_{2i}(s)y_*(s) + h_{1i}(s)x_*(s)}{[x_*^2(s) + y_*^2(s)]^2} [x_*^2(s) - y_*^2(s)] \sin 2\theta(\sigma) ds + \\
 & \left. + \frac{1}{\pi} \int_{L_i} \frac{h_{2c}(s)y_*(s) + h_{1c}(s)x_*(s)}{[x_*^2(s) + y_*^2(s)]^2} 2x_*(s)y_*(s) \cos 2\theta(\sigma) ds \right\} = \\
 & = p_{1c}(\sigma), \quad c = 1, 2, \dots, k
 \end{aligned} \tag{3.27}$$

and

$$\begin{aligned}
 & \frac{1}{\pi} \int_{L_c} \frac{h_{2c}(s)y_*(s) + h_{2c}(s)x_*(s)}{[x_*^2(s) + y_*^2(s)]^2} [x_*^2(s) - y_*^2(s)] \cos 2\theta(\sigma) ds + \\
 & + \frac{1}{\pi} \int_{L_c} \frac{h_{2c}(s)y_*(s) + h_{1c}(s)x_*(s)}{[x_*^2(s) + y_*^2(s)]^2} 2x_*(s)y_*(s) \sin 2\theta(\sigma) ds + \\
 & + \sum_{\substack{i=1 \\ i \neq c}}^k \left\{ \frac{1}{\pi} \int_{L_i} \frac{h_{2i}(s)y_*(s) + h_{2i}(s)x_*(s)}{[x_*^2(s) + y_*^2(s)]^2} [x_*^2(s) - y_*^2(s)] \cos 2\theta(\sigma) ds + \right. \\
 & \left. + \frac{1}{\pi} \int_{L_i} \frac{h_{2i}(s)y_*(s) + h_{1i}(s)x_*(s)}{[x_*^2(s) + y_*^2(s)]^2} 2x_*(s)y_*(s) \sin 2\theta(\sigma) ds \right\} = \\
 & = -p_{2c}(\sigma), \quad c = 1, 2, \dots, k
 \end{aligned} \tag{3.28}$$

subject to the following conditions for single-valuedness of the displacements

$$\int_{\mathcal{L}} h_{1i}(s) ds = 0, \quad i = 1 \dots k$$

$$\int_{\mathcal{L}} h_{2i}(s) ds = 0, \quad i = 1 \dots k \tag{3.29}$$

3.3 Numerical Solution for a Single Crack

For the solution of equations (3.22) and (3.23) the *Gauss-Chebyshev* numerical integration scheme for singular integrals of Cauchy type proposed by Erdogan and Gupta (1972) is employed. The integration scheme is based on the methodology proposed for the fundamental Cauchy integral in the linear interval $[-1, 1]$

$$I = \int_{-1}^1 \frac{\varphi(t)}{t - z} dt \tag{3.30}$$

The decomposition of the density into a singular and a regular part is performed by setting $\varphi(t) = w(t) \cdot \hat{\varphi}(t)$, with $w(t)$ to be an appropriate weight function. Since the Cauchy integral refers to a derivative of a potential (derivative of displacements, hence stresses) the weight function that will be used is, as proposed, the following

$$w(t) = \frac{1}{\sqrt{1 - t^2}} \tag{3.31}$$

Thus, the integral (3.30) can be approximately calculated as follows

$$I = \int_{-1}^1 \frac{\varphi(t)}{t - t_0} dt = \int_{-1}^1 \frac{\hat{\varphi}(t)}{\sqrt{1 - t^2}(t - t_0)} dt \cong \frac{\pi}{n} \sum_{j=1}^n \frac{\hat{\varphi}(t_j)}{t_j - t_{0r}}, \quad r = 1, 2, \dots, n - 1 \tag{3.32}$$

where t_j are the roots of the Chebyshev polynomials of first type and order n

$$t_j = \cos \frac{(2j - 1)\pi}{2n}, \quad j = 1, 2, \dots, n \tag{3.33}$$

and t_{0r} are the roots of the Chebyshev polynomials of second type and order $n - 1$

$$t_{0r} = \cos \frac{j\pi}{n}, \quad r = 1, 2, \dots, n - 1 \tag{3.34}$$

We can apply this integration scheme also for the case of curvilinear cracks of arbitrary shape following the methodology by Liolios and Exadaktylos (2006).

By applying the above numerical integration scheme to equations (3.22) and (3.23) we derive the following linear system of equations for the calculation of the unknown densities $h_1(s)$ and $h_2(s)$

$$\begin{aligned} & \frac{1}{n} \sum_{j=1}^n h_1(s_j) \left[\frac{y(s_j) - y'(\sigma_r)}{[x(s_j) - x'(\sigma_r)]^2 + [y(s_j) - y'(\sigma_r)]^2} - \right. \\ & - \sin 2\theta(\sigma_r) \frac{[x(s_j) - x'(\sigma_r)][x(s_j) - x'(\sigma_r)]^2 - [y(s_j) - y'(\sigma_r)]^2}{[[x(s_j) - x'(\sigma_r)]^2 + [y(s_j) - y'(\sigma_r)]^2]^2} + \\ & \left. + \cos 2\theta(\sigma_r) \frac{2[x(s_j) - x'(\sigma_r)]^2 [y(s_j) - y'(\sigma_r)]}{[[x(s_j) - x'(\sigma_r)]^2 + [y(s_j) - y'(\sigma_r)]^2]^2} \right] + \\ & + \frac{1}{n} \sum_{j=1}^n h_2(s_j) \left[\frac{x(s_j) - x'(\sigma_r)}{[x(s_j) - x'(\sigma_r)]^2 + [y(s_j) - y'(\sigma_r)]^2} - \right. \\ & - \sin 2\theta(\sigma_r) \frac{[y(s_j) - y'(\sigma_r)][x(s_j) - x'(\sigma_r)]^2 - [y(s_j) - y'(\sigma_r)]^2}{[[x(s_j) - x'(\sigma_r)]^2 + [y(s_j) - y'(\sigma_r)]^2]^2} + \\ & \left. + \cos 2\theta(\sigma_r) \frac{2[x(s_j) - x'(\sigma_r)][y(s_j) - y'(\sigma_r)]^2}{[[x(s_j) - x'(\sigma_r)]^2 + [y(s_j) - y'(\sigma_r)]^2]^2} \right] = \\ & = p_{11}(\sigma_r), \quad r = 1, 2, \dots, n-1 \end{aligned} \tag{3.35}$$

and

$$\begin{aligned} & \frac{1}{n} \sum_{j=1}^n h_1(s_j) \left[\cos 2\theta(\sigma_r) \frac{[x(s_j) - x'(\sigma_r)][x(s_j) - x'(\sigma_r)]^2 - [y(s_j) - y'(\sigma_r)]^2}{[[x(s_j) - x'(\sigma_r)]^2 + [y(s_j) - y'(\sigma_r)]^2]^2} + \right. \\ & \left. + \sin 2\theta(\sigma_r) \frac{2[x(s_j) - x'(\sigma_r)]^2 [y(s_j) - y'(\sigma_r)]}{[[x(s_j) - x'(\sigma_r)]^2 + [y(s_j) - y'(\sigma_r)]^2]^2} \right] + \\ & + \frac{1}{n} \sum_{j=1}^n h_2(s_j) \left[\cos 2\theta(\sigma_r) \frac{[y(s_j) - y'(\sigma_r)][x(s_j) - x'(\sigma_r)]^2 - [y(s_j) - y'(\sigma_r)]^2}{[[x(s_j) - x'(\sigma_r)]^2 + [y(s_j) - y'(\sigma_r)]^2]^2} + \right. \\ & \left. + \sin 2\theta(\sigma_r) \frac{2[x(s_j) - x'(\sigma_r)][y(s_j) - y'(\sigma_r)]^2}{[[x(s_j) - x'(\sigma_r)]^2 + [y(s_j) - y'(\sigma_r)]^2]^2} \right] = \\ & = -p_{12}(\sigma_r), \quad r = 1, 2, \dots, n-1 \end{aligned} \tag{3.36}$$

The above system (3.35), (3.36) represents a system of $2(n-1)$ linear algebraic equations with $2n$ unknowns. The additional two equations required for the solution of the system is derived from equations (3.26) as follows

$$\begin{aligned}\sum_{j=1}^n h_1(s_j) &= 0 \\ \sum_{j=1}^n h_2(s_j) &= 0\end{aligned}\tag{3.37}$$

After the calculation of the densities $h_1(s)$ and $h_2(s)$ from the above algorithm, the calculation of the stresses at any point of the plane can be found by calculating the complex potentials $\Phi(z)$ and $\Psi(z)$ from the expressions (3.8) and (3.12), respectively, by virtue of an analogous numerical integration scheme that was described above. The stresses are then calculated from the set of equations (3.1).

3.4 Numerical Solution for a System of Non-Intersecting Cracks

Following a similar methodology as before, we derive the system of linear equations for a system of k non-intersecting cracks of arbitrary shape by applying numerical integration to equations (3.27), (3.28) and (3.29)

$$\begin{aligned}
 & \frac{1}{n} \sum_{j=1}^n h_{1c}(s_{jc}) \left[\frac{y(s_{jc}) - y'(\sigma_{rc})}{[x(s_{jc}) - x'(\sigma_{rc})]^2 + [y(s_{jc}) - y'(\sigma_{rc})]^2} - \right. \\
 & - \sin 2\theta(\sigma_{rc}) \frac{[x(s_{jc}) - x'(\sigma_{rc})][x(s_{jc}) - x'(\sigma_{rc})]^2 - [y(s_{jc}) - y'(\sigma_{rc})]^2}{[[x(s_{jc}) - x'(\sigma_{rc})]^2 + [y(s_{jc}) - y'(\sigma_{rc})]^2]^2} + \\
 & \left. + \cos 2\theta(\sigma_{rc}) \frac{2[x(s_{jc}) - x'(\sigma_{rc})]^2 [y(s_{jc}) - y'(\sigma_{rc})]}{[[x(s_{jc}) - x'(\sigma_{rc})]^2 + [y(s_{jc}) - y'(\sigma_{rc})]^2]^2} \right] + \\
 & + \frac{1}{n} \sum_{j=1}^n h_{2c}(s_{jc}) \left[\frac{x(s_{jc}) - x'(\sigma_{rc})}{[x(s_{jc}) - x'(\sigma_{rc})]^2 + [y(s_{jc}) - y'(\sigma_{rc})]^2} - \right. \\
 & - \sin 2\theta(\sigma_{rc}) \frac{[y(s_{jc}) - y'(\sigma_{rc})][x(s_{jc}) - x'(\sigma_{rc})]^2 - [y(s_{jc}) - y'(\sigma_{rc})]^2}{[[x(s_{jc}) - x'(\sigma_{rc})]^2 + [y(s_{jc}) - y'(\sigma_{rc})]^2]^2} + \\
 & \left. + \cos 2\theta(\sigma_{rc}) \frac{2[x(s_{jc}) - x'(\sigma_{rc})][y(s_{jc}) - y'(\sigma_{rc})]^2}{[[x(s_{jc}) - x'(\sigma_{rc})]^2 + [y(s_{jc}) - y'(\sigma_{rc})]^2]^2} \right] + \\
 & + \sum_{\substack{i=1 \\ i \neq c}}^k \left\{ \frac{1}{n} \sum_{j=1}^n h_{1i}(s_{ji}) \left[\frac{y(s_{ji}) - y'(\sigma_{rc})}{[x(s_{ji}) - x'(\sigma_{rc})]^2 + [y(s_{ji}) - y'(\sigma_{rc})]^2} - \right. \right. \\
 & - \sin 2\theta(\sigma_{rc}) \frac{[x(s_{ji}) - x'(\sigma_{rc})][x(s_{ji}) - x'(\sigma_{rc})]^2 - [y(s_{ji}) - y'(\sigma_{rc})]^2}{[[x(s_{ji}) - x'(\sigma_{rc})]^2 + [y(s_{ji}) - y'(\sigma_{rc})]^2]^2} + \\
 & \left. + \cos 2\theta(\sigma_{rc}) \frac{2[x(s_{ji}) - x'(\sigma_{rc})]^2 [y(s_{ji}) - y'(\sigma_{rc})]}{[[x(s_{ji}) - x'(\sigma_{rc})]^2 + [y(s_{ji}) - y'(\sigma_{rc})]^2]^2} \right] + \\
 & + \frac{1}{n} \sum_{j=1}^n h_{2i}(s_{ji}) \left[\frac{x(s_{ji}) - x'(\sigma_{rc})}{[x(s_{ji}) - x'(\sigma_{rc})]^2 + [y(s_{ji}) - y'(\sigma_{rc})]^2} - \right. \\
 & - \sin 2\theta(\sigma_{rc}) \frac{[y(s_{ji}) - y'(\sigma_{rc})][x(s_{ji}) - x'(\sigma_{rc})]^2 - [y(s_{ji}) - y'(\sigma_{rc})]^2}{[[x(s_{ji}) - x'(\sigma_{rc})]^2 + [y(s_{ji}) - y'(\sigma_{rc})]^2]^2} + \\
 & \left. + \cos 2\theta(\sigma_{rc}) \frac{2[x(s_{ji}) - x'(\sigma_{rc})][y(s_{ji}) - y'(\sigma_{rc})]^2}{[[x(s_{ji}) - x'(\sigma_{rc})]^2 + [y(s_{ji}) - y'(\sigma_{rc})]^2]^2} \right] \Big\} = \\
 & = p_1(\sigma_{rc}), \quad r = 1, 2, \dots, n-1 \quad c = 1, 2, \dots, k
 \end{aligned} \tag{3.38}$$

$$\begin{aligned}
 & \frac{1}{n} \sum_{j=1}^n h_{1c}(s_{jc}) \left[\cos 2\theta(\sigma_{rc}) \frac{[x(s_{jc}) - x'(\sigma_{rc})][x(s_{jc}) - x'(\sigma_{rc})]^2 - [y(s_{jc}) - y'(\sigma_{rc})]^2}{[[x(s_{jc}) - x'(\sigma_{rc})]^2 + [y(s_{jc}) - y'(\sigma_{rc})]^2]^2} + \right. \\
 & \left. + \sin 2\theta(\sigma_{rc}) \frac{2[x(s_{jc}) - x'(\sigma_{rc})]^2 [y(s_{jc}) - y'(\sigma_{rc})]}{[[x(s_{jc}) - x'(\sigma_{rc})]^2 + [y(s_{jc}) - y'(\sigma_{rc})]^2]^2} \right] + \\
 & + \frac{1}{n} \sum_{j=1}^n h_{2c}(s_{jc}) \left[\cos 2\theta(\sigma_{rc}) \frac{[y(s_{jc}) - y'(\sigma_{rc})][x(s_{jc}) - x'(\sigma_{rc})]^2 - [y(s_{jc}) - y'(\sigma_{rc})]^2}{[[x(s_{jc}) - x'(\sigma_{rc})]^2 + [y(s_{jc}) - y'(\sigma_{rc})]^2]^2} + \right. \\
 & \left. + \sin 2\theta(\sigma_{rc}) \frac{2[x(s_{jc}) - x'(\sigma_{rc})][y(s_{jc}) - y'(\sigma_{rc})]^2}{[[x(s_{jc}) - x'(\sigma_{rc})]^2 + [y(s_{jc}) - y'(\sigma_{rc})]^2]^2} \right] + \\
 & + \sum_{\substack{i=1 \\ i \neq c}}^k \left\{ \frac{1}{n} \sum_{j=1}^n h_{1i}(s_{ji}) \left[\cos 2\theta(\sigma_{rc}) \frac{[x(s_{ji}) - x'(\sigma_{rc})][x(s_{ji}) - x'(\sigma_{rc})]^2 - [y(s_{ji}) - y'(\sigma_{rc})]^2}{[[x(s_{ji}) - x'(\sigma_{rc})]^2 + [y(s_{ji}) - y'(\sigma_{rc})]^2]^2} + \right. \tag{3.39} \\
 & \left. + \sin 2\theta(\sigma_{rc}) \frac{2[x(s_{ji}) - x'(\sigma_{rc})]^2 [y(s_{ji}) - y'(\sigma_{rc})]}{[[x(s_{ji}) - x'(\sigma_{rc})]^2 + [y(s_{ji}) - y'(\sigma_{rc})]^2]^2} \right] + \\
 & + \frac{1}{n} \sum_{j=1}^n h_{2i}(s_{ji}) \left[\cos 2\theta(\sigma_{rc}) \frac{[y(s_{ji}) - y'(\sigma_{rc})][x(s_{ji}) - x'(\sigma_{rc})]^2 - [y(s_{ji}) - y'(\sigma_{rc})]^2}{[[x(s_{ji}) - x'(\sigma_{rc})]^2 + [y(s_{ji}) - y'(\sigma_{rc})]^2]^2} + \right. \\
 & \left. + \sin 2\theta(\sigma_{rc}) \frac{2[x(s_{ji}) - x'(\sigma_{rc})][y(s_{ji}) - y'(\sigma_{rc})]^2}{[[x(s_{ji}) - x'(\sigma_{rc})]^2 + [y(s_{ji}) - y'(\sigma_{rc})]^2]^2} \right] \Big\} = \\
 & = -p_2(\sigma_{rc}), \quad r = 1, 2, \dots, n-1 \quad c = 1, 2, \dots, k
 \end{aligned}$$

and finally the additional equations

$$\begin{aligned}
 \sum_{j=1}^n h_{1i}(s_{ji}) &= 0, \quad i = 1, 2, \dots, k \\
 \sum_{j=1}^n h_{2i}(s_{ji}) &= 0, \quad i = 1, 2, \dots, k
 \end{aligned} \tag{3.40}$$

4 Solution of the Pore Pressure

The solution of the field equation (2.4a) for multiple cracks of arbitrary shape subjected to Dirichlet and Neumann, as well as to mixed boundary conditions has been presented in detail in (Liolios and Exadaktylos, 2006). In this work the solution for the pore pressure that satisfies (2.4a) was set as follows

$$p(z) = 2 \operatorname{Re}(F(z)) \tag{4.1}$$

where $F(z)$ is an analytic function of the complex variable z . Further, the fluid mass flow or specific discharge vector $q[L/T]$ is given by Darcy’s law as follows

$$q(z) = -K \left(\frac{\partial}{\partial x} p(z) + i \frac{\partial}{\partial y} p(z) \right) \tag{4.2}$$

The unknown function F was set in the form of a Cauchy integral

$$F(t_0) = \frac{1}{\pi} \int_L \frac{f(t) dt}{|t - t_0|} \tag{4.3}$$

Subsequently, by taking into consideration the nature of the pore pressure solution this integral was decomposed as follows

$$F(t_0) = \frac{1}{2\pi} \int_L \sqrt{(1-t^2)} \frac{\hat{f}(t)}{|t - t_0|} dt \tag{4.4}$$

The integration rule also followed for the stresses was adopted

$$I = \int_{-1}^1 \frac{f(t)}{|t - t_0|} dt = \int_{-1}^1 \sqrt{1-t^2} \frac{\hat{f}(t)}{|t - t_0|} dt \cong \sum_{j=1}^n w_j(t) \frac{\hat{f}(t)}{|t_j - t_{0r}|}, \quad r = 1, 2, \dots, n+1 \tag{4.5}$$

where

$$w_j(t) = \frac{\pi}{n+1} \sin^2 \left(\frac{j\pi}{n+1} \right) \tag{4.6}$$

The integration points are given by

$$t_j = \cos \frac{j\pi}{n+1}, \quad j = 1, 2, \dots, n \tag{4.7}$$

and the collocation points also given by the relations

$$t_{0r} = \cos \frac{\pi(2r-1)}{2(n+1)}, \quad r = 1, 2, \dots, n+1 \tag{4.8}$$

Based on the above integration scheme the system of complex singular integral equations along the curvilinear cracks subjected to Dirichlet or Neumann boundary conditions is transformed into a linear algebraic system of equations with unknowns the densities of the Cauchy integrals $\hat{f}_i(t)$, $i = 1, \dots, k_1$ along the lips of the cracks.

5 Numerical Examples

In the following, some numerical exercises by virtue of the proposed method are demonstrated.

5.1 Example 1: Single Linear Crack on Ox Axis

For the validation of the Gauss Chebyshev scheme presented above we consider the problem of a single straight crack that occupies the interval $[-1, 1]$ on Ox -axis. The crack is under uniform dimensionless pore pressure $p(s) = -1$ (thereafter compressive stresses are taken as negative quantities), where s is a real variable along the length of the crack. Hence, the dimensionless normal stress that acts on the lips of the crack is $\sigma_n(s) = -1$ and the medium is free of far field stresses. Further, the dimensionless permeability coefficient $K = 1$ and we assume that steady-state conditions have reached. For the numerical solution of the pore diffusion equation and stress equations (3.35)-(3.37) we have used 30 integration points.

If we neglect the pore pressure for a moment, then the problem (straight crack under normal loading) has a closed form solution regarding the normal stresses in Oy -direction. The solution is given by Muskhelishvili as follows

$$\sigma_n = \frac{z}{\sqrt{z^2 - 1}} - 1 \quad (5.1)$$

Fig. 5.1 shows the perfect agreement of the closed form solution (5.1) with the Gauss – Chebyshev numerical integration scheme. Fig's 5.2 – 5.9 illustrate respectively the pore pressure distribution, the fluid flow distribution along Ox and Oy directions, the total stress distributions on

the plane σ_x , σ_y and τ_{xy} , and finally the effective stresses distributions σ'_x and σ'_y .

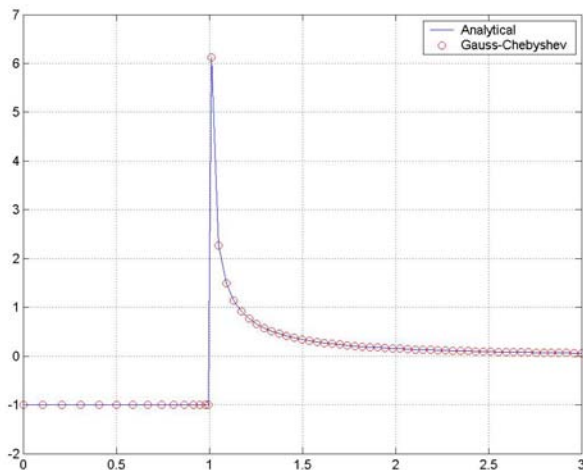


Fig. 5.1. Comparison between analytical and numerical solutions referring to the distribution of σ_y along Ox-axis

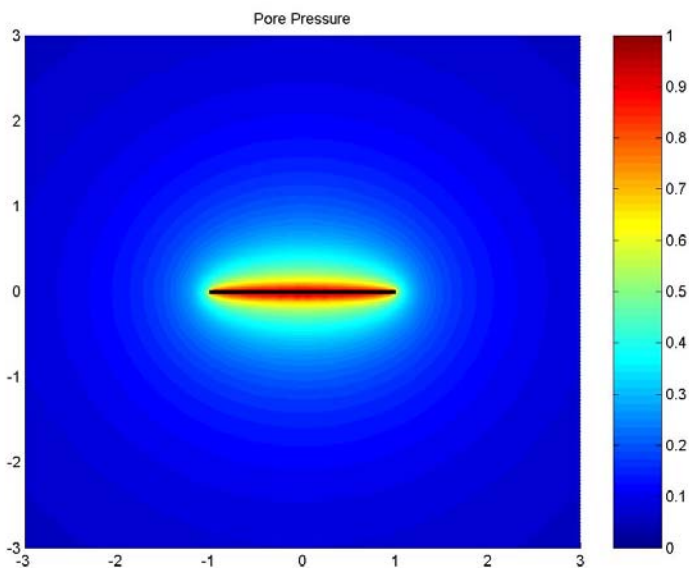
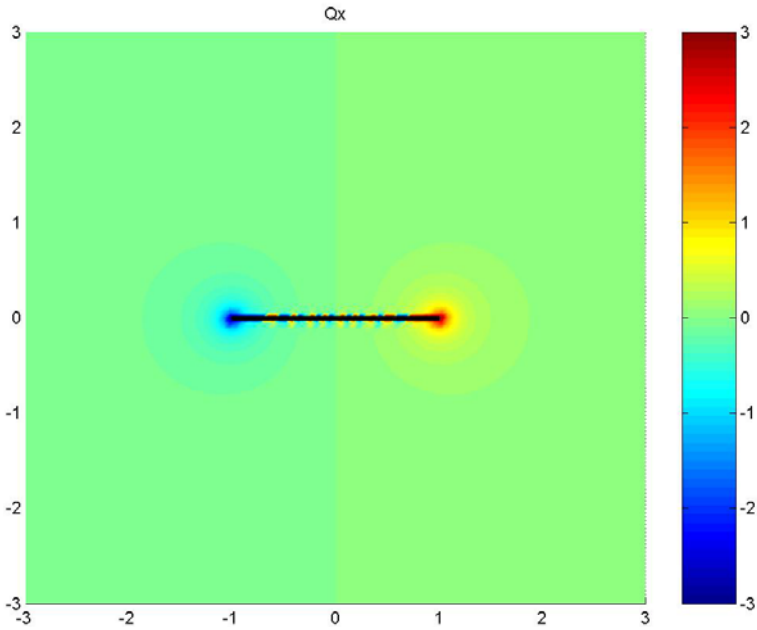
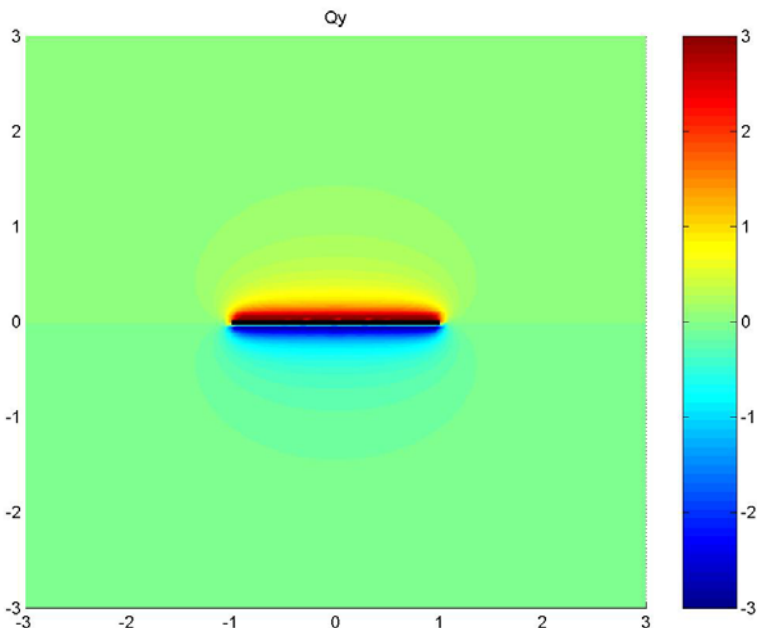


Fig. 5.2. Absolute pore pressure distribution on the plane

Fig. 5.3. Fluid flow towards $O x$ directionFig. 5.4. Fluid flow towards $O y$ direction

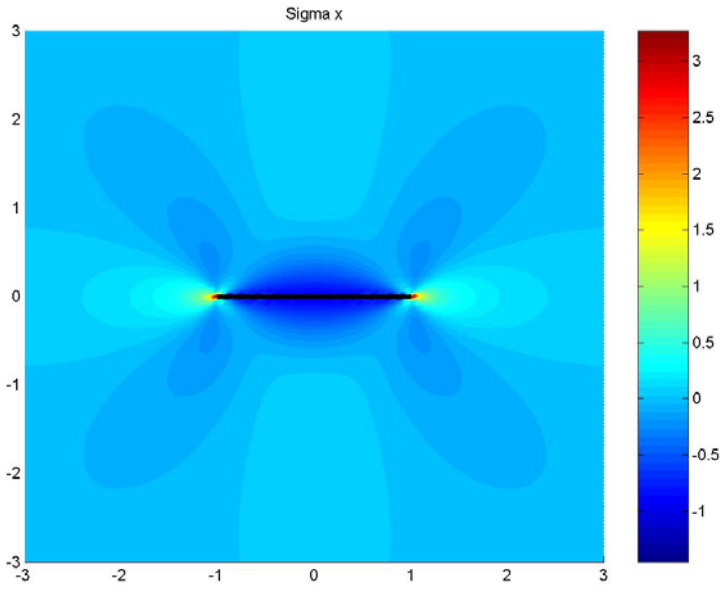


Fig. 5.5. Distribution of total stress σ_x

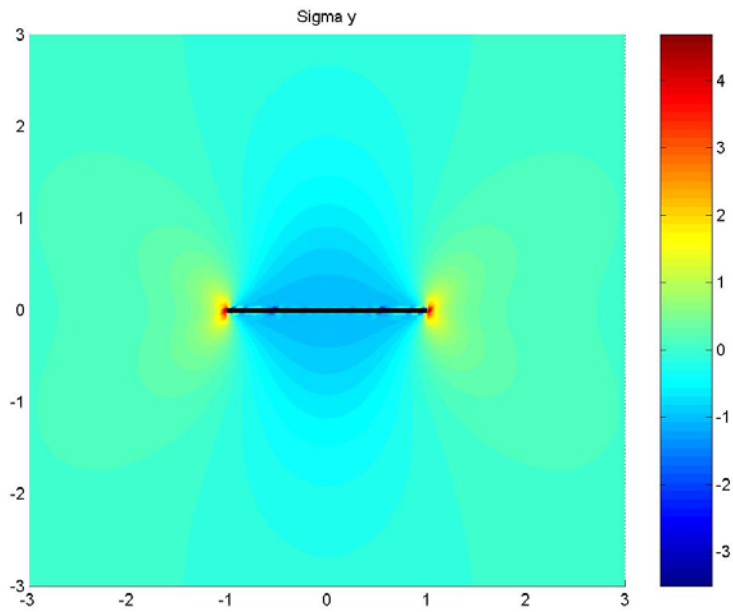


Fig. 5.6. Distribution of total stress σ_y

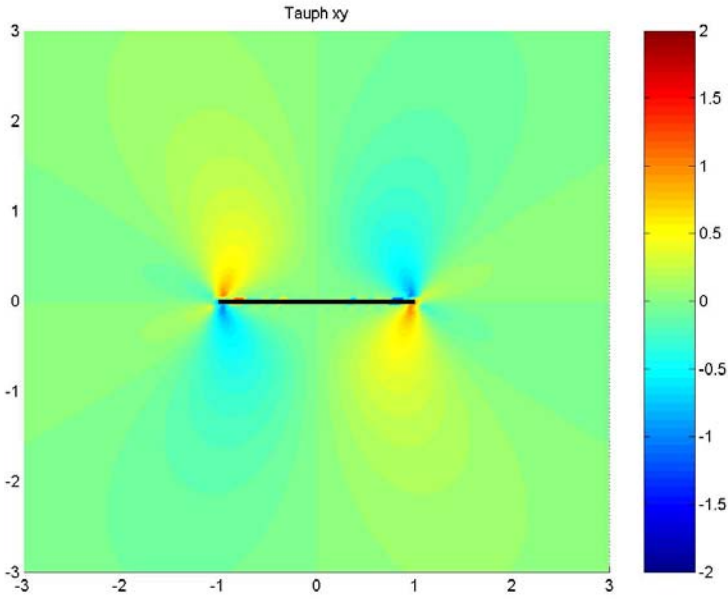


Fig. 5.7. Distribution of shear stresses τ_{xy}

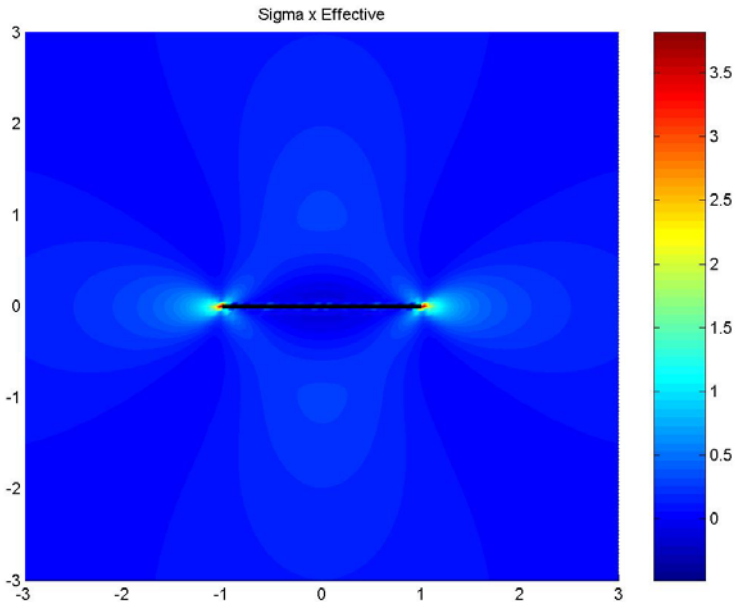


Fig. 5.8. Distribution of effective stress σ_x

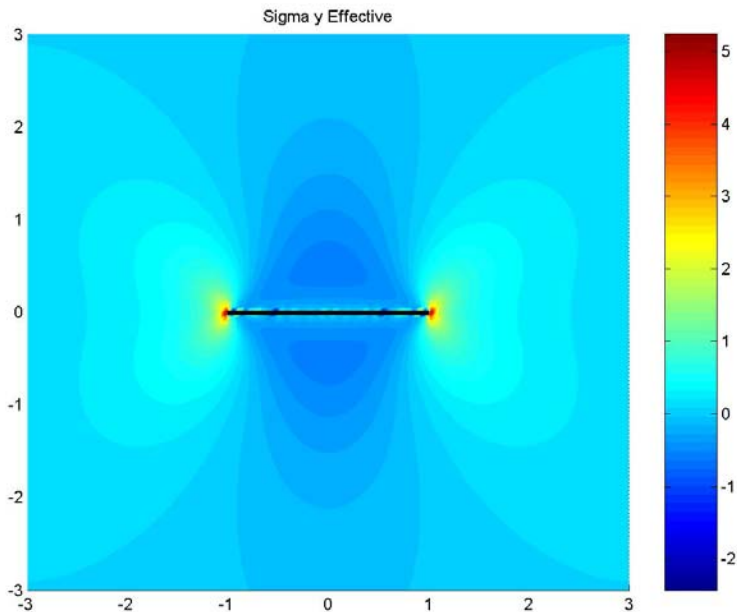


Fig. 5.9. Distribution of effective stress σ_y

5.2 Example 2: System of Three Parallel Cracks

Assume that we have a system of three (3) linear cracks as shown in Fig. 5.10. In all the cracks a uniform pore pressure equal to 1 (which means normal loading equal to -1) is specified. Also, the system is under far field N_2 stress (along Oy-axis) equal to 1 (tensile). The steady state solution of this problem is presented in Fig's 5.10 – 5.15.

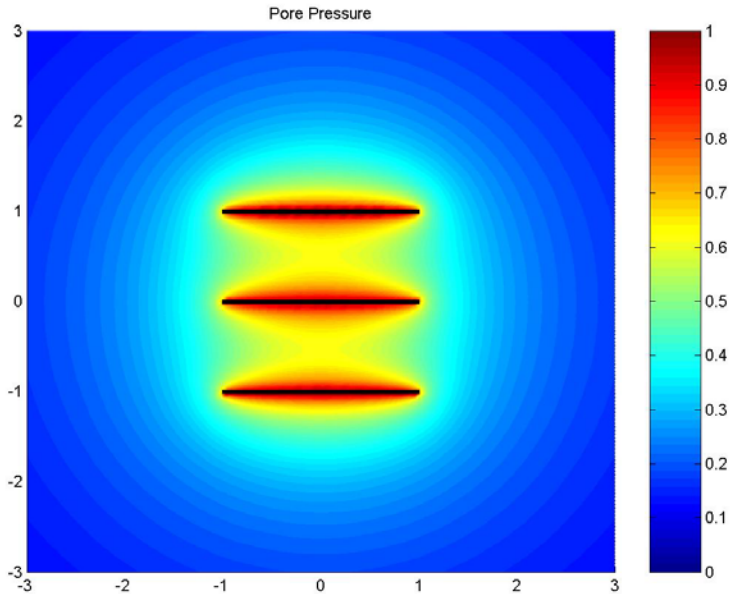
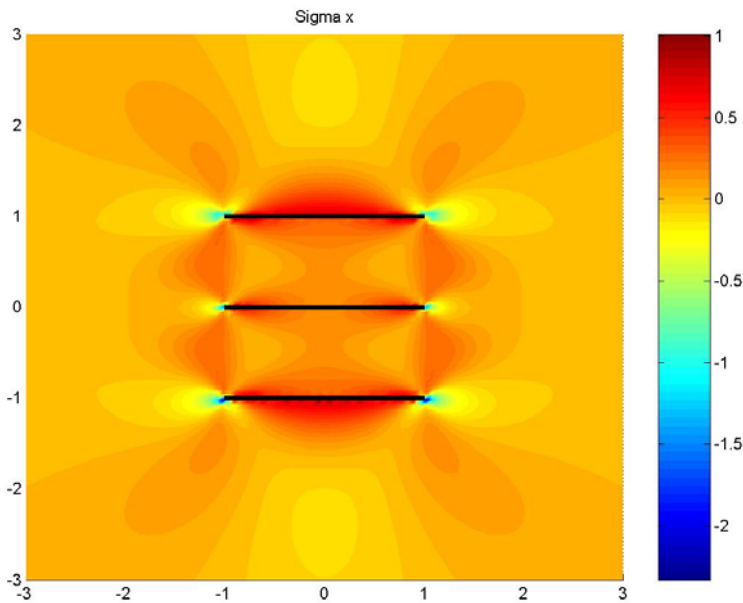


Fig. 5.10. Absolute pore pressure distribution

Fig. 5.11. Distribution of total stress σ_x

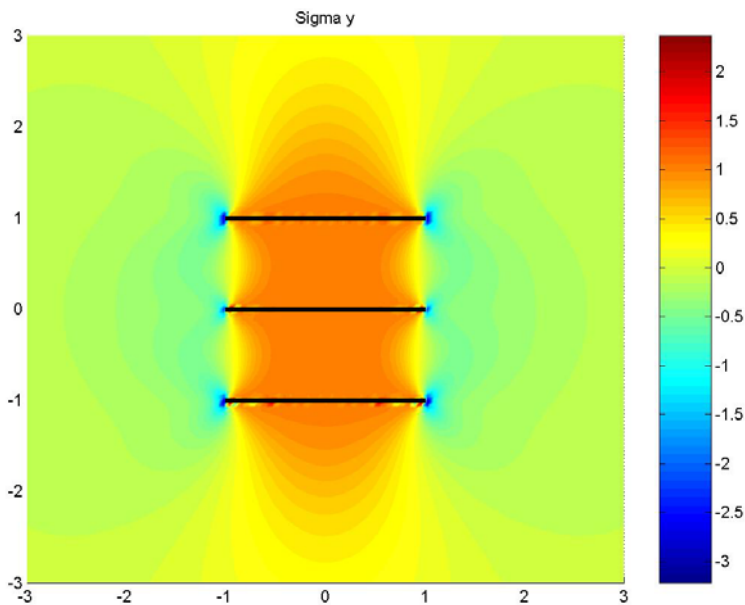


Fig. 5.12. Distribution of total stress σ_y

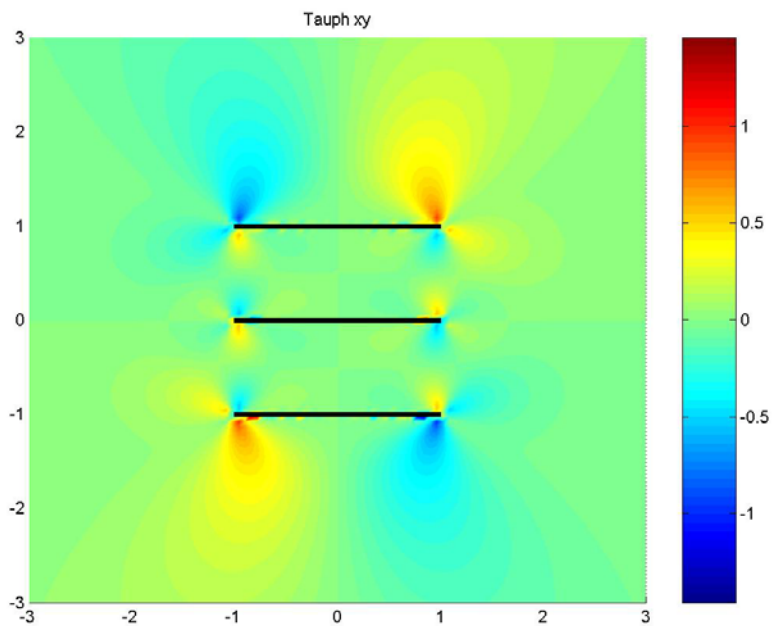


Fig. 5.13. Distribution of shear stresses τ_{xy}

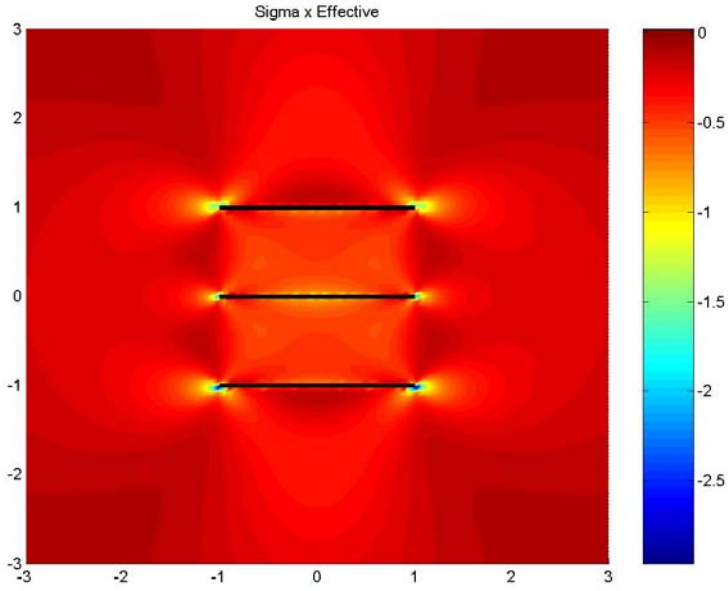


Fig. 5.14. Distribution of effective stress σ'_x

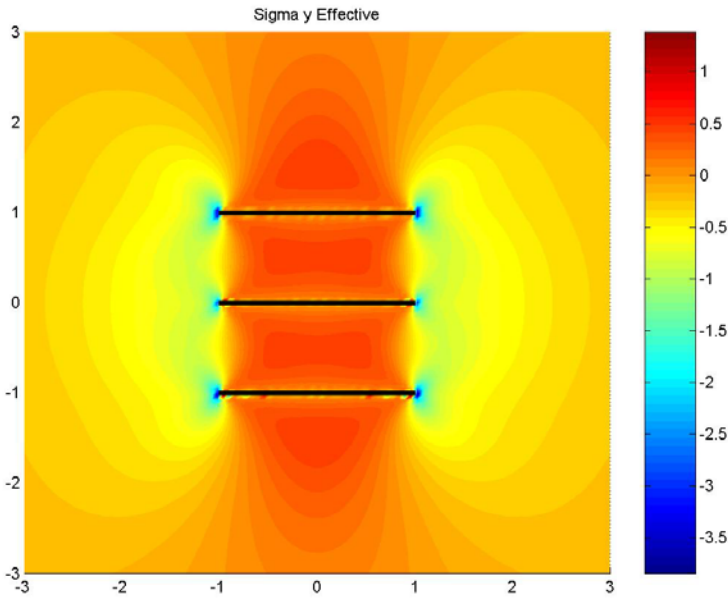


Fig. 5.15. Distribution of effective stress σ'_y

5.3 Example 3: Multiple (40) Cracks Ahead of a Horizontal Crack under Uniform Pore Pressure (Steady State)

Assume that we have a main crack along which a uniform pore pressure equal to 1 (which means normal loading equal to -1) is applied with its left tip surrounded by a swarm of microcracks with pore pressure zero. The steady-state solution of this problem for the pore pressure diffusion and stresses is presented in Fig's 5.16 – 5.21.

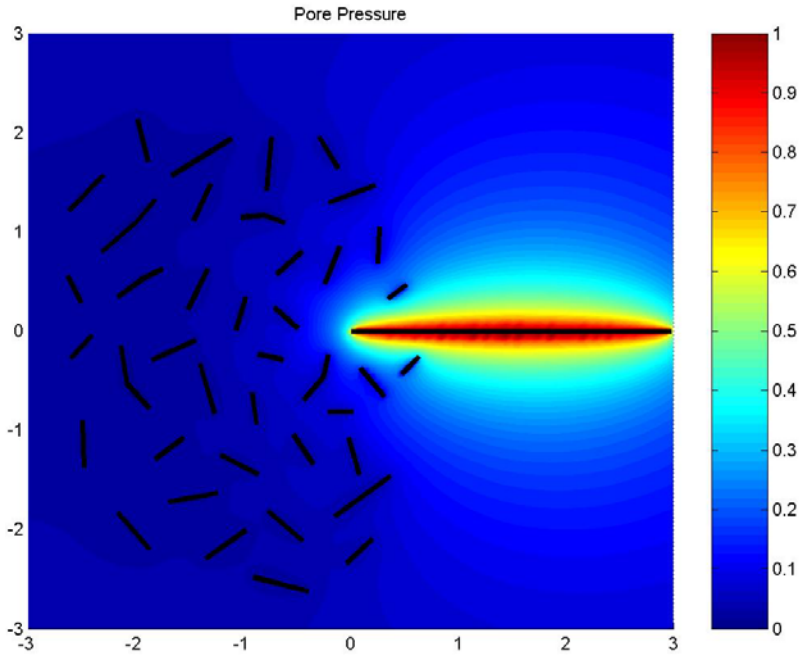
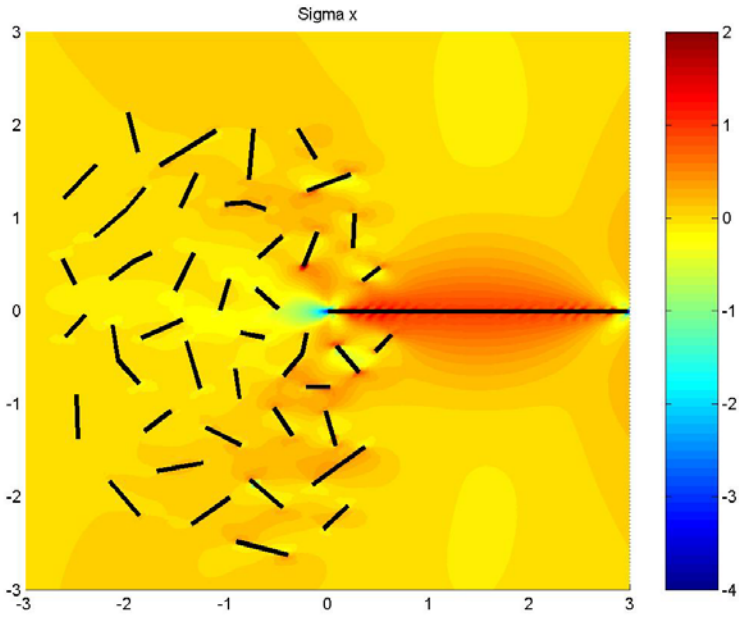
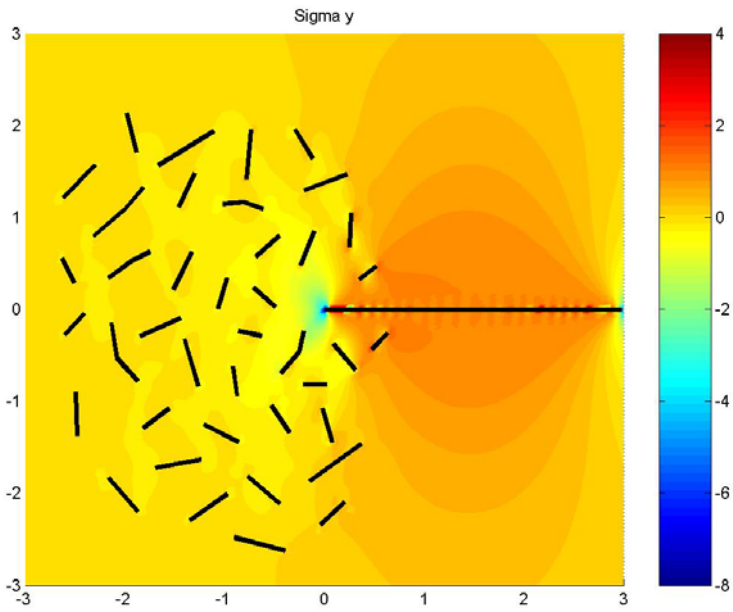


Fig. 5.16. Pore pressure distribution

Fig. 5.17. Distribution of total stress σ_x Fig. 5.18. Distribution of total stress σ_y

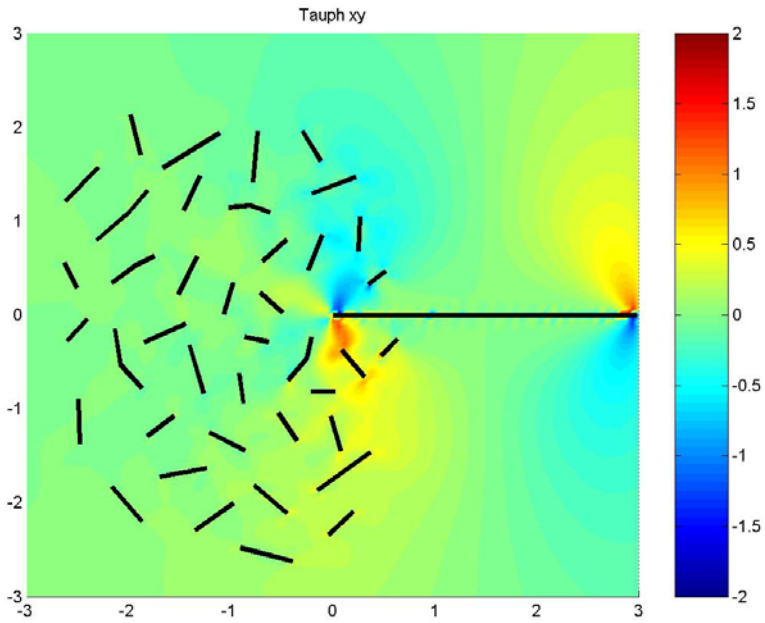


Fig. 5.19. Distribution of shear stresses τ_{xy}

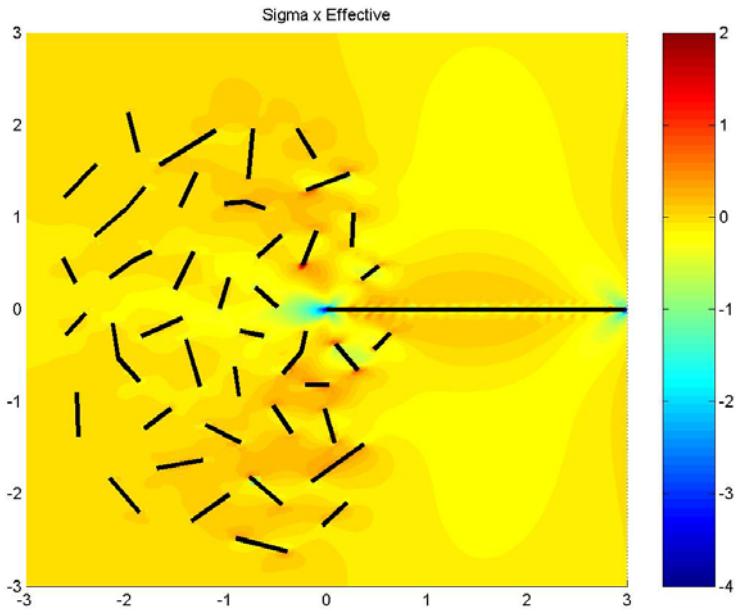


Fig. 5.20. Distribution of effective stress σ_x

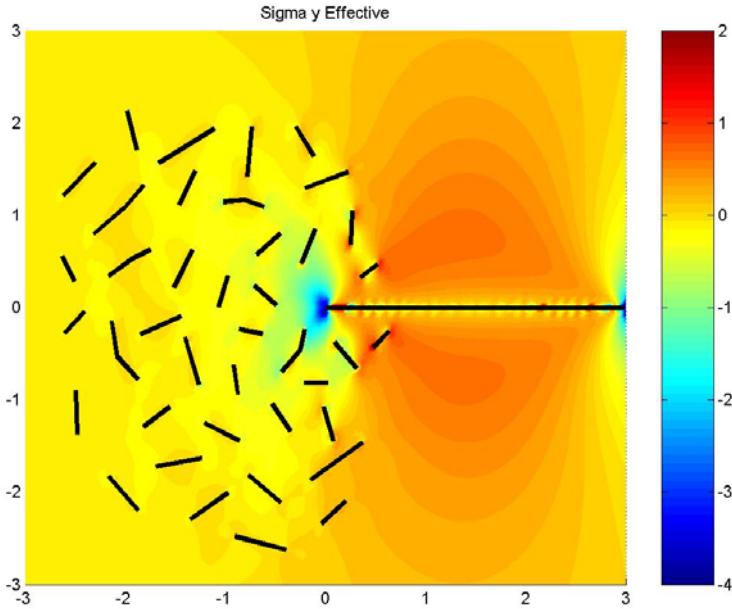


Fig. 5.21. Distribution of effective stress σ_y

References

1. Liolios, P. and Exadaktylos, G. (2006), A solution of steady-state fluid flow in multiply fractured isotropic porous media, *Int. J. Solids Structures*, 43, 3960–3982
2. Muskhelishvili, N.I., 1953. *Singular Integral Equations*. P. Noordhoff Ltd., Groningen, Holland.
3. Erdogan, F., Gupta, G.D., 1972. On the numerical solution of singular integral equations. *Quart. Appl. Math.* 30, 525–534.
4. Dyskin, A.V. and Pasternak, E. A mechanism of fracture development in rocks and the Earth's crust, this volume.
5. Pichler, B., Hellmich, Ch. and Dormieux, L. Potentials and limitations of Griffith's energy release rate criterion for mode I type microcracking in brittle materials, this volume.

Index

- Agioutantis, 429
Andresen, 357
anisotropy, 85, 125
associated flow rule, 21, 321
axisymmetric compression, 33
band formation, 7, 18, 19, 20, 26,
32, 34, 37, 38, 43, 44, 45, 46,
48, 49, 170, 198, 292, 299
barotropy, 175, 298
Bauer, 196, 278, 279, 285, 287,
294, 295, 296, 297, 298
Baxevanis, 171
bending, 330
Bésuelle, 142
biaxial, 6, 12, 71, 73, 74, 140,
199, 204, 209, 224, 225, 226,
229, 342
bifurcation, 9, 10, 11, 17, 19, 20,
26, 50, 54, 58, 69, 70, 95, 97,
105, 118, 130, 135, 142, 278,
279, 292, 293, 294, 295, 296,
297, 298, 356
bifurcation, 3, 10, 11, 12, 55, 70,
103, 124, 171, 199, 297, 298
Bilbie, 231
Bingham fluid, 383, 400
Bingham model, 384, 385, 386
Bobiński, 319
Bolton, 82, 93, 155, 159, 168,
171
borehole, 49, 53, 54, 55, 56, 69,
70, 157, 317
brazilian disc, 403, 405, 406, 408
brittle materials, 245, 246, 262,
263, 273, 275, 276, 339, 340,
404, 428, 461
buckling, 6, 7, 53, 55, 56, 57, 58,
59, 69, 72, 79, 80, 152, 225,
246, 268, 273
Caillerie, 11, 142, 197, 231
cataclastic flow, 39, 50, 51, 95,
96, 97, 99, 101, 112, 118, 121,
123, 124
Cauchy, 148, 177, 180, 213, 214,
280, 284, 367, 431, 438, 443,
448, 449
Challa, 30, 33, 35, 45, 49, 50
Chambon, 11, 12, 142, 197, 199,
231, 297, 298
chemo-thermo-mechanical, 361,
362, 379
clays, 94, 198, 341, 347, 348,
352, 356, 357
cohesion, 3, 107, 241, 382, 386,
395
Collin, 142
compaction, 17, 34, 36, 37, 38,
39, 41, 42, 48, 50, 96, 124,
125, 126, 155, 156, 163, 171
compaction bands, 42, 96
concrete, 50, 106, 127, 128, 130,
133, 138, 139, 140, 141, 142,
275, 276, 317, 319, 320, 324,
325, 326, 327, 328, 330, 331,
337, 338, 339, 340, 404, 429
confinement, 77, 79, 92, 246,
247, 254, 256, 257, 261, 270,
271, 272
confining pressure, 18, 39, 76,
98, 99, 102, 103, 117, 118,
119, 120, 121, 122, 123, 184,
188, 297, 302, 309

- constitutive law, 72, 79, 91, 127, 128, 133, 176, 178, 179, 235, 236, 237, 258, 297, 324
 constitutive model, 17, 19, 21, 44, 45, 49, 50, 72, 91, 93, 98, 106, 116, 125, 142, 174, 192, 197, 198, 230, 297, 298, 319, 325, 339, 356, 361, 362, 369, 371, 387
 contact, 12, 72, 78, 79, 83, 93, 147, 148, 149, 152, 153, 155, 157, 158, 159, 162, 166, 167, 175, 179, 202, 203, 204, 205, 206, 210, 211, 213, 214, 215, 216, 217, 218, 219, 220, 221, 222, 223, 225, 226, 231, 233, 234, 278, 302, 310, 404, 427, 428
 Cosserat, 8, 54, 55, 146, 178, 179, 180, 198, 199
 Coulomb, 3, 11, 82, 204, 232, 302, 315, 381, 382, 386, 400
 coupled flow, 343
 coupling, 95, 121, 124, 132, 133, 138, 139, 202, 274, 356, 362
 crack, 248, 262, 275, 305, 307, 423, 428, 437, 443, 449, 458
 cracks, 50, 56, 58, 59, 62, 63, 70, 96, 99, 102, 125, 127, 170, 171, 181, 245, 246, 247, 249, 255, 256, 257, 259, 260, 261, 262, 263, 264, 265, 266, 267, 270, 272, 273, 275, 278, 301, 302, 303, 304, 305, 307, 308, 309, 310, 311, 312, 313, 315, 316, 319, 326, 405, 420, 426, 427, 428, 431, 432, 433, 435, 436, 442, 443, 445, 448, 449, 454
 crushing, 19, 50, 51, 101, 116, 125, 155, 156, 157, 158, 159, 161, 162, 164, 165, 166, 168, 169, 170, 171, 175, 178, 280, 281
 damage, 48, 51, 97, 124, 126, 127, 128, 129, 130, 133, 134, 135, 136, 137, 138, 139, 140, 141, 142, 163, 171, 247, 261, 263, 271, 274, 275, 319, 320, 321, 322, 324, 328, 329, 330, 331, 332, 333, 335, 336, 337, 338, 339, 340, 381, 382
 damage mechanics, 127, 128, 130, 133, 136, 138, 139, 141, 142, 324, 336, 337, 339, 340
 damage mechanics, 127
 Darcy's law, 342, 344, 448
 Dascalu, 231, 242
 decohesion, 231, 232, 235, 237, 238, 239, 240, 241
 deformation, 4, 6, 7, 8, 12, 18, 19, 21, 26, 27, 29, 32, 37, 38, 39, 43, 45, 48, 49, 50, 51, 54, 56, 71, 72, 73, 76, 79, 80, 81, 83, 86, 90, 97, 98, 99, 103, 104, 105, 106, 111, 118, 123, 124, 125, 133, 142, 146, 150, 151, 152, 153, 166, 173, 174, 175, 177, 180, 181, 183, 184, 193, 194, 195, 196, 197, 201, 202, 203, 207, 208, 209, 210, 223, 225, 227, 229, 231, 232, 233, 234, 235, 236, 237, 242, 257, 278, 281, 282, 284, 296, 298, 316, 320, 324, 337, 338, 341, 342, 343, 348, 349, 350, 351, 352, 356, 357, 361, 362, 363, 365, 373, 379, 380, 382, 386
 degradation, 10, 11, 124, 171
 Delaunay Triangulation, 145
 deviatoric, 17, 20, 21, 22, 23, 24, 29, 31, 36, 39, 40, 42, 43, 44, 46, 80, 95, 97, 101, 119, 121,

- 124, 177, 178, 285, 315, 321,
322, 369, 372
- dilatancy, 4, 5, 6, 11, 12, 13, 71,
72, 82, 93, 94, 97, 126, 176,
201, 202, 203, 204, 205, 207,
208, 209, 213, 217, 218, 219,
222, 227, 228, 229, 230, 278,
286, 291, 301, 310, 313, 316,
321, 332, 342, 348
- dilation bands, 49
- disaggregation, 78
- discontinuity, 4, 6, 86, 279, 292,
293, 294
- discontinuous, 4, 50, 306
- discrete element method, 78, 203
- discretization, 136, 174, 339, 373
- disintegration, 277
- dissipation, 345
- distinct element, 405
- Dormieux, 245, 261, 274, 275,
461
- drained, 73, 77, 92, 119, 173,
352, 353
- Drucker-Prager criterion, 320
- Dyskin, 69, 274, 298, 302, 303,
304, 306, 312, 316, 432, 461
- elasticity, 4, 25, 55, 85, 94, 104,
142, 258, 319, 324, 327, 331,
379, 410, 424, 433
- elasto-plastic, 5, 6, 7, 116, 123,
175, 181, 319, 320, 325, 326,
328, 334, 336, 337, 339, 356,
379
- elasto-viscoplastic, 361, 362,
369, 380
- ellipticity, 7, 231, 232, 235, 236,
237, 238, 240
- elongation, 303, 329, 331, 332
- energy release, 57, 61, 69, 245,
247, 248, 249, 253, 254, 263,
266, 267, 271, 272, 275, 461
- entropy, 145, 148, 245
- Eshelby, 57, 250, 251, 258, 274
- Exadaktylos, 13, 428, 429, 430,
431, 443, 448, 461
- fabric, 71, 72, 73, 74, 79, 87, 88,
93, 94, 159, 160, 198, 201,
202, 203, 204, 205, 206, 207,
214, 218, 219, 223, 224, 227,
228, 229, 230
- failure criterion, 3, 82, 108, 127,
304, 339, 381, 382, 386, 400,
404
- fault, 9, 13
- FE-simulations, 175, 324, 326,
334, 335
- finite element, 54, 63, 133, 140,
141, 142, 174, 199, 231, 237,
304, 338, 339, 341, 342, 343,
348, 351, 352, 355, 356, 361,
373, 401, 403, 405
- flow-rule, 5
- Fourier, 80, 231, 346
- fracture, 49, 53, 55, 56, 61, 62,
63, 64, 65, 66, 67, 69, 99, 102,
124, 125, 142, 171, 231, 237,
245, 247, 248, 255, 256, 262,
263, 265, 266, 268, 269, 272,
273, 275, 276, 301, 302, 304,
308, 315, 316, 317, 319, 338,
339, 340, 403, 404, 405, 427,
428, 429, 430, 431, 461
- fracture mechanics, 53, 55, 56,
62, 69, 245, 247, 248, 262,
273, 276
- fracturing, 58
- friction angle, 3, 82, 188, 192,
194, 204, 206, 211, 214, 217,
218, 219, 222, 223, 224, 278,
286, 287, 288, 290, 291, 321,
332, 382, 386, 395, 396, 398,
400
- frictional material, 5, 342
- gas hydrate, 361

- geomaterials, 7, 8, 10, 20, 43, 97,
 142, 340, 356, 357, 363, 381,
 382, 383, 386, 391, 431
 geomechanics, 3, 10, 11, 12, 48,
 49, 51, 70, 94, 141, 142, 153,
 171, 197, 199, 276, 296, 298,
 299, 340, 357
 Goddard, 12, 92, 94, 145, 146,
 148, 149, 150, 151, 152, 153,
 202, 228
 gradient, 8, 22, 24, 54, 70, 128,
 130, 131, 132, 133, 134, 135,
 138, 139, 140, 141, 142, 146,
 147, 148, 150, 173, 174, 178,
 181, 182, 183, 184, 186, 188,
 190, 192, 193, 195, 199, 232,
 233, 236, 242, 281, 292, 293,
 320, 325, 330, 338, 340, 342,
 351, 356, 367, 383
 grain size, 8, 54, 63, 174, 176,
 278, 304, 383
 granular materials, 4, 5, 7, 11,
 12, 13, 19, 50, 51, 71, 72, 92,
 93, 94, 141, 153, 155, 173,
 174, 175, 196, 197, 198, 199,
 201, 202, 203, 205, 206, 208,
 213, 225, 227, 228, 229, 277,
 278, 279, 281, 282, 288, 297,
 298, 338
 Griffith, 70, 245, 247, 248, 252,
 263, 266, 267, 271, 272, 274,
 404, 415, 420, 421, 427, 429,
 461
 Guo, 13, 73, 94, 214, 224, 227,
 230, 404, 429
 Hadush, 382, 401
 hardening, 24, 26, 27, 29, 37, 44,
 50, 51, 77, 81, 83, 92, 105,
 106, 112, 113, 115, 116, 121,
 123, 125, 129, 175, 193, 247,
 320, 321, 323, 337, 357, 370
 Hellmich, 245, 461
 hydrate, 361, 362, 363, 367, 368,
 375, 379, 380
 hydrostatic, 95, 97, 101, 106,
 107, 109, 111, 112, 113, 114,
 116, 117, 121, 123, 124, 386,
 434
 hypoplasticity, 173, 175, 299,
 301
 ill-posed problems, 4
 impact force, 381
 instabilities, 5, 10, 11, 70, 71, 94,
 124, 153, 155, 161, 163, 170,
 171, 197, 231, 236, 237, 238,
 239
 Issen, 19, 20, 29, 30, 33, 35, 45,
 49, 50, 97, 125
 Ito, 401
 Jostad, 357
 Kaklis, 428, 429
 Kast, 288, 289, 297, 298
 Kimoto, 369, 371, 380
 kinematical, 5, 8, 72, 82, 202,
 211
 kinematics, 8, 72, 133, 146, 149,
 152, 232, 342
 Kotronis, 127, 142
 Kourkoulis, 429, 430
 Liolios, 431, 443, 448, 461
 localization, 3, 4, 5, 6, 8, 11, 18,
 19, 26, 28, 30, 34, 35, 39, 44,
 45, 48, 49, 50, 51, 55, 70, 73,
 94, 95, 96, 97, 98, 99, 101,
 103, 106, 118, 123, 124, 125,
 133, 136, 137, 138, 139, 142,
 145, 151, 153, 171, 173, 174,
 178, 186, 197, 198, 214, 231,
 236, 246, 256, 297, 298, 316,
 319, 320, 329, 333, 334, 337,
 338, 340, 342, 348, 349, 350,
 352, 353, 354, 355, 356, 357,
 379, 380

- macrocrack, 255, 256, 301, 304, 306, 307, 308, 309, 315, 316
- Marketos, 155, 159, 168, 171
- Mazars, 130, 133, 134, 138, 140, 141, 142
- methane, 361, 379
- microcracks, 97, 245, 246, 247, 256, 258, 259, 262, 263, 264, 265, 266, 267, 268, 270, 273, 274, 275, 458
- micro-mechanical, 5, 56, 405
- micro-polar, 6, 173, 174, 178, 180, 183, 186, 188, 189, 192, 193, 195, 198, 340
- microstructure, 8, 54, 71, 72, 83, 84, 85, 93, 188, 202, 230, 231, 237, 256, 276, 320, 323
- mode-I, 56, 263, 435
- mode-II, 56, 435
- Mohr, 3, 4, 12, 82, 188, 204, 302, 315, 381, 382, 386, 400
- Mohr-Coulomb, 3, 302, 386
- moisture, 277, 285
- Moriguchi, 382, 386, 401
- Newton-Raphson method, 135
- non-coaxiality, 216
- non-linearity, 175
- non-local, 141, 192, 338, 339
- Nordal, 357
- Oka, 297, 340, 363, 372, 380
- overconsolidation, 370, 371, 372
- packing, 206, 208, 211, 219
- Papamichos, 69, 70, 156, 171, 276
- Papanastasiou, 53, 70, 141, 199
- Pasternak, 179, 198, 298, 432, 461
- penny-shaped cracks, 249, 260
- perforation failure, 53, 64
- permeability, 19, 51, 95, 96, 97, 98, 119, 121, 122, 123, 124, 125, 126, 155, 165, 170, 274, 341, 342, 349, 366, 373, 379, 431, 433, 434, 449
- photoelastic disks, 71, 72, 74
- photoelasticity, 73, 75
- Pichler, 245, 432, 461
- plane strain compression, 173, 174, 183, 188, 193, 194, 195, 199, 278, 279, 292, 294, 295, 296
- plastic potential, 5, 21, 22, 23, 24, 29, 30, 31, 37, 38, 39, 40, 46, 48, 91, 92, 104, 107, 108, 109, 111, 175, 176, 371
- plasticity, 5, 12, 49, 50, 51, 54, 72, 88, 90, 91, 93, 94, 130, 141, 142, 150, 174, 176, 184, 197, 198, 199, 203, 228, 229, 278, 320, 323, 327, 335, 336, 337, 338, 339
- Poisson's ratio, 61
- poroelasticity, 274, 434
- post-failure, 4
- postpeak, 101
- potential energy, 57, 58, 251, 252, 361
- principal stress, 17, 18, 20, 21, 27, 29, 30, 31, 58, 75, 109, 111, 113, 129, 155, 156, 157, 188, 202, 205, 206, 207, 209, 213, 222, 225, 287, 436
- propagation, 12, 248, 262, 305
- pyncnotropy, 176, 178
- quasi-brittle, 141, 319, 338, 339
- quasi-static, 4, 145, 152, 173, 174, 184, 236, 245, 247, 249, 319, 347
- Rankine criterion, 321, 331
- representative volume, 231, 232, 236, 245, 255
- Rudnicki, 17, 19, 20, 21, 25, 26, 27, 29, 30, 35, 49, 50, 51, 97,

- 105, 125, 126, 171, 298, 304,
316, 342, 357
- sand, 5, 6, 12, 13, 48, 54, 71, 72,
73, 82, 94, 96, 106, 155, 156,
157, 159, 164, 165, 170, 171,
173, 178, 180, 183, 184, 186,
188, 192, 193, 197, 201, 202,
203, 204, 205, 227, 228, 229,
277, 278, 282, 297, 299, 362,
392, 394, 395, 396, 397, 398,
399, 400
- sandstone, 19, 20, 22, 33, 45, 48,
49, 50, 51, 54, 63, 64, 65, 66,
69, 96, 125, 126, 156, 157,
158, 159, 165, 170, 171
- Sarris, 429
- Sawada, 401
- scale effect, 53, 54, 70, 302
- shear band, 4, 6, 7, 18, 35, 36,
40, 42, 43, 44, 45, 118, 124,
196, 198, 199, 278, 279, 292,
293, 294, 295, 296, 297, 298,
299, 341, 342, 347, 348, 350,
351, 352, 353, 354, 355, 356
- shear localization, 174
- shear modulus, 61, 199, 348, 375,
425
- shear zone, 173, 301, 341
- singular integral equations, 431,
440, 441, 449, 461
- size effect, 53, 55, 69, 141, 174,
319, 320, 324, 325, 326, 327,
328, 335, 336, 337, 338, 339
- sliding, 72, 74, 93, 184, 201,
202, 203, 204, 206, 210, 211,
213, 215, 216, 217, 218, 219,
220, 221, 223, 225, 226, 227,
246, 268, 315
- slip-lines, 4
- softening, 6, 7, 8, 55, 73, 83, 94,
99, 113, 115, 116, 118, 121,
127, 129, 130, 132, 134, 137,
138, 141, 174, 176, 186, 197,
198, 231, 232, 237, 238, 239,
245, 246, 247, 265, 267, 273,
319, 320, 321, 322, 323, 325,
326, 327, 328, 330, 331, 332,
333, 334, 335, 336, 338, 339,
340, 341, 347, 352, 354, 355,
356, 370, 373
- stability, 7, 10, 11, 53, 70, 71, 72,
73, 80, 81, 92, 94, 184, 232,
235, 236, 237, 238, 240, 324,
357, 361, 362, 379
- stiffness, 85, 129, 135, 158, 177,
178, 186, 193, 245, 247, 249,
250, 251, 257, 258, 259, 260,
261, 262, 263, 273, 274, 275,
277, 278, 285, 286, 288, 294,
307, 321, 343, 348
- stiffness matrix, 186
- strain localization, 7, 18, 39, 48,
51, 72, 125, 130, 151, 193,
231, 256, 319, 320, 323, 332,
336, 337, 338, 342, 350, 356,
357
- stress intensity factor, 418, 419,
424
- tangent, 135, 138, 215, 233, 236,
281, 348, 391, 440
- tectonic, 9
- Tejchman, 173, 198, 199, 319,
338, 339, 340
- tensile strength, 61, 273, 325,
331, 404
- Thakur, 352, 357
- thermodynamical, 9, 149
- thermodynamics, 128, 148
- three-point bending, 319, 320,
330
- triaxial compression, 290
- undrained condition, 342, 347
- undrained conditions, 173, 435

- uniaxial compressive strength,
53, 265, 269, 273
- unsaturated soils, 361, 379, 380
- Vardoulakis, 12, 13, 70, 141,
156, 171, 192, 197, 199, 228,
276, 298, 342, 357, 363, 380,
429, 430
- viscoplastic, 367, 369, 371, 372,
373, 380
- viscoplastic flow rule, 372
- void ratio, 79, 80, 83, 173, 174,
175, 177, 178, 184, 186, 187,
188, 189, 190, 191, 193, 194,
195, 198, 224, 280, 281, 282,
283, 285, 286, 288, 289, 290,
291, 294, 295, 296, 340, 369,
375
- volumetric strain, 73, 99, 101,
104, 111, 113, 114, 115, 121,
151, 205, 370, 434
- Wan, 13, 73, 91, 93, 94, 224,
227, 230
- weathering, 278
- wellbore, 53, 56
- well-posedness, 174, 320, 323
- wing crack, 301, 302, 303, 310,
312
- Yashima, 297, 401, 402
- yield surface, 17, 49, 371
- Young's modulus, 61